VEHICLE CRASH MECHANICS

MATTHEW HUANG

CRC PRESS

Boca Raton London New York Washington, D.C.

Library of Congress Cataloging-in-Publication Data

Catalog record is available from the Library of Congress

Direct all inquiries to CRC Press LLC, 2000 N.W. Corporate Blvd., Boca Raton, Florida 33431.

Visit the CRC Press Web site at www.crcpress.com

International Standard Book Number 0-8493-0104-1
Printed in the United States of America 1 2 3 4 5 6 7 8 9 0
Printed on acid-free paper

PREFACE

This textbook, Vehicle Crash Mechanics, has grown out of a series of my lectures on vehicle crashworthiness at the University of Michigan, Dearborn. Since 1991, these lectures have been presented to automotive engineers from the Ford Motor Company, full service suppliers to the Ford Motor Company, and engineers from various consulting firms.

The primary goals of this book are to provide the fundamentals of engineering mechanics and to apply these fundamentals to the study of vehicle crashworthiness. Also the book was written to present a number of interesting and informative ancillary topics related to vehicle crashes but extending beyond purely fundamental theory.

In the automotive-related industry, the goal of engineering effort in the field of crashworthiness is to satisfy, or, to the extent possible, exceed the safety requirements mandated by the Federal Motor Vehicle Safety Standards (FMVSS) and administered by the National Highway Traffic Safety Administration (NHTSA).

Governed as it is by strict adherence to regulations and the balancing of complex interactions among the variables, the application of mechanics to crashworthiness is not a simple task. The importance of understanding the fundamentals of mechanics cannot be overemphasized. In this book, I have strived to present the fundamentals as clearly as possible, and with an aim toward applications to problems.

This field can be subdivided into four groups: (1) Vehicle crash dynamics, (2) Computer aided engineering, (3) Occupant impact dynamics, and (4) Design analysis and accident reconstruction. In each of these groups, knowledge of the fundamental principles of mechanics is essential. Also, the ability to apply such knowledge to hardware, to developmental work, or analytical modeling is required.

First, the fundamentals, which range from particle dynamics to rigid body kinetics, are presented. Then, Newton's Second Law, the principle of impulse and momentum, and the principle of work and energy are applied to engineering problems. It is assumed that the reader has had courses in mathematics through calculus and engineering statics. Formulas are presented as needed; as each one is presented for the first time, a short derivation of the formula is provided. Throughout the book, when analyzing vehicle tests, both the analysis of actual test results and the interpretation of mathematical models related to the tests will be developed in parallel. This approach is done in an orderly fashion in order to provide an insight into the parameters and interactions that influence the results.

In the study of crashworthiness, three main elements can be defined: vehicle, occupant, and restraints (VOR). In this book, the dynamic interactions among these three elements will be illustrated by the use of analytical models, experimental methods, and test data from actual vehicle crash tests. As an example, the occupant-vehicle kinematics in the restraint coupling phase and the use of the ridedown concept are presented in both analytical and experimental terms.

The book contains seven chapters, each having an introduction which describes the objectives of the chapter and the material to be covered.

Chapter 1 presents an overview of the crash pulse and kinematics, the kinematic principles used in VOR analysis and digital filtering techniques which satisfy the frequency response requirements of SAE J211. The filtering process is used to analyze vehicle, occupant, and crash sensor test data for crash severity. Also covered are analyses of crash sensor and air bag performance for an accident using on-board recorder data as they are related to the crash pulse analysis.

Chapter 2 presents ways of characterizing the crash pulse. An approximation method is developed which describes the crash pulse with a few parameters. Eight approximation methods are presented, ranging from the Tipped Equivalent Square Wave (TESW) with two boundary conditions to the Fourier Equivalent Wave (FEW) with or without boundary conditions. Physical significance of crash pulse centroid and residual deformation are discussed. Use of crash pulse approximation to the testings of an air bag crash sensor and vehicle interior-headform impact is illustrated.

Chapter 3 deals with the use of digital convolution methods for the prediction of responses of an object in a system test such as vehicle/Hyge sled test, and in a component test such as body mount. The basic operation of convolution theory, the derivation of the transfer function, and an algorithm using a snow-ball effect to increase the computation efficiency are discussed. A dynamic system is characterized by a set of FIR coefficients, i.e., a transfer function. Applications of FIR in vehicle, occupant, and component test forward prediction (predicting the low frequency output from a high frequency input) are presented. Applications of FIR transfer functions and inverse filtering method yield the RIF (response inverse filtering) method, which is utilized to make backward prediction (predicting the high frequency output from a low frequency input). Case studies on the use of transfer functions include: (1) effect of the full-powered and depowered air bags, (2) effect of the front- and rear-loaded crash pulses, (3) effect of the different body mounts and restraint systems, and (4) effect of the approximated crash pulse (such as a halfsine sled test pulse) and test crash pulse.

Chapter 4 covers the basic modeling techniques using Newton's Second Law. Transient and major model responses are formulated starting with simple models using Kelvin elements to hybrid models using both Kelvin and Maxwell elements. Since any crash event involves impact and excitation, the formulas derived are applicable to the analysis of model with a slack. Factors affecting the system output, such as natural frequency, damping factor, and coefficient of restitution are described. Applications of the closed form formulas to the VOR analysis are illustrated.

Chapter 5 covers the numerical methods applied to the response prediction. The solution to an impact or excitation model with more than two masses and/or non-linear energy absorbers becomes too complex to solve in closed-form. In such cases, numerical evaluation and integration techniques are necessary to solve for the dynamic responses. In a multi-mass model, the unloading characteristics of a spring element are as equally important as the loading characteristics. The unloading of one mass in a model may become a loading to the neighboring masses, therefore affecting the total system model responses. Power curve loading and unloading simulation with hysteresis energy loss and permanent deformation are covered. To help solve some dynamic models quickly, a lumped-parameter model, CRUSH II, is utilized. The force-deflection formulas of some simple structures are listed for ease of determining the spring stiffness for the modeling. Some lumped-parameter models for the full frontal, side, and frontal offset impacts are described. The basic concepts of splitting a simple spring mass model for the frontal offset impact and the model validation are also presented.

In Chapter 6, the principle of impulse and momentum and the principle of work and energy, derived from the Newton's Second Law, are utilized to solve the impulsive loading problems. The CG (center of gravity) motion theorem in the multiple vehicle collision analysis and the circle of constant acceleration (COCA) on a rigid body subjected to an eccentric loading are analyzed. Specific design analysis is presented. The formulation of critical sliding velocity, rollover dynamics, and detection of an incipient rollover are introduced. Methods of determining the vehicle inertia properties, such as the CG height and the moment of inertia of a vehicle, are covered. The formulation of the critical sliding velocity (CSV), the rollover dynamics, and detection of an incipient rollover using a simple vehicle model are introduced.

Chapter 7 discusses vehicle and occupant impact severity and accident reconstruction methodology. Vehicle components, such as body mounts, and engine size and location are evaluated for their roles in the absorption of vehicle energy, deceleration, and dynamic crush. Restraint devices, such as a pretensioner in a belt restraint system, are also evaluated for their values in reducing the

severity of occupant impact. The test results, principles, and functions of the pretensioner are analyzed. The use of the damage boundary curve (DBC) in assessing the vehicle, occupant, and sensor impact is covered. In the section on accident reconstruction, the derivation of a formula used to compute the vehicle stiffness coefficients is presented and discrepancies between the built-in stiffness coefficients in the data base and those obtained from crash data are analyzed. The consequences of using improper coefficients are illustrated by drawing upon real-world accident cases.

There are many aspects to vehicle crashworthiness, and it is hoped that this book will provide the fundamentals of engineering mechanics, which can be revealing in applications and will also serve as a helpful reference on up-to-date techniques used in this field of study.

In preparing this book I am greatly appreciative of the considerable help from my former colleague, Mr. Calvin C. Matle, a retired Senior Research Engineer at the Ford Motor Company. His critiques on the details of the subjects on mechanics were enlightening and the review of the entire manuscript was not a simple task. I am grateful that Mr. Matle created several artworks for use in the text including the car and dummy drawing on the book cover. Also, I would like to express my sincere appreciation to Dr. Clifford C. Chou, a Senior Staff Technical Specialist at the Ford Motor Company for his technical input and review of the manuscript. I would also like to gratefully acknowledge Mr. Jianming Li, an outstanding senior student at the University of Michigan, Dearborn, for his artistic skills in creating a major portion of the artwork used in this book. As inspired by those before us, and enhanced by those among us, I wish to extend many thanks to all of my students, my colleagues for their contributions. Although the list is too long to mention individually, it is hoped that those who have shared in the discussions and who have helped will accept this recognition, CRC Press staff has been very helpful and its contributions to this endeavor are gratefully recognized. Lastly, I am deeply indebted to my wife, Becky, for her ever-lasting patience and care over the years while I worked on this book. I am also grateful to my daughters Dr. Caroline B. Huang and Ms. Kelly M. Huang for their concerns and understandings; and to my nephew David C. Huang for his help making the contents consistent.

In closing, I would like to dedicate this book to my parents who were so helpful in my life.

Matthew Huang
(黃正雄)

Dearborn, Michigan, USA
May, 2002

TABLE OF CONTENTS

LIST OF FIGURES

1.48 Rocker B-Post Kinematics of a Mid-Size Car in a 14 mph Rigid Barrier Test
1.49 Sled Test Set Up
1.50 Unbelted Occupant Kinematics in a Mid-Size Sedan 14 mph Barrier Test
1.51 Mid-Size Sedan 14 mph Rigid Barrier and Sled Test Kinematics
1.52 Vehicle-Barrier 14 mph Crash and Sled (Occupant free-flight) Displacement
1.53 Dummy Seating Position
1.54 Unbelted Driver Motion from Crash Test Film
1.55 Vehicle Crush, Sled Displacement, and Centroid
1.56 Vehicle Deceleration in Two Barrier and One Pole (21mph) Crash Tests
1.57 Vehicle Velocity vs. Time in Three Crash Tests
1.58 Vehicle Displacement vs. Time in Three Crash Tests
1.59 Vehicle Energy Densities in Three Crash Tests
1.60 Vehicle Front Center Pole Test Set-up
1.61 Vehicle Front Center Pole Post Test
1.62 Unbelted Occupant Velocity vs. Displacement in Three Crash Tests
1.63 Unbelted Occupant Displacement vs. Time in Three Crash Tests
1.64 Special Pulses
1.65 Sensor Activation Threshold Window
1.66 A Single Point Crash Sensing Algorithm
1.67 Air Bag Deployment Sequence
1.68 The Car and Right Front Damage
1.69 The tree
1.70 The Driver and Bags
1.71 Vehicle Deceleration vs. Time from Flight Recorder (Sampling Rate = 2k Hz)
1.72 Deceleration vs. Time for Low (Test #1) and High (Test #2) Speed Pole Tests
1.73 Deceleration Comparison of Case and Test #1 Vehicles
1.74 Deceleration Comparison of Case and Test #3 (High Speed Car-Car) Vehicles
1.75 Unbelted Occupant Displacement vs. Time
1.76 Unbelted Occupant ΔV vs. Time
1.77 Unbelted Occupant ΔV vs. Displacement
1.78 Fourier Power Spectrum of the Case, Tests #3 and #4
1.79 Residual Energy Density (red) vs. displacement
1.80 A Simple Occupant-Vehicle Impact Model
1.81 Truck and Chest Decelerations vs. Time in a 35 mph Barrier Test
1.82 Restraint Slack and Stiffness of an Air Bag System in a Truck 35 mph Test
1.83 Chest Onset Rate (j) in a Truck 35 mph Fixed Barrier Test
1.84 A Sled Impact Model
1.85 A Constant Sled Excitation Pulse
1.86 Model Chest g as a Function of Restraint, f; Slack, δ; and ESW
1.87 Model Chest g Time as a Function of Restraint, f; Slack, δ; and ESW
1.88 VOR Chart #2 – Example
1.89 VOR Chart #1 – Example
1.90 VOR Chart #3 – Example
1.91 VOR Chart #4 – Example
1.92 VOR Chart #2
1.93 VOR Chart #1
1.94 VOR Chart #3
1.95 VOR Chart #4
1.96 Comparison of Responses: Model vs. Tests
1.97 Chest g as a Function of Restraint, f; Slack, δ; and Four Crash Test Data
1.98 Chest g vs. Dynamic Crush in 31 mph Rigid Barrier Tests
1.99 Chest g vs. Restraint Natural Frequency in 31 mph Rigid Barrier Tests

2.29 Test and FEW Decelerations at Rocker/B-Pillar of Three Full-Size Tests
2.30 Power Rate Density with Original FEW Coefficients of Three Tests
2.31 Power Rate Density Curves with All-Negative FEW Coefficients
2.32 Crash Pulse Data Points (from 2.17)
2.33 Pulse Curve Length vs. Time from Four Sets of Crash Data Filtered at 100 Hz
2.34 Pulse Curve Length vs. Time from Four Sets of Crash Data Filtered at 300 Hz
2.35 Truck Body on Frame
2.36 A Typical Body Mount on a Body-on-Frame Vehicle
2.37 Frame Wideband Data
2.38 Frame Data Filtered by Butterworth at 100 Hz Cutoff Freq
2.39 FEW Coefficients for the Frame Data
2.40 Body Deceleration Wideband Data
2.41 Body Data Filtered by Butterworth at 100 Hz Cutoff Freq
2.42 FEW Coefficients for the Body Data
2.43 Frame and Body Filtered Crash Pulses (Butterworth rolloff freq. = 100 Hz)
2.44 Frequency Spectrum Magnitude of Frame and Body Filtered Crash Pulses
2.45 A Sensor Module bracket
2.46 Coefficients of Fourier Equivalent Wave at ECS Module
2.47 Bracket 100 Hz Resonance
2.48 Velocity and Displacement Changes of the Resonance $A_2(t)$
2.49 Composition of Accelerometer Data at ECS: Signal A_1 and Resonance A_2
2.50 Velocity and Displacement of the FEW With and Without Resonance $A_2(t)$
2.51 Trapezoidal Wave Approximation and Its Integrals
2.52 Bi-Slope Approximation (BSA)
2.53 Crash Pulse Comparison between Test and BSA (Bi-Slope Approximation)
2.54 Velocity Comparison between Test and BSA (Bi-Slope Approximation)
2.55 Displacement Comparison between Test and BSA (Bi-Slope Approximation)
2.56 Harmonic Pulses
2.57 Normalized Halfsine, Haversine and Velocity Changes
2.58 Halfsine
2.59 Haversine
2.60 Triangle
2.61 Harmonic Pulses with Same Magnitude
2.62 Harmonic Pulses with Same Velocity Change
2.63 Halfsine: Relative Centroid Location vs. b
2.64 Halfsine: Normalized Peak Deceleration
2.65 Halfsine Normalized Peak Deceleration
2.66 Halfsine: Normalized Deceleration at t_m
2.67 Haversine: Relative Centroid Location vs. b
2.68 Haversine: Normalized Peak Deceleration
2.69 Haversine: Normalized Time at Peak
2.70 Halfsine: Normalized Deceleration at t_m
2.71 Crash Pulse Comparison between Test, Halfsine, and Haversine Waves
2.72 Velocity Comparison between Test, Halfsine, and Haversine Waves
2.73 Displacement Comparison between Test, Halfsine, and Haversine Waves
2.74 An Air bag Ball-in-Tube (BIT) Crash Sensor
2.75 Ball-in-Tube Crash Sensor Components
2.76 Input Pulses to a BIT Model
2.77 Sensor Velocity Changes at Activation Times
2.78 Sensor Ball Displacements
2.79 Calibration of a 10 mph Crash Sensor
2.80 A Sensor Model

UNIT CONVERSIONS

Example: Length (in) × 25.4 = Length (mm); Length (mm) × .03937 = Length (in)

Quantity	Unit	×	Unit	×	Unit
Length	in	25.4	mm	.03937	in
	ft	.3048	m	3.281	ft
Area	in^2	645.16	mm^2	1550×10^{-3}	in^2
	ft^2	.0929	m^2	10.76	ft^2
	ft^2	2.3×10^{-5}	Acre	43500	ft^2
Volume	cubic yard	21.7	Bushels	1.244	ft^3
	in^3	1.639×10^{-4}	mm^3	6.102×10^{-5}	in^3
Mass	slug slug	14.594 32.2	kg lb_m	2.205 .454	lb_m kg
Moment of Inertia	$ft\text{-}lb\text{-}s^2$	1.356	$kg\text{-}m^2$	.7375	$ft\text{-}lb\text{-}s^2$
Pressure	lb/in^2	6.895	kPa	.1450	lb/in^2
	lb/ft^2	.0479	kPa	20.89	lb/ft^2
	psi	6.895	kPa	.1450	psi
	ksi	6.895	MPa	.1450	ksi
	psi	6.895×10^{-6}	GPa	1.450×10^5	psi
	ksi	6.895×10^{-3}	GPa	145	ksi
	lb_m/ft^3	16.02	kg/m^3	.0624	lb_m/ft^3
Force	lb_f	4.448	N	.2248	lb_f
Moment	lb·in	.1130	N·m	8.851	lb·in
	lb·ft	1.356	N·m	.7376	lb·ft
Energy	in·lb	.113	Joule	8.85	in·lb
	kw-h	2655.18	klbs-ft	3.766×10^{-4}	kw-h
Velocity	m/s	2.237	mph	.447	m/s
	mph	1.467	ft/s	.682	mph
	mph	17.6	in/s	5.68×10^{-2}	mph
Power	watt	.73755	ft-lb/s	1.356	watt
	watt	1.341×10^{-3}	hp	745.7	watt

Acceleration of Gravity (1g) = 32.2 ft/s^2 (at latitude 45° near Alpena or Gaylord, Michigan)

CHAPTER 1

CRASH PULSE AND KINEMATICS

1.1 INTRODUCTION

A basic characteristic of a vehicle structural response in crash testing and model simulation is the "crash signature," commonly referred to as the crash pulse [1] (numbers refer to references at the end of each chapter). This is the deceleration time history at a point in the vehicle during impact. The crash pulse at a point on the rocker panel at the B-pillar is presumed to identify the significant structural behavior and the gross motion of the vehicle in a frontal impact. Other locations, such as the radiator and the engine, are frequently chosen to record the crash pulse for component dynamic analysis. The nature of the crash response depends on the mass, structural stiffness, damping at that location, and on external interactions from neighboring components. In this chapter, techniques for analyzing the basic vehicle, occupant and restraint system interactions, digital filtering, and the crash pulse are reviewed; also, applications of the kinematic relationships in the analysis of restraint coupling and ridedown efficiency [2-5] are covered. Case studies involving air bag crash sensing, deployment, and crash recorder data analysis are also presented.

1.2 VEHICLE IMPACT MODES AND CRASH DATA RECORDING

Figs. 1.1 and 1.2 show two structure types commonly found in vehicles. These types are unitized-body and body-on-frame structures. The unitized-body vehicle has no separate frame or steel girders. It has comparatively thin pieces of body sheet metal which are stamped into complex shapes and welded together to provide the strength required for the chassis. The resultant structure is usually stiffer and lighter than one using separate frame and body construction. Unitized bodies are commonly found on small and compact vehicles.

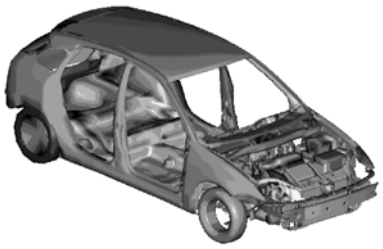

Fig. 1.1 Unitized Body Vehicle

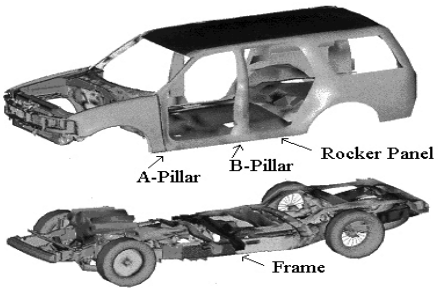

Fig. 1.2 Body-on-Frame Vehicle

The disadvantages of unitized body construction are that (1) more road noise and vibration are transmitted, (2) a serious safety problem is posed if rust attacks the attachment points for the engine, transmission, or suspension, (3) repair costs for body damage are usually higher because a large expanse of the body may have to be cut away and replaced in order to maintain structural integrity, and (4) manufacturing costs are higher due to the need for more sophisticated metal stamping and welding equipment. However, a unitized body using subframes supporting a powertrain or platform chassis, plus modern rustproofing, can overcome some of these disadvantages.

Some large North American passenger cars and most trucks and sport utility vehicles (SUV) have a separate frame and body or cab. The frame is made of heavy rectangular, or box section, steel tubes that are welded together. The frame design includes cross members forming a series of open rectangles which provide rigidity and powertrain support. A separate frame is heavy and not especially rigid without the use of X-shaped bracing across the passenger compartment. Rust is not a serious safety concern with separate frame construction.

In the body-on-frame vehicle, the body or cab is fastened to the frame by body mounts. A typical

body mount is shown in Fig. 1.3. It consists of two rubber bushings (on top and bottom of the frame bracket), a bolt, and a retainer. Typically, there are four body mounts on each side frame and two front end sheet metal (FESM) mounts. Body mounts are designed to carry the horizontal impact load in an accident and to isolate the noise, vibration, and harshness (NVH) due to road surface excitation from entering the passenger compartment.

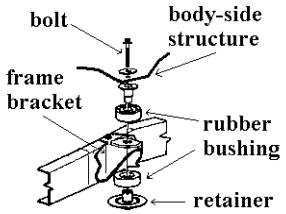

Fig. 1.3 A Typical Body Mount on a Body-on-Frame Vehicle

The crash pulse, which describes the nature and severity of a vehicle crash, depends not only on the type of structure, but also on the measurement site and the impact mode. Figs. 1.4 and 1.5 depict typical crash sensor and accelerometer locations on a unitized body vehicle where the crash pulses are measured.

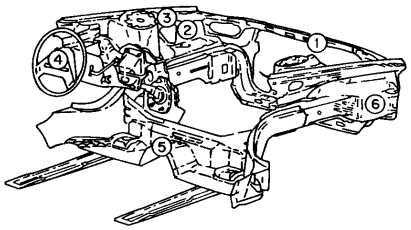

Fig. 1.4 Crash Test Sensor and Accelerometer Locations

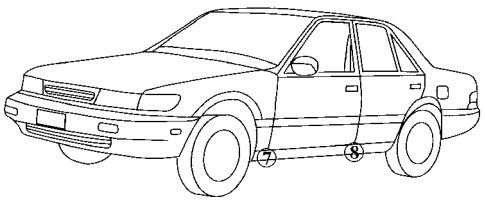

Fig. 1.5 Crash Test Sensor/Accelerometer Locations

1. Upper radiator support bracket 2. Front left/right shotguns (inside fender) 3. Left/right shotguns at spring tower 4. Steering wheel	5. Centerline tunnel in passenger compartment 6. Front left/right frame rails 7. Left/right rockers at A-pillar 8. Left/right rockers at B-pillar

Figs. 1.6 and 1.7 show the frontal impact crash test configurations used in a project on the optimization of an advanced air bag sensor system [6]. The crash tests were chosen after a thorough review of previous air bag work worldwide, accident statistics, and experience with the Ford Tempo air bag fleet based on a real world crash investigation. Some of the tests were car-to-car tests versus barrier and fixed pole tests. Crash data were collected on twenty-two vehicles; the tests selected represented a broad range of accident encounters at or near the expected threshold of air bag deployment. The threshold tests were designed to produce a vehicle barrier equivalent velocity

(BEV)[1/] of about 12 mph, which is the approximate crash severity threshold at which, in the judgment of the project engineers, an air bag should deploy.

Twenty-two vehicles in sixteen tests, as shown in Figs. 1.6 and 1.7, were used to collect the crash pulse data. The impact speed in each test configuration was chosen so the system performance under the air bag sensor must- or must-not- activate condition could be evaluated.

The types of impact include the following:

1. A perpendicular (90-degree) barrier
2. A low and high speed rigid pole
3. A front-to-front overlap
4. An oblique front to front (three types)
5. A vehicle front to an MDB (moving deformable barrier) perpendicular
6. A vehicle front-to-side
7. A front-to-rear
8. A bumper over-ride (or truck under-ride)

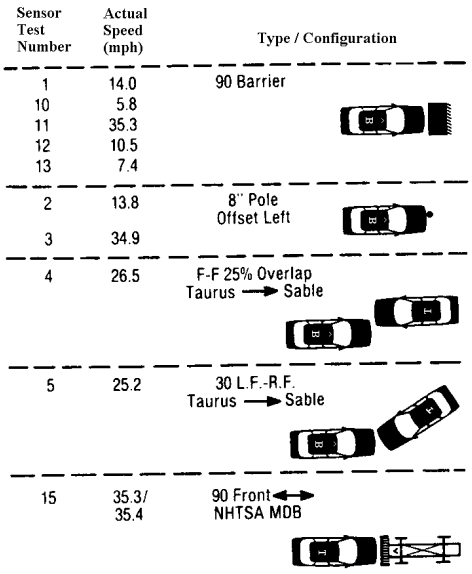

Fig. 1.6 Crash Test Mode – 1

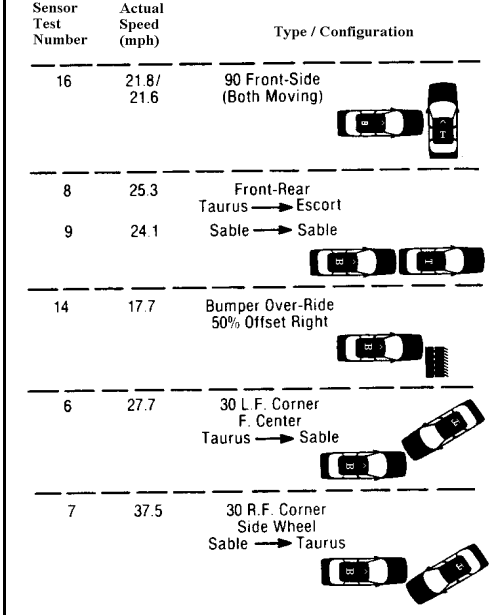

Fig. 1.7 Crash Test Mode – 2

1.2.1 Accelerometer Mounting and Coordinate Systems

The crash test data are recorded by accelerometers. Shown in Fig. 1.8 are the accelerometer types and the schematic of an accelerometer model. A typical accelerometer uses either a strain gauge mounted on a beam surface or a piezo-electric crystal. Those used in the vehicle crush zone have a range of about ±2000 g, and those at the engine, transmission, passenger compartment, and dummies, ±750 g. During crash test preparation, accelerometers with the specified ranges and sensitivities are instrumented in the vehicle. A typical crush zone accelerometer has a sensitivity of 0.25 millivolts/g

[1/]BEV is the vehicle speed in the rigid barrier test which yields the same crush energy absorbed by the structure as that in the non-rigid barrier test condition.

with a 10-volt excitation. Damage to accelerometers and pulling-off of wires from accelerometer blocks are not uncommon in the crash tests.

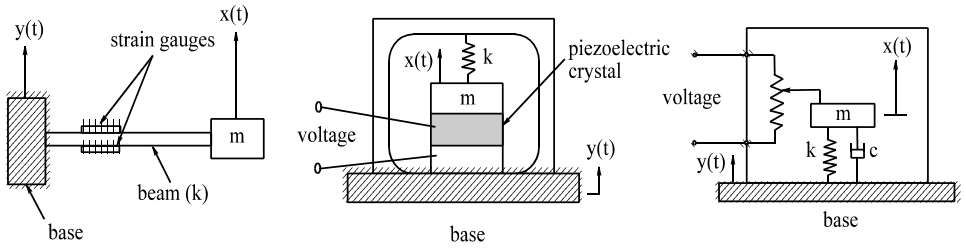

Fig. 1.8 Accelerometer Types and Schematic

The axes of a triaxial accelerometer, an assembly of three accelerometers on a mounting block, are oriented along the vehicle axes. The initial angles of the accelerometer axes from the reference axes should not exceed 5°. Each axis should pass within 10 mm of a prescribed mounting point, and the center of gravity of each accelerometer should be within 30 mm of that point [7].

The coordinate systems for the vehicle and occupant are shown in Figs. 1.9 and 1.10, respectively. The X, Y, and Z directions in the 3-dimensional reference frame are referred to as longitudinal, lateral, and vertical directions.

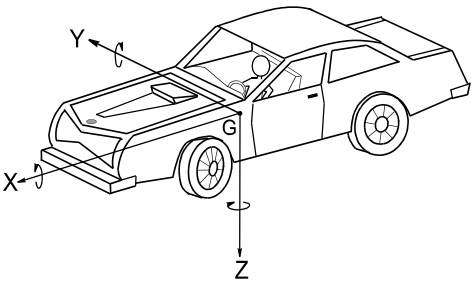

Fig. 1.9 Vehicle Coordinate System

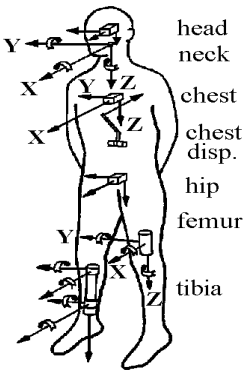

Fig. 1.10 Occupant Coordinate System

1.3 DIGITAL FILTERING PRACTICE PER SAE J211 AND ISO 6487

The crash test data, recorded by an accelerometer, is pre-filtered before sampling at a rolloff frequency of 4,000 Hz. The pre-filtered data, referred to as wideband data, contains the same signal as the raw data (the impact stress recorded by an accelerometer). This data is then sampled at a rate of 12,500 points per second (or 0.08 milli-seconds per data point) and yields an input acceleration, A_{in}. To obtain the signal in its useful frequency range, a digital filtering technique which satisfies the frequency response corridor specified by SAE J211 (SAE Recommended Practice on the "Instrumentation for Impact Tests") [8] should be used. The filtered output acceleration, designated as A_{out}, satisfies the amplitude gain relationship shown below.

Consider an instrumentation system that has an input power of P_{in} and an input voltage of V_{in} and produces an output power of P_{out} and an output voltage of V_{out}. Then, the gain G, in decibels (db), of the system is given by

$$G_{db} = 10 \log_{10} \frac{P_{out}}{P_{in}} = 10 \log_{10} \frac{v_{out}^2/z_{out}}{v_{in}^2/z_{in}} \quad (1.1)$$

If Z_{out} and Z_{in}, the output and input impedances, respectively, are equal, Eq. (1.1) becomes

$$G_{db} = 10 \log_{10} \frac{v_{out}^2}{v_{in}^2} = 20 \log_{10} \frac{v_{out}}{v_{in}} = 20 \log_{10} \frac{A_{out}}{A_{in}} \quad (1.2)$$

This formula will be used later to compute the filtered output magnitude provided that the unfiltered input magnitude of a given frequency and the corresponding attenuation are specified.

The purpose of SAE J211 is to provide guidelines for filtering specifications and the selection of a class of frequency response. The aim is to achieve uniformity in instrumentation practice and in reporting test results.

The channel classes recommended by SAE J211 are shown in Table 1.1. A filter frequency-band plot for Channel Class 60 is shown in Fig. 1.11. The frequency response corridor and limit values in the pass band, transition band, and stop band are shown for each channel class. For example, if the vehicle structural acceleration is used as a test measurement for total vehicle comparison, Channel Class 60 is selected according to Table 1.1. The tolerances in the pass band for the Channel Class 60 are a = −.5 to .5 db at f = 10 Hz; b = −1 to .5 db at f_H = 60 Hz; and c = −4 to .5 db at f_N (rolloff or cutoff frequency) = 100 Hz. The upper and lower slopes in the transition band are d = −9 and e = −24 db/octave, respectively. The stop band extends downward from the ends of the transition band at g = −30 db.

The International Standard, ISO 6487 (the International Organization for Standardization), titled "Road Vehicles – Measurement Techniques in Impact Tests – Instrumentation" was issued on May 1, 2000 as the third edition. The standard is basically the same as SAE J211, which was issued in March 1995.

There are four channel classes in which frequency response values are specified for the passband, transition band, and stop band. The specifications for the channel classes (or CFC, channel frequency class) 60 and 180 are the same for both SAE J211 and ISO 6487.

Table 1.1 Band Pass Frequency Response Values For Various Channel Classes

Channel Class	f_L, Hz	a, db	f_H, Hz	b, db	f_N, Hz	c, db	d	e	g, db
							db/octave		
1000	0.1	.5, −.5	1000	.5, −1	1650	.5, −4	−9	−24	−30
600	0.1	.5, −.5	600	.5, −1	1000	.5, −4	−9	−24	−30
180	0.1	.5, −.5	180	.5, −1	300	.5, −4	−9	− 24	−30
60	0.1	.5, −.5	60	.5, −1	100	.5, −4	−9	−24	−30

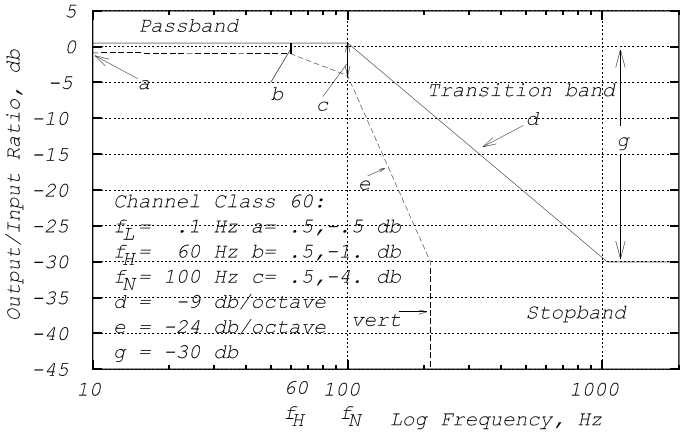

Fig. 1.11 SAE J211 Frequency Response Corridor

Table 1.2 Channel Class Selection – SAE J211

Typical Test Measurement	Channel Class
Vehicle structural acceleration for use in:	
Total vehicle comparison	**60**
Collision simulation (for example, impact sled) input	60
Component analysis	600
Integration for velocity or displacement	180
Barrier face force	**60**
Belt restraint system load	**60**
Occupant	
Head acceleration	**1000**
Chest acceleration	**180**
deflection	180
Pelvis	
acceleration	**1000**
forces	1000
moments	1000
Femur/knee/tibia/ankle	
forces	**600**
moments	600
displacements	180
Sled acceleration	**60**
Steering column load	**600**
Headform acceleration	**1000**

The channel class selected for a particular application in Table 1.2 does not imply that all the frequencies passed by that channel are always significant for that application. In the case of measurements of occupant head and headform accelerations and femur force, the channel class band pass may be higher than necessary in order to cover biomechanical uncertainties.

Crash test data generally has high-frequency components above the frequency f_H (e.g., Channel Class 1000, where $f_N = 1650$ Hz). This can occur more often with undamped accelerometers. To prevent these components from causing aliasing errors in the sampling process, a presampling filter should be used. The minimal acceptable sampling rate should be at least five times the −3db frequency of the presampling filter. Since the −3db frequency is f_N (rolloff) frequency (see Table 1.1), the minimum sampling rate for Channel Class 1000 should then be at least $5 \times 1650 = 8250$ Hz.

In order to derive a mathematical relationship between any two points on the frequency response plot, the terms ***decibel*** and ***octave*** are introduced as follows:

Alexander Graham Bell defined a unit, the Bel, to measure the ability of people to hear. The deciBel (db), one tenth of a Bel, is the most common unit used in frequency domain analysis. The combination of ear and brain is an excellent frequency domain analyzer. The brain processes the signal received from the ear, splits the audio frequency spectrum into different narrow bands and determines the power present in each band.

The ***decibel***, db, is a unit expressing the ratio of two signals of electric current, voltages, acceleration, or sound pressure. The gain G_{db} is equal to 20 times the common logarithm of the ratio. From Eq. (1.2), G_{db} in terms of acceleration is defined in Eq. (1.3).

$$G_{db} = 20 \log_{10} \frac{A_{out}}{A_{in}} \tag{1.3}$$

where A_{in}: input or unfiltered acceleration,
A_{out}: output or filtered acceleration.

The ***octave***, a term used in vibration analysis, is a frequency interval analogous to a musical octave. Fig. 1.12 shows the arrangement of piano keys in one octave. The frequency of a typical keynote C (C5) is 523.25 Hz. There are a total of twelve notes in one octave ranging from C, $C^{\#}$, D,...., B with the corresponding note number of j equal to 0,1,2,3,....,11. The frequency relationship between the j^{th} note and keynote C is shown in Eq. (1.4).

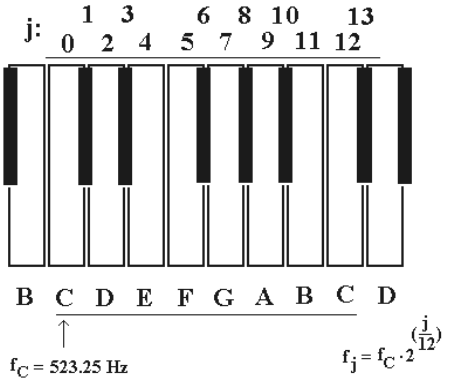

Fig. 1.12 Piano Keys Covering One Octave

$$f_j = f_C \, 2^{\frac{j}{12}}, \quad \textit{then for} \quad j = 5 \quad (F \textit{ Note})$$
$$f_5 = (523.25) \, 2^{(\frac{5}{12})} = 698.46 \textit{ Hz} \tag{1.4}$$

For example, given the frequency of note C, 523.25 Hz, we like to compute the frequency of note F. One can use j = 5 for note F in Eq. (1.4), and its frequency is then 698.46 Hz.

Since the process of filtering a crash pulse involves the attenuation of deceleration magnitudes at different frequencies, the basic frequency relationship between any two points on the frequency response plot should be understood. The formula given in Eq. (1.4) is derived in the next section.

1.3.1 Relationship Between Two Points in a Frequency Response Plot

In a plot of decibel vs. log of frequency, the frequency relationship between two points depends on the number of octaves between them. To derive this relationship, let b and log f be the vertical and horizontal coordinates, respectively; then, a straight line equation can be defined as shown in Eq. (1.5) in the following derivation.

Deriving the Frequency Relationship Between Two Points in a Frequency Response Plot

$$b = A + B \log f \quad \ldots\ldots\ldots\ldots\ldots (1)$$

where b is in db, and f is the frequency in Hz

At point 1: $b_1 = A + B \log f_1 \quad \ldots\ldots\ldots (2)$

At point 2: $b_2 = A + B \log f_2 \quad \ldots\ldots\ldots (3)$

Substracting (2) *from* (3) *gives*: $B = \dfrac{b_2 - b_1}{\log f_2 - \log f_1} = \dfrac{b_2 - b_1}{\log \dfrac{f_2}{f_1}}$

Let $f_2 = 2 f_1$ (*one octave*), *and* $b_2 - b_1 = s$ (*db/octave*)

$$\therefore B = \frac{s}{\log 2} \quad \ldots\ldots\ldots\ldots\ldots (4)$$

Substituting B from (4) *into* (1) *yields*

$$b = A + \frac{s}{\log 2} \log f \quad \ldots\ldots\ldots\ldots (5)$$

At point 1: $b = b_1$, $f = f_1$ *and* (5) *becomes*

$$A = b_1 - \frac{s}{\log 2} \log f_1 \quad \ldots\ldots\ldots\ldots (6)$$

Substituting A from (6) *into* (5), *then*

$$b = b_1 + \frac{s}{\log 2} (\log f - \log f_1)$$

$$= b_1 + \frac{s}{\log 2} \log \frac{f}{f_1} \quad \ldots\ldots\ldots\ldots (7)$$

At point 2: $b = b_2$, $f = f_2$ *and* (7) *becomes*

$$\left(\frac{b_2 - b_1}{s} \right) \log 2 = \log \frac{f_2}{f_1}$$

Let n (*no. of octaves changed*) $= \dfrac{b_2 - b_1}{s}$,

then: $\log \dfrac{f_2}{f_1} = n \log 2 = \log 2^n$

$$\therefore \frac{f_2}{f_1} = 2^n \quad \text{or} \quad f_2 = f_1 2^n \quad \ldots\ldots (8)$$

(1.5)

Case Study (exercise): Frequency Response Corridor

The transition band specified by SAE J211 is shown in Fig. 1.13.

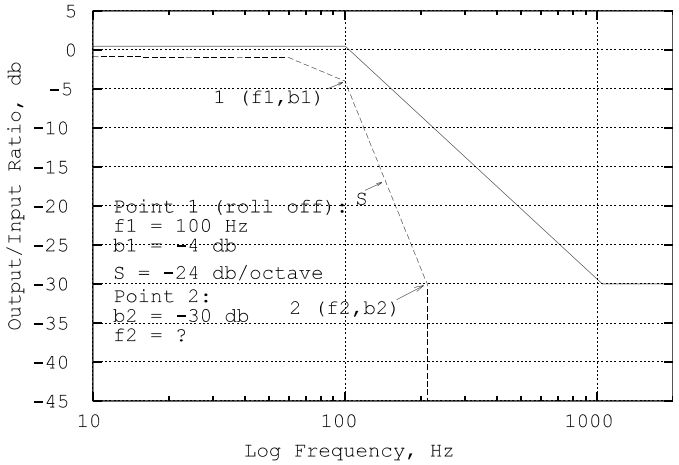

Fig. 1.13 Case Study: Frequency Response Corridor

(1) The lower bound of the band has a slope of −24 db/octave, the frequency and output/input ratio in decibels at point 1 being 100 Hz and −4 db. The output/input ratio in decibels at point 2 is −30 db. Compute the output/input deceleration ratio at point 1 and the frequency at point 2.

(2) The upper bound has a slope of −9 db/octave, and the frequency and output/input ratio in decibels at the beginning point are 100 Hz and 0.5 db, respectively. The output/input ratio in decibels at the ending point is −30 db. Compute the output/input deceleration ratio at the beginning point and the frequency at the end point.

[Ans. (1) 0.63, 212 Hz, (2) 1.1, 1048 Hz]

1.3.2 Chebyshev and Butterworth Digital Filters

Two digital filters, commonly known as Chebyshev and Butterworth filters, are used in processing vehicle crash test data. These filters are described by their frequency response characteristics and compared to the frequency response corridors specified in SAE J211. The parametric relationships between the deceleration attenuation (output/input ratio, db), f (frequency content of the crash pulse), and $f_{rolloff}$ (rolloff frequency) are shown below in Figs. 1.14 and 1.15 for the Butterworth and Chebyshev n^{th} order digital filters, respectively.

Since the frequency response curves fall within the specified frequency response corridor, both Butterworth and Chebyshev 2^{nd} order digital filters satisfy the SAE J211 requirements. Although Butterworth 3^{rd} and 4^{th} order filters also satisfy the requirements, they tend to have higher signal attenuation at a given frequency component than that of the Butterworth 2^{nd} order filter as shown in Fig. 1.14. Shown in Fig. 1.15, only the Chebyshev 2nd order filter fulfills the SAE J211 response corridor requirement.

Note that the entire frequency plots shown in Fig. 1.14 and Fig. 1.15 are made by using the two frequency response equations, Eq. (1.6) and Eq. (1.7), respectively. The two equations provide the relationships between the acceleration attenuation and the normalized frequency. The normalized frequency is defined as the component frequency of the signal normalized with respect to (w.r.t.) either the f_N frequency (rolloff) for the Butterworth filter or the f_H frequency for the Chebyshev filter as shown in both Eqs. (1.6) and (1.7), respectively. The same equations are also used to plot the passband responses of the Butterworth and Chebyshev filters shown in the following.

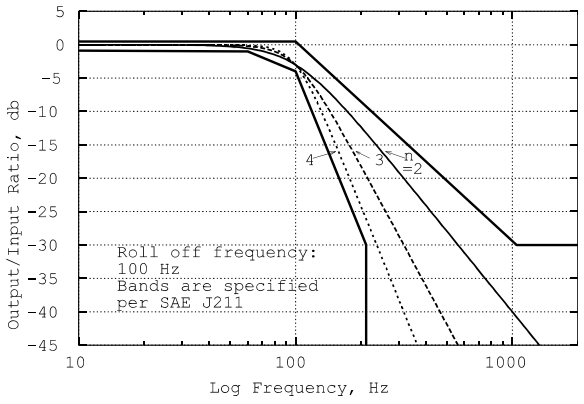

$$\frac{Output}{Input} = \frac{1}{\sqrt{1+\left(\frac{f}{f_{rolloff}}\right)^{2n}}}$$

$$db = 20\log_{10}\frac{Output}{Input} = -20\log_{10}\sqrt{1+\left(\frac{f}{f_{rolloff}}\right)^{2n}}$$

(1.6)

Fig. 1.14 Butterworth n[th] Order Filter

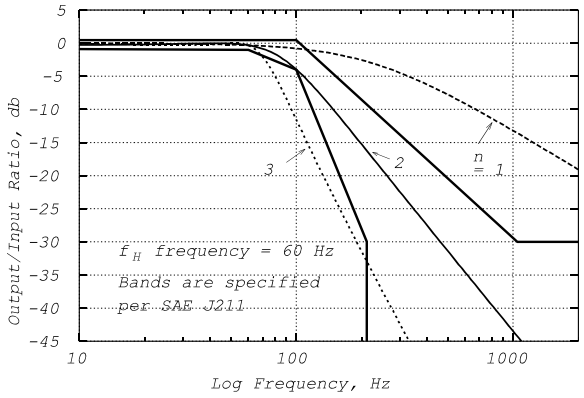

$$\frac{Output}{Input} = \frac{1}{\sqrt{1+\varepsilon^2 C_n^{\,2}(\omega)}}$$

Where

$$\varepsilon = \sqrt{10^{\alpha_{max}/10}-1}$$

$$C_n(\omega) = \cosh(n\cosh^{-1}\omega), \quad |\omega| \geq 1$$

$$C_n(\omega) = \cos(n\cos^{-1}\omega), \quad |\omega| \leq 1$$

ω: *normalized frequency w.r.t.* f_H

α_{max}: *passband attenuation, e.g.,* 0.3 *db*

(1.7)

Fig. 1.15 Chebyshev n[th] Order Filter

Butterworth low-pass filters are designed to have an amplitude response characteristic that is as flat as possible at low frequency and decreases with increasing frequency (Fig. 1.16).

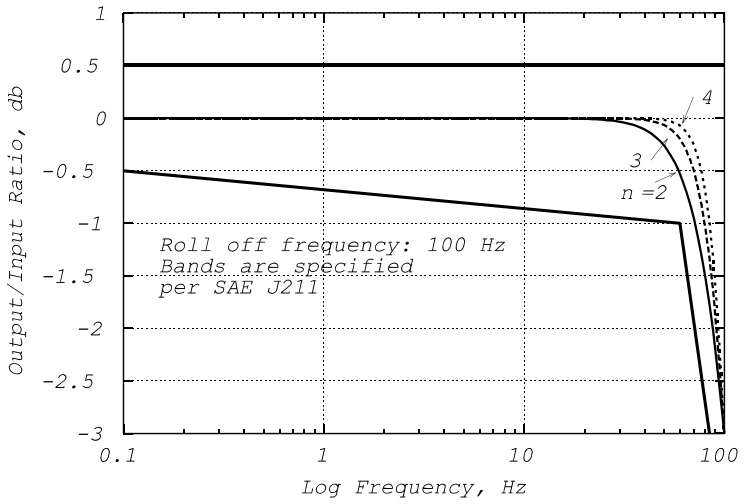

Fig. 1.16 Butterworth n[th] Order Passband Response Function

On the contrary, Chebyshev filters are designed to have a relatively sharp transition from the pass band to the stop band in the amplitude response characteristics plot as shown Fig. 1.17. This sharpness is accomplished at the expense of ripples (waves) that are introduced into the response. For a Chebyshev n^{th} order filter, there are n ripples in the passband.

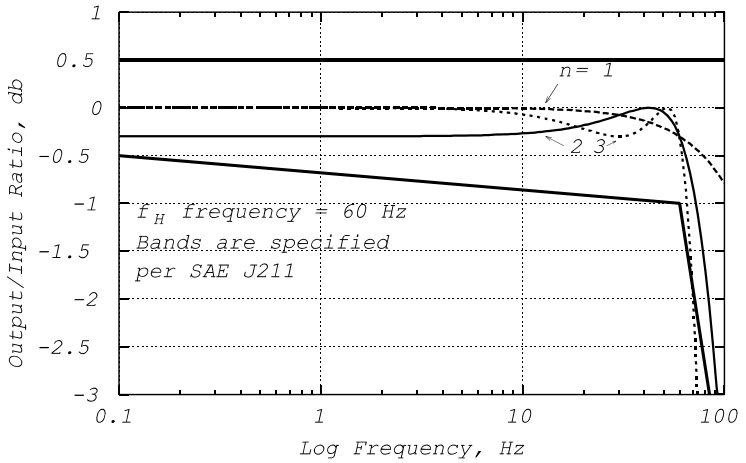

Fig. 1.17 Chebyshev n^{th} Order Passband Response Function

1.3.3 Filter Type, Deceleration Magnitude, and Phase Delay

The attenuation of magnitude and phase delay (angle) of deceleration depend on the filter type. If the wideband data are to be filtered at a low rolloff frequency using a 2^{nd} order Chebyshev filter, such filtering alters information content, including phase angle. The resulting data filtered by Chebyshev are then commonly scaled and/or shifted so that the observed vehicle kinematics is compatible with that obtained from photographic film analysis. However, the use of the 2^{nd} order Butterworth filter does not present any phase delay problem.

Five sinusoidal pulses with a duration of 100 ms, magnitude of plus/minus 10 g and frequencies of 40, 100, 200, 300, and 500 Hz were sampled at a rate of 12,500 Hz. The pulses were filtered using both Chebyshev channel class 60 and Butterworth 2^{nd} order filters with a rolloff frequency of 100 Hz. The deceleration attenuation (output/input ratio) and phase delay were then obtained from the filtering output and plotted on a frequency response plot as shown in Fig. 1.18. Note that the phase delay is 360°, if the filtered output is one cycle off from the sinusoidal input. It is observed that there is no phase delay for all the pulses filtered by Butterworth. The phase delay caused by the Chebyshev filter varies considerably depending on the component frequency of the excitation signal.

In addition to phase delay, the deceleration attenuation by the 2^{nd} order Butterworth is greater than that produced by the 2^{nd} order Chebyshev filter. The difference in attenuation between the two filter types depends on the component frequency. As shown in the upper plot in Fig. 1.18, the higher the component frequency, the larger the attenuation difference between the two filter types.

Unless otherwise noted, the default filter type and filtering rolloff frequency are the 2^{nd} order Butterworth filter and 100 Hz (Channel Class 60 shown in Table 1.2), respectively. In the special case where the input deceleration has a frequency component the same as the rolloff frequency, the deceleration attenuation is then −3 db and the magnitude ratio of output deceleration (filtered) to the input is 0.707.

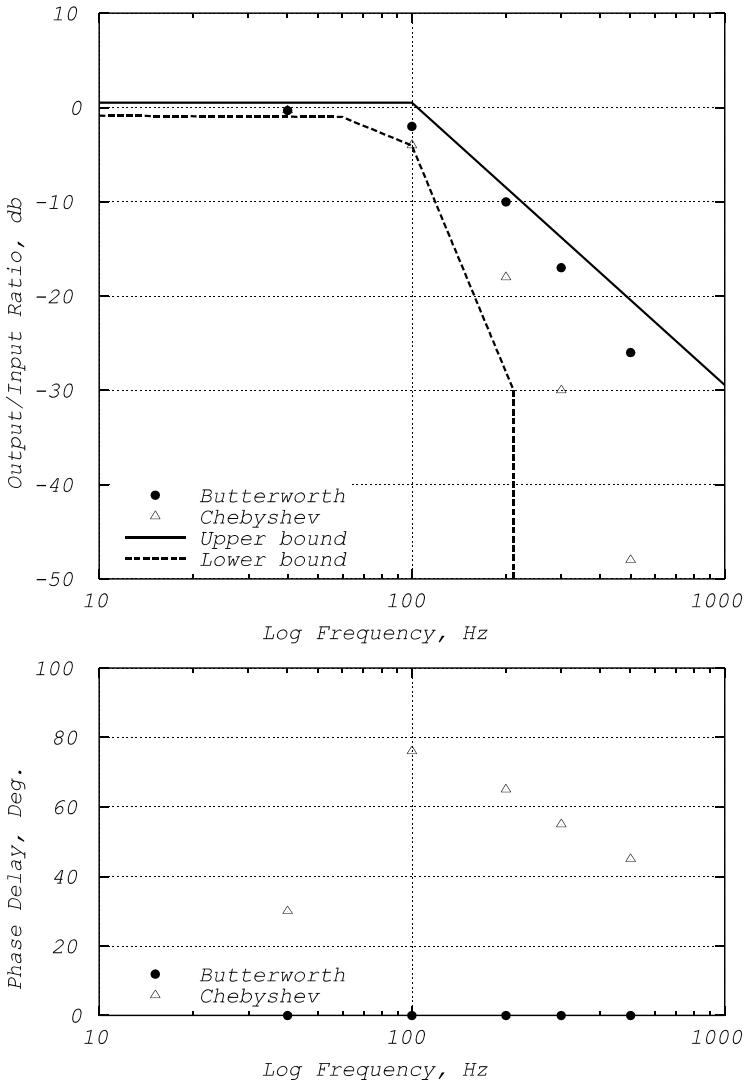

Fig. 1.18 Effects of Filter on Magnitude and Phase Delay

For example, given a sinusoidal pulse with a frequency of 100 Hz filtered by the Butterworth filter with a rolloff frequency of 100 Hz, 70.7% of the peak magnitude still passes through the filtering. Using the formulas for the Butterworth n^{th} order filter, the computation is shown in Eq. (1.8):

$$\begin{aligned} &\textit{for} \quad f = 100\ \textit{Hz}, \quad f_{\textit{rolloff}} = 100\ \textit{Hz} \\ &\frac{a_{\textit{output}}}{a_{\textit{input}}} = \frac{1}{\sqrt{1+\left(\frac{f}{f_{\textit{rolloff}}}\right)^{2n}}} = \frac{1}{\sqrt{1+1}} = .707 \\ &\textit{attenuation, db} = 20 \log_{10} \frac{a_{\textit{output}}}{a_{\textit{input}}} = -3\ \textit{db} \end{aligned} \tag{1.8}$$

The effects of the filter type on the deceleration magnitude and phase delay of the filtered responses are compared using the three input pulses described in the following:

A. *Single-step and multiple-step function inputs*

The data set shown in Fig. 1.19 contains a step (or fast rise) input and is filtered with Channel Class 60. The output from the Butterworth filter contains data prior to and after the actual step event in the unfiltered data, and has no phase shift.

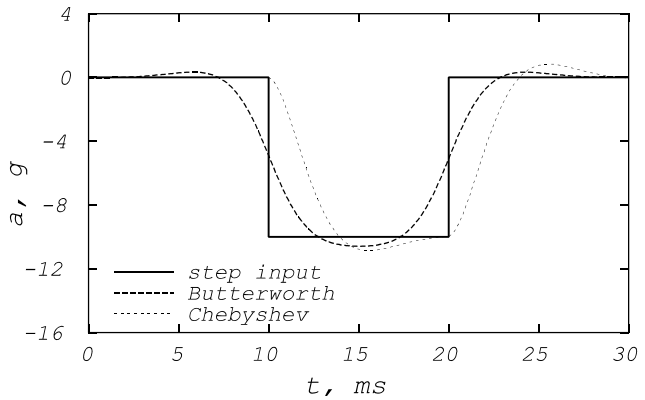

Fig. 1.19 Filtered Response Comparison – Single-Step Function and Channel Class 60

The data filtered by the Chebyshev filter, shown in Fig. 1.20, matches the initiation point of the step input closely, but with considerable phase delay. Comparing the location of the peak magnitude of the filtered pulse with the mid-point of the rectangular step input, the Chebyshev peak magnitude is delayed by half of the duration of the step input, and the Butterworth peak occurs right at the mid-point of the step input. Note that the peak magnitude of the Butterworth filtered output is slightly less than that of the step input, while the peak magnitude of the Chebyshev filtered output is slightly higher than that of the step input.

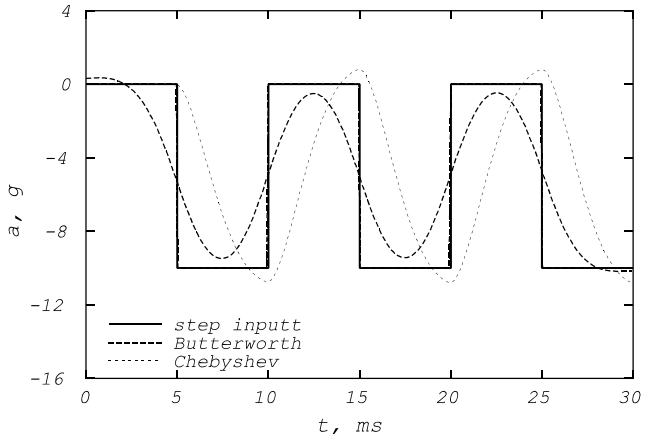

Fig. 1.20 Filtered Response Comparison – Multiple-Step Function and Channel Class 60

Applying the same analysis to the raw data of the vehicle crash pulse, the differences in the magnitude attenuation, phase delay, and initiation point between the filtered data and raw data become clear. Shown in Fig. 1.21, the first impulse, between 4 and 8 ms, can be approximated by a unit step input. The relationships between the filter type, initiation point, attenuation magnitude, and phase delay applied to the step input can also be applied to the test data analysis.

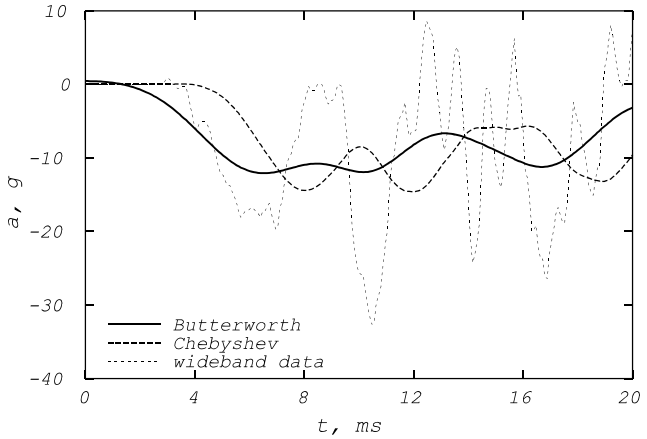

Fig. 1.21 Close-Up of Filtered and Wideband Crash Pulse Comparison

B. *Vehicle crash pulse and Driver chest deceleration*

The wideband crash pulse from an accelerometer on the left rocker at B-pillar of a mid-size passenger car struck by a truck in a 58 mph full frontal test is shown in Fig. 1.22. The data set is filtered with Channel Class 60, with a rolloff frequency of 100 Hz according to Table 1.2 on Channel Class Selection - SAE J211. Peaks in the data sets filtered by Butterworth occur at the same time as the peaks in the unfiltered data. However, there are considerable phase delays between the Chebyshev-filtered and the wideband data sets. Since the deceleration attenuation by Butterworth (2^{nd} order) is more than that by Chebyshev (2^{nd} order), the peak magnitudes of the Butterworth filtered data are smaller than those by Chebyshev. The peak magnitude filtered by the Butterworth, about 12.5 g in the region of T = 30 ms, is about 1g less than that of the Chebyshev.

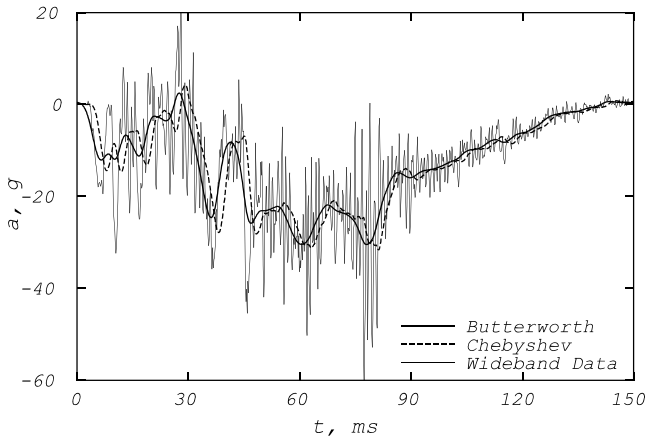

Fig. 1.22 Vehicle Pulse Filtered by Channel Class 60 – Butterworth and Chebyshev

The wideband data of driver chest deceleration in the same truck-to-car test is shown in Fig. 1.23. The data set of chest deceleration is filtered with Channel Class 180 with a rolloff frequency of 300 Hz according to Table 1.2 on Channel Class Selection - SAE J211. The outputs filtered by both Butterworth and Chebyshev algorithms are practically the same compared to the unfiltered data. This is due to the fact that the frequency content in the wideband data of the chest deceleration is low and the rolloff frequency is high. Therefore, the attenuation by the filter becomes small (see Eqs. 1.6 and 1.7), and the output to input deceleration ratio approaches one.

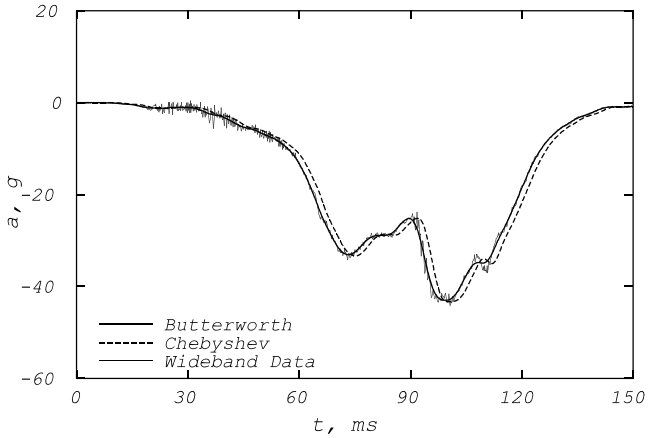

Fig. 1.23 Chest Decel. Filtered by Channel Class 180 – Butterworth and Chebyshev

According to SAE J211, March 1995, Section 9.4.1 on digital filtering, the Butterworth filter should be used for the Channel Class 180 or 60. In the same section, it also states that any filtering algorithm can be used for Channel Class 1000 or 600 as long as the results conform to the data channel performance requirements shown in Fig. 1.24. For simplicity, NHTSA uses the Butterworth filtering for all four channel classes (see Table 1.3 for the Fortran subroutine), even though it is not mandatory for channel class 600 and 1000.

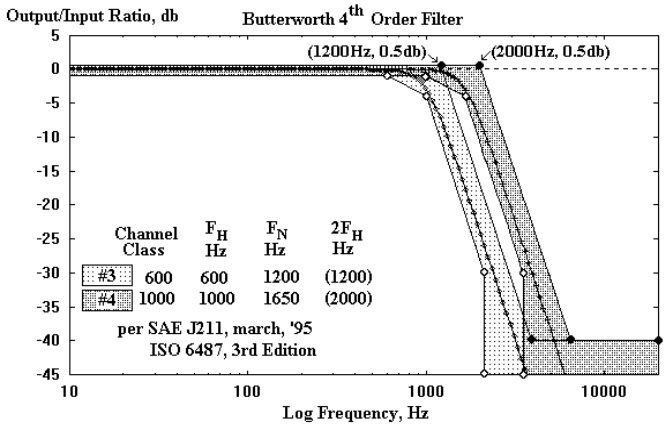

Fig. 1.24 Revised Transition Bands for Channel Class #3 & #4 per SAE J211, March 1995

Table 1.3 FORTRAN SUBROUTINE – BUTTERWORTH FILTER

```
      COMMON/I/YF(-10:2505),YY(2505)
C  (portion of) MAIN program:  2nd order Butterworth digital filter...
C  FILTER THE ENTIRE WIDEBAND DATA READ FROM THE DATA FILE
       NFP = 1              !  NFP:  FIRST DATA POINT NUMBER
       DO I = 1, NPT        !  NPT:  NO. OF DATA POINTS
        YF(I) = YY(I)       !  YY(I): ORIGINAL WIDEBAND ACCELERATION AT POINT I
       ENDDO
         DO I=0,9
       YF(NFP-1-I) = -YF(NFP+I)
      ENDDO
        DEL = .08         !  DEL: DATA STEP, 0.08 MS.  (SAMPLING RATE = 12,500 POINTS/SEC)
C  FCUT: (Fn) CUTOFF FREQUENCY, Hz
      CALL FILTER(YF(NFP-10),DEL,NFP-10,NUM,FCUT*1.25)
C       YF(I): FILTERED DATA POINTS, I=1,2,.., NUM
      STOP
      END
      SUBROUTINE FILTER(Y,DEL,N1,N2,FM6DB)
C       SOURCE: NHTSA Crashworthiness Research, DOT.
C       Function: Filters data forward and backward with a second order
C       Butterworth algorithm, giving zero phase shift and -3dB
C       at FM6DB/1.25.
C      Principal Variables:
C            A1,A2,B0,B1,B2    - Difference equation coefficients
C            Y(I)              - Data array (pre- and post-filtered)
C            FM6DB             - Filter (-6 dB) frequency (Hz)
C            DEL               - Time increment of data (sec)
C            N1                - Index of first data point
C            N2                - Index of last data point
C      Programmer:
C            ASGI - C. Louie                    11/78
C            ASGI - S. Mentzer                   7/83

      DIMENSION Y(N1:N2)
C     Compute filter coefficients
      PI = 3.141592654
      WD = 2*PI*FM6DB
      WA = SIN(WD*DEL/2.)/COS(WD*DEL/2.)
      B0 = WA**2/(1.+SQRT(2.)*WA+WA**2)
      B1 = 2.*B0
      B2 = B0

A1=-2.*(WA**2-1.)/(1.+SQRT(2.)*WA+WA**2)

A2=(-1.+SQRT(2.)*WA-WA**2)/(1.+SQRT(2.)
*WA+WA**2)
C     Filter forward
      Y1 = 0.0
     DO 201 I=N1,N1+9
      Y1 = Y1+Y(I)
  201 CONTINUE
      Y1 = Y1/10.0
      X2 = 0.0
      X1 = Y(N1)
      X0 = Y(N1+1)
      Y(N1) = Y1
      Y(N1+1) = Y1
     DO 202 I=N1+2,N2
         X2 = X1
         X1 = X0
         X0 = Y(I)
Y          (          I          )                    =
B0*X0+B1*X1+B2*X2+A1*Y(I-1)+A2*Y(I-2)
  202 CONTINUE
C       Filter backwards
       Y1 = 0.0
     DO 203 I=N2,N2-9,-1
         Y1 = Y1+Y(I)
  203 CONTINUE
       Y1 = Y1/10.0
       X2 = 0.0
       X1 = Y(N2)
       X0 = Y(N2-1)
       Y(N2) = Y1
       Y(N2-1) = Y1
     DO 204 I=N2-2,N1,-1
         X2 = X1
         X1 = X0
         X0 = Y(I)
Y          (          I          )                    =
B0*X0+B1*X1+B2*X2+A1*Y(I+1)+A2*Y(I+2)
  204 CONTINUE
     RETURN
     END
```

1.3.4 Moving Window Averaging and Equivalent Cutoff Frequency

The purpose of using window averaging in processing the crash test wideband (raw) data is to reduce the total number of discrete data points and to average (filter) out the noise. A simple moving window averaging is used for this purpose and the techniques used to integrate the new set of averaged data points are presented. The window length, the number of data points in a window, controls the component frequency of the crash pulse, equivalent to the effect of cutoff frequency in signal attenuation.

1.3.4.1 *Moving Window Averaging*

Moving window averaging is a simple digital filtering technique that filters out noise by averaging the data within the window length. The averaged deceleration value is then placed at the mid-point of the window. By moving this window through the entire crash pulse, the total number of data points is reduced n-fold, where n is the window length, the number of points (bites) in the window. Note that in the raw data, the length of each bite is 0.08 ms, corresponding to a sampling rate of 12,500 points (bites) per second.

Using an accelerometer on the left frame at the A-pillar, the crash data for a light truck in a 31 mph rigid barrier impact was obtained. The data are plotted and shown in Fig. 1.25. Assume that the window length is 50 bites and 1 bite = 0.08 ms (sampling rate=12,500 Hz); the step size (window length), δ, is then 4 ms (50 bites/window × 0.08 ms/bite). However, the distance between the mid-point of the first window and time zero is only half of the window step size. Any window after the first one has the full step size. This is the distance between the mid-points of the consecutive windows. Consequently, the first window has only a half-step, which is 2 ms.

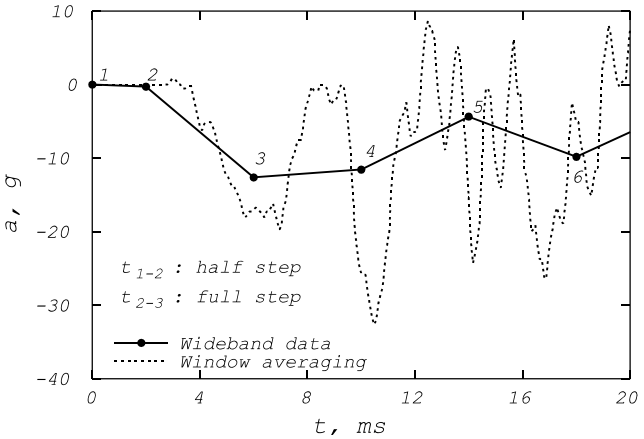

Fig. 1.25 Crash Test Data (Acceleration) with Moving Window Averaging

The duration of the wide-band data shown is 20 ms, and each bite is .08 ms; therefore, the total number of points is 20/0.08 + 1 = 251. Since the window length (step) is 50 bites or 4 ms/step, the total number of points is reduced from 251 to 6 (251/50 + 1 = 6, or 20/4 + 1 = 6) which includes the first point at time zero. The integration scheme using moving window averaging for crash data should therefore use only a half step size when integrating the first data point at time zero. The full step size should then be used when integrating points after the first one as shown in the integration scheme in Eq. (1.9). Note that v_o and d_o denote the initial velocity and initial displacement (at time zero) and δ, the integration time step.

1^{st} *and* 2^{nd} *integrals, velocity and displacement*:

$$v_1 = v_o, \quad v_2 = v_1 + \frac{a_1+a_2}{2}\frac{\delta}{2}, \quad v_{i+1} = v_i + \frac{a_i+a_{i+1}}{2}\delta$$
$$d_1 = d_o, \quad d_2 = d_1 + \frac{v_1+v_2}{2}\frac{\delta}{2}, \quad d_{i+1} = d_i + \frac{v_i+v_{i+1}}{2}\delta \tag{1.9}$$

The entire wideband crash pulse of the truck frame at A-pillar in the rigid barrier 31 mph test is shown in Fig. 1.26 along with the window averaged curve. Since the pulse duration is 150 ms, and the data step is 0.08 ms, the total number of data points is 1,876 points. The dotted solid curve is the window averaged curve with window length of 50 bites.

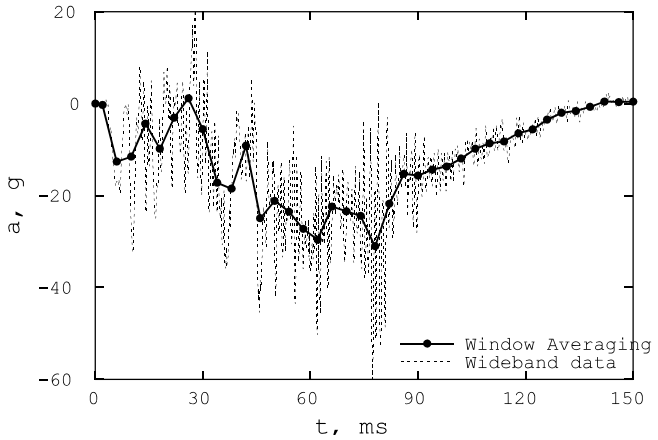

Fig. 1.26 A Truck Crash Test Raw Data with Moving Window Averaging

Although the number of points of the wideband data is reduced by 50 times, the first and second integrals (relative velocity and displacement) of the window-averaged data points still retain the integration accuracy. For practical purposes, they are identical to the integrals of the wideband data as shown in Fig.1.27.

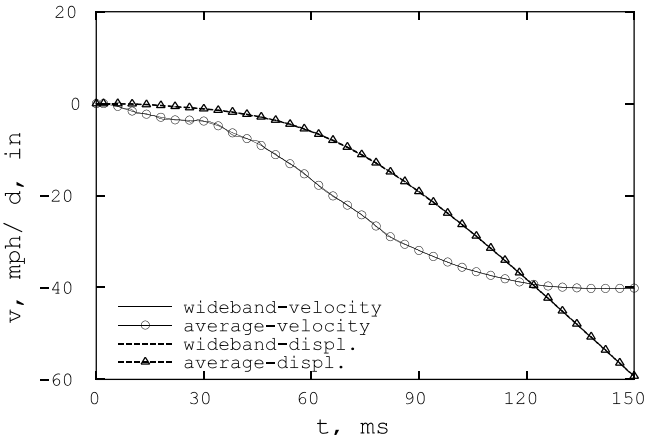

Fig. 1.27 1^{st} and 2^{nd} Integrals of Crash Test Raw Data with Moving Window Averaging

1.3.4.2 *Equivalent Cutoff Frequency*

The moving average operation can be regarded as a low pass filtering process. It averages out the high frequency noise. The filtering effect by window averaging depends on the window length and is equivalent to a low pass filter with a cutoff frequency [14] given by Eq. (1.10).

$$f_c = \frac{f_s}{2(M+1)}, \quad \textit{where}$$

$$f_c\text{: equivalent cutoff frequency, Hz}$$
$$f_s\text{: sampling frequency, Hz} \tag{1.10}$$
$$M\text{: length of window in points}$$

In the previous section, a truck crash pulse with a duration of 20 ms was used for the moving window averaging. A window length of 50 bites (4 ms step) was used and the total number of points after averaging was six. Since the sampling rate, f_s is 12,500 Hz, and window length, M=50, the equivalent cutoff frequency, f_c is therefore equals to 12,500/[2×(50+1)] = 123 Hz.

A comparison of three curves, window averaging, the Butterworth filter at 123 Hz, and the raw test data, is shown in Fig. 1.28. Note that the initiation point for both window averaging and the Butterworth filtered curves occurs at about the same time, a half-step of 2 ms. Throughout the 20 ms duration, the window averaging tends to average out the Butterworth filtered responses.

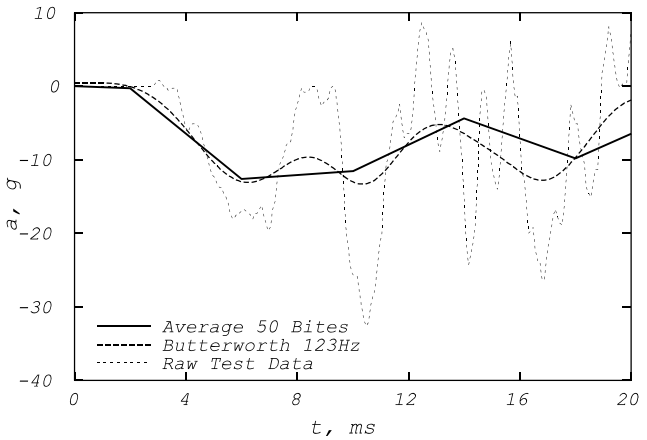

Fig. 1.28 Crash Pulse Comparison between Window Averaging and the Butterworth Filter

Instead of fixing the window length, one can compute the window length based on the required cutoff frequency. Let the equivalent cutoff frequency, f_s, be 100 Hz, for filtering the vehicle structural deceleration. Since the sampling rate is 12,500 Hz, from Eq. (1.10), one can compute M, the window length:

$$M = \frac{f_s}{2f_c} - 1 = \frac{12{,}500}{2\times 100} - 1 = 61 \tag{1.11}$$

Using the window length of 61 bites, the body crash pulse of a mid-size vehicle struck by a truck at 58 mph is filtered by the window averaging method. Fig. 1.29 shows the raw data of the crash pulse overlapped with the two filtered outputs by the window averaging of 61 bites and Butterworth filter with cutoff frequency of 100 Hz.

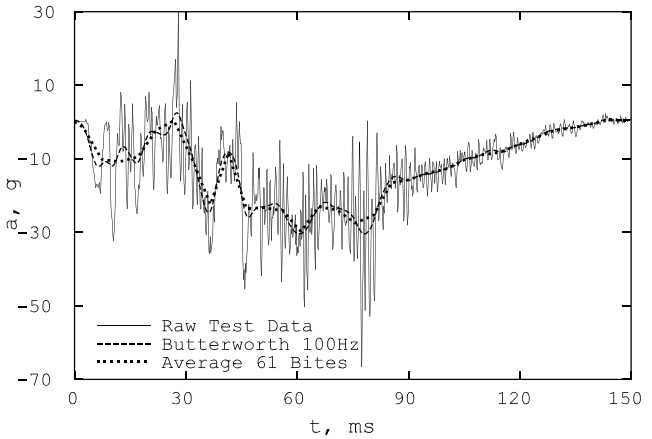

Fig. 1.30 Raw Data of Body Pulse of a Mid-Size Car Struck by a SUV at 58 mph

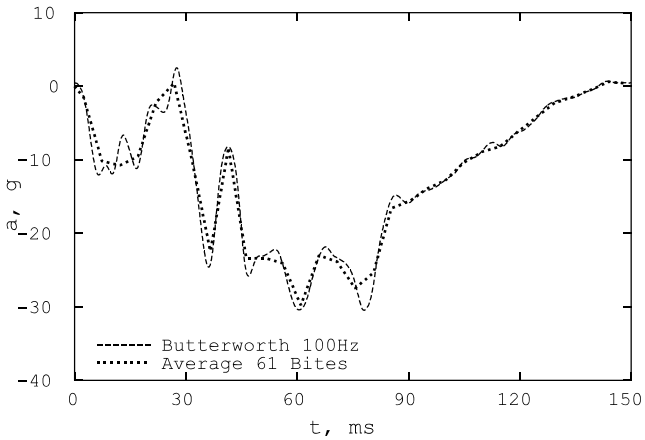

Fig. 1.29 Body Pulse With Butterworth 100 Hz Cutoff and 61-bite Averaging

Fig. 1.30 shows a comparison between the two filtered curves over the entire 150 ms duration. Both curves are fairly close to each other in terms of magnitude and timing in the peaks and valleys. Just like the Butterworth filter, the window averaging method does not possess a phase delay problem.

To properly overlay the wideband and window average data points, the averaged data point should be placed at the mid-point of the window and the half-step should be used in the first point integration. The location of the first half-step data point in time is critical in terms of the accuracy of timing and magnitude of integrals. This is especially true when the window length is long.

Due to the reduced number of data points and given the accuracy of the integral, the window averaging technique is especially useful in obtaining a transfer function. Topics on transfer functions are covered in Chapter 3.

The forthcoming sections describe the basic kinematic relationships, principles, and their applications in analyzing the crash pulse data for crashworthiness study.

1.4 BASIC KINEMATIC RELATIONSHIPS

Using the three basic kinematic relationships relating the deceleration, velocity, and displacement shown below, crash test data can be further processed to yield the particle kinematics of a vehicle or occupant in the time and displacement domain.

$$v = \frac{dx}{dt} \quad \ldots\ldots (1)$$
$$a = \frac{dv}{dt} \quad \ldots\ldots (2), \quad \textit{and}$$
$$adx = vdv \quad \ldots\ldots (3), \quad \textit{where} \tag{1.12}$$
x: *displacement (change of position)*
v: *velocity (rate of change of displacement)*
a: *acceleration (rate of change of velocity)*
d: *differential operator*

(1) and (2) of Eq. (1.12) represent the basic kinematic relationships in the time domain. By combining (1) and (2) and eliminating the time variable, a kinematic relationship in the displacement domain is obtained as shown in (3).

Define *e:* energy density (or specific energy, defined as energy per unit mass). Then

$$e = \int adx, \quad \textit{then} \quad de = adx = vdv, \quad \textit{and} \quad a = \frac{de}{dx} \tag{1.13}$$
$$\textit{where} \quad de\textit{: differential energy density}$$

Note that the slope at a point on the energy versus displacement plot is the acceleration at that point in time. The four basic kinematic variables, a, v, d, and e in the time domain are the transient response variables. The same response variables expressed in the displacement domain offer a new perspective in evaluating the impact severity of a crash.

Although the transient acceleration data, a(t), and displacement, x(t), are readily available from the recorded accelerometer data and their integrals, the energy density at any given time, t, is <u>not</u> equal to the product of the two quantities as shown below.

$$e \neq a(t) \times x(t) \tag{1.14}$$

To obtain the correct energy density, the differential energy density should be integrated over a specified range of displacement on the acceleration versus displacement curve. The energy density can also be computed using the velocity information shown in Eq. (1.15) where v_o is the initial velocity of a vehicle in an impact.

$$e = \int_{v_o}^{v} vdv = \frac{v^2 - v_o^2}{2} \tag{1.15}$$

1.4.1 Computing Acceleration from a Velocity-Displacement Curve

Given a velocity (v) vs. displacement (x) curve as shown in Fig. 1.31, the acceleration (a) corresponding to any point on the curve can be computed using kinematic relationship (3) of Eq. (1.12). Note if v and x are relative quantities, then the computed a is also a relative quantity. Similarly, if v and x are absolute, so is a.

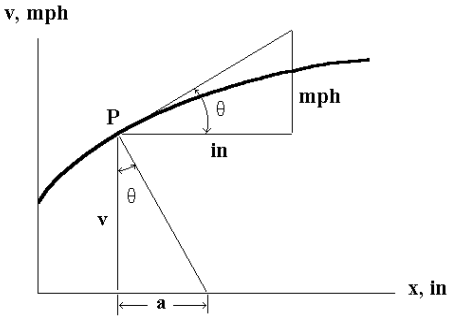

Fig. 1.31 Velocity vs. Displacement Curve

The slope at point P on the v-x curve is

$$dv/dx = (dv/dt)/(dx/dt) = a/v = \tan\theta$$
$$a = v \tan\theta \tag{1.16}$$

If conventional units (a, g; v, mph; x, in) are used, then the formula becomes

$$a = 0.8\, v \tan\theta, \qquad \tan\theta = \frac{\textit{opposite side}}{\textit{adjacent side}} \tag{1.17}$$
(*using same scale on v and x*)

Note that if the angle is to be measured off the curve and the tangent function is to be used to compute the slope, the scales on both x and v axes have to be the same. As an example, if the scale on the x axis is 2 inches per division, the scale on the v axis would have to be 2 mph per division, and the measured lengths per division along x and v would have to be the same.

Case Study: A full-size passenger car was tested in a 14 mph rigid barrier test. The magnitude of the longitudinal deceleration at the left rocker/B-pillar is shown in Fig. 1.32. (1) Plot the velocity versus displacement curve for an unbelted occupant with respect to the vehicle, and (2) Compute the relative acceleration of the unbelted occupant at the relative displacement of 8 inches.

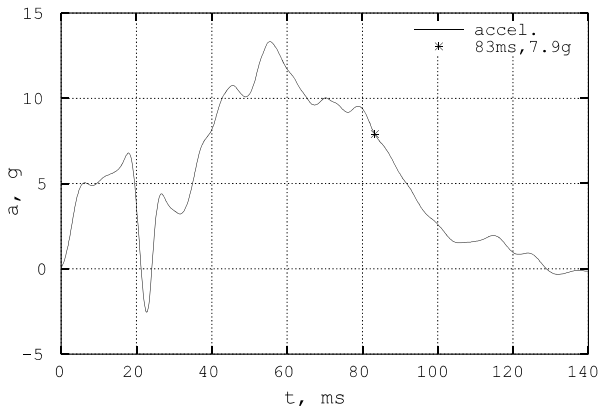

Fig. 1.32 Unbelted Occupant Relative a vs. t

In the case of a free-flying (unrestrained) occupant in the passenger compartment during a crash,

it can be shown that the slope (deceleration) at a point on the relative occupant velocity vs. relative displacement curve is the corresponding vehicle deceleration.
Let us define:
a_o = free-flying occupant acceleration (= 0), a_v = vehicle acceleration
$a_{o/v}$ = deceleration of occupant relative to vehicle
then $a_{o/v} = a_o - a_v = 0 - a_v$; therefore, $a_v = -a_{o/v}$

The vehicle deceleration is equal to the negative of the free-flying occupant relative to vehicle acceleration. The first and second integrals of the unbelted occupant acceleration with zero initial velocity yield the relative velocity and displacement of the unbelted occupant, respectively. The relative acceleration versus relative displacement (a vs. d), and the relative velocity versus relative displacement (v vs. d) are shown in Figs. 1.33 and 1.34, respectively.

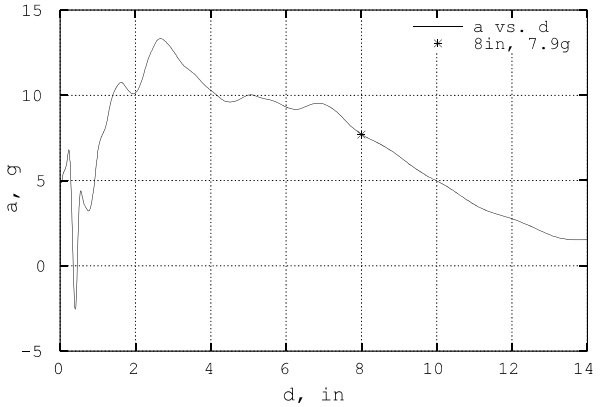

Fig. 1.33 Unbelted Occupant Relative a vs. d

To illustrate the proper use of the relationship between a and v in the displacement domain plot, two different displacement scales shown in Fig. 1.34 are used.

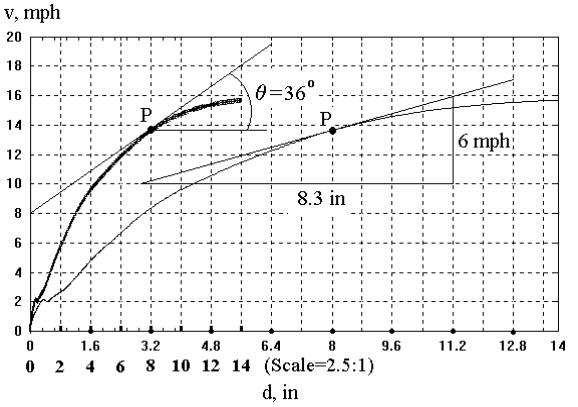

Fig. 1.34 Unbelted Occupant Relative Velocity vs. Relative Displacement in Two Scales

To compute the relative acceleration at point P from the velocity vs. displacement curve, the relative displacement and velocity at point P are found to be 8 inches and 13.7 mph, respectively. Since the first x scale is different from y scale, the slope at point P is determined by taking the ratio of the opposite side to the adjacent side: 6 mph/8.3 in = 0.72 mph/in. Therefore, the relative acceleration, a, at point P, is

$$a = 0.8\, v \tan\theta = 0.8\, v \frac{opposite\ \ side}{adjacent\ \ side} = 0.8 \times 13.7 \times (0.72) = 7.9\, g \tag{1.18}$$

If the angle is to be measured from the plot to compute the tangent function, the x and y scales would have to have the same magnitude (same length per division). A scale factor of 2.5 is used to change the x scale such that it has the same magnitude as the y scale as shown in Fig. 1.34. The angle of the tangent at point P from the scaled-down curve is about 36°. Therefore, the relative acceleration at point P is then

$$a = 0.8\, v \tan\theta = 0.8 \times 13.7 \times \tan(36^o) = 7.9\, g \tag{1.19}$$

The value of the relative acceleration at point P computed from the velocity versus displacement plot is checked against that from the relative acceleration versus relative displacement plot as shown in Fig. 1.33.

The plot of v vs. d, the relative velocity versus relative displacement, shown in Fig. 1.34 is useful in comparing the impact severity of an unbelted occupant in different crash modes in air bag development tests. Section 1.6.3, Occupant Kinematics in Different Test Modes, is devoted to such an application.

A particle kinematics analysis in a two-dimensional gravitational field is described in the next section. The example shown is a case study modified from an accident investigation where a speeding vehicle became air borne after going over an uphill pavement.

1.4.2 Particle Kinematics in a Gravitational Field

An accident involving an airborne car is used to review the particle kinematic principles often used in accident reconstruction. The "take-off" speed of a vehicle accelerating on an up-hill country road and becoming airborne (called jumping) and landing on a flat surface is to be estimated. Using kinematic relationships, the particle kinematics problem can be formulated. The kinematic solutions to this problem are expressed in closed-form and a trend and sensitivity analysis reveal the parametric relationships that are useful in engineering analysis. The formulas presented here are also applicable to the ski jump analysis on the takeoff, distance, and landing kinematic relationships.

1.4.2.1 *Car Jumping and Landing*

The horizontal and vertical distances, d and h, between the launching and landing sites are shown in Fig. 1.35. The ramp angle at the takeoff is θ. Case [A]: find the minimum takeoff velocity v that the vehicle needs to go over the obstacle, and Case [B]: find the takeoff velocity and takeoff ramp angle, θ, needed to avoid a crash on the landing ramp where the angle is ϕ as shown, and Case [C]: find the impact velocity of the vehicle upon reaching the landing ramp with an arbitrary angle of ϕ.

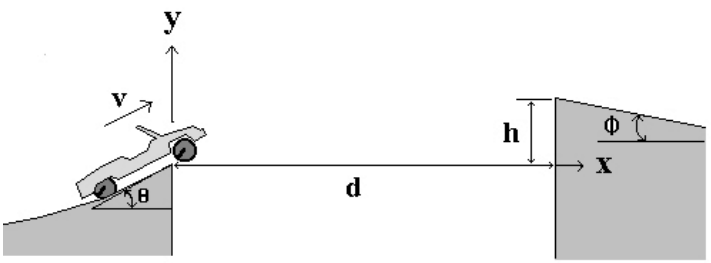

Fig. 1.35 Car Jump – Particle Kinematics

Case [A]: Minimum Velocity Needed to Go over an Obstacle

Assuming the take-off point is at the origin of a Cartesian coordinate system, the displacement relationships for the x and y directions are shown in Eq. (1.20). Given d, h, and θ, the two unknowns v and t can be obtained from these two equations. Note that θ has to be greater than the elevation angle defined by h and d, or arctangent of h/d.

[A] Solutions: minimum velocity for going over obstacle

define vehicle displacements along x and y:

$$x: \quad d = v\cos(\theta)t \quad \ldots\ldots\ldots\ldots \quad (1)$$

$$y: \quad h = v\sin(\theta)t - \frac{1}{2}gt^2 \quad \ldots\ldots\ldots \quad (2)$$

solve for v by eliminating t in the equations above:

$$v = \frac{d}{\cos(\theta)}\sqrt{\frac{g}{2[d\tan(\theta) - h]}} \quad \ldots\ldots \quad (3)$$

solve for t from the equation for x:

$$t = \frac{d}{v\cos(\theta)} \quad \ldots\ldots\ldots\ldots\ldots \quad (4)$$

Normalizing v and simplifying the expression for v:

$$\frac{v}{\sqrt{2gd}} = \frac{1}{2\cos(\theta)\sqrt{\tan(\theta) - \frac{h}{d}}} \quad \ldots\ldots \quad (5)$$

Note: $\theta > \tan^{-1}\left(\frac{h}{d}\right)$ (1.20)

The take-off velocity, v, is normalized with respect to (w.r.t.) a fixed velocity quantity (square root of 2gd) as shown in (5) of Eq. (1.20). Figs. 1.36–37 show the plots needed to find the take-off velocity, v. Given the ratio of h/d and θ in degrees, the normalized velocity multiplied by the square root of 2gd yields the takeoff velocity v.

Example 1: Given a takeoff ramp angle θ = 30°, d=25ft, h=5ft, determine the minimum velocity needed for the vehicle to go over the obstacle.

Using the following data: $\frac{h}{d} = \frac{5}{25} = 0.2$, *and* $\theta = 30^o$

from Fig. 1.36 *and* (5) *of Eq.* (1.20),

$\frac{v}{\sqrt{2gd}} = 0.94$; *therefore,* $v = 0.94\sqrt{2\times32.2\times25} = 37.7\ \frac{ft}{sec}$, *or*

from Fig. 1.37, $\sqrt{2gd} = 27.4$ *mph, then* $v = 0.94\times27.4 = 25.7$ *mph* (1.21)

The takeoff velocity of 37.7 ft/sec is based on a takeoff angle of θ = 30°. However, the real minimum takeoff velocity can be even lower than 37.7 ft/sec if a proper takeoff angle is chosen.

Fig. 1.38 shows the minimum normalized takeoff velocity at different takeoff ramp angles, θ, and values of h/d. When θ = 50°, the normalized velocity for h/d = 0.2 is 0.78, and the minimum takeoff velocity is then equal to 31.3 ft/sec which is lower than 37.7 ft/sec.

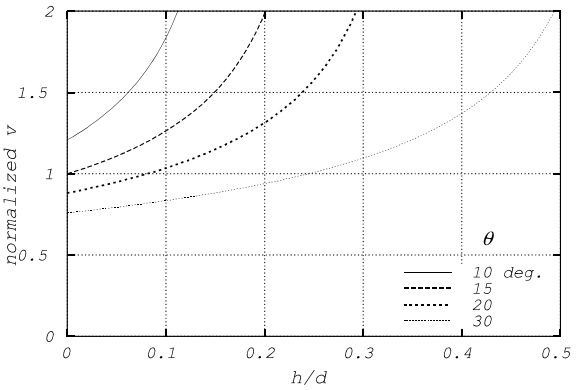

Fig. 1.36 Normalized Take-Off Velocity

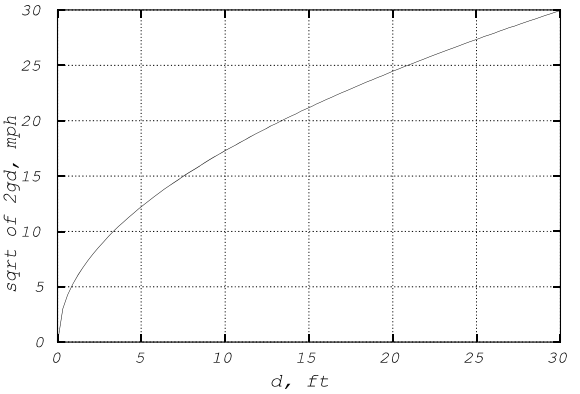

Fig. 1.37 A Quantity to Normalize Velocity

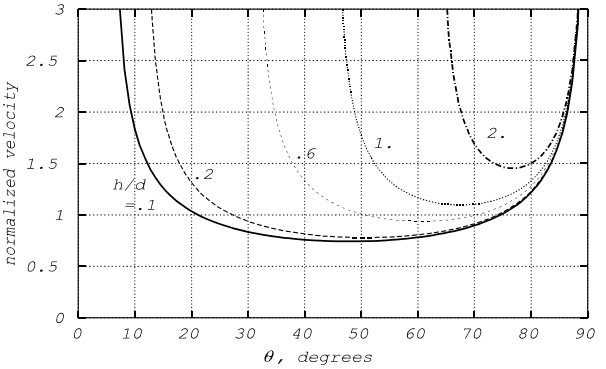

Fig. 1.38 Min. Norm. Velocity To Go Over an Obstacle

The trajectories in the two cases at the takeoff ramp angles of 30°and 50° are shown in Fig. 1.39. For the ramp angle of 30°, the vertical velocity is zero near the top of the obstacle where it is the highest point of the trajectory. For the ramp angle of 50°, the vertical velocity of the vehicle is negative (on the way down) and landing occurs after the highest point of the trajectory has been reached.

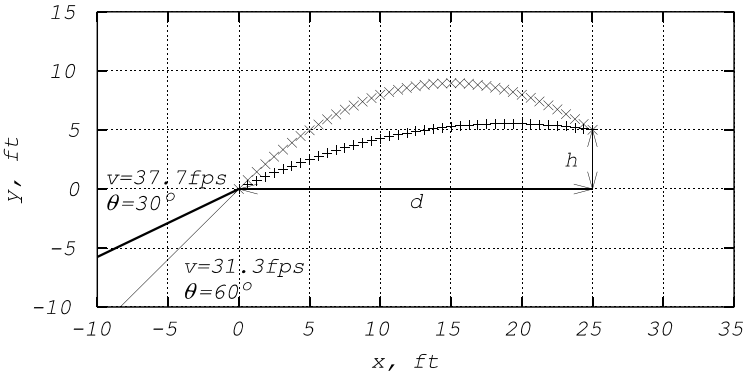

Fig. 1.39 Trajectories with Different Ramp Angles and Velocities To Clear an Obstacle

Case [B]: Perfect Landing Without a Crash

Given a length d, height h, and the landing ramp angle, ϕ, there exists one unique set of solutions of the takeoff velocity, v, and the takeoff ramp angle, θ. Such a solution will render a perfect landing where the slope of the trajectory at the touch down point is the same as that of the landing ramp surface. (13) and (14) of Eq. (1.22) determine the takeoff ramp angle and velocity required for the car jump without having a crash landing.

[*B*] *At landing point*: $y = v\sin(\theta)t - \frac{1}{2}gt^2$ . . (6), $x = v\cos(\theta)t$ . . . (7)

The slope of the trajectory at the landing point is the same as that of the landing ramp; *then* $\frac{dy}{dx} = -\tan(\phi)$ . . . . . (8)

$$\therefore \frac{dy}{dx} = \frac{dy}{dt}\frac{dt}{dx} = [v\sin(\theta) - gt]\frac{1}{v\cos(\theta)} = -\tan(\phi) \quad . . (9)$$

Eliminating t between (7) *and* (9), *one gets the constraint equation* (*slope* = $\tan\phi$) *between v and* θ:

$$\tan(\theta) + \tan(\phi) = \frac{gx}{[v\cos(\theta)]^2} \quad . . . . . (10)$$

By eliminating t between (6) *and* (7), *the trajectory equation is obtained*:

$$y = x\tan(\theta) - \frac{g}{2}\left[\frac{x}{v\cos(\theta)}\right]^2 \quad . . . . . (11) \qquad (1.22)$$

There are two contraint equations on the slope and trajectory: *unknowns, v and* θ, *can be solved by eliminating the term* $[v\cos(\theta)]^2$ *between* (10) *and* (11), *then*

$$\tan(\phi) + \frac{2y}{x} = \tan(\theta) \quad . . . . . (12)$$

Let coordinates at landing point be x=d, and y=h, then

$$\tan(\theta) = \tan(\phi) + \frac{2h}{d} \quad . . . . . (13)$$

Eliminating $\tan(\phi)$ *between*(10) *and* (13):

$$v = \frac{d}{\cos(\theta)}\sqrt{\frac{g}{2[d\tan(\theta) - h]}} \quad . . . . . (14)$$

Fig. 1.40 shows two cases where the landing is perfect. Case 1, where the trajectory in a thick solid curve is plotted with a symbol "+" has a takeoff velocity of 37.7 ft/s with a takeoff ramp angle $\theta = 30°$, and a landing ramp angle of 10°. Case 2, where the trajectory is plotted with a symbol "×" has a takeoff velocity of 34.0 ft/s with a takeoff ramp angle $\theta = 65°$, and a landing ramp angle of 60°.

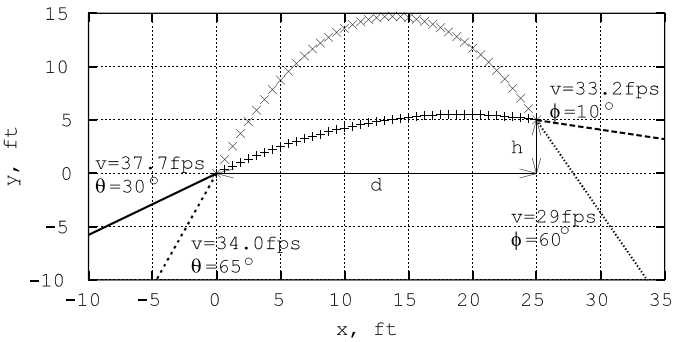

Fig. 1.40 Perfect Landing Without a Crash

Case [C]: Crash Landing Velocity Computation and Perfect Landing Criterion

The velocity components along x and y at the landing point can be computed as shown in (15) and (16) of Eq. (1.23). These velocity components can be transformed into the components along x′ (parallel to the landing ramp surface) and y′ shown in (17) and (18) of Eq. (1.23), respectively. A simplified solution for the landing velocity along the landing ramp is shown in (22) of Eq. (1.23).

$$
\begin{aligned}
&[C]\text{: } \textit{Computing Crash Landing Velocity} \\
&\quad v_x\text{: } \textit{initial velocity along } x, \quad v_y\text{: } \textit{velocity along } y \\
&\quad v_x = v\cos(\theta) \qquad \ldots\ldots\ldots\ldots\ldots\ldots \quad (15) \\
&\quad v_y = v\sin(\theta) - gt \qquad \ldots\ldots\ldots\ldots\ldots \quad (16) \\
&\textit{Let } x'\text{-}y' \textit{ be a coordinate system with } x' \textit{ along the landing ramp} \\
&\quad v_x'\text{: } \textit{velocity along } x' \\
&\quad v_y'\text{: } \textit{velocity along } y' (\textit{perpendicular to landing ramp}) \\
&\quad v_x' = -v_y\sin(\phi) + v_x\cos(\phi) \qquad \ldots\ldots\ldots\ldots \quad (17) \\
&\quad v_y' = v_y\cos(\phi) + v_x\sin(\phi) \qquad \ldots\ldots\ldots\ldots \quad (18) \\
&\textit{Substituting } t = \frac{d}{v\cos(\theta)} \textit{ and } (15),\ (16) \textit{ into } (18) \\
&\quad v_y' = v\sin(\theta+\phi) - \frac{gd\cos(\phi)}{v\cos(\theta)} \qquad \ldots\ldots\ldots\ldots \quad (19) \\
&\textit{Normalizing } v_y' \textit{ by } v\text{: } \frac{v_y'}{v} = \sin(\theta+\phi) - \frac{\cos(\phi)}{\cos(\theta)}\left(\frac{gd}{v^2}\right) \\
&\textit{Substituting } \left(\frac{gd}{v^2}\right) \textit{ by using } (5) \textit{ of Eq. } (1.20), \textit{ one gets} \\
&\quad \frac{v_y'}{v} = \sin(\theta+\phi) - 2\cos(\theta)\cos(\phi)\left[\tan(\theta) - \frac{h}{d}\right] \quad \ldots\ldots \quad (20) \\
&\textit{For a landing without a crash, } v_y' = 0, \textit{ and } (20) \textit{ becomes} \\
&\quad \frac{\tan(\theta)}{2} = \frac{\tan(\phi)}{2} + \frac{h}{d} \qquad \ldots\ldots\ldots\ldots \quad (21) \\
&\textit{Substuting } v_x \textit{ and } v_y \textit{ from } (15) \textit{ and } (16) \textit{ into } (17), \textit{ one gets} \\
&\quad v_x' = v\cos(\theta+\phi) + \frac{gd\sin(\phi)}{v\cos(\theta)} \qquad \ldots\ldots\ldots\ldots \quad (22)
\end{aligned}
\tag{1.23}
$$

For a perfect landing without a crash, the computed $v_{y'}$ is equal to zero. The geometric relationship in terms of takeoff and landing ramp angles is that the ratio of height to length (h/d) are related by (21) of Eq. (1.23). The height to distance ratio, h/d, plus one half tangent of landing ramp angle (ϕ) equals one half tangent of takeoff angle (θ). Since h/d is always zero or positive, the feasible solution space for perfect landing is that the takeoff ramp angle (θ) is always equal to or greater than the landing ramp angle (ϕ). The only time that the takeoff ramp angle equals the landing ramp angle is when h/d = 0, when no elevation change occurs between the takeoff and landing ramps.

A surface contour plot based on (21) of Eq. (1.23) for perfect landing is shown in Fig. 1.41. Note that for h/d = 5/25 = 0.2 and a landing ramp angle (ϕ) of 10°, the takeoff angle (θ) of 30° is found from the surface contour plot. This agrees with the computation for Case #1 (the curve with a + sign) shown in Fig. 1.40, where the landing is perfect, i.e., without a crash. The formulas presented here are also valid for the long distance ski jump analysis. Since the elevation at the landing site is lower than that at the takeoff point, h in (21) of Eq. (1.23) should be treated as a negative quantity.

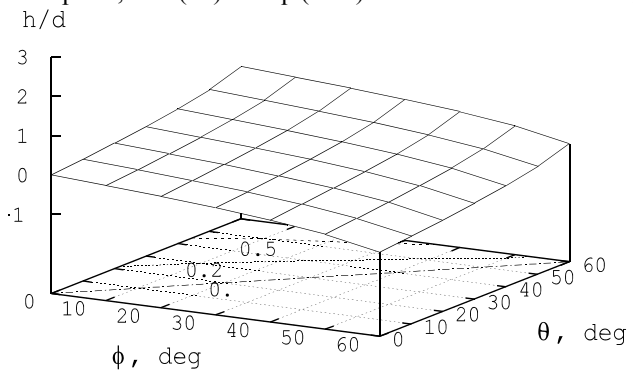

Fig. 1.41 Geometric Relationship for Perfect Landing

1.4.3 Slipping on an Incline – Down Push and Side Push

A side impact or rollover of a vehicle is a kinematic problem involving friction. A vehicle on the verge of impending motion on an incline is a static equilibrium problem where the frictional force required for equilibrium equals the maximum available friction. The maximum available friction is the product of the normal force supporting the vehicle and the static coefficient of friction. The following case study shows the application of static equilibrium and the procedures needed for problems such as vehicle skidding and fastener (nut and bolt) loosening.

Case Study: A uniform block of mass m is at rest on an incline at an angle θ, as shown in Fig. 1.42. Case (1): Side push. Determine the maximum side-push force P_s that can be applied to the block in the direction shown before slipping begins. The coefficient of friction between the block and the

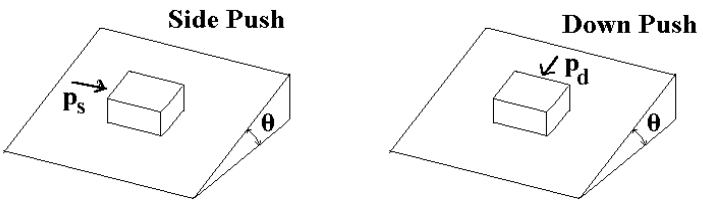

Fig. 1.42 Slipping on an Incline due to Side or Down Push

incline is μ. Also determine the angle β between the horizontal direction of P_s and the direction of initial movement of the block. Repeat the problem for Case (2): Down push.

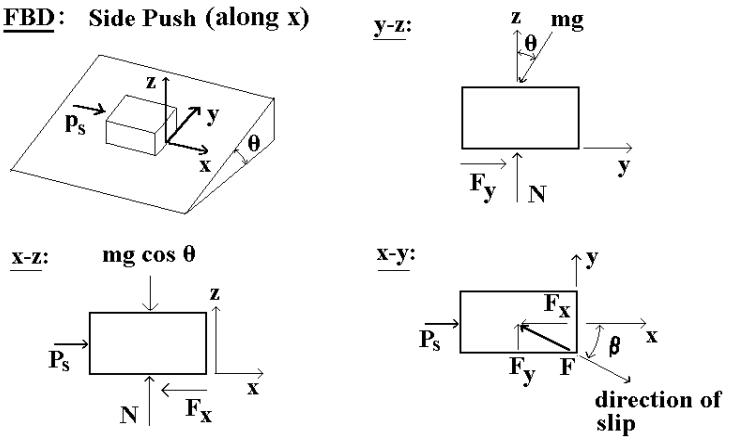

Fig. 1.43 Slipping on an Incline due to Side Push

Case (1): Side push. Using the free body diagram (FBD) and the static force equilibrium in the x and y directions, the maximum side push force that would cause the block to start sliding can be derived as follows.

$$\Sigma F_x = 0: \quad F_x = P_s$$
$$\Sigma F_y = 0: \quad F_y = mg\sin\theta$$
$$\Sigma F_z = 0: \quad N = mg\cos\theta$$
$$F\ (\max\ \textit{available friction}) = \mu N = \sqrt{F_x^2+F_y^2} \tag{1.24}$$
$$(\mu mg\cos\theta)^2 = P_s^2+(mg\sin\theta)^2$$
$$\therefore\ P_s = mg\sqrt{\mu^2\cos^2\theta - \sin^2\theta}$$
$$\textit{For}\ \ P_s \geq 0,\ \ \textit{then}\ \ \mu \geq \tan\theta$$

As long as the coefficient of friction is greater than the tangent of the inclination angle, a side-push force is required to initiate the impending motion of the block. If the inclination angle is large enough such that the tangent of inclination angle is greater than the coefficient of friction, the block slides down on the incline by itself without any side push force required.

The angle β between the side push direction and the direction of initial movement of the block is defined and expressed as follows.

$$\textit{In the x–y plane}: \quad \beta = \tan^{-1}\frac{F_y}{F_x} = \tan^{-1}\frac{mg\sin\theta}{P_s}$$
$$\textit{Substituting the expression for } P_s \textit{ into the equation for } \beta: \tag{1.25}$$
$$\beta = \tan^{-1}\frac{\tan\theta}{\sqrt{\mu^2 - \tan^2\theta}}$$

Case (2) Down push (along y):

Using the free body diagram (FBD) and the static force equilibrium in the x and y directions, the maximum down push force that would cause the block to start sliding can be derived as follows.

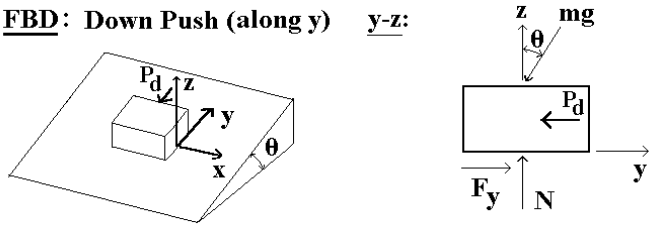

Fig. 1.44 Slipping on an Incline due to Down Push

$$\Sigma F_y = 0: \quad -P_d + F_y - mg\sin\theta = 0,$$
$$\Sigma F_z = 0: \quad N = mg\cos\theta$$
$$\textit{where} \quad F_y = \mu N = \mu\, mg\cos\theta, \quad P_d = mg(\mu\cos\theta - \sin\theta) \tag{1.26}$$
$$\textit{For} \quad P_d \geq 0, \quad \textit{then} \quad \mu \geq \tan\theta$$

From the solutions for P_s and P_d above, the relationship between them can be obtained and is shown as follows:

$$P_d = P_s\sqrt{\frac{\mu\cos\theta - \sin\theta}{\mu\cos\theta + \sin\theta}} \tag{1.27}$$
$$\textit{Since} \quad \sqrt{\frac{\mu\cos\theta - \sin\theta}{\mu\cos\theta + \sin\theta}} \leq 1, \quad \textit{one gets} \quad P_d \leq P_s$$

Given a coefficient of friction, μ, and an inclination angle, θ, it can be concluded that
(1) $P_d < P_s$ for $0 < \theta < \theta_r$ where θ_r(angle of repose)$= \tan^{-1}\mu$
(2) $P_d = P_s$ for $\theta = 0$ and $\theta = \theta_r$

The relationship $P_d \leq P_s$ can also be verified by the curves shown for the side and down pushes shown in Fig. 1.45.

Special Cases: (1) for no inclination, $\theta = 0$, the normalized push P/W (where W=mg) is equal to the coefficient of friction, μ (i.e., P/W = .9 for both side push and down push when $\mu = 0.9$ shown in the plot); (2) for no normalized push, P/W = 0, then the inclination angle, θ, is equal to the angle of repose, $\tan^{-1}\mu$ (i.e., for $\mu = 0.9$, $\theta = \tan^{-1}\mu = 42$ deg. shown in the plot).

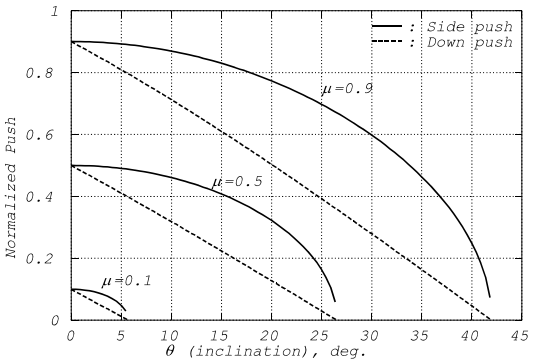

Fig. 1.45 Normalized Push to Slide on an Incline

1.4.4 Calculation of Safe Distance for Following Vehicle

Use the kinematic relationships and derive the formula below for the safe distance as a function of initial velocities and decelerations of both leading and following vehicles [10,11].

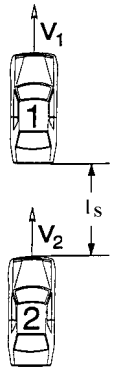

$$l_s = \frac{1}{2b_2}v_2^2 - \frac{1}{2b_1}v_1^2 + v_2T_r$$

where

T_r : *Following driver's reaction time*

b_1, b_2 : *Deceleration rates*

l_s : *Safe distance*

(1.28)

Fig. 1.46 Safe Distance

The first term in the equation for l_s, based on the kinematic relationship (3) in Eq. (1.12), is the total braking distance required for the following vehicle, (2), to stop; the second term for the leading vehicle #1. The difference of the first two terms is then the minimum safe distance needed for no collision. The third term is the extra distance needed due to the reaction time of the driver in the following vehicle to apply his brakes.

Special Cases: If $v_1 = 0$, the minimum safe distance needed is the braking distance to stop for the following vehicle (the first term). If $v_1 = v_2$, and $b_1 = b_2$, the minimum safety distance is zero. (This excludes the reaction times of the drivers shown in Table 1.4.)

Table 1.4 Typical Braking Performances on Various Road Surfaces

Road Surface	Leading Vehicle Deceleration, b_1 m/s^2 (g)	Trailing Vehicle Deceleration, b_2 m/s^2 (g)	Reaction Time, T_R s
Dry	6.5 (.66)	6.0 (.61)	1.0
Wet	6.5 (.66)	5.5 (.56)	1.0
Ice	2.6 (.27)	2.0 (.20)	1.0

Case Study (Exercise): Radar Braking Kinematics

For a given set of initial traffic conditions:

1. Following Distance (ΔX), ft
2. Lead Vehicle Speed (V_L), mph
3. Following Vehicle Speed (V_F), mph
4. Lead Vehicle Deceleration (A_L), g
5. Following Vehicle Deceleration (A_F), g

Determine T, the time at which the following vehicle must brake to just avoid a crash, i.e., the two vehicles reach the same velocity at the same position. If a collision is inevitable, determine the speeds of the two vehicles and the time at collision.

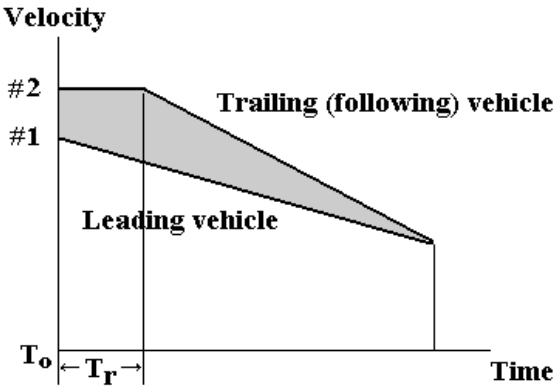

Fig. 1.47 Radar Braking Velocity Diagram

NOTES:

(1) Lead vehicle starts to brake at T_o

(2) T includes the radar warning time and reaction time of following vehicle driver before applying brakes

(3) Use the velocity diagram and derive a set of closed-form kinematic relationships to solve the problem

(4) There are four possible kinematic combinations:

Case 1: $V_L \preceq V_F$, $A_L \prec A_F$, Case 2: $V_L \preceq V_F$, $A_L \succeq A_F$

Case 3: $V_L \succ V_F$, $A_L \prec AF$, Case 4: $V_L \succ V_F$, $A_L \succeq A_F$

1.5 IMPACT AND EXCITATION: VEHICLE AND SLED TEST KINEMATICS

In a rigid barrier test, the vehicle is subjected to a direct impact and the occupant is then excited by the crash pulse of the passenger compartment. It is often more cost effective to test certain components (such as an air bag, belt and steering column restraint system, or instrument panel) on a Hyge sled than in a rigid barrier test. In a Hyge sled test, the sled is impacted on by an accelerator which produces a sled test pulse similar to the barrier crash pulse. The occupant is subsequently excited by the sled pulse. Since deceleration forward in the barrier test is equal to acceleration backward in the sled test, the effect of component design changes on the occupant responses can then be quickly evaluated using the sled test setup.

In this section, the basic kinematic relationships applicable to vehicle and occupant impact analysis are presented. The unbelted occupant kinematics in the vehicle compartment are analyzed for an air bag deployment decision in a crash. How the kinematic variables, such as energy density and its derivative, can be utilized in detecting an occupant crash severity for activating an air bag sensor is also covered.

1.5.1 Vehicle Kinematics in a Fixed Barrier Impact

The first and second integrals of the vehicle deceleration, a, are shown below. The initial velocity and initial displacements of the vehicle are v_o and x_o, respectively.

$$a = \frac{dv}{dt}, \quad dv = a\,dt, \quad \int_{v_o}^{v} dv = \int_{t_o}^{t} a\,dt, \quad v = v_o + \int_{t_o}^{t} a\,dt$$
$$x = x_o + v_o t + \int_{t_o}^{t}\int_{t_o}^{t} a\,dt\,dt, \quad Let\ x_o = 0, \quad then \quad x = v_o t + \int_{t_o}^{t}\int_{t_o}^{t} a\,dt\,dt \tag{1.29}$$

The longitudinal deceleration, a, measured at the Left/Rocker on the B-pillar of an aluminum intensive vehicle, in a 14 mph perpendicular barrier test, is shown in Fig. 1.48.

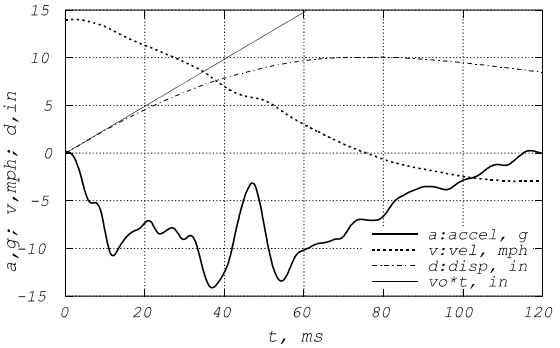

Fig. 1.48 Rocker B-Post Kinematics of a Mid-Size Car in a 14 mph Rigid Barrier Test.

Plotted along with the deceleration curve are the integrated velocity and displacement. The line segment tangent to the vehicle displacement curve at time zero is the free-flying displacement where the slope is the vehicle initial impact velocity, v_o. The maximum displacement of the vehicle (dynamic crush) is about 10 inches and occurs at 76 ms, as shown in Fig. 1.48. The vehicle stops against the barrier at the time of dynamic crush, then rebounds until it separates from the barrier at 115 ms. At the time of vehicle-barrier separation, the vehicle rebound velocity becomes constant over a small window of time and would remain constant if there were no external impulses acting on the vehicle. The vehicle rebound velocity (or separation velocity) in this test is −3 mph and the vehicle displacement at the separation time (static crush) is about 9 inches. Since the dynamic crush is 10 inches, the elastic rebound displacement (springback) of the vehicle structure (dynamic crush−static crush) is 10−9 = 1 inch. The coefficient of restitution (relative separation velocity / relative approach velocity) is 3/14 = 0.21.

In the fixed barrier test, vehicle speed is reduced (velocity decreases) by the structural collapse, therefore, the vehicle experiences a deceleration in the forward direction. To study the effect of vehicle deceleration on occupant-restraint performance in the laboratory, the crash pulse is duplicated on the sled. A schematic showing an accelerator which imparts the acceleration to the sled is shown in Fig. 1.49. Consequently, it can be stated that "deceleration forward in a barrier test is equal to an acceleration backward in a sled test." The sled test is more economical than the barrier test for studying the dynamic performance of occupant and restraint systems in an impact.

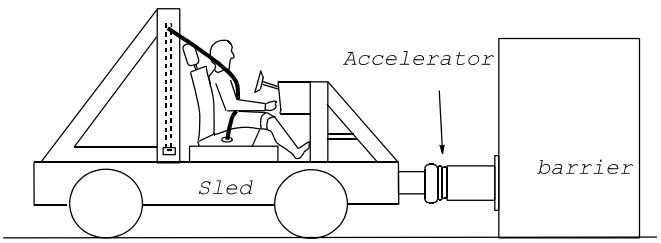

Fig. 1.49 Sled Test Set Up

1.5.2 Unbelted Occupant Kinematics

In a fixed barrier impact, the initial velocity of a free-flying occupant is constant, v_o. Therefore, the acceleration is zero (a_o = 0), and the free-flying displacement is equal to $v_o t$. The relative

kinematics of an unbelted occupant with respect to the vehicle are defined as follows.
a', v', x': Relative acceleration, velocity, and displacement of an unbelted occupant w.r.t. vehicle,
a, v : Vehicle acceleration and velocity, measured with respect to inertial frame (e.g., ground)

$$
\begin{aligned}
a' &= a(occupant) - a(vehicle) = 0 - a = -a \\
v' &= v_o - v = -\int_{t_o}^{t} a\,dt = \int_{t_o}^{t} a'\,dt \\
x' &= x_o - x = v_o t - x = -\int_{t_o}^{t}\int_{t_o}^{t} a\,dt\,dt \\
&= \int_{t_o}^{t}\int_{t_o}^{t} a'\,dt\,dt = \int_{t_o}^{t} v'\,dt
\end{aligned}
\tag{1.30}
$$

1.5.2.1 *Kinematics Based on Accelerometer Data*

The kinematic relationship between the unbelted occupant and the vehicle during a crash is expressed in the equations above. It should be noted that the magnitude of the unbelted occupant acceleration relative to the vehicle is equal to that of the vehicle deceleration. The kinematics of the unbelted occupant with respect to a vehicle in a 14 mph rigid barrier test is shown in Fig. 1.50.

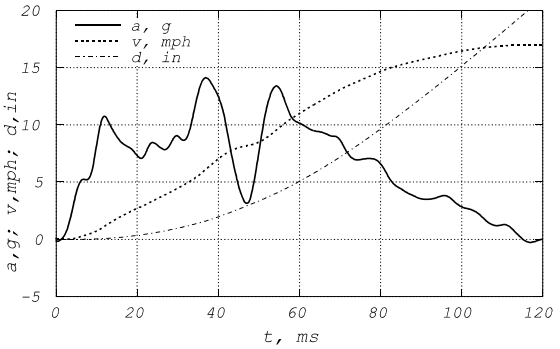

Fig. 1.50 Unbelted Occupant Kinematics in a Mid-Size Sedan 14 mph Barrier Test.

The differences between the barrier and sled test kinematic analysis are the sign of the acceleration and initial velocity. The vehicle velocity profile in the barrier test is then parallel to that in the sled test as shown in Fig. 1.51.

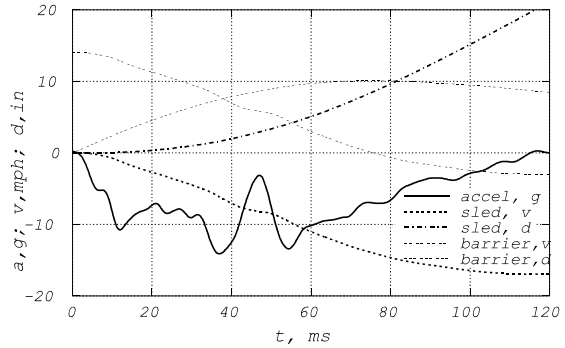

Fig. 1.51 Mid-Size Sedan 14 mph Rigid Barrier and Sled Test Kinematics

The kinematic relationships (deceleration, velocity, displacement) between the fixed barrier and sled tests are summarized as follows (for the in-depth analysis, see Section 4.2 of Chapter 4).

A: The sled pulse is the negative of the vehicle barrier crash pulse,

B: The sled velocity profile is a shifted barrier velocity curve, by the magnitude of the initial barrier impact velocity, v_o. At t_m , the time of dynamic crush, the sled velocity is equal to v_o. The magnitude of velocity change between time zero and t_m for both barrier and sled tests is v_o.,

C: The sled displacement at any time t is equal to $v_o t$ - d (free-flying occupant absolute displacement minus vehicle-barrier displacement in a fixed barrier test, see Fig. 1.52). The sled displacement at t_m is equal to $v_o t_m$ - c, where c is the vehicle dynamic crush in the barrier test.

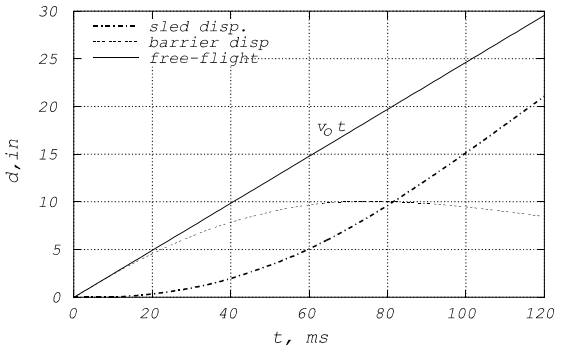

Fig. 1.52 Vehicle-Barrier 14 mph Crash and Sled (Occupant free-flight) Displacement

The sled displacement curve is useful in obtaining the timing, t, when the sled or unbelted dummy moves a displacement of d; or obtaining the displacement when the time, t, is given. For example, it would take an unbelted dummy 60 ms to move 5 inches in a 14 mph mid-size sedan to barrier test. Therefore, according to the 5"–30 ms criterion, an air bag sensor system would need to activate at 60–30 = 30 ms after impact.

Assuming that the distance between the hub of steering wheel to the torso of the occupant is 15 inches, as shown in Fig. 1.53, the torso-hub contact time is about 100 ms and the relative contact velocity is about 16.5 mph. At the time of hub contact, the unbelted occupant is still accelerating w.r.t. the vehicle (a') at –3 g as shown in Fig. 1.51. Since the vehicle rebounds (v = 0) at 76 ms where the torso relative velocity, v', is 14 mph, the torso contacts the hub during the rebound phase of the vehicle. Therefore, the torso-hub contact velocity in this test is greater than the initial vehicle impact velocity of 14 mph due to vehicle rebound. The 14 mph rigid barrier test is a threshold test condition where an air bag deployment is warranted since there is an injury potential to an unbelted occupant in a frontal crash at this speed or higher speeds [6].

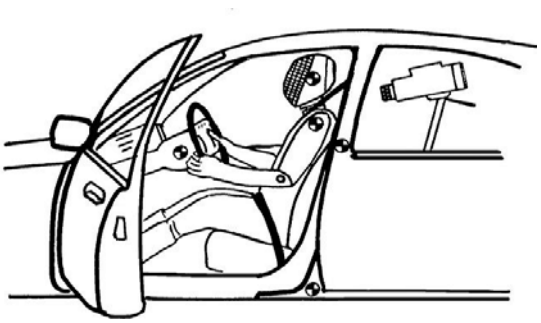

Fig. 1.53 Dummy Seating Position

1.5.2.2 *Kinematics Based on Crash Film Records*

The kinematic analysis of an unbelted crash dummy in a mid-size car in a 14 mph rigid barrier test is compared to that based on accelerometer data. The relative displacements of the head and shoulder targets w.r.t. the target on the rocker at B-pillar are shown in Fig. 1.54. The two curves are fairly close to each other due to the free-flight motion of the unbelted dummy. However, due to seat friction and minor resistance acting on the lower extremities, the upper body has a small amount of pitching motion and moves a little bit ahead of the shoulder after 60 ms. This timing from crash film analysis agrees fairly well with that obtained from the double integral of the accelerometer signal shown in Fig. 1.50.

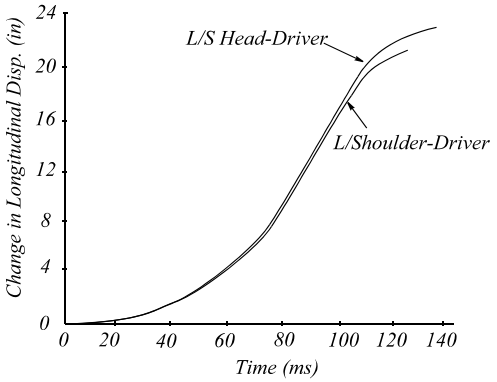

Fig. 1.54 Unbelted Driver Motion from Crash Test Film

1.5.2.3 *Vehicle Crush, Sled Displacement, and Crash Pulse Centroid*

It will be shown that at any given time, the sum of the vehicle displacement and the corresponding sled displacement (or unbelted occupant relative displacement to vehicle) equals the occupant free-flight distance. This is evident from Eq. (1.30) in that $x + x' = v_o t$, where x is the vehicle displacement (crush), x' is the sled displacement, and $v_o t$ is simply the occupant free-flight displacement. Fig. 1.55 shows the relationship between the vehicle crush, sled displacement, and crash pulse centroid.

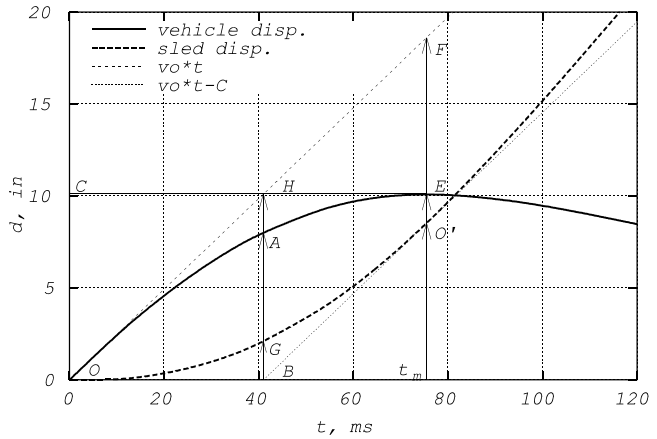

Fig. 1.55 Vehicle Crush, Sled Displacement, and Centroid

The dynamic crush of the vehicle at t_m is C = 10.1 inches and the sled displacement is 8.5 inches; these add up to 18.6 inches, the occupant free-flight displacement as shown by point F. Since the vehicle stops momentarily at t_m (= 76 ms, at point E), the corresponding occupant relative velocity at

t_m is then the same as the initial impact velocity. Since line segment O′B is a tangent to the sled curve OGO′ at O′, and line segment OHF is a tangent to the curve OAE at O, the two line segments O′B and OHF are parallel.

The horizontal intercept, H, of line segment CE (dynamic crush) and the slope (initial velocity), OF, tangent to the vehicle displacement at time zero, is the area centroid of the crash pulse. It is shown in Chapter 2 that the intercept, B, of the tangent O′B and the zero displacement reference axis is also the centroid time. The shape of a crash pulse is mainly controlled by the relative centroid location which is the ratio of centroid time, t_c, to the time of dynamic crush, t_m.

The point E on the vehicle displacement curve is where the vehicle dynamic crush occurs and the corresponding point on the sled displacement curve is O′ at t_m. It will be shown in Chapter 2 that in general, points E and O′ do not coincide. In other words, vehicle dynamic crush does not equal the sled displacement at t_m . Points E and O′ will coincide only when the crash pulse is symmetrical at its centroid location. Crash pulses such as square, halfsine, haversine, and symmetrical triangular pulses are examples of pulses where points E and O′ coincide. Recognition of such a special condition makes the impact analysis easier. The severity of headform impact in terms of head injury criteria (HIC) will be covered at the end of Chapter 2. The analysis is made easier because only the displacement change of a symmetrical crash pulse, such as a halfsine pulse, is needed.

In summary, use of crash film digitized data of the unbelted occupant displacement relative to the vehicle (or the sled displacement with zero initial velocity) provides more than just the occupant/sled displacement information. It also provides the vehicle transient kinematics such as the displacement, velocity, relative centroid location, and crash pulse shape.

1.6 VEHICLE AND OCCUPANT KINEMATICS IN FIXED OBJECT IMPACT

The vehicle and occupant kinematics using various threshold speeds and impact modes are compared. Two of the modes are rigid barrier tests, one at 8 mph and one at 14 mph, and one mode is a rigid pole test at 21 mph for a full-size passenger car. The objective is to evaluate the occupant-vehicle impact severity in a crash where an air bag deployment decision is to be made. Shown in Table 1.5, the 14 mph rigid barrier and 21 mph pole tests are for an air bag "must deploy" test condition, while the 8 mph test is a "must not deploy" condition.

Table 1.5 Air Bag Deployment Threshold Tests

Vehicle Test	Impact Speed/Mode
C1	14 mph perpendicular barrier
C2	8 mph perpendicular barrier
C3	21 mph center pole

1.6.1 Vehicle Kinematics in Different Test Modes

Three crash tests (C1, C2, C3) involving a full-size passenger car in an 8 and 14 mph perpendicular rigid barrier test and in one 21 mph center pole test were made in order to compare the vehicle kinematics for a fixed object impact. The compartment crash pulses obtained from the three tests are shown in Fig. 1.56. The crash pulse duration for the 8 and 14 mph rigid barrier tests are about the same, 125 ms, while that for the 21 mph pole test is about 170 ms. This duration is longer due to the softer localized impact. The times of dynamic crush (the maximum crush during collision) for the three tests can be found from the velocity and displacement curves shown in Figs. 1.57 and 1.58. These are about 80 ms for the barrier tests and 140 ms for the pole test. For a given vehicle structure, the crash pulse duration, and time of dynamic crush depend greatly on the crash mode. For a given impact mode, these timings do not vary significantly with the initial impact velocity.

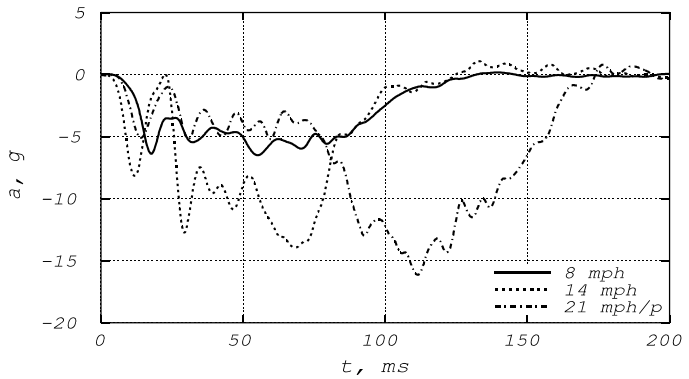

Fig. 1.56 Vehicle Deceleration in Two Barrier and One Pole (21mph) Crash Tests

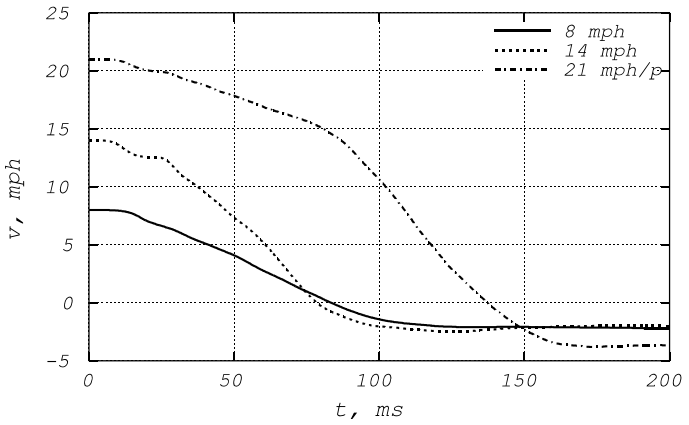

Fig. 1.57 Vehicle Velocity vs. Time in Three Crash Tests

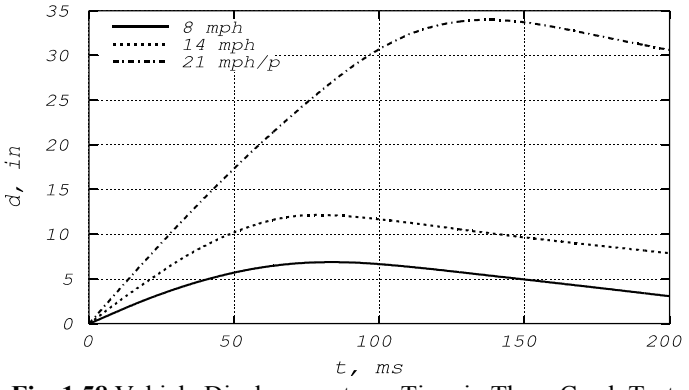

Fig. 1.58 Vehicle Displacement vs. Time in Three Crash Tests

1.6.2 Vehicle Energy Density

The energy density (e = energy/mass) of a vehicle during a crash can be computed by integrating the accelerometer data, given an initial velocity. The energy density at the time of dynamic crush can then be expressed as $e = .4\ v^2$, where the unit of e is g-in, and v, mph. The formula is derived as follows.

$$
\begin{aligned}
&\textit{Given:}\quad e = \int_{v_o}^{v} v\,dv = \frac{1}{2}(v^2 - v_o^2)\\
&\textit{At the time of dynamic crush:}\quad v = 0,\quad \textit{then}\quad e = -0.5\ v_o^2\\
&\textit{For the units:}\quad e\textit{: g-in,}\quad v\textit{: mph,}\quad a\textit{: g,}\quad \textit{and}\quad x\textit{: in}\\
&\textit{then}\quad e = -0.4\ v_o^2\\
&\textit{The slope on the e vs. d plot (Fig. 1.59) is}\\
&a = \frac{de}{dx}
\end{aligned}
\tag{1.31}
$$

Shown in Fig. 1.59, the energy density curve for the 8 mph test has only one slope, which is the average deceleration of the vehicle in that period. However, there exist two line segments for the 14 mph barrier and 21 mph pole tests. The slope of the second segment is higher than the slope of the first. Therefore, the vehicle experiences a low deceleration first and then a high deceleration later due to encountering higher structure and/or component resistance. Using the formula $e = .4\ v^2$, the total energy density for the 8, 14 mph rigid barrier, and 21 mph rigid pole tests are 25.6, 78.4, and 176.4 g-in, respectively. The computed values based on the formula agree fairly well with those maximum energy densities at the test dynamic crush shown in Fig. 1.59.

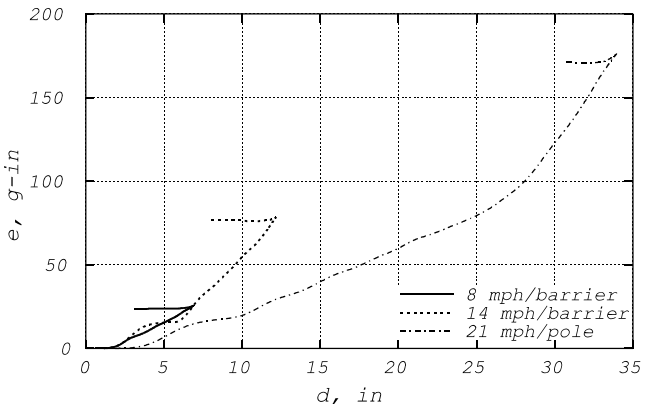

Fig. 1.59 Vehicle Energy Densities in Three Crash Tests

In a localized impact test where a passenger car was crashed at a speed of 21 mph into a rigid pole, the pre- and post-test kinematics of the engine compartment are shown in Figs. 1.60 and 1.61. The engine bottoms out on the pole and the total vehicle crush is 34 inches with a total energy density, $e = 0.4\ v^2 = 0.4 \times (21\ \text{mph})^2 = 176.4$ g-in. The pole starts interacting with the engine block at about 27 inches of penetration, where the vehicle deceleration magnitude (slope of a point on e vs. x), a, increases from 4 to 14 g. The vehicle energy density in the pole test shown in Fig. 1.59 increases from zero at 4 inches and reaches 90 g-in at about 27 inches. Therefore, the slope of the first segment of the e vs. x curve is $90/(27-4) \doteq 4$ g.

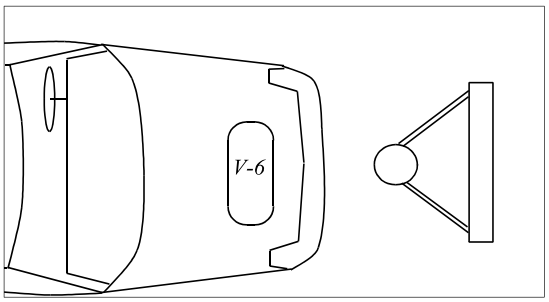

Fig. 1.60 Vehicle Front Center Pole Test Set-up

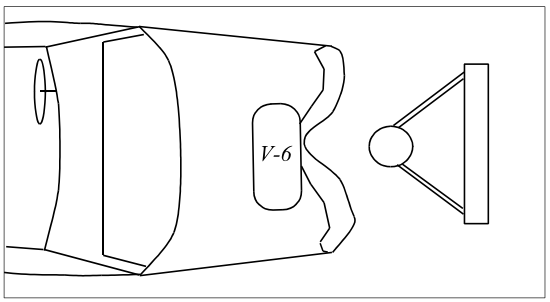

Fig. 1.61 Vehicle Front Center Pole Post Test

Based on the 21 mph pole test, where the air bag system is designed to deploy, the energy density curve can be used to interpolate the threshold test speed at which air bag deployment is not warranted. At this threshold speed, the engine is not expected to bottom-out on the rigid pole; therefore, the vehicle deceleration will not exceed 4 g, the initial slope of the energy density curve in the 21 mph pole test. At this low vehicle deceleration level, air bag deployment is not warranted. Since the end of the 4-g segment of the curve ends at about 25 inches without engine bottoming-out, the corresponding energy density is about 76 g-in. Therefore, in the rigid pole test, the air bag must-not-deploy test speed, v', can be computed as follows:

$$v' = \sqrt{\frac{e'}{.4}} = \sqrt{\frac{76\ g\text{-}in}{.4}} \doteq 14\ mph \tag{1.32}$$

1.6.3 Occupant Kinematics in Different Test Modes

Using an initial velocity of zero in integrating the passenger compartment accelerometer data, the free-flying occupant kinematics w.r.t. the vehicle is obtained, as shown in Figs. 1.62 and 1.63. Using the crash data for a full-size passenger car in 8 and 14 mph perpendicular rigid barrier tests and one 21 mph center pole test, the v-x plots show the unbelted occupant velocity w.r.t. the vehicle before contacting the vehicle interior surface such as steering wheel/hub or instrument panel. The total velocity change of the unbelted occupant in the 8 mph test is about 10 mph. This is due to a vehicle rebound velocity of 2 mph. The vehicle momentarily stops against the barrier when the occupant has moved about 5 inches and his velocity is 8 mph. After that, the vehicle rebounds from the barrier at 2 mph. The 8 mph rigid barrier test is considered to be an air bag must-not-deploy condition. The overall velocity changes of the 14 mph rigid barrier and 21 mph pole are larger than that in the 8 mph test. Therefore, the 14 mph rigid barrier test and 21 mph pole are considered to be

an air bag "must deploy" condition. Note that in the period when the unbelted occupant moves less than 5 inches, he moves at a slower velocity in the 21 mph pole test than in the 8 mph rigid barrier test. After that, the occupant picks up a higher speed in the 21 mph pole test than in the 8 mph test. This is due to the engine bottoming out on the rigid pole, which accelerates the occupant forward at a higher rate.

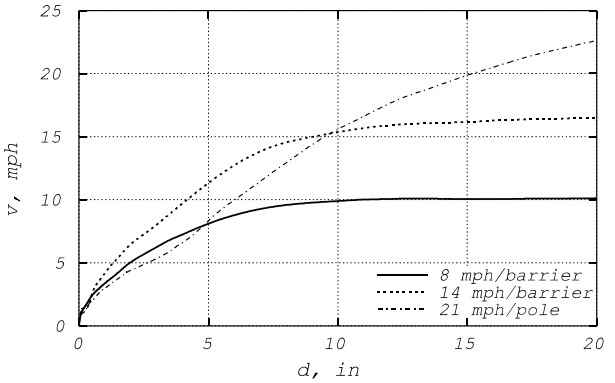

Fig. 1.62 Unbelted Occupant Velocity vs. Displacement in Three Crash Tests

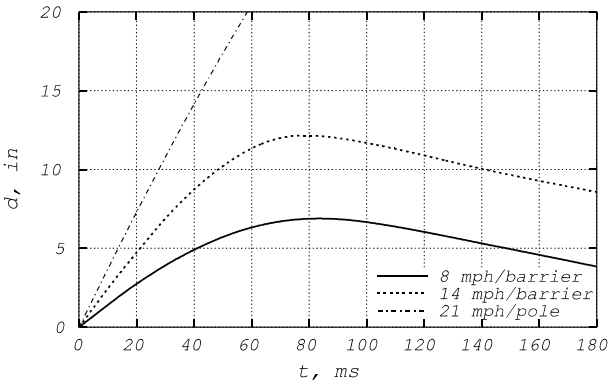

Fig. 1.63 Unbelted Occupant Displacement vs. Time in Three Crash Tests

As shown in the previous deceleration plot in Fig. 1.56, the deceleration magnitude in the 21 mph pole test is lower than that in the 8 mph rigid barrier test before the engine bottoms out at around 80 ms. At this time, the vehicle displacement (pole penetration) is 27 inches when the vehicle experiences a large jerk, a sudden deceleration.

Observing the v-d and d-t plots shown in Figs. 1.62 and 1.63 and at 10 inches travel (about 5 inches before impacting on the steering hub or at the midpoint of a fully deployed air bag), the unbelted occupant relative velocity in the 21 mph pole test (Fig. 1.62) is the same as that in the 14 mph barrier test. This observation applies equally well to a vehicle-to-vehicle offset testing. This velocity change at 10 inches of travel gives an indication that the unbelted occupant impact severity in both tests is about the same. Therefore, the 21 mph pole test is also considered as an air bag "must deploy" test.

1.7 KINEMATIC VARIABLES

A total of nine kinematic variables associated with a crash pulse are defined in Table 1.6. Since they are related to the particle kinematic responses, some have been used in crashworthiness studies, such as occupant-vehicle ridedown performance evaluations and air bag electronic crash sensing algorithm development.

Table 1.6 Kinematic Variables

Kinematic Variable	*Unit*	*Expression*
1. *Acceleration*	ft/s^2	$a = \frac{dv}{dt}$
2. *Velocity*	ft/s	$v = \int a dt = \frac{dx}{dt}$
3. *Displacement*	ft	$x = \int v dt = \int\int a dt dt$
4. *Jerk*	ft/s^3	$j = \frac{da}{dt}$
5. *Energy Density*	$(ft/s)^2$	$e = \int_{x_0}^{x} a dx = \int_{v_o}^{v} v dv = \frac{1}{2}(v^2 - v_0^2)$
6. *Energy*	$lb{\cdot}ft$	$E = \frac{1}{2} m (v^2 - v_0^2)$, m: *mass*
7. *Power*	$lb{\cdot}ft/s$	$\bar{p} = \frac{dE}{dt} = mva$
8. *Power Density*	ft^2/s^3	$p = \frac{\bar{p}}{m} = va$
9. *Power Rate Density*	$(ft/s^2)^2$	$p' = \frac{dp}{dt} = vj + a^2$

(1.33)

The closed-form expressions of the kinematic variables for some special pulses such as the square, haversine, and halfsine pulses shown in Fig. 1.64 are listed in Eq. (1.34). In one particular application, the crash pulse is mathematically represented by a Fourier series in halfsines (described in Chapter 2) with magnitudes associated with a multiple of the fundamental frequency. The closed-form expression for the halfsine wave power rate density (p.r.d.) offers an effective way of computing the p.r.d. of an entire crash pulse without using numerical integrations. Representing a crash pulse by p.r.d. serves to discriminate the crash severity of a vehicle in a crash.

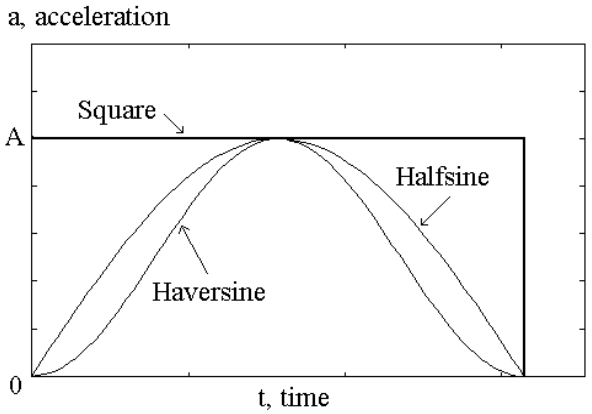

Fig. 1.64 Special Pulses

$$
\begin{aligned}
&\textit{Square: } a = A \ (\textit{constant}) \\
&v = At \\
&j = 0 \\
&p' = vj + a^2 = A^2 \\
&\textit{Halfsine: } a = A \sin \omega t \\
&v = \frac{A}{\omega}(1 - \cos \omega t) \\
&j = A\omega \cos \omega t \\
&p' = vj + a^2 = A^2 \left[1 + \cos \omega t (1 - 2\cos \omega t)\right] \\
&\textit{Haversine: } a = \frac{A}{2}(1 - \cos \omega t) \\
&v = \frac{A}{2}\left(t - \frac{\sin \omega t}{\omega}\right) \\
&j = \frac{A}{2}(\omega \sin \omega t) \\
&p' = vj + a^2 = A^2 \left[\frac{\omega \sin \omega t - 2\cos \omega t (1 - \cos \omega t)}{4}\right]
\end{aligned}
\tag{1.34}
$$

The power rate density (p.r.d.), kinematic variable #9 in Table 1.6, has been used in the development of the single point sensing algorithm [12]. A modified version of kinematic variable #5, residual energy density (r.e.d.) in the displacement domain, has been shown to be simple and effective in analyzing air bag deployment. This is because the r.e.d. describes the energy distribution as a function of the displacement of a free-flying body (unbelted occupant) in the vehicle compartment [13].

1.7.1 Use of Residual Energy Density in Air Bag Sensor Activation

The method using residual energy density (r.e.d.) in air bag deployment applications [13] is described as follows. The term residual refers to the portion of energy density content above a certain acceleration level, a bias g, at the single-point sensing (SPS) location.

Bias g, Residual Energy Density and Threshold Window (Fig. 1.65):

$$
\begin{aligned}
&\textit{Differential energy density: } a\,dx = v\,dv \\
&\textit{Define:} \\
&e = \textit{energy density (energy per unit mass)}, \\
&b = \textit{constant bias g}, \\
&\textit{r.e.d.} = \textit{residual energy density then}
\end{aligned}
\tag{1.35}
$$

$$
\begin{aligned}
&e = \int a\,dx = \int v\,dv, \ \textit{For } v_o = 0 \textit{ and } x_o = 0 \quad \textit{at } t = 0 \\
&e = \int_0^x a\,dx = \int_0^v v\,dv = \frac{v^2}{2} \\
&r.e.d. = \int_0^x (a - b)\,dx = \int_o^x a\,dx - \int_o^x b\,dx = \frac{v^2}{2} - bx \\
&\textit{Note: } v = \int a\,dt, \quad \textit{and} \quad x = \int v\,dt = \iint a\,dt\,dt
\end{aligned}
\tag{1.36}
$$

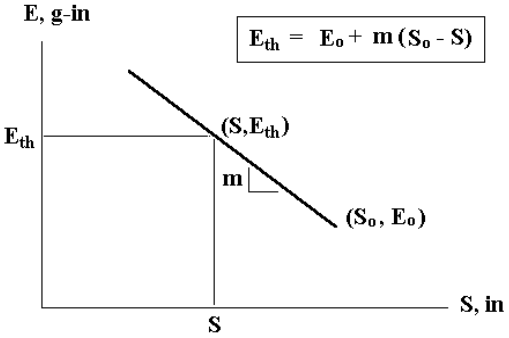

Fig. 1.65 Sensor Activation Threshold Window

A threshold window, a slanted line segment, as shown in Fig. 1.65, is set up with a starting point (defined by a displacement S_o and r.e.d. E_o) and a slope m on the r.e.d. (E, g-in) vs. displacement plot. As the r.e.d. is computed at time t, it is checked for the intersection with the window. When intersection occurs, the air bag sensor system is activated. The window is positioned and tilted in such a way that (1) The r.e.d. curve for the must-not-activate test condition stays below the window, and (2) The r.e.d. curve for the must-activate condition intersects the window at a time no later than that specified by the sensor design criterion as described in Section 1.7.2.

An algorithm [13] based on r.e.d. is shown in the flow chart, Fig. 1.66.

1.7.2 Time Requirement for Air Bag Sensor Activation

For a test condition where an air bag deployment is warranted, the desired sensor activation time is determined by the relative travel (displacement) of an unbelted occupant in the compartment. The computation of sensor activation time is based on the assumption that (1) an unbelted occupant moves forward 5 inches in the compartment before the air bag is fully deployed, (2) the time to fully inflate the air bag is 30 ms, (3) the depth of the fully deployed air bag is 10 inches, and (4) the initial distance between the torso and the steering hub where the air bag is packaged is 15 inches. This method of computing the desired sensor activation time is often referred to as the '5"–30 ms' criterion. This criterion is designed to protect an unbelted occupant from moving into the zone of a deploying air bag in a crash where the air bag deployment is warranted. The occupant free movement zone without interacting with the deploying air bag is then 15 in – 10 in = 5 in.

From Fig. 1.52, the displacement plot of an unbelted occupant in a 14 mph rigid barrier impact, the occupant has traveled 5 inches in the compartment at 60 ms. According to the '5"–30 ms' criterion, the desired sensor activation time is then equal to 60 ms–30 ms = 30 ms.

1.7.3 Vehicle-Occupant-Restraint (VOR) Interaction

In a vehicle crash test, the restraint system couples the vehicle and occupant dynamic responses. Fig. 1.67 shows the VOR interaction in a test where the vehicle is equipped with an air bag and a belt. In a moderate to severe impact, sensors close causing the inflator to ignite and the air bag to be inflated. After inflation, gas is vented through the openings in the air bag. In a ruling by the National Highway Traffic Safety Administration (NHTSA), a regulation permits automobile manufacturers to test a depowered air bag restraint system using a Hyge sled. An accelerator impacts on the sled and imparts a generic halfsine pulse with a peak magnitude of about 17.5 g and duration of 120 ms. The generic sled pulse simulates a crash with a total velocity change of about 30 mph. In a depowered air bag system, both inflation pressure and mass flow rate are less than those in a full-powered air bag.

SPS Crash Algorithm Flow Chart

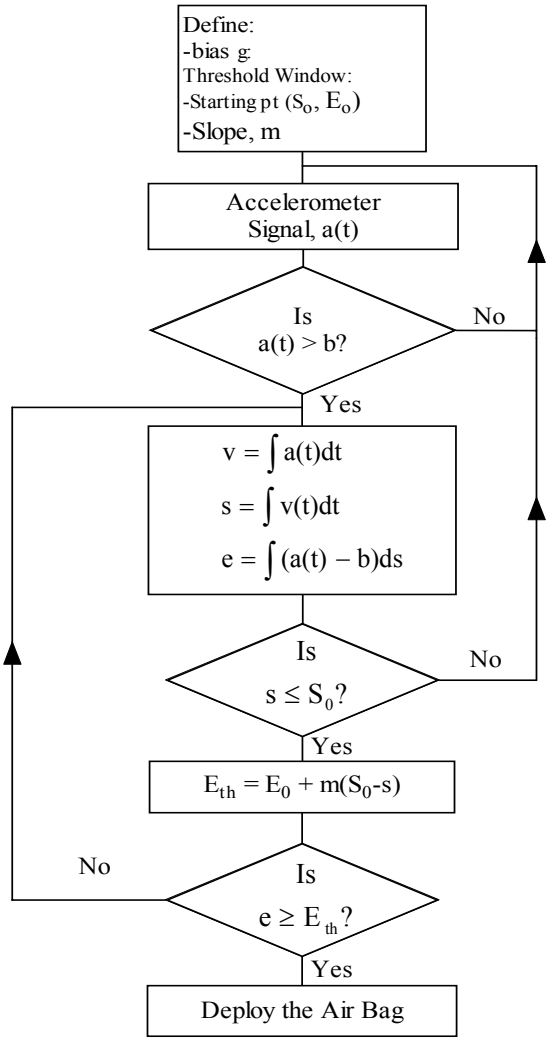

Fig. 1.66 A Single Point Crash Sensing Algorithm

However, the effectiveness of a driver-side air bag restraint system also depends on the design of the steering column system. A steering column absorbs a portion of driver's impact energy while it strokes several inches with a loading of about 900 lb. force in a high speed frontal impact. The steering column may be pushed rearward and then rotated upward due to dashboard intrusion. In such a case, the steering column does not stroke as effectively as intended which may result in a high loading on the torso.

A detailed analysis of the VOR interaction is presented in Section 1.9. The concepts of restraint coupling, occupant response, and ridedown efficiency are covered.

A real world accident involving a full-size sedan impacting a tree is analyzed in the next section. Since the vehicle was equipped with a crash event data recorder (flight recorder), the kinematic analysis of the crash pulse downloaded from the flight recorder was performed in both time and frequency domains.

Vehicle, Occupant, and Restraint Interaction in a Sedan Equipped with an Air Bag and a Belt at 35 mph Barrier Impact

t = 0 ms Bumper contacts barrier	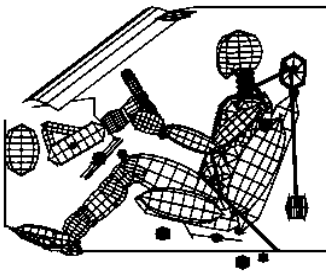
t = 20 ms Front crash sensor activated at t=17 ms; 3 ms later, air bag deployment door bursts open. Air bag is being inflated.	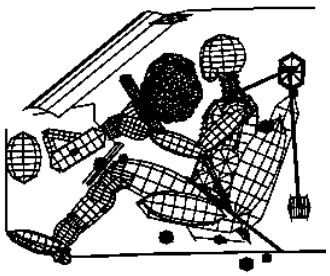
t = 50 ms Air bag fully inflated at 47 ms (full inflation time of 30 ms plus sensor activation time of 17 ms)	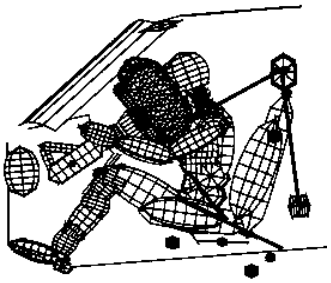
t = 80 ms Air bag is deflating and cushioning the head and torso.	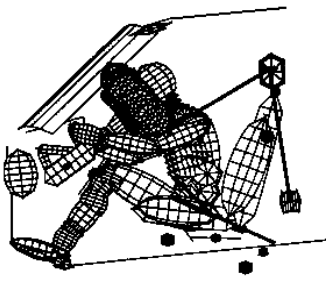

Fig. 1.67 Air Bag Deployment Sequence

1.8 CASE STUDY: SINGLE VEHICLE-TREE IMPACT ACCIDENT

A late 1990 model year full-size passenger car (case vehicle), shown in Fig. 1.68, equipped with a depowered air bag restraint system and a "flight recorder" was involved in a tree impact accident. The vehicle, driven by a 20th percentile female, inadvertently hit a street curb and then struck a tree in a residential neighborhood on a sunny morning as shown in Fig. 1.69. The road was clear and dry but curved. Part of the wheel rim was stripped and the side wall of the tire was punctured which resulted in a flat tire. Subsequently, the right tire and wheel, pushed back by the tree, left a tire imprint on the inner plastic of the right front wheel well.

Fig. 1.68 The Car and Right Front Damage

Fig. 1.69 The tree

Fig. 1.70 The Driver and Bags

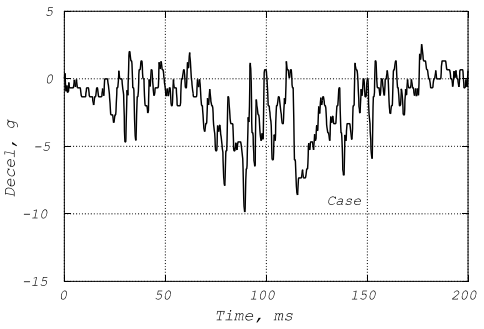

Fig. 1.71 Vehicle Deceleration vs. Time from Flight Recorder (Sampling Rate = 2k Hz)

The impact activated the air bag electronic crash sensor (ECS) inside a diagnostic control module located on the right side near the A-pillar and floor. Subsequently, both the driver and passenger side air bags deployed as shown in Fig. 1.70. The driver sustained no injuries. However, her right hand received a minor abrasion and her left lower arm had a bruise due to impacting with the side door trim panel as a result of air bag deployment. Her eyeglasses were knocked off by the air bag and fell to the floor in front of the front passenger seat.

1.8.1 Analysis of the Recorder Crash Data

The information from the flight recorder indicated that the electro-mechanical crash sensor (ball-in-tube sensor) located at the top center of the radiator bracket support was not activated. Therefore, the activation of the ECS resulted in the air bag deployment. The recorded crash data (deceleration vs. time), which was internally filtered in the control module at a cutoff frequency of about 400 Hz and sampled at a rate of 2000 Hz, is shown in Fig. 1.71.

The crash data of the case vehicle were compared with that of crash data for the similar type of vehicle tested at the threshold conditions (see Table 1.7). The crash data from two rigid pole tests conducted at low speeds are shown in Fig. 1.72. Test # 1, where the right front of the subject vehicle hits the pole at 10 mph, is judged to be a must-not-activate condition, while Test #2, front center of the vehicle hitting the pole at 23 mph, is a must-activate condition.

For comparing signals, all the crash pulses were filtered by a Butterworth 2nd order filter with a cutoff frequency of 100 Hz. The impact severity of the case vehicle is closer to Test # 1 than Test #2 as shown by the deceleration plots in Fig. 1.73. The response of a similar full-size car struck by a mid-size car head-on at a relative speed of 38 mph (Test #3) is shown in Fig. 1.74. Although the case vehicle response is less severe than the subject vehicle in Test #3, the pulse shapes are approximately proportional and the jerks are about the same at times up to about 110 ms when rebound occurs.

Table 1.7 Case Vehicle and Other Vehicle Test Conditions

Vehicle	Description	Note
Case	Tree impact accident (car hit the right curb, then a tree, on a curved street)	Control module on right cowl side (A-pillar) contains electronic crash sensor and flight data recorder
Test #1	10 mph right pole	Sensor must not activate
Test #2	23 mph center pole	Sensor must activate
Test #3	38 mph car-car	Sensor must activate
Test #4	14 mph fixed barrier	Sensor must activate

The velocity and displacement changes of an "unbelted occupant" in time and displacement domains are shown in Figs. 1.75–1.77. Based on the velocity change, the case vehicle accident is the least severe of all the cases considered. The relative velocity changes of the unbelted occupants at 10 inches compartment travel are less than 14 mph, a velocity change at that reference point where an air bag deployment is desired. In the case vehicle, the longitudinal velocity change is about 7.5 mph. By estimating the angle of the principal direction of force (PDOF) from the longitudinal axis to be about 45°, the case vehicle-tree impact velocity is then computed to be $V_o = 7.5/\cos(45°) = 10.6$ mph. Considering the posted speed limit of 25 mph, the case vehicle can be judged to be traveling below the speed limit. Since Test #1 is a must-not-activate condition, the case vehicle accident did not necessarily require the air bags to deploy. Considering the belt usage by the driver and the low speed impact, the air bag deployment decision by the ECS is not warranted.

The impact severity at the sensor location is mainly responsible for the deployment of the air bag. The effect of the off-center (not along the vehicle center line through C.G.) impact on the off-center crash sensing is covered in Section 6.4 of Chapter 6 on the circle of constant acceleration (COCA).

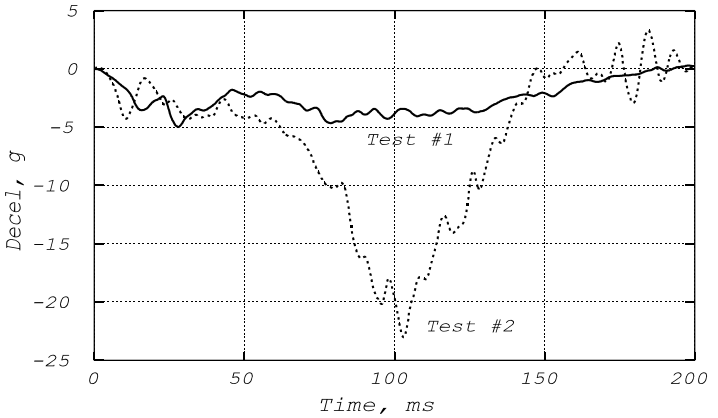

Fig. 1.72 Deceleration vs. Time for Low (Test #1) and High (Test #2) Speed Pole Tests

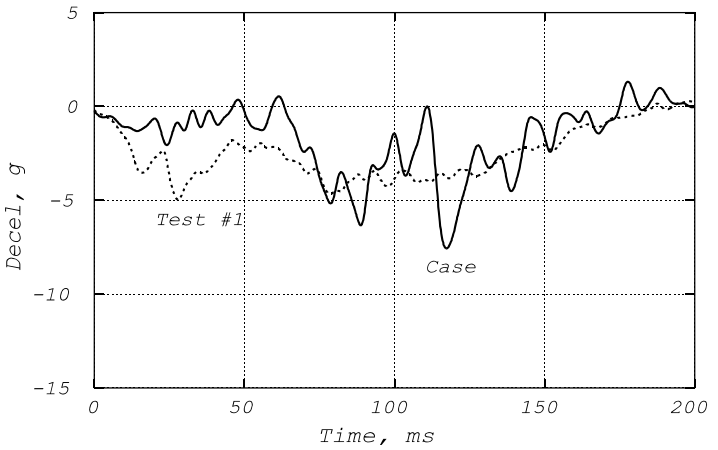

Fig. 1.73 Deceleration Comparison of Case and Test #1 Vehicles

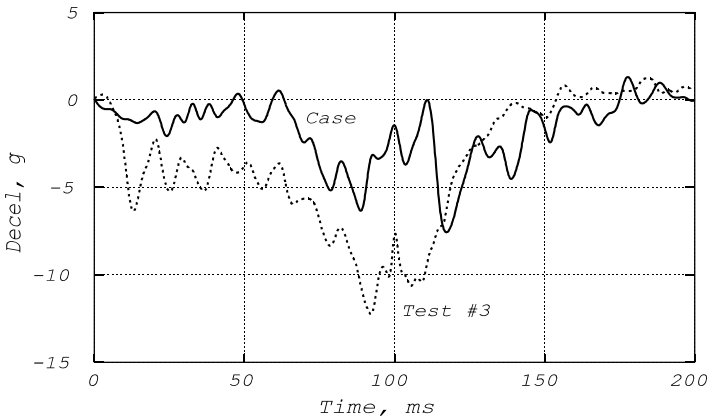

Fig. 1.74 Deceleration Comparison of Case and Test #3 (High Speed Car-Car) Vehicles

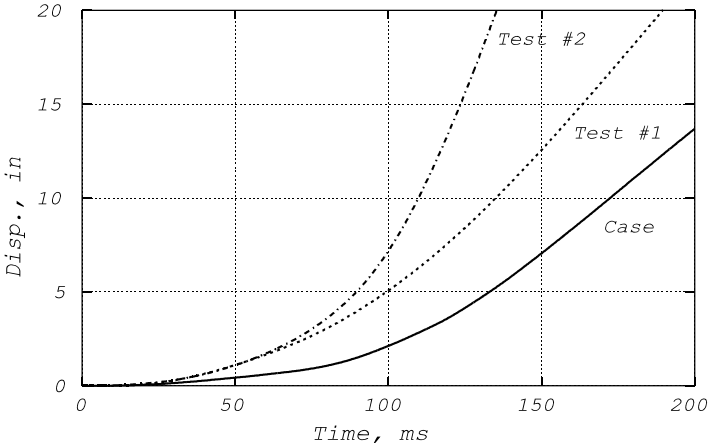

Fig. 1.75 Unbelted Occupant Displacement vs. Time

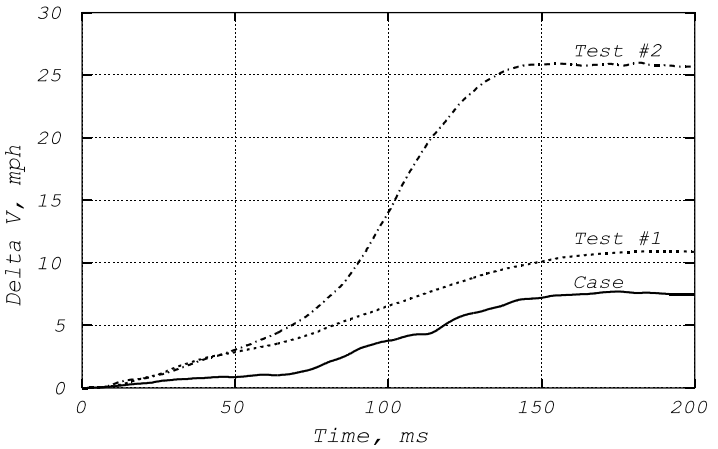

Fig. 1.76 Unbelted Occupant ΔV vs. Time

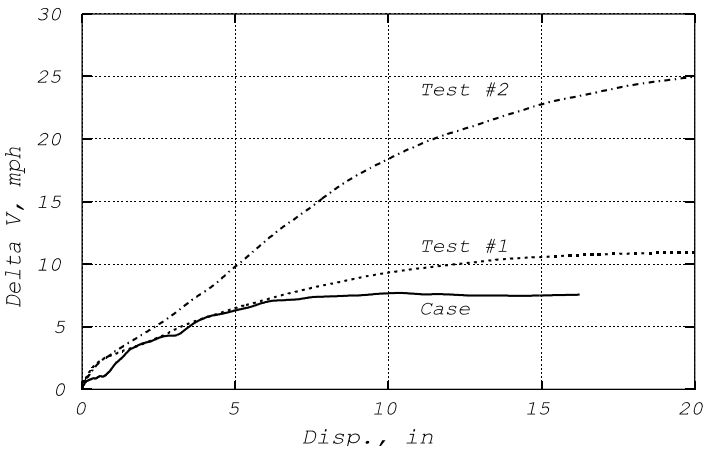

Fig. 1.77 Unbelted Occupant ΔV vs. Displacement

1.8.2 Frequency Spectrum Analysis for Electronic Crash Sensing

Using a Fourier frequency spectrum analysis technique (covered in Section 2.4.1 of Chapter 2), the spectra at the right A-pillar cowl side sensor locations in the crash of the case vehicle and the Test #3 and #4 vehicles were compared and are shown in Fig. 1.78. Test #4, a 14 mph full frontal rigid barrier test, has the largest power spectrum magnitude, reflecting the intensity of impact; it is the largest among the three vehicles. This is due to the fact that the effective stiffness of the vehicle in Test #4 and the deceleration levels are higher than those involved in the localized impacts such as for the case and Test #3 vehicles.

The spectrum magnitudes of the case and Test #3 (car-to-car impact at 38 mph) are almost identical beyond the frequency of 20 Hz. This explains the high frequency pulse shape similarity between the two vehicles shown by the deceleration plots in Fig. 1.74. For frequencies below about 15 Hz, which includes the fundamental and the first few multiples of the fundamental frequency, Test #3 has a higher spectrum magnitude than the case vehicle which can be visualized from Fig. 1.78. Therefore, the deceleration magnitude and crash severity of the subject vehicle in Test #3 is also higher than those of the case vehicle.

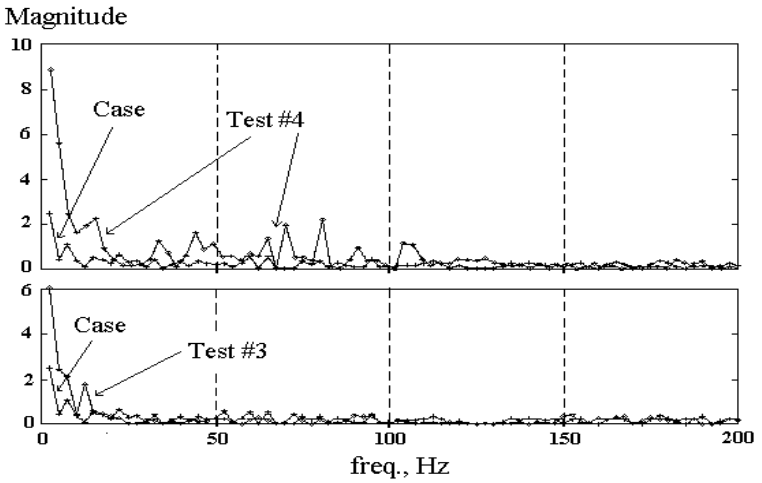

Fig. 1.78 Fourier Power Spectrum of the Case, Tests #3 and #4

An electronic crash sensing algorithm can be implemented to count the number of oscillations of a crash signal in a fixed time interval. It is equivalent to comparing the frequency content to a reference value. However such an algorithm is not sufficient to discriminate the impact severity of a crash between the case and Test #3 vehicles. An crash sensing algorithm developed to tackle such a frequency similarity problem can be found in a patent.[2/] The Polynomial Windowing Algorithm was originally developed to discriminate the side impact condition where the frontal air bag deployment in a side struck vehicle is not warranted. In such a condition, the longitudinal velocity change is below the deployment threshold but the frequency and magnitude of the crash pulse are high due to impulsive loading. The impulsive loading at the onset of a crash is more prevalent in a body-on-frame vehicle than the unitized-body vehicle. This is mainly attributed to the dynamic characteristics of the body mounts in transmitting the frame impulse to the body where the ECS module is located (see Section 2.4.6 of Chapter 2 on body mount attenuation).

[2/] U.S. Patent No.5948032: "Polynomial Windowing Algorithm for Impact Responsive Activation," Matthew Huang and Parag Jitendra Parikh, Sept. 7, 1999.

1.8.3 Application of a Residual Energy Density Algorithm

The algorithm based on the integral of deceleration in the displacement domain yields the energy density. As described in previous sections in this chapter, a residual energy density (r.e.d) algorithm with zero bias g was tested for five impact conditions including the case vehicle accident and Test #4 where a similar car (C5) struck a rigid barrier at 14 mph. Fig. 1.79 shows the deployment window which determines the activation timings when the r.e.d. curves of Tests #2, #3, and #4 intercept the window. Since the r.e.d. curves of the case vehicle and Test #1 did not intercept the window, no sensor activation is expected. The activation timings shown by the r.e.d. algorithm satisfy the 5"–30 ms requirements for those cases which can be checked by the displacement vs. time curves in Fig. 1.75. Note that using a bias of 2 g's would yield the same results.

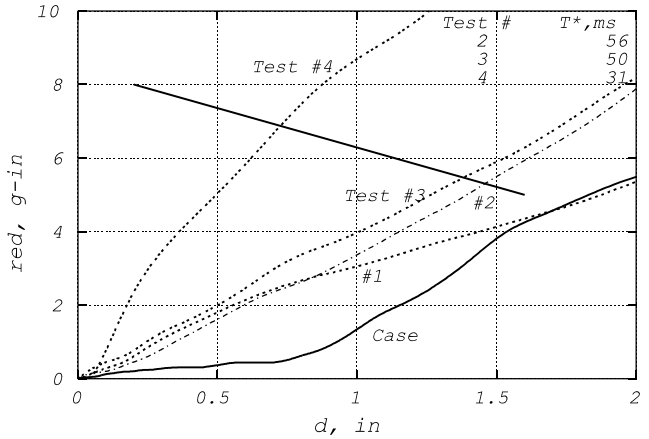

Fig. 1.79 Residual Energy Density (red) vs. displacement

1.9 RESTRAINT COUPLING

In a crash test, accelerometers are installed on both vehicle structural components and occupant body segments to record their dynamic responses during the crash events. The recorded data are then used to analyze the occupant energy distribution during the crash. The effectiveness of the restraint system in coupling the vehicle and occupant responses has been presented in the previous sections using the occupant restraint and ridedown energy densities. To further understand the characteristics of the restraint system, which acts as a transfer function between the vehicle and occupant, a simple model with a constant spring stiffness, K, and restraint slack, δ, shown in Fig. 1.80, is used in the following study.

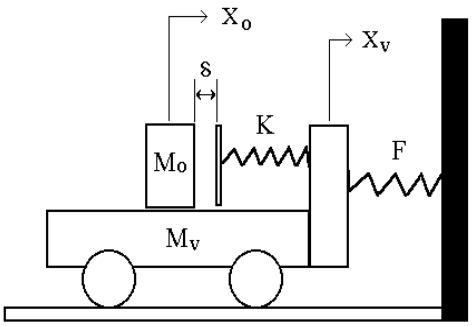

Fig. 1.80 A Simple Occupant-Vehicle Impact Model

1.9.1 Restraint Specific Stiffness and Onset Rate of Occupant Deceleration

The restraint stiffness, force per unit of deflection, can be computed using the test data. However, since the accelerometer is instrumented in the dummy chest, it is more convenient to use the natural frequency to evaluate the system consisting of the torso effective mass and restraint stiffness.

The vehicle and chest decelerations of a driver in a truck in a 35 mph rigid barrier test are shown in Fig. 1.81. Double integration of the two accelerometer data sets yield the displacements where the difference is the chest displacement w.r.t. the vehicle. The chest deceleration is plotted against the relative chest displacement in Fig. 1.82. A linear regression with a least square error approach was used to approximate the chest loading curve by a straight line. The time during which the chest is being loaded is referred to as the coupling phase. The horizontal intercept distance, δ, represents the slack in the restraint system. It will be shown in Section 1.9.2 that the natural frequency of the restraint system, f, is related to the slope, k, the restraint specific stiffness or restraint stiffness per unit of effective occupant weight as follows: f (Hz) equals 3.13 times the square root of k (g/in).

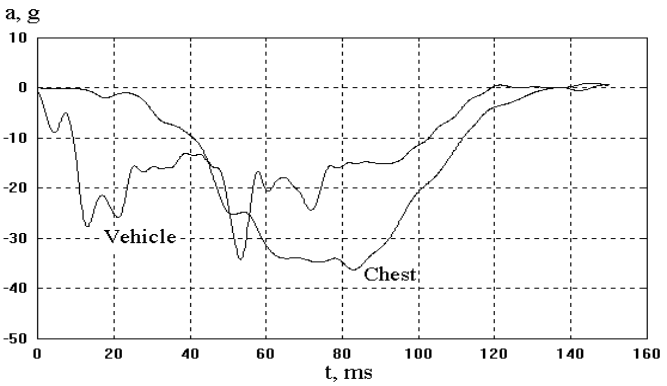

Fig. 1.81 Truck and Chest Decelerations vs. Time in a 35 mph Barrier Test

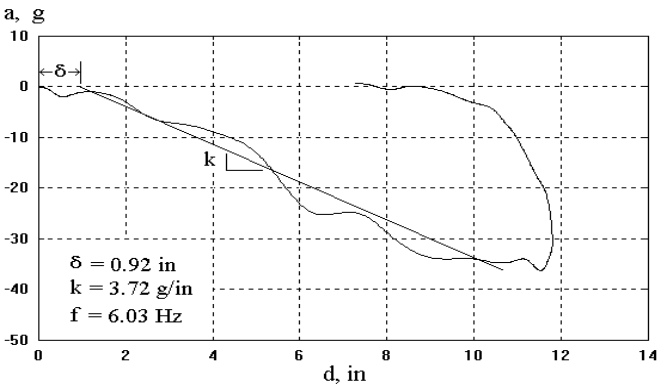

Fig. 1.82 Restraint Slack and Stiffness of an Air Bag System in a Truck 35 mph Test

The onset rate of the occupant deceleration, j, is the slope of the chest deceleration vs. time curve at the time of restraint contact. The term j is also the jerk (rate of change of deceleration) at time t*, the time that the occupant takes to move a relative distance δ. The onset rate, j, is the product of the specific stiffness, k, and the relative restraint contact velocity, Δv_c (or ΔV). The derivation of the formula is shown in Eq. (1.44) in Section 1.9.3. As shown in Fig. 1.83, ΔV is the difference between the chest velocity and vehicle velocity at the restraint contact time, t*. The truck tested in a 35 mph rigid barrier condition is used as an example. The corresponding ΔV of 7 mph and specific stiffness of 3.72 g/in are shown in Fig. 1.83. The computed onset rate, j, of 0.458 g/ms shown in Eq. (1.37) agrees fairly well with that from the test. The derivation of the onset rate relationship is shown in the following sections.

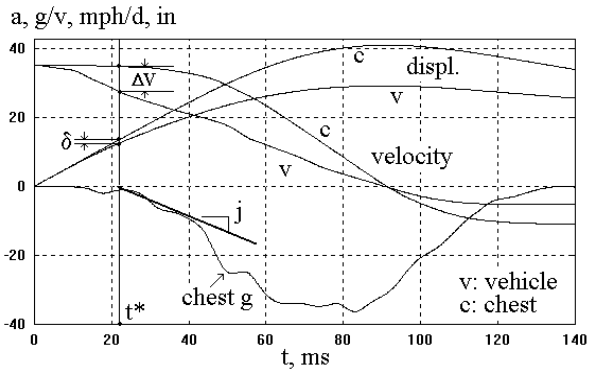

Fig. 1.83 Chest Onset Rate (j) in a Truck 35 mph Fixed Barrier Test

$$
\begin{aligned}
&j(\textit{onset rate}) = \Delta v_c k, \textit{ where } \quad \Delta v_c = v_c - v_v \\
&\Delta v_c\textit{: restraint contact velocity} \\
&v_c\textit{: chest velocity at } t^*, \qquad v_v\textit{: vehicle velocity at } t^* \\
&t^*\textit{: restraint contact time}, \quad k\textit{: specific stiffness} \\
&\textit{Using the data for the truck, then} \\
&j = (v_c - v_v)k \;=\; (34.7 - 27.7)\,mph \times \frac{17.6\,in/s}{1\,mph} \times 3.72\,\frac{g}{in} \\
&\quad = 458\,\frac{g}{\sec} = 0.458\,\frac{g}{ms}
\end{aligned}
\tag{1.37}
$$

Using the vehicle and occupant test data, the performance of the restraint system can be characterized by the slack between the restraint and occupant and the restraint specific stiffness. The transient occupant response in the restraint coupling phase can be analytically derived based on an equivalent square wave (ESW) which approximates a test crash pulse.

1.9.2 Occupant Response in the Restraint Coupling Phase

In the simple occupant-vehicle impact model shown in Fig. 1.84, a vehicle deceleration in the form of equivalent square wave (ESW), shown in Fig. 185, is imparted on the model. The occupant, M_o, contacts the restraint system, K, at t* after traveling a distance δ with a relative contact velocity of ΔV_c. Occupant response formulas during the restraint coupling phase can then be derived.

Let us define:

a_o : occupant absolute acceleration
a_v : vehicle absolute acceleration
$a_{o/v}$: occupant relative to vehicle acceleration
$v_{o/v}$: occupant relative to vehicle velocity
$x_{o/v}$: occupant relative to vehicle displacement
k : slope of a_o vs. $x_{o/v}$ in the coupling phase (specific stiffness, g/in)
ω : circling frequency of the restraint system, rad/sec (= $2\pi f$)
f : restraint natural frequency, Hz
δ : restraint slack
t* : occupant-restraint contact time
t : time variable in restraint coupling phase, starting from t* as time zero
Δv_c : occupant-restraint contact velocity (= a_v t*)

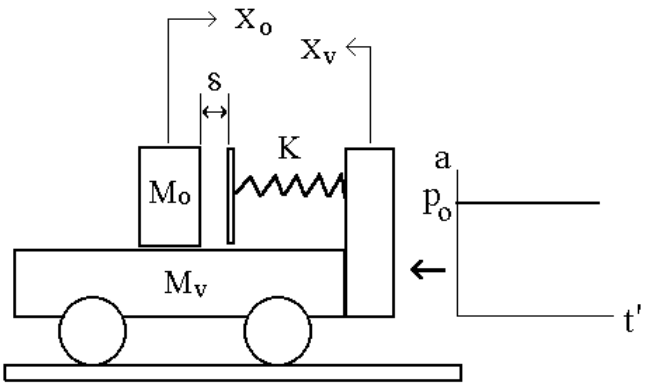

Fig. 1.84 A Sled Impact Model

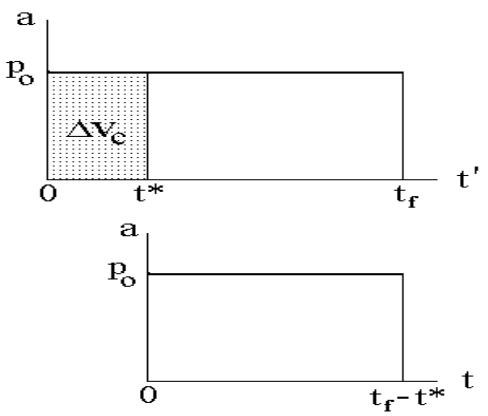

Fig. 1.85 A Constant Sled Excitation Pulse

Define an equivalent square wave (ESW) as follows:

$a_v = p_o$

where p_o = ESW acceleration = constant

The final expressions for the two unknowns, the phase angle ϕ and A, the occupant deceleration magnitude and onset rate, are shown as follows.

Summaries of Occupant Response and Onset Rate Equations

$$a_o = A \sin(\omega t+\phi) + a_v \qquad \ldots\ldots\ldots (1)$$

$$\phi = \tan^{-1}\frac{-p_o}{\omega \Delta v_c} = -\tan^{-1}\frac{1}{\omega t^*}$$

$$A = -\sqrt{p_o^2 + (\omega \Delta v_c)^2}$$

$$a_o|_{\max} = ESW\,[1 - \cos(\omega t^*)] \quad \ldots \; a\ haversine\ wave \qquad (1.38)$$

$$= ESW\,[1 + \sqrt{1 + (2\pi f t^*)^2}]$$

$$where \quad \Delta v_c = p_o t^* \quad and \quad t^* = \sqrt{\frac{2\delta}{p_o}}$$

$$j(onset\ rate\ of\ occupant\ deceleration) = \Delta v_c\ \omega^2 = \Delta v_c\, k$$

Based on the definition of the specific stiffness and the relative motion between the sled and the occupant mass, a second order differential equation in terms of occupant and sled accelerations can be derived. The equations involving the interaction between the occupant and sled are valid in the restraint coupling phase. What happens before the occupant contacts the restraint system is solely determined by the sled kinematics, since the occupant is stationary.

The procedures used to derive the closed-form solution for the occupant deceleration are shown in two steps shown in Eqs. (1.39) and (1.40), respectively.

The slope of the occupant chest g versus relative displacement curve is given by

$$\frac{da_o}{dx_{o/v}} = -k, \quad then$$

$$\frac{-a_o}{x_{o/v}} = \frac{K}{M_o} = -\frac{da_o}{dx_{o/v}} = k,$$

$$\frac{dx_{o/v}}{da_o} = \frac{dx_{o/v}}{dt}\frac{dt}{da_o} = -\frac{1}{k} \qquad (1.39)$$

$$let \quad a_{o/v} = \frac{d^2x_{o/v}}{dt^2} = \frac{d}{dt}\left(\frac{dx_{o/v}}{da_o}\frac{da_o}{dt}\right) = -\frac{1}{k}\frac{d^2a_o}{dt^2},$$

$$\because \quad a_o = a_o/v + a_v,$$

$$\therefore \quad a_o + \frac{1}{k}\frac{d^2a_o}{dt^2} = a_v, \quad or \quad a_{o/v} + \frac{1}{k}\frac{d^2a_o}{dt^2} = 0 \qquad \ldots\ldots (2)$$

It is assumed that the solution for the occupant relative acceleration, $(a_o - a_v)$, is sinusoidal, as shown by (1) of Eq. (1.38). The occupant relative acceleration along with the second derivative of the occupant acceleration satisfy the equality constraint shown by (2) of Eq. (1.39). Note that the time variable, t (a local time), is referenced as time zero when the occupant contacts the restraint. The corresponding time variable, t′(a global time), with time zero set at the time of sled impact, is equal to the restraint contact time plus the local time used in the restraint coupling. Therefore, $t' = t^* + t$. That is, the global time is equal to the restraint contact time plus the local time.

In the restraint coupling phase

then $\frac{da_{ov}}{dt} = A\omega \cos(\omega t+\phi)$, $\frac{d^2a_{ov}}{dt^2} = -A\omega^2 \, Sin(\omega t+\phi)$ . . (3)

Substituting (1) *and* (3) *into* (2) *and simplifying, one gets*

$1 - \frac{\omega^2}{k} = 0, \quad \therefore \quad \omega = \sqrt{k}$ *is solution condition for* (1)

Initial Conditions:

I. $t = 0, \quad a_{ov} = 0 - p_o = -p_o$ *then*

Eq.(1) *becomes*: $a_{ov} = -p_o = A \, Sin \, \phi$ . . . . . (4)

II. $t = 0, \quad v_{ov} = \Delta v_c$

$$\Delta v_c = \int (a_o - a_v)dt = \int A \, \sin(\omega t+\phi)dt = -\frac{A}{\omega}\cos(\omega t+\phi) \qquad . \; . \; . \; . \; . \; (5)$$

III: *at* $t = 0 \qquad \Delta v_c = -\frac{A}{\omega}Cos(\phi)$ (1.40)

IV: $A \sin \phi = -p_o$ . . . . . (6)

V: $A \cos \phi = -\omega \, \Delta v_c$ . . . . . (7)

Dividing eq. (6) *by* (7): $\tan \phi = \frac{p_o}{\omega \, \Delta v_c}$,

squaring both sides of equations (6) & (7) *and summing up,*

$\therefore \quad A = \sqrt{p_o^2 + (\omega \, \Delta V_c)^2}$

Set $\frac{da_{ov}}{dt} = A\omega \cos(\omega t+\phi) = 0$, *then* $\omega t_G + \phi = \frac{\pi}{2}$

$\because \quad \tan \phi = \frac{-p_o}{\omega \, \Delta V} = \frac{-p_o}{\omega \, (p_o t^*)} = \frac{-1}{\omega t^*}, \qquad \phi = \tan^{-1}\frac{-1}{\omega \, t^*} = -\tan^{-1}\frac{1}{\omega \, t^*}$

$$t_G = \frac{\frac{\pi}{2} - \phi}{\omega} = \frac{\frac{\pi}{2} + \tan^{-1}\frac{1}{\omega \, t^*}}{\omega} \qquad . \; . \; . \; . \; . \; . \; . \; . \; . \; (8)$$

Since the two unknowns ϕ and A define the occupant relative sinusoidal acceleration, the absolute occupant acceleration is equal to the sum of sled constant and the occupant relative sinusoidal acceleration.

For the special case where the restraint slack, $\delta = 0$, then $t^* = 0$, $\Delta v_c = 0$, and $\phi = -90°$, and the occupant absolute acceleration becomes a haversine as shown in (2) of Eq. (1.41). The haversine is the output response of a simple spring-mass model subjected to an input excitation of constant acceleration. The simple spring-mass model consists of a constant stiffness restraint system without slack. The occupant haversine acceleration is the sum of two acceleration components. The first component is the occupant-relative-to-vehicle (or sled) sinusoidal acceleration with phase advance of quarter cycle ($\pi/2$) and magnitude equal to the vehicle constant acceleration. The second component is the vehicle constant acceleration itself.

$$\phi = -\tan^{-1}\frac{1}{\omega t^*} = -\tan^{-1}\frac{1}{0} = -\tan^{-1}\infty = -\frac{\pi}{2}$$

since $\delta = 0$, $\Delta V_c = 0$, *then*

$$A = -\sqrt{p_o^2 + (\omega \Delta v_c)^2} = -\sqrt{p_o^2 + 0} = -p_o \tag{1.41}$$

$$a_o = A\sin(\omega t + \phi) + a_v = -p_o \sin(\omega t - \frac{\pi}{2}) - p_o \quad \ldots (1)$$

$$= -p_o[1 - \cos(\omega t)] \quad \ldots \textit{ a haversine wave} \quad \ldots (2)$$

1.9.3 Maximum Occupant Response, Timing, and Onset Rate

Given the closed-form solution of the occupant response shown by (2) of Eq. (1.41), the maximum occupant chest response, the corresponding timing, and the onset rate of the impact model can be derived. The approach using the specific stiffness is more direct than the method using Newton's second law [14]. The derivation procedures are shown in Eqs. (1.42) to (1.44).

Deriving Maximum Occupant Response:

(*I*) *From Eq.* (1.38), $a_o|_{\max} = A + p_o$, *then*

$$a_o|_{\max} = \sqrt{p_o^2 + (\omega \Delta v_c)^2} + p_o,$$

$$\because \quad \Delta v_c = p_o t^*, \quad \omega = 2\pi f, \quad \textit{and } p_o = ESW \tag{1.42}$$

$$\therefore \quad a_o = ESW\,[1 + \sqrt{1 + (2\pi f t^*)^2}]$$

Deriving Time at Maximum Occupant Response:

(*II*) *set* $\frac{da_{ov}}{dt} = A\omega\cos(\omega t + \phi) = 0$, *then* $\omega t_g + \phi = \frac{\pi}{2}$

$$\because \quad \tan\phi = \frac{-p_o}{\omega \Delta v} = \frac{-p_o}{\omega(p_o t^*)} = \frac{-1}{\omega t^*}, \quad \phi = -\tan^{-1}\frac{1}{\omega t^*}$$

$$t_g = \frac{\frac{\pi}{2} - \phi}{\omega} = \frac{\frac{\pi}{2} + \tan^{-1}\frac{1}{\omega t^*}}{\omega} \tag{1.43}$$

$$\because \quad \tan^{-1}x + \tan^{-1}\frac{1}{x} = \frac{\pi}{2}, \quad \textit{and} \quad -\tan^{-1}x = \tan^{-1}-x$$

$$\therefore \quad \tan^{-1}\frac{1}{\omega t^*} = \frac{\pi}{2} - \tan^{-1}\omega t^*, \quad \textit{then } t_G = \frac{\pi - \tan^{-1}\omega t^*}{\omega}$$

Note that t_g *is measured from* t^*, $t_g' = t^* + \frac{\pi - \tan^{-1}\omega t^*}{\omega}$

t_g' *is measured from the time of impact*

Deriving Occupant Onset Rate:

$$
\begin{aligned}
&\because \quad a_o = A\sin(\omega t+\phi) + a_v \\
&\text{At restraint contact time, } \quad t' = t^* \quad \text{or} \quad t = 0 \\
&\text{let } \quad j = \frac{da_o}{dt}\Big|_{t=0} = A\omega\cos(\omega t+\phi)\Big|_{t=0} = A\omega\cos(\phi) \\
&\because \quad \tan(\phi) = \frac{-1}{\omega t^*} \qquad \therefore \quad \cos(\phi) = \frac{\omega t^*}{\sqrt{1+(\omega t^*)^2}} \\
&\text{and } \quad A = -\sqrt{p_o^2+(\omega\Delta V_c)^2} = -p_o\sqrt{1+(\omega p_o t^*)^2} = -p_o\sqrt{1+(\omega t^*)^2} \\
&\text{Substituting } A \text{ and } \cos(\phi) \text{ into } j, \text{ it becomes:} \\
&j = A\omega\cos(\phi) = -p_o t^*\omega^2 = -\Delta V_c\omega^2 = -\Delta V_c k \quad \ldots\ldots \text{ onset rate}
\end{aligned}
\tag{1.44}
$$

1.9.4 Vehicle, Occupant, and Restraint (VOR) Analysis Charts

Two basic model parametric relationships for use in the analysis of the restraint coupling phase [14] are listed. The relationships are for (1) Vehicle ESW and Occupant Chest G, and (2) Restraint Specific Stiffness (see Section 1.9.2) and Natural Frequency as shown in Eq. (1.45).

$$
\begin{aligned}
&(I)\text{: } ESW \text{ (Equivalent Square Wave)} = .4\frac{V^2}{C} \\
&DAF = 1 + \sqrt{1+(2\pi f t^*)^2}, \quad \text{where } \quad f = \frac{\sqrt{386\ k}}{2\pi}\ Hz \\
&t^*(\text{restraint contact time, sec}) = .072\sqrt{\frac{\delta}{ESW}} \\
&C.G.(\text{maximum chest } G) = ESW \times DAF \\
&(II)\text{: Let } k \text{ (restraint specific stiffness)} = \frac{K}{m} = \frac{K}{W}g \\
&\because \quad \omega \text{ (circular frequency)} = \sqrt{\frac{K}{m}} = \sqrt{kg} \\
&\text{then } \quad f \text{ (natural frequency)} = \frac{\omega}{2\pi} = \frac{\sqrt{kg}}{2\pi} \\
&\text{For the units of: } \quad K\text{: lb/in}, \qquad W\text{: lb}, \\
&\text{dimensional analysis on } k \text{ becomes:} \\
&k \text{ (specific stiffness)} = \frac{lb/in}{lb}g = \frac{g}{in}, \quad \text{since} \quad g = 386\ \frac{in}{s^2} \\
&f = \frac{\sqrt{386k}}{2\pi} = 3.13\sqrt{k}
\end{aligned}
\tag{1.45}
$$

1.9.4.1 *3-D Contour Plots of the Occupant Response and Timing*

Given a vehicle structural ESW, restraint parameters in terms of slack and natural frequency, the trend analyses on the occupant maximum chest deceleration (or C.G., short for chest g) and corresponding timing are performed. Figs. 1.86 and 1.87 show the 3-D surface contour plots for the model chest g and the corresponding timing, respectively, as a function of the restraint natural frequency, f; restraint slack, δ; and equivalent square wave. The respective formula for the chest g and timings are shown in Eqs. (1.46) and (1.47), respectively.

For a given vehicle structural deceleration level, ESW, the chest g increases as the restraint stiffness (or natural frequency) and/or slack increases as shown in Fig. 1.86. Within the practical

ranges of the restraint stiffness and slack, the chest g is more sensitive to the restraint slack than the stiffness. This trend is evident by comparing the slopes along the axis of restraint stiffness and the axis of the slack on the ESW surface shown in the figure. In general, assuming no preloading on the occupant, the chest g is at least double the ESW. In the special case where the slack is reduced to zero, either by taking out the restraint slack or by using a pretensioner (a pyrotechnic device, assuming the preloading on the occupant is negligible compared to the overall loading [15]), the chest g becomes two times the ESW. The dynamic amplification factor of two, the ratio of dynamic loading to the static loading, is the theoretical minimum that can be achieved without preloading. Similarly, given a vehicle structural deceleration level, ESW, the chest g timing (t_g' becomes longer when the stiffness (or natural frequency) decreases and/or the restraint slack increases as shown in Fig. 1.87.

$$a_o = ESW\,[1 + \sqrt{1 + (2\pi f t^*)^2}]$$
$$t^* = 0.072\sqrt{\frac{\delta}{ESW}} \tag{1.46}$$

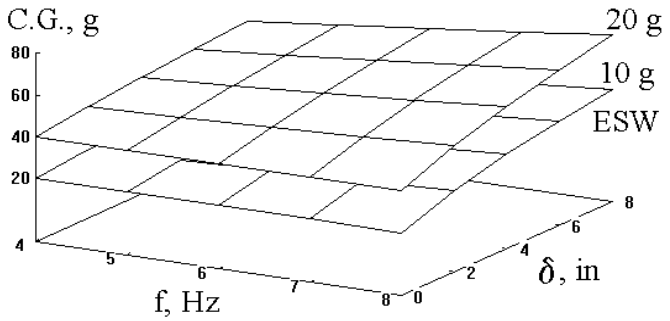

Fig. 1.86 Model Chest g as a Function of Restraint, f; Slack, δ; and ESW

$$t_G' = t^* + \frac{\pi - \tan^{-1}\omega t^*}{\omega}, \qquad \omega = 2\pi f \tag{1.47}$$

Note t_G' is measured from the time of impact

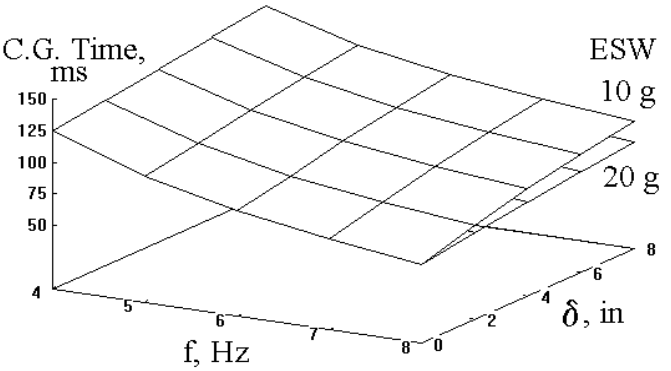

Fig. 1.87 Model Chest g Time as a Function of Restraint, f; Slack, δ; and ESW

To prevent the sudden increase of the occupant-relative-to-vehicle contact velocity in the vehicle rebound phase, it is desirable to have the peak chest g occur before vehicle rebounds. By doing this, the occupant takes advantage of the ridedown, a phenomenon that will be described in Section 1.10. Based on the model, the condition for the peak chest g to occur before vehicle rebounds is shown as follows:

$$t_g' = t^* + \frac{\pi - \tan^{-1}\omega t^*}{\omega} < t_m, \quad \textit{where} \tag{1.48}$$

t_g': *time of maximum occupant response measured from time of vehicle impact*
$t*$: *occupant–restraint contact time*
ω: *circle frequency of restraint system*
t_m: *time when vehicle rebounds or time at dynamic crush*

1.9.4.2 *Vehicle, Occupant, and Restraint (VOR) Analysis Charts*

To summarize the application of the derived formulas in the occupant response analysis, four VOR charts are shown in Figs. 1.88 to 1.91. The chart sequence starts from the upper right hand corner as VOR(chart) #1 and goes counter-clockwise to VOR #4 at the lower right corner. They are used to estimate the occupant-restraint contact time (t*), dynamic amplification factor (DAF), and chest g based on the vehicle to barrier impact speed and dynamic crush from a test. The respective formula for each chart is shown inside the chart.

The variables are defined as follows:

ESW	:	vehicle equivalent square wave, g
V	:	vehicle barrier impact velocity, mph
C	:	vehicle dynamic crush, in
δ	:	restraint slack, in
t*	:	restraint contact time, ms
f	:	restraint natural frequency, Hz
DAF	:	dynamic amplification factor
C.G.	:	chest g (occupant response)

VOR Chart #1 is for vehicle analysis, #2 and #3 for the restraint analysis, and #4 for the occupant response computation.

Case Study: Estimate the occupant response with the following conditions:

V, barrier impact speed = 30 mph
C, dynamic crush = 24 in
δ, occupant-restraint slack = 4 in
f, occupant-restraint natural frequency = 7 Hz.

The steps to use the VOR analysis charts are shown as follows:

Chart #1. Fig. 1.89: Draw a vertical line at C=24 in, intersect the curve with V=30 mph. Draw a horizontal line and get the ESW, 15 g,

Chart #2. Fig. 1.88: Extend the ESW horizontal line, intersect the curve wiht δ = 4 in. Draw a vertical line and get the occupant restraint contact time, t* =37 ms,

Chart #3. Fig. 1.90: Extend the t* vertical line, intersect the curve with f = 7 Hz. Draw a horizontal line and get the DAF, 2.9,

Chart #4. Fig. 1.91: Extend the DAF horizontal line, intersect the curve with ESW = 15 g. Draw a vertical line and get the occupant chest g, C.G. = 44 g.

VOR (Vehicle Occupant Restraint) Analysis Charts (VOR#1 => VOR#4) – Example

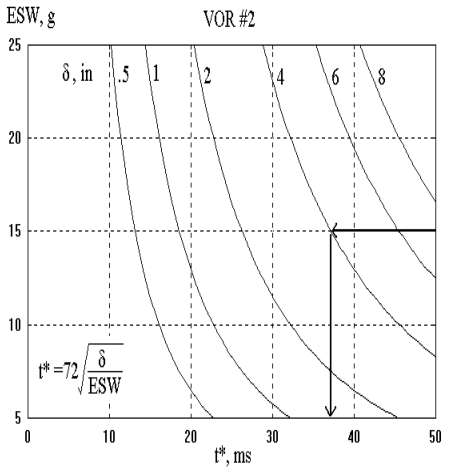

Fig. 1.88 VOR Chart #2 – Example

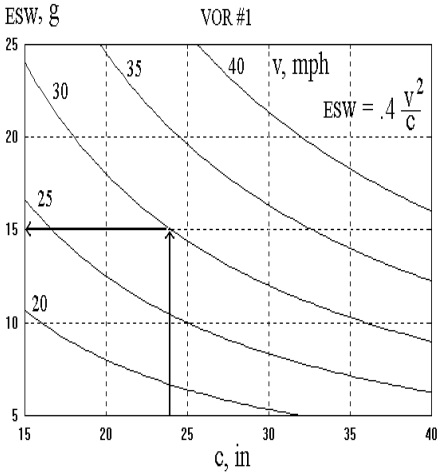

Fig. 1.89 VOR Chart #1 – Example

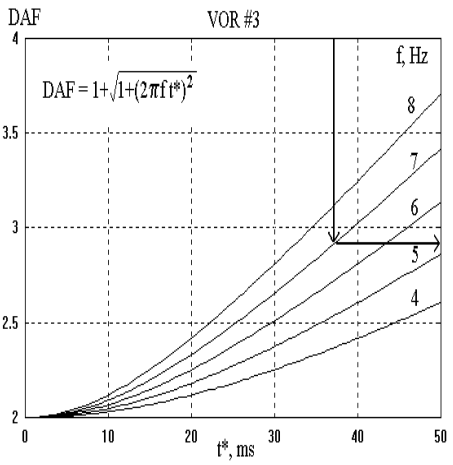

Fig. 1.90 VOR Chart #3 – Example

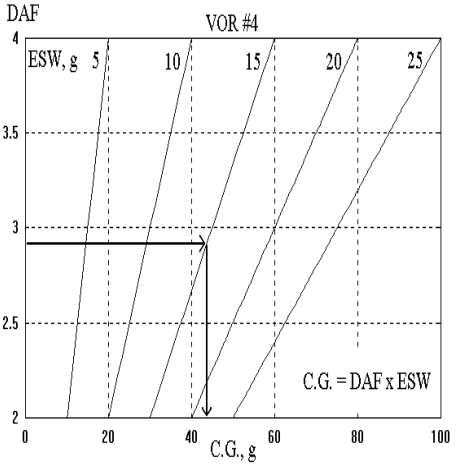

Fig. 1.91 VOR Chart #4 – Example

VOR (Vehicle Occupant Restraint) Analysis Charts (VOR#1 => VOR#4)

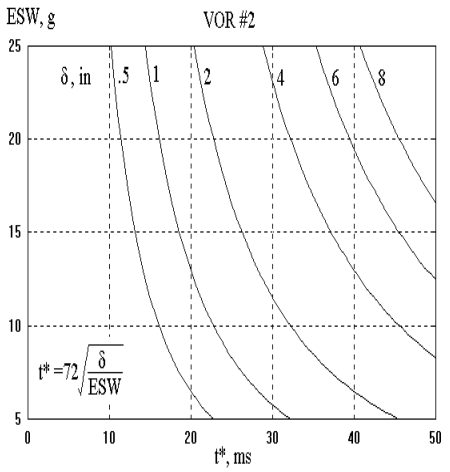

Fig. 1.92 VOR Chart #2

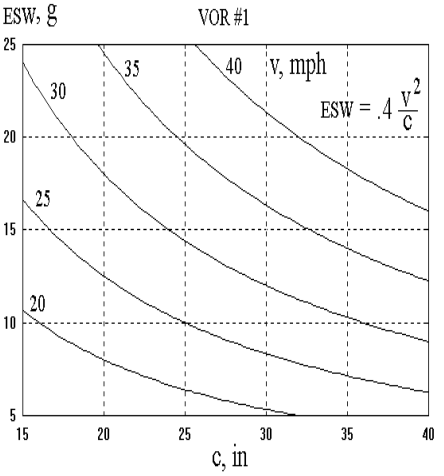

Fig. 1.93 VOR Chart #1

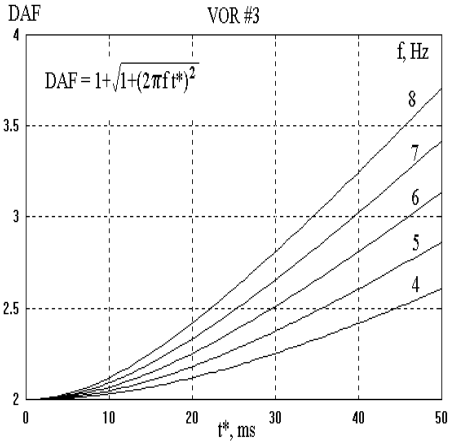

Fig. 1.94 VOR Chart #3

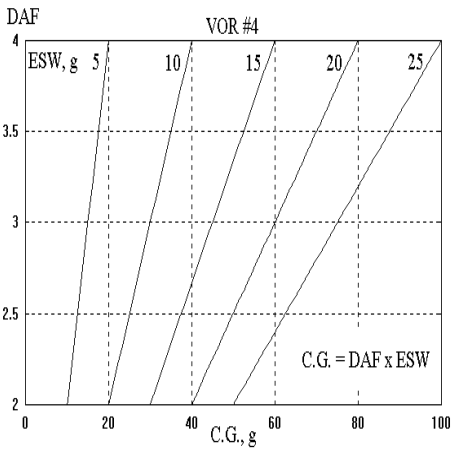

Fig. 1.95 VOR Chart #4

Using the formulas or the VOR charts, four separate tests, where the trucks impacted on the rigid barrier at 31 mph, were examined and a trend analysis was performed. The parameters involved in the sensitivity analysis were vehicle structural ESW (equivalent square wave), restraint slack (longitudinal distance between the fully deployed air bag and torso), and the restraint system stiffness. The computation of the restraint system stiffness is described in Section 1.10.2.2 and Eq. (1.58).

The test results for four light trucks in a 31 mph fixed barrier impact are shown in Table 1.8. The tests were conducted with unbelted dummies, where only the air bag restraint system was used. The vehicle dynamic crush and timing, equivalent square wave (ESW), and chest responses are listed. The restraint slack and natural frequency of the restraint system in each test are computed by using linear regression applied to the loading portion of the chest g vs. chest relative displacement curve. The computed restraint slack, which is the horizontal distance between the initial torso position and the fully inflated air bag surface, ranges from 0.5 to 5.4 inches. The variations in the computed slack are mainly due to the initial dummy seating position and air bag inflation characteristics. The test chest g's and model prediction using the ESW and restraint parameters are shown in the last column of the table. The trend prediction of the chest g by the model compares reasonably well with that from the tests as shown by the histogram in Fig. 1.96.

Table 1.8 Rigid barrier tests with air bag only (unbelted dummy), V = 31 mph

Test #	Vehicle	C, Dynamic Crush, in @ ms	ESW, g	δ, Restraint Slack, in	f, Restraint Natural Frequency, Hz	Chest g Test [Model]
T9	Truck	26.0 @ 90	14.8	5.4	6.1	46 [44]*
T1	Truck	20.5 @ 63	19.2	2.8	5.9	54 [47]
T10	Truck	20.3 @ 69	19.2	1.5	5.8	42 [43]
T11	Truck	24.1 @ 77	16.0	0.5	5.6	39 [34]

* The number in [ ] is the predicted chest g = ESW x DAF (Dynamic Amplification Factor).
k: restraint specific stiffness in the coupling phase, g/in

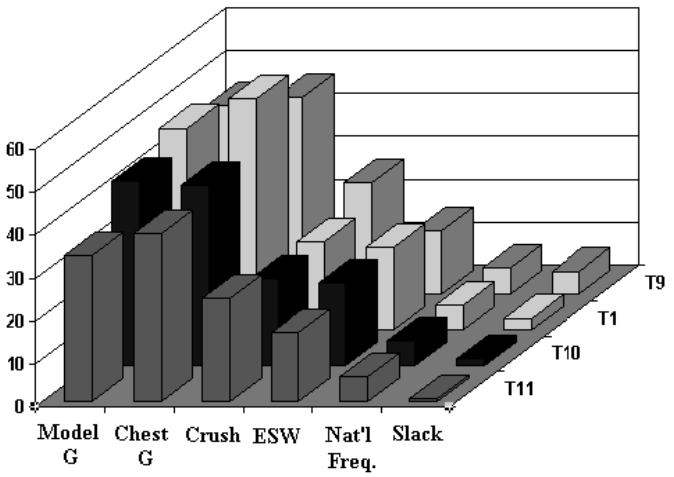

Fig. 1.96 Comparison of Responses: Model vs. Tests

From Table 1.8, the results of occupant chest g from the four rigid barrier tests at 31 mph with air bag only are plotted and shown in Fig. 1.97. To compare the test chest responses with those from the model prediction, the 3-D surface plots are superimposed. As an example, test T9, which has f = 6.1 Hz, δ = 5.4 inches, and chest g of 46 g, is shown as a dot in the plot. The ESW of test T9 is 14.8 g which is located between the two model ESW surfaces of 10 g and 20 g. Similarly, the ESW of the other three tests is also within the vicinity of the two ESW values. Therefore, the trend of the model occupant response in terms of structural deceleration level, restraint stiffness, and slack is comparable to that of the test results.

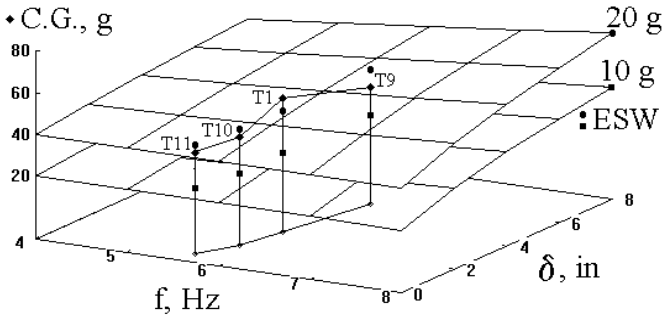

Fig. 1.97 Chest g as a Function of Restraint, f; Slack, δ; and Four Crash Test Data

1.9.5 VOR Trend Analysis Based on Car and Truck Test Results

Two sets of test data involving a mid-size car and a truck in rigid barrier 31 mph tests were collected and a trend analysis of the VOR (vehicle, occupant, and restraint) interactions was performed. In each test, the chest g versus chest relative displacement was plotted, and the restraint slack and restraint specific stiffness were then estimated by approximating a straight line to the chest loading curve.

Fig. 1.98 shows the scattered data and a linear regression of the occupant chest g versus dynamic crush data. The chest g of both car and truck decreases as the dynamic crush increases. Since the larger the dynamic crush, the lower the ESW (equivalent square wave), the chest g is lower for both car and truck tests. The trend relationship based on the linear regression analysis indicates that the chest g has a negative correlation with dynamic crush for both car and truck.

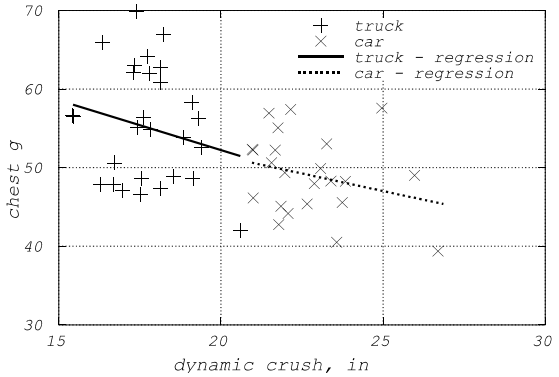

Fig. 1.98 Chest g vs. Dynamic Crush in 31 mph Rigid Barrier Tests

Since for a given barrier test speed, the ESW (equivalent square wave) is inversely proportional to dynamic crush, the chest g has a positive correlation with ESW. The typical DAF (dynamic amplification factor), the ratio of chest g to the ESW, can be computed using the average values of

chest g and dynamic crush. For the truck, using the approximate average of 55 g for chest g and 18 inches for dynamic crush (ESW=21 g), the DAF is equal to 2.6. Similarly, for the car, using 47 for the chest g and 23 inches for the crush (ESW=16.7 g), the DAF is 2.8.

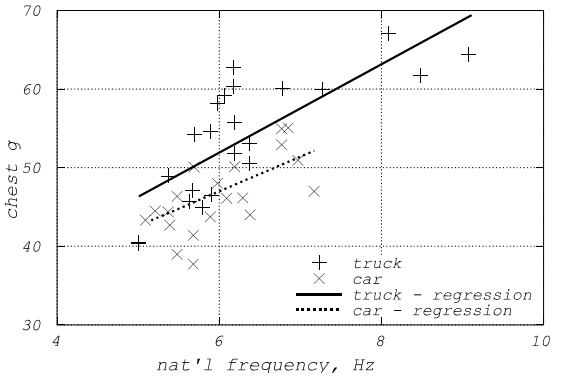

Fig. 1.99 Chest g vs. Restraint Natural Frequency in 31 mph Rigid Barrier Tests

The relationship between the chest g and the restraint natural frequency for both car and truck is shown in Fig. 1.99. The average restraint natural frequency is about 6 Hz and as it increases, the chest g increases. Although the rate of increase is about the same for both car and truck, the chest g is higher for the truck than the car. The observed relationship is best explained by the chest g equation derived in Section 1.9.4.

The relationship between the chest g and the restraint slack, δ, for both car and truck is shown in Fig. 1.100. Since the two sets of tests are with air bags only, the average restraint slack is larger than that with the belt. The average slack, about 4–5 inches, has a positive correlation with the chest g. This correlation can also be explained by the functional relationship shown in Section 1.9.4.

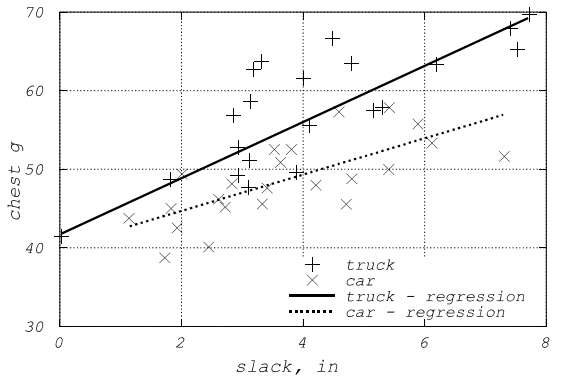

Fig. 1.100 Chest g vs. Restraint Slack in 31 mph Rigid Barrier Tests

1.10 OCCUPANT RIDEDOWN ANALYSIS AND ENERGY MANAGEMENT

In a vehicle crash test, an unbelted occupant's kinetic energy is absorbed by restraints such as an air bag and/or knee bolster and by the vehicle structure during occupant ridedown. Both the energy absorbed by the restraints and the ridedown energy absorbed by the structure through restraint coupling are studied in time and displacement domains using crash test data. Using both vehicle and occupant accelerometer data from a 31 mph truck-to-barrier impact, the restraint and ridedown energy components were computed for the lower extremity of the occupant, e.g., the femur. Relationships

between ridedown efficiency (μ, ratio of ridedown energy to initial occupant kinetic energy) and unbelted occupant response in air bag equipped vehicles are presented [5].

The left front unbelted occupant seating position in a vehicle-into-barrier impact is shown in Fig. 1.101. The restraint system consists of an air bag module in the steering wheel and a knee bolster underneath the instrument panel.

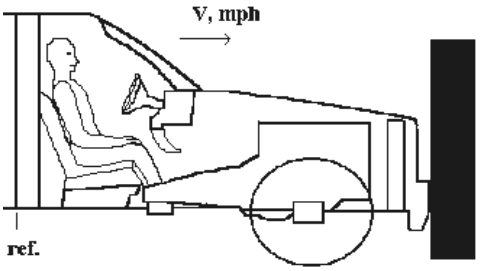

Fig. 1.101 Left Front Occupant Seating Position in a Vehicle-to-Barrier Impact

Using the kinematic relationship vdv = adx, where v: velocity, d: differential operator, a: acceleration, and x: displacement, the energy density of an occupant, e, can be expressed as follows.

$$e = \int \ddot{x}_o dx_o = \int \ddot{x}_o d(x_v + x_{o/v}) = e_{rd} + e_{rs}$$

where (1.49)

e_{rd}(*ridedown energy density*)$= \int \ddot{x}_o dx_v$

e_{rs}(*restraint e.d.*)$= \int \ddot{x}_o dx_{o/v}$

x_v : *vehicle displacements w.r.t. ground*

x_o : *occupant displacements w.r.t. ground*

$x_{o/v} = x_o - x_v$: *occupant–vehicle relative displacement*

$\ddot{x}_o$: *occupant deceleration*

If the vehicle were infinitely stiff such that no structural deformation occurs, the occupant ridedown energy would be zero because the vehicle displacement becomes zero in the integral. On the other hand, if the restraint system were infinitely stiff, the restraint energy would be zero because the occupant-vehicle relative displacement (or restraint deformation) during restraint loading becomes zero, and all the occupant kinetic energy goes into the deforming vehicle structure.

The vehicle and left front occupant responses in the light truck test with an air bag alone (without belt) at 31 mph are shown in Fig. 1.102. For comparison purposes, all the crash data in this study were filtered by the second-order Butterworth filter with a cutoff frequency of 100 Hz. Due to the stiffer front rail in the truck, the impact produces a front-loaded crash pulse with a high impulse at 22 ms. The front-loaded crash pulse forces the occupant femur to contact the knee bolster sooner. Shown in Fig. 1.102, the femur contacts the knee bolster at 48 ms and starts decelerating. The femur displacement relative to the vehicle at 48 ms shown in Fig. 1.103 is about 6 inches, which is the initial clearance between the femur and knee bolster. The maximum femur relative displacement is about 12 inches and occurs at 75 ms, about 10 ms after the truck reaches its maximum deformation of 22.5 inches. Therefore, the knee bolster deformation due to femur loading is 6 inches (=12 – 6) as shown by the deformation range of the restraint curve in Fig. 1.104.

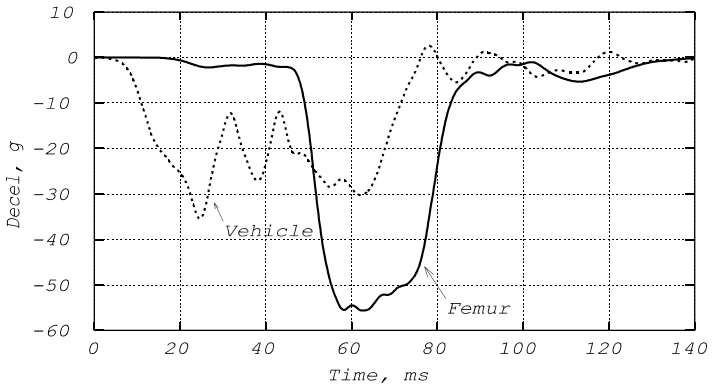

Fig. 1.102 Decelerations of Driver Left Femur and Truck in 31 mph Barrier Test

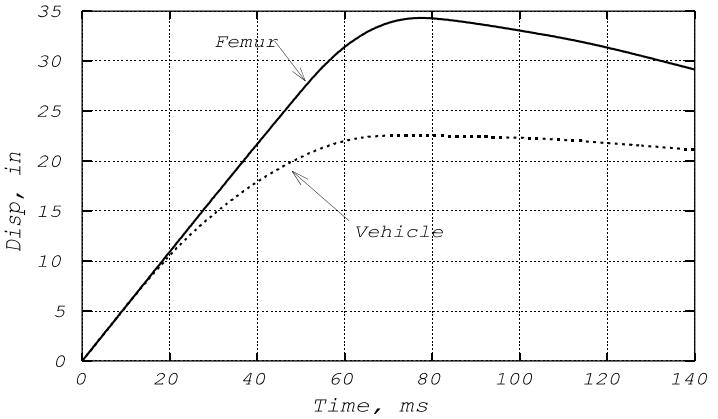

Fig. 1.103 Displacements of Driver Left Femur and Truck in 31 mph Barrier Test

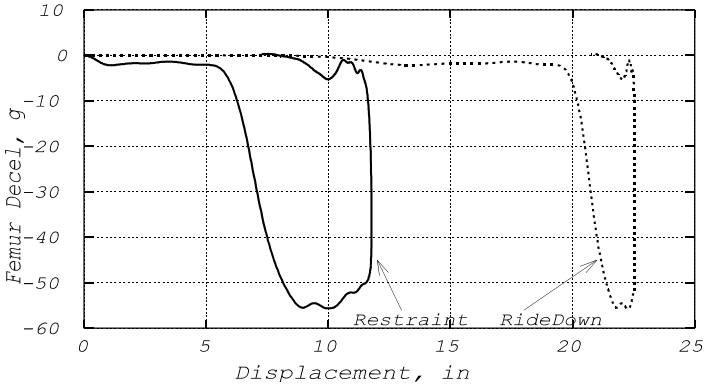

Fig. 1.104 Restraint and Ridedown Curves of Left Femur in 31 mph Test

Using the femur deceleration and the double integral of the truck accelerometer data with an initial velocity of 31 mph, the ridedown curve of the femur deceleration versus vehicle absolute displacement (crush) is obtained. This is shown in Fig. 1.104. Because both ridedown and restraint curves were plotted using the same femur deceleration, they have the same peak deceleration of about 55 g. The area between each of the two curves and the zero g reference line in Fig. 1.104 or the integral of the femur deceleration over the respective displacement is the energy density as shown in Fig. 1.105.

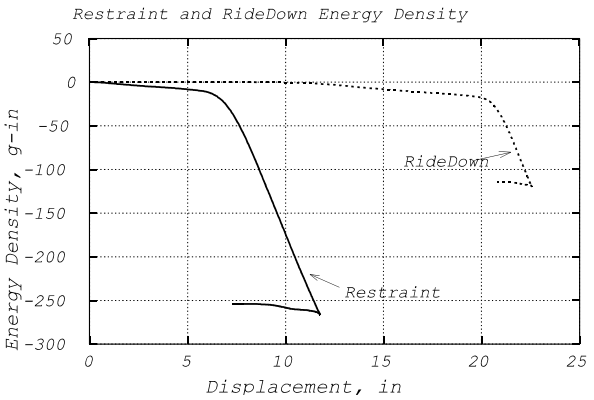

Fig. 1.105 Restraint and Ridedown Energy Densities of Left Femur in 31 mph Test

Since ridedown efficiency (μ) is defined as the ratio of maximum ridedown energy density to the initial occupant kinetic energy density, the femur ridedown efficiency for a light truck can be computed from Fig. 1.105 as follows.

$$\mu\ (ridedown\ \ efficiency) = \frac{e_{rd}\big|_{\max}}{\frac{1}{2}v_o^2} \tag{1.50}$$

$$\frac{1}{2}v_o^2 = \frac{1}{2}\left(31mph \times \frac{44}{30}\right)^2 \times \frac{1}{32.2} \times 12 \;=\; .4(31\ mph)^2 = 385\ g\text{-}in$$

$$\mu = \frac{120}{385} = 31\ \% \quad \ldots\ldots\ light\ \ truck$$

The femur ridedown efficiency is proportional to the ridedown energy density, or the total area under the ridedown curve shown in Fig. 1.104. The femur deceleration in the ridedown curve does not pick up until the truck has a displacement (crush) of 20 inches, at which point the femur starts contacting the knee bolster (at 48 ms). Since in this test, the vehicle structural deformation accompanying the occupant ridedown is only 2.5 inches (22.5 - 20.0), the ridedown energy density is limited and so is the ridedown efficiency. There are two basic principles that can be used to improve the ridedown efficiency in a crash test. One is reducing the occupant-restraint contact time (by positioning dummy closer to the instrument panel, using belt pre-tensioner, or using a more front-loaded crash pulse), and the other is increasing the vehicle available crush space.

Note that in Fig. 1.105 for the light truck, the sum of the maximum ridedown energy density (120 g-in) and the maximum restraint energy density (260 g-in) is 380 g-in, which is not equal to the initial kinetic energy (385 g-in) although it is very close. This is because the maximum vehicle and femur displacements do not, in general, occur at the same time, as shown in the displacement curves in Fig. 1.103. It should be noted that the femur ridedown efficiency for a passenger car can be twice as much as that for a truck due to a larger vehicle crush for the same test condition.

1.10.1 Energy Density Model

An analytical model simulating the interaction between the occupant and restraint system in a passenger compartment shown in Fig. 1.106 can be analyzed using Newton's Second Law. The analytical expressions for the equations of motion (EOM), restraint and ridedown energy densities, parametric sensitivity, and design constraints are presented in Eqs. (1.51)–(1.53).

Equations of Motion and Energy Density of a Crash Model

A. EOM FOR VEHICLE

$$\ddot{x}_v = -\frac{F}{M_v} = -ESW$$
$$\dot{x}_v = v_o - ESW\ t \qquad (1.51)$$
$$x_v = v_o t - \frac{1}{2} ESW\ t^2$$

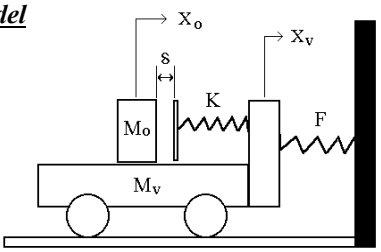

Fig. 1.106 A Crash Model

B. EOM FOR OCCUPANT

$$\ddot{x}_o = -ESW\ \{1 - C(p) + \omega t^* S(p)\}$$
$$\dot{x}_o = \dot{x}_v + \frac{ESW}{\omega}\{S(p) + \omega t^* C(p)\}$$
$$x_o = x_v + \delta + \frac{ESW}{\omega^2}\{1 - C(p) + \omega t^* S(p)\} \qquad (1.52)$$
$$\ddot{x}_o\big|_{max} = -ESW\ \{1 + \sqrt{1 + (\omega t^*)^2}\ \}$$

Where $p = \omega(t - t^*)$ *for* $t \geq t^*$

$$\omega = \sqrt{\frac{K}{M_o}}, \quad t^* = \sqrt{\frac{2\delta}{ESW}} \ \ldots\ \textit{restraint contact time}$$

$C(p) = Cosine(p), \quad S(p) = Sine(p)$

C. ENERGY DENSITY

$$e = \int \ddot{x}_o dx_o = \int \ddot{x}_o d(x_v + x_{o/v}) = \int \ddot{x}_o (dx_v + dx_{o/v}) = \int \ddot{x}_o dx_v + \int \ddot{x}_o dx_{o/v} = e_{rd} + e_{rs}$$

$$e_{rd}\ (\textit{ridedown energy density}) = \int \ddot{x}_o dx_v = \int \ddot{x}_o (v_o - t\ ESW) dt$$

$$e_{rs}\ (\textit{restraint energy density}) = \int \ddot{x}_o dx_{o/v} = \int \ddot{x}_o d(x_o - x_v)$$

$$e_{rd} = (ESW)^2 \left[\frac{v_o t}{ESW} - \frac{1}{\omega^2} - \frac{t^2 + t^{*2}}{2} + \frac{S(p)}{\omega}\left(\frac{-v_o}{ESW} + t - t^* \right) + C(p)\left(\frac{-v_o t^*}{ESW} + \frac{1}{\omega^2} + t t^* \right) \right]$$

$$e_{rs} = \left(\frac{ESW}{\omega} \right)^2 \left[1 - C(p) + \omega t^* S(p) + \frac{(\omega^2 t^{*2} - 1)}{2} S^2(p) - \frac{\omega t^*}{2} S(2p) \right] \qquad (1.53)$$

$$e_{rd}\big|_{max} = \frac{v_o^2}{2} - (ESW)^2 \left[\frac{t^{*2}}{2} + \frac{t^* S(p)}{\omega} - \frac{C(p) - 1}{\omega^2} \right]$$

Maximum e_{rd} *occurs at* $t_v = \dfrac{v_o}{ESW}$ $\ldots$ *time of dynamic crush*

$$e_{rs}\big|_{max} = \left(\frac{ESW}{\omega} \right)^2 \left[1 + \frac{(\omega t^*)^2}{2} + \sqrt{1 + (\omega t^*)^2} \right]$$

Maximum e_{rs} *occurs at* $t_g = t^* + \dfrac{\pi + \tan^{-1}(-\omega t^*)}{\omega}$ $\ldots$ *time of* $\ddot{x}_o\big|_{max}$

1.10.1.1 *Equations of Motion and Energy Density of a Crash Model*

A simple occupant-vehicle model, shown in Fig. 1.106, is used to study the ridedown and restraint energy distribution and the effect of vehicle structural deformation and restraint stiffness on the ridedown efficiency, and occupant response. The model consists of an occupant mass, restraint stiffness, restraint slack, and a vehicle structure with a constant force level. Using the equations of motion for a simple occupant-vehicle model [14], a set of closed-form solutions for the transient ridedown and restraint energy densities was derived. These solutions are presented in the following analysis. The accuracies of the transient energy density expressions have been verified using a numerical integration technique where occupant and vehicle transient responses are used. Expressions for the maximum ridedown and restraint energy densities and the corresponding times at which the maximum densities occur are also shown.

1.10.1.2 *Ridedown, Restraint Energy Densities, and Timings*

Shown in the previous section in Eq. (1.53), the maximum ridedown energy density occurs at the time of dynamic crush and the maximum restraint energy density occurs at the time of peak occupant deceleration. Since the time of dynamic crush is in general different from the time of maximum occupant response, the sum of the maximum restraint and ridedown energy densities does not add up to the total occupant kinetic energy density. The expressions for the ridedown and restraint energy densities are shown in Eq. (1.54) for δ (restraint slack) greater than zero.

(A) δ (restraint slack) > 0

$$
\begin{aligned}
&\textit{For } \delta \textit{ (restraint slack)} > 0\textit{:}\\
&e_{rd}\big|_{\max} = 0.5\, v_o^{\,2} - (ESW)^2\left[\frac{t^{*2}}{2} + \frac{t^{*}S(p)}{\omega} - \frac{C(p)-1}{\omega^2}\right]\\
&\textit{Define } \mu \textit{ : ridedown efficiency,}\\
&\qquad e \textit{ : energy density, then}\\
&\mu = \frac{e_{rd}\big|_{\max}}{0.5\, v_o^{\,2}} = 1 - \frac{(ESW)^2}{e}\left[\frac{t^{*2}}{2} + \frac{t^{*}S(p)}{\omega} - \frac{C(p)-1}{\omega^2}\right] \qquad \ldots\ldots \quad (1)\\
&\textit{Where} \quad p = \omega(t_m - t^{*}) \quad \textit{for} \quad t_m > t^{*}\\
&\omega = \sqrt{\frac{K}{M_o}}\,, \quad t^{*} = \sqrt{\frac{2\delta}{ESW}}, \quad t_m = \frac{v_o}{ESW}\\
&C(p) = Cosine(p), \qquad S(p) = Sine(p), \qquad e = .5\, v_o^{\,2}\\
&e_{rs}\big|_{\max} = \left(\frac{ESW}{\omega}\right)^2\left[1 + \frac{(\omega t^{*})^2}{2} + \sqrt{1 + (\omega t^{*})^2}\right] \qquad \ldots\ldots \quad (2)
\end{aligned}
\tag{1.54}
$$

For the model shown in Fig. 1.106, there exist certain conditions for which the sum of the restraint and ridedown energy densities equals the occupant initial kinetic energy density, and for the timings when the maximum restraint and ridedown energy densities occur coincide.

(B) δ (restraint slack) = 0

When the restraint slack, δ, is equal to zero, (1) of Eq. (1.54) is simplified as shown in Eq. (1.55). A ratio of maximum restraint energy density to the occupant initial kinetic energy density is defined as a restraint factor (λ). Formula (3) of Eq. (1.55) shows the normalized relationship between the occupant kinetic energy density, restraint energy density, and ridedown energy density. It is shown that when δ is zero, the sum of ridedown efficiency (μ) and restraint factor (λ) equals one. In other words, the sum of the restraint and ridedown energy densities is equal to the occupant initial kinetic energy density; and the time of the maximum restraint energy density (t_g, time of maximum occupant

deceleration) and the time of maximum ridedown energy density (t_m, time of dynamic crush) coincide as shown by (6) of Eq. (1.55).

For δ (*restaint slack*) = 0

Define: λ: *restraint factor*, $\lambda = \dfrac{e_{rs}|_{\max}}{e}$

t_m: *time of dynamic crush*, $t_m = \dfrac{v_o}{ESW}$

t_g: *time of maximum occupant deceleration*

$C(p) = Cosine(p)$, *where* $p = \omega t_m$

$$\mu = 1 - \frac{(ESW)^2}{e}\left[\frac{1 - C(p)}{\omega^2}\right] \quad \ldots\ldots \quad (1)$$

$$e_{rs}|_{\max} = 2\left(\frac{ESW}{\omega}\right)^2 \quad \ldots\ldots\ldots \quad (2) \qquad (1.55)$$

Substituting (2) *into* (1), *one gets*

$$\mu = 1 - .5\lambda[1 - C(p)] \quad \ldots\ldots \quad (3)$$

$$C(p) = C(\omega t_m) = C\left(\frac{\omega v_o}{ESW}\right) \quad \ldots\ldots \quad (4)$$

Note: $\mu + \lambda = 1$ *if* $[1 - C(p)] = 2$, *or* $C(p) = -1$

therefore $p = \pi = \dfrac{\omega v_o}{ESW}$ $\ldots\ldots$ (5)

then $t_g = \dfrac{\pi}{\omega} = \dfrac{v_o}{ESW} = t_m$ $\ldots\ldots$ (6)

Using (5) of Eq. (1.55), a relationship is derived in Eq. (1.56) which shows how the occupant restraint and vehicle structural parameters affect the timings, t_m and t_g. The conditions shown in (4) of Eq. (1.56) determine the relative magnitudes of the two timings. By adjusting the restraint and/or structural parameters, the relative magnitudes of the two timings can be changed. Case study using this relationship is presented in Section 1.10.2.2.

Since $\dfrac{\omega v_o}{ESW} = \pi$ $\ldots\ldots\ldots\ldots$ (1)

Using the conventional units such as

ESW (*equivalent square wave*): *g*, v_o (*initial velocity*): *mph*

f (*restraint natural frequency*): *Hz*, *and*

ω (*circular natural frequency*): *radians*/sec

Since $\omega = 2\pi f$, (1) *becomes* (*in natural units*)

$$\frac{2fv_o}{ESW} = 1 \quad \ldots\ldots\ldots\ldots\ldots \quad (2)$$

Converting to conventional units: (2) *becomes* (1.56)

$$\frac{fv_o}{ESW} = 11 \quad \ldots\ldots\ldots\ldots\ldots \quad (3)$$

if $f < \dfrac{11\,ESW}{v_o}$, *then* $t_g > t_m$

if $f = \dfrac{11\,ESW}{v_o}$, *then* $t_g = t_m$ $\ldots\ldots$ (4)

if $f > \dfrac{11\,ESW}{v_o}$, *then* $t_g < t_m$

1.10.2 Validation of Energy Density Model in High Speed Crash

A pick-up truck equipped with an air bag and belt restrained dummies was crashed into a rigid barrier at 35 mph. Based on the test data, the ridedown and restraint energy densities of the driver dummy can be computed. These test energy densities are then compared with those computed from the simple model for validation.

1.10.2.1 *Test Energy Densities*

The vehicle compartment and left-front dummy torso decelerations and displacements from the test results are shown in Figs. 1.107 and 1.108, respectively. The vehicle dynamic crush and maximum occupant travel (relative to vehicle) are 25.7 and 9.5 inches, respectively. The time of dynamic crush (t_m) is 70 ms, and the time of maximum occupant deceleration (t_g) is 63 ms.

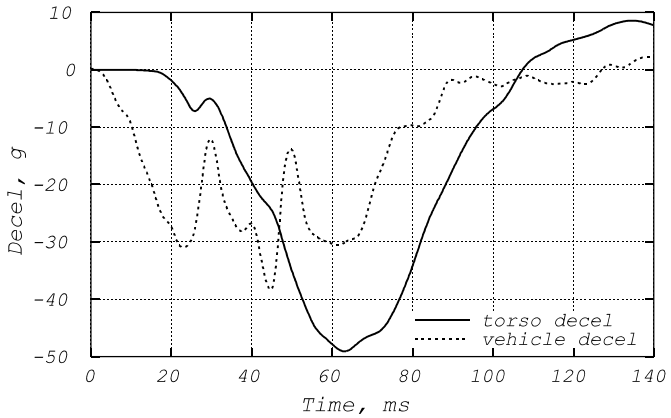

Fig. 1.107 Test Decelerations of a Truck and L.F. Torso

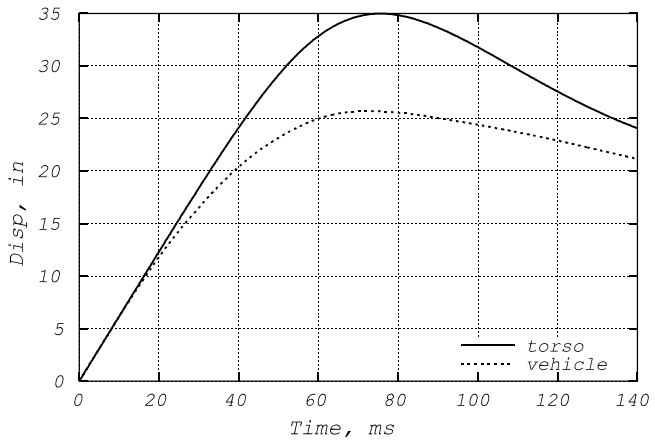

Fig. 1.108 Test Displacements of a Truck and L.F. Torso

The occupant restraint and ridedown curves can then be plotted. These are shown in Fig. 1.109. Note that the plot of the restraint curve is based on the torso deceleration and relative torso-vehicle displacement (torso travel). The restraint curve onset time (at zero-plus torso travel) is about 20 ms, which is found from the torso and truck displacement curves shown in Fig. 1.108. At 20 ms, the chest deceleration starts picking up as shown by the torso deceleration curve in Fig. 1.107, which is also

reflected in Fig. 1.109. At the same time, the ridedown curve starts picking up. At this time, the vehicle had crushed about 12 inches already. Occupant ridedown starts from this point on until the vehicle reaches a dynamic crush of 25.7 inches.

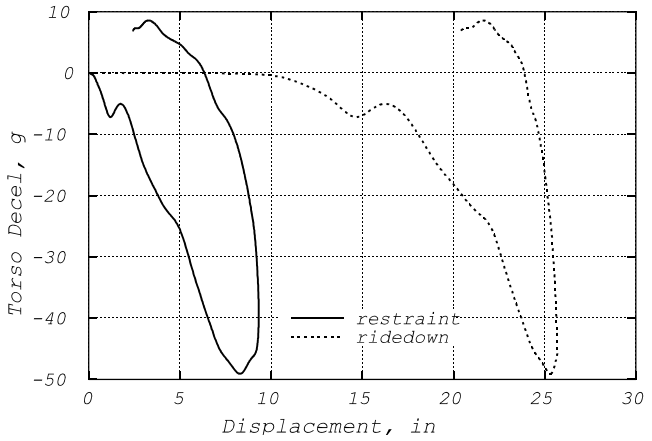

Fig. 1.109 Test Restraint and Ridedown Curves

The torso restraint and ridedown energy densities in the 35 mph test are then computed from Fig. 1.109. These are shown in Fig. 1.110. The computed maximum ridedown energy density is about 250 g-in and restraint energy density is about 235 g-in. Therefore, the ridedown efficiency is 250/(250+235) = 51%.

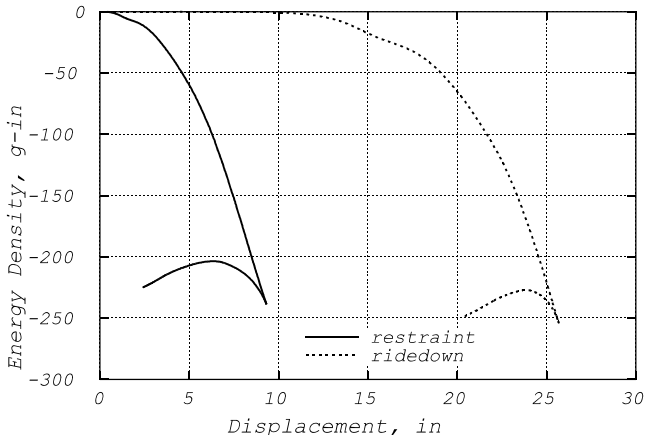

Fig. 1.110 Test Restraint and Ridedown Energy Densities

1.10.2.2 *Model Energy Densities*

Since the dynamic crush of the truck in the 35 mph test is 25.7 inches, the equivalent square wave (ESW) is computed to be:

$$ESW = .4\frac{v^2}{c} = .4\frac{(35\ mph)^2}{25.7\ in} = 19.1\ g \tag{1.57}$$

The comparison of the ESW with the vehicle compartment crash pulse is shown in Fig. 1.111.

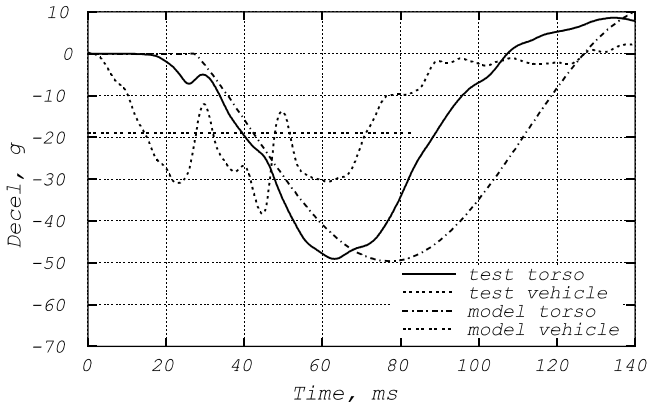

Fig. 1.111 Test and Model Comparisons of Vehicle and Torso Decelerations

The restraint slack can be estimated from the torso deceleration onset time which is about 28 ms from the torso deceleration curve shown in Fig. 1.111.

$$t^* = 0.072\sqrt{\frac{\delta}{ESW}} \qquad (\textit{units are in inches, mph, and g}).$$
$$\delta = ESW\left(\frac{t^*}{0.072}\right)^2 = 19.1\,g\left(\frac{0.028\ \text{sec}}{0.072}\right)^2 = 2.8\ in \tag{1.58}$$

The restraint specific stiffness, k, used in the test can be estimated from the test restraint curve in the loading phase shown in Fig. 1.112. k (the slope of the line segment) is computed to be about 5.3 g/in and the restraint natural frequency, f, can then be computed as follows:

$$f = \frac{1}{2\pi}\sqrt{\frac{K}{W}} = \frac{1}{2\pi}\sqrt{386.4\,k}$$
$$\textit{here } k\ (\textit{specific stiffness}) = 5.3\ g/in, \quad \textit{then}$$
$$f = 7.2\ Hz \tag{1.59}$$

Having obtained ESW, restraint slack, δ, and natural frequency, f, the occupant deceleration, restraint and ridedown energy densities, can then be computed using the formulas shown in Eqs. (1.51)–(1.53).

The model torso deceleration, shown in Fig. 1.111, is compared to the test curve. The peak torso deceleration is about the same, but the timing is late by 15 ms. Both test and model torso decelerations resemble the haversine pulse. This is due to the fact that the output response of a simple crash model subjected to a constant g-force input is a haversine.

The occupant restraint and ridedown curves for both test and model are shown in Fig. 1.112. Both model and test curves are comparable. Since only the restraint stiffness in the model loading is specified, the model unloading slope in the restraint curve is the same as the loading slope.

Shown in Fig. 1.113, the computed model energy densities using the closed-form formula compare closely with those from the test. The computed model ridedown efficiency is 53 % compared to 51 % from the test.

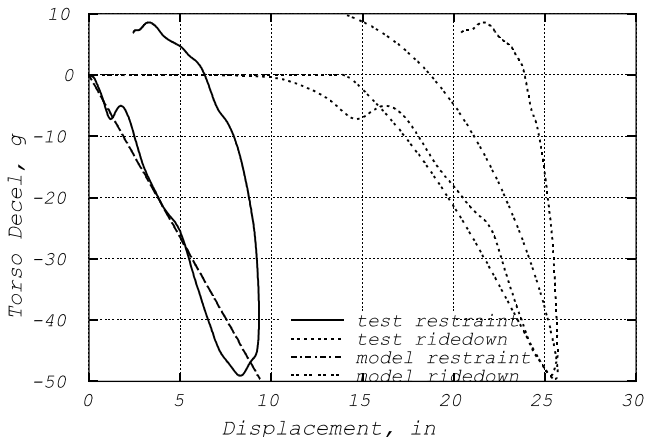

Fig. 1.112 Test and Model Comparisons of Restraint and Ridedown Curves

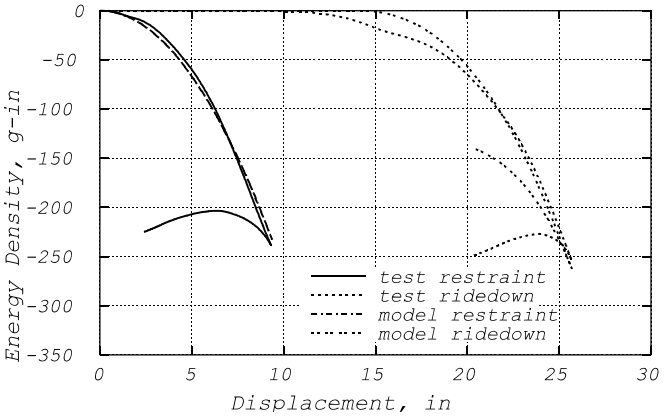

Fig. 1.113 Test and Model Comparisons of Restraint and Ridedown Energy Densities

Case Study: Using the pick-up truck test data analyzed in this section, verify the occupant and vehicle response timing relationship shown in (4) of Eq. (1.56).

The pick-up truck is equipped with an air bag and belt restraint system. The restraint natural frequency, f, has been estimated to be 7.2 Hz, as shown in Eq. (1.59). The ESW of the vehicle is 19.1 g computed in Eq. (1.57), and the barrier test speed is 35 mph.

From the formula (4) of Eq. (1.56), the right-hand side of the term [11 ESW/v_o] is equal to [11×19.1/35] = 6. Since f is 7.2 Hz, greater than [11 ESW/v_o], it is expected that $t_g < t_m$. Based on the test results shown in Figs. 1.107 and 1.108, t_g and t_m from the test are 63 and 70 ms, respectively. From Eq. (1.55) and Fig. 1.111, t_g and t_m from the model are 78 and 82 ms, respectively. In both test and model, $t_g < t_m$, which agrees with the relationship defined by the formula (4) of Eq. (1.56).

Let us define f_{tt} to be the transition timing frequency, equal to [11 ESW/v_o]. If the stiffness of the restraint system is increased beyond f_{tt}, then the maximum occupant deceleration occurs before the time of dynamic crush. It will be shown in Eq. (4.17) of Section 4.3.4.5 of Chapter 4 that t_g is a function of the restraint contact time t* and restraint natural frequency, f. When f increase, so does t_g.

1.10.3 Contour Plots of Ridedown Efficiency and Occupant Response

Normalizing the maximum ridedown energy density, shown in Eq. (1.53), by the occupant energy density, e, yields the ridedown efficiency, as shown by (1) of Eq. (1.54). For the special case where the restraint slack is zero, the ridedown efficiency, shown by (1) of Eq. (1.55), becomes a maximum.

Shown in Fig. 1.114 is the ridedown efficiency surface contour for the truck in the 31 mph barrier test from Section 1.10.2. The femur to instrument panel slack, δ, is 6 inches. As ESW decreases and/or f (restraint natural frequency) increases, the ridedown efficiency increases.

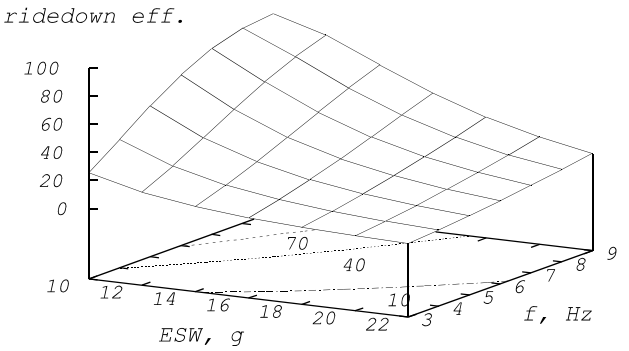

Fig. 1.114 Ridedown Efficiency Contour Plot (δ=6 in)

While the ESW decreases, the ridedown efficiency increases, as shown in Fig. 1.114, and the femur deceleration decreases, as shown in Fig. 1.115. However, as the restraint natural frequency increases, even though the ridedown efficiency increases, the femur deceleration also increases. It can therefore be stated that the higher ridedown efficiency does not guarantee that the occupant response is always lower.

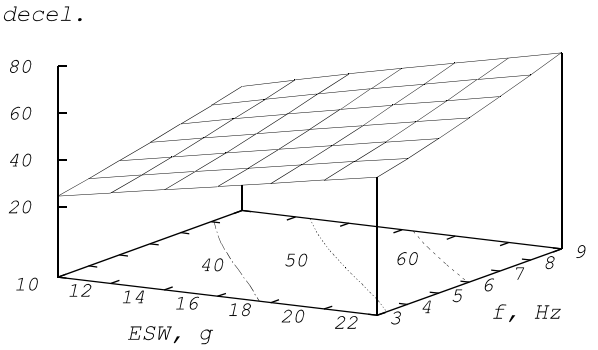

Fig. 1.115 Femur Deceleration Contour Plot (δ=6 in)

From the vehicle structural point of view (considering ESW as a variable), the higher ridedown efficiency always guarantee a lower occupant response. However, from the restraint point of view (considering restraint natural frequency as a variable), the higher ridedown efficiency does not always

guarantee lower occupant response.

To mitigate the effect of the restraint slack, a knee bolster air bag for example can be utilized. By adding this, the restraint slack is quickly taken out in a crash. For cases without restraint slack, the ridedown efficiency is the maximum for a set of design parameters such as the ESW and restraint natural frequency, as shown in Fig. 1.116.

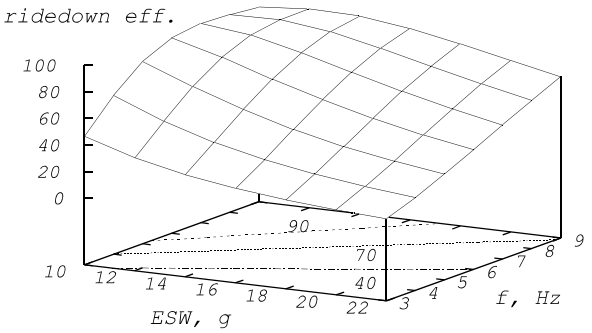

Fig. 1.116 Ridedown Efficiency Contour Plot (δ=0 in)

The effect of the restraint natural frequency on the occupant response depends on the slack (see B. EOM for Occupant in Eq. (1.52)). When the slack is taken out (δ=0), any change in the restraint stiffness (f) has no effect on the femur deceleration, as shown in Fig. 1.117.

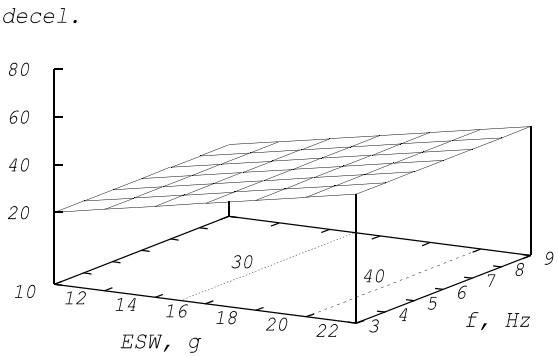

Fig. 1.117 Femur Deceleration Contour Plot (δ=0 in)

In the absence of restraint slack, the magnitude of the femur deceleration becomes two times that of the ESW. Although the restraint natural frequency does not affect the magnitude of the occupant response when the restraint slack is zero, it nevertheless affects the restraint deformation. When the restraint natural frequency is small, both the restraint deformation and restraint energy become large, and the ridedown energy (initial occupant kinetic energy−restraint energy) and ridedown efficiency become small, as shown in Fig. 1.116.

In a restraint design, the maximum component force level can be kept constant by a design constraint. For example, the steering column can be designed to yield a constant force level with the use of a break-away shear pin. In addition, the column can be designed to meet the varying stroking distance requirement. As far as the air bag and inflator design, the depth (deformation) and stiffness of a fully deployed air bag can be controlled to meet the force-deflection requirement with the use of tethers inside the air bag and adjustment of the vent size and inflator rise rate.

1.10.4 Restraint Design with Constant Occupant Deceleration

A simple means to achieve a constant peak occupant deceleration (a haversine pulse) is to have zero restraint slack. This peak occupant deceleration is two times that of vehicle ESW.

Assuming a truck in a 35 mph rigid barrier test with the following data:

ESW (equivalent square wave) = 19.1 g
δ (restraint slack) = 0 inch

Find the occupant response and energy density distribution for three cases with restraint natural frequencies (f) as shown below. Note that the case #2 frequency, 6 Hz, derived using (3) of Eq. (1.56) for the restraint system with slack equal to zero, is termed the restraint critical frequency, f_c.

$$f_c = 11\frac{ESW}{v_o} = 11\frac{19.1g}{35mph} = 6Hz \tag{1.60}$$

Using Eqs. (1.51)–(1.54), all the other responses can be computed for the three cases as shown in Table 1.9. Case #2 shows that the timing, t_m, of vehicle dynamic crush coincides with the timing, t_g, of maximum occupant response, a_o, and that the sum of restraint and ridedown energy densities equals the initial occupant kinetic energy density, e.

Table 1.9 Occupant Response with Restraint Slack Equal To Zero

Case	f, Hz	t_v, ms	t_g, ms	$d=x_{ov}$, in	a_o, g	e_{rd}, g-in	e_{rs}, g-in	$e_{rd}+e_{rs}$, g-in
#1	5	83	100	15	38.2	222	288	510
#2	6	83	83	10.4	38.2	290	200	490
#3	7	83	71	7.66	38.2	352	147	499

Formula (4) of Eq. (1.56) also shows the timing relationship between t_v and t_g. In this example, the transient ridedown and restraint energy densities for the three cases are plotted and shown in Fig. 1.118. The heavy curves are for the restraint energy densities, and the thin curves, ridedown energy densities. Note that for case #2 with a critical frequency of 6 Hz, the ridedown and restraint energy densities add up to the total occupant kinetic energy density, $e = .4\ v^2 = .4\ (35\ mph)^2 = 490$ g-in.

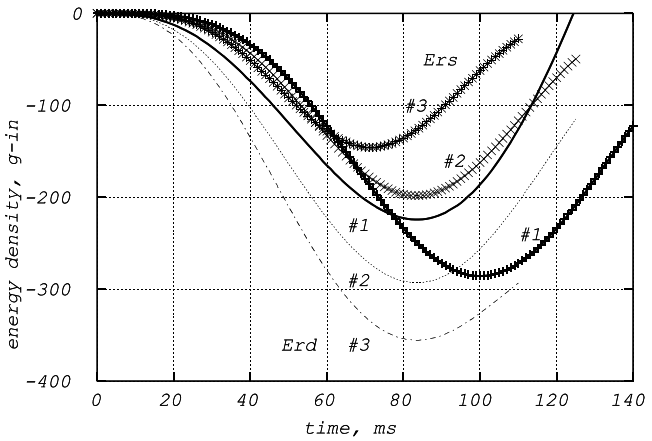

Fig. 1.118 Energy Densities versus Time for 3 Cases with Restraint Slack = 0

Fig. 1.119 shows the occupant deceleration versus relative displacement for the three cases. The slope of each line segment represents the specific stiffness of that case. Case #1 has the softest restraint (5 Hz) and the largest restraint deformation while case #3 (7 Hz) has the stiffest restraint and the least deformation. However, all the three cases have the same occupant deceleration.

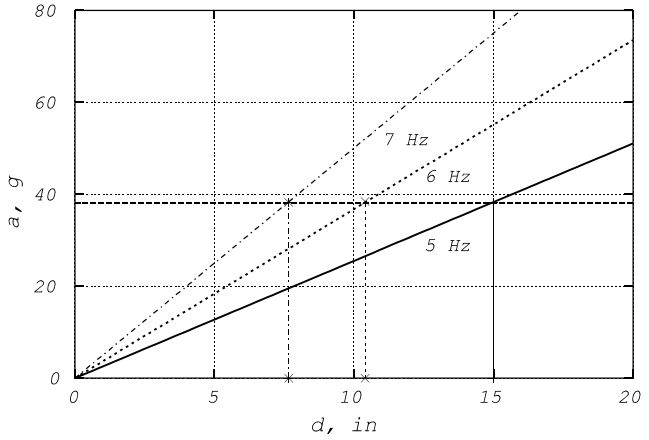

Fig. 1.119 Occupant Acceleration vs. Restraint Deformation

The relationship between the three variables, occupant deceleration (a), restraint deformation (d), and restraint natural frequency (f), observed in Fig. 1.119 can also be derived by method in Eq. (1.61).

$$f = \frac{1}{2\pi}\sqrt{\frac{k}{m}}, \quad \text{then} \quad \frac{k}{m} = (2\pi f)^2 \quad \ldots\ldots \quad (1)$$

Define a: occupant deceleration, then

$$a = \frac{F}{m} = \frac{k\,d}{m} = (2\pi f)^2\, d \quad \ldots\ldots\ldots \quad (2) \qquad (1.61)$$

for case #3: $f = 7\ Hz, \quad d = 7.66\ in,$ *then*

$$a = (2\pi \times 7\ Hz)^2\,(7.66\ in) = 14{,}818\ in/s^2 = 38.3\ g$$

The relationship between the restraint energy density (e_{rs}) and the restraint deformation (e) can also be derived separately from the plot shown in Fig. 1.120. The straight line segment of e_{rs} vs. d is plotted using the data shown in Table 1.9.

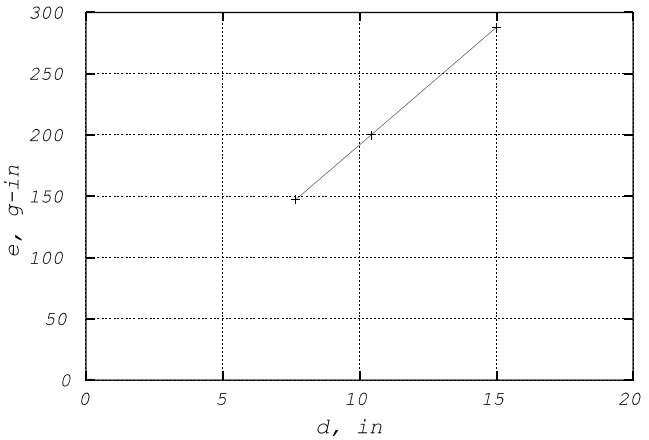

Fig. 1.120 Restraint Energy Density vs. Deformation

Since restraint energy density is the area under the a vs. d line segment shown in Fig. 1.119, the relationship can then be derived as shown in Eq. (1.62).

$$\Delta e_{rs} = \frac{a_o \Delta d}{2} \quad \ldots\ldots\ldots\ldots \quad (1)$$

The slope of line segment in e_{rs} *vs. d plot*:

$$\frac{a_o}{2} = ESW = \frac{\Delta e_{rs}}{\Delta d} \quad \ldots\ldots\ldots\ldots (2)$$

$$\frac{a_o}{2} = \frac{(288 - 147)\, g\text{-}in}{(15 - 7.66)\, in} = 19.2\, g, \quad a_o = 38.4\, g \qquad (1.62)$$

1.10.5 Design Constraint and Trade-Off

In this design example, the design limit and trade-off between the knee bolster and vehicle structure available crush spaces are discussed. In practice, the femur deceleration or loading is not only governed by the vehicle dynamic crush and knee bolster stiffness, but also by the knee bolster available crush space. Assuming that the available knee bolster crush space, D, is 6 inches before it bottoms out and the design target force level, F, is 1800 pounds, then the bolster stiffness, K, is computed to be 300 lb/in. This knee bolster design, having the constant restraint energy force-deflection relationship shown in Fig. 1.121, yields the same ridedown efficiency despite differences in knee bolster deformation.

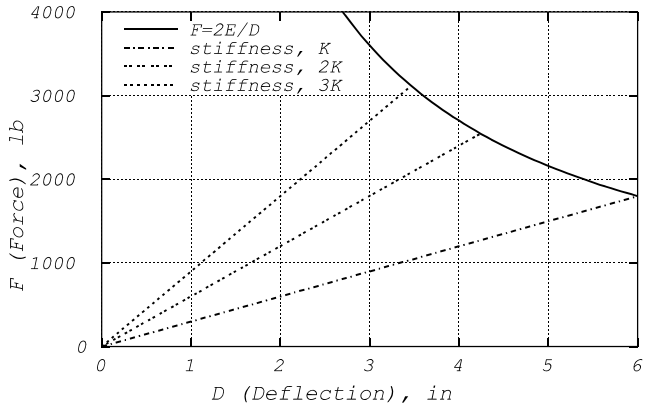

Fig. 1.121 Constant Energy Knee Bolster Force vs. Deflection

The knee bolster restraint energy, E_{rs}, at this design level, the femur (w = 35 lbs) kinetic energy, E, at the 31 mph impact, and the femur ridedown efficiency are shown by (1), (2), and (3) of Eq. (1.63), respectively.

$$E_{rs} = \frac{1}{2} D F = \frac{1}{2}(6\ in \times 1{,}800\ lb) = 5{,}400\ in\text{-}lb \quad \ldots\ (1)$$

$$\therefore\ The\ constant\ energy\ F\text{-}D\ curve\ is\ D F = 10{,}800\ in\text{-}lb$$

$$E = M(\frac{1}{2} V_o^2) = 35\ lb\ (385\ g\text{-}in) = 13475\ in\text{-}lb \quad \ldots\ (2) \qquad (1.63)$$

The ridedown efficiency is:

$$\mu = \frac{E_{rd}}{E} = \frac{E - E_{rs}}{E} = \frac{13475 - 5400}{13475} = 60\,\% \quad \ldots\ldots\ (3)$$

If the restraint energy remains the same and the knee bolster stiffness has to be doubled to 2K due to limited knee bolster crush space, then the corresponding knee bolster deflection, D, and the femur force, F, are shown in Eq. (1.64). The constant energy knee bolster force-deflection curve with stiffness of 2K is shown in Fig. 1.121.

$$D = \sqrt{\frac{2E_{rs}}{(2K)}} = \sqrt{\frac{2 \times 5400\ in\text{-}lb}{(2 \times 300)\frac{lb}{in}}} = 4.243\ in$$
$$\textit{The femur force is:}\quad F = (2K)\,D = (600\frac{lb}{in}) \times 4.243\ in = 2546\ lb \tag{1.64}$$

Since this femur force exceeds both the design level of 1800 pounds and the FMVSS limit of 2250 pounds, the vehicle structure must be changed such that the vehicle ESW is decreased according to the surface contour plot in Fig. 1.114. The trade-off between the vehicle dynamic crush and knee-bolster available crush space is evident in the vehicle design needed to meet the safety design limit.

1.11 REFERENCES

1. Huang, M., Lawson, G.P., Powell, B.K., and Walker, J.H., "Characterization of Vehicle Deceleration Time Histories in the Analysis of Impact Dynamics," SAE 770013, 1977, SAE International Automotive Engineering Congress and Exposition, February 28 – March 4, Detroit, Michigan.
2. Katoh, H. and Nakahama, R., "A Study on the Ridedown Evaluation," Proceeding, 9th International Technical Conference on Experimental Safety Vehicles, pp. 190-195, 1982.
3. Bonello, K.J., "Occupant Energy Management Technique for Restraint System Analysis and Design – Understanding the Physics of the System," SAE 922083.
4. Evans, N.C., Furton, L.M. and Cok, D.A.,"Occupant Energy Management Technique for Restraint System Analysis and Design – Theory and Validation," SAE 922082.
5. Huang, M., Laya, J., Loo, M., "A Study on Ridedown Efficiency and Occupant Responses in High Speed Crash Tests, " SAE 950656, Detroit, Feb., 1995.
6. Adams, T.G., Huang, M., Hultman, R.W., Marsh, J.C., and Henson, S.E., "The Development of an Advanced Air Bag Crash Sensing System," pp. 159–164, Paper no. 905140, XXIII FISITA Congress, Torino, Italy, 7–11 May, 1990.
7. "SAE Vehicle Occupant Restraint Systems and Components Standards Manual," 1999 Edition, SAE HS–13, Society of Automotive Engineers, Inc., Warrendale, Pa.
8. "Instrumentation for Impact Tests – Part 1– Electronic Instrumentation – SAE J211/1 March 1995," pp. 34.344–34.353; "Instrumentation for Impact Tests – Part 2– Photographic Instrumentation – SAE J211/2 March 1995," pp. 34.354–34.355, 1999 SAE Handbook, Society of Automotive Engineers, Inc.
9. Solnes, J., "Stochastic Processes and Random Vibration, Theory and Practice," John Wiley and Sons, New York, 1997.
10. "Radar Detection of Traffic Obstacles," Automotive Engineering, September, 1994.
11. Farber, E. and Huang, M.,"Rear-end Collision-Warning Algorithms with Headway Warning and Lead Vehicle Deceleration Information," pp.1128–1133, Proceeding, Second World Congress on Intelligent Transportation System, Yokohama, Japan, Nov., 1995.
12. Allen, J.L., "Power-Rate Crash Sensing Method for Safety Device Actuation," Paper #920478, pp. 55–60, SAE SP-903, 1992.
13. Huang, M. "Method for Activating an Occupant Restraint in a Vehicle," 1995, U.S. Patent 5,394,328, granted February 28, 1995.
14. Huang, M., "An Analysis of the Vehicle-Occupant Impact Dynamics and its Application," SAE 830977, Passenger Car Meeting, Dearborn, Michigan, June 6–9, 1983.

15. Lane, W.C., "The Interaction of Pretensioner With Restraints And Supplemental Restraints," pp.77–80, International Body Engineering Conference, Proceedings of Automotive Body Interior & Safety Systems, September 26–29, 1994, Detroit, Michigan.

CHAPTER 2

CRASH PULSE CHARACTERIZATION

2.1 INTRODUCTION

To supplement full scale dynamic testing of vehicle crashworthiness, mathematical models and laboratory tests (such as those using a Hyge sled or a vehicle crash simulator) are frequently employed. The objective of these tests is the prediction of changes in overall safety performance as vehicle structural and occupant restraint parameters are varied. To achieve this objective, it is frequently desirable to characterize vehicle crash pulses such that parametric optimization of the crash performance can be defined. Crash pulse characterization greatly simplifies the representation of crash pulse time histories and yet maintains as many response parameters as possible. The response parameters used to characterize the crash pulse are those describing the physical events occurring during the crash such as (maximum) dynamic crush, velocity change, time of dynamic crush, centroid time, static crush, and separation (rebound) velocity. In addition, the kinematic responses of the test such as transient acceleration, velocity, displacement in time domain, and energy absorption in the displacement domain are compared. Frequency contents and spectrum magnitudes of harmonic pulses in a Fourier series pulse characterization can be utilized for frequency domain analysis.

A number of crash pulse approximations and techniques have been developed for the characterization. These are divided into two major categories according to whether or not the initial deceleration is zero.

- Pulse approximations with non-zero initial deceleration
  - * Average Square Wave (ASW)
  - * Equivalent Square Wave (ESW)
  - * Tipped Equivalent Square Wave (TESW)
- Pulse approximations with zero initial deceleration
  - * Fourier Equivalent Wave (FEW) and Sensitivity Analysis
  - * Trapezoidal Wave Approximation (TWA)
  - * Bi-Slope Approximation (BSA)
  - * Basic Harmonic Pulses

Each one of the approximation techniques is solved analytically for a closed-form formula which satisfies certain boundary conditions based on the crash test results. Since the mechanism of each impact involves two distinct phases, the deformation phase and the rebound phase, the boundary conditions at the end of the deformation phase are utilized to derive the parametric relationship. The dynamic crush and/or velocity change at the end of deformation phase are the basic boundary conditions frequently used in the analysis.

2.2 MOMENT-AREA METHOD

Given the accelerometer output from a crash pulse, the velocity and displacement can be obtained from the first and second integrals of the output data. However, the displacement can also be determined directly from the accelerometer data and only the first integral by using the moment-area method. This method yields a kinematic relationship between the maximum dynamic crush, the corresponding velocity change, and the centroid of the crash pulse.

The centroid is the geometric center of the area defined by the acceleration curve from time zero up to the time of dynamic crush. The centroid of a crash pulse defines the characteristic length (crush per mph) of the structure and determines whether the crash pulse is front-loaded, even-loaded, or rear-loaded. The shape of the crash pulse as influenced by the location of a centroid affects the occupants' responses. The centroid method is also used in the derivation of Tipped Equivalent Square Wave (TESW) for the crash pulse analysis described in Sections 2.3.3 and 2.3.4 of this chapter.

2.2.1 Displacement Computation Without Integration

The moment-area method is applied to derive the displacement equation without using the double integral of the accelerometer data. Letting the initial conditions be $x = x_o$ and $v = v_o$ at $t = 0$, the displacement x_1, the position of particle at $t = t_1$, can then be derived. In the v–t diagram shown in Fig. 2.1, the displacement change, $x_1 - x_o$, is the area under the v–t curve. The area consists of a rectangle, $v_o\, t_1$, plus the area between the horizontal line v_o and the velocity curve. The derivation of the displacement formula is shown in Eq. (2.1).

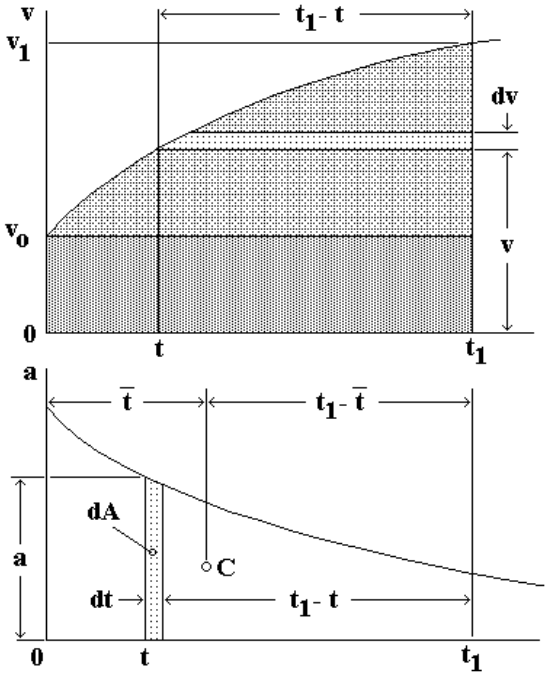

Fig. 2.1 Moment-Area Method and Displacement Equation

$$x_1 - x_o = v_o t_1 + \int_{v_o}^{v_1} (t_1 - t)\, dv \qquad \ldots\ldots\ (1)$$

since $dv = a\,dt$,
let $t_1 - t = y$,
differential area: $dA = a\,dt$,
and $t_1 - \bar{t} = \bar{Y}$ (*horiz. location of centroid under a vs. t curve*)

$$\therefore \quad \int_{v_o}^{v_1} (t_1 - t)\, dv = \int_{t_o}^{t_1} (t_1 - t)\, a\, dt = \int y\, dA \qquad (2.1)$$
$$= \bar{Y}A = (t_1 - \bar{t}) \int_0^{t_1} a\, dt$$

Substituting this into (1):

$$x_1 = x_o + v_o t_1 + (t_1 - \bar{t}) \int_0^{t_1} a\, dt \qquad \ldots\ldots\ (2)$$

where $\int_o^{t_1} a\, dt$ *is area under the a–t curve between* 0 *and* t_1

2.2.2 Centroid Time and Characteristics Length

Since the centroid time is the time at the geometric center of area of the crash pulse from time zero to the time of dynamic crush, it can be computed using the displacement equation derived in the previous section.

In a fixed rigid barrier impact where the initial velocity is v_o, and the dynamic crush, C (x_1 at t_1), the centroid time is simplified as follows:

$$\because \quad x_1 = x_o + v_o t_1 + (t_1 - \bar{t}) \int_o^{t_1} a\,dt$$

$$where \quad \int_0^{t_1} a\,dt = v_1 - v_o = 0 - v_o = -v_o$$

$$\therefore \quad C = x_1 = 0 + v_o t_1 + (t_1 - \bar{t})(-v_o) = v_o \bar{t} = v_o t_c \tag{2.2}$$

$$then,\ centroid\ time\ t_c\ is\ simplified\ to$$

$$t_c = \frac{C}{v_o} \quad \ldots\ldots\ldots\ldots\ldots \quad (1)$$

In a general case, where a bullet vehicle impacts on a target vehicle, the centroid times of both vehicles are the same. Using the concept of relative motion described in Section 4.7.1.1 in Chapter 4, the centroid time can be computed using Eq.(2.3) where ΔC is the total dynamic crush and Δv_o is the relative approach velocity or the closing speed of the two vehicles.

$$t_c = \frac{\Delta C}{\Delta v_0} \tag{2.3}$$

From the formula derived for a rigid barrier impact, the expression for the centroid time is the same as that for the characteristic length of the vehicle structure. For the conventional units such as C (in), v_o (mph), and t_c (ms), the centroid time formula becomes:

$$t_c = 56.8 \frac{C}{v_o} \qquad where$$

$$C:\ in,\quad v_o:\ mph,\quad and\quad t_c:\ ms \tag{2.4}$$

Since C is the dynamic crush and v_o is the vehicle-rigid barrier impact velocity, the ratio of C/v_o (the amount of crush per unit of impact speed, inch/mph) is defined as the characteristic length of the vehicle structure. Based on eleven fixed barrier impact tests of a mid-size passenger car and a linear regression analysis, the characteristic length is found to be approximately 0.92 inch/mph, the slope of the regression line as shown in Fig. 2.2. For light trucks, the characteristic length is about 0.7 inch/mph.

The intercept of the regression line with the x-axis (velocity) is about 2 mph, at which there is no dynamic crush. Since any impact at a low speed yields a dynamic deformation, the only case to have zero dynamic crush is when the impact velocity is zero. This suggests that a higher order regression curve be used if the accuracy in the low speed prediction is critical. In a study by Lundstrom [1], about thirty mid-1960 production domestic automobiles were run into rigid barrier at speeds of 10–50 mph. The characteristic length was found to be 1.2 inch/mph and the horizontal intercept was about 8 mph. Therefore, the linear regression line is $C = -8 + 1.2\,V$ where C is the dynamic crush in inches and V is the barrier impact velocity in mph.

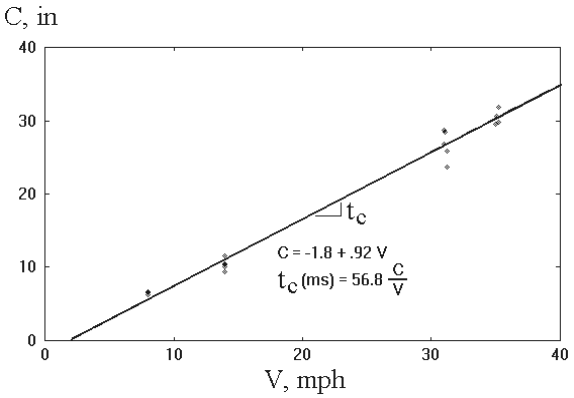

Fig. 2.2 Centroid Time of a Mid-Size Passenger Car (slope of C vs. V line)

The significance of the characteristic length lies in the fact that it is related to the vehicle stiffness per unit of vehicle weight (specific stiffness) which is presented in Chapter 4. Thus, the specific stiffness (pounds/inch/pound), k/w, is inversely proportional to the square of characteristic length (inches/mph). For example, for mid-1960 automobiles, the characteristic length is 1.2 inches/mph; then the specific stiffness is equal to 0.555 pounds/in/pound. For a typical automobile weight of 4,000 pounds, the front end structure stiffness of the mid-1960 vehicle is then equal to 2222 pounds/inch. For a more modern mid-size vehicle as shown in Fig. 2.2, the specific stiffness is 0.945 pounds/in/pound (use C/V=.92 in the formula for k/w in Section 4.5.1 in Chapter 4). For a typical vehicle weight of 3500 pounds, the front end stiffness is then 3308 pounds/inch, which is stiffer than that of the mid-1960 vehicles. In other words, modern vehicles are smaller, lighter but stiffer than those in mid-1960.

2.2.3 Construction of Centroid Time and Residual Deformation

The centroid time can be constructed for a given displacement-time history of a crash test as shown in Fig. 2.3.

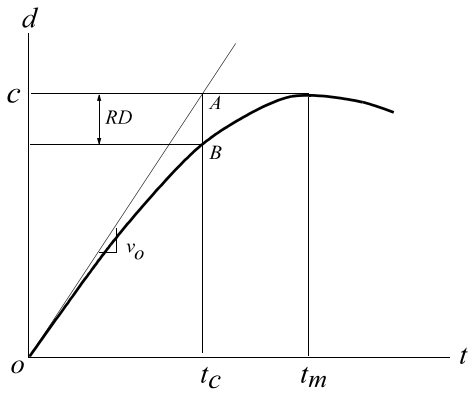

Fig. 2.3 Centroid Location and Residual Deformation

Residual deformation (RD) is the displacement difference between the dynamic crush (maximum displacement) and the displacement at the centroid time. Graphically, RD can be constructed from the transient displacement curve obtained from the single- or multiple-vehicle test.

Given a transient displacement (crush) profile from a barrier crash test, the residual deformation and its centroid location on the time axis can be constructed as follows.

Construction:
1. On the d–t curve, draw a slope at time zero. The slope is the initial barrier impact velocity, v_o.
2. The slope intersects the horizontal line through dynamic crush, C, at A.
3. Draw a vertical line from A which intersects the displacement curve at B and time axis at t_c.
4. The distance between A and B is RD.

From Section 2.2.2, the relationship between the dynamic crush, centroid time, and the initial impact speed is shown as follows.

$$v_o = \frac{opposite\ side}{adjacent\ side} = \frac{C}{t_c} \tag{2.5}$$

From Eq. (2.5), C/v_o (a characteristic length) is also the centroid time of the crash pulse in the deformation phase. t_c is the centroid time where RD (residual deformation) is located. Shown in Fig. 2.3, RD is equal to the dynamic crush minus the vehicle displacement (or deformation) at the centroid time. Note that Eq. (2.5) is also applicable to vehicle-to-vehicle impact where C is then the maximum dynamic crush of the two vehicles combined and v_o is the relative approach velocity (or closing speed). Both vehicles yield the same centroid time and time at dynamic crush.

It has been found that in a rigid barrier impact, the effect of RD in reducing the occupant injury numbers in an impact is similar to the effect of dynamic crush (see Fig. 1.98 in Section 1.9.5 in Chapter 1). The test data of the mid-size passenger car and full-size truck in the 31 mph rigid barrier tests are analyzed for the correlation between the chest g and RD. Shown in Fig. 2.4 is the scatter plots of chest deceleration versus RD for both car and truck, respectively. The effect of RD in reducing chest deceleration is more pronounced in light trucks than in passenger cars. This is because the slope of the regression line for the truck is steeper than that of the car as shown in Fig. 2.4.

From Fig. 2.4, the mean values of the RD for the car and truck in the 31 mph tests are about 5.2 and 4.3 inches, respectively. The mean values of the dynamic crush for both car and truck from Fig. 1.98 are about 23 and 18 inches, respectively. Therefore, the percentage of RD in terms of the dynamic crush for both car and truck is about 23%. It will be shown in the next section that for a vehicle structure represented by a linear spring mass system which yields the halfsine transient displacement, the RD is 16% of the dynamic crush, and the centroid time is 64% of the time of dynamic crush (t_m). In production vehicles, the typical range of the relative centroid location (ratio of centroid time to the time of dynamic crush) is between 46 and 57% less than that of a spring mass model (64%). However, the percentage of RD w.r.t. the dynamic crush of a production vehicle is a few percentage points larger than that of the spring mass model (16%). The differences in the timing and magnitude of response between the test and the spring mass model are attributed to the absence of damping in the model. The detailed discussions on this subject are presented in Section 4.10 of Chapter 4.

2.2.3.1 *Centroid of a Quarter-Sine Pulse*

The x and y coordinates of the area centroid of the quarter-sine pulse shown in Fig. 2.5 are to be determined. The derivation steps to obtain the x and y coordinates are shown in Eqs. (2.6) and (2.7), respectively. The x coordinate of the area centroid is equal to 64% of the duration of the quarter-sine wave. The use of centroid of a quarter-sine wave in approximating a test crash pulse and in simple spring-mass impact modeling will be explored in this chapter and Chapter 4, respectively.

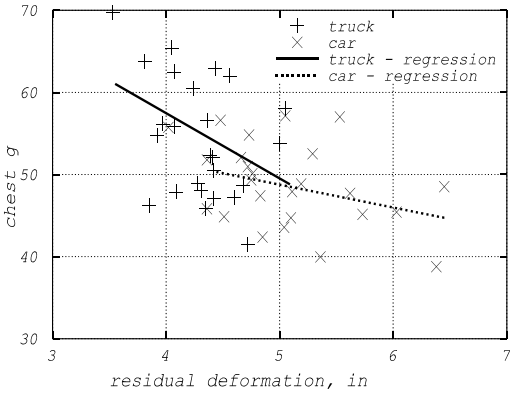

Fig. 2.4 Chest g vs. RD in 31 mph Rigid Barrier Tests

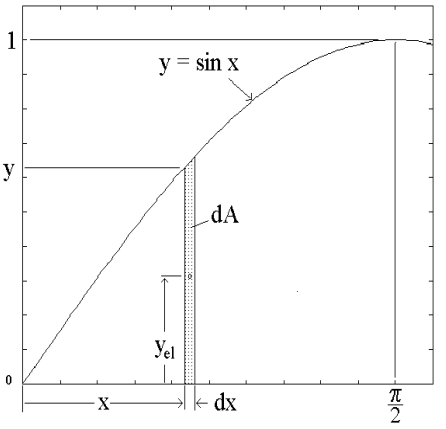

Fig. 2.5 Derivation of x & y Coordinates of Quarter-Sine Centroid

$$\bar{X}=\frac{\int xdA}{A} \quad where \quad dA=ydx=(sinx)dx,$$

$$and \quad A=\int dA=\left[-cosx\right]_0^x=1-cosx$$

$$Integrating: \quad \int xdA=\int_0^x x(sinx)dx,$$

one can use integration by parts $(dvu=vdu+udv)$:

Use $u=x,\quad du=dx,$ *and let* $dv=(sinx)dx,$ *then* $v=-cosx$

$$\therefore \quad \int udv=uv-\int vdu=-x(cosx)+\int_0^x(cosx)dx=\sin x-x(cosx) \tag{2.6}$$

$$and \quad \bar{X}=\int\frac{xdA}{A}=\frac{sinx-x(cosx)}{1-cosx} \quad . \; . \; . \; . \; . \; . \; . \; (1)$$

$$For \quad x=\frac{\pi}{2}, \quad \bar{X}=1 \quad \left(or \; 64\% \; of \; \frac{\pi}{2}\right)$$

$$then \quad RD(residual \; deformation)=1-\sin(\bar{X})=1-\sin(1)=.16$$

$$= 16\% \; of \; dynamic \; crush$$

$$\bar{Y}=\frac{\int y_{el}dA}{A}, \quad where \quad dA=ydx$$

$$let \quad y_{el}(midpoint \; of \; y \; of \; the \; element \; dA)=\frac{y}{2}, \quad then$$

$$\int y_{el}dA=\frac{1}{2}\int y^2dx \qquad where \quad y=sinx \; ,$$

$$\therefore \quad \frac{1}{2}\int y^2dx=\frac{1}{2}\int\sin^2xdx=\frac{1}{4}\int_0^x(1-\cos2x)dx=\frac{1}{4}\left(x-\frac{sin2x}{2}\right) \tag{2.7}$$

$$For \; x=\frac{\pi}{2}, \; A=1, \quad \frac{1}{2}\int y^2dx=\frac{1}{4}\left(\frac{\pi}{2}\right)=\frac{\pi}{8}, \quad \therefore \quad \bar{Y}=\frac{\frac{1}{2}\int y^2dx}{A}=\frac{\pi}{8}\approx 0.393$$

2.2.3.2 *Residual Deformation of a Quarter-Sine*

A quarter-sine displacement curve is the displacement-time history of a simple spring mass model impacting a rigid barrier. Since the deceleration response of the spring mass model is also a halfsine, the area centroid locations of both displacement and deceleration responses are the same. The centroid location of the simple spring mass model response provides a reference value for those derived from the crash test results. Residual deformation (RD) is defined as the difference between the dynamic crush and the crush at the centroid time. Higher RD has been found to correlate well with the higher occupant ride down efficiency and the lower occupant torso deceleration in an impact.

For a quarter-sine displacement curve, the relative centroid location, t_c/t_m, equals to .64 as shown in Eq. (2.8). It has been derived in the previous section that RD = 0.16 C.

$$t_c = \frac{C}{v_o} = \frac{1}{\omega_n} = \frac{t}{2\pi} = \frac{4t_m}{2\pi} = \frac{2}{\pi}t_m, \quad \textit{where}$$
$$\textit{t is the period of the sinusoidal wave}$$
$$\therefore \quad t_c = .64t_m \tag{2.8}$$

2.3 PULSE APPROXIMATIONS WITH NON-ZERO INITIAL DECELERATION

A crash pulse is a collection of accelerometer data points recorded in a test. The duration of the collision lasts from the time of impact (time zero) to the time of separation. The deceleration value at both of these times is zero in any collision. In the following section concerning the crash pulse approximations using ASW (Average Square Wave), ESW (Equivalent Square Wave), and TESW (Tipped Equivalent Square Wave), the deceleration at time zero is non-zero. The approximation of a crash pulse with non-zero deceleration at time zero is simpler since only one line segment needs to be defined during the deformation phase. The number of parameters needed to define the pulse approximation depends on the number of boundary conditions to be satisfied. It ranges from one parameter for both the ASW and ESW approximations to two parameters for the TESW approximation.

2.3.1 ASW (Average Square Wave)

Using kinematic relationship (2) of Eq. (1.12) in Section 1.4, we have

$$a = \frac{dv}{dt} \tag{2.9}$$

Let t_m be the time of dynamic crush, C. Since the magnitude of velocity change between time zero and t_m in the fixed barrier impact is V_o, the deceleration of the average square wave, A_{avg}, can then be expressed as

$$a = A_{avg} = \frac{\Delta v_m}{t_m} = \frac{v_o}{t_m} \tag{2.10}$$

Note that Eq. (2.10) uses consistent units, such as a in ft/s^2 , v_o in ft/s, and C in ft.

where: A_{avg}: Average Square Wave (ASW) in g's
v_o: barrier impact speed in mph
t_m: time at dynamic crush in ms

After converting to conventional units shown above, Eq.(2.10) becomes:

$$A_{avg} = 45.55\frac{v_o}{t_m} \tag{2.11}$$

Since ASW is defined by the velocity change between time zero and t_m, it satisfies the test velocity boundary condition at t_m. Since the energy per unit of mass (energy density) in the deformation phase up to t_m is equal to the energy density difference between time zero and t_m, $0.5V_o^2$, the energy contained in the ASW up to t_m, is the same as that of the test. However, the test dynamic crush is not met in general by the ASW. Therefore, the energy density computed by the product of ASW and its dynamic crush will be different from that in the test. The details and comparisons are presented in the following sections.

Just as ASW satisfies only the test velocity change but not dynamic crush, ESW satisfies the test dynamic crush but not t_m. The characteristics of ESW are described in the next section.

2.3.2 ESW (Equivalent Square Wave)

Using kinematic relationship #3 of Section 1.4, we have

$$\begin{aligned} a\,dx &= v\,dv \\ \int_{x_o}^{x} a dx &= \int_{v_o}^{v} v dv \end{aligned} \tag{2.12}$$

There are two differential variables shown in Eq. (2.12) which are differential displacement (dx) and differential velocity (dv). The term adx or vdv is referred to as the differential energy density, where the time variable is not involved. Furthermore, adx is related to the differential change in structural energy absorption and is equal to vdv, the differential change in kinetic energy of a particle.

The initial conditions at t = 0 are $v = v_0$, $x = x_0 = 0$, and the boundary conditions (b.c.) at $t = t_m$ (time of dynamic crush) are $v = 0$, $x = C$ (from the test).

Let a = constant with positive magnitude, and $v_0 = V$, then the integrals yield Eq. (2.13).

$$a = .5\,\frac{V^2}{C} \tag{2.13}$$

Note the equation above uses consistent units, such as a in ft/s^2, V in ft/s, and C in ft. Then, after converting to conventional units, Eq. (2.13) becomes Eq. (2.14).

$$ESW = .4\,\frac{V^2}{C} \tag{2.14}$$

where ESW: Equivalent Square Wave in g's
V: Barrier impact speed, mph
C: Dynamic crush, in

As an example, for a mid-size passenger vehicle in a barrier impact test at V = 30 mph, the dynamic crush is C = 24 inches. Using Eq. (2.14), the magnitude of ESW is then equal to 15 g. The dynamic crush due to ESW is the same as that from the test. However, t_m, the time at dynamic crush due to ESW, is later than that in the test.

2.3.2.1 *ESW Transient Analysis*

There are several parameters defining an ESW in the deformation phase and its integrals. Assuming the deceleration in the restitution phase is a ramp extending from ESW to zero, then the parametric relationship can be obtained for the ESW transient analysis. Given the vehicle barrier impact speed (V), dynamic crush (C), and rebound velocity (V_r), the formulas for (ESW), time of dynamic crush (T), rebound displacement (d_r), static crush ($C_s = C - d_r$), rebound duration (ΔT), and coefficient of restitution (e) can be derived as follows:

<u>*Deformation Phase (0 → T)*</u>: The dynamic crush, C, can be derived as a function of initial velocity, V, and time of dynamic crush, T. Note that T defined here is for ESW only and is not necessarily the same as t_m from the test.

$$\begin{aligned} &\textit{since} && a = .5\frac{v^2}{C} && \ldots\ldots\ldots && (1), \\ &\textit{and} && a = \frac{v}{T} && \ldots\ldots\ldots\ldots && (2), \\ &\because\ (1) = (2), && C = .5vT && \ldots\ldots\ldots && (3) \end{aligned} \tag{2.15}$$

Using the units of g, mph, in, and ms, (3) of Eq. (2.15) becomes C = 0.0088 vT.

<u>For a full- size car in a rigid barrier impact</u>: T ≈100 ms, then C = 0.9 v, where the slope is (C/v) is 0.9 in/mph and is referred to as the characteristic length of the vehicle for the given impact mode.

<u>For a full-size car in a rigid pole impact</u>: T ≈180 ms, then, C = 1.6 v and the characteristic length is 1.6 in/mph, larger than that in the rigid barrier impact. This is due to the fact that the structure in the pole localized impact is softer than that in the frontal barrier test.

<u>*Restitution Phase*</u> (T → T+$_\Delta$T)

The rebound displacement, d_r, and rebound velocity, v_r, can be obtained explicitly as follows:

$$\begin{aligned} &\textit{Deceleration in the restitution phase: } \ddot{x} = a + \left(\frac{-a}{\Delta T}\right)t \\ &\textit{where } t: 0 \rightarrow \Delta T, \quad \textit{then} \quad \dot{x} = \int_0^t \ddot{x}dt = at + \left(\frac{-a}{\Delta T}\right)\frac{t^2}{2} \\ &\textit{and} \qquad x = \int_0^t \dot{x}dt = \frac{at^2}{2} + \left(\frac{-a}{\Delta T}\right)\frac{t^3}{6} \\ &\therefore\ v_r = \int_o^{\Delta T}\ddot{x}dt = \frac{a\,\Delta T}{2} \qquad \ldots\ldots (4), \quad \textit{and} \\ &\quad d_r = \int_o^{\Delta T}\dot{X}dt = \frac{a\,(\Delta T)^2}{3} \qquad \ldots\ldots (5) \end{aligned} \tag{2.16}$$

Using units of g, mph, in, ms:

$$\begin{aligned} &\textit{Eq.(4) becomes } v_r = .011\ a\ \Delta T, \quad \textit{Eq.(5) becomes } d_r = .000129a\ (\Delta T)^2 \\ &\because \quad a = .4\ \frac{v^2}{C} \quad \textit{and} \quad \Delta T = 2\ e\ T \quad (e\textit{: coeff. of restitution}), \\ &\therefore\ d_r = .00\textit{let } (1) = (2), 02064\ \frac{(evT)^2}{C} \qquad \ldots\ldots\ldots\ (6) \\ &\textit{For} \quad e = .15, \quad T = 100\ ms, \quad \textit{then} \quad d_r = .05\frac{v^2}{C} \end{aligned} \tag{2.17}$$

2.3.3 Tipped Equivalent Square Wave (TESW) – Background

The general requirement for a vehicle crash pulse approximation is that (1) it should characterize the crash pulse with the smallest possible number of parameters needed to describe the vehicle dynamic responses, and (2) it adequately evaluates occupant response. The ASW (Average Square Wave) satisfies the velocity change requirement at t_m, while the ESW (Equivalent Square Wave) satisfies the test dynamic crush of the vehicle only and not necessarily the timing at test dynamic crush. Since both the ASW and ESW require only one unknown, a constant deceleration, for definition, they are zero-order approximations to the crash pulse. In order to satisfy simultaneously the two boundary conditions, velocity change and dynamic crush at t_m, a method using the Tipped Equivalent Square Wave (TESW) was developed [2]. This is defined below.

The TESW is a crude approximation to the actual vehicle crash pulse and is equivalent to it only in the sense of providing equal velocity change and dynamic crush at $t = t_m$. The t_m signals a marked change in the behavior of the vehicle structure from a crushing to an "unloading" condition with a consequent marked effect upon vehicle deceleration. In the actual vehicle-to-barrier (VTB) test, t_m can be obtained from the velocity curve where the velocity is zero. In the vehicle-to-vehicle (VTV) test, t_m is simply the time when both vehicles reach a common velocity and the dynamic crush is simply the maximum relative deformation of the two vehicles involved.

(1) Case Study (Exercise): Displacement Analysis of Simple Pulses

Given: A vehicle-to-barrier impact condition: $x_o = 0$ and $v_o = 30$ mph (44 ft/sec),

Compute: The vehicle displacement (crush) at $t_1 = .091$ sec for the following three special cases using the Moment-Area Equation shown by (2) of Eq. (2.1).

Case 1: Equivalent Square Wave (ESW), a = -15 g (even-loaded)

Case 2: Rear-Loaded Triangular Wave, a = -30 g (extremely rear-loaded)

Case 3: Front-Loaded Triangular Wave, a = -30 g (extremely front-loaded)

The transient accelerations of the three cases are shown in Fig. 2.6. Plot the corresponding transient velocity and displacement responses.

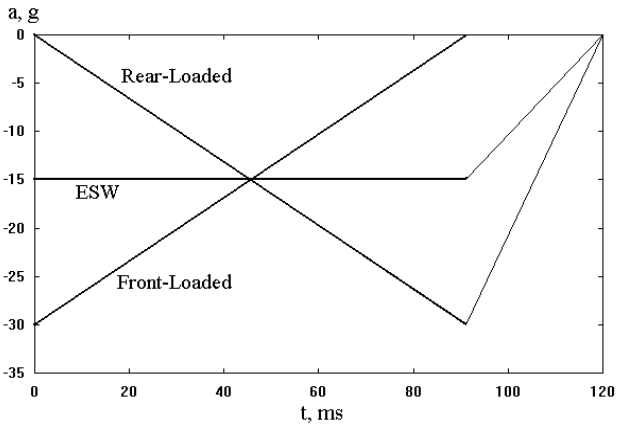

Fig. 2.6 Even, Extremely Rear-, and Front-Loaded Pulses

(2) Case Study: Pulse Shape and Centroid Location

The test summary of the crash of a luxury passenger car into a fixed barrier is shown below:

x_o (initial crush at t_o) = 0, v_o (initial VTB velocity) = 31 mph = 545.6 in/s

$x_1 = C$ (dynamic crush) = 31.5 in, $t_1 = t_m$ (time at x_1) = 93 ms = .093 sec

v_1 (velocity at t_1) = 0, $t_o = 0$

Determine: the centroid time of the crash pulse (the centroid location of the area under the deceleration curve between t_o and t_1) and the centroid location (t_c/t_1).

Derivation of Centroid Time, $\bar{t}$:

$$x_1 = x_o + v_o t_1 + (t_1 - \bar{t})\int_0^{t_1} a\,dt$$

where $\int_0^{t_1} a\,dt = v_1 - v_o = -v_o = -545.6$ *in/s*

$$\therefore \quad x_1 = 0 + v_o t_1 + (t_1 - \bar{t})(-v_o) = v_o \bar{t} \tag{2.18}$$

then $\bar{t} = \dfrac{x_1}{v_o} = \dfrac{31.5}{545.6} = .058$ sec

Note: $\bar{t} \geq \dfrac{t_1}{2}$, *and the centroid location is:* $\dfrac{\bar{t}}{t_1} = .624$

2.3.4 Derivation of TESW Parameters

The derivation of the TESW parameters needed to approximate the crash pulse for car-to-barrier and car-to-car impacts is based on two boundary conditions of the vehicle test. One is the velocity change at the time of dynamic crush shown by (1) of Eq. (2.19) and the other is the dynamic crush, (2). To complete the rebound phase approximation, a straight line is used to represent the rebound portion of the deceleration curve shown by rebound velocity, formula (3) of Eq. (2.19).

Let us define the TESW parameters shown in Fig. 2.7.

t_m : time at vehicle dynamic crush, t_f : final separation time

ΔV_m : velocity change up to t_m, ΔV_R : velocity change in rebound phase

$$\Delta v_m = \int_0^{t_m} \ddot{x}\,dt = \int_0^{t_m} \ddot{p}(t)\,dt = \frac{\ddot{p}(0) + \ddot{p}(t_m)}{2} t_m \quad \ldots\ldots (1)$$

$$C = \int_0^{t_m} \dot{x}(t)\,dt = \int_0^{t_m} \dot{p}(t)\,dt \quad \ldots\ldots\ldots\ldots (2) \tag{2.19}$$

$$\Delta v_R \doteq \int_{t_m}^{\infty} \ddot{x}(t)\,dt = \int_{t_m}^{t_f} \ddot{p}(t)\,dt = \frac{t_f - t_m}{2} \ddot{p}(t_m) \quad \ldots\ldots (3)$$

where $\ddot{p}(0)$, $\ddot{p}(t_m)$: *two decelerations at the end points of TESW.*

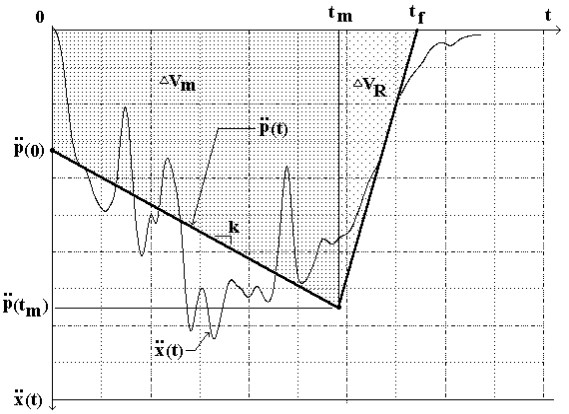

Fig. 2.7 TESW Parameters

2.3.4.1 *Deformation and Rebound Phases*

The solutions to (1) and (2) of Eq. (2.19) (which define the two end points of TESW) are shown in equations (4) and (5) of Eq. (2.20) (see the TESW Formula Derivation in Eq. (2.22)). Since in the deformation phase, the decelerations at the two end points of TESW are negative, it can be shown that the relative centroid location, t_c/t_m, of a crash pulse is located between 1/3 and 2/3 of the deformation period, t_m.

$$\ddot{p}(0) = \frac{2\Delta v_m}{t_m^2}(2t_m - 3t_c) \quad \ldots\ldots\ldots\ldots \quad (4)$$

$$\ddot{p}(t_m) = \frac{2\Delta v_m}{t_m^2}(3t_c - t_m) \quad \ldots\ldots\ldots\ldots \quad (5)$$

$$\text{where} \quad t_c = t_m + \frac{t_m\dot{x}(0) - x(t_m)}{\Delta v_m} \quad \ldots\ldots (6)$$

$$\because \quad \ddot{p}(0) \le 0,$$

$$\ddot{p}(t_m) \le 0, \quad \text{and}$$

$$\Delta v_m \le 0 \qquad (2.20)$$

$$\text{From (4) and (5), one gets}$$

$$2t_m - 3t_c \ge 0 \quad \text{and}$$

$$3t_c - t_m \ge 0, \quad \text{then}$$

$$\frac{2}{3} \ge \frac{t_c}{t_m} \ge \frac{1}{3}$$

$$\text{and from (3) of Eq. (2.19):}$$

$$t_f = t_m + \frac{2\Delta v_R}{\ddot{p}(t_m)} \quad \ldots\ldots\ldots\ldots\ldots\ldots (7)$$

In order to have the same rebound velocity between the test and TESW, the final time, t_f, is computed and shown in equation (7) of Eq. (2.20).

For the special case of a rigid barrier impact, the displacement of the subject vehicle at t_m becomes the dynamic crush, C, and the centroid time is then equal to C/v_o, the characteristic length of the subject vehicle.

$$x(t_m) = C$$

$$\Delta v_m = -\dot{x}(0) = -v_o$$

$$\text{from (6):} \qquad (2.21)$$

$$t_c = -\frac{x(t_m)}{\Delta v_m} = \frac{C}{v_o}$$

TESW Formula Derivation

$$\ddot{p}(t) = \ddot{p}(0) + kt \qquad \text{where} \quad k = \frac{\ddot{p}(t_m) - \ddot{p}(0)}{t_m} \quad \ldots (8)$$

$$\dot{p}(t) = \int \ddot{p}(t)\,dt = \ddot{p}(0)t + \frac{k}{2}t^2 + c_1 \quad \ldots\ldots\ldots (9)$$

at $t = 0$, $\dot{p}(t) = \dot{x}(0)$, *where* c_1: *integration constant*

from (9): $c_1 = \dot{x}(0)$, $\therefore \quad \dot{p}(t) = \dot{x}(0) + \ddot{p}(0)t + \frac{k}{2}t^2 \quad \ldots\ldots (10)$

Substituting (8) *into* (10), *one gets the integrals at* t_m:

$$\dot{p}(t_m) = \dot{x}(0) + \frac{\ddot{p}(0) + \ddot{p}(t_m)}{2}t_m \quad \ldots\ldots\ldots\ldots (11)$$

$$p(t_m) = \int_0^{t_m} \dot{p}(t)dt = \int_0^{t_m} \left[\dot{x}(0) + \ddot{p}(0)t + \frac{k}{2}t^2\right]dt$$

$$= \dot{x}(0)t_m + \frac{\ddot{p}(0)}{2}t_m^2 + \frac{kt_m^3}{6} \quad \ldots\ldots\ldots\ldots (12)$$

Substituting k *from* (8) *into* (10), *then* $\dot{p}(t)$ *from* (10) *into* (2): $\int_0^{t_m} \ddot{x}(t)\,dt = \int_0^{t_m} \dot{p}(t)\,dt$ *and integrate*:

$$x(t_m) = p(t_m) = \left[\dot{x}(0) + \frac{\ddot{p}(t_m) + 2\ddot{p}(0)}{6}t_m\right]t_m \quad \ldots\ldots (13) \qquad (2.22)$$

$$(1): \quad \ddot{p}(0) + \ddot{p}(t_m) = \frac{2\Delta v_m}{t_m} \quad \ldots\ldots\ldots\ldots\ldots (14)$$

$$(13): \quad 2\ddot{p}(0) + \ddot{p}(t_m) = \frac{6}{t_m}\left[\frac{x(t_m)}{t_m} - \dot{x}(0)\right] \quad \ldots\ldots (15)$$

Using (14) *and* (15) *to solve for* 2 *unknowns* $\ddot{p}(0)$ *and* $\ddot{p}(t_m)$:

$$(15)-(14): \quad \ddot{p}(0) = \frac{6}{t_m}\left[\frac{x(t_m)}{t_m} - \dot{x}(0)\right] - \frac{2\Delta v_m}{t_m} \quad \ldots\ldots (16)$$

Rearranging (6): $\frac{x(t_m)}{t_m} - \dot{x}(0) = \left(1 - \frac{t_c}{t_m}\right)\Delta v_m \quad \ldots (17)$

$$(17) \rightarrow (16): \quad \ddot{p}(0) = \frac{2\Delta v_m}{t_m^2}(2t_m - 3t_c) \quad \ldots\ldots\ldots\ldots (4) \triangleleft$$

$$(1): \quad \ddot{p}(t_m) = \frac{2\Delta v_m}{t_m^2}(3t_c - t_m) \quad \ldots\ldots\ldots\ldots (5) \triangleleft$$

2.3.5 Construction of TESW Parameters

Given the velocity change of a vehicle in the deformation phase, the dynamic crush and the time at dynamic crush, TESW parameters, can be computed from the equations or the graphs shown below. It is shown that the average of the decelerations at the two end points of the TESW is equal to the magnitude of the average deceleration, A_{avg}, or the ASW (average square wave). In addition to the average deceleration, the TESW line segment is tilted in such a way that the boundary condition at the test dynamic crush is satisfied.

Relationship between the TESW and ASW:

Since

$$\ddot{p}(0) = \frac{2\Delta v_m}{t_m^2}(2t_m - 3t_c)$$

$$\ddot{p}(t_m) = \frac{2\Delta v_m}{t_m^2}(3t_c - t_m)$$

Rearranging the two equations:

$$\ddot{p}(0) = 2A_{avg}\left(2 - 3\frac{t_c}{t_m}\right) \quad \ldots . \quad (18)$$

$$\ddot{p}(t_m) = 2A_{avg}\left(3\frac{t_c}{t_m} - 1\right) \quad \ldots . \quad (19)$$

where

$$A_{avg} = \frac{\Delta v_m}{t_m} \quad \ldots . \quad \textit{average deceleration} \qquad (2.23)$$

$$\frac{t_c}{t_m}: \quad \ldots \ldots \ldots \quad \textit{relative centroid location}$$

NOTE: *from* (6) *of Eq.*(2.20):

$$t_c = t_m + \frac{t_m\dot{x}(0) - x(t_m)}{\Delta v_m}$$

For the rigid barrier test: $t_c = -\frac{x(t_m)}{\Delta v_m} = \frac{c}{v_o}$

Adding both sides of (18) *and* (19), *one gets*

$$A_{avg} = \frac{\ddot{p}(0) + \ddot{p}(t_m)}{2} \quad \ldots . \quad (20)$$

2.3.5.1 *Relationships Between TESW and ASW*

Given a Δv_m of 30 mph and a t_m of 68 ms, from Fig. 2.8, the average deceleration, A_{avg}, is found to be 20 g ($A_{avg} = \Delta v_m / t_m$).

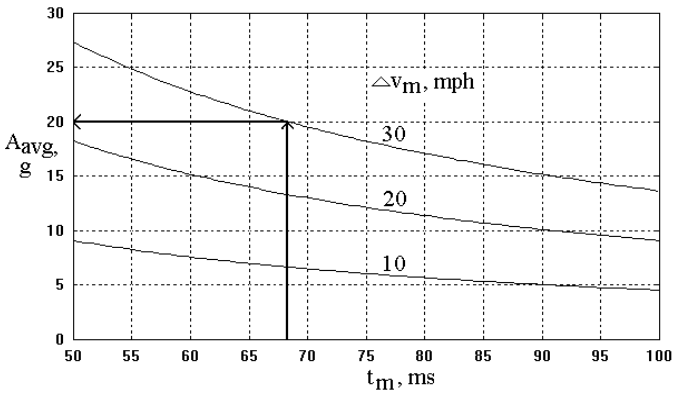

Fig. 2.8 A_{avg} as a Function of ΔV_m and t_m

The centroid time, constructed from the crush (displacement) vs. time curve, is found to be 37.4 ms. Since $t_c/t_m = 0.55$ and a vertical line through this point, shown in Fig. 2.9, intersects the two lines for which A_{avg}=20g at two points. The horizontal lines through those two points give the deceleration (to the left) of the first point of TESW, which is 14 g, and that (to the right) of the second point of TESW, 26 g. The values of those two end points of TESW are also verified by the formula computations shown in Eq. (2.24).

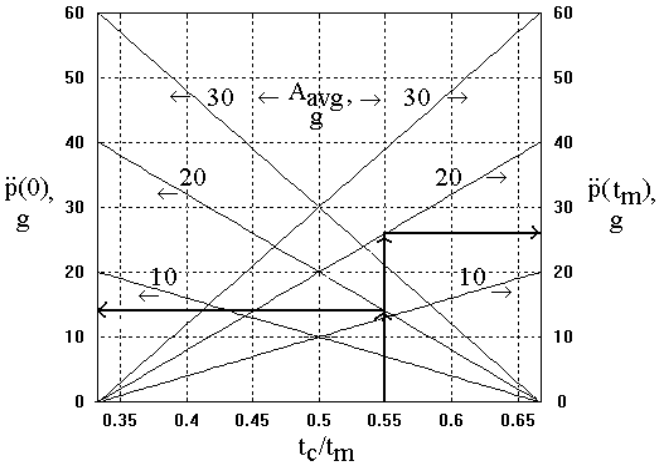

Fig. 2.9 TESW Deceleration as a Function of A_{avg} and t_c/t_m

$$\ddot{p}(0) = 2A_{avg}\left(2 - 3\frac{t_c}{t_m}\right) = 14\ g, \qquad \ddot{p}(t_m) = 2A_{avg}\left(3\frac{t_c}{t_m} - 1\right) = 26\ g \tag{2.24}$$

Case Study: Front and Rear Loaded Crash Pulses

A summary of test data of the prototype trucks A and B in the 31 mph rigid barrier tests is shown below:

Truck A:	Dynamic Crush	Time of C	Rebound velocity
Proto-type #1:	C = 23.7 in,	t_m= 90.4 ms	(Δv_R= 2.67 mph)
Proto-type #2:	C = 23.7 in,	t_m= 77.7 ms	(Δv_R= 1.96 mph)

Note that the prototypes have the same amount of dynamic crush but different timings.

Truck B:			
Proto-type #3:	C = 20.1 in,	t_m= 74.0 ms	(Δv_R= 5.5 mph)
Proto-type #4:	C = 22.6 in,	t_m= 72.9 ms	(Δv_R= 3.3 mph)

Note that the trucks have different amounts of dynamic crush but similar timings.

Let us define the TESW parameters for the four prototype vehicles and justify the differences in the dynamic response and crash pulse shape. The rigid barrier impact speed is v_o= 31 mph and the crash data for both trucks, dynamic crush, time of dynamic crush and rebound velocity are shown in Table 2.1.

Using the following formulas shown in Eqs. (2.25) and (2.26), where the units are in ms, inches, mph, and g, the centroid time and average deceleration are computed and shown in Table 2.1.

$$t_c = 56.8\ \frac{C\ (in)}{v_o\ (mph)} \tag{2.25}$$

$$A_{avg} = 45.55 \frac{v_o\ (mph)}{t_m\ (ms)} \tag{2.26}$$

Table 2.1 Parametric Comparisons between Front- and Rear-Loaded Pulses, v_o =31 mph

Prototype	C, in	ESW, g	t_c, ms	t_m, ms	A_{avg}, g	P_0, g	P_1, g	t_c/t_m
#1 (Front Loaded)	23.7	16.3	43.4	90.4	15.6	17.5	13.7	0.48
#2 (Rear-Loaded)	23.7	16.3	43.4	77.7	18.2	11.6	24.7	0.56
#3 (Even-Loaded)	20.1	19.1	36.9	74.0	19.1	19.1	19.1	0.50
#4 (Rear-Loaded)	22.6	17.0	41.4	72.9	19.4	113	27.5	0.57

Since the relative centroid location (t_c/t_m) of prototype #1 is less than 0.5 and that of #2 greater than 0.5, it can be stated that the #1 prototype structure is front-loaded and the #2 is rear-loaded. The dynamic responses of the two prototypes are shown in Fig. 2.10. The velocity curve in the front-loaded pulse is slightly concave upward due to the decreasing deceleration magnitude, while the velocity curve in the rear loaded pulse is convex downward. If t_m had been the same for both cases, then the area of the velocity curve (dynamic crush) in the front-loaded crash pulse would be smaller due to the concave-upwarded velocity curve. However, the two crash pulses of the two prototypes yield the same amount of dynamic crush; therefore, the duration of the front-loaded crash pulse would have no choice but to be longer as shown in Table 2.1 and Fig. 2.10 (curves for #1 are in bold). t_m for the front-loaded pulse is about 13 ms longer than that for the rear-loaded pulse.

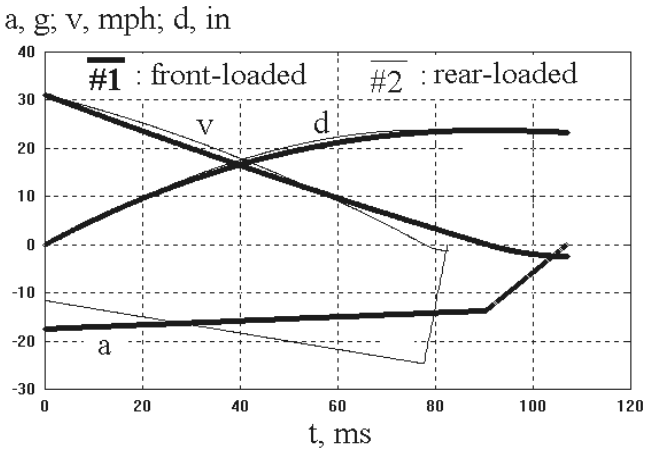

Fig. 2.10 Front- / Rear-Loaded Pulses and Integrals

Similarly, in the two prototypes of truck B, #3 (curves for #3 are in bold shown in Fig. 2.11) is even-loaded due to the value of the relative centroid location being 0.5, and #4 is rear-loaded with centroid location at 0.57. The times at the dynamic crush are about the same; however, the dynamic crush of #3 (even-loaded) is about 2.4 inches shorter than that of #4 (rear-loaded). Due to the facts that (1) the velocity curve of the even-loaded pulse is a straight line and that of rear-loaded is concave

downward, and (2) duration up to the time of dynamic crush is about the same for the two curves, the area under the rear-loaded velocity curve is more than that of the even loaded velocity line segment. Consequently, the dynamic crash of the #4 prototype crash pulse yields about 2.4 inches more dynamic crush than #3.

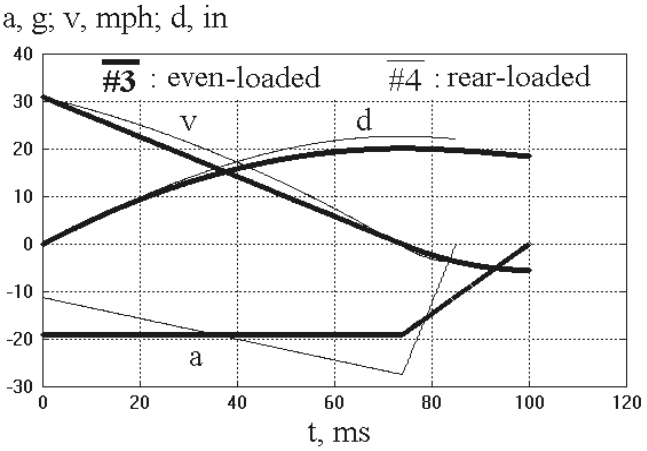

Fig. 2.11 Even / Rear-Loaded Pulses and Integrals

2.3.6 Kinematic Comparisons of Test Pulse and Approximated Pulses

It will be shown in this section that (1) the magnitude of the ASW (Average Square Wave) is the average of the decelerations at the two end points of the TESW (Tipped Equivalent Square Wave), (2) for the rear-loaded crash pulse, the magnitude of ASW is greater than that of ESW (Equivalent Square Wave), but the duration and dynamic crush are shorter, and (3) for the front-loaded crash pulse, the relationships are opposite to those of the rear-loaded. It will be shown that TESW combines the advantages of both ASW and ESW when it comes to approximating a crash pulse.

The acceleration, velocity, and displacement transient responses between the test and approximated pulses are compared. In addition, the energy relationships between the test and approximated crash pulses are also compared (based on the deceleration and displacement data). It will be shown that for a rear loaded pulse, since the magnitude of ASW is greater than that of ESW, the energy absorption computed by the product of ASW and dynamic crush from the test will be greater than the kinetic energy input and therefore over-estimated. Conversely, for a front-loaded pulse, the energy computed using the ASW and test dynamic crush will be underestimated. However, the energy estimate by the product of ESW and dynamic crush will be the same as kinetic energy input. The difference in energy estimate by the use of ASW is due to the fact that ASW is based on velocity change rather than energy equivalence between the test and approximated pulse.

2.3.6.1 *Rear-Loaded*

The crash pulse at the right rocker at the B-pillar of a truck in a 35 mph rigid barrier test is approximated by ASW, ESW, and TESW, respectively. The crash pulse and its integrals and those of the approximated pulses are shown in Figs. 2.12–2.14. The response comparison is shown in Table 2.2. Since the computed t_c of the test pulse is 48.2 ms and t_m= 83.4 ms, the relative centroid location is 48.2/83.4 = 0.58, and the test crash pulse is rear-loaded.

It is seen from Figs. 2.12–2.14 and Table 2.2 that for a rear-loaded crash pulse, the deceleration of ASW (19.2 g) is higher than that of ESW (16.5 g) and the loading-phase duration (t_m) of ASW (same as that in the test, 83.4 ms) is shorter than that of ESW (96.4 ms). Like the duration, the dynamic crush of ASW (25.7 in) is also shorter than that of ESW or the test (29.7 in). Since TESW meets the two boundary conditions of the test crash pulse (dynamic crush at t_m and velocity change at t_m, the approximation using TESW is the best among the three approximation methods.

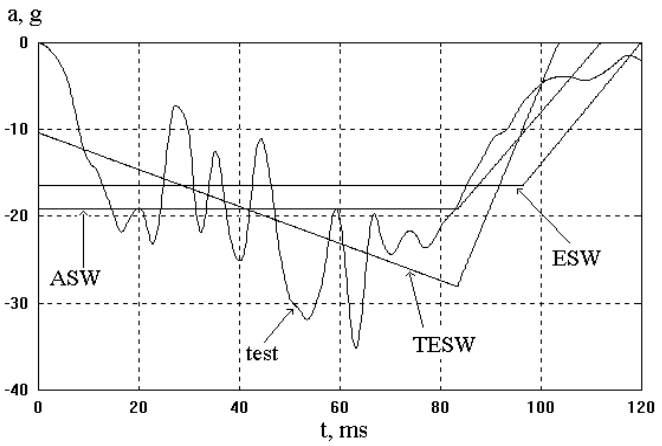

Fig. 2.12 Crash Pulse Comparison (rear-loaded)

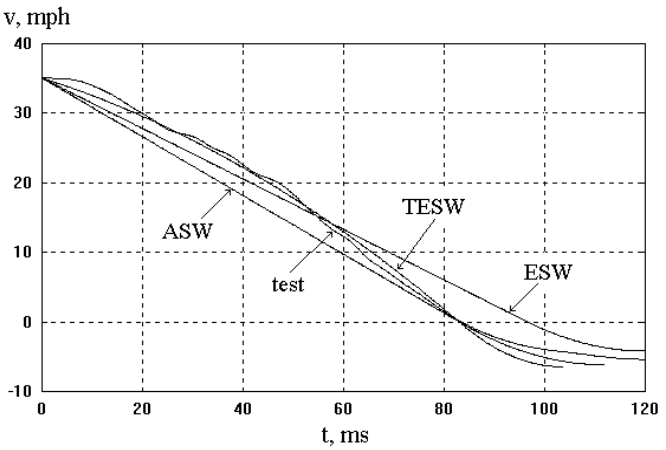

Fig. 2.13 Velocity Comparison (rear-loaded)

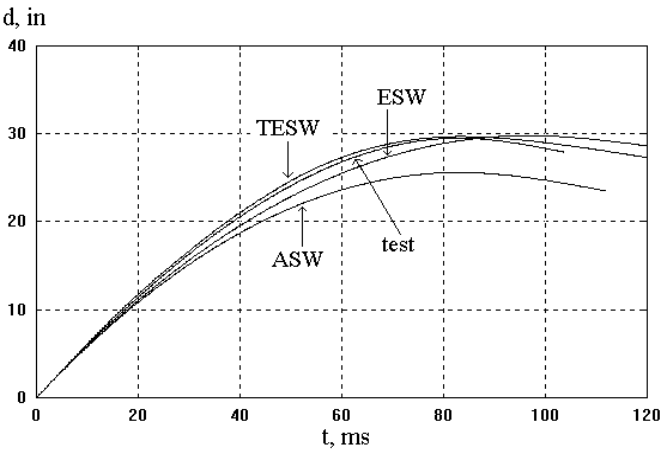

Fig. 2.14 Displacement Comparison (rear-loaded)

Table 2.2 Rear-Loaded Crash Pulse (SUV, 35 mph Barrier Test) and Approximated Pulses

Response	**test**	**ASW**	**ESW**	**TESW**
Deceleration, g	Rear-Loaded	(-19.2)	(-16.5)	(-10.3, -28)
C (dynamic crush),	29.7	25.7[3/]	29.7	29.7
t_m, Time at C, ms	83.4	83.4	$2*t_c = 96.4$[4/]	83.4

In Fig. 2.15, the area between the deceleration versus displacement curve and the zero reference line is the amount of energy absorbed by the structure per unit of mass. Fig. 2.16 shows the energy density versus displacement for the test and approximated pulses. Among the three approximated pulses, TESW approximates both the deceleration and energy density (e) versus displacement better than ESW, and ESW better than ASW. Note that all of the approximated pulses predict the same maximum e, $e_{max}(g\text{-in}) = 0.4\ v(mph)^2$. This is due to the fact that the velocity at dynamic crush for all the three approximated pulses is zero. However, the dynamic crush at which e_{max} occurs for ASW is shorter (25.7 in) compared to the others (29.7 in), as shown in Table 2.2 and Fig. 2.16. The maximum energy densities for the test and approximated pulses are the same as the kinetic energy density.

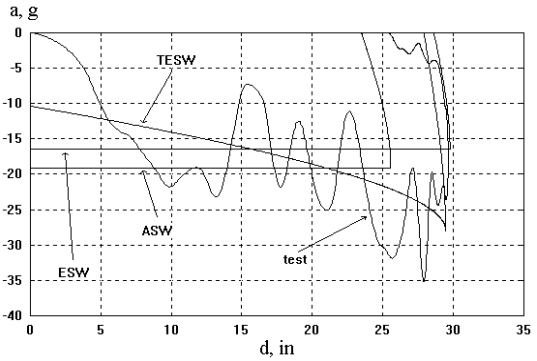

Fig. 2.15 Deceleration vs. Displacement Comparison

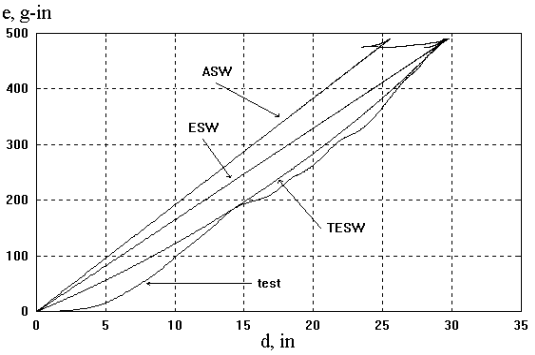

Fig. 2.16 Energy Density vs. Displacement Comparison

[3/] For ASW: $C|_{ASW} = 0.5\ V\ t_m$

[4/] For ESW: $t_m|_{ESW} = 2\ t_c = 2\ C/V$

For a rear-loaded pulse, the deceleration magnitude of ASW is higher than that of ESW and the dynamic crush due to ASW is shorter than that from any one of the tests, ESW and TESW. Therefore, for a rear-loaded test vehicle, the energy computation based on the product of ASW deceleration and test dynamic crush will be overestimated.

2.3.6.2 *Front-Loaded*

In the previous case study, the crash pulse for the truck #1 crash in a 31 mph rigid barrier test was approximated by ASW, ESW, and TESW. The crash pulse was front-loaded, since the computed relative centroid location was 0.48. From Table 2.3, it is seen that for a front-loaded crash pulse, the deceleration of ASW (15.6g) is lower than that of ESW (16.3g), and the loading-phase duration of ASW (same as the test, 90.4 ms) is longer than that of ESW (86.9 ms). Note the dynamic crush of ASW (24.6 in) is also larger than that of ESW (23.7 in) or the test.

Table 2.3 Front-Loaded Crash Pulse (SUV, 35 mph Test) and Approximated Pulses

Response	**Test**	**ASW**	**ESW**	**TESW**
Deceleration, g	Front-Loaded	(-15.6)	(-16.3)	(-17.5, -13.7)
C (Dynamic Crush),	23.7	24.6	23.7	23.7
t_m, Time of C, ms	90.4	90.4	$2t_c$ = 86.9	90.4

2.4 PULSE APPROXIMATIONS WITH ZERO INITIAL DECELERATION

One realizes that, in a test crash pulse, the deceleration at time zero is zero. However, in the crash pulse approximations so far, using ASW, ESW, and TESW, the deceleration at time zero is finite. Although the effect of an approximation with non-zero deceleration on the over-all vehicle response is minimal, the evaluation of other responses such as g-force or energy density vs. displacement (or crush) requires a better approximation, especially in the early portion of the time history. For example, the evaluation of energy absorption capability of a bumper and/or front rail section of a vehicle in a frontal impact requires a good estimate of the deceleration versus deflection data for integration. To take into account the zero deceleration at time zero, the Fourier Equivalent Wave (FEW), Trapezoidal Wave Approximation (TWA), and Bi-Slope Approximation (BSA) are presented.

2.4.1 Fourier Equivalent Wave (FEW)

Over one hundred years ago, Baron Jean Baptiste Joseph Fourier showed that any waveform can be generated by adding up sine waves and that the combination of sine waves is unique for each waveform. Given a crash pulse described by discrete data points as shown in Fig. 2.17, the deceleration value and time at any given point j are A_j and t_j , respectively.

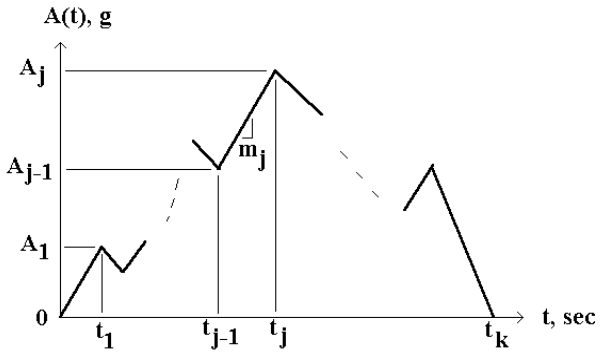

Fig. 2.17 Crash Pulse Discrete Data Points

The slope of the line segment ending at point j is m_j. The total number of discrete data points is k, and the deceleration value at time t_k is presumed to be zero. The fundamental harmonic frequency of the crash pulse is computed using the half period of t_k. The Fourier series approximation to a crash pulse which has been derived and applied to characterize a crash pulse [2] is called the Fourier Equivalent Wave (FEW). An n^{th} order FEW is shown by (1) of Eq. (2.27), which consists of a 1^{st} order harmonic of a fundamental frequency, ω, up to an n^{th} rder harmonic of n times the fundamental frequency, nω. The magnitude of the sine wave corresponding to the i^{th} harmonic is a_i.

$$
\begin{aligned}
&n^{th}\ order\ FEW: \quad A(t) = \sum_{i=1}^{n} a_i \sin(i\omega t) \quad . \ . \ . \ . \ . \ . \ . \quad (1)\\
&where\\
&A(t)\text{: acceleration at } t, \quad and \quad a_i\text{: } i^{th} \text{ coefficient of FEW}\\
&\omega\,(natural\ angular\ frequency) = 2\pi f = \frac{\pi}{t_k}\\
&t_k\text{: crash pulse duration, and } T(period) = 2t_k\\
&f(fundamental\ frequency) = \frac{1}{T}\\
&where \quad a_i = \frac{2t_k}{(i\pi)^2} \sum_{j=1}^{k} m_j \left[\sin\left(\frac{i\pi t_j}{t_k} \right) - \sin\left(\frac{i\pi t_{j-1}}{t_k} \right) \right] \quad . \ . \quad (2)\\
&and \quad m_j = \frac{A_j - A_{j-1}}{t_j - t_{j-1}} \quad . \ . \ . \ . \ . \ . \ . \ . \ . \ . \ . \ . \quad (3)
\end{aligned}
\tag{2.27}
$$

The Fourier Equivalent Wave is particularly useful in approximating the crash pulse using a superposition of harmonics of various orders. Based solely on the crash pulse, preliminary FEW coefficients, a_i, can be computed using the closed-form expression shown in (2) of Eq. (2.27). By imposing boundary conditions on the integrals such as velocity change and dynamic crush, the preliminary FEW coefficients can then be modified by sensitivity analysis.

The frequency spectrum of some common signals can be generated by Eq. (2.27) where formula (2) defines the spectrum amplitude of a particular frequency component. In general, given a crash pulse signal, the estimate of the natural angular frequency, ω, is based on crash pulse duration, t_k. At that time, the deceleration of the vehicle is zero. However, in a vehicle to fixed barrier impact, ω can also be estimated quickly using the formula shown in Section 4.9 of Chapter 4, ω = v/c. In a simple spring mass model, v is the initial impact speed and c is the dynamic crush of the vehicle.

2.4.2 FEW Sensitivity Analysis with Boundary Conditions

The FEW expression for the crash pulse can be further integrated to yield velocity and displacement equations. In order to adjust the coefficients a_i to meet the boundary conditions of the test results, the two equations are further differentiated with respect to a_i, which yields the following velocity and displacement sensitivity equations.

$$
\begin{aligned}
v(t) &= v_o - \frac{1}{\omega}\left[\sum_{i=1}^{n} \frac{a_i}{i} \cos(i\omega t) - \sum_{i=1}^{n} \frac{a_i}{i} \right]\\
d(t) &= v_o t - \frac{1}{\omega^2}\left[\sum_{i=1}^{n} \frac{a_i}{i^2} \sin(i\omega t) - \omega \sum_{i=1}^{n} \frac{a_i}{i} t \right]\\
\frac{\partial v(t)}{\partial a_i} &= \frac{1 - \cos(i\omega t)}{i\omega}, \qquad \frac{\partial d(t)}{\partial a_i} = \frac{t - \dfrac{\sin(i\omega t)}{i\omega}}{i\omega}
\end{aligned}
\tag{2.28}
$$

where v_o is the initial velocity at t_o and the typical response variables with the boundary conditions specified are shown in Table 2.4. In order to meet the boundary conditions, as many FEW coefficients as the boundary conditions would have to be modified.

Table 2.4 Boundary Conditions for FEW Sensitivity Analysis

i	u_i	Boundary
1	$d(t_m)$	displacement at t_m (dynamic crush)
2	$v(t_m)$	velocity at t_m (common velocity)
3	$v(t_f)$	velocity at t_f (separation velocity)
4	$d(t_c)$	displacement at t_c (centroid displacement)
5	$d(t_f)$	displacement at t_f (static crush)

Let Δu_i be the difference between the test and original (unmodified) FEW for the response variable i. The response variables are shown above and Δu_i can then be $\Delta d(t_m)$, $\Delta v(t_m)$, $\Delta v(t_f)$, $\Delta d(t_c)$, or $\Delta d(t_f)$, where t_m and t_f are times of dynamic crush and vehicle separation from the barrier, respectively. Using the sensitivity relationships, the amount of change to the original coefficient a_i, Δa_i, can then be solved using a set of simultaneous linear equations shown in Eq. (2.29). Note that to solve as many unknowns as the conditions, the number of coefficients (M) is set equal to number of variables (N).

$$\left[\frac{\partial u_i}{\partial a_j}\right]^{i\times j} [\Delta a_i]^{j\times 1} = [\Delta u_i]^{i\times 1}, \quad \textit{where}$$
$$i = 1 \textit{ to } N, \quad j = 1 \textit{ to } M \qquad \textit{then}$$
$$\textit{modified } a_i = \textit{original } a_i + \Delta a_i \tag{2.29}$$

The following section describes the differences between the FEW approximations with and without the modification of the FEW coefficients.

2.4.3 Kinematics and Energy Comparison

The test and FEW approximations are compared using the transient kinematic and energy responses for a case where a light truck was tested in a 31 mph rigid barrier crash. Table 2.5 contains the test pulse and the FEW approximations with and without modifications to the coefficients.

The crash pulse in the left rocker at B-pillar shown in Fig. 2.18 is to be characterized by a 5th order FEW with and without coefficient modification. Four boundary conditions, $d(t_m)$, $v(t_m)$, $v(t_f)$, and $d(t_c)$, are used to modify the first four coefficients. The fundamental frequency (of the first harmonic) is computed to be ω= 5.38 Hz. The magnitude of the first harmonic, coefficient a_1, dominates the signal of the crash pulse. However, the second harmonic determines how well the FEW fits the test responses.

The modified FEW, where the second coefficient is smaller in magnitude than that in the unmodified FEW, has a better response fit as shown in Figs. 2.18–2.20. The 5th order FEW gives a double-humped approximation, a rear-loaded crash pulse which can be checked by noting that the second hump is higher than the first. The centroid time, t_c, of the crash pulse can be checked by its location. Computing C(dynamic crush) / V (velocity change) gives a centroid time, t_c, of 41 ms; since the time of dynamic crush, t_m , is 72.8 ms, the relative centroid location, t_c / t_m, is 0.56. Therefore, the crash pulse can be considered to be rear-loaded.

Table 2.5 FEW Crash Pulses with and without Modified Coefficients

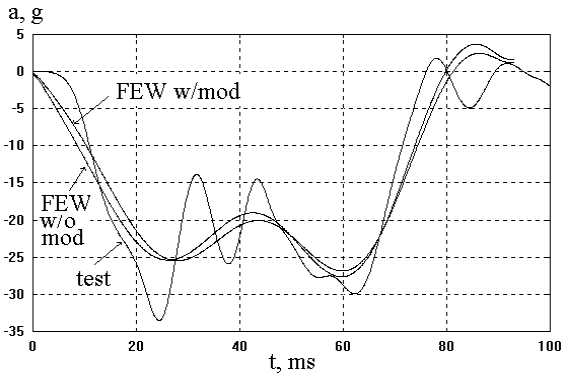

Fig. 2.18 Pulses of Truck Test at 31 mph and FEW with and without Modification

$$n^{th}\ order\ FEW: \quad A(t) = \sum_{i=1}^{n} a_i \sin(i\omega t)$$

where $A(t)$: *acceleration at* t, *and* (2.30)

a_i: i^{th} *coefficient of FEW*

ω (*angular frequency*) = 5.38 *Hz*

i	Is coefficient a_i modified?	
	no (without)	yes (with)
1	-25.11	-25.23
2	-3.49	-2.90
3	-.65	-.23
4	-5.24	-3.76

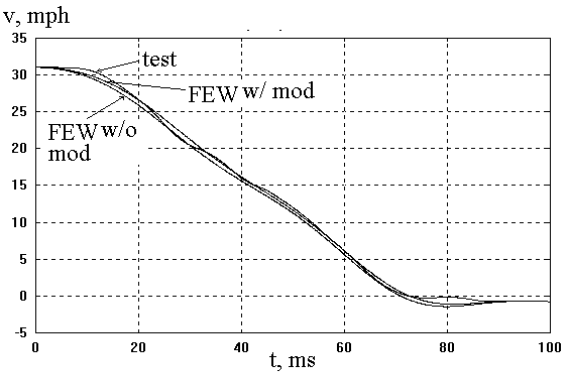

Fig. 2.19 Velocities of a Truck Test at 31mph and FEW w/ and w/o Modification

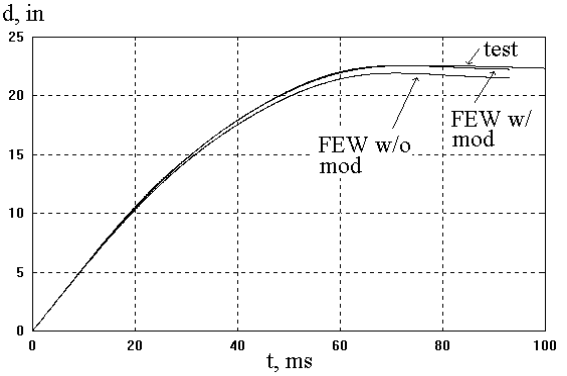

Fig. 2.20 Displacements of Truck Test at 31 mph and FEW w/ and w/o Modification

The deceleration and energy density versus displacement curves for the test and FEW are shown in Figs. 2.21–22, respectively. The FEW with modified coefficients appears to be better matched with the test data than the FEW without modification. This is because the transient velocity curve (v vs. t) of FEW with modification is better matched with the test curve than the FEW without modification. Consequently, the energy density, e(g-in) = .4 [v_o^2 (mph) - v^2 (mph)], of the FEW with modification should also be better matched with the test data than the FEW without modification.

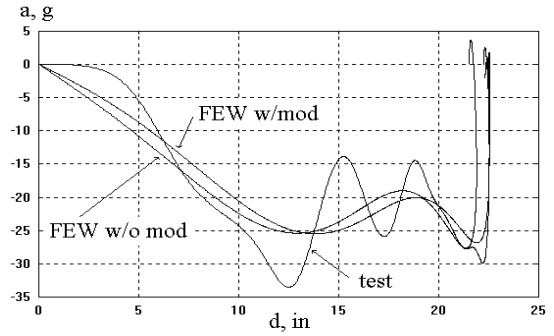

Fig. 2.21 Deceleration vs. Displacement

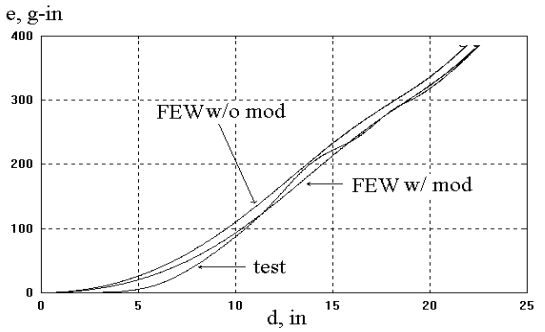

Fig. 2.22 Energy Density vs. Displacement of Truck Test at 31 mph and FEW

2.4.4 Use of FEW and Power Rate Density in Crash Severity Detection

In Section 1.7, Chapter 1, one of the formulated kinematic variables is power rate density (prd). The definition of prd, p′(t), is as follows:

$$p'(t)\text{: power rate density of the crash pulse, } A(t)$$
$$p'(t) = v(t)j(t) + A^2(t) \tag{2.31}$$

For a crash pulse which is a simple halfsine wave, the expression of power rate density is shown as follows and plotted in Fig. 2.23.

$$\text{For } A(t) = \sin(\omega t), \quad \text{then}$$
$$p'(t) = 1 + \cos(\omega t)[1 - 2\cos(\omega t)] \tag{2.32}$$

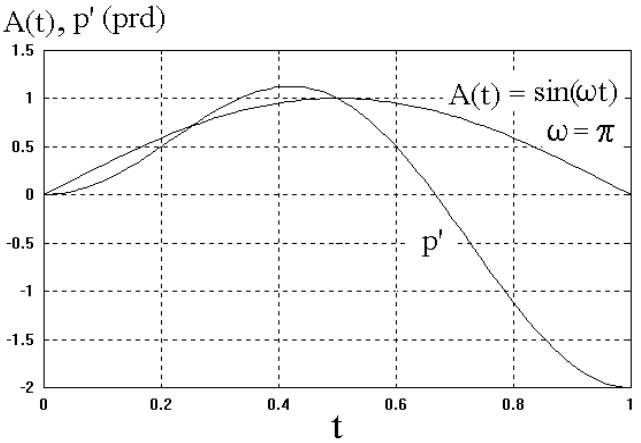

Fig. 2.23 A Simple Halfsine Wave and its Power Rate Density (prd)

Given a set of crash pulse data, the FEW approximation yields a set of coefficients with the corresponding frequencies expressed as multiples of fundamental frequency of a sinusoidal wave. Using the equation above, the power rate density, p′(t), can then be computed directly from the summation of the individual power rate densities, p_i' (i refers to the i^{th} frequency component). The prd thus obtained by the technique described above is therefore referred to as a Fourier Transformed Power Rate Density. The application of the technique in detecting the vehicle pole impact severity is described in the following.

2.4.4.1 *Discrimination of Pole Impact Crash Severity*

Two vehicles, one mid-size (front-wheel drive) and the other full-size (rear-wheel drive), were tested in the rigid barrier and rigid pole (8" diameter) impact conditions. There are four rigid barrier tests, and three center pole (pole impacting at the center line of the vehicle) tests. The crash pulse analysis using FEW with five unmodified coefficients for each test is shown in Table 2.6.

Table 2.6 Crash Pulse Analysis using FEW

Mid-size Vehicle (Centerline Tunnel)				Full-size Vehicle (Left Rocker at B-pillar)			
Test # , Mode	n	A(n)	**-|A(n)|**	Test # , Mode	n	A(n)	**-|A(n)|**
#1, 10 mph rigid barrier (ω=4.55Hz)	1	-8.21	-8.21	#1, 8 mph rigid barrier (ω=3.91Hz)	1	-5.66	-5.66
	2	-1.46	-1.46		2	-.78	-.78
	3	**.80**	**-.80**		3	-.03	-.03
	4	-1.47	-1.47		4	-.62	-.62
	5	-1.31	-1.31		5	-.09	-.09
#2, 10 mph center pole (ω=2.79Hz)	1	-4.77	-4.78		1		
	2	**.26**	**-.26**		2		
	3	-.10	-.10		3		
	4	-.33	-.33		4		
	5	-.12	-.12		5		
#3 14 mph rigid barrier (ω=4.31Hz)	1	-10.82	-10.82	#2, 14 mph rigid barrier (ω=3.94Hz)	1	- 9.76	- 9.76
	2	-2.23	-2.23		2	-7.04	-7.04
	3	**.64**	**-.64**		3	**2.05**	**-2.05**
	4	-1.61	-1.61		4	-.70	-.70
	5	-.65	-.65		5	-.83	-.83
#4, 17 mph center pole (ω=3.15Hz)	1	-10.65	-10.65	#3, 21 mph center pole (ω=2.83Hz)	1	-9.96	-9.96
	2	**3.07**	**-3.07**		2	**3.92**	**-3.92**
	3	**1.19**	**-1.19**		3	-.34	-.34
	4	-3.01	-3.01		4	-2.3	-2.3
	5	-.42	-.42		5	**.2**	**-.2**

The structural interaction of a vehicle impacting a rigid pole is quite different from that in a rigid barrier impact. In the pole test, there is a soft impact followed by the stiff contact between the pole and the engine/power train subsystem. The use of Fourier analysis in rigid barrier and pole impact crashes yields a fundamental sign difference in the FEW coefficients. In the pole test, the positive sign of the second FEW coefficient (in bold for the #2 and #4 mid-size vehicle tests in Table 2.6) contributes to the lower deceleration in the beginning of the crash pulse, while in the rigid barrier impact, the sign of the second FEW coefficient is negative which makes the deceleration higher in the beginning of the crash.

The crash severities of these tests will be examined using the Fourier Transformed Power Rate Density. In each vehicle test series, the low speed rigid barrier and center pole impacts are must-not-activate conditions for the air bag sensing application and the medium speed impacts are must-activate conditions. Shown in Fig. 2.24 are the deceleration curves of the mid-size vehicle and the corresponding FEW approximations. Both #1, the 10 mph into a rigid barrier test, and #2, the 10 mph center pole test, are must-not-activate conditions. Similarly, both #3, the mid-size vehicle at 14 mph into a rigid barrier , and #4, the 17 mph center pole test, are must- activate conditions, as shown in Fig. 2.25.

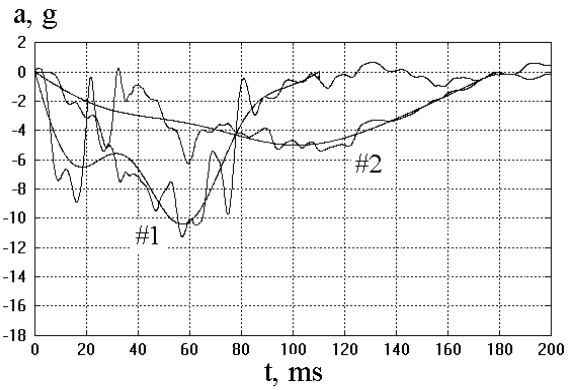

Fig. 2.24 Test and FEW Decelerations at Tunnel of Two Must-Not-Activate Tests

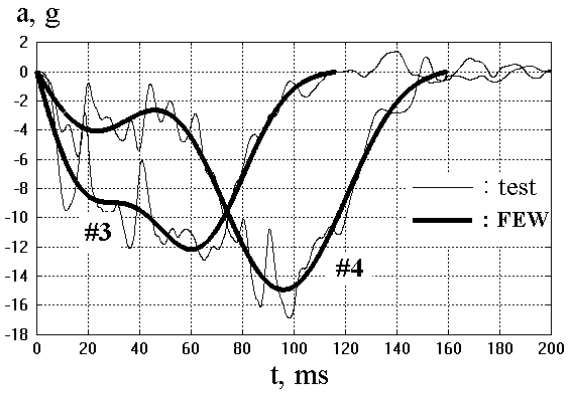

Fig. 2.25 Test and FEW Decelerations at Tunnel of Two Must-Activate Tests

According to the 5"–30 ms criteria described in Section 1.7.2 of Chapter 1, the air bag sensor activation times for these tests were between 30 and 40 ms. However, comparing crash pulse of the #4 pole test with those of #1 and #2 before 40 ms, the deceleration signal of #4 was weaker. The probable activation time due to the #4 crash pulse was somewhere between 60 and 100 ms, where the acceleration signal was stronger. Therefore, the activation time due to the #4 crash pulse may have been 20 ms later than the desired timing of 40 ms.

The 5^{th} order FEW approximations for the four mid-size vehicle crash tests have been computed using the method without meeting the test boundary conditions. The coefficients of the FEW are A(n), n=1,..,5. These are shown in Table 2.6. By studying the coefficients in the four tests, it is found that the A(2) and A(3) coefficients of the #4 pole test are positive and relatively large while the corresponding coefficients of the other tests are mostly negative and relatively small. Since the A(2)

and A(3) coefficients represent the magnitudes of the second and third harmonics in the Fourier series, the positive coefficients yield sine waves which are 180° out of phase with those having negative coefficients. Thus, positive A(2) and A(3) FEW coefficients tend to decrease the deceleration magnitude in the first one-third of the crash pulse duration. The lower deceleration magnitudes for both #2 and #4 pole tests can be seen in Figs. 2.24 and 2.25.

Using the FEW coefficients in each test and the prd (power rate density) summation formula, p′(t), shown in Eq. (2.33), the prd of the four mid-size vehicle crash tests has been computed and is shown in Fig. 2.26. By comparing the power rate densities of test #1, a must-not-activate test, with test #4, a must-activate one, it is seen that the timing when #4 prd becomes greater than #1 prd occurs around 50 ms, which is still 10 ms later than the desired timing of 40 ms.

$$
\begin{aligned}
&\textit{For an } n^{th} \textit{ order FEW:}\\
&A(t) = \sum_{i=1}^{n} a_i \sin(i\omega t)\\
&\textit{where}\\
&\omega = 2\pi f, \quad \textit{where}\\
&f\textit{: fundametal frequency, Hz}\\
&p'(t)\textit{: power rate density (prd) of the crash pulse, } A(t)\\
&p'(t) = \sum_{i=1}^{n} p_i'(t)\\
&\textit{where } p_i'(t)\textit{: prd of a sine component of } i, \textit{ and}\\
&p_i'(t) = v(t)j(t) + A^2(t) = a_i^2\left(1 + \cos(i\omega t)[1 - 2\cos(i\omega t)]\right)
\end{aligned}
\tag{2.33}
$$

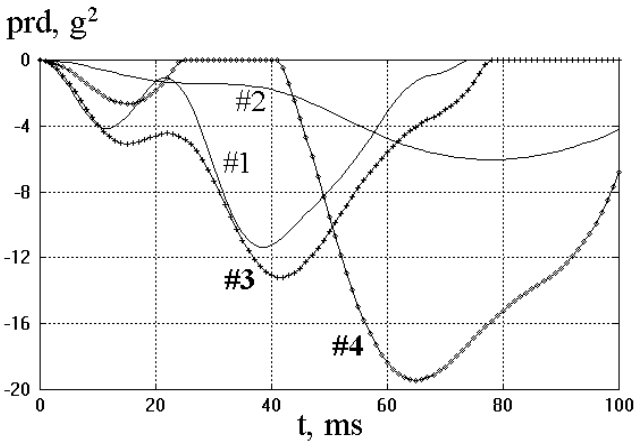

Fig. 2.26 Power Rate Density With Original FEW Coefficients of Four Mid-Size Tests

2.4.4.2 *Use of All Negative FEW Coefficients in Pole Tests*

Assuming that all the original FEW coefficients for the four tests have been given, a new power rate density, p′(t), is defined and computed by using all-negative coefficients. Fig. 2.27 shows the new prd, p′(t), for the four tests where the crash severities between the must-not-activate tests, #1 and #2, and the must-activate tests, #3 and #4, are well separated up to 30 ms. A prd discrimination threshold can then be established between the two groups such that the activation time can be tailored to meet the 5"–30 ms criteria in either time or displacement domain.

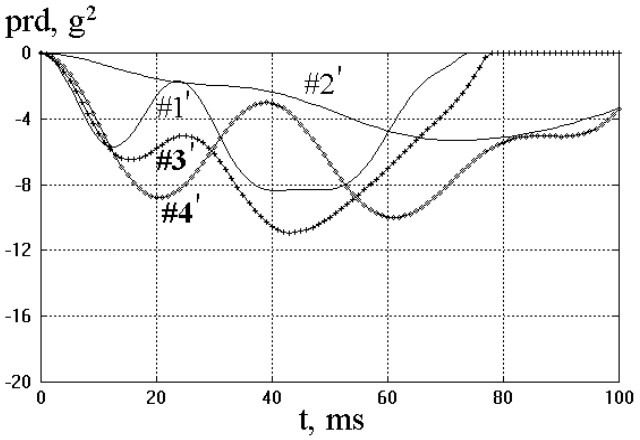

Fig. 2.27 Power Rate Density Curves With All-Negative FEW Coefficients

Using the all negative FEW coefficients, the new decelerations are synthesized using the FEW summation formula. After transformation, the original #1 and #4 crash pulses become #1' and #4', respectively, and are shown in Fig. 2.28. Before 70 ms, the #4 deceleration magnitude is less than #1. The conversion of the FEW coefficients A(2) and A(3) to negative values makes the magnitude of deceleration in test #4' greater than that in test #1'.

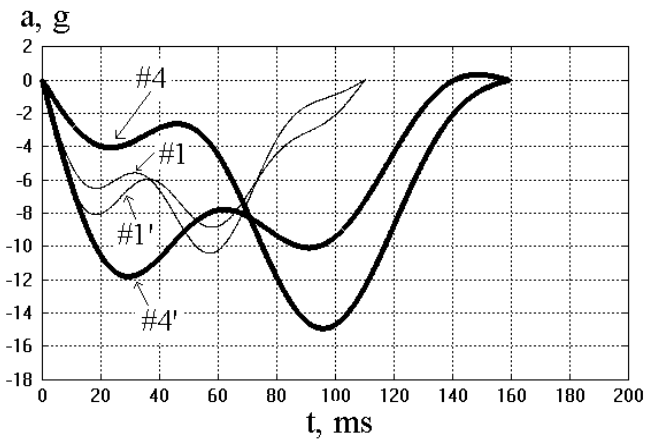

Fig. 2.28 Effect of All-Negative FEW Coefficients on #1' and #4' Decelerations

The phenomenon of having a positive A(2) FEW coefficient in the rigid pole test is not incidental. It exists not only in the front wheel drive vehicle but also in the rear wheel drive vehicle. Fig. 2.29 shows the crash pulse at the left rocker on the B-pillar of a rear wheel drive full-size vehicle for three test conditions: #1, 8 mph rigid barrier, #2 ,14 mph rigid barrier, and #3, 21 mph pole impact test. The computed original FEW coefficients are shown in the right column in the previous Table 2.6.

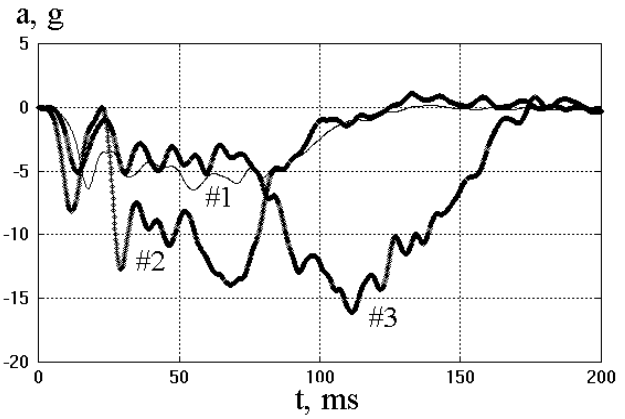

Fig. 2.29 Test and FEW Decelerations at Rocker/B-Pillar of Three Full-Size Tests

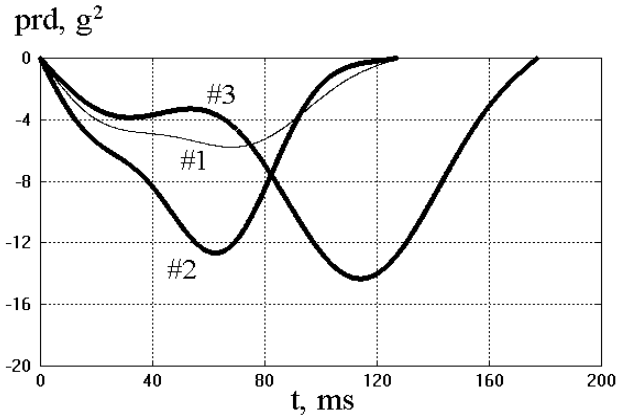

Fig. 2.30 Power Rate Density with Original FEW Coefficients of Three Tests

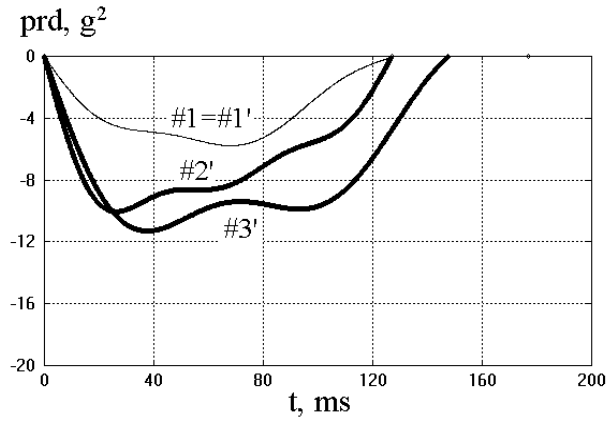

Fig. 2.31 Power Rate Density Curves with All-Negative FEW Coefficients

The power rate densities based on the original FEW coefficients and the all-negative coefficients for the three full-size vehicle tests are shown in Figs. 2.30 and 2.31, respectively. Note that in Fig. 2.31, the must-activate tests, #2' and #3', are well separated from the #1 test after the introduction of the all-negative coefficients.

In crash severity analyses using power rate density (prd) and FEW coefficients, it has been assumed that the FEW coefficients be given before the prd computation. The application of the methodology to real time sensing application, however, needs to be explored further. Nevertheless, the analysis points out the unique features of the FEW coefficients in the non-perpendicular barrier tests where the coefficients can be manipulated and the crash severity can then be distinguished.

2.4.5 Use of Pulse Curve Length in Crash Severity Detection

An algorithm using the curve length concept to analyze vehicle crash severity is explored here. Its purpose is to test its usefulness in discriminating non-perpendicular impacts, such as the rigid pole test, and for meeting the desired sensor activation criteria. Since curve length of a crash pulse depends on how the crash pulse is filtered, the use of the same filtering technique for different impact modes is necessary. In the algorithm based on the curve length concept, it is postulated that the curve length of the crash pulse in a "softer" impact, such as an 8"-diameter rigid pole test, is longer than that in the perpendicular rigid barrier tests.

The computation of the curve length, ΔL, of a given crash pulse can be carried out using the notations shown in Fig. 2.32 and algebraic relationships shown in Eq. (2.34):

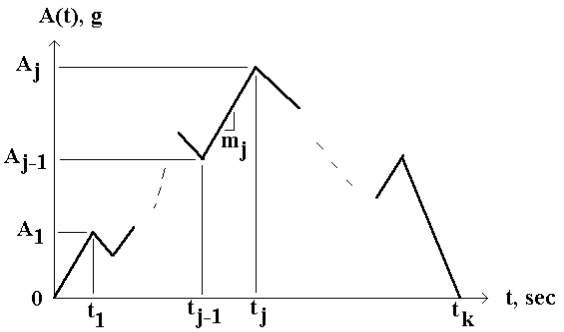

Fig. 2.32 Crash Pulse Data Points (from Fig. 2.17)

$$
\begin{aligned}
&\Delta L: \textit{ curve length of a crash pulse}\\
&\Delta L_i: \textit{ length of line segment } j\\
&\Delta L = \sum_{j=1}^{k} \Delta L_j \quad \textit{where}\\
&k: \textit{ no. of line segments in the crash pulse}\\
&\Delta L_j = \sqrt{(\Delta t_j)^2 + (\Delta A_j)^2} = \Delta t_j \sqrt{1 + m_j^2}\\
&\Delta A_j = A_j - A_{j-1} \quad \textit{and} \quad \Delta t_j = t_j - t_{j-1}\\
&m_j = \frac{\Delta A_j}{\Delta t_j} \ldots . \quad \textit{slope of line segment } j
\end{aligned}
\tag{2.34}
$$

The test data from the four mid-size vehicle tests shown in Table 2.6, filtered by a Butterworth 100 Hz cutoff frequency, are shown in the previous Figs. 2.24 and 2.25. These are analyzed for the curve length comparison as shown in Fig. 2.33. Note that at any given time, #3 test, a 14 mph rigid

barrier test, has the longest curve length. However, the curve length of #4 test, a 17 mph center pole must-activate test, is sandwiched between the two must-not-activate tests of #1 and #2. There exists no curve length relationship that would cause the sensor to activate for the #4 must-activate test condition.

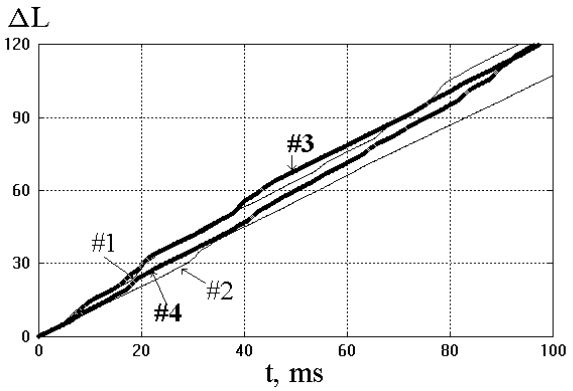

Fig. 2.33 Pulse Curve Length vs. Time from Four Sets of Crash Data Filtered at 100 Hz

A similar analysis was carried out using a higher Butterworth filter cutoff frequency of 300 Hz and the curve length comparison is shown in Fig. 2.34. The curve length of each of the four tests filtered at 300 Hz is longer than that filtered at 100 Hz. The conclusion is the same that an algorithm using the curve length concept is not sufficient to discriminate the crash severity of the must-activate center pole test from the other must-not-activate tests.

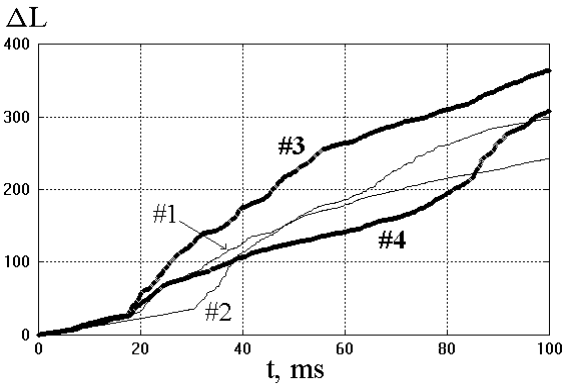

Fig. 2.34 Pulse Curve Length vs. Time from Four Sets of Crash Data Filtered at 300 Hz

2.4.6 FEW Analysis on Body Mount Attenuation

In a body-on-frame vehicle, Fig. 2.35, the body or cab is fastened to the frame by body mounts. One type of truck body mount, shown in Fig. 2.36, consists of rubber bushings on the top and bottom of the frame bracket, plus a bolt and retainer. A typical rubber bushing is made of Butyl, a man-made rubber. There are four body mounts on each side frame and two front end sheet metal (FESM) mounts. Body mounts are designed to carry the horizontal impact load in an impact, and to isolate the noise, vibration, and harshness (NVH) from entering the passenger compartment during driving.

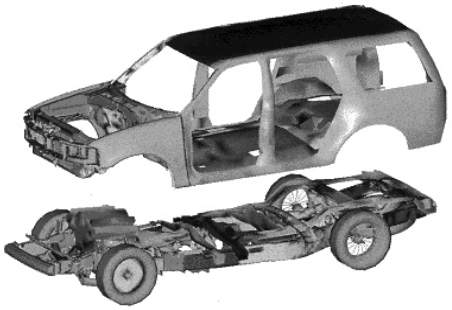

Fig. 2.35 Truck Body on Frame

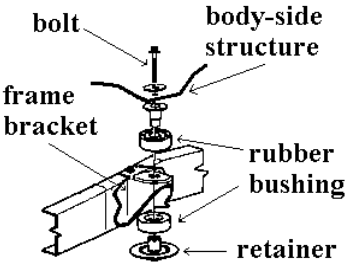

Fig. 2.36 A Typical Body Mount on a Body-on-Frame Vehicle

The impact responses of the frame and body of a truck in a 31 mph rigid barrier test will be analyzed using the FEW method. The dynamic performance of the body mounts in attenuating the frame pulse to the body can be better understood using analyses in both the time and frequency domains. The frame responses are shown in Figs. 2.37–2.39 and the body responses are shown in Figs. 2.40–2.42. Note the differences in the response intensity and peak response location between the frame and body.

2.4.6.1 *Frame Impulse Attenuation by Body Mount*

The frame, body, and body mount impact performances of a truck in a 31 mph rigid barrier test are analyzed. The wideband data of the frame and body crash pulse are shown in Figs. 2.37 and 2.40, respectively. Note the frame pulse contains higher frequency contents and magnitudes than those for the body pulse. The filtered frame and body data sets using a Butterworth 2nd-order filter at a roll-off frequency of 100 Hz are plotted in Figs. 2.38 and 2.41. Figs. 2.39 and 2.42 show the coefficients of FEW, which approximate the frame and body pulses, respectively. The number of coefficients, n, is 100, and the fundamental frequency, f, is equal to 2.91 Hz, which is based on the pulse duration of the test data.

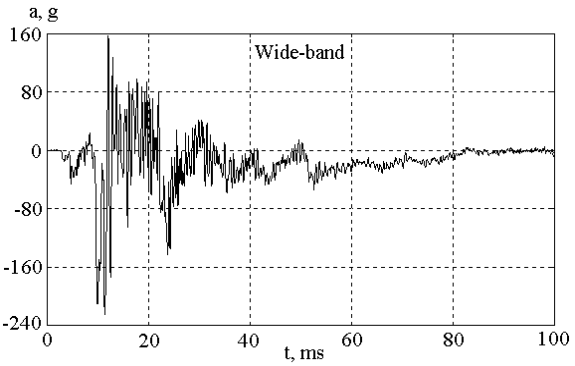

Fig. 2.37 Frame Wideband Data

For comparison purposes, the filtered frame and body data sets shown in Figs. 2.38 and 2.41 are combined and shown in Fig. 2.43. The initial frame impulse can be approximated by a halfsine with duration and magnitude of about 7 ms and 71 g, respectively. The corresponding velocity change of the impulse is $\Delta v = .014 \times 7 \text{ ms} \times 71 \text{ g} = 7$ mph (see the closed-form shown in Table 2.7). The impulse frequency of 1000 ms/(2×7 ms) = 71 Hz dominates the frequency spectrum as shown in Fig. 2.39. Due to body mount attenuation (see Section 3.5.1 in Chapter 3), only a small fraction of frame impulse is transmitted to the body.

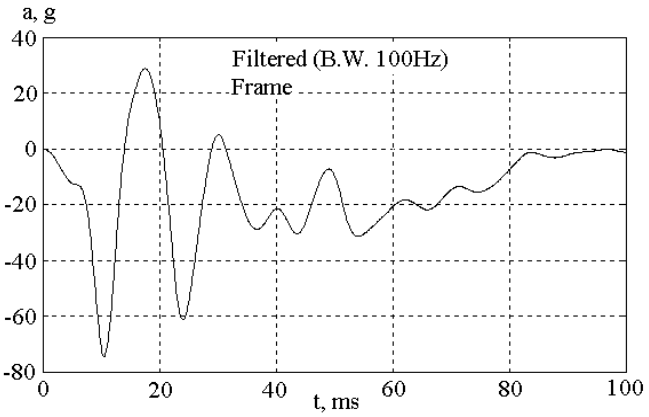

Fig. 2.38 Frame Data Filtered by Butterworth at 100 Hz Cutoff Freq.

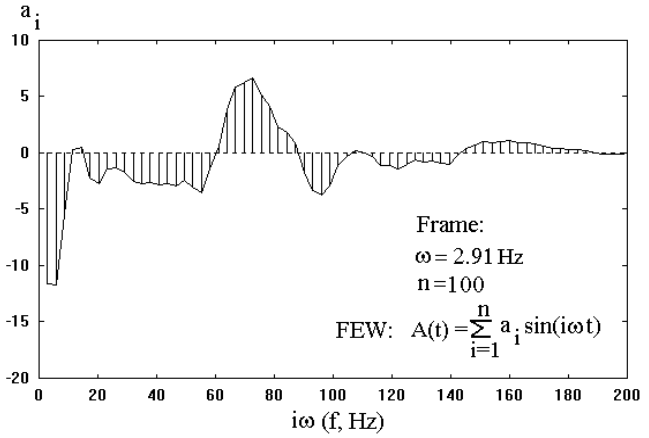

Fig. 2.39 FEW Coefficients for the Frame Data

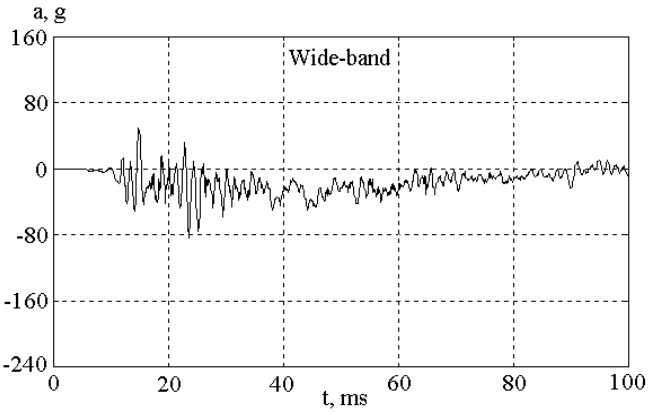

Fig. 2.40 Body Deceleration Wideband Data

Fig. 2.41 Body Data Filtered by Butterworth at 100 Hz Cutoff Freq.

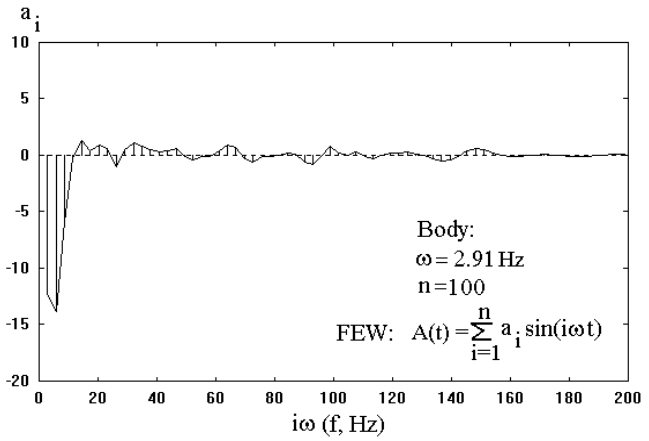

Fig. 2.42 FEW Coefficients for the Body Data

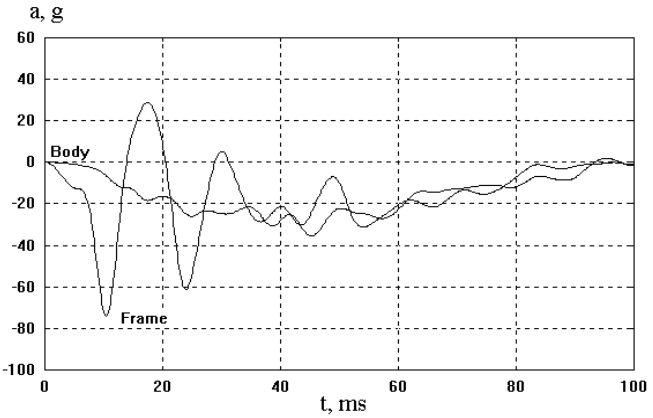

Fig. 2.43 Frame and Body Filtered Crash Pulses (Butterworth rolloff freq. = 100 Hz)

Those FEW coefficients shown in Figs. 2.39 and 2.42 are converted to positive spectrum magnitudes and combined in Fig. 2.44. From these figures, it is evident that the peak frame g-loading is attenuated before it is transmitted to the body by the body mounts. Shown in Fig. 2.39, the spectrum magnitudes of the frame, between 70 and 100 Hz, reflect the decelerations of the initial shock impulse and the subsequent oscillatory signals. However, due to the effect of body mount attenuation, the body does not carry any significant crash pulse components with frequency content above 30 Hz.

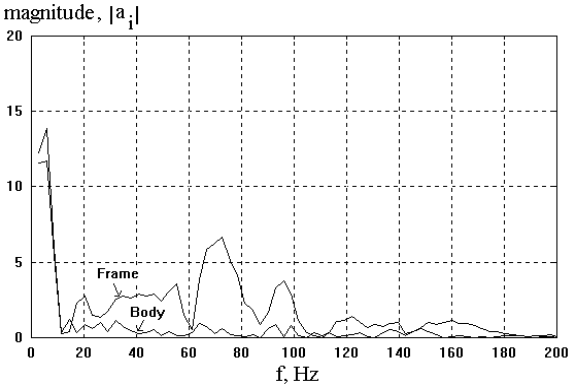

Fig. 2.44 Frequency Spectrum Magnitude of Frame and Body Filtered Crash Pulses

2.4.7 FEW Analysis on Resonance

In the previous section, FEW was used to analyze and display the frequency contents of a crash pulse and the magnitudes of their spectra. It will be shown that the FEW approach can also be used to identify and remove certain frequency content, such as resonant frequencies, during a component design process. Therefore, using the FEW approach, an existing crash pulse can be re-synthesized to include or exclude certain frequency content for the purposes of design analysis.

Since removing the resonant frequency in a Fourier Series expression is equivalent to strengthening the component where the resonance occurs, it provides a quick way of evaluating a crash pulse free of resonance during a component redesign process.

2.4.7.1 *Air Bag Sensor Bracket Design Analysis*

In evaluating the performance of an air bag system with a single point electronic crash sensor (ECS) in a van in an 8 mph rigid barrier impact, a mounting bracket supporting the ECS module was designed as shown in Fig. 2.45.

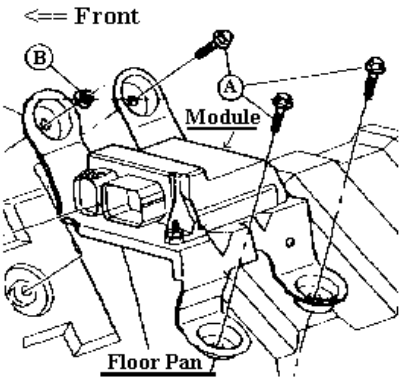

Fig. 2.45 A Sensor Module bracket

The bracket, a stamped sheet metal with three segments, was installed at the center line tunnel near the dash panel. An accelerometer, mounted on top of the module, recorded the deceleration (shown as $A_1(t)$ in Fig. 2.49).

Frequency Domain Analysis of Resonance

A FEW analysis shows the FEW coefficients, a_i, of the crash pulse, where i ranges from 1 to n. The total number of coefficients, n, used in the analysis is 100 with a fundamental frequency, ω, of 4.24 Hz, as shown in Fig. 2.46. The maximum magnitude of the coefficients occurs between i = 22 and i = 25, where resonance occurs. It should be noted that the magnitude and sign of the pair of coefficients #22 and #25 are about the same but opposite in sign; so are those of the pair of #23 and #24. Therefore, these four coefficients as a group cancel out their effects on the signal generation, and yield the resonance shown in the transient response.

Time Domain Analysis of Resonance

Since both ends of the bracket are fixed to the floor pan, the bracket behaves as a four-bar linkage with flexible joints between the segments. The resonance of the bracket at about 100 Hz is mainly due to the vibration of the flexible bracket excited at its own natural frequency.

To visualize the transient response of the resonance, the Fourier expression using the four coefficients ranged from i = 22 to i = 25 is plotted and shown in Fig. 2.47.

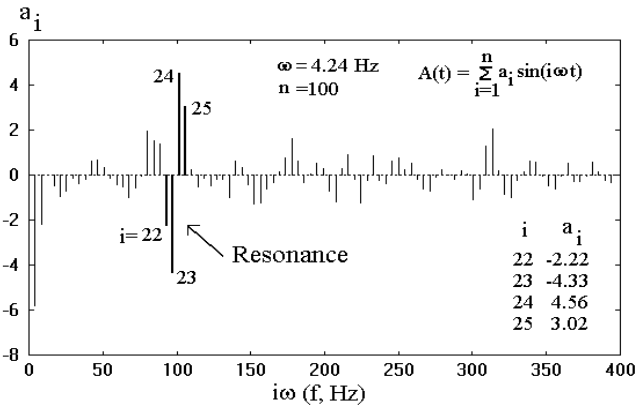

Fig. 2.46 Coefficients of Fourier Equivalent Wave at ECS Module

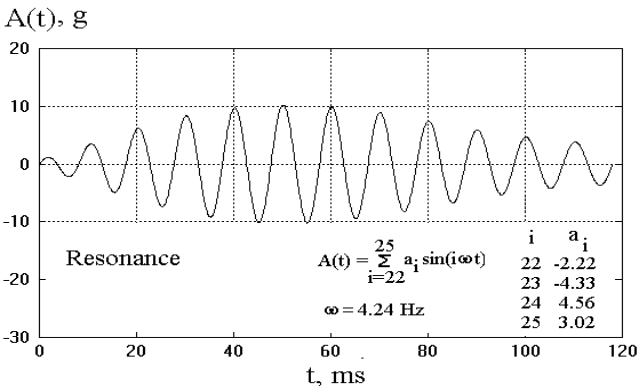

Fig. 2.47 Bracket 100 Hz Resonance

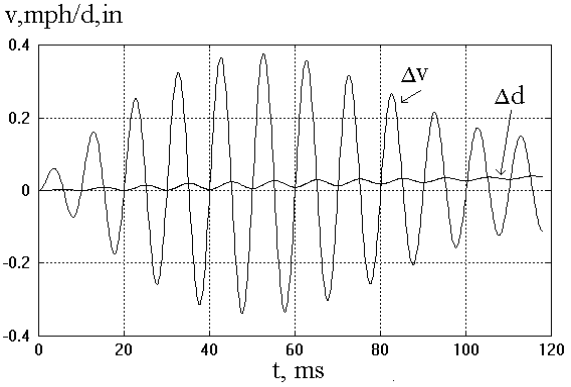

Fig. 2.48 Velocity and Displacement Changes of the Resonance $A_2(t)$

Shown in Fig. 2.48 are the first and second integrals of the resonance deceleration. The magnitudes of the velocity and displacement changes are fairly small even though the resonance deceleration magnitudes are fairly large.

Since resonance is an undesirable vibration in the signal detection, the removal of the resonance will not affect significantly the contents of the signals such as velocity and displacement changes.

2.4.7.2 *Re-synthesis of a Crash Pulse Without Resonance*

Re-synthesis of a crash pulse is a process in which the resonance is removed, and the crash pulse is reconstructed using the FEW approach. Before making a new and stiffer bracket to test the ECS performance, the original crash pulse, A(t), shown in Fig. 2.49, is decomposed into two sets, signal $A_1(t)$ and resonance $A_2(t)$.

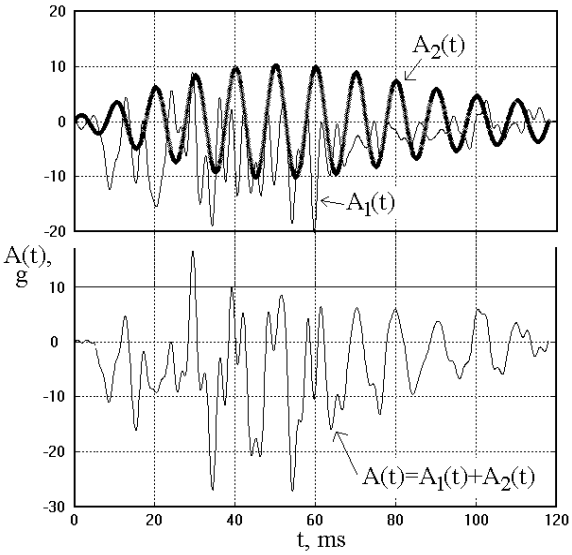

Fig. 2.49 Composition of Accelerometer Data at ECS: Signal A_1 and Resonance A_2

$A_2(t)$ is identified by observing the group of the FEW coefficients (i = 22 to 25) whose magnitudes are the largest, as shown in Fig. 2.46. Note that the coefficients in the second half of the group (i = 24, 25) are approximately mirror images of those in the first half of the group (i = 23, 22). The effect of mirror imaging of the FEW coefficients of the resonance set is that the signal due to each of the coefficients cancels out. The first and second integrals of the resonance $A_2(t)$; (velocity and displacement changes) is very small. Therefore, the signal contribution due to the resonance is also small.

By subtracting the resonance $A_2(t)$ from the original crash pulse A(t), the re-synthesized pulse $A_1(t)$ is thus obtained, as shown in Fig. 2.49. The integrals of the re-synthesized pulse $A_1(t)$ are compared with those of the original pulse (A). Comparison of the first integrals, Δv, between the original pulse, A(t), and re-synthesized pulse, $A_1(t)$, shows very little difference, as shown in Fig. 2.50, even though a large oscillation from the resonance is removed. Similarly, the difference of the second integrals, Δd, between the original and re-synthesized pulses is also very small. The underlying reasons are attributed to the first and second integrals, Δv and Δd, of the resonance, $A_2(t)$, which are very small as shown in Fig. 2.50.

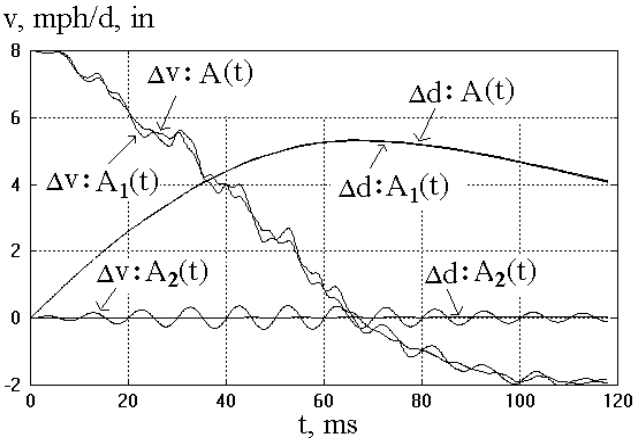

Fig. 2.50 Velocity and Displacement of the FEW With and Without Resonance $A_2(t)$

2.4.8 Trapezoidal Wave Approximation (TWA)

The deceleration of the TWA starts with zero deceleration at time zero and rises along a constant slope, e, until it reaches a constant deceleration A at time T_1, as shown in Fig. 2.51. The constant deceleration extends from T_1 to T_m, when the maximum deformation occurs. Since there are two unknowns, T_1 and A, two equations based on two boundary conditions are needed. The two boundary conditions for the barrier impact are (1) the velocity at T_m being equal to zero and (2) the displacement at T_m being equal to the test dynamic crush. The derivation and the solution for the two unknowns are shown as follows. TWA is a useful crash pulse approximation when the kinematics occurring in the beginning of test pulse duration can be well duplicated. In that early portion of the crash, structure deformation and energy and air bag sensor crash performance can be accurately assessed by the TWA.

2.4.8.1 *Deriving the Closed-form Solutions for TWA Parameters*

The derivation of the TWA parameters is preceded by the kinematic relationships in the deformation phase (Step 1). Thereafter, the boundary conditions are applied to derive the solutions (Step 2). The two-step procedure is shown as follows.

Trapezoidal Wave Approximation (TWA) and Kinematic Relationships–Step 1

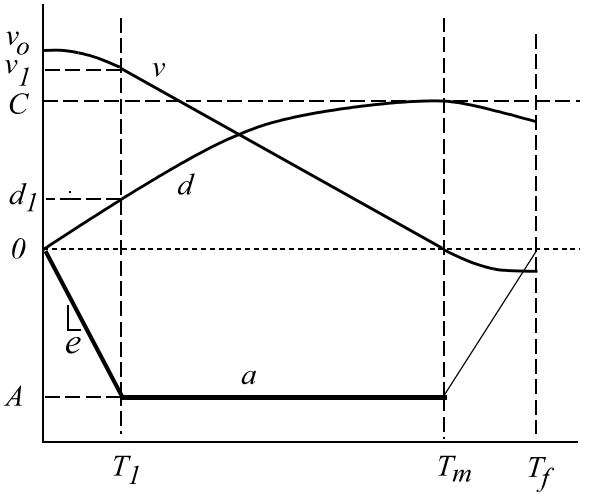

Fig. 2.51 Trapezoidal Wave Approximation and Its Integrals

$$
\begin{aligned}
&\textit{Deformation Phase: } 0 \rightarrow T_1 \\
&a = et = \frac{A}{T_1}t \\
&v = v_o + \int_0^t a\,dt = v_o + \frac{e}{2}t^2 \\
&d = v_o t + \frac{e}{6}t^3
\end{aligned}
\tag{2.35}
$$

$$
\begin{aligned}
&\textit{Boundary conditions at } T_1\text{:} \\
&\textit{for } t=T_1, \quad \textit{then } a = eT_1 = A, \\
&\therefore\ v_1 = v_o + \frac{e}{2}T_1^2 \left(= v_o + \frac{AT_1}{2} \right), \quad \textit{and} \\
&d_1 = v_o T_1 + \frac{e}{6}T_1^3 \left(= v_o T_1 + \frac{AT_1^2}{6} \right)
\end{aligned}
\tag{2.36}
$$

Trapezoidal Wave Approximation (TWA) and Kinematic Relationships–Step 2

$$
\begin{aligned}
&\textit{Constant Decel: } T_1 \rightarrow T_m\text{:} \\
&v = v_1 + \int_{T_1}^t a\,dt = v_o + \frac{AT_1}{2} + A(t-T_1), \qquad \textit{where } t \geq T_1 \\
&d = d_1 + \int_{T_1}^t v\,dt = \ldots = \frac{At^2}{2} + \left(v_o - \frac{AT_1}{2} \right) t + \frac{AT_1^2}{6} \\
&\textit{where } d_1 \textit{ is determined by the boundary conditions at } T_1
\end{aligned}
\tag{2.37}
$$

Boundary conditions at T_m:

$$\text{BC \#1:}\quad v = v_m = 0,$$

$$0 = v_o + \frac{AT_1}{2} + A(T_m - T_1)$$

$$\therefore \quad T_1 = \frac{2}{A}(v_o + AT_m) \qquad \triangleleft \tag{2.38}$$

$$\text{BC \#2:}\quad d = C,$$

$$\therefore \quad C = \frac{AT_m^2}{2} + \left(v_o - \frac{AT_1}{2}\right)T_m + \frac{AT_1^2}{6}$$

Substituting expression for T_1 *into that for C, and rearranging, it becomes*

$$T_m^2A^2 + 2(4v_oT_m - 3C)A + 4v_o^2 = 0 \quad \textit{then}$$

solving for the feasible solution of A : (2.39)

$$A = \frac{-(4v_oT_m - 3C) + \sqrt{(4v_oT_m - 3C)^2 - 4v_o^2T_m^2}}{T_m^2} \qquad \triangleleft$$

Case Study:

A test was conducted of a mid-size passenger car in a 31 mph rigid barrier impact. The crash pulse at the left rocker panel at the B-post is shown in Fig. 2.53. The TWA and the integrals are shown in Figs. 2.53–55, along with those for the BSA (Bi-Slope Approximation). Note that the test velocity and displacement boundary conditions at T_m= 86.5 ms are satisfied by the TWA.

2.4.9 Bi-slope Approximation (BSA)

In the Trapezoidal Wave Approximation (TWA), there are two consecutive line segments of which the slopes are e and zero, respectively. In the Bi-Slope Approximation (BSA) shown in Fig. 2.52, there are also two consecutive line segments but with finite slopes of e and f. Since there are three unknowns in the BSA, the ramp-up time of T_1 and two slopes, e and f, it needs three boundary conditions for a solution. In addition to the two boundary conditions for the TWA, which are the velocity at T_m equal to zero and the displacement at T_m equal to the test dynamic crush, the third boundary condition is for the displacement at T_c, the centroid time of the test crash pulse.

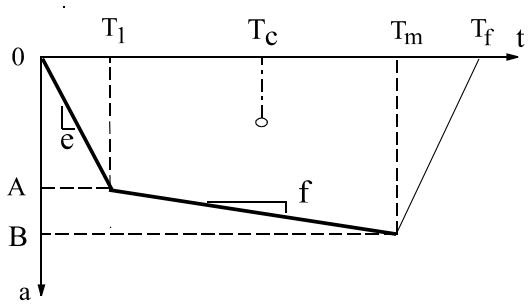

Fig. 2.52 Bi-Slope Approximation (BSA)

There are three unknowns: T_1, e, and f. The three boundary conditions for BSA are:

1. Velocity at T_m= 0

2. Displacement at T_m = test dynamic crush
3. Displacement at T_c = test displacement at centroid time

The procedures used to determine these unknowns (A, e, f) of BSA are shown in Eq. (2.40).

$$T_1 = \frac{-b + \sqrt{b^2-4ac}}{2a}, \quad e = \frac{1+y}{x}, \quad f = \frac{y}{x}$$

$$\textit{Note:} \quad A = eT_1, \quad B = A + f(T_m - T_1)$$

$$\textit{where}$$

$$a = \frac{q-p}{6}, \quad b = \frac{1}{2}\left(-T_c q + \frac{d_c p}{v_o}\right)$$

$$c = qT_m\left(T_c - \frac{T_m}{2}\right) - pT_m\left(\frac{T_c^2}{2T_m} - T_c + \frac{d_c}{v_o}\right)$$

$$p = \frac{1}{3} - \frac{1}{2}\frac{T_c}{T_m} \tag{2.40}$$

$$q = \frac{1}{2}\frac{T_c}{T_m} - \frac{1}{2}\frac{d_c}{v_o T_m} - \frac{1}{6}\left(\frac{T_c}{T_m}\right)^3$$

$$y = \frac{\frac{1}{6}\left(\frac{T_1}{T_m}\right)^3 - \frac{1}{2}\frac{T_c}{T_m}\left(\frac{T_1}{T_m}\right)^2 + \left(\frac{T_c}{T_m} - \frac{1}{2}\right)\frac{T_1}{T_m}}{\frac{1}{3} - \frac{1}{2}\left(\frac{T_c}{T_m}\right)}$$

$$x = \frac{T_m^2}{v_o}\left[\frac{y}{2} + \frac{T_1}{T_m} - \frac{1}{2}\left(\frac{T_1}{T_m}\right)^2\right]$$

2.4.9.1 *Comparison of Test Pulse, BSA, and TWA*

The rear-loaded crash pulse of a truck in a 35 mph rigid barrier test was used in Section 2.3.6.1 for the ASW, ESW, and TESW analyses. All three approximated pulses have two boundary conditions. The crash pulse shown in Fig. 2.12 is re-plotted and shown in Fig. 2.53 for the BSA (Bi-Slope Approximation) analysis. The solutions of BSA which have three boundary conditions are as follows:

T_1 = 23.1 ms
T_m = 83.4 ms
C (dynamic crush) = 29.7 in
A (deceleration at T_1) = −20.8 g
T_c = 48.1 ms
d at T_c = 24 in
B (deceleration at T_m) = −24.1 g

In the BSA, in addition to satisfying the two boundary conditions for the velocity and displacement at T_m (83.4 ms), the third boundary condition of the displacement at T_c (48.1 ms) is also satisfied, as shown in Fig. 2.55. Also shown in the figures are the responses for the Trapezoidal Wave Approximation (TWA).

Based on the closely approximated velocity curves shown in Fig. 2.54, the comparison of energies for the test, TWA and BSA, should be fairly close.

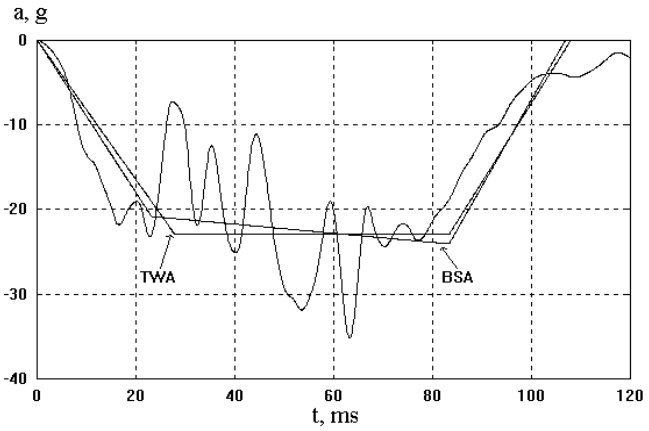

Fig. 2.53 Crash Pulse Comparison between Test and BSA (Bi-Slope Approximation)

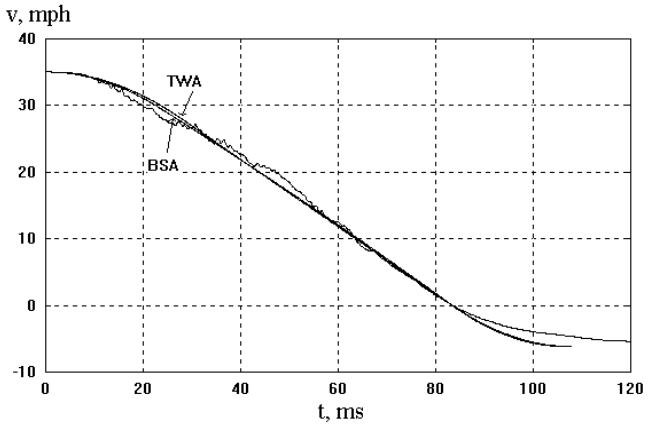

Fig. 2.54 Velocity Comparison between Test and BSA (Bi-Slope Approximation)

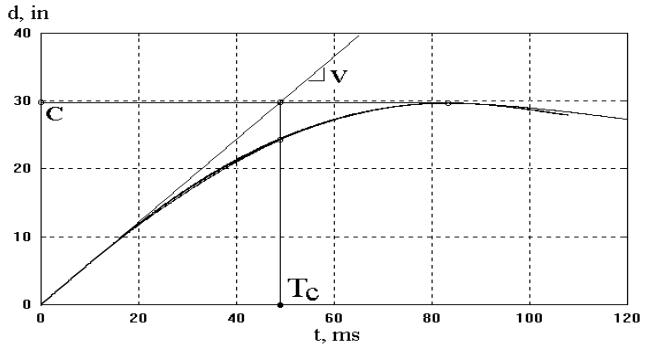

Fig. 2.55 Displacement Comparison between Test and BSA (Bi-Slope Approximation)

2.4.10 Harmonic Pulses – Background

Two harmonic pulses are used for crash pulse approximation: the halfsine and the haversine pulses. Both of these are derived from a simple harmonic pulse but with different coordinate systems being specified. Fig. 2.56 shows a harmonic pulse in which a sine, a cosine, and a haversine are defined with coordinate systems a-t, a'-t', and a"-t", respectively. Since both the halfsine and haversine start from zero magnitude (which agrees with the crash test deceleration value at time zero), they are useful in crash pulse approximations. Normalized halfsine and haversine pulses (r_a), their velocities (r_v), and the time (r_t) are plotted in Fig. 2.57.

y-x Coordinate	Pulse
a-t	Sine
a'-t	Cosine
a"-t"	Haversine

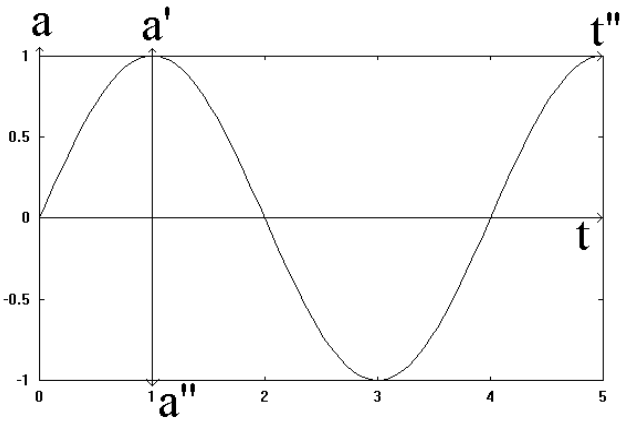

Fig. 2.56 Harmonic Pulses

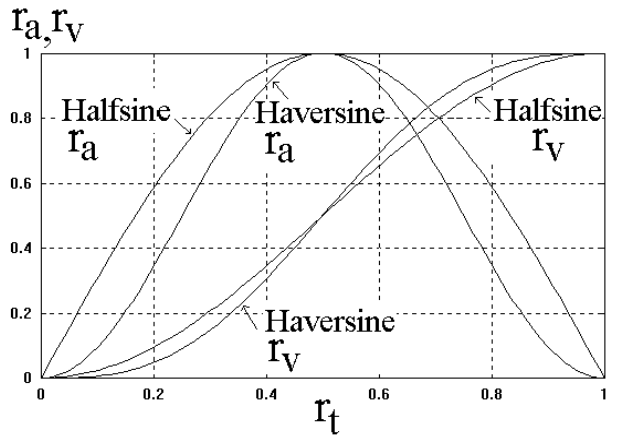

Fig. 2.57 Normalized Halfsine, Haversine and Velocity Changes

Table 2.7 contains the kinematic expressions and their plots shown in Figs. 2.58 and 2.59, respectively. In addition, a triangular pulse shown in Fig. 2.60 is included as a reference. Given the same magnitude and duration as shown in Fig. 2.61, the total velocity and displacement changes of the halfsine pulse are about 27 and 21 percent more than those of the haversine, respectively. However, given the same velocity change and duration, the peak magnitude of the halfsine pulse is only about 79 percent of that of the haversine pulse as shown in Fig. 2.62.

Table 2.7 Simple Pulses and Normalized Kinematic Variables

Pulse Type	Formula
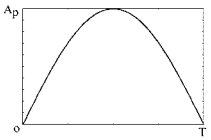 **Fig. 2.58** Halfsine	$r_a = \frac{a_t}{A_p} = Sin(\pi\frac{t}{T})$ $r_v = \frac{v_t}{\Delta V} = .5\left[1-Cos\left(\pi\frac{t}{T}\right)\right]$ $\Delta V = 13.98\ A_p\ T$ $\Delta D = 122.9\ A_p T^2$ (2.41)
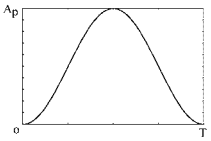 **Fig. 2.59** Haversine	$r_a = \frac{a_t}{A_p} = .5\left[1-Cos\left(2\pi\frac{t}{T}\right)\right]$ $r_v = \frac{v_t}{\Delta V} = \frac{t}{T}-\frac{1}{2\pi}Sin\left(2\pi\frac{t}{T}\right)$ $\Delta V = 10.98\ A_p\ T$ $\Delta D = 101.5\ A_p T^2$ (2.42)
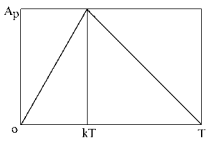 **Fig. 2.60** Triangle	$r_a = \frac{t}{kT}A_p \quad for \quad 0 < t \le kT$ $r_a = \frac{T-t}{T(1-k)}A_p \quad for \quad kT < t < T$ $\Delta V = 10.98 A_p T$ $\Delta D = 64.37(1+k)A_p T^2$ (2.43)

Where t: time, sec
T: total duration, sec
a_t: acceleration at t
A_p: peak acceleration magnitude, g
v_t: velocity at t
ΔV: total velocity change, mph
ΔD: total displacement, in.
r_t, r_a, r_v: normalized time, acceleration, and velocity, respectively

The triangular pulse in Figs. 2.61–2.62 has the same total velocity change as that of the haversine pulse. The side of the triangular pulse intersects the haversine at the inflection point of the haversine, the mid-point of the magnitude. However, the total displacement of the symmetrical triangular pulse is about 5 percent less than that of the haversine pulse.

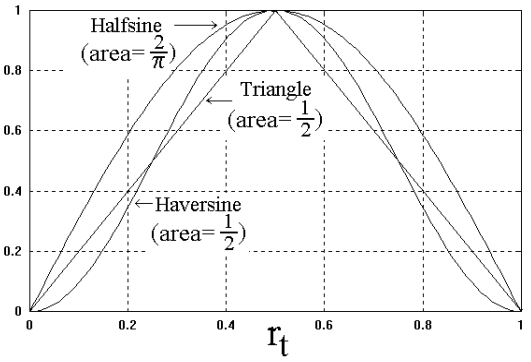

Fig. 2.61 Harmonic Pulses with Same Magnitude

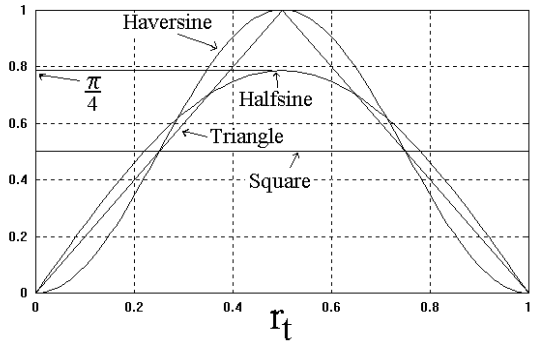

Fig. 2.62 Harmonic Pulses with Same Velocity Change

2.4.11 Halfsine Approximation

The two boundary conditions for the halfsine approximation are the maximum dynamic crush, C, and the time at dynamic crush, t_m. Since there are two constraint equations, two unknowns can be computed: ω_n (circular frequency) and A_n (peak halfsine magnitude). The process of deriving the formula of the two unknowns is shown in Eq. (2.44). A case study and the construction steps needed to apply the formula are described in Section 2.4.11.1.

The unknown term b in (5) of Eq. (2.44) can be found by using the Newton-Raphson method, as shown in Eq. (2.45). Then the unknowns ω_n can be computed from the relationship $b = \omega_n t_m$, and A_p, (4) of Eq. (2.44), can be solved for. If the relative error, ϵ, of the unknown b between two successive iterations is less than .001 shown in Eq. (2.45), the current value of b is then the solution to (5) of Eq. (2.44).

The solution process usually takes no more than three iterations to arrive at a solution. However, the iteration process may get trapped if the initial guess is not in the range where a solution is feasible. This is because the method requires calculation of the derivative of a function to evaluate the slope (tangent) at a reference point. The slope at a point on the curve in the region where there is no feasible solution can become zero at the peak or the valley and cause a computational error. It is recommended that the function f(b) be plotted against b to understand the nature of the function and to select a proper value for the initial guess.

Formula Derivations for the Halfsine Approximation

$$a = A_p \, Sin(\omega_n t) \quad \ldots\ldots\ldots\ldots \quad (1)$$

$$\textit{Integrating: } v = -\frac{A_p}{\omega_n} Cos(\omega_n t) + c_1$$

$$\textit{I.C.: } \quad t=0, \quad v=v_0 \quad \textit{then} \quad c_1 = v_0 + \frac{A_p}{\omega_n}$$

$$\therefore \quad v = v_0 + \frac{A_p}{\omega_n}[1 - Cos(\omega_n t)] \quad \ldots\ldots \quad (2)$$

$$\textit{Integrating: } \quad d = v_0 t + \frac{A_p}{\omega_n}\left[t - \frac{Sin(\omega_n t)}{\omega_n}\right] + c_2$$

$$\textit{I.C.: } \quad t=0, \quad d=0 \quad \Rightarrow \quad c_2 = 0$$

$$\textit{and} \quad d = v_0 t + \frac{A_p}{\omega_n}\left[t - \frac{Sin(\omega_n t)}{\omega_n}\right] \quad \ldots\ldots \quad (3) \qquad (2.44)$$

Given: v_0 *(initial velocity),* C *(dynamic crush), and* t_m *(time of* C*)*
solve for two unknowns, ω_n *and* A_p

B.C. 1: $v = 0$ *at* $t = t_m$ *then, letting* $b = \omega_n t_m$:

$$\textit{from (2): } \quad A_p = \frac{-v_0 \omega_n}{1 - Cos(b)} \quad \ldots\ldots\ldots \quad (4)$$

B.C. 2: $d = C$ *(dynamic crush) at* $t = t_m$ *then*
from (3) *and* (4):

$$\frac{t_c}{t_m} = 1 - \frac{b - Sin(b)}{b[1 - Cos(b)]} \quad \ldots\ldots\ldots\ldots \quad (5)$$

$$\textit{where } \quad t_c \textit{ (centroid time)} = \frac{C}{v_0} \quad \ldots\ldots\ldots \quad (6)$$

Solving for Unknown Term b in (5) of Eq. (2.44):

Applying the Newton–Raphson Method:
From (5) *in Eq.*(2.44), *a function* $f(b)$ *is set as*

$$f(b) = 1 - \frac{b - Sin(b)}{b[1 - Cos(b)]} - \frac{t_c}{t_m}$$

$$f'(b) = \frac{\partial f(b)}{\partial b} = \frac{b - Sin(b)}{b^2[1 - Cos(b)]} - \frac{2 - 2Cos(b) - bSin(b)}{b[1 - Cos(b)]^2} \qquad (2.45)$$

$$\because \quad f'(b_i) = \frac{f(b_i)}{b_i - b_{i+1}}, \quad \therefore \quad b_{i+1} = b_i - \frac{f(b_i)}{f'(b_i)}$$

$$\epsilon = \frac{|b_{i+1} - b_i|}{b_i} \le .001, \quad \textit{where } i\textit{: iteration index}$$

Using a Newton-Raphson technique for the halfsine approximation, ω_n and A_p can then be computed from (4) and (5) of Eq. (2.44).

Based on formulas shown in Eq. (2.44), the construction steps for halfsine approximation are listed in the following page.

Given: v (initial velocity, ft/sec) = 14 mph = 20.53 ft/s,
C (dynamic crush, ft) = 5.86 in,
t_m (time at C)= 38.5 ms

Chart 1: Relative centroid location vs. b
[from (5) of Eq. (2.44)].
Given: $C/(vt_m)$= .617,
find b=1.96, then compute
ω_n (=b/t_m) =50.9 rad/s,
$f = \omega_n/(2\pi)$ = 8.1 Hz

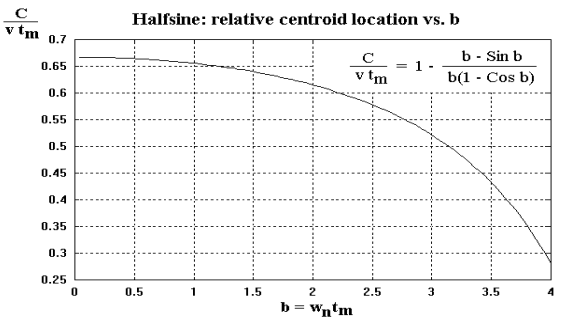

Fig. 2.63 Halfsine: Relative Centroid Location vs. b

Chart 2: Normalized peak deceleration
[from (4) of Eq. (2.44)]
Given: b = 1.96,
find $A_p/(v\omega_n)$ = .724, then
A_p=756.7 ft/s^2 =23.5 g

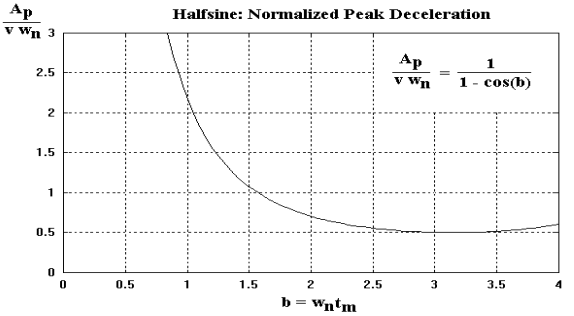

Fig. 2.64 Halfsine: Normalized Peak Deceleration

Chart 3: Normalized time at peak deceleration
[from (1) of Eq. (2.44)]
Given: b=1.96,
find t_p/t_m = .8, then
t_p=30.9 ms.

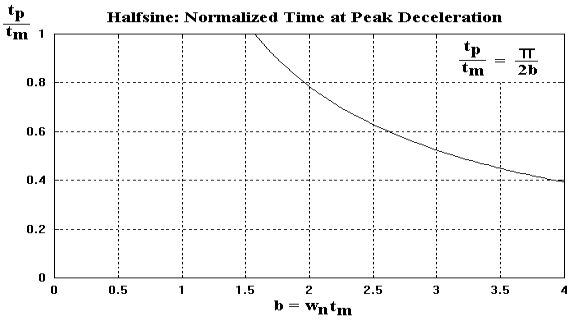

Fig. 2.65 Halfsine Normalized Peak Deceleration

Chart 4: Normalized deceleration at t_m
[from (1) of Eq. (2.44)]
Given: b=1.96,
find A_m/A_p=.925, then
A_m=21.74 g

Draw halfsine wave on top of crash pulse.

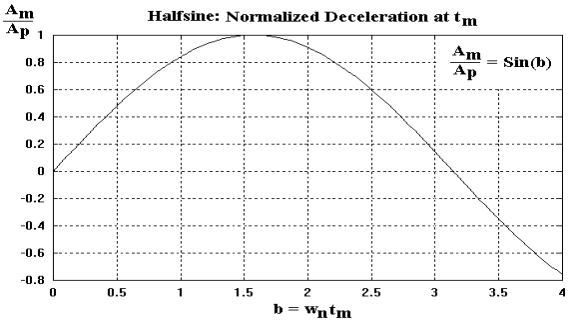

Fig. 2.66 Halfsine: Normalized Deceleration at t_m

2.4.12 Haversine Approximation

Crash pulse approximation using haversine is similar to that using halfsine, wherein the two boundary conditions are the maximum dynamic crush, C, and the time, t_m. Since there are two constraint equations, two unknowns can be computed: ω_n (circular frequency) and A_p (peak haversine magnitude). The process of deriving the formulas for the two unknowns is shown in Eq. (2.46).

Derivation of Formulas for the Haversine Approximation

$$a = \frac{A_p}{2}[1 - Cos(\omega_n t)] \quad \ldots\ldots\ldots\ldots\ldots\ldots \quad (7)$$

$$Integrating: \quad v = \frac{A_p}{2}\left[t - \frac{Sin(\omega_n t)}{\omega_n}\right] + c_1 \quad \ldots\ldots\ldots \quad (8)$$

$$I.C.(initial\ condition): \quad t = 0,\ v = v_0. \quad Then \quad c_1 = v_0$$

$$\therefore \quad v = v_0 + \frac{A_p}{2}\left[t - \frac{Sin(\omega_n t)}{\omega_n}\right]$$

$$then: \quad d = v_0 t + \frac{A_p}{2}\left[\frac{t^2}{2} + \frac{Cos(\omega_n t)}{\omega_n^2}\right] + c_2$$

$$I.C.: \quad t = 0, \quad d = 0, \quad then \quad C_2 = \frac{-A_p}{2\omega_n^2},$$

$$and \quad d = v_0 t + \frac{A_p}{4}t^2 + \frac{A_p}{2\omega_n^2}[Cos(\omega_n t) - 1] \quad \ldots\ldots\ldots \quad (9) \qquad (2.46)$$

$$Given: v_0\ (initial\ velocity),\ C\ (dynamic\ crush)\ and\ t_m\ (time\ at\ C)$$

$$solve\ for\ two\ unknowns,\ \omega_n\ and\ A_p:$$

$$B.C.(boundary\ condition)\ 1: v = 0\ at\ t = t_m$$

$$from\ (8): \quad A_p = \frac{-2 v_0 \omega_n}{b - Sin(b)} \quad \ldots\ldots\ldots\ldots\ldots\ldots \quad (10)$$

$$B.C.\ 2: d = C\ at\ t = t_m,$$

$$from\ (9)\ and\ (10): \quad \frac{t_c}{t_m} = 1 - \frac{b^2 + 2\,Cos(b) - 2}{2b[b - Sin(b)]}$$

$$where\ t_c\ (centroid\ time) = \frac{C}{v_0}\ and$$

$$b = \omega_n t_m$$

Using the Newton-Raphson technique for the haversine approximation, ω_n and A_p can then be computed from (7) and (8) of Eq. (2.46).

Based on formulas shown in Eq. (2.46), the construction steps for haversine approximation are listed in the following page.

Given:
v (initial velocity, ft/sec)
= 31 mph = 45.5 ft/s,
C (dynamic crush, ft) = 22.54 in
= 1.878 ft,
t_m (time at C) = 72.8 ms
= .0728 sec

Chart 1: Relative centroid location vs. b
[from (5) of Eq. (2.46)]
Given: $C/(vt_m)$= .567,
find b=5.49, then compute
ω_n (=b/t_m) =75.4 rad/s,
$f = \omega_n/(2\pi)$ = 12 Hz

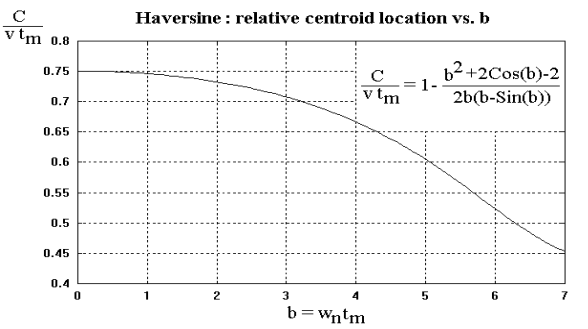

Fig. 2.67 Haversine: Relative Centroid Location vs. b

Chart 2: Normalized peak deceleration
[from (4) of Eq. (2.46)]
Given: b = 5.49,
find $A_p/(v\omega_n)$ = .322, then
A_p=1104.5 ft/s^2 =34.3 g

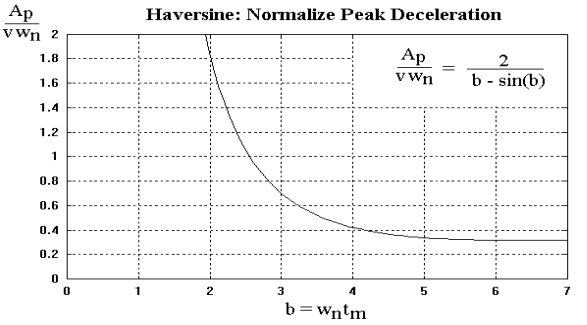

Fig. 2.68 Haversine: Normalized Peak Deceleration

Chart 3: Normalized time at peak deceleration
[from (1) of Eq. (2.46)]
Given: b=5.49,
find t_p/t_m = .572, then
t_p=41.7 ms

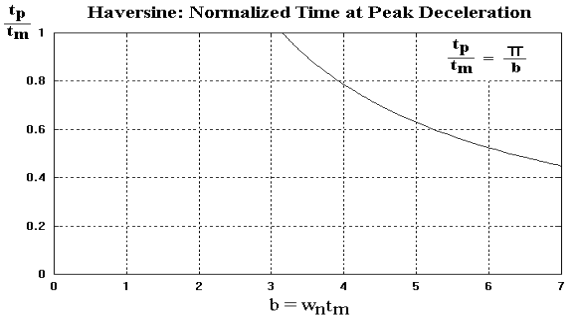

Fig. 2.69 Haversine: Normalized Time at Peak

Chart 4: Normalized deceleration at t_m
[(1) of Eq. (2.46)]
Given: b=5.49,
find A_m/A_p=.149, then
A_m=5.12 g

Draw haversine wave on top of crash pulse.

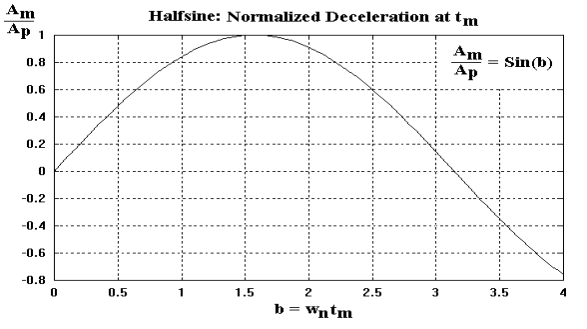

Fig. 2.70 Halfsine: Normalized Deceleration at t_m

2.4.13 Comparison of Halfsine and Haversine Pulses

A light truck, T5, was tested using a 31 mph rigid barrier condition. The crash pulse at the left rocker at the B-pillar can be characterized by halfsine and haversine pulses. As shown in Figs. 2.71–2.73, both the halfsine and haversine produce a dynamic crush of about 23 inches at 73 ms, which is the same as that of the test. However, the halfsine approximates the velocity and displacement responses better than the haversine does. Also, the magnitude of the peak deceleration of the halfsine, 27 g, is closer to that of the test than that of the haversine. The main reason for the better approximation by the halfsine is that both the front and rear engine cross members of the light truck frame structure are stiff. The early portion of the test crash pulse is better approximated by the halfsine than the haversine, as shown in Fig. 2.71. Since the halfsine wave is also the transient response (deceleration and displacement) of a simple spring mass model, the light truck structure stiffness (force-deflection relationship) can be modeled by a simple spring-mass system. Depending on the effective weight of the vehicle, the spring stiffness of the light truck can then be computed to yield the specified dynamic responses.

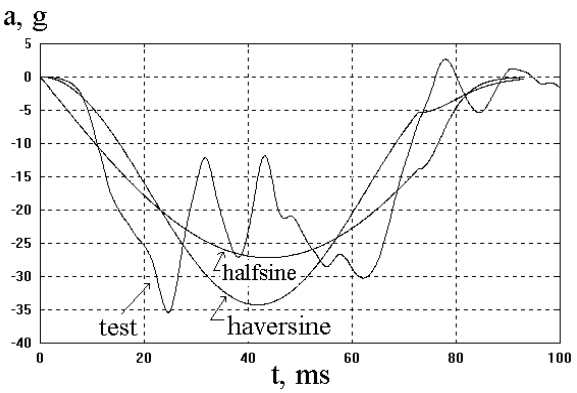

Fig. 2.71 Crash Pulse Comparison between Test, Halfsine, and Haversine Waves

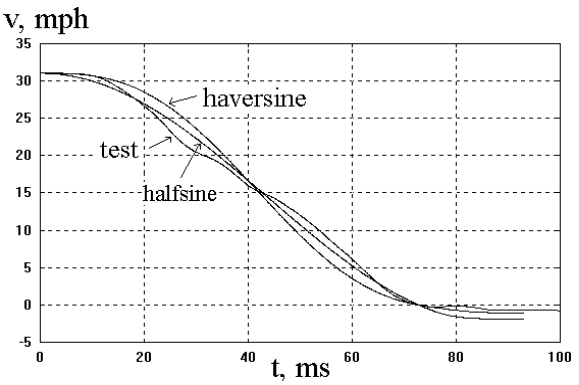

Fig. 2.72 Velocity Comparison between Test, Halfsine, and Haversine Waves

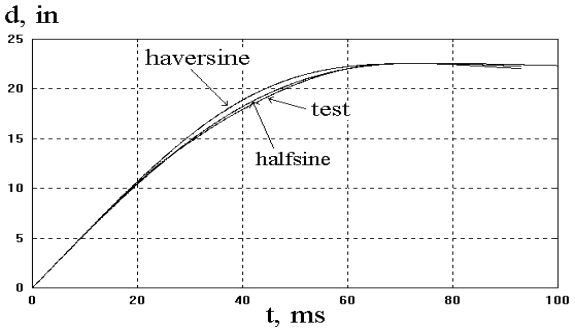

Fig. 2.73 Displacement Comparison between Test, Halfsine, and Haversine Waves

2.4.14 Response of Air Bag Sensor to Harmonic Pulses

A ball-in-tube (BIT) crash sensor and its components, used in an air bag equipped vehicle, are shown in Figs. 2.74–2.75. The sensor contains a gold-plated steel ball, held in place by a magnet located outside a plastic cylindrical housing. The ball moves forward when subjected to a deceleration sufficient to overcome the force of magnetic attraction. The gap between the ball and spring contact is 0.25 in and the ball bottoms out on the cap at 0.5 in. Due to the tight clearance between the ball and cylinder (about 0.0015 inches, approximately the diameter of a human hair), the sensor is highly gas-damped [3,4]. Being gas-damped, the sensor is not sensitive to short duration impulses, such as hammer blows. This helps prevent inadvertent activations of the sensor.

The dynamic behavior of the gas-damped crash sensor is explained by the equation of motion of the sensor subjected to an input excitation. The mathematical relationship between the sensor displacement (output response) and velocity change (input excitation) is presented in the next section.

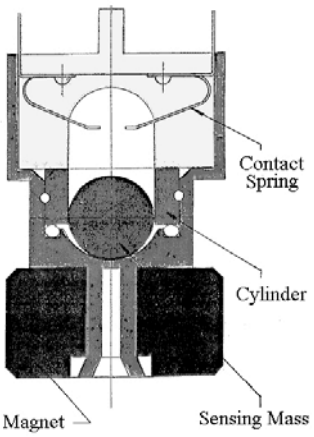

Fig. 2.74 An Air bag Ball-in-Tube (BIT) Crash Sensor

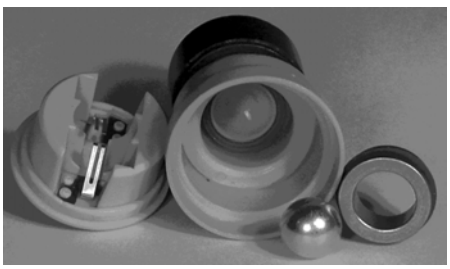

Fig. 2.75 Ball-in-Tube Crash Sensor Components

To study the effect of halfsine and haversine pulses on the sensor responses, three pulses with the specifications shown in Table 2.8 are plotted in Fig. 2.76. The three pulses were used to excite a BIT sensor model. Pulse #1 is a haversine ($T = 38$ ms, $A_p = 32$ g). When tested, it is required to activate the crash sensor at a time between the mid-point and the final time of the haversine. Pulse #2 is a halfsine with the same magnitude and duration as pulse #1; it has a total Δv of 17 mph, about 27% higher than that of pulse #1. Pulse #3 is a halfsine with the same total Δv and duration as #1; it has a peak magnitude of only 25.2 g, about 21% lower than that of pulse #1.

Table 2.8 Specifications of Three Haversine and Halfsine Pulses

No.	Pulse	T, ms	A_p, g	Δv, mph	t*, ms	Δv, mph
1	Haversine	38	32	13.4	24	10
2	Halfsine	38	32	17.0	21	10
3	Halfsine	38	25.2	13.4	25	10

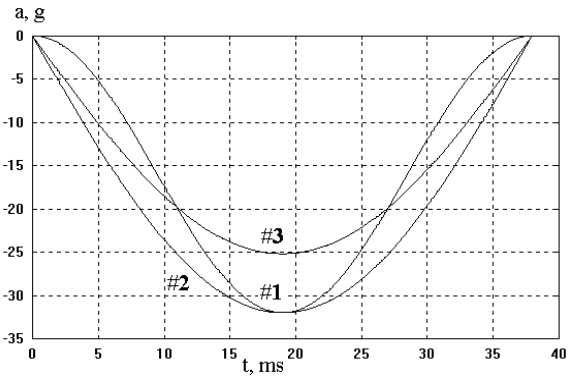

Fig. 2.76 Input Pulses to a BIT Model

Fig. 2.77 shows that the sensor velocity change is about 10 mph at the time of sensor activation for all three pulses. The crash sensor is therefore categorized as a 10 mph crash sensor.

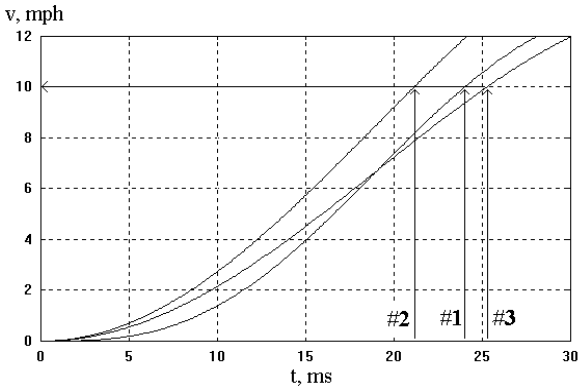

Fig. 2.77 Sensor Velocity Changes at Activation Times

Fig. 2.78 shows the displacement change and the activation times, t_m, of the three pulses using a crash sensor model [3]. The activation occurs when the ball travels 0.25 inches and contacts the springs inside the sensor housing. Pulse #2 has the shortest activation time, 21 ms, followed by pulses #1, 24 ms, and last #3, 25 ms. Although the activation times due to the three pulses are different, the velocity changes experienced by the sensor for the three pulses are the same.

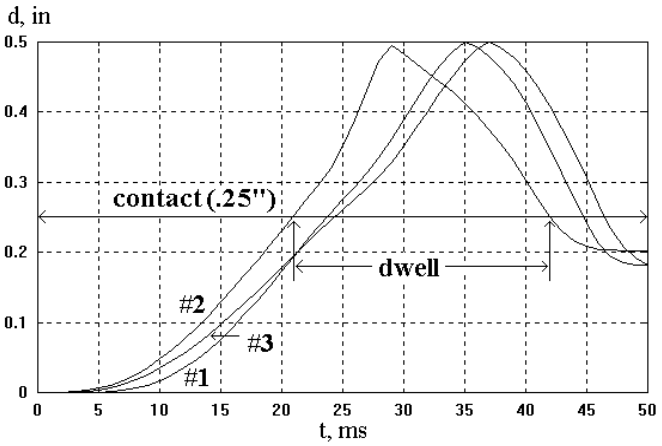

Fig. 2.78 Sensor Ball Displacements

Since the BIT crash sensor is highly damped, it is nearly a velocity-sensitive device. Therefore, the displacement (output) of the ball in the sensor is approximately proportional to the sensor velocity change (input). To compare the shape and curvature of the input velocity change and the output ball displacement, the displacement magnitude in the three tests is amplified by 40 times and overlapped with the velocity change. At the crash sensor calibration of 10 mph velocity change, the corresponding sensor displacement, d, is 0.25 inches (d×40 = 10) when the sensor is activated. From Fig. 2.79, the sensor activation times (the corresponding timings at Δv = 10 mph) for #1, #2, and #3 tests are about 24, 21, and 25 ms, respectively. This shows that a relationship exists between the velocity change (input) at the sensor location and the sensor ball displacement (output).

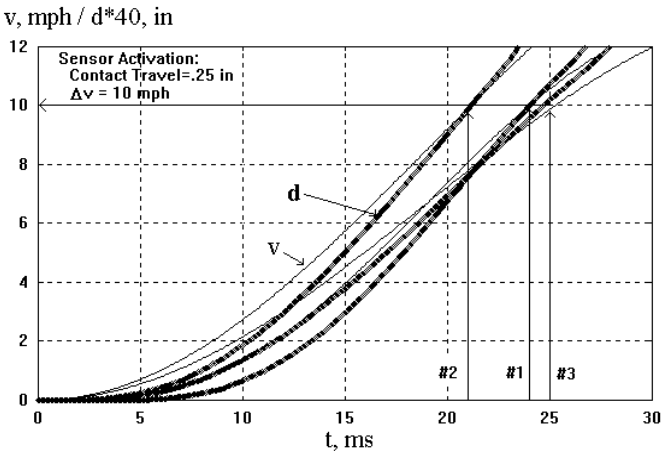

Fig. 2.79 Calibration of a 10 mph Crash Sensor

2.4.14.1 *Sensor Dynamic Equations*

To simulate the ball-in-tube (BIT) sensor dynamics, a simple spring-mass-damper model, shown in Fig. 2.80, is used. The equation of motion of the ball is developed in Eq.(2.47).

$$\uparrow \sum F = ma$$

$$-F_{mag} - c\dot{x} = m(\ddot{x}+\ddot{X}) \quad \ldots\ldots\ldots \quad (1)$$

$$\ddot{x} = -\left[\ddot{X} + \frac{F_{mag}}{m} + \frac{c}{m}\dot{x}\right] \quad \ldots\ldots\ldots \quad (2)$$

where

$\ddot{x}$: *acceleration of ball relative to the tube*

$\dot{x}$: *velocity of ball*

x: *displacement of ball*

$\ddot{X}$: (*input excitation*) *deceleration of the tube*

$\dot{X}$: *velocity of the tube*

m: *mass of the ball*

F_{mag}: *magnetic force acting on the ball*

F_o: *magnetic force at* $x=0$

$F_{mag} = F_o + kx$

k: *slope of magnetic force vs.* x (k, *a negative quantity*)

c: *damping coefficient*

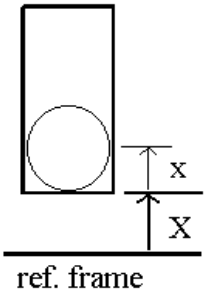

Fig. 2.80 A Sensor Model

(2.47)

2.4.14.2 *Gas-Damped Sensor Mathematical Relationship*

In a gas-damped crash sensor, the damping force acting on the sensing element during the crash dominates the overall force. This is because the bias force due to the magnet is insignificant compared to the damping force. Therefore the term due to the magnetic force, F_{mag}, in (2) of Eq. (2.47) can be eliminated, and the simplified equation is shown in (3) of Eq.(2.48).

To see the effect of input excitation on the maximum ball travel in the tube, the ball relative velocity in (4) of Eq. (2.48) is set to zero. (5) of Eq. (2.48) shows that the maximum ball travel of a gas-damped sensor is proportional to the input velocity change at the tube. This analytical observation has been made by Chan [5].

$$\ddot{x} = -[\ddot{X} + \frac{c}{m}\dot{x}] \quad \ldots\ldots\ldots\ldots \quad (3)$$

Integrating, this becomes

$$\dot{x} = -[\dot{X} + \frac{c}{m}x] \quad \ldots\ldots\ldots\ldots \quad (4)$$

Set $\dot{x}$ *to zero to get maximum ball travel.*

Then $\quad 0 = -[\dot{X} + \frac{c}{m}x_{max}]$

therefore $\quad x_{max} = -\frac{m}{c}\dot{X} \quad \ldots\ldots\ldots \quad (5)$

(2.48)

2.4.15 Head Injury Criteria

The two principal criteria for head injury are the Severity Index (SI) and the head injury criterion (HIC). The definitions of both SI and HIC are shown in Eq. (2.49).

$$SI = \int_0^T a^{2.5}\,dt = c, \quad HIC = \max\left[\frac{1}{t_2-t_1}\int_{t_1}^{t_2} a\,dt\right]^{2.5}(t_2 - t_1) \quad (2.49)$$

The weighting factor of 2.5 is the power, n, in each equation , where a is the effective acceleration in g's, and t is the duration in milliseconds. Eiband [6] and Gadd [7] proposed a value of c = 1000 in which the human tolerance data are fitted by the equation. The fitted curve is referred to as the

Wayne State Tolerance Curve. Versace [8] examined and published the detailed relationship between the Wayne State Curve and the Severity Index. NHTSA, in response to Versace's review, proposed a new response variable, named HIC, which has become part of the occupant crash protection requirements for frontal barrier crash tests.

The HIC, specified in the FMVSS 208 (Federal Motor Vehicle Safety Standard), states that the resultant acceleration at the center of gravity of the head of a 50th percentile male dummy must be such that the value of the HIC does not exceed 1000, where "a" is the resultant acceleration expressed in g's (the acceleration of gravity), and t_1 and t_2 are any two points in time (milliseconds) during the crash separated by not more than a 36 ms interval.

Note that both t_1 and t_2 are two independent scanning times and there exists a pair of t_1 and t_2 such that the HIC is maximized. Given a pair of t_1 and t_2, the integral of the deceleration in Eq. (2.49) yields the velocity change of the crash pulse in that duration. Furthermore, dividing the velocity change by the duration ($T = t_2 - t_1$) yields an average deceleration (A) in the duration, T. This average deceleration is then raised to the power of 2.5 and multiplied by the duration to produce a HIC value. By advancing t_2 while fixing t_1 (where $t_2 > t_1$) and computing another HIC, a set of t_1 and t_2 with maximum HIC can then be found. It has been shown by Chou and Nyquist [9] that for the maximum HIC the deceleration values at the corresponding t_1 and t_2 are exactly equal.

Therefore, Eq.(2.49) can be rewritten as a matter of convenience as follows.

$$1000 = A^{2.5}\, T \tag{2.50}$$

Eq. (2.50) is the injury threshold line shown in Fig. 2.81, the log-log plot of average acceleration (A) versus duration ($T = t_2 - t_1$). This injury threshold is the linear regression line based on the test data of human and animal tolerance under rapid acceleration conditions. According to Eiband [6], the potential of getting a severe head injury is high if the test condition in terms of A and T is above this threshold line. Similarly, the potential of getting no injury or a moderate head injury is high if the test condition in terms of A and T is below this threshold line.

HIC formula would change if different tolerance test data result in different regression lines such as #1 and #3 in Fig. 2.81. If the #1 regression line is used as a head injury criterion, the HIC limit would become 3780 instead of 1000 and the exponent would be 2.9 instead of 2.5.

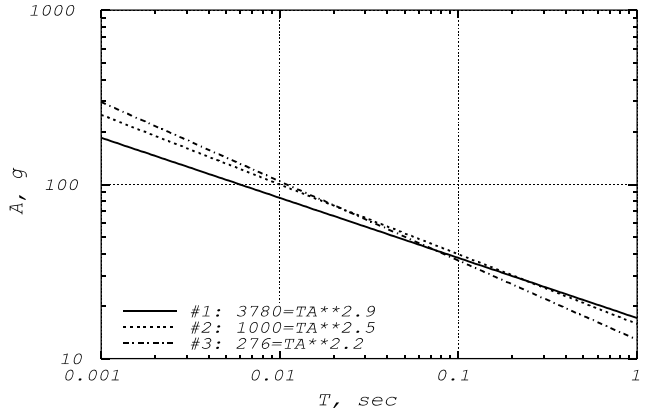

Fig. 2.81 HIC Formula for Three Tolerance Regression Lines

Given an exponent n and a corresponding HIC expression, as shown in (1) of Eq. (2.51), the HIC value for a sinusoidal head acceleration can then be computed by the closed formula shown in (2) of Eq. (2.51). As an example, for n = 2.5, formula (2) becomes HIC = 0.4146 $A_p^{2.5}$ T for a sinusoidal pulse, where A_p is the peak magnitude of the halfsine deceleration and T is the halfsine duration.

$$For \quad HIC = \left[\frac{1}{t_2 - t_1}\int_{t_1}^{t_2} a\,dt\right]^n (t_2 - t_1) \quad \ldots \quad (1)$$

$$HIC = \frac{2(\sin\mu)^n}{\pi\,\mu^{n-1}} T A_p{}^n \quad \ldots \quad (2)$$

$$\bar{t}_1 = T\left(\frac{1}{2} - \frac{\mu}{\pi}\right) \quad \ldots \quad (3)$$

$$\bar{t}_2 = T - \bar{t}_1 \quad \ldots \quad (4) \qquad (2.51)$$

$$where \quad \mu = \frac{n-1}{n}\tan\mu \quad \ldots \quad (5)$$

Newton–Raphson method is used to solve for μ *in* (5)*, a recursive equation. The solution of* μ *for a given n is shown below*:

For $n = 2.5$, $\mu = 1.0527943$ *radians*
For $n = 2.9$, $\mu = 0.9828248$
For $n = 3.2$, $\mu = 0.9386134$

For simple pulses such as harmonic, triangular, and square pulses, the HIC can be computed by a closed-form formula without using a numerical searching technique [9]. The closed-form HIC formulas and the integrals for four simple pulses are shown in Table 2.9.

Table 2.9 Closed-Form HIC Formulas and Integrals of Four Simple Pulses[9]

	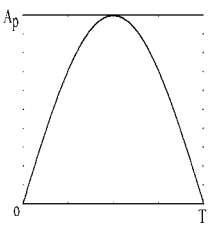 **Fig. 2.82** Halfsine	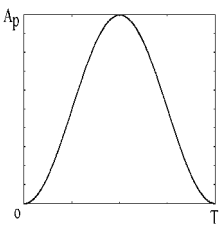 **Fig. 2.83** Haversine	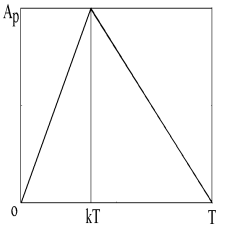 **Fig. 2.84** Triangle	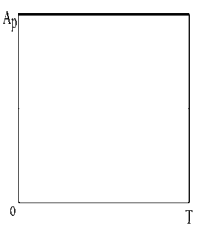 **Fig. 2.85** Square
a, g	$A_p Sin\left(\frac{\pi}{T}t\right)$	$\frac{A_p}{2}\left[1-\cos\left(\frac{2\pi}{T}t\right)\right]$	$\frac{A_p}{kT}t, \quad 0<t<kT$ $\frac{A_p(T-1)}{T(1-k)}, \quad kT<t<T$	A_p
ΔV, mph	$13.98 A_p T$	$10.98 A_p T$	$10.98 A_p T$	$21.95 A_p T$
Δd, in.	$122.9 A_p T^2$	$101.5 A_p T^2$	$64.37 A_p T^2(1+k)$	$193.2 A_p T^2$
t_1, sec	$0.1651 T$	$0.25 T$	$\frac{3}{7}kT$	0
t_2, sec	$0.8349 T$	$0.75 T$	$\frac{4+3k}{7}T$	T
HIC	$0.4146 A_p^{2.5} T$	$0.303 A_p^{2.5} T$	$0.2464 A_p^{2.5} T$	$A_p^{2.5} T$

2.4.15.1 *HIC Topographs*

(A) HIC Topograph of a Square Pulse

Given a pair of scan timings at t_1 and t_2, a HIC value can be computed. If the deceleration versus time data are plotted on each of the two timing axes, then a 3-D HIC surface (topograph), including the point of the maximum HIC (with a symbol of triangle), can then be displayed. Fig. 2.86 shows the topograph of a square crash pulse. The deceleration magnitude of the crash pulse, a, has been multiplied by a factor of 10 in order to use the same scale as the HIC. Therefore, the vertical axis with the caption of "HIC/a×10" represents both the HIC and head deceleration values. Since in scanning for the maximum HIC, t_2 is always greater than t_1, this relationship results in a flat surface with zero HIC in the horizontal triangular base where t_2 is less than or equal to t_1. The maximum HIC occurs at the corner point (t_1 = 0 ms and t_2 = 36 ms) of the inclined triangular surface where the gradient is constant. Therefore, the change in HIC with respect to the change in time is also constant.

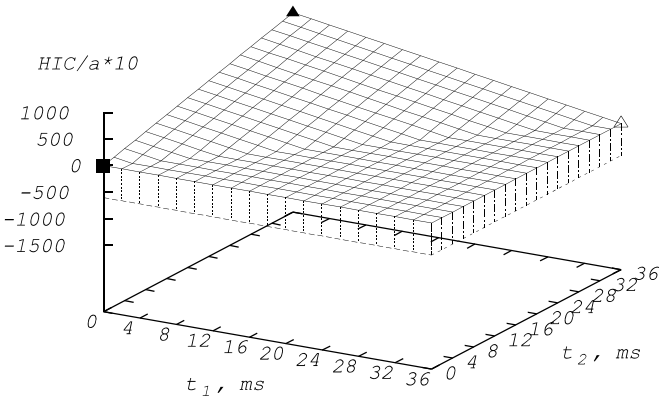

Fig. 2.86 HIC Topograph of a Square Pulse

(B) HIC Topographs of Other Simple and Test Pulses

Figs. 2.87–2.89 display the topographs of triangular, halfsine, and haversine pulses.

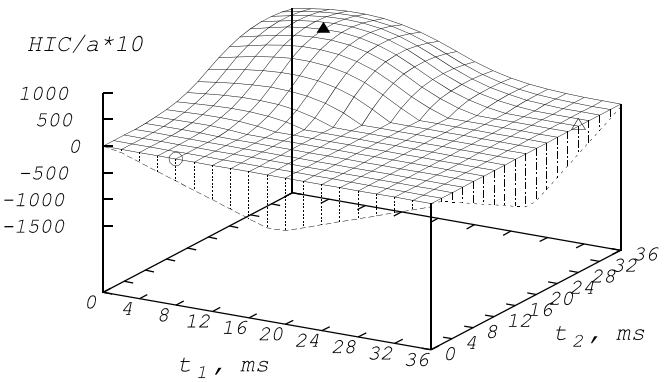

Fig. 2.87 HIC Topograph of a Triangular Pulse

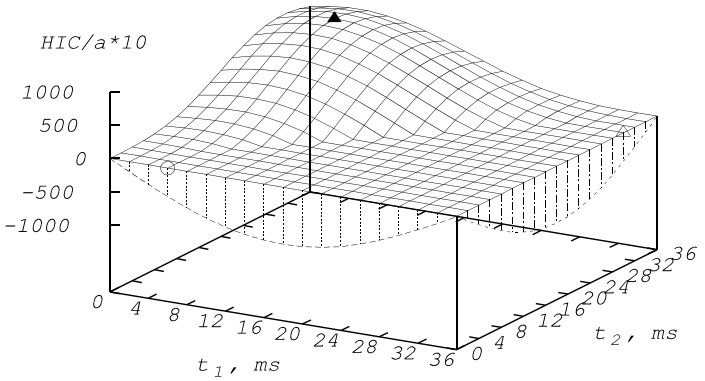

Fig. 2.88 HIC Topograph of a Halfsine Pulse

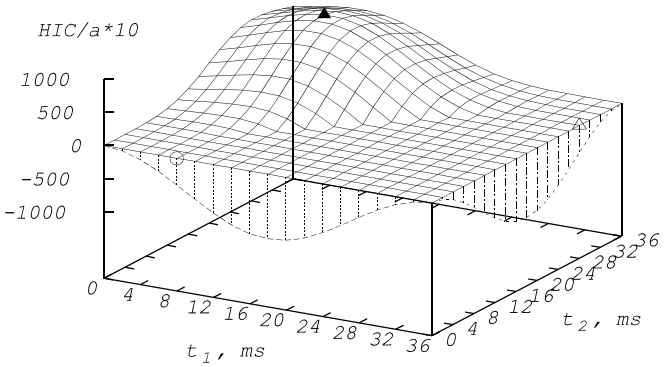

Fig. 2.89 HIC Topograph of a Haversine Pulse

The maximum HIC for these pulses occurs at the peak of a dome surface marked with a triangular point symbol. Although the HIC surface around the peak is relatively flat, the gradients at the maximum HIC are slightly negative in both t_1 and t_2 directions. Therefore, as $(t_2 - t_1)$ expands or contracts, the HIC would decrease.

The head deceleration of a driver in a pick-up truck tested in a 35 mph fixed barrier condition is shown in Fig. 2.90.

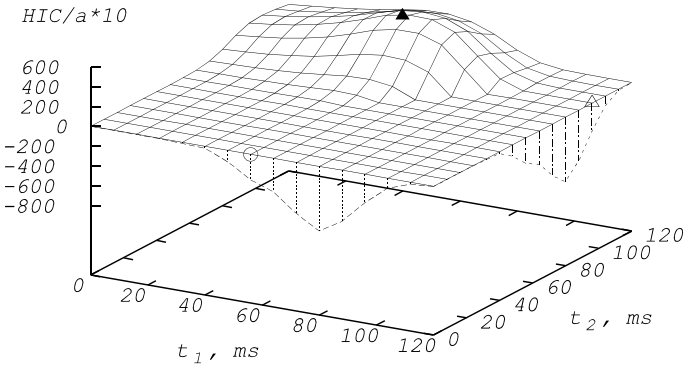

Fig. 2.90 HIC Topograph of a R/F Dummy in a Truck 35 mph Barrier Test

The duration of the head deceleration is 110 ms and the peak deceleration is -66 g (shown in the figure as $-66\times10=-660$) at 77 ms. The maximum HIC from the numerical computation is 595. This occurred between t_1 = 56 ms (with a circle mark) and t_2 = 96 ms (with a triangle mark) where the duration is $t_2 - t_1$ = 40 ms. The gradient around the maximum HIC is relatively small in both t_1 and t_2 directions.

According to government regulations covering occupant protection, if the duration $(t_2 - t_1)$ of the maximum HIC is more than 36 ms, then the HIC needs to be re-computed using a duration of 36 ms. To estimate such a HIC, t_1 is increased from 56 to 58 ms, and t_2 is decreased from 96 to 94 ms so $t_2 - t_1$ becomes 36 ms. The new HIC value can be estimated from the topograph if the HIC resolution is decent. Otherwise, the closed-form HIC formula can be used.

The head deceleration versus time curve can be approximated by a haversine pulse which is symmetrical about a vertical through the point of peak deceleration. It can be shown numerically that HIC is approximately proportional to Δt, the duration between t_1 and t_2. Since maximum Δt for a haversine pulse can not exceed half of the haversine duration (see Table 2.9) and A_p remains the same, the HIC is proportional to the time interval, $\Delta t = t_2 - t_1$, as shown in Eq. (2.52).

$$\begin{aligned} &\because \quad HIC \propto A_p^{2.5}\,\Delta t, \quad where \;\; \Delta t = t_2 - t_1 \\ &\therefore \quad HIC_{\Delta t=36} = HIC_{\Delta t=40}\,\frac{36\,ms}{40\,ms} = 595\times 0.9 = 535 \end{aligned} \tag{2.52}$$

Therefore, the estimated HIC with a duration of 36 ms is about 535.

2.4.16 Application of HIC Formula in Head Interior Impact

One of the useful applications of the closed-form HIC formulas for various simple pulses shown in the previous section is in head interior impact. This impact testing is required by FMVSS 201 (Federal Motor Vehicle Safety Standard) to meet the vehicle upper interior impact safety requirement. The regulation requires that the HIC value should be 1000 or less in a test where a headform of 10 lbs impacts on various vehicle interior surfaces at a speed of 15 mph. The crush space requirement of a padded material in the impact location therefore can be estimated by the use of the HIC formula [10,11]. A process to normalize the head impact test data to 24 km/h provides a fair comparison among tests and a process to assess a structure/foam padding system performance has been undertaken by Lim, Chou, Wu, and Zhao [12].

Assuming the material stack-up in the headform impact is negligible, the maximum crush of the material (dynamic crush) in the test is then identical to the available crush space. The closed-form HIC expressions in terms of acceleration magnitude and duration are shown in Table 2.9. Eq. (2.53) shows the HIC as a function of the velocity change (impact velocity) and the displacement change (dynamic crush) for the four simple pulses such as square, halfsine, triangle, and haversine pulses.

$HIC = \alpha\,\Delta V^4 / S^{1.5}$:	*Square*	*Halfsine*	*Triangle*(k=0.5)	*Haversine*
α:	0.0116	0.0148	0.0160	0.0213

(2.53)

Note that for an impact where the crash pulse is symmetrical and the impact velocity is the same as the entire area of the crash pulse (the velocity change), the impact is perfectly inelastic, i.e., the coefficient of restitution is equal to zero. It will be shown in Chapter 4 that the dynamic crush (maximum crush, the double integral of the crash pulse with an initial impact velocity) is the same as the displacement change (maximum displacement, the double integral of the crash pulse with zero impact velocity).

The kinematic formula for the symmetrical crash pulses shown in Table 2.9 can therefore be directly used to compute the impact responses and the HIC values.

Fig. 2.91 shows the HIC as a function of other response variables such as dynamic crush, for a given impact velocity of 15 mph. The minimum crush space requirement which would produce a specified HIC value of 1000 can then be obtained from the curves in the figure.

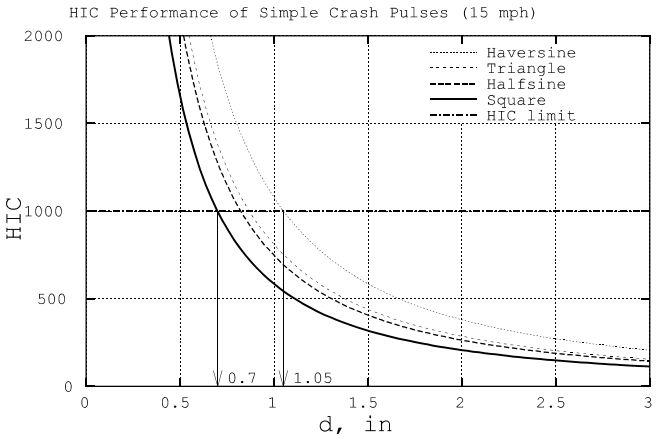

Fig. 2.91 Relationship between HIC, Impact Velocity, and Crush Space

To obtain a HIC limit of 1000, the minimum crush space or the thickness of a padded material which yields a haversine pulse in the head form impact is 1.05 inches (27 mm); while for a square pulse, it is only 0.7 in (18 mm). The material which produces the square pulse on the headform is therefore considered to be the most efficient and that for the haversine pulse is the least efficient. The HIC performances due to the halfsine and triangular pulses are inbetween those of the square and haversine pulses.

2.5 REFERENCES

1 Ludstrom, L.C., "The Safety Factor in Automotive Design," pp.511–516, Highway Vehicle Safety (Collected SAE Papers, 1961–1967), Society of Automotive Engineers.

2. Huang, M., Lawson, G.P., Powell, B.K., and Walker, J.H., "Characterization of Vehicle Deceleration Time Histories in the Analysis of Impact Dynamics," SAE 770013, 1977, SAE International Automotive Engineering Congress and Exposition, February 28 – March 4, Detroit, Michigan.
3. Huang, M., "Dynamics and Animation of an Air Bag Ball-in-Tube Sensor System," AMD-Vol.106, BED-Vol.13, ASME Winter Annual Meeting, San Francisco, California, December 10–15, 1989.
4. Huang, M., Cuddihy, M., and Drummond, J.B., "Effects of Vehicle Impact Mode and Speed on Air Bag Single Point Sensing Requirements," ASME Winter Annual Meeting, New Orleans, LA, Nov. 28 – Dec. 3, 1993.
5. Chan,C.Y., " Fundamentals of Crash Sensing in Automotive Air Bag Systems," SAE 2000.
6. Eiband, A. M., "Human Tolerance to Rapidly Applied Accelerations: A Summary of the Literature," NASA Memo 5-19-59E, June, 1959.
7. Gadd, C.W., "Use of a Weighted-Impulse Criterion for Estimating Injury Hazard," SAE Paper No. 660793, Tenth Stapp Car Crash Conference Proceeding.
8. Versace, J., "A Review of the Severity Index," SAE Paper No.710881, Fifteenth Stapp Car Crash Conference Proceeding.

9. Chou, C. C. and Nyquist, G. W., "Analytical Studies of the Head Injury Criterion (HIC)," SAE Paper 740082, Detroit, MI, February 25 – March 1, 1974.
10. Wooley, R.L. et al., "Graphical Solution of Reconstruction Equation," 27th AAAM (American Association for Automotive Medicine, San Antonio, Texas, October 3–6, 1983.
11. Naick, P.A. and Cranago, K.M., "Theoretical Relationship of HIC(d) to Crush Space for FMVSS 201 Head Impact Tests, and the Effective Use of FEA in Predicting HIC for Design, Verification and Optimization of Countermeasures," IBEC (International Body Engineering Conference) 1998 Proceedings, Vol. 6, pp.97–105.
12. Lim, G., Chou, C., Wu, F. and Zhao, Y., "Normalization of Head Impact Data to 24 km/h," SAE Paper 970389, International Congress and Exposition, Detroit, Michigan, February 24–27, 1997.

CHAPTER 3

CRASH PULSE PREDICTION BY CONVOLUTION METHODS

3.1 INTRODUCTION

A crash pulse is the time history of the response of a vehicle system subjected to an impact or excitation. The dynamic characteristics of the system can be described by using a "hardware" or a "software" model. A "hardware" model is a system consisting of masses interconnected by energy absorbers (springs and dampers). This will be presented in Chapters 4 and 5. The present chapter covers the use of a "software" model utilizing digital convolution theory for crash pulse prediction. In a study by Eppinger and Chan [1], the concept of a finite impulse response (FIR) model based on convolution theory is used to assess thoracic injury in a side impact. Using accelerometer data from both the impacting side (rib cage) and the non-impacting side (spine) of a thorax, the torso dynamic system is characterized by a set of FIR coefficients, i.e., a transfer function. Then, under a different impact condition, the torso response in the non-impacting side can then be predicted by convoluting the FIR coefficients with the accelerometer data for the impacting side of the thorax.

The basic operation of convolution theory, the derivation of the transfer function, and an algorithm using a snow-ball effect to increase the computation efficiency are discussed. Cases are presented which include but are not limited to the (1) Use of transfer functions in assessing the occupant response prediction using various crash pulse approximations, (2) Characterization of truck body mounts by FIR coefficients and the prediction of body pulses with different frame pulses, (3) Evaluation of the performance of air bag and steering column restraint systems for both unbelted and belted occupant responses, and (4) Assessment of sled test pulses and the prediction of its occupant crash severity in a barrier test condition.

In body-on-frame vehicles, two types of body mounts, using man-made or natural rubbers, are evaluated for their transient transmissibility (TT), the ability of the body mount to transfer the frame impulse to the body. Two trucks with different body mounts and restraint systems were tested in high speed barrier crashes. The dynamic properties of two body mounts are characterized by transfer functions. Similarly, two restraint systems are characterized by their respective transfer functions. The occupant response in a high speed barrier crash of one truck using the interchanged body mount and restraint system from the other can then be predicted and the performance assessed.

Using a Kelvin model, in which the spring and damper are connected in parallel, a digital convolution formula can be derived using the Laplace transform. The closed-form formulas in terms of two model parameters, K (spring stiffness) and C (damping coefficient), describe the transfer function. The dynamic properties of the components, such as air bag and body mount systems, can then be compared for crashworthiness evaluation. Other applications of FIR transfer functions including the development of RIF (response inverse filtering) are discussed.

RIF is based on finite impulse response (FIR) and inverse filtering (IF) methods. The accuracy in validation and prediction via FIR transfer functions depends on the frequency content of the input and output accelerometer data from which the transfer function is developed. The prediction accuracy is low if the output data contain higher frequency components than the input. Taking advantage of these forward prediction properties of FIR , the method of inverse filtering is thus utilized to develop the RIF for the backward prediction.

The new RIF transfer function is created by the IF operation applied to the FIR transfer function. The IF technique involves four sequential matrix operations applied to the column matrix of the FIR coefficients. These matrix operations include transpose, multiplication, inverse, and multiplication. The accuracy of RIF in predicting the high frequency output (such as frame impulse) with the low frequency input (such as body excitation) has been shown to be high. One of the applications in predicting the truck frame pulse based on an optimized or desired body pulse is illustrated.

3.2 TRANSFER FUNCTION VIA CONVOLUTION INTEGRAL

A dynamic system can be characterized by its ability to convert a set of discrete-time data (input) into another sequence (output). Such a conversion process shown in the S domain (Laplace transformation) and time domain (convolution integral) in Fig. 3.1 is defined as a transfer function.

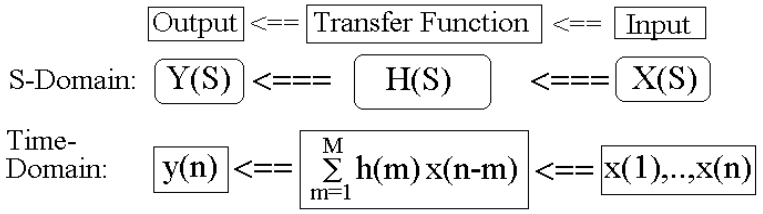

Fig. 3.1 A Transfer Function – A Convolution Process

A system with an input variable x and an output variable y is linear if the following conditions are satisfied.

Condition 1:	output: ay	<===	input: ax
Condition 2:	output: by	<===	input: bx
Condition 3:	output: (a+b)y	<===	input: (a+b)x

A system can consist of multiple subsystems. In a frontal barrier test, the front end of a vehicle can be modeled as two subsystems, as shown in Fig. 3.2 . These are subsystem #1: frame rails (m_1) and body rocker panels (m_2), connected by body mounts (k and c), and subsystem #2: upper front end structure (m′) connected to the body (m_2), through the dash panels (k′ and c′).

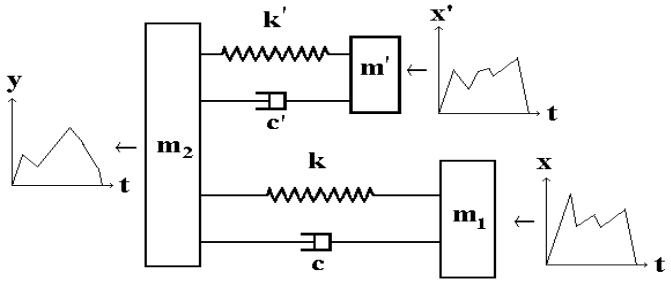

Fig. 3.2 A Dynamic System with Multiple Transfer Functions

Relative to the body (m_2) response, the two subsystems (m′ and m_1) are parallel. In frontal impact occupant kinematics analysis, multiple subsystems also exist. Subsystem #1 may represent the belt and air bag restraint system (and the steering column for the driver side), and subsystem #2 may represent the knee bolster, as shown in Table 3.1.

Table 3.1 A System with Multiple Transfer Functions [TF]

System	[TF]′: k′ and c′	[TF]: k and c
Vehicle Front Structure	Upper Front End	Body Mount
Occupant Restraint System	Belt and Air Bag Restraint System	Knee Bolster

Awareness of the existence of multiple transfer functions is essential in the analysis and computation of the finite impulse response coefficients of a specific system. The relationship between the transfer functions and the overall input and output data is described by Eq. (3.1).

$$y = [TF]'x' + [TF]x \tag{3.1}$$

To define a transfer function, the load paths need to be identified. As an example, to accurately compute the body mount transfer function, the input frame (m_1) and output body (m_2) data associated with the load path through the body mount should be processed first before the upper structure starts affecting the body response. This is because, in a vehicle frontal impact, the bumper comes in contact with the barrier followed by the deformation of the front rail. Subsequently, the upper structure, such as the shotgun and fender, may start interacting with the barrier. The upper front end structure thus provides a separate load path to the occupant compartment (body).

The loadings acting on the upper and lower structures can be obtained from the crash test data, such as the accelerometer data or the barrier load cell data. In computing the FIR coefficients of a component such as the body mounts on a frame vehicle, the accelerometer data of the frame and body in the first 20 ms after impact should be utilized. This is due to the fact that after 20 ms, the upper structure contributes a portion of the deceleration to the body.

3.2.1 Convolution Method and Applications

The response of a linear system to a time varying input can be defined by the convolution integral shown in Eq. (3.2).

$$y(t) = \int_{-\infty}^{t} h(t-\tau)x(\tau)d\tau$$

where $y(t)$: *the output response at time* t,
$x(\tau)$: *the input excitation at time* τ, *and*
$h(t)$: *response at time* t *to an unit impulse at* $t=0$ (3.2)

Similarly to the analytical simulation using the spring-damper-mass model described in Chapters 4 and 5, a model is also linear if the spring and damper forcing functions have linear relationships with the deformation and deformation rates, respectively. A linear system can be described by a set of finite impulse response (FIR) coefficients obtained by digital convolution theory. The relationships between the FIR coefficients and the two model parameters, spring stiffness (or natural frequency) and damping coefficient (or damping factor), are described in the following sections.

The FIR coefficients are useful in describing the dynamic characteristics of a system and in predicting the system response under a different input condition. As an example, in a frontal barrier crash, the chest deceleration and vehicle deceleration can be processed to obtain the set of FIR coefficients which describes the dynamic characteristics of the restraint system. The set of FIR coefficients is therefore the transfer function between the vehicle and occupant systems and represents the dynamic characteristics of the restraint system. The transfer function can then be used to predict occupant responses in a vehicle with a new or modified vehicle structures.

In describing the body mount dynamic behavior in light truck barrier crashes, the transfer function of the body mount between the frame and the body (or cab) can be obtained from the accelerometer data at the frame and body of the truck. Consequently, the body response can be predicted once given a set of new frame accelerometer data.

The method using input and output discrete data points to obtain the FIR coefficients is described in the following. Since the computation of the FIR coefficients is numerically intensive, an efficient algorithm based on matrix symmetry and a technique called the "snow-ball effect" are presented. The variables for the input, the actual and predicted outputs, and the FIR coefficients are defined as follows:

$\hat{y}(n)$: predicted output at point n
y(n): actual output at point n
x(n−m): system input at a discrete point n−m
h(m): FIR coefficient at point m
M: total number of FIR coefficients
n: a discrete point index
N: total number of discrete

Given a set of FIR coefficients, the predicted output is then expressed by the digital convolution formula shown in Eq. (3.3):

$$\hat{y}(n) = \sum_{m=1}^{M} h(m)\, x(n-m) \tag{3.3}$$

Fig. 3.3 shows the convolution process where a set of M FIR coefficients overlaps the same number of input discrete data points.

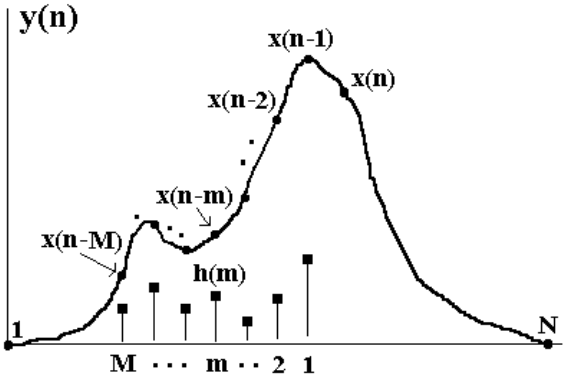

Fig. 3.3 Input Discrete Data Points and FIR Coefficients

The FIR coefficients are numbered from 1 to M in reverse order compared to the input discrete data points, which are numbered from (n-m) to (n-1), with a total of M discrete points. Taking the sums of each pair of the input data and FIR coefficient yields a predicted output, $\hat{y}(n)$, at point n, where the corresponding input data is x(n).

At the beginning and the end of computation, where the number of overlapping data points is less than the number of FIR coefficients, the values of those input data points outside the range from 1 to N are assigned a value of zero.

3.2.2 Solution by the Least Square Error Method

Using the least square error method shown in Eq. (3.4), the steps needed to create a set of finite impulse response (FIR) coefficients are presented below. The set of the FIR coefficients, h(m), for the given input and output pulses can then be solved from a set of simultaneous linear equations shown in (3) of Eq. (3.5).

$$\begin{aligned}
&\textit{Let the predicted response be } \hat{y}(n) = \sum_{m=1}^{M} h(m)\, x(n-m), \textit{ and} \\
&\textit{e be the error between the actual and predicted responses,} \\
&\textit{then } e = y(n) - \hat{y}(n), \textit{ and the sum of the error squared is} \\
&\sum_{n=1}^{N} e^2 = \sum_{n=1}^{N} y^2(n) - 2\sum_{n=1}^{N} y(n) \sum_{m=1}^{M} h(m)\, x(n-m) + \sum_{n=1}^{N} \left[\sum_{m=1}^{M} h(m)\, x(n-m) \right]^2 \\
&\textit{To minimize } e^2\textit{, set a sensitivity coefficient to zero.}
\end{aligned} \tag{3.4}$$

$$\text{Letting} \quad \frac{\partial \sum_{n=1}^{N} e^2}{\partial h(m)} = 0, \text{ the sum becomes}$$

$$-2\sum_{n=1}^{N} y(n)\,x(n-m) + 2\sum_{n=1}^{N}\left[\sum_{m=1}^{M} h(m)\,x(n-m)\right]x(n-m) = 0$$

After rearrangement, one gets

$$\sum_{n=1}^{N}\left[\sum_{m=1}^{M} h(m)\,x(n-m)\right]x(n-m) = \sum_{n=1}^{N} y(n)\,x(n-m) \quad or: \tag{3.5}$$

$$[A_{ij}]^{MxM}\,[h_i]^{Mx1} = [B_i]^{Mx1}$$

where matrices $[h]$ and $[B]$ are column matrices

$$A_{ij} = \sum_{n=1}^{N} x(n-i)\,x(n-j) \qquad \ldots\ldots\ldots\ldots \quad (1)$$

$$B_i = \sum_{n=1}^{N} y(n)\,x(n-i) \qquad \ldots\ldots\ldots\ldots\ldots \quad (2)$$

$$\text{Then} \qquad [h_i] = [A_{ij}]^{-1}[B_i] \qquad \ldots\ldots\ldots\ldots\ldots \quad (3)$$

A_{ij} is an auto-correlation matrix, which provides a comparison of a signal (x) with itself as a function of time shift, while B_i is a cross-correlation matrix, which provides a comparison of two signals (x and y) as a function of time shift.

The time needed to compute the matrix elements of A_{ij} and B_i can be extremely long if a straight forward (with repetitive computation of each of the matrix elements) method is used. However, an efficient method based on the symmetry of the matrix and a "snow-ball technique" have been devised. The method has been tested and is about 25 times faster than the repetitive computation approach. The snow-ball method is described in the following section.

3.2.3 Matrix Properties and Snow-Ball Effect

The two sets of matrices derived from the least square error method possess certain repetitive properties which may be computation-intensive. In Eq. (3.6), the properties related to the numerical operation are described, and the snow-balling technique is utilized to perform the computation of the matrix elements. Subsequently, the solutions of the FIR coefficients can be solved efficiently on a computer.

Special Properties of Matrices A and B

Since the i^{th} FIR coefficient is $[h_i] = [A_{ij}]^{-1}[B_i]$,

where $A_{ij} = \sum_{n=1}^{N} x(n-i)\,x(n-j)$ and $B_i = \sum_{n=1}^{N} y(n)\,x(n-i)$;

for $(n-i) \geq 1$ and $(n-j) \geq 1$ and

Due to the symmetry of the matrix A_{ij},

replace the start index $n=1$ by $n=k$,

where k is the larger of i and j. Then: (3.6)

$$A_{ij} = \sum_{n=k}^{N} x(n-i+1)\,x(n-j+1) \quad and \quad B_i = \sum_{n=k}^{N} y(n)\,x(n-i+1)$$

Example: $N = 9$, $M = 5$, and $i = 5$, $j = 5$; then $k = 5$

$$\therefore \quad A_{55} = \sum_{n=5}^{9} x(n-5+1)\,x(n-5+1)$$

$$= x(1)\,x(1) + x(2)\,x(2) + \ldots + x(5)\,x(5)$$

The composition of each of the elements in A_{ij} has been analyzed for the number sequence repetition. This repetition can be eliminated from the computation to shorten computation time. The technique used to eliminate this repetitiveness, as shown in Eq. (3.7), uses the snow-ball effect. The process begins by computing the elements of the last column (j = m) in matrix A; then, the snow-balling starts from the elements in the last column and generates the rest of the elements in the upper half of the matrix. Due to the symmetry of matrix [A], the lower half of the matrix is simply: $A_{ji} = A_{ij}$. The snow-ball and straightforward techniques have been tested on a personal computer, and the computation time difference was determined. Given N (number of data points) = 250 and M (number of FIR coefficients) = 150, the snow-ball technique was found to be 25 times faster than the straight-forward method on the same computer.

Matrix Element Computation Methods

1) *Straightforward method*:

$$A_{ij} = \sum_{n=1}^{N} x(n-i)\,x(n-j), \quad \text{for} \quad i=1, \quad j=5, \quad N = 9; \quad \text{then}$$

$$A_{15} = x(0)x(-4)+x(1)x(-3)+x(2)x(-2)+x(3)x(-1)+x(4)x(0)+ \\ +x(5)x(1) \;+x(6)x(2) \;+x(7)x(3) \;+x(8)x(4) \;+x(9)x(5), \qquad (3.7)$$

$$\text{where} \quad x(n-i) = 0 \quad \text{for} \quad n-i \le 0 \quad \text{and} \\ x(n-j) = 0 \quad \text{for} \quad n-j \le 0.$$

2) *Snow-ball technique*:
Using the previous example, where
N (no. of data points) = 9 and
M (no. of FIR coefficients) = 5
(*i*) *Snow-ball Seed generator*: *Matrix elements* A_{ij}, *where* $i=1,2,..,M$ *and* $j=M$.

$$A_{ij} = \sum_{n=k}^{N} x(n-i+1)\,x(n-j+1) \qquad (3.8)$$

i	j	k	N	
1	5	5	9	$A_{15} = x(5)x(1)+x(6)x(2)+...+x(9)x(5)$
2	5	5	9	$A_{25} = x(4)x(1)+x(5)x(2)+...+x(8)x(5)$
3	5	5	9	$A_{35} = x(3)x(1)+x(4)x(2)+...+x(7)x(5)$
4	5	5	9	$A_{45} = x(2)x(1)+x(3)x(2)+...+x(6)x(5)$
5	5	5	9	$A_{55} = x(1)x(1)+x(2)x(2)+...+x(5)x(5)$

Matrix Element Computation Methods (Continued)

As shown by the computation sequence from "Order" 1 to 2 in Eq. (3.9), the seed element A_{55}, generated in Eq. (3.8), is snow-balled into the computation of A_{44}. In the operation, only one multiplication of a pair of numbers is executed and the product is summed up with the seed to get A_{44}. Similarly, A_{44} is snow-balled into the computation of A_{33} as shown in "Order" 3. By repeating the same procedure for the other seeds, the upper half of the matrix is completed. Due to the symmetry of the matrix, the element computation for the lower half of the matrix is not required. A Fortran computer program based on the computation algorithm presented is listed in Table 3.2. It includes the snow-ball technique and a subroutine using a Gaussian method [2] to solve the set of simultaneous equations for the FIR coefficients.

ii) Snow-balling from the seed location, A_{i5}, $i=5, 4, 3, 2, 1$, up in diagonal direction in the matrix A_{ij}

$$[A_{ij}] = \begin{bmatrix} A_{11} & A_{12} & A_{13} & A_{14} & A_{15} \\ A_{21} & A_{22} & A_{23} & A_{24} & A_{25} \\ A_{31} & A_{32} & A_{33} & A_{34} & A_{35} \\ A_{41} & A_{42} & A_{43} & A_{44} & A_45 \\ A_{51} & A_{52} & A_{53} & A_{54} & A_{55} \end{bmatrix}$$

Order	*Matrix Elements*
5	$A_{11} = A_{22} + x(9)x(9)$
4	. . $A_{22} = A_{33} + x(8)x(8)$
3	. . . . . $A_{33} = A_{44} + x(7)x(7)$
2	. . . . . $A_{44} = A_{55} + x(6)x(6)$
1	. . . . . A_{55} (*seed*)
9	. . $A_{12} = A_{23} + x(9)x(8)$
8	. . . . . $A_{23} = A_{34} + x(8)x(7)$
7	. . . . . $A_{34} = A_{45} + x(7)x(6)$
6	. . . . . A_{45} (*seed*)
12	. . . . $A_{13} = A_{24} + x(9)x(7)$
11	. . . . . $A_{24} = A_{35} + x(8)x(6)$
10	. . . . . A_{35} (*seed*)
14	. . . . . $A_{14} = A_{25} + x(9)x(6)$
13	. . . . . A_{25} (*seed*)
15	. . . . . A_{15} (*seed*)

(3.9)

Table 3.2 Gaussian Routine for Determining Finite Impulse Response Coefficients (FIR)

```
c   main routine
    COMMON/SOL/a(151,152),h(151)
    dimension xy(251,2)
   write(*,"(' no. of pts (t=100ms)=',$)")
    read(*,*) n
    npb = n
    step = 100./float(npb-1)
   write(*,"(' step=',f9.3)") step
   pi = 3.1415926
   f = 10.   ! hz
   w = 2*pi*f    ! rad./sec,
    do i = 1, npb
    tms = (i-1)* step
    t = .001 * tms
    gin = -15                ! input data
   gout = gin*(1.-cos(w * t))   ! output haversine
     xy(i,1) = gin
     xy(i,2) = gout
   end do
 2 write(*,"(' # of fir coeff.(max=',i3,') =>',$)") n
   read(*,*) m
      if(m.gt.n) goto 2
c  prepare a(i,j) matrix with order of m x m
      do i = m,1,-1
       i1 = n-i+1
       j = m
       j1 = n-j+1
       a(i,j) = 0.
       aij = a(i,j)
c   generating Seed, aij
       do while (i1.gt.0 .and. j1.gt.0)
       a(i,j) = a(i,j) + xy(i1,1)*xy(j1,1)
       aij = a(i,j)
       i1 = i1 - 1
       j1 = j1 - 1
       end do
      end do
      do i = 2,m
       i1 = i-1
       j1 = m-1
c   snow-balling from Seed A_im
       do while (i1.gt.0)
```

```
      i2 = i1+1
      j2 = j1+1
      i3 = n-i1+1
      j3 = n-j1+1
      a(i1,j1) = a(i2,j2) + xy(i3,1)*xy(j3,1)
      i1 = i1-1
      j1 = j1-1
     end do
    end do
c  copy upper right hand elements to the lower c
left hand due to matrix symmetry
    do i = 2, m
     do j = 1, i-1
      a(i,j) = a(j,i)
     end do
    end do
c  prepare Bb(i) matrix with order of m x 1
c   store in  a(i,k),i=1,2,..,m;     k=m+1
      m1 = m+1
    do i = 1, m
     a(i,m1) = 0.
     do j = i, n
      l = j-i+1
      a(i,m1) = a(i,m1) + xy(j,2)*xy(l,1)
     end do
    end do
    call gauss(m)
c   Compute the predicted response, xy(n,1)
    do n = 2, npb+1        !  Fir prediction..
      n1 = n-1
      xy(n1,2) = 0.
      xyn=xy(n1,2)
     do j = 1, m
       nj = n-j
     if(nj .gt. 0) then
      xy(n1,2) = xy(n1,2) + h(j)*xy(nj,1)
      xyn = xy(n1,2)
     end if
    end do
   end do
   stop
   end
   subroutine gauss(n)
c  to solve for simultaneous equations [2]
   COMMON/SOL/a(151,152),h(151)
    m = n+1
    l = n-1
    do k = 1, l
     kk = k+1
     do i = kk,n
      qt = a(i,k)/a(k,k)
       do j = kk,m
        a(i,j) = a(i,j)-qt*a(k,j)
       end do
     end do
      do i = kk,n
       a(i,k) = 0.
      end do
    end do
    h(n) = a(n,m)/a(n,n)
     do nn = 1, l
      sum = 0.
      i = n-nn
      ii = i+1
       do j = ii,n
        sum = sum+a(i,j)*h(j)
       end do
      h(i) = (a(i,m)-sum)/a(i,i)
     end do
    return
    end
```

3.2.4 Case Studies: Computing Transfer Functions

The procedures described above are applied to an example where the transfer function converts an input of square wave into an output of haversine pulse. The data sets for the input (x) and output (y) decelerations versus time (t) are shown in Table 3.3. Shown in Fig. 3.4, the input is a constant deceleration of -15 g and the output is a haversine wave with a duration of 100 ms and a peak magnitude of -30 g. The total number of data points, N, is nine. The number of FIR coefficients, M, is set to either five or nine.

Table 3.3 Input and Output Data Sets and Generation of Matrices A_{ij} and B_{ij}

i	1	2	3	4	5	6	7	8	9
t, ms	0	12.5	25	37.5	50	62.5	75	87.5	100
X(i), g	-15	-15	-15	-15	-15	-15	-15	-15	-15
Y(i), g	0	-4.39	-15	-25.61	-30	-25.61	-15	-4.39	0

For M (number of FIR coefficients) = 5

Generation of Matrix Elements, A_{ij}:

(i) Generating Seeds:

A_{55} = X(5)*X(5)+X(4)*X(4)+X(3)*X(3)+X(2)*X(2)+X(1)*X(1) = 1125.0
A_{45} = X(6)*X(5)+X(5)*X(4)+X(4)*X(3)+X(3)*X(2)+X(2)*X(1) = 1125.0
A_{35} = X(7)*X(5)+X(6)*X(4)+X(5)*X(3)+X(4)*X(2)+X(3)*X(1) = 1125.0
A_{25} = X(8)*X(5)+X(7)*X(4)+X(6)*X(3)+X(5)*X(2)+X(4)*X(1) = 1125.0
A_{15} = X(9)*X(5)+X(8)*X(4)+X(7)*X(3)+X(6)*X(2)+X(5)*X(1) = 1125.0

(ii) Snow-balling from Seeds:

$A_{14} = A_{25}$+X(9)*X(6) = 1125.0 + -15.0 * -15.0 = 1350.0
$A_{24} = A_{35}$+X(8)*X(6) = 1125.0 + -15.0 * -15.0 = 1350.0
$A_{13} = A_{24}$+X(9)*X(7) = 1350.0 + -15.0 * -15.0 = 1575.0
$A_{34} = A_{45}$+X(7)*X(6) = 1125.0 + -15.0 * -15.0 = 1350.0
$A_{23} = A_{34}$+X(8)*X(7) = 1350.0 + -15.0 * -15.0 = 1575.0
$A_{12} = A_{23}$+X(9)*X(8) = 1575.0 + -15.0 * -15.0 = 1800.0
$A_{44} = A_{55}$+X(6)*X(6) = 1125.0 + -15.0 * -15.0 = 1350.0
$A_{33} = A_{44}$+X(7)*X(7) = 1350.0 + -15.0 * -15.0 = 1575.0
$A_{22} = A_{33}$+X(8)*X(8) = 1575.0 + -15.0 * -15.0 = 1800.0
$A_{11} = A_{22}$+X(9)*X(9) = 1800.0 + -15.0 * -15.0 = 2025.0

Generation of Matrix Elements, B_i:

B_1 = y(1)*X(1)+y(2)*X(2)+. . .+y(9)*X(9) = 1800.0
B_2 = y(2)*X(1)+y(3)*X(2)+. . .+y(9)*X(8) = 1800.0
B_3 = y(3)*X(1)+y(4)*X(2)+. . .+y(9)*X(7) = 1734.1
B_4 = y(4)*X(1)+y(5)*X(2)+. . .+y(9)*X(6) = 1509.1
B_5 = y(5)*X(1)+y(6)*X(2)+. . .+y(9)*X(5) = 1125.0

M = 5: The computations of matrix elements, A_{ij} and B_i, the FIR coefficients, and the predicted output, $\hat{y}$, are shown in the Table 3.3 and Eq. (3.11). For the case where the number of FIR coefficients is five, the matrix elements of A_{ij} generated by the snow-balling approach are shown in Table 3.3, as are the matrix elements of B_i.

M = 9: For the case where the number of FIR coefficients is equal to nine, the matrix elements of A_{ij} and B_i are also shown in Eqs. (3.10) and (3.11). Comparing the two sets of matrices, for M = 5 and M = 9, it is noted that the set of matrix elements for the case of M = 5 is only a subset of the case where M = 9. The first 5 by 5 subset matrix in the 9 by 9 matrix A is the same as that matrix A for M = 5. The subset observation also applies to the B matrix elements.

FIR Coefficients and Predicted Output with M =5 and 9, and N = 9

$M(no.\ of\ FIR\ coefficients) = 5: \quad [A][h] = [B]$

$$\begin{bmatrix} 2025 & 1800 & 1575 & 1350 & 1125 \\ 1800 & 1800 & 1575 & 1350 & 1125 \\ 1575 & 1575 & 1575 & 1350 & 1125 \\ 1350 & 1350 & 1350 & 1350 & 1125 \\ 1125 & 1125 & 1125 & 1125 & 1125 \end{bmatrix} \begin{bmatrix} h(1) \\ h(2) \\ h(3) \\ h(4) \\ h(5) \end{bmatrix} = \begin{bmatrix} 1800.0 \\ 1800.0 \\ 1734.1 \\ 1509.1 \\ 1125.0 \end{bmatrix} \quad and \quad \begin{bmatrix} h(1) \\ h(2) \\ h(3) \\ h(4) \\ h(5) \end{bmatrix} = \begin{bmatrix} .0 \\ .293 \\ .707 \\ .707 \\ .707 \end{bmatrix}$$

Using FIR coefficients to compute the predicted output, $\hat{y}(i)$: (3.10)

$$\hat{y}(1) = h(1) * x(1) = 0$$
$$\hat{y}(2) = h(1) * x(2) + h(2) * x(1) = -4.393$$
$$\hat{y}(3) = h(1) * x(3) + h(2) * x(2) + h(3) * x(1) = -15.000$$
$$\hat{y}(4) = h(1) * x(4) + h(2) * x(3) + \ldots + h(4) * x(1) = -25.607$$
$$\hat{y}(5) = h(1) * x(5) + h(2) * x(4) + \ldots + h(5) * x(1) = -15.000$$
$$\hat{y}(6) = h(1) * x(6) + h(2) * x(5) + \ldots + h(5) * x(2) = -15.000$$
$$\hat{y}(7) = h(1) * x(7) + h(2) * x(6) + \ldots + h(5) * x(3) = -15.000$$
$$\hat{y}(8) = h(1) * x(8) + h(2) * x(7) + \ldots + h(5) * x(4) = -15.000$$
$$\hat{y}(9) = h(1) * x(9) + h(2) * x(8) + \ldots + h(5) * x(5) = -15.000$$

$M(no.\ of\ FIR\ coefficients) = 9: \quad [A][h] = [B]$

$$\begin{bmatrix} 2025 & 1800 & 1575 & 1350 & 1125 & 900 & 675 & 450 & 225 \\ 1800 & 1800 & 1575 & 1350 & 1125 & 900 & 675 & 450 & 225 \\ 1575 & 1575 & 1575 & 1350 & 1125 & 900 & 675 & 450 & 225 \\ 1350 & 1350 & 1350 & 1350 & 1125 & 900 & 675 & 450 & 225 \\ 1125 & 1125 & 1125 & 1125 & 1125 & 900 & 675 & 450 & 225 \\ 900 & 900 & 900 & 900 & 900 & 900 & 675 & 450 & 225 \\ 675 & 675 & 675 & 675 & 675 & 675 & 675 & 450 & 225 \\ 450 & 450 & 450 & 450 & 450 & 450 & 450 & 450 & 225 \\ 225 & 225 & 225 & 225 & 225 & 225 & 225 & 225 & 225 \end{bmatrix} \begin{bmatrix} h(1) \\ h(2) \\ h(3) \\ h(4) \\ h(5) \\ h(6) \\ h(7) \\ h(8) \\ h(9) \end{bmatrix} = \begin{bmatrix} 1800.0 \\ 1800.0 \\ 1734.1 \\ 1509.1 \\ 1125.0 \\ 675.0 \\ 290.9 \\ 65.9 \\ .0 \end{bmatrix}$$ (3.11)

where FIR coefficients are: $h(m)$, $m = 1,2,\ldots,M$

$h(1)=.0$ $\quad h(2)=.293$ $\quad h(3)=.707$ $\quad h(4)=.707$ $\quad h(5)=.293$
$\quad h(6)=-.293$ $\quad h(7)=-.707$ $\quad h(8)=-.707$ $\quad h(9)=-.293$

The two sets of FIR coefficients and the predicted outputs for M (number of FIR coefficients) equal to five and nine are plotted and shown in Figs. 3.4 and 3.5, respectively. For the case M= 5, the predicted output matches the actual output for the first four data points. For the case where the number of FIR coefficients is equal to the number of data points, M = N = 9, the predicted output matches completely the actual output as shown in Fig. 3.5.

The plot of FIR coefficients for M = 9 has a pattern of a sine wave as shown in Fig. 3.5, while that for M = 5 has a pattern of a halfsine wave, as shown in Fig. 3.4. Note that the magnitudes of the FIR coefficients are relative. They depend on the time step of the data points. In this example, the time step is 12.5 ms, and the peak magnitude of the FIR coefficients shown in Fig. 3.6 is 0.7. It will be shown in the next section that the magnitudes of the FIR coefficients are proportional to the data time step.

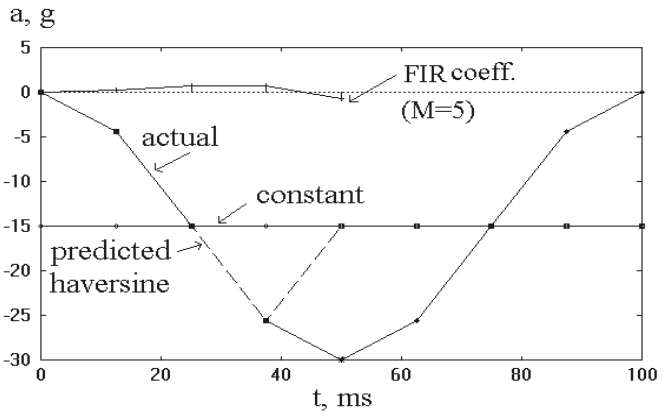

Fig. 3.4 FIR Prediction with M=5 and Constant Input

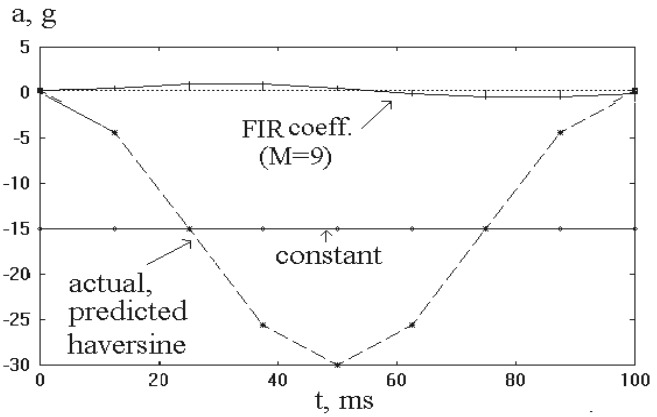

Fig. 3.5 FIR Prediction with M=9 and Constant Input

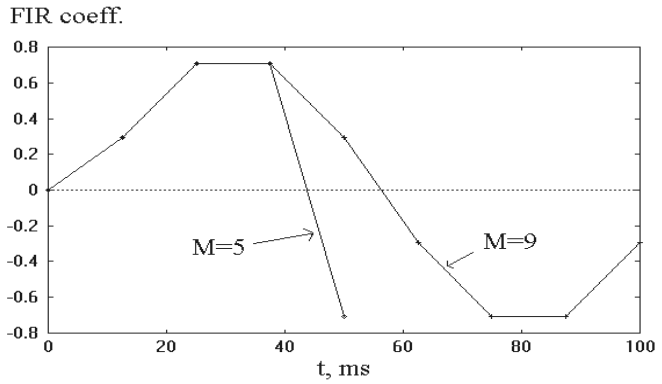

Fig. 3.6 FIR Coefficient Comparison with M=5 and 9 (Δt=12.5 ms)

3.3 TRANSFER FUNCTION AND A SPRING-DAMPER MODEL

The spring-damper model shown in Fig. 3.7 when subjected to an input excitation, p(t), yields an output response of q(t). The process of the model transforming the input to an output in either the time domain (Fig. 3.7) or in the S domain (Fig. 3.8) is defined as a transfer function as shown in the following.

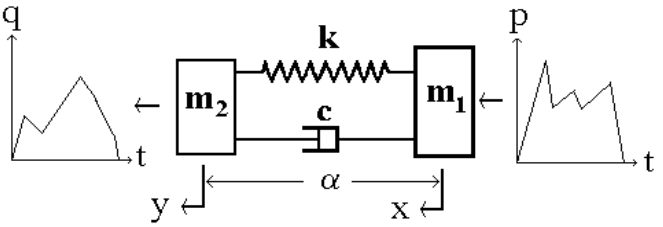

Fig. 3.7 A spring-damper model subjected to an input excitation, p(t).

$$q(t) \doteq \Delta\tau \sum_{\tau_i=0}^{t} h(\tau_i)\, p(t-\tau_i)$$

$$h(t) = \frac{\omega_o}{\sqrt{1-\zeta^2}}\, e^{-\zeta\omega_o t} \sin[\omega_o\sqrt{1-\zeta^2}\,t + \psi] \qquad (3.12)$$

$$\text{where} \quad \psi = \tan^{-1}\left[\frac{2\zeta\sqrt{1-\zeta^2}}{1-2\zeta^2}\right]$$

$p(t)$, $q(t)$: *input, output decelerations at t, respectively*
$h(\tau_i)$: *finite impulse response coefficient at time* τ_i
$\Delta\tau$: *fixed time step size*

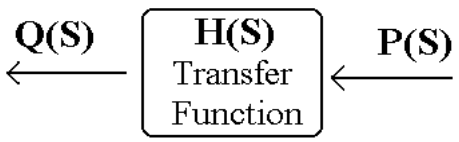

Fig. 3.8 Input P(s), Output Q(s), and Transfer Function H(s) in S Domain

$$H(s) = \frac{Q(s)}{P(s)} = \frac{2\zeta\omega_o s + \omega_o^2}{s^2 + 2\zeta\omega_o s + \omega_o^2}$$

$$\text{where} \quad \omega_o = \sqrt{\frac{k}{m}} \quad \ldots\ldots \textit{undamped natural freq.} \qquad (3.13)$$

$$\zeta = \frac{c}{c_c} \quad \ldots\ldots \textit{damping factor,}$$

$$c = 2m\omega_o \quad \ldots\ldots \textit{critical damping coefficient}$$

3.3.1 FIR Coefficients and K-C Parameters of a Spring-Damper Model

Given an input excitation to a Kelvin model, consisting of a spring (K) and damper (C) in parallel, the output response of the model can be obtained. By solving the second order differential equation of the spring-damper model using the Laplace transformation, the finite impulse response (FIR)

coefficients can be derived. The FIR coefficients are expressed by a closed-form formula in terms of the spring and damper parameters.

The closed-form formula, commonly referred to as the digital convolution formula, is useful in characterizing any set of transfer functions by two parameters K and C of the Kelvin spring-damper model. The process involves the extraction of the signal by digitally filtering the FIR coefficients and curve-fitting the signal by the closed-form FIR formula. Case studies are presented.

Derivation of FIR Coefficients From a Spring-Damper Model – Step 1

(*I*) *Input excitation* (*deceleration*): $\ddot{x} = p(t)$ . . . . (1)

Taking the transform: $s^2\,\bar{X}(s) = P(s)$, *then* $\bar{X}(s) = \dfrac{P(s)}{s^2}$ . . (2)

(*II*) *Output Equation of Motion*: $\ddot{y} = \dfrac{k}{m}(x-y)+\dfrac{c}{m}(\dot{x}-\dot{y})$ . . (3)

Let $\omega_o = \sqrt{\dfrac{k}{m}}$ . . . . . *undamped natural freq., and*

$\zeta = \dfrac{c}{c_c}$ . . *damping factor,* $c_c = 2m\omega_o$ . . . *critical damping coefficient*

then $\dfrac{k}{m} = \omega_o^2$ *and* $\dfrac{c}{m} = 2\zeta\omega_o$

Substituting the above expressions into (3) *yields*:

$\ddot{y} = \omega_o^2(x-y) + 2\zeta\omega_o(\dot{x}-\dot{y})$ . . . . . (4)

Taking the Laplace Transform:

$s^2\bar{Y}(s) = \omega_o^2[\bar{X}(s)-\bar{Y}(s)] + 2\zeta\omega_o s[\bar{X}(s)-\bar{Y}(s)]$

and rearranging in the form: $\bar{Y}(s) = H(s)\bar{X}(s)$ . . . . (5)

where $H(s) = \dfrac{2\zeta\omega_o s + \omega_o^2}{s^2 + 2\zeta\omega_o s + \omega_o^2}$ . . . . . (6)

and substituting (2) *into* (5), *then* (3.14)

$H(s) = \dfrac{\bar{Y}(s)}{\bar{X}(s)} = \dfrac{s^2\bar{Y}(s)}{P(s)} = \dfrac{Q(s)}{P(s)}$ . . . . . (7)

where $Q(s) = \mathcal{L}[\ddot{y}(t)] = s^2\bar{Y}(s)$, $P(s) = \mathcal{L}\ddot{X}(t)]$

$\mathcal{L}$ *is the Laplace Transform*

Rewriting (6): $H(s) = 2\zeta\omega_o\left[\dfrac{s + \dfrac{w_o}{2\zeta}}{(s + \zeta\omega_o)^2 + \omega^2}\right]$ . . . . . (8)

where $\omega = \omega_o\sqrt{1-\zeta^2}$ *damped natural frequency* . . . . (9)

and taking the inverse Laplace transform of (8):

$h(t) = \mathcal{L}^{-1}[H(s)]$

$$= 2\zeta\omega_o\left[\frac{\sqrt{\omega^2 + (\dfrac{\omega_o}{2\zeta} - \zeta\omega_o)^2}}{\omega}\right] e^{-\zeta\omega_o t}\sin(\omega t + \psi) \quad \ldots . (10)$$

where $\psi = \tan^{-1}\left[\dfrac{\omega}{\dfrac{\omega_o}{2\zeta} - \zeta\omega_o}\right]$ . . . . . (11)

Derivation of FIR Coefficients From a Spring-Damper Model – Step 2

Simplifying (10) *and* (11) *by using* (9) *gives*:

$$h(t) = \frac{\omega_o}{\sqrt{1-\zeta^2}}\, e^{-\zeta\omega_o t} \sin[\omega_o\sqrt{1-\zeta^2}t + \psi] \quad \ldots . \quad (12)$$

and $$\psi = \tan^{-1}\left[\frac{2\zeta\sqrt{1-\zeta^2}}{1-2\zeta^2}\right] \quad \ldots \ldots . \quad (13)$$

Since $Q(s) = H(s)P(s)$, *and*

$$q(t) = \mathcal{L}^{-1}[Q(s)] = \mathcal{L}^{-1}[H(s)P(s)] = \int_0^t h(\tau)p(t-\tau)d\tau \quad (3.15)$$

$$\therefore \quad q(t) \doteq \Delta\tau \sum_{\tau_i=0}^{t} h(\tau_i)\, p(t-\tau_i) \quad \ldots \ldots . \quad (14)$$

where

$p(t)$, $q(t)$: *input and output decelerations at time* t

$h(\tau_i)$: *finite impulse response coefficient at time* τ_i

$\Delta\tau$: *fixed time step size*

(14) of Eq. (3.15) is known as a digital convolution formula where p(t) and q(t) are the input and output, respectively, in the time domain, and $\Delta\tau\, h(\tau_i)$ is the finite impulse response (FIR) coefficients convoluting with the input to yield the output.

3.3.2 Transfer Functions of Special Pulses

Without a damper, ζ becomes zero, and the model degenerates into an undamped spring mass model. Then, the set of FIR coefficients of the spring (k) model is simply a sine wave, shown in Eq. (3.16), and also the curve with legend of 10Hz/0 (zero damping) in Fig. 3.9. From Eq. 3.16, note that the magnitude of the FIR coefficient at point m, h(m), is proportional to the time step, $\Delta\tau$.

$$\begin{aligned} &c\ (\textit{damping coefficient}) = 0, \quad \textit{and} \quad \zeta = 0, \\ &\textit{From}\ (13): \quad \psi\ (\textit{phase angle}) = 0 \\ &(12)\ \textit{becomes} \quad h(t) = \omega_o \sin(\omega_o t) \\ &\textit{FIR coefficient at point } m: \quad h(m) = \Delta\tau\, h(t) \end{aligned} \quad (3.16)$$

Case Study: Without Damping. A spring model with a natural frequency of 10 Hz is subjected to an input excitation which is a constant deceleration of -15 g. Determine the transfer function as expressed by the FIR coefficients and compute the output deceleration. The data step is set to 0.8 ms.

Without a damper in the system, the damping factor is zero. From (12) of Eq. (3.15), the peak magnitude of h(t) is computed to be $\omega_o = 2\pi\times(10\ \text{Hz}) = 67.8$ rad/sec. Since each FIR coefficient is proportional to h(t) times one data step in seconds, the peak magnitude of the FIR coefficient is equal to 67.8 rad/sec x 0.0008 sec=0.05 radians, as shown by the curve with zero damping in Fig. 3.9.

The peak magnitude of the FIR coefficient in this example is 0.05 radians with a data step of 0.8 ms. In the previous example, shown in Fig. 3.6, the data step is 12.5 ms and the corresponding peak magnitude is 0.78 radians (Fig. 3.6), or 15.6 times (12.5 ms/0.8 ms = 15.6), and the peak magnitude of 0.05 radians (Fig. 3.9), where the data step is 0.8 ms.

Using the convolution formula shown in (14) of Eq. (3.15) and $\Delta t = 0.8$ ms, the output deceleration q(t) is computed and the peak output magnitude is found to be two times that of the constant deceleration shown in Fig. 3.10.

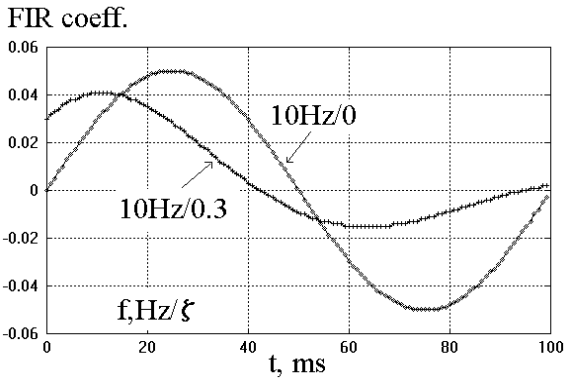

Fig. 3.9 Model FIR coefficients with f = 10 Hz and ζ= 0 and 0.3, respectively (Δt=.8 ms)

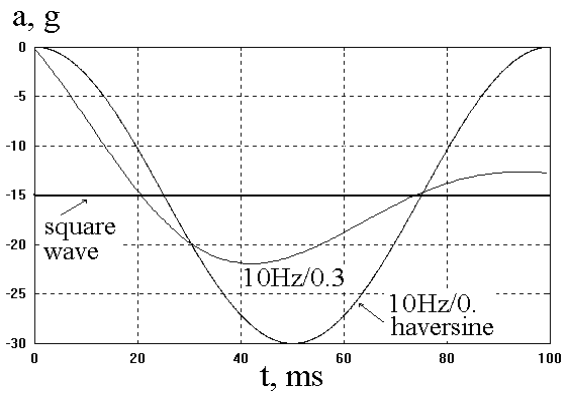

Fig. 3.10 Output Responses of a Spring-Damper Model with Square Wave Input

With Damping: Using the closed-form formulas, the FIR coefficients and the output can also be computed for a system with a finite damping factor. Given a natural frequency of 10 Hz and a damping factor of 0.3, the FIR coefficients and output response are shown in Figs. 3.9 and 3.10, respectively. Note that the magnitudes of the coefficients start higher when the damping factor is greater than zero. The end result from using the convolution formula is that the output response would also start higher in a system with higher damping. The overall output response becomes a shifted and modified haversine.

Instead of using a haversine as the output, a triangular pulse which has the same peak magnitude and duration as the haversine will be used as the output. Note that both the haversine and triangular outputs have the same velocity change (see Fig. 2.61). The set of FIR coefficients for transferring a constant input to the triangular output is derived next.

Special Case: Constant Input and Triangular Output

In the previous example, the haversine pulse is replaced by a triangular pulse as output shown in Fig. 3.11. The transfer function then becomes an integrator. The magnitude of the FIR coefficients on both sides of the mid-point at 50 ms then becomes constant but with opposite sign as depicted in Fig. 3.12. In this special case, the data step is 0.8 ms and the total number of FIR coefficients is the same as the total number of data points, namely 125.

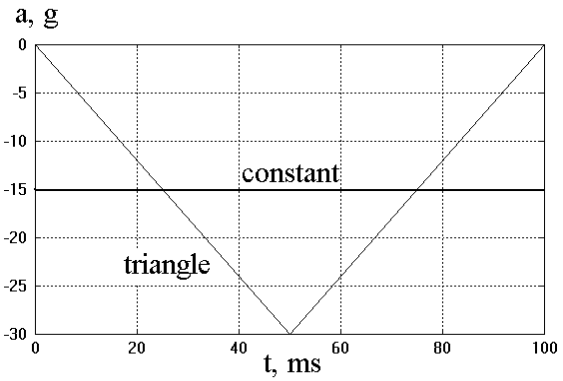

Fig. 3.11 Constant Input and Triangular Output

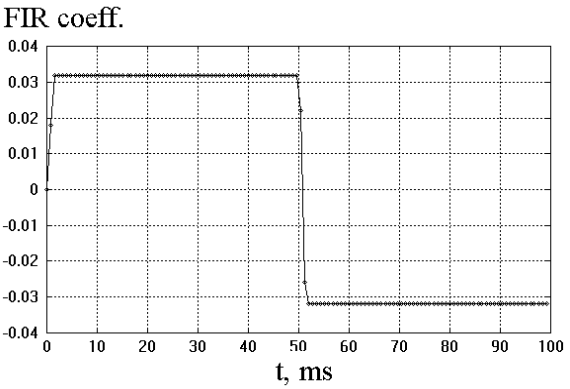

Fig. 3.12 FIR Coefficients Transferring Constant Input to Triangular Output

According to the convolution formula, the constant magnitude of the FIR coefficients becomes the constant integration step when the coefficients are convoluting with the constant input. Since the integration of a constant is a ramp (or a constant slope), the output, following the ramp, reaches its maximum magnitude when the convolution reaches the mid-point at 50 ms. After that, the second part of the coefficients becomes negative and the predicted output magnitude starts decreasing. This constant magnitude of FIR coefficients with opposite sign approximates the sinusoidal FIR coefficient for the haversine output (see Figs. 3.9 and 3.12). Note that both the haversine and triangular pulses have the same velocity change, the magnitude of FIR coefficients (.032) for the triangular output is less than that (.05) for the haversine output.

3.4 BELTED AND UNBELTED OCCUPANT PERFORMANCE WITH AIR BAG

In establishing the transfer function for the occupant restraint system, the objectives of the study in this section are two-fold. One is to evaluate the crash pulse approximation techniques in predicting test occupant performance, the other, to assess the belted and unbelted left front occupant performance in air bag equipped vehicles. Since the air bag module is attached to the steering wheel system, the impact dynamics of the steering column in belted and unbelted occupant conditions plays an important role in the occupant responses.

In Chapter 1, crash pulse characterization methods were developed to approximate an original crash pulse by the use of only a few parameters. These techniques utilize only a few parameters for crash pulse approximation and capture the major responses of a dynamic system in a test. The

accuracy of the approximation technique in predicting the occupant response depends on the number of parameters used.

The crash test data, such as vehicle and occupant accelerometer data, for two trucks in rigid barrier 31 mph tests are used in this study. Table 3.4 shows the summaries of the occupants and vehicles, truck #1 and truck #2. The data for the two trucks are used to obtain the transfer functions of the air bag and knee bolster restraint systems, respectively. The TWA (trapezoidal wave approximation) and FEW (Fourier equivalent wave) pulses are used as inputs to excite the occupant-restraint systems. The transfer functions are then used to predict the responses of the occupant in the trucks subjected to TWA and FEW pulses. The predicted occupant responses from these approximated pulses are compared with those from the tests

Table 3.4 Vehicle and Occupant Responses in the Truck 31 mph Rigid Barrier Tests

Truck (type, restraint condition)	Vehicle		**Torso** / Femur		
	Dy. Cr*., in @ T_m, ms	ESW, g	t*, restraint contact time,ms	Peak Decel, g @ T, ms	DAF**
#1: pickup truck, unbelted, w/ full-powered air bag	22.5 @ 73	17.1	42/46	**51 @ 86** / 55 @ 60	**3.0** / 3.2
#2: SUV, Belted w/ depowered air bag	26.2 @ 90	14.7	15/ - - -	**35 @ 70** / - - -@ - - -	**2.4** / - - -

* Dy. Cr.: Dynamic Crush, in

** DAF (Dynamic Amplification Factor) = peak occupant deceleration, g / ESW, g

3.4.1 Test Vehicle and Occupant Responses

Two trucks, one a pickup truck with a full-powered air bag for an unbelted occupant and the other an SUV (sport utility vehicle) with a depowered air bag for a belted occupant, were tested in 31 mph rigid barrier impacts. The essential data describing the vehicle and occupant responses are shown in Table 3.4. Truck #1 with an equivalent square wave (ESW) of 17.1g is stiffer than Truck #2 with an ESW of 14.7 g, and the peak torso deceleration of 51 g in Truck #1 is higher than that of 35 g in Truck #2. The dynamic amplification factor (DAF) (ratio of the peak torso decelerations to vehicle ESW) is 3 for Truck #1 and 2.4 for Truck #2. Occupant performance in Truck #2 is superior to that in Truck #1 due to the lower torso g (deceleration).

Referring back to the closed-form formula shown in Section 1.9.4 of Chapter 1, the peak occupant deceleration is a function of three factors: ESW, restraint stiffness, and restraint slack (or restraint contact time, t*). It is shown that of these three factors, the controlling factors in the two cases are the ESW and restraint slack.

Shown in Fig. 3.13 are curves for the torso deceleration versus torso relative displacement for both trucks. The effective slack between the torso and the shoulder belt in the left front occupant of Truck #2 is almost zero, while that for the Truck #1, δ_1, is about five inches, this being the distance between the fully deployed air bag and the left front occupant torso. Fig. 3.14 shows that the torso ridedown efficiencies for both trucks #1 and #2 are 7.4% and 49.0%, respectively.

The higher torso deceleration in Truck #1 is attributed to the unbelted condition. The occupant simply freely flew into the deployed air bag. The left front occupant horizontal motion in Truck #1 forces the steering column (see Fig. 3.15) to stroke and rotate upward, resulting in head-windshield contact.

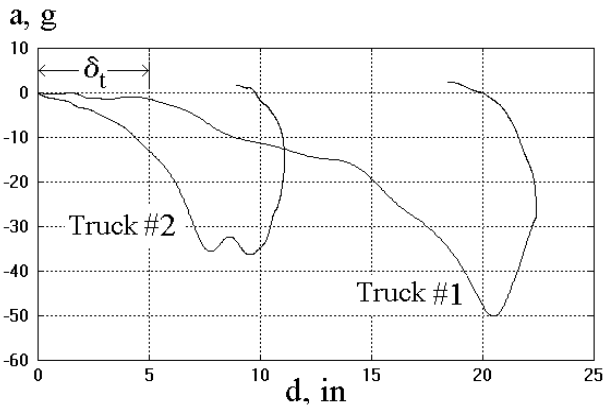

Fig. 3.13 Torso Restraint Curves (Decel. vs. Relative Disp.) for Two Trucks

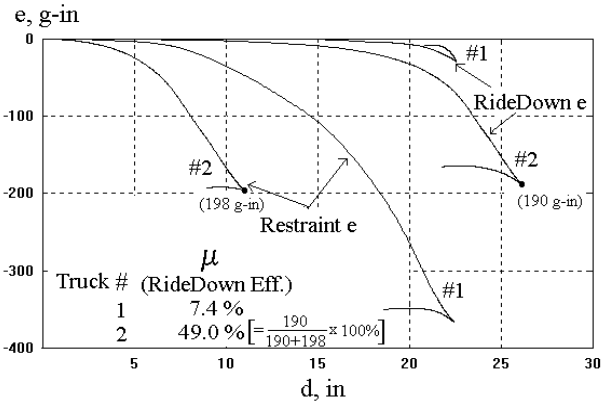

Fig. 3.14 Torso Ridedown Efficiencies in Trucks #1 and #2

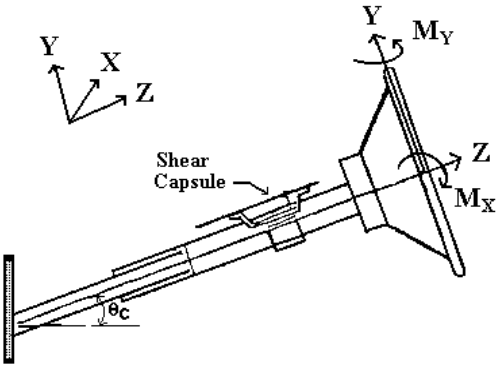

Fig. 3.15 A Steering Column and Local Coordinate System

The steering column transient loadings are shown in Fig. 3.16 and summarized in Table 3.5. Note that the higher column loadings along the three orthogonal directions result in a higher torso deceleration in Truck #1 than in Truck #2.

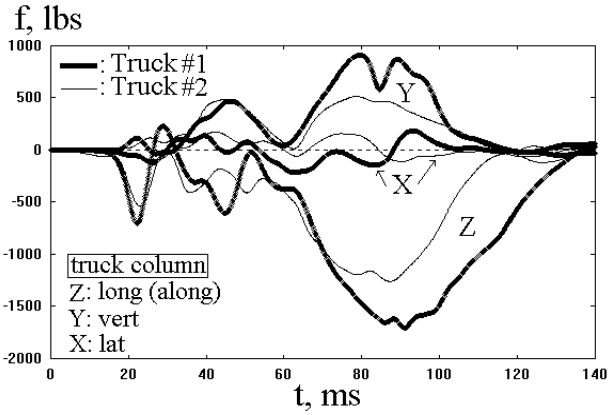

Fig. 3.16 Steering Column Transient Loading in Truck #1 and #2, 31 mph Test

Table 3.5 Steering Column Loadings and Timings of Two Trucks, 31 mph Tests

Truck (restraint types)	Left Front Chest G @ ms	Steering Column Loading and Bending				
		F_z, lb @ ms	F_y, lb @ ms	F_x, lb @ ms	M_x, in-lb @ ms	M_y, in-lb @ ms
#1 (pickup truck, unbelted, w/ full-powered air bag)	51 @ 86	-1937 @ 91	1034 @ 83	248 @ 95	-2000 @ 49	-1312 @ 68
#2 (SUV, 3-Pt. Belted w/ de-powered air bag)	35 @ 70	-1261 @86	512 @ 89	158 @ 75	-2262 @ 80	766 @76

Considering the loading along the steering column itself, in the Z (longitudinal) direction, the effective torso weight[5/] (W_{eff}, based on peak column loading and peak torso deceleration in the longitudinal direction) can be computed. W_{eff} for Truck #1 with an unbelted occupant is 38 pounds as shown in Eq. (3.17). For Truck #2 with belted occupant, the resultant loading due to torso belt, air bag, and column has to be computed before W_{eff} can be estimated.

$$\textit{For Truck \#2:}$$

$$W_{eff} = \frac{\textit{column longitudinal loading}}{\textit{torso longitudinal deceleration}} = \frac{1937\ lb}{51\ g} = 38\ lb$$

$$f = \frac{1}{2\pi}\sqrt{386.4\,k}, \quad \textit{and} \quad K = W_{eff}k \qquad (3.17)$$

$$\textit{where} \quad k\textit{: restraint specific stiffness, g/in}$$
$$K\textit{: overall restraint stiffness, lb/in}$$
$$f\textit{: restraint natural frequency, Hz}$$

[5/]The instantaneous weight is based on the loading and deceleration at the same timing. The average of instantaneous weights over the loading duration approximates the effective weight.

W_{eff} can be used in a simple occupant-restraint model for dynamic analysis. The natural frequency of a typical depowered air bag restraint system is about 6 Hz. The slope of the restraint curve, shown in Fig. 3.13, is the restraint specific stiffness for Truck #2 and equals 4 g/in. Using the formula presented in Section 1.10.2.2 of Chapter 1, the resultant stiffness of the restraint system of Truck #2 is $K = W_{eff}\, k = 38 \times 4 = 152$ lb/in.

3.4.2 Truck #1: Unbelted Occupant with Full-Powered Air Bag

In this section, the restraint transfer function for Truck #1 will be computed and validated using the test data. The occupant response subject to a TWA (trapezoidal wave approximation) will be predicted using the test transfer function and compared with the test occupant performance.

Truck #1, with an unbelted occupant, was subjected to a rigid barrier impact at 31 mph. The vehicle left rocker deceleration (input: x) and the torso and femur decelerations (output: y) of the left front unbelted occupant are shown in Figs. 3.17 and 3.18, respectively. The truck rebounded at 73 ms, and the peak torso deceleration occurred at 86 ms, after the rebounding of the truck. Having late peak torso deceleration results in a low torso ridedown efficiency. However, due to the small slack between the knee and knee bolster, the peak femur deceleration occurred at 60 ms, before the rebounding of the truck.

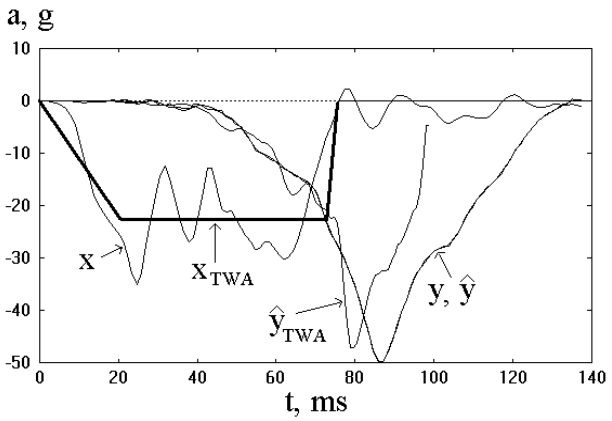

Fig. 3.17 Truck #1/Torso G: Test(x,y), Validation(x, $\hat{y}$), and FIR Prediction (x_{TWA}, $\hat{y}_{TWA}$)

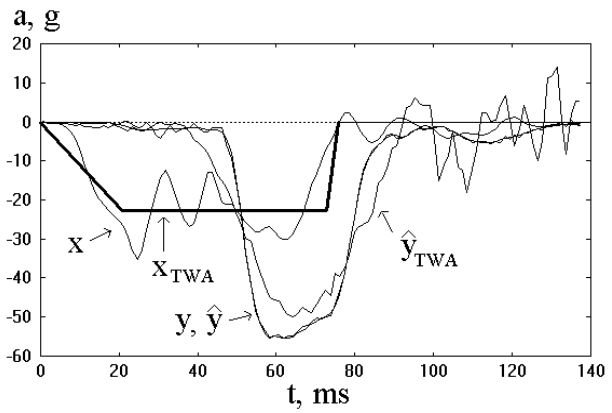

Fig. 3.18 Truck #1/Femur G: Test(x,y), Validation(x, $\hat{y}$), and FIR Prediction (x_{TWA}, $\hat{y}_{TWA}$)

3.4.2.1 *Restraint FIR Model Validation Using Test Results*

The number of FIR coefficients in the transfer functions is set at 75 percent of the number of data points. Since the data step is small, a window averaging of 14 bites is used to reduce the total number of data points by 14 times. The total number of data points in the duration of 140 ms is then N = 140 ms/(0.08 ms×14 bites) = 125 points. Then, the number of FIR coefficients is M = 0.75×125 = 93 points. The computed transfer functions (FIR models) of the air bag and knee bolster restraint systems are shown in Fig. 3.19 and 3.20, respectively.

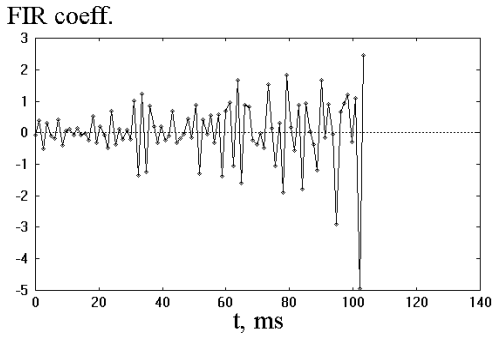

Fig. 3.19 Truck #1: FIR Coefficients of Air Bag Restraint System

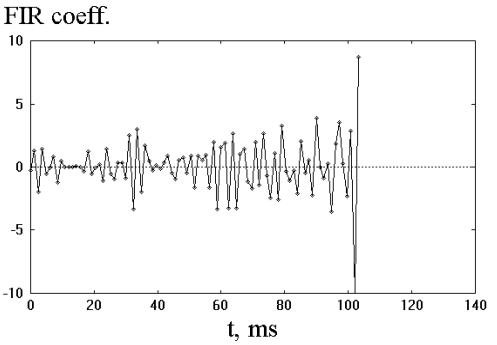

Fig. 3.20 Truck #1: FIR Coefficients of Knee Bolster Restraint System

To validate the FIR model, the test vehicle pulse (x) is convoluted with the FIR coefficients. The predicted torso and femur outputs (ŷ) are found to be practically identical to those obtained in the tests (y) as shown in Figs. 3.17 and 3.18 in the previous section.

3.4.2.2 *Filtered Signals of FIR Coefficients*

The signals contained in the two sets of highly oscillatory FIR coefficients, shown in Figs. 3.19 and 3.20, can be extracted by digital filtering. To improve the curve fitting between the FIR coefficients and the filtered curve (signal), the FIR coefficients for both the air bag and knee bolster restraints were reversed in sequence and then filtered by a Butterworth filter. The backward-filtered signals of the two transfer functions are shown in Fig. 3.21.

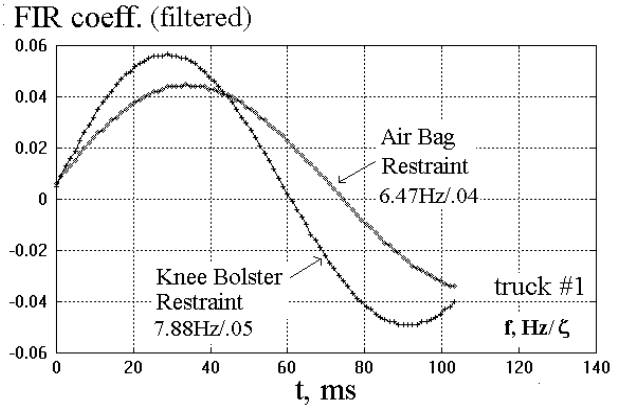

Fig. 3.21 Butterworth-Filtered FIR Coefficients of Truck #1

Using formulas (12)–(14) in Eq. (3.15) and the Imbedded Random Searching (IRS) technique for curve matching (see Chapter 5), the specific stiffness and the damping factor of the respective restraint system can be found. As shown in Fig. 3.21, the damping factors for the air bag and knee bolster

restraint systems are 0.04 and 0.05, respectively. The specific stiffness of the knee bolster (f = 7.88 Hz) is larger than that of the air bag restraint (f = 6.47 Hz). The difference in specific stiffness can also be checked using the loading slopes of the test restraint curves. In this particular test, the effective slack between the torso and the fully deployed air bag is about five inches, as is the slack between the knee (femur) and the knee bolster.

3.4.2.3 *Response Prediction using TWA*

Using the transfer function for the torso restraint system of Truck #1, the torso response is predicted with the TWA crash pulse as input. The predicted occupant torso decelerations ($\ddot{y}_{TWA}$) using TWA input (x_{TWA}) are shown in Fig. 3.22. The peak deceleration magnitudes of both the predicted and the test torso responses occur during the vehicle rebounding phase and result in a relative high deceleration. However, the magnitudes of the peak femur deceleration for both the predicted and test responses occur before vehicle stops against the rigid barrier as shown in Fig. 3.18. The parameters describing TWA are the constant deceleration magnitude and the onset time at the beginning of the constant deceleration. Since a constant deceleration pulse is close to an ideal crash pulse, the predicted output occupant deceleration subjected to the TWA crash pulse yields a smaller peak magnitude (48 g) than that of the test (51 g) (see Fig. 3.22).

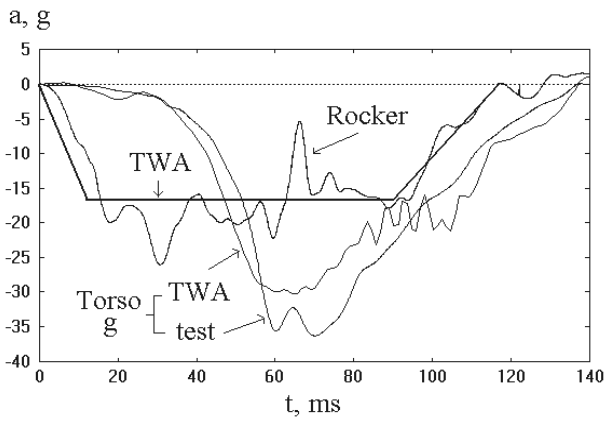

Fig. 3.22 Truck #2: Test, Validation, and Prediction of Torso Response using TWA

3.4.3 Truck #2: Belted Occupant with Depowered Air Bag

In this section, the restraint transfer function in Truck #2 will be computed and validated using the test data. The occupant response subjected to TWA (trapezoidal wave approximation) will then be predicted using the transfer function from the test.

In Truck #2, with a 3-point belt and an air bag system in a rigid barrier test at 31 mph, the vehicle left rocker and left front occupant torso decelerations are shown in Fig. 3.22. The TWA (trapezoidal wave approximation), satisfying two boundary conditions of the vehicle dynamic crush and velocity change, is overlapped with the test crash pulse, as shown in the figure.

3.4.3.1 *Restraint Transfer Function Validation*

The number of FIR coefficients (not shown) for the air bag restraint system in the Truck #2 test is also set at 75 percent of the number of data points as is the case for Truck #1. Since the data step is small, a window averaging 14 bites is also used to reduce the total number of data points fourteen-fold. The total number of data points and the number of FIR coefficients are greater than those for truck #1, due to the longer duration of the crash pulse. To validate the FIR model, the test vehicle pulse (x) is convoluted with the FIR coefficients. Similar to the Truck #1 FIR model validation

(plotted in Fig. 3.17), the predicted torso output ($\hat{y}$, not plotted in Fig. 3.22) for Truck #2 matches quite well with that from the test (y).

In Fig. 3.23, the filtered signal of the FIR coefficients for Truck #2 is compared to that of Truck #1. Due to the higher steering column loading and bending, the specific stiffness of the torso restraint system for Truck #1 is higher than that for Truck #2. However, due to higher sliding friction attributed to the column stroking in Truck #2, the damping factor (0.17) of the torso air bag restraint in Truck #2 is higher than that (0.04) in Truck #1. The higher damping would have provided more attenuation effect on the lower torso deceleration in Truck #2.

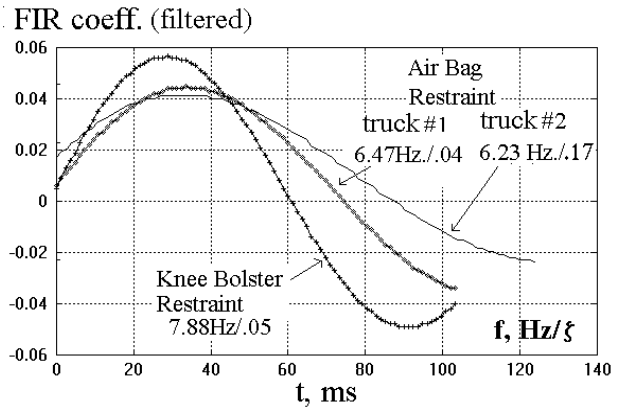

Fig. 3.23 Filtered Signals of FIR Coeff. of Truck #1 and #2 with Air Bag Restraints

3.4.3.2 *Response Prediction Using TWA*

To assess the effect of the TWA (Trapezoidal Wave Approximation) crash pulse on the occupant response, a TWA is used as the input in the derived FIR model. The predicted output torso deceleration with a TWA is compared to the test torso deceleration and shown in Fig. 3.22. The predicted peak torso deceleration of 30 g, lower than the test torso deceleration of 36 g, occurs around 65 ms, before the vehicle comes to a stop at the rigid barrier around 90 ms.

3.4.3.3 *Response Prediction Using Fourier Equivalent Wave (FEW)*

A 5th order Fourier Equivalent Wave (FEW) derived from the crash pulse alone without satisfying any test boundary conditions can be computed by Eq. (2.27) in Chapter 2. In the Truck #2 rigid barrier 31 mph test, the FEW has been computed and is shown in Eq. (3.18) and Fig. 3.24.

$$\textit{Truck \#2: } 5^{th} \textit{ order FEW (Fourier Equivalent Wave)}$$

$$A(t) = \sum_{i=1}^{5} a_i \sin(i\,\omega\, t) \quad \textit{for} \quad \omega = 5.38\ \textit{Hz} \tag{3.18}$$

i	1	2	3	4	5
$i\omega$	4.10	8.20	12.30	16.39	20.49
a_i	−20.31	−3.72	−3.95	−.93	1.22

The 5th order FEW, shown in Fig. 3.24, exhibits a double hump wave and approximates the test vehicle crash pulse very closely. To assess the effect of the FEW crash pulse on the occupant response, the FEW is used as the input to the derived transfer function. The FEW predicted torso and test torso deceleration are shown in Fig. 3.24. Both the predicted and test peak torso decelerations occur around 70 ms. The overall profiles of the predicted and test torso deceleration match very closely, and the peak magnitudes of the two curves are almost identical (about 35 g). In general, using the transfer function in crash pulse prediction, the higher the order of the approximated FEW pulses used, the more accurate the predicted output deceleration will be.

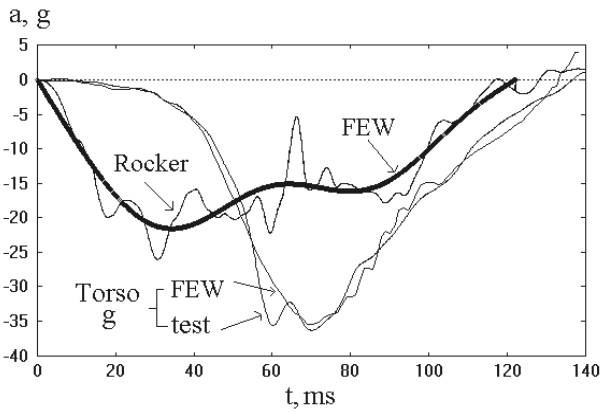

Fig. 3.24 Truck #2: Test, Validation, and Prediction of Torso Response using (FEW)

3.5 BODY MOUNT AND TORSO RESTRAINT TRANSFER FUNCTIONS

In a body-on-frame vehicle, Fig. 3.25, the body or cab is fastened to the frame by body mounts. One type of truck body mount, as shown in Fig. 3.26 (Type F), consists of rubber bushings on the top and bottom of the frame bracket, a bolt, and a retainer. The rubber bushing is made of Butyl, a man-made rubber. There are four body mounts on each side frame and two front end sheet metal (FESM) mounts. Body mounts are designed to carry the horizontal impact load in an impact and to isolate the noise, vibration, and harshness (NVH) from the passenger compartment during driving.

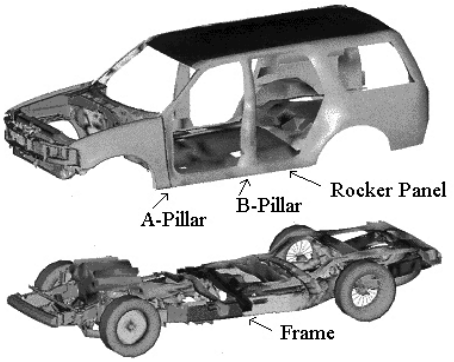

Fig. 3.25 Two Body Mount Locations

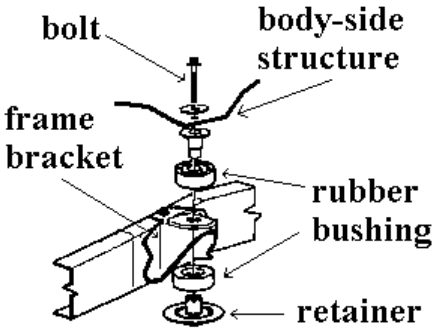

Fig. 3.26 Type F Body Mount (= Fig. 2.36)

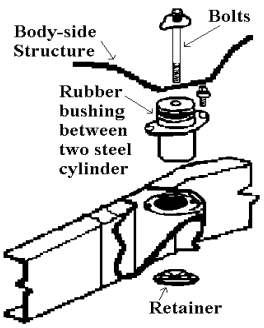

Fig. 3.27 Type T Body Mount

Fig. 3.28 Body Mount Deformation (Type F)

An alternate body mount design, Type T, consists of two concentric steel cylinders, as shown in Fig. 3.27. The space between the two cylinders is filled with a rubber bushing consisting of natural rubber mixed with a carbon black compound. Due to the vertical shear loading on both sides of rubber bushing, Type T body mount is also referred to as a shear mount. Since the inner cylinder movement is constrained by the outer cylinder, the inner cylinder bottoms out on the outer cylinder as it moves forward. Both Types F and T body mounts are analyzed using the component test data and the spring-mass-damper model.

3.5.1 Body Mount Characteristics and Transient Transmissibility

A body mount is a complex joint assembly where not only pre-loading due to installation torque exists, but also shearing, axial loadings, and bending from a crash (Fig. 3.28). It has been suggested [3,4] that body mounts provide attenuation of the frame and body decelerations. However, few attempts have been made to investigate the mechanism of attenuation by body mounts. In this section, the dynamic characteristics of various body mounts in the component and full vehicle tests are described by the sets of FIR coefficients and the associated stiffness and damping properties of a spring-mass-damper model.

The damping characteristics of two rubber bushing materials and one of steel are compared in the frequency plots for the steady-state force transmissibility (T) (shown in Fig. 3.29). The steel has very little damping and it resonates strongly when the ratio of the forced to natural frequency (R) is equal to one.

For the natural rubber bushing, the force transmissibility, T, is about 9 at the resonant frequency. Therefore, from Fig. 3.30 for T versus R, the damping factor, ζ, for natural rubber is estimated to be about 0.06. It is expected that the damping factor for natural rubber with a carbon black compound for engineering application will be between 0.1 and 0.15. For Butyl rubber, the transmissibility is about 2 and the damping factor from Fig. 3.30 is about 0.3.

The ability of a body mount to transfer the frame impulse to the body is defined as transient transmissibility (TT)[3]. The numerical value of TT is equal to the ratio of the first peak magnitude of the body deceleration to that of the frame deceleration. TT plays an important role in the truck crashworthiness which affects directly the occupant compartment response. This is because the front rail design determines the size and shape of the frame impulse, and the spring stiffness and damping of the body mount determine how the frame impulse is transferred to the body.

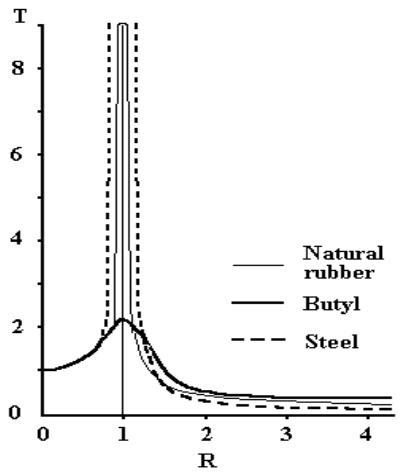

Fig. 3.29 Material Damping Properties

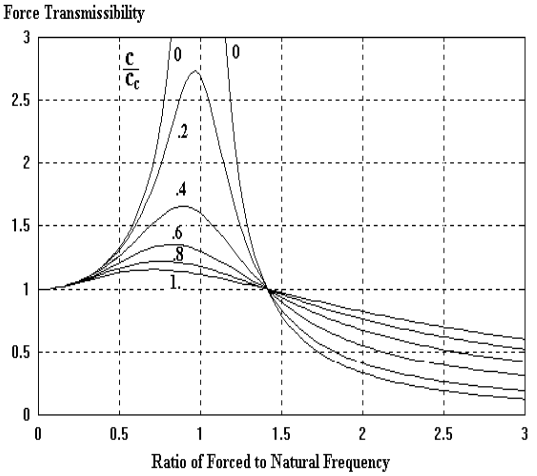

Fig. 3.30 Force Transmissibility as a Function of Damping Factor and Frequency Ratio

Fig. 3.31 shows the accelerometer data of the frame and body at the B-Pillar of truck F (with type F body mount) with a duration of 20 ms in a 35 mph rigid barrier test. The data were filtered by a Butterworth 2nd-order filter at a roll-off frequency of 100 Hz according to SAE J211, Instrumentation for Impact Tests. The duration of the frame impulse lasts about 10 ms and the peak magnitude is about -135 g at 7 ms. The first peak magnitude of the body deceleration is about -35 g at 11 ms, about 4 ms later than the timing of peak frame acceleration. The TT of the body mount is then equal to 35/135 = 0.26 as shown in the figure.

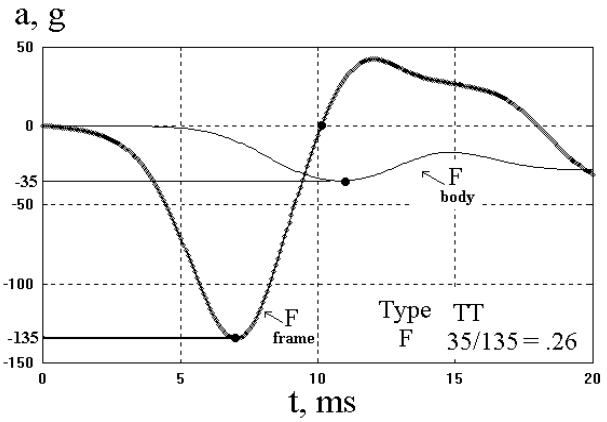

Fig. 3.31 TT of the Body Mount in Truck F

The dynamic characteristics of the body mount will be analyzed by the transfer function. It is desirable to isolate the portion of the body deceleration which is attributed to the frame impulse only. Shown in Fig. 3.32, the frame and body displacements at 11 ms are about 6 and 7 inches, respectively. The corresponding body mount deformation, Δd, at 11 ms therefore is about 1 inch.

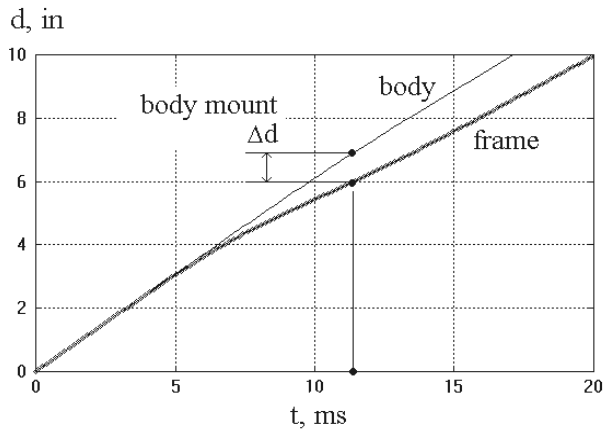

Fig. 3.32 Type F Body Mount Deformation in Truck #1
35 mph test

Due to the overhang of the bumper attached to the frame, the frame deformation of 6 inches is not large enough to cause the upper end of the structure above the frame to interact with the rigid barrier. Since the upper structure is not contributing significant resistance or deceleration to the body in the early portion of the crash, the excitation that generates the body pulse in that period is the frame impulse. Thus the transfer function obtained is that of the body mount between the body and frame.

Using a haversine pulse with a duration of ΔT = 10 ms as input to a Kelvin model, the TT can be expressed as a function of body mount natural frequency (stiffness), f, and damping factor, ζ. Figs. 3.33 and 3.34 show the 3-D surface and constant contour plots, respectively. As either of the natural frequency, f, and damping factor, ζ, increases, TT increases.

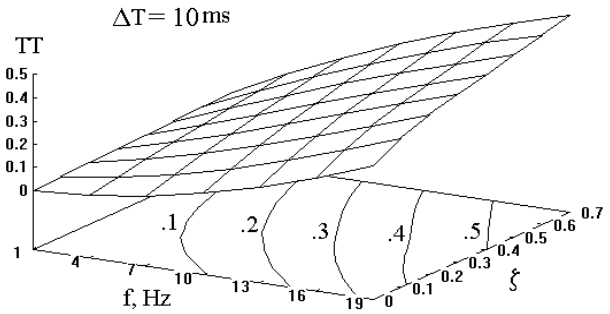

Fig. 3.33 3-D Plot of TT, a Function of f and ζ, Given Haversine with ΔT=10 ms

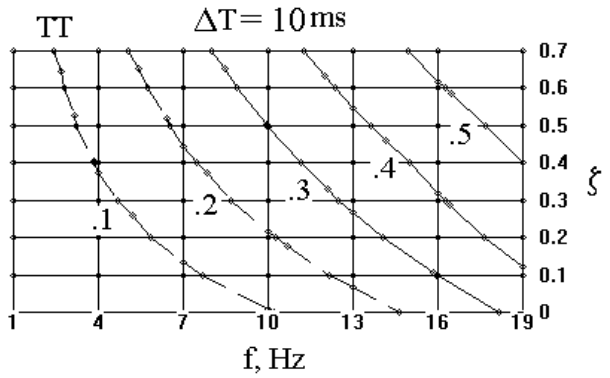

Fig. 3.34 Contour Plot of TT, a Function of f and ζ, Given Haversine with ΔT = 10 ms

3.5.2 Types F and T Body Mount Transfer Functions

Truck F, equipped with a Type F body mount, was tested in a 35 mph rigid barrier condition. The frame and body decelerations up to 20 ms with TT = 0.26 are shown in Fig. 3.31. The two deceleration data sets are used to compute the transfer function with M (no. of FIR coefficients) = 18 and N (no. of data points) = 25. The set of FIR coefficients (transfer function) is filtered (without reversing the data sequence) by a Butterworth 2nd-order filter with a cutoff frequency of 100 Hz, as shown in Fig. 3.35. Using the convolution integral formula to curve fit the filtered FIR coefficients, a smoother K-C model curve is also shown in Fig. 3.35. The natural frequency and the damping factor from the curve fitting are f = 11.2 Hz and ζ = 0.26. The value of damping factor of the Type F body mount is fairly close to that of the component test results.

The same procedure was applied to Truck T which was equipped with Type T body mounts. The frame and body decelerations (curves indicated by T frame and T body) up to 20 ms are shown in Fig. 3.36. The natural frequency and the damping factor from the curve fitting are f = 9.6 Hz and ζ= 0.15, as shown in Fig. 3.36. As expected from the component test analysis, the damping factor for Truck T, equipped with natural rubber body mounts, is less than that for Truck F, equipped with man-made rubber (Butyl) body mounts.

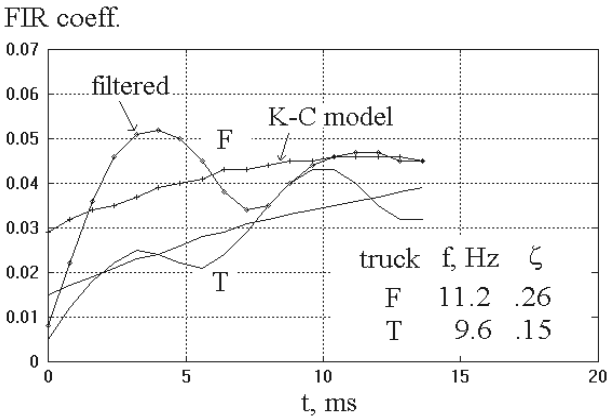

Fig. 3.35 Body Mount FIR Coefficients and K-C Parameters of Trucks F and T

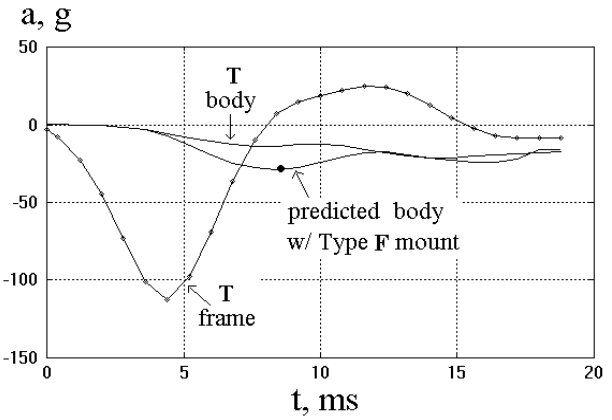

Fig. 3.36 Body Response of Truck T with Type F Body Mount

3.5.3 Body Response Prediction of Truck T with Type F Body Mount

In the previous section, the body mount transfer functions were derived using the frame and rocker accelerometer data for trucks F and T, respectively. One of the most frequently asked questions is what would the body response become if Truck T were equipped with Type F mounts. Since the transfer function of the Type F body mount used in Truck F has been obtained, it can be used to convolute with the frame pulse of Truck T to predict its body response.

Fig. 3.36 shows the predicted body response of Truck T with a Type F body mount installed. The peak body deceleration has increased from a magnitude of 14 g to 26 g. Therefore, the new TT (transient transmissibility) is equal to 26/110 = 0.24 which is twice as high as the 0.12 obtained when the original body mount Type T was used. The increase of TT is attributed to the high damping factor of Type F body mount. The body response is dominated by the damping due to the large velocity change over the duration of the frame impulse.

3.5.3.1 *Frame Impulse Duration and Transient Transmissibility*

The TT of Truck T equipped with the Type F body mount has been estimated to be 0.24. It would have been the same as the original obtained for Truck F, 0.26, if the duration of the frame impulse of Truck T (ΔT = 8 ms) were as long as that of Truck F, 10 ms. As mentioned in the publications on

body mounts [3,4], for a given body mount, there is a positive correlation between TT and ΔT. Fig. 3.37 shows the 3-D surface contour plot of TT as a function of damping factor, ζ, and frame (haversine) impulse duration, ΔT. The natural frequency of a body mount used in generating the TT is 8 Hz.

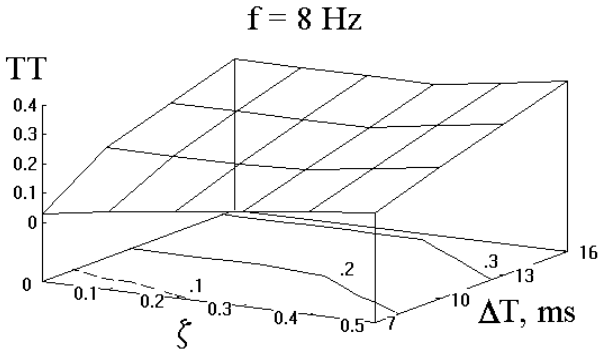

Fig. 3.37 3-D Contour Plot of TT in Terms of ζ and ΔT of Frame Impulse

3.5.3.2 *Testing Frame Rail for a Desired Impulse Duration*

In an impact test, the frame structure produces a crash pulse that can be approximated by a haversine pulse. Depending on the initial impact velocity, the frame deformation associated with the peak magnitude and duration of a haversine pulse can be modified by a two-step process:

Step 1: The kinematic relationship between the peak amplitude, displacement change, and duration of the haversine pulse has been shown in Section 2.4.15 in Chapter 2 and is plotted in Fig. 3.38. The derivation of the relationship shown is based on the first and second integral with the initial velocity and displacement equal to zero. This is equivalent to a test conducted on a power thruster (a pulse generating machinery) where a test object is excited with the specified peak haversine acceleration magnitude and duration. The resulting displacement change can then be estimated.

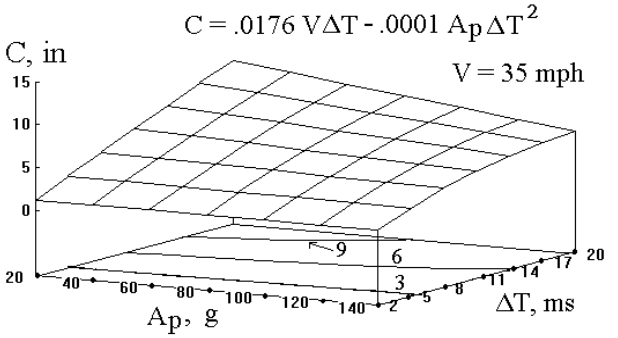

Fig. 3.38 Haversine Frame Crush versus Peak Deceleration amd Duration –Impact

Step 2: By subtracting the displacement change, as shown in Fig. 3.38, from the free-flying displacement at ΔT (ms) with an initial velocity of V (mph), the frame crush, C (in), can be computed by the formula shown in Fig. 3.39.

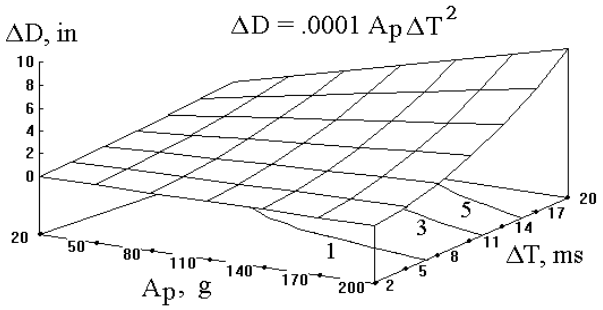

Fig. 3.39 Haversine Displacement versus Peak Deceleration and Duration – Excitation

For the Truck F in the 35 mph barrier impact, the peak deceleration and duration of the frame haversine pulse are about 135 g and 7 ms, respectively, and the frame crush is then C = 6.2 – 1.4 = 4.8 inches. For Truck T, the peak deceleration and duration are 110 g and 8 ms, and the frame crush is C = 4.9 – 0.7 = 4.2 inches. To increase the duration of Truck T impulse from 8 to 10 ms, the frame crush needed is 5 inches, an increase of about 0.8 inches. Note that in the frontal impact, the amount of frame crush includes those due to the bumper and front frame horn which supports the bumper.

3.5.4 Torso Restraint Transfer Functions

The two trucks used in the body mount transfer function analysis in Section 3.5.2 were crash tested in a 35 mph rigid barrier impact. The body mount transfer function in one truck (Truck F) is used to predict the body responses of the other truck (Truck T, a prototype vehicle) for body (compartment) crash performance comparisons. In this section, a similar study on the torso restraint transfer function is performed to validate and predict the occupant torso responses for the prototype truck at 35 mph impact.

Given the crash test results of Truck F, the restraint transfer functions for both the left front and right front restraint systems can be obtained. In a new prototype truck development, the front end structure has more available crush space while the basic restraint systems for both trucks remain unchanged. It is imperative that the occupant responses in the new prototype truck be estimated.

By analyzing the test performance of truck F, the respective transfer function for the left and right front occupant restraint systems can then be computed. These restraint transfer functions are then applied to predict the occupant responses in Truck T.

3.5.4.1 *Vehicle and Belted Occupant Performances in Trucks F and T*

Both trucks in the 35 mph barrier impact were equipped with belt and air bag systems. Each restraint system utilized a pyrotechnic pretensioner, a load limiter, and a web grabber in both left and right front seating positions. Truck F had a regular air bag system, while Truck T had ARS (advanced restraint system) dual-stage inflator systems. Thus, the restraint transfer function, obtained from the input vehicle compartment (body) and output torso decelerations, represents the dynamic characteristics of the restraint system in that test condition.

Figs. 3.40 and 3.41 show the vehicle and occupant responses of trucks F and T, respectively, in the 35 mph barrier test. The higher initial acceleration magnitude of the body in Truck F makes both the ESW (equivalent square wave) and ASW (average square wave, deceleration average of two points on the TESW) higher than those for Truck T. Consequently, the dynamic crush of Truck F is less than that of Truck T. Truck F is stiffer than Truck T and the left front occupant chest deceleration is greater than that in the Truck T test.

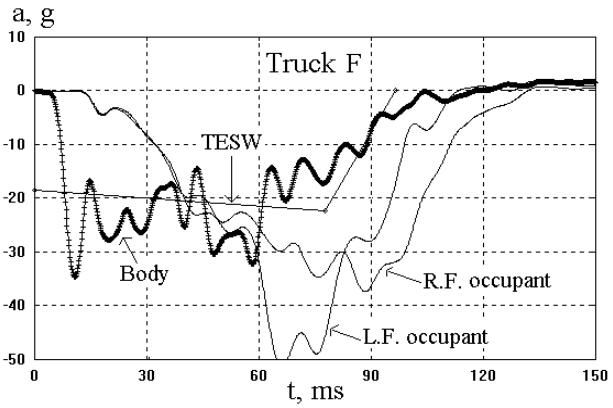

Fig. 3.40 Vehicle and Occupant Responses of Truck F in a 35 mph Barrier Impact

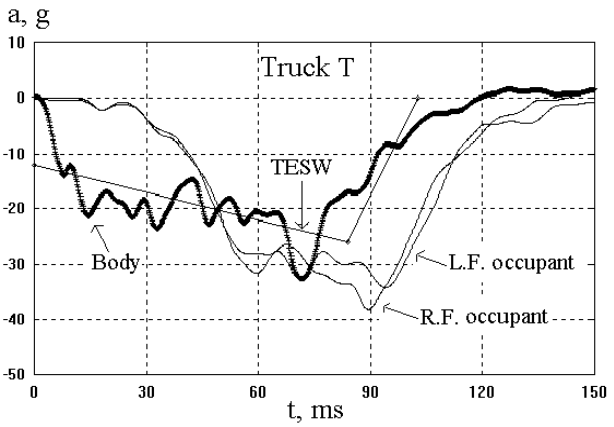

Fig. 3.41 Vehicle and Occupant Responses of Truck T in a 35 mph Barrier Impact

Table 3.6 lists the structural responses of the two vehicles in terms of the tipped equivalent square wave (TESW), relative centroid location, and dynamic crush of the left rocker panel at the B-pillar. The crash pulse of Truck T, with relative centroid location of 0.56, is tipped more rearward than Truck F. Truck T, which was more rear-loaded than truck F, had about 29 inches dynamic crush compared to about 25 inches for Truck F.

Table 3.6 Tipped Equivalent Square Wave (TESW) and Dynamic Crush of Trucks F and T

Truck (Belted Occupant)	TESW				Dynamic Crush, in @ T_m, ms
	P_0 , g	P_1 , g	T_c/T_m	T_f , ms	
F, Type F body mount	-18.5	-22.4	.52	97	24.7 @ 78
T, Type T body mount	-12.1	-26.0	.56	103	28.9 @ 84

The equivalent square wave and the left and right front occupant chest (torso) decelerations of both trucks F and T are shown in Table 3.7. Because of the advanced restraint systems, the test chest decelerations of both left and right front occupants in the tests are relatively low except for the left front occupant in Truck F. Post-crash analysis of the steering column in Truck F indicates that the steering column rotated upward and did not stroke as much as that in truck T. The high left front chest deceleration of 51 g in truck F is attributed to the high column loading.

Table 3.7 Chest G, ESW, and DAF of Trucks F and T

Truck	Test Chest Deceleration, g		ESW, g	DAF, Dynamic Amplification Factor	
	Left Front	Right Front		Left Front	Right Front
F	51 @ 66	38 @ 88	19.8	2.6	1.9
T	34 @ 94	38 @ 90	16.9	2.0	2.3

Fig. 3.42 shows the left front occupant restraint and ridedown curves for both trucks in the 35 mph barrier tests. Comparison of the restraint curves (chest decelerations versus chest displacements) indicates that Truck F has a steep second slope due to the steering column rotation. This results in a higher column loading and higher chest deceleration (51 g) and less torso travel (12 inches) than the torso responses (34 g and 14 inches) in Truck T.

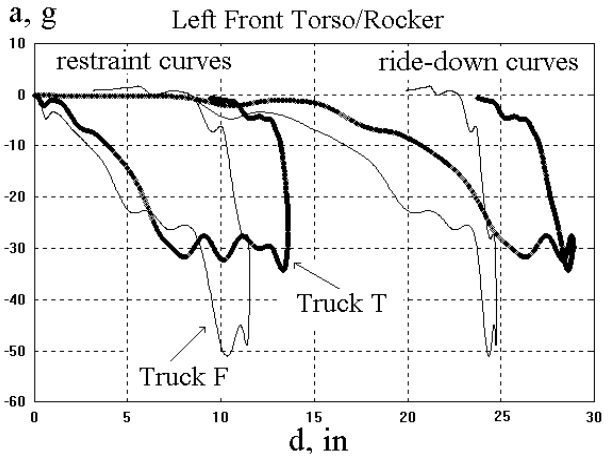

Fig. 3.42 Left Front Occupant Restraint and Ridedown Curves of Both Trucks F and T

Fig. 3.43 shows the right front occupant restraint and ridedown curves for both trucks in the 35 mph barrier tests. Compared to the steering column movement, the right front air bag module is mounted inside the instrument panel where no intrusion has occurred. Therefore, the restraint curves of the right front occupants in both trucks are almost identical.

The ridedown efficiencies of both the left front and right front occupants in both trucks are shown in Table 3.8. The ridedown efficiencies of the left front occupants for both trucks are the same, 47%; however, the chest deceleration of truck T is lower due to its advanced restraint system (with a 2-stage inflator) and a low steering column loading.

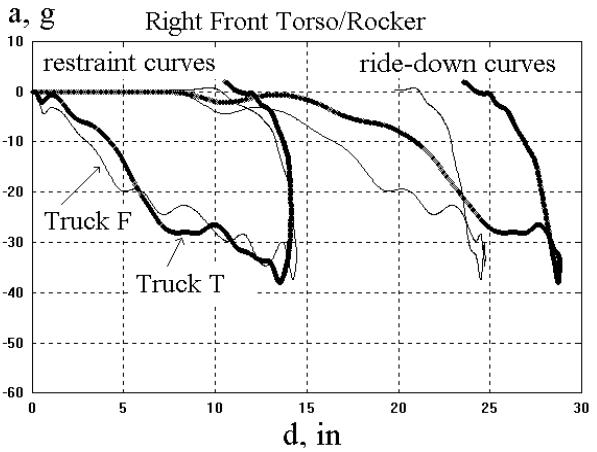

Fig. 3.43 Right Front Occupant Restraint and Ridedown Curves of Both Trucks F and T

Table 3.8 Occupant Ridedown Efficiencies in Both Trucks

Truck	η, Ridedown Efficiency	
	Left Front	Right Front
F	47 %	41 %
T	47 %	44 %

Note that the ridedown efficiency does not have a direct bearing on occupant deceleration. Higher ridedown efficiency indicates that the restraint energy is lower. However, even though the restraint energy is the same in two tests, the occupant response such as chest deceleration may be still different. This difference depends on the nature of the restraint force-deflection characteristics as shown by the two left front occupant restraint curves in Fig. 3.42.

3.5.4.2 *Truck T Response Prediction with Truck F Restraints*

The restraint transfer functions (T.F.) for the left and right front occupants in the Truck F test, shown in Fig. 3.44, have been computed using the respective vehicle rocker panel and occupant deceleration data.

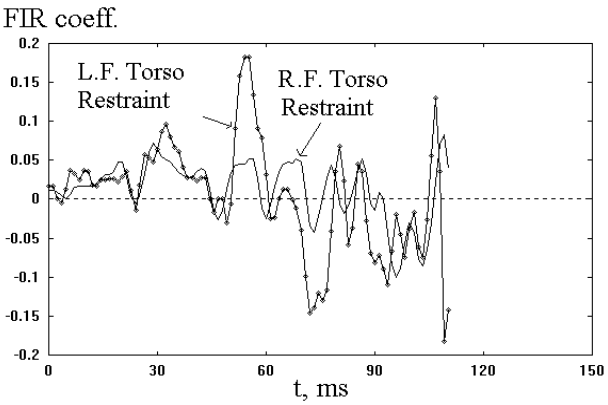

Fig. 3.44 Transfer Functions of Left and Right Torso Restraints of Truck F

The duration of the crash pulse is set at 150 ms where the data step is 0.08 ms. The number of bites used for averaging is 15, which yields a new data step of 1.2 ms. The total number of points used in the T.F. computation is then equal to N = 125 points. The number of FIR coefficients, M, is set at 75% of N. Therefore, M is equal to 93 points and the corresponding duration of the FIR coefficients is equal to 75% of 150 ms which is 112 ms as shown in Fig. 3.44. Note that the FIR coefficients of the left front torso restraint between 55 and 70 ms are higher than those of the right front restraint. The difference reflects the effects of steering column loading.

In predicting the response of the left front occupant response in Truck T, the left rocker deceleration at B-pillar of Truck T is used as the input, X, to the restraint transfer function of Truck F. This yields the predicted left front occupant response $\hat{y}$ in Truck T, as shown in Fig. 3.45. The predicted left front torso peak deceleration for Truck T using Truck F restraint is about 6 g higher than that of the original Truck T test. The higher predicted Truck T torso deceleration is attributed to the upward rotation and higher stroking load of the steering column which was present in the Truck F test but not in the Truck T test.

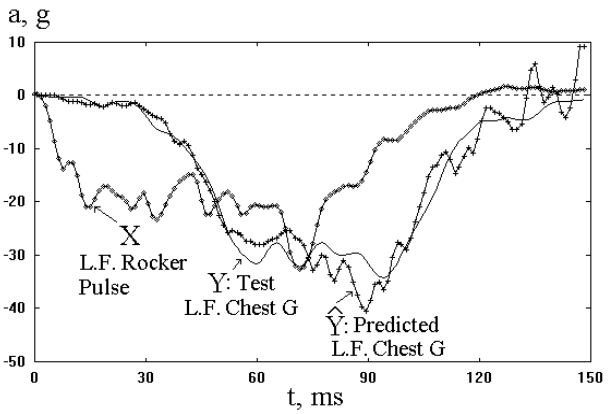

Fig. 3.45 Prediction of LF Chest g in Truck T using LF T.F. from Truck F

The effect of steering column loading on the occupant response can be better understood by comparing the driver and passenger responses. In the passenger side (right front), only the air bag inflator is stored inside the instrument panel. In predicting the right front occupant response for Truck T, the right rocker deceleration at the B-pillar is used as the input, X, to the respective transfer function and yields the predicted right front occupant response, $\hat{y}$, as shown in Fig. 3.46.

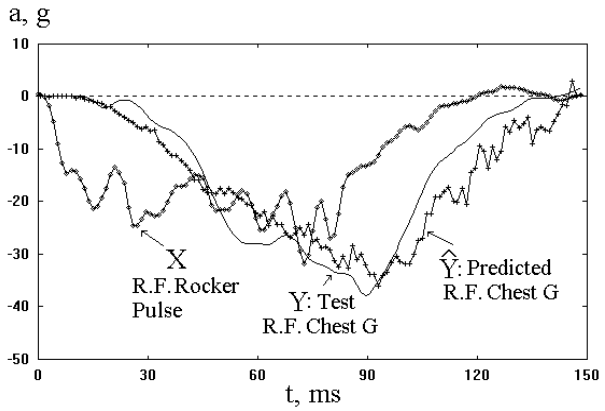

Fig. 3.46 Prediction of Right Front Chest G in Truck T using RF T.F. from Truck F

The use of Truck F restraint for the right front occupant in the Truck T test yields almost the same overall occupant response as in the original Truck T test. This agreement in the response prediction is due to the absence of the external impulse, such as the impact by the steering column on the occupant.

As illustrated in Fig. 3.2, there exists a dynamic system which has multiple transfer functions. To predict the system output, the input and output data for the two subsystems need to be obtained to compute the respective transfer function. In the case where a system consists of the air bag and belt restraint subsystem, and the steering column subsystem, both transfer functions need to be evaluated to make a better response prediction.

3.6 EFFECT OF SLED AND BARRIER PULSES ON OCCUPANT RESPONSE

In a laboratory test where a Hyge sled is used, the acceleration is imparted to the sled by the impactor. The sled test pulse is designed to duplicate the crash pulse recorded at the vehicle compartment in a test. Fig. 3.47 shows a crash pulse for a full-size sedan in a 35 mph barrier test. The sled test pulse approximates the barrier pulse reasonably well up to about 25 ms. Thereafter, the sled pulse missed the peaks of the double-hump in the barrier test deceleration.

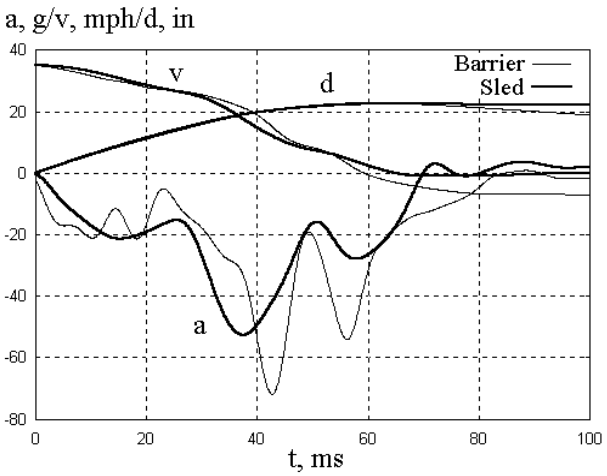

Fig. 3.47 Kinematics of Barrier and Sled Test Pulses with Initial Velocity

For comparison with the vehicle kinematics in a barrier test, the sled test pulse is integrated with an initial velocity of 35 mph. As shown in Fig. 3.47, even though the barrier and sled crash pulses do not match well, they do yield the same dynamic crush. The dynamic crush in the barrier test is 22.7 inches at 63 ms, and the centroid time is computed to be 37 ms. Since the relative centroid location is $37/63 = 0.59 > 0.5$, the test pulse is rear loaded.

Similarly, for comparison with the sled impact kinematics, the barrier test pulse is integrated with zero initial velocity. Both the velocity and displacement curves of the barrier and sled tests shown in Fig. 3.48 match very closely in the region of the double-hump acceleration.

Despite the similarity in both velocity and displacement responses, the difference in crash pulse shape between the barrier and sled test conditions may result in a different occupant response. To investigate the effect of the crash pulse shape on the occupant response, the transfer function of the restraint system in the barrier test is computed and then the occupant response due to the sled test pulse is predicted.

The left front (driver) occupant chest deceleration in the barrier test is shown in Fig. 3.49. Using the accelerometer data measured at the vehicle compartment and occupant torso, the FIR coefficients of the transfer function were computed, as shown in Fig. 3.50.

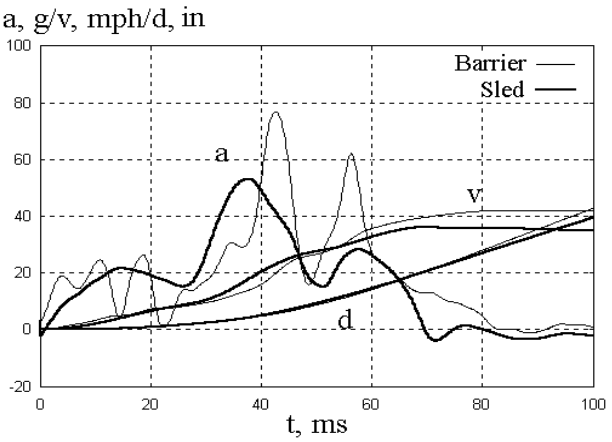

Fig. 3.48 Kinematics of Barrier and Sled Test Pulses without Initial Velocity

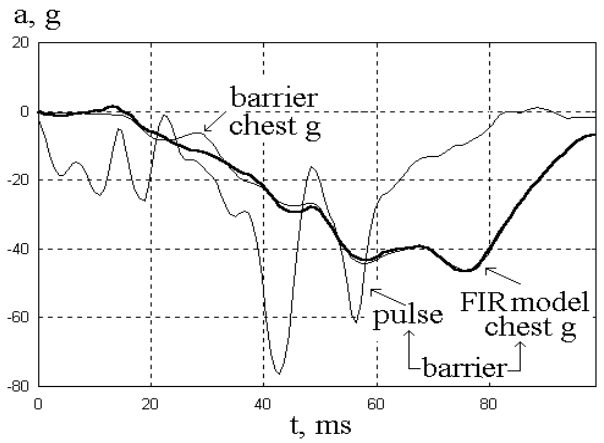

Fig. 3.49 Chest g Comparisons between the FIR Model and Barrier Test

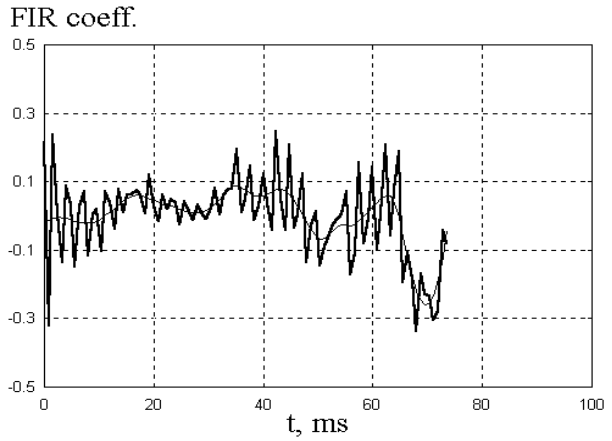

Fig. 3.50 A Driver Restraint Transfer Function in a 35 mph Sedan-Barrier Test

To validate the restraint FIR Model, the vehicle rocker crash pulse is convoluted with the restraint FIR coefficients, and the predicted FIR model chest g is overlapped with the barrier test chest g, as shown in Fig. 3.49. Since the test and predicted chest responses are almost identical, the FIR model is considered to be valid.

The validated restraint transfer function is used to predict the driver chest deceleration due to a sled test pulse. The predicted driver chest deceleration, shown in Fig. 3.51, has a double-hump, where the first hump of 53 g is larger than the second of 52 g, while the driver chest deceleration in the barrier test has peak magnitudes of 43 and 45 g in its first and second humps, respectively. Regarding the occupant response, the sled test pulse is more severe than the barrier test pulse. This is attributed to the difference in the crash pulse shape since the transient velocity and displacement profiles between the barrier and sled test pulses, shown in Figs 3.47 and 3.48, are about the same.

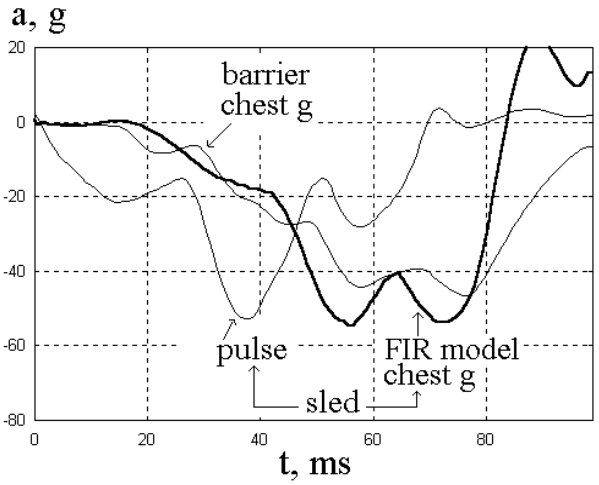

Fig. 3.51 Barrier and FIR Model Chest g

3.7 OTHER APPLICATIONS

1. *Development of restraint systems using sled tests:* The approach here is to obtain torso/knee restraint transfer functions from laboratory sled or component tests and then predict the occupant responses by convoluting the respective restraint transfer functions (such as torso restraint or knee bolster) with the vehicle crash pulse obtained from the full frontal barrier tests.
2. *Prediction of head deceleration with neck transfer function*: The torso deceleration from another test (the input) is convoluted with the neck transfer function to yield the head deceleration. The underlying assumption is that the environmental conditions (such as dummy, belts, and air bag restraint systems) where the neck transfer function is obtained should be similar to those where the prediction is to be made.
3. *Prediction of fuel tank motion in an angular barrier impact*: Fig. 3.52 shows a schematic of a truck with a fuel tank strapped to the left side frame rail. Assume that in a perpendicular barrier impact, there is enough friction between the fuel tank and the two straps that both fuel tank and straps move as one unit. Then, the fuel tank/strap transfer function can be obtained by using the left frame rail and fuel tank strap accelerometer data as input and output, respectively. To predict the fuel tank longitudinal motion in a 30° angular barrier at 31 mph test as shown in Fig. 3.52, the fuel tank/strap transfer function is convoluted with the left frame rail longitudinal accelerometer data. The fuel tank relative displacement in a 35 mph perpendicular barrier test is about 2 inches and in the right angular barrier 30°, 1.8 inches.

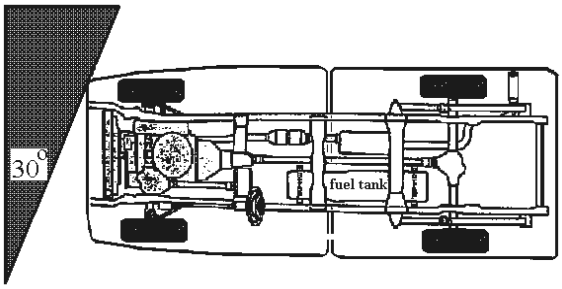

Fig. 3.52 31 MPH 30º Right Angular Barrier Test

3.8 RESPONSE INVERSE FILTERING (RIF)

In this section, a sequence of matrix operations is utilized to convert a set of finite impulse response (FIR) coefficients into a response inverse filtering (RIF) matrix for reverse prediction [5,6]. To predict the input from output, the use of RIF is more efficient and accurate than creating a new set of FIR. In the previous section, a method of obtaining the FIR coefficients, h(m), based on the input and output data sets has been presented. The application of FIR coefficients is two-fold: one is to predict a new output response given a new input excitation, and the other is to characterize the dynamic property of the system or component by the stiffness and damping extracted from a filtered FIR function.

The use of the time convolution method and least square error to compute the FIR coefficients, h(m), is based on the input and output data, x(n) and y(n), respectively. In theory, the reverse process of finding a new h(m) with x(n) and y(n) interchanged should still work. However, in practice, x(n) and y(n) are not independent sets of numbers. Rather, they are related to the properties of the component which connects them. For example, in a component test on a body mount of a truck, x(n) is the frame (input) accelerometer data on the impacting side, and y(n) is the body (output) accelerometer data measured on the non-impacting side. The output response y(n) is therefore the filtered output of the body mount subjected to an input excitation. The magnitude and frequency content of the output depend on the stiffness and damping properties of the body mount.

For instance, given the crash pulse of a frame rail of a truck in a frontal crash test, the response of the body or cab can be predicted with high accuracy with a body mount transfer function. The transfer function thus obtained serves as a low pass filter which filters out the high frequency components of the frame pulse.

If the convolution process is reversed, such that given a body crash pulse as input and the frame rail crash pulse as output, a set of FIR coefficients can also be derived. However, the coefficients thus obtained become very large and act like an amplifier which yields a high frequency and magnitude in the output.

In this section, the convolution process is utilized to obtain the FIR transfer function for the forward prediction. The process of transforming FIR into a RIF is then described. The application of RIF in predicting a frame pulse based on a predetermined optimal (target setting) body pulse is presented.

3.8.1 Forward Prediction by Finite Impulse Response (FIR)

The convolution equation shown in Eq. (3.3) is repeated and shown in Eq. (3.19). The set of finite impulse response (FIR) coefficients is represented by a variable which is a one-dimensional array, h(n), where n ranges from 1 to M, and M is the number of FIR coefficients.

$$\hat{y}(n) = \sum_{m=1}^{M} h(m)\, x(n-m) \tag{3.19}$$

The convolution operation shown can be expressed in matrix notation, as shown in Eq. (3.20). The input and output data sets are represented by column matrices [X] and [Y], respectively. The transfer function [H] is defined by a set of FIR coefficients, which are computed by the convolution process and least square error approach as described in Section 3.2.2.

$$
\begin{aligned}
&[Y]^{N\times 1} = [H]^{N\times N}\,[X]^{N\times 1}, \quad \textit{where}\\
&[H] \textit{ is a banded matrix with}\\
&H_{i,j}=0, \quad \textit{for} \quad i > j+M-1, \quad j > i,\\
&\textit{where} \quad N > M\\
&N\text{: number of discrete points,}\\
&M\text{: number of FIR coefficients}
\end{aligned}
\tag{3.20}
$$

As an example of constructing the matrix [H] from the one dimensional h(m), let N be nine and M, five. A square matrix of N by N or 9 × 9 is constructed by sliding the FIR coefficient h(1) to the first row, followed by h(1), h(2) to the second row, and so forth. as shown in Eq. (3.21). Matrix [H] is a banded matrix as shown in a 3-dimensional plot in Fig. 3.53. It has a banded section below the main diagonal that is distinguished from the other sections of the matrix where the elements are zeros.

$$N = 9, \quad M = 5: \quad [H]^{N\times N}\ [X]^{N\times 1} = [Y]^{N\times 1}$$

$$
\begin{bmatrix}
h(1) & .000 & .000 & .000 & .000 & .000 & .000 & .000 & .000\\
h(2) & h(1) & .000 & .000 & .000 & .000 & .000 & .000 & .000\\
h(3) & h(2) & h(1) & .000 & .000 & .000 & .000 & .000 & .000\\
h(4) & h(3) & h(2) & h(1) & .000 & .000 & .000 & .000 & .000\\
h(5) & h(4) & h(3) & h(2) & h(1) & 000 & .000 & .000 & .000\\
.000 & h(5) & h(4) & h(3) & h(2) & h(1) & .000 & .000 & .000\\
.000 & .000 & h(5) & h(4) & h(3) & h(2) & h(1) & .000 & .000\\
.000 & .000 & .000 & h(5) & h(4) & h(3) & h(2) & h(1) & .000\\
.000 & .000 & .000 & .000 & h(5) & h(4) & h(3) & h(2) & h(1)
\end{bmatrix}
\begin{bmatrix} X(1)\\ X(2)\\ X(3)\\ X(4)\\ X(5)\\ X(6)\\ X(7)\\ X(8)\\ X(9) \end{bmatrix}
=
\begin{bmatrix} Y(1)\\ Y(2)\\ Y(3)\\ Y(4)\\ Y(5)\\ Y(6)\\ Y(7)\\ Y(8)\\ Y(9) \end{bmatrix}
\tag{3.21}
$$

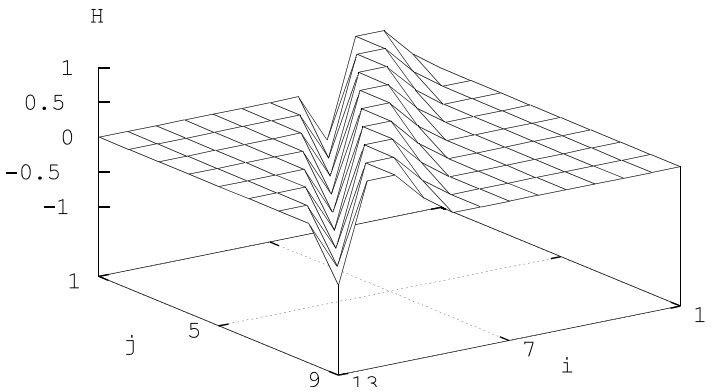

Fig. 3.53 3D Plot of Transfer Function [H] from Body to Frame

The predicted [Y] is computed by multiplying matrices [H] and [X]. The multiplication process is identical to that using the sum of products of pairs of h(m) and x(n−m) shown in Eq. (3.11).

The matrix operation of [H][X] = [Y], shown in Eq. (3.21), cannot be used to compute h(m), even if input x and output y data sets are available. In the example, shown in Eqs. (3.10) and (3.11) in Section 3.2.4, the values of h(1) for both cases where M = 5 and M = 9 are zeros. Since the main diagonal elements in the respective [H] matrix in Eq. (3.21) are zeros, the determinants for both [H] are zeros and the matrices [H] are singular and not invertible.

3.8.2 Inverse Filtering (IF)

With the FIR coefficients generated from the convolution and least square error approaches, the square matrix of the [H] transfer function is modified to one non-square matrix, followed by a sequence of matrix operation to produce an expanded square matrix, [IF], an inverse filtering matrix.

Matrix [H] is expanded from the order of N × N to the that of [N+M−1] × N. By sliding FIR coefficients to the ensuing row one column at a time, the last coefficient h(M) then appears in the last element of the [H] matrix. at row (N+M−1) and column (N) as shown in Eq. (3.22).

$$N = 9,\quad M = 5,\quad (N+M-1) = 13:\qquad [H]^{(N+M-1)\times N}\,[X]^{N\times 1} = [Y]^{(N+M-1)\times 1}$$

$$\begin{bmatrix}
h(1) & .000 & .000 & .000 & .000 & .000 & .000 & .000 & .000 \\
h(2) & h(1) & .000 & .000 & .000 & .000 & .000 & .000 & .000 \\
h(3) & h(2) & h(1) & .000 & .000 & .000 & .000 & .000 & .000 \\
h(4) & h(3) & h(2) & h(1) & .000 & .000 & .000 & .000 & .000 \\
h(5) & h(4) & h(3) & h(2) & h(1) & .000 & .000 & .000 & .000 \\
.000 & h(5) & h(4) & h(3) & h(2) & h(1) & .000 & .000 & .000 \\
.000 & .000 & h(5) & h(4) & h(3) & h(2) & h(1) & .000 & .000 \\
.000 & .000 & .000 & h(5) & h(4) & h(3) & h(2) & h(1) & .000 \\
.000 & .000 & .000 & .000 & h(5) & h(4) & h(3) & h(2) & h(1) \\
.000 & .000 & .000 & .000 & .000 & h(5) & h(4) & h(3) & h(2) \\
.000 & .000 & .000 & .000 & .000 & .000 & h(5) & h(4) & h(3) \\
.000 & .000 & .000 & .000 & .000 & .000 & .000 & h(5) & h(4) \\
.000 & .000 & .000 & .000 & .000 & .000 & .000 & .000 & h(5)
\end{bmatrix}
\begin{bmatrix} X(1) \\ X(2) \\ X(3) \\ X(4) \\ X(5) \\ X(6) \\ X(7) \\ X(8) \\ X(9) \end{bmatrix}
=
\begin{bmatrix} Y(1) \\ Y(2) \\ Y(3) \\ Y(4) \\ Y(5) \\ Y(6) \\ Y(7) \\ Y(8) \\ Y(9) \\ Y(10) \\ Y(11) \\ Y(12) \\ Y(13) \end{bmatrix}
\tag{3.22}$$

To visualize the matrix [H] of 13 × 9, it is plotted as a 3D surface and is shown in Fig. 3.53. The numbers on the axes i and j represent the row and column indices in [H]. The sections where the peaks and valleys are located represent the width of the banded matrix.

The matrix multiplication [H] [X] shown in Eq. (3.22) yields a column matrix [Y] with an order of (N+M−1)×1. Due to the increase in the rows of matrix [H] by M−1, the number of [Y] elements is also increased by M−1. For the previous example in Table 3.4 in Section 3.2.4, where M = 5 and N = 9, then N+M−1 = 13. In this example, the FIR coefficients are h(1) = 0., h(2) = 0.293, h(3) = h(4) = 0.707, and h(5) = −0.707.

Since the newly developed matrix [H] is a non-square matrix, it can not be inverted. Therefore, the transformation $[X] = [H]^{-1}[Y]$ can not be used to predict the input [X] from the output [Y]. However, with several matrix operations on the matrix [H], an inverse filtering matrix, [IF], can be developed to perform the transformation [X] = [IF][Y].

Eq. (3.23) shows the derivation of [IF]. It starts out with the normal transformation of [X] into [Y] by using the forward transformation [H] shown by (1) of Eq. (3.23) followed by the multiplication of the transpose matrix of [H] to yield a square matrix shown by (2) of Eq. (3.23). The inverse

filtering matrix [IF] of N×(N+M−1) order shown in (4) of Eq. (3.23) is a non-square matrix and is a product of three matrices. However, it serves to transfer the output [Y] into input [X].

$$[H][X] = [Y] \quad \ldots\ldots\ldots\ldots\ldots\ldots \quad (1)$$

The order of the matrices are:

$[H]$: $(N+M-1)\times N$

$[X]$: $N\times 1$,

$[Y]$: $(N+M-1)\times 1$

Multiplying both sides of (6) *by the transpose of* $[H]$,

$$[H]^T[H][X] = [H]^T[Y] \quad \ldots\ldots\ldots\ldots \quad (2)$$

here $[H]^T[H]$ *is a square matrix with an order of* $N\times N$, *it can then be inverted, provided the matrix is non-singular.* (3.23)

Multiplying both sides of (7) *by* $[H]^T[H]^{-1}$, *one gets*

$$[X] = ([H]^T[H])^{-1}[H]^T[Y] \quad \ldots\ldots\ldots\ldots \quad (3)$$

Let $[IF]$ *be the inverse filtering matrix as follows*

$$[IF] = ([H]^T[H])^{-1}[H]^T \quad \ldots\ldots\ldots\ldots \quad (4)$$

then (8) *becomes*

$$[X]^{N\times 1} = [IF]^{N\times(N+M-1)}\,[Y]^{(N+M-1)\times 1} \quad \ldots\ldots \quad (5)$$

3.8.3 Crash Pulse Prediction using FIR and RIF

Using a set of crash pulses, input [X] and output [Y], three transfer functions are to be developed and compared for their validation accuracy. These are (1) FIR Forward Prediction: Transferring [X] to [Y] with [H], (2) FIR Backward Prediction: Transferring [Y] to [X] with [H]′, and (3) RIF Backward Prediction: Transferring [Y] to [X] with [IF] (an inverse filtering matrix).

3.8.3.1 *Transferring [X] to [Y] with [H].*

The accelerometer data of the front frame rail and the rocker panel at B-pillar of a truck in a 31 mph rigid barrier test are shown in Fig. 3.54. Curve x (thin solid line) indicates the frame crash pulse and curve y (thin dashed line), the rocker (body) pulse.

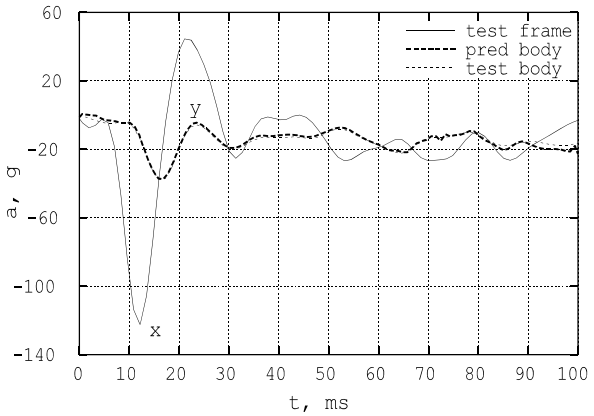

Fig. 3.54 Validation on [H]: Transferring Frame (x) Pulse to Body (y) Pulse

Using the time convolution and least square error method, the transfer function [H] can be computed. This is shown in Fig. 3.55. The 3-D surface mapping is the plot of non-zero matrix

elements of the banded matrix [H] transferring [X] to [Y]. To validate the matrix [H], the predicted [Y] computed by convoluting [H] with [X] is shown as a heavy dashed line in Fig. 3.54. Since the predicted output is almost identical to the output even though M is only about 83% of N, the transfer function [H] is considered to be accurate and validated.

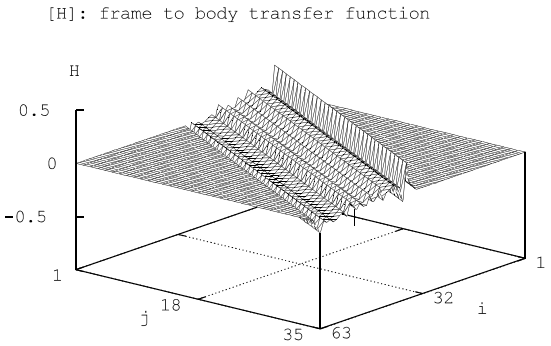

Fig. 3.55 [H] (x⇒y): N=35, M=29, Δt=2.8ms

3.8.3.2 *Transfer [Y] to [X] with [H]′*

Since [H], used in transferring [X] of the frame pulse to [Y] of the body pulse, is a non-square matrix, it cannot be inverted directly. However, using the same test data and the time convolution principle with the least square error approach, a transfer function [H]′ transferring [Y] of body pulse to [X] of frame pulse can then be derived.

Curve x (thick solid line) in Fig. 3.56 is the test frame crash pulse and curve y (thin solid line), the test rocker (body) pulse. To validate the matrix [H]′, the predicted [X] evaluated by convoluting [H] with [Y] is shown as a heavy dotted line in Fig. 3.56. The test frame pulse before 10 ms is not predicted by the transfer function [H]′ to the satisfaction of frame engineers although the prediction is fairly accurate afterwards.

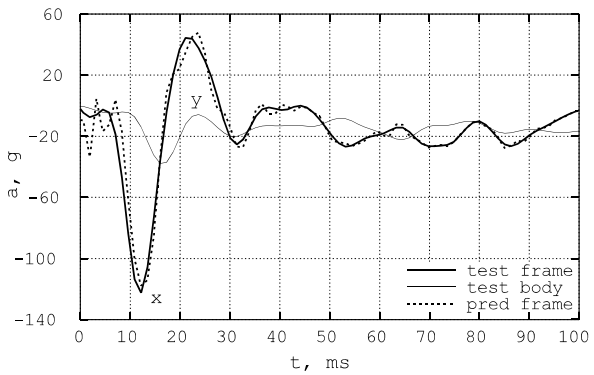

Fig. 3.56 Validation on [H]′: Transferring Body (y) Pulse to Frame (x) Pulse

Shown in Fig. 3.57 is the 3-D surface plot of the non-zero matrix elements of the banded matrix [H]′ transferring [Y] to [X].

Comparing the two 3-D surface plots for the two cases, transferring [X] to [Y] using [H] and transferring [Y] to [X] using [H]′, there are some distinct differences between the two transfer functions. The surface slopes are opposite to each other and the magnitudes of the FIR coefficients are about 1,000 times different. The transfer function [H]′ having very large FIR coefficients acts like an amplifier with high oscillations.

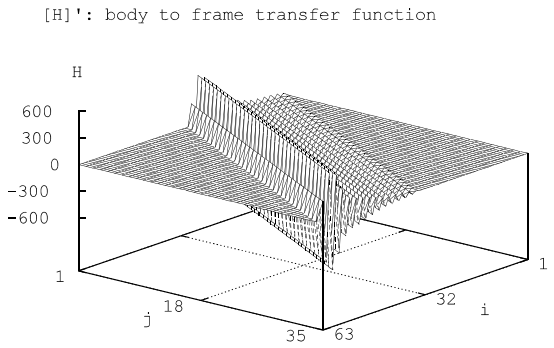

Fig. 3.57 [H]′ (y⇒x): N=35, M=29, Δt=2.8ms

3.8.3.3 *Transferring [Y] to [X] using [IF]*

Having obtained the forward transfer function matrix [H], which transfers the input [X] to the output [Y], the inverse filtering matrix [IF] obtained in Eq. (3.23) can then be used to transfer [Y] to [X]. The previous accelerometer data sets from the truck crash test are used to derive [IF]. Curve x (thin solid line) shown in Fig. 3.58 indicates the frame crash pulse and curve y (thin dash line), the rocker (body) pulse. To validate the matrix [IF], the predicted [X], evaluated by convoluting [IF] with [Y], is shown as a thin dotted line in Fig. 3.58. The test frame pulse, having large impulses before 30 ms, is practically identical to the predicted frame pulse [X]. Although the prediction is a little bit off after 30 ms, this is not a concern because the variation in vehicle frame crush from the second integral of the frame pulse is about 5% (1 inch difference out of dynamic crush of 20 inches), which is less than the test variation of about 10% for a high speed 31 mph crash test.

Shown in Fig. 3.59 is the 3-D surface plot of [IF], the inverse filtering transfer function. Note that the row and column orders have been reversed in [IF], compared to that in [H], shown in Fig. 3.55. This is because [H] is a forward transfer function, while [IF] is a backward transfer function. The 3-D surface plot shows that [IF] is not a banded matrix and that the magnitudes of the matrix elements

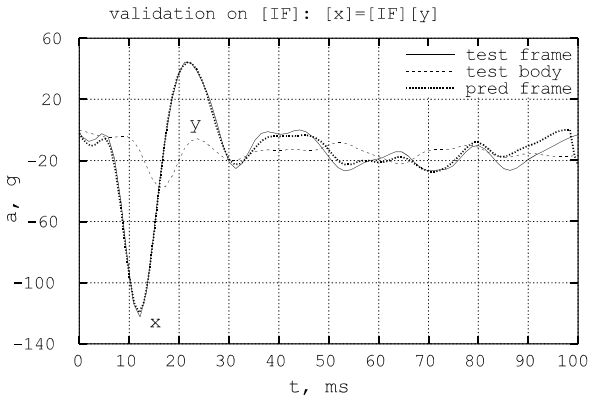

Fig. 3.58 Validation on [IF], N=93, M=80, Δt=1.28ms

appear to spread out through the entire matrix.

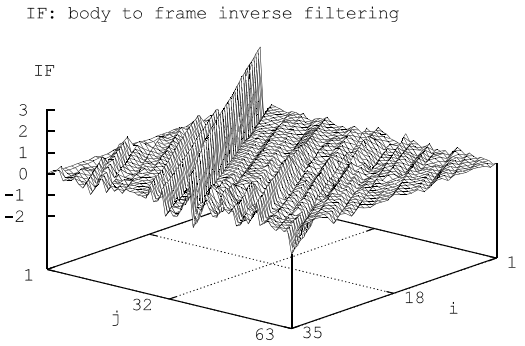

Fig. 3.59 [IF] Function: N=35, M=29, Δt=2.8ms

3.8.4 RIF Application in Frame Pulse Prediction

Case I: Target Body Pulse with High Constant Deceleration and Short Duration

The [IF] transfer function derived in the previous section and shown in Fig. 3.59 is used to predict the frame response requirement [X], given a desired target pulse at the vehicle compartment (body), [Y]. The target body pulse is predetermined in the early design stage to be the "optimal" pulse that would offer a better occupant protection in a 31 mph truck barrier crash test. The thin dotted line shown in Fig. 3.60 is the ideal target body pulse with an overshot ramp-up followed by a constant deceleration of – 17 g. The predicted frame pulse [X] = [IF] [Y] is shown as a thick solid line in Fig. 3.60.

Observing the frame and body pulses in Fig. 3.60, it is found, as expected, that the frequency components and magnitude of the frame pulse are higher than those of the target body pulse. The magnitude of the predicted frame pulse at the onset (in the first 5 ms of the frame crash) is higher in the prediction than that in the test (see Fig. 3.58).

This is due to the fact that the ramp-up portion of the target body pulse in both cases is higher which results in the higher ramp-up frame pulse. If the target body pulse in the beginning of the crash is a haversine, the predicted frame pulse would also be a haversine, just like those in the test shown in Fig. 3.58.

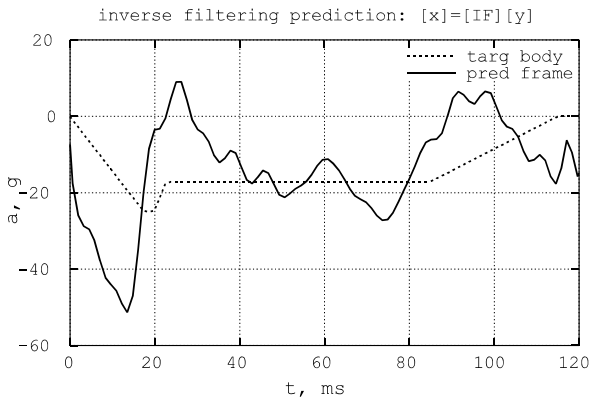

Fig. 3.60 Frame Pulse by Inverse Filtering on the Target Body Pulse #1 (Case I)

To compare the target vehicle frame and body crushes with those of the test, four crash pulses were double-integrated with an initial velocity of 31 mph. Fig. 3.61 compares the body and frame displacements between the test pulse (thin dashed line for frame, thick dotted line for body) and target pulse (thick solid line for body, thin line for frame). The results show a consistent trend for both target pulse and test pulse. That is, the body displacement is greater than the frame displacement.

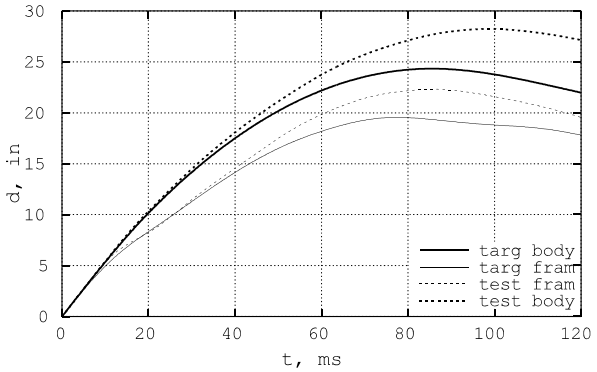

Fig. 3.61 Body-Frame Displacements of Test and Target Body Pulse #1 (Case I)

Case II: Target Body Pulse with Low Constant Deceleration

To check for the sensitivity of the body constant deceleration level on the frame pulse prediction, the magnitude of the constant deceleration is reduced from 17 g to 13 g, as shown in Fig. 3.62. In order to maintain the same velocity change of 31 mph in the deformation phase, the timing at rebound is increased from 84 ms to 104 ms.

Using the sequence of matrix operations on FIR, [IF] transfer function can then be computed. The predicted frame pulse is shown in Fig. 3.62. As expected, the predicted frame pulse before the ramp-up time of 20 ms on the body remains the same as in Case I. Since the given target body pulse is softer in Case II (13 g) than in Case I (17 g) and the transfer function of the body mount is the same in both cases, the predicted frame crush for Case II (24.5 inches at 106 ms on the thin solid curve in Fig. 3.63) should be larger than that for Case I (19.5 inches at 77 ms on the thin solid curve in Fig. 3.61).

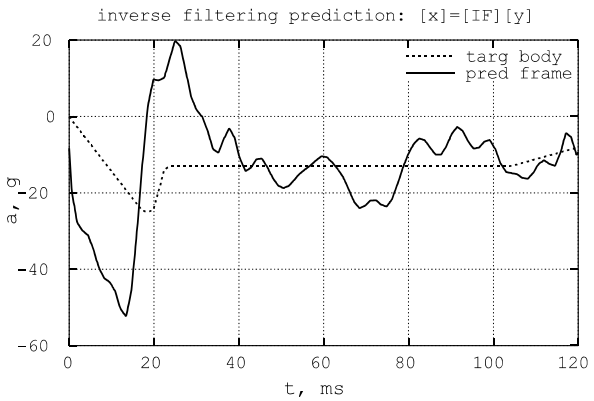

Fig. 3.62 Frame Pulse by Inverse Filtering on the Target Body Pulse #2 (Case II)

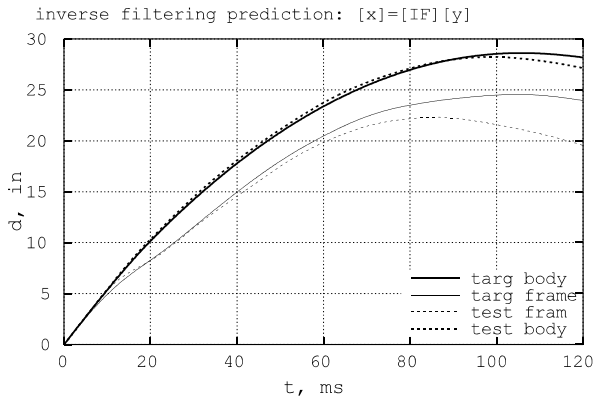

Fig. 3.63 Body-Frame Displacements of Test and Target Body Pulse #2 (Case II)

3.9 REFERENCES

1. Eppinger, R. and Chan, H.S., "Thoracic Injury Prediction via Digital Convolution Theory," SAE Paper No. 811010, Proceeding, SAE-P-97, Society of Automotive Engineering, 1981.
2. Chapra, S.C., Canale, R.P., "Numerical Methods for Engineers," McGraw-Hill, 1985.
3. Huang, M., "On Body Mount Crash Characteristics," SAE paper No. 1999-01-3186, International Body Engineering Conference and Exposition, Detroit, Michigan, September 28–30, 1999. Also in Journal of Passenger Cars, SAE 1999 Transactions, Section 6, pp.3330–3342.
4. Kang, S., Huang, M., Peng, J., Yang, H., and Culbertson, P., "Use of Body Mount Stiffness and Damping in CAE Crash Modeling," SAE Paper 2000-01-0120, SAE Congress, March, 2000.
5. Solnes, J., "Stochastic Processes and Random Vibrations, Theory and Practice," John Wiley & Sons,1997.
6. Huang, M. and Jayachandran, R., "Crash Pulse Prediction via Inverse Filtering," SAE paper No. 2001-01-3110, SAE Congress, March, 2002.

CHAPTER 4

BASICS OF IMPACT AND EXCITATION MODELING

4.1 INTRODUCTION

Any crash dynamic event involves impact and/or excitation. The mechanisms of impact and excitation for full vehicle crash testing and laboratory Hyge sled testing are covered in this chapter. A simple occupant ridedown criterion using kinematic relationships is formulated. This criterion specifies the minimum vehicle crush space needed when a given occupant free travel space in the compartment is specified. During the ridedown, the vehicle undergoes a deformation process which is the first collision of the event, followed by the second collision where the occupant travels and contacts the vehicle interior surface or restraint. It will be shown that for a satisfactory ridedown, the relative contact speed is always less than the initial vehicle to rigid barrier impact speed.

Using a simple occupant vehicle model, the ridedown mechanism is described mathematically and the computation of the ridedown efficiency is shown in closed-form solutions. Consequently, the sensitivity of the occupant response to the vehicle structure and restraint parameters can be examined. Regression analysis of the test data confirms the analytical trend prediction.

Taking advantage of closed-form solutions, the effects of physical parameters on model output responses can be evaluated. To illustrate the application of the various mathematical models in analyzing the vehicle impact and sled excitation dynamics, the basic concepts and solution techniques used in deriving solutions of the models are presented. To the extent possible, closed-form solution techniques are utilized. The use of interior space or restraint slack in the modeling requires a time shift which makes the closed-form approach more complex. However, once the slack is taken out during impact, the analysis of the occupant response in the restraint coupling phase is the same as the model without slack.

The mathematical dynamic models, consisting of springs and dampers in various combinations, are used in analyzing the VOR (vehicle, occupant, and restraint) interaction in an impact (such as vehicle to rigid barrier and vehicle to vehicle tests) and/or excitation (such as the Hyge sled test) conditions. Case studies involving two-parameter and three-parameter modeling for the transient analysis are illustrated.

The occupant response performance in a vehicle subjected to various simple crash pulses are analyzed. Given the same dynamic crush, the relative centroid location and the residual deformation determine the shapes of the approximated crash pulses, such as ESW (equivalent square wave), TESW (tipped equivalent square wave), and halfsine wave. The correlation between the occupant response and the relative centroid location of a crash pulse can then be established.

4.2 IMPACT AND EXCITATION – RIGID BARRIER AND HYGE SLED TESTS

In a rigid barrier test, the vehicle is subjected to a direct impact, and the occupant is then excited by the crash pulse of the passenger compartment. It is often more cost effective to test certain components (such as air bags, belt and steering column restraint systems, and instrument panels) in a Hyge sled test rather than a rigid barrier test. In a Hyge sled test, the sled is impacted by an accelerator which produces a sled test pulse similar to the barrier crash pulse. The occupant is subsequently excited by the sled pulse. Since deceleration forward in the barrier test is equal to acceleration backward in the sled test, the effect of component design changes on the occupant responses can then be quickly evaluated using the sled test setup.

The kinematic relationships (deceleration, velocity, displacement) between the fixed barrier (a,v,d) and sled ($\ddot{\alpha}$,$\dot{\alpha}$,α) tests are noted below and illustrated in Figs. 4.1 and 4.2.

1. The sled pulse is the negative of the vehicle barrier crash pulse ($\ddot{\alpha}$ = -a)
2. The sled velocity profile, $\dot{\alpha}$ (shown by the heavy curve in Fig. 4.1), is a barrier velocity curve shifted by an amount of the initial barrier impact velocity, v_o. At t_m, the time of dynamic

crush, the sled velocity is equal to v_o. The magnitude of velocity change between time zero and t_m for both barrier and sled tests is v_o.

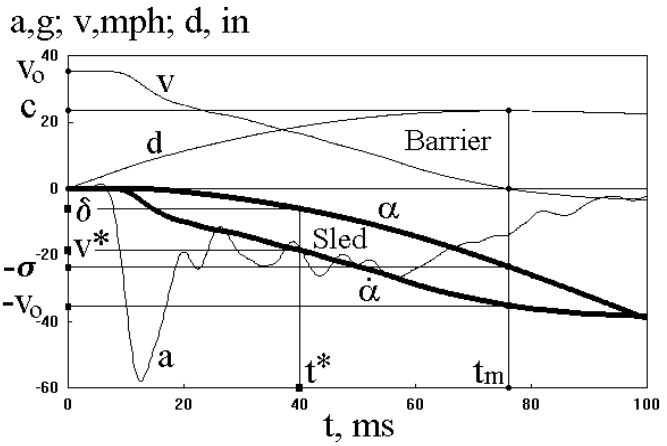

Fig. 4.1 Truck Kinematics in 35 mph Barrier and Sled Tests

3. The sled displacement, α (shown by the heavy curve in Fig. 4.2), is equal to $v_o t - d$ (free-flying occupant absolute displacement minus vehicle displacement). σ (sled displacement at t_m) is equal to $v_o t_m - c$. Shown in Fig. 4.2 is an area enclosed by the vertical lines through t_o, and t_m and horizontal lines through $v = 0$ and $v = -v_o$. At any time t, the rectangular area equals $v_o t$ and is the sum of the sled displacement (upper right portion of the area) and vehicle crush (lower left portion of the area).

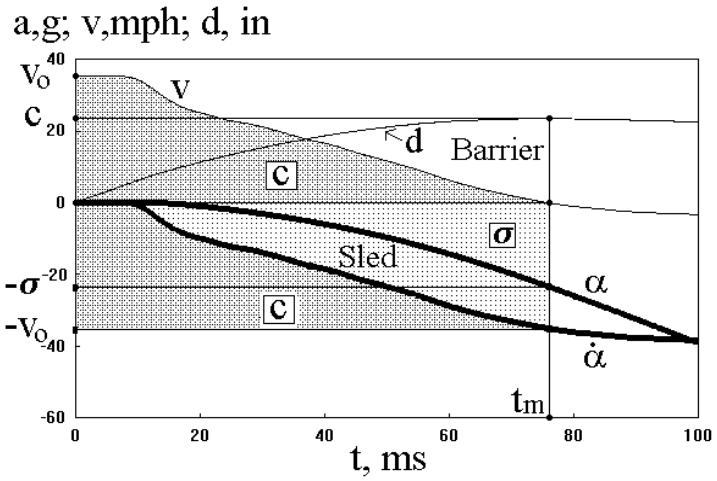

Fig. 4.2 Displacements of a Truck in 35 mph Barrier and Sled Tests

4. The vehicle dynamic crush (c) equals the sled displacement (σ at t_m) if and only if the crash pulse has a relative centroid location (t_c / t_m) of 0.5. The proof of this is given in Eq. (4.1).

Define:

c: *vehicle dynamic crush*, t_m: *time of* c, t_c: *centroid time*,

σ: *sled displacement at* t_m, v_o: *vehicle impact velcocity*,

$$\because \quad t_c = \frac{c}{v_o},$$

$$\therefore \quad \frac{t_c}{t_m} = \frac{c}{v_o t_m} = \frac{c}{c+\sigma} \tag{4.1}$$

for $c = \sigma$, *then*

$$\frac{t_c}{t_m} = \frac{1}{2}$$

In a truck-to-fixed barrier crash at 35 mph, the crash pulse, a, at the left rocker panel at the B-post, has been shown in Fig. 4.1. The vehicle transient velocity and displacement in the barrier test are shown as curves v and d, respectively. The sled transient velocity and displacement are shown as curves $\dot{\alpha}$ and α, respectively. The dynamic crush, c, is 23 inches at t_m of 75 ms. The sum of the sled displacement and vehicle dynamic crush (σ and c) is equal to $v_o t_m$, 46 inches. This particular crash pulse has a centroid time t_c of 37.5 ms, or $t_c = c/v_o = 23$ inches $/(35 \times 17.6$ in/sec$) = .0374$ sec; the relative centroid location, t_c / t_m, is $.0374/.075 = .5$. Therefore, the sled displacement at t_m is equal to the dynamic crush.

There exists a condition where a symmetrical crash pulse, such as a halfsine or havesine pulse, has a dynamic crush equal to the sled displacement at t_m. The condition is that the initial impact velocity must be equal to the velocity change (area under the entire curve) of the crash pulse. The dynamic analysis of such a crash pulse is made easier since only the integrals of such a crash pulse without an initial velocity are necessary for the analysis. Examples are given in Section 2.4.16, Chapter 2, where the analyses of the relationship between HIC, impact velocity, and crush space for the vehicle interior headform impact are presented.

Fig. 4.3 shows three symmetrical crash pulses which have the same velocity change of 30 mph. These are the haversine, front-loaded, and rear-loaded triangular pulses. The velocity changes versus time of the three symmetrical pulses are shown in Fig. 4.4. The velocity change between the two endpoints of each velocity curve is 30 mph. The displacement change, the area under the velocity curve, is the smallest for the triangular front loaded pulse and is the largest for the triangular rear-loaded pulse.

Note that in Fig. 4.4, only the haversine pulse is symmetrical about the diagonal connecting the two end points of the velocity curve. This velocity symmetry results in the same dynamic crush (area below the S curve) as the sled displacement (area above the S curve) at t_m. There are two displacement curves for each of the three crash pulses: vehicle crush (concave downward) and sled displacement (convex upward), as shown in Fig. 4.5. The sum of the vehicle crush and sled displacement is equal to the occupant free-flight displacement at t_m (0.091 seconds) shown in Eq. (4.2).

$$\begin{aligned} &\textit{Occupant free-flight displacement} = v_o t_m \\ &= (30\ \textit{mph})\left(17.6\ \frac{\textit{in/sec}}{\textit{mph}}\right)(0.091\,\text{sec}) \\ &= 48\ \textit{in.} \end{aligned} \tag{4.2}$$

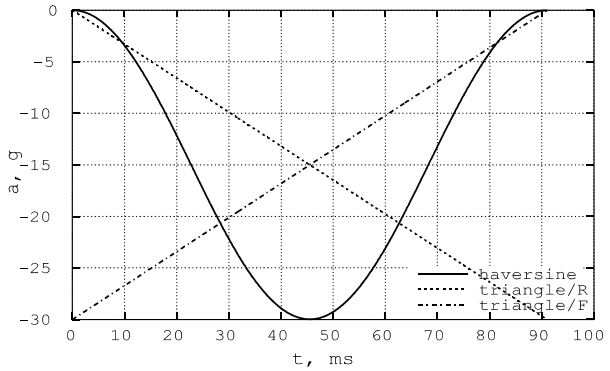

Fig. 4.3 Vehicle and Sled Accelerations: Haversine and Triangular Pulses

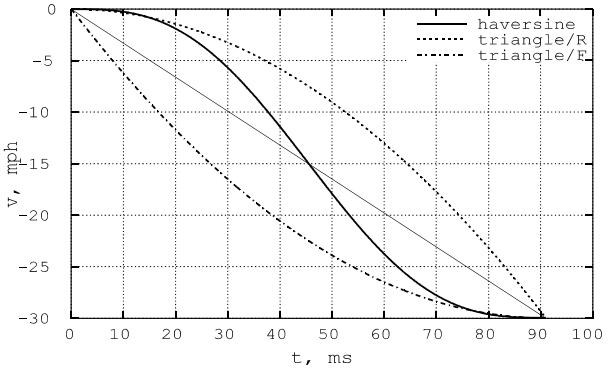

Fig. 4.4 Velocity vs. Time: Haversine and Triangular Pulses

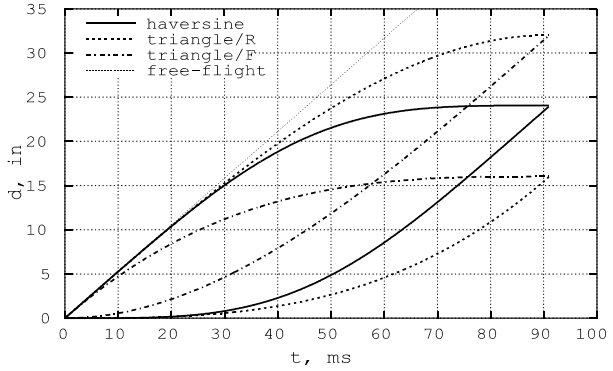

Fig. 4.5 Displacement vs. Time: Haversine and Triangular Pulses

For the haversine pulse, the sum of the vehicle crush and sled displacement is 24 + 24 = 48 inches; for the triangular front-loaded it is 16 + 32 = 48 inches; and for the triangular rear-loaded it is 32 + 16 = 48 inches. Note that the end points of the vehicle crush and sled displacement curves for the haversine pulse meet at the same point at t_m (0.091 seconds). However, the end points for the other two triangular pulses do not meet at the same point. This is because the haversine pulse is not

only symmetrical about the vertical line through the centroid of the deceleration curve, but also is symmetrical about the diagonal connecting the two end points of the velocity curve.

The sled displacement curve is useful in obtaining the timing, t, when the sled or unbelted dummy moves through a displacement d or in obtaining the displacement when the time, t, is given. For example, it would take an unbelted dummy 40 ms to move 5 inches in a 35 mph truck to barrier test, as shown in Fig. 4.6. Therefore, according to the 5"–30 ms criterion, an air bag sensor system would need to activate at 40 – 30 = 10 ms after impact.

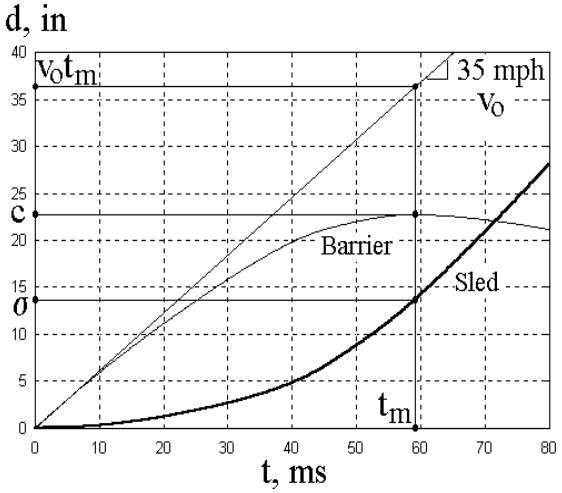

Fig. 4.6 Vehicle and Sled Displacements of a Truck in 35 mph Test

4.2.1 Vehicle and Sled/Unbelted Occupant Impact Kinematics

A simple spring mass model, shown in Fig. 4.7, represents a vehicle structure in a rigid barrier impact. An unbelted occupant displacement relative to the vehicle or the sled displacement can then be related to vehicle crush in the barrier test. The kinematic relationships between the transient barrier crush and sled displacement are analyzed in-depth for understanding the crash pulse characteristics. The derivations of the formulas for the vehicle, unbelted occupants, and the vehicle and occupant sensitivity coefficients are presented.

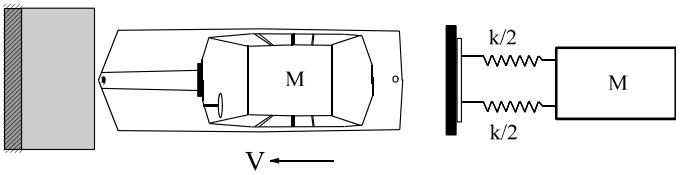

Fig. 4.7 A Spring-Mass Vehicle Model

4.2.1.1 *A Vehicle-to-Barrier Displacement Model*

The vehicle transient displacements (deformations) for three rigid barrier tests at different speeds for a mid-size sedan (test #1, 5 mph; test #2, 14 mph; test #3, 31 mph) are shown in Fig. 4.8.

Let us define: v_o: barrier impact velocity
ω: vehicle structure natural frequency in radian
p: normalized time (w.r.t. t_c)
q: normalized vehicle displacement (w.r.t. c).

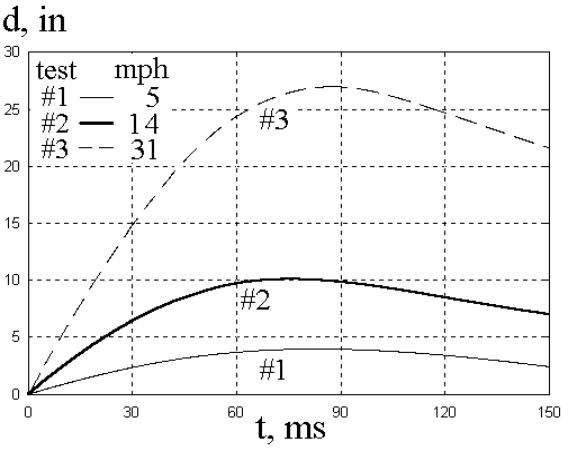

Fig. 4.8 Displacements of a Sedan at Three Speeds in Rigid Barrier Tests

The vehicle transient displacement curve is normalized in order to compare the vehicle-to-barrier impact responses at different speeds. The vehicle displacement is normalized by c, dynamic crush; and the time, by t_c, the centroid time for both the model and test. The accuracy of using the sine wave formula, q = sin(p) in estimating the test vehicle displacement in a range of test speed depends on the timing location, p, as shown in Fig. 4.9.

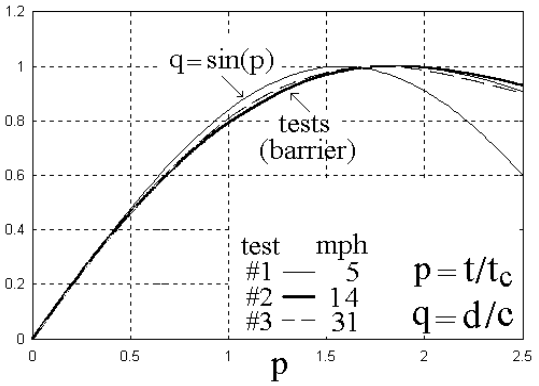

Fig. 4.9 Normalized Vehicle Displacements: Model and Test at Three Speeds

If p is located in the first one-third of t_m, the estimated displacement would be closer to the test value than that in the last two-thirds of t_m. To reveal the difference, the test displacement curves of the three tests are normalized. When p = 1, t = t_c, and when p = 1.56, t = p t_c = 1.56 t_c = t_m. Note that for a spring mass model, where the model response is sinusoidal, the relative centroid location is t_c / t_m = .64 =1. / 1.56.

As seen in the plot, when the normalized displacement is less than 0.5 (vehicle displacement being less than half of the dynamic crush), the model displacement matches closely that of the test. Since the normalized vehicle displacement curves for the same vehicle are matched closely, they are

practically test speed invariant. The mathematical derivation and application of these normalized variable relationships are shown in the following sections.

4.2.1.2 *Unbelted Occupant Kinematics*

Since a vehicle-to-barrier displacement is approximated by a sinusoidal curve, an unbelted occupant relative displacement is equal to its free-flight displacement minus the vehicle displacement. Such a displacement is then normalized with respect to the vehicle dynamic crush.

(2) of Eq. (4.3) gives the normalized unbelted occupant displacement, α/c. q is defined as the normalized occupant displacement, α/c, and p as the normalized time (real time normalized w.r.t. centroid time). Centroid time occurs when p equals 1.0, as shown by (4) of Eq. (4.3). By definition, $t_c = c/v_o$; p also represents the normalized occupant free-flight displacement w.r.t. the dynamic crush.

$$c = \frac{v_o}{\omega}, \qquad \alpha = v_o t - c\sin(\omega t) \tag{1}$$

$$\textit{Dividing (1) by } c, \quad \frac{\alpha}{c} = \frac{v_o}{c}t - \sin(\omega t) \tag{2}$$

$$\textit{where } \omega = \frac{v_o}{c} = \frac{1}{t_c}. \quad \textit{Let us define:} \tag{4.3}$$

$$q\textit{: Normalized sled displacement, } q = \frac{\alpha}{c} \tag{3}$$

$$p\textit{: Normalized time, } p = \frac{v_o}{c}\,t = \omega t = \frac{t}{t_c} \tag{4}$$

$$\textit{Then (2) becomes } q = p - \sin(p) \tag{5}$$

The normalized vehicle displacement, sin(p), and the normalized sled displacement, q = p – sin(p), are shown in Fig. 4.10. The sum of the two normalized displacements becomes p [= q + sin(p)].

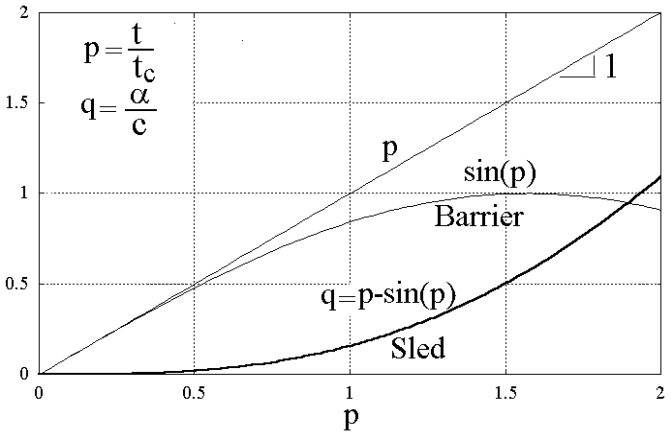

Fig. 4.10 Normalized Vehicle and Sled Displacements vs. Normalized Time

Case (I): In a vehicle-to-barrier crash test at 14 mph, the dynamic crush is 10 inches and occurred at 75 milliseconds, as shown in Fig. 4.8. Case (I) Estimate the time for the unbelted occupant to move five inches in the vehicle compartment, and Case (II) assess the effect of a change in the air bag module to occupant clearance (e.g., using a smaller air bag such as a face bag) on the sensor activation requirement.

Case (I) Computing time at a given sled/unbelted occupant displacement

The activation time of an air bag sensor is based on how far an unbelted occupant moves before the air bag is fully deployed. If the initial clearance between the torso and air bag module is 15 inches and the depth of a fully deployed air bag is 10 inches, the occupant should move forward 5 inches when the air bag is fully deployed. If it takes 30 ms to fill up the air bag, the time to activate the sensor is then the time for the unbelted occupant to move five inches minus 30 ms which is commonly known as 5"−30 ms criterion. The computation steps are shown in Eq. (4.4).

$$
\begin{aligned}
&\textit{since} \quad \alpha = 5\ \textit{in}, \quad \textit{and} \quad c = 10\ \textit{in}. \\
&q = \frac{\alpha}{c} = \frac{5}{10} = .5, \quad \textit{then} \\
&\textit{from the normalized sled displacement curve, Fig.}4.10, \\
&\textit{for } q = .5, \quad \textit{one gets} \quad p = 1.5 = \frac{t}{t_c} \\
&\textit{Since } t_c = \frac{c}{v_o} = \frac{10\ \textit{in}}{14x17.6\ \textit{in/s}} = .041\ s \\
&\textit{one gets} \qquad t = t_c\, p = .061\ s = 61\ ms
\end{aligned}
\tag{4.4}
$$

Therefore, in Case (I), 5"−30 ms is equal to 61 ms minus 30 ms, or 31 ms.

A pictorial comparison of the movement of the unbelted occupant relative to the vehicle between time zero and 61 ms is shown in Fig. 4.11.

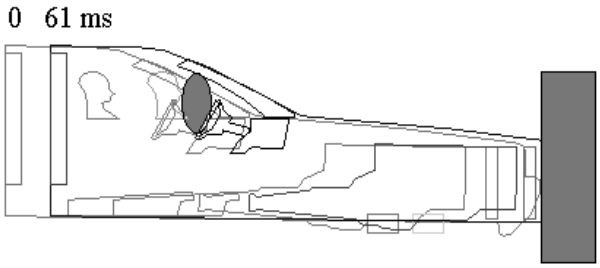

Fig. 4.11 Unbelted Dummy and Vehicle Motion in a 14 mph Barrier Test

The absolute displacement of the free flying occupant is $v_0 t$ = (14 mph × 17.6 in/s/mph) × .061 s = 15 inches. Since in a 14 mph rigid barrier test the steering wheel rearward displacement due to intrusion is minimal, the steering wheel absolute displacement is then equal to the vehicle crush at 61 ms which is about 10 inches (see Fig. 4.8). Therefore, the unbelted occupant moves 5 inches (=15 − 10) in the vehicle compartment before contacting the fully deployed air bag. The relative contact velocity between the occupant and air bag at t = 61 ms can be estimated and whether an occupant ridedown exists will be presented.

Case (II) Effect of clearance change on sensor activation time

Fig. 4.10 can also be used to estimate the sensor activation time if the interior clearance (free travel space) or air bag size changes. In the case of a smaller air bag or face bag, the occupant free

travel is assumed to be 20% more than for the Full-Size bag. Then α is 6 inches instead of 5 inches. The computation steps are shown in Eq. (4.5).

$$q = \frac{\alpha}{c} = \frac{6}{10} = .6, \quad \textit{from the normalized displacement curve in Fig. 4.10 and Eq. (4.3), for } q = .6, \quad \textit{one gets}$$
$$p = 1.6 = \frac{v_o}{c} t = .0176 \left(\frac{14\ mph}{10\ in} \right) t, \quad \textit{then } t = 65\ ms \tag{4.5}$$

The time for the unbelted occupant to move 6 inches is then 65 ms and the sensor activation time becomes 35 ms instead of 31 ms, a less stringent sensor activation requirement.

4.3 RIDEDOWN EXISTENCE CRITERIA AND EFFICIENCY

In the simple vehicle and occupant model shown in Fig. 4.12, once the free travel space or restraint slack is expended, the occupant contacts the vehicle interior surface or restraint system. To ensure that the occupant relative contact velocity is less than the initial barrier impact speed, it will be shown the free travel space should be less than the dynamic crush. Eq. (4.6) shows the relationships between the ratio of contact velocity to impact speed and the ratio of free travel to dynamic crush. Note that the same relationship exists for the ratio of contact time to time of dynamic crush.

Two methods will be used to derive the ridedown existence criteria shown in Eq. (4.6).

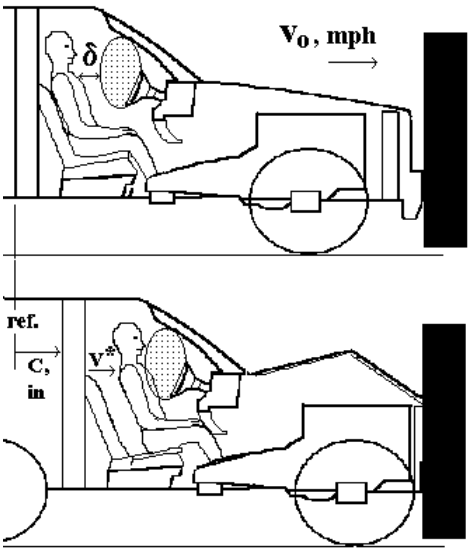

Fig. 4.12 Vehicle and Occupant Kinematics in a Frontal Rigid Barrier Test

Ridedown Criteria: (4.6)

For $\delta < c$, *then* $v^* < v_o$

$$\frac{v^*}{v_o} = \sqrt{\frac{\delta}{c}}, \qquad \frac{t^*}{t_m} = \sqrt{\frac{\delta}{c}}$$

where

v^*: *occupant–interior surface contact velocity*
v_o: *initial vehicle rigid barrier impact velocity*
δ: *occupant free travel space*
c: *vehicle dynamic crush at time* t_m
t^*: *time when occupant contacts restraint*
t_m: *time of dynamic crush*

4.3.1 Vehicle and Occupant Transient Kinematics

The equations of motion for a simple vehicle–occupant model are reviewed. In a study by Huang [1] on vehicle and occupant crash dynamics, a simple model with a constant force level structure and a restraint system was used. The equations of motion for the vehicle and occupant are derived based on the vehicle equivalent square wave (ESW). These are shown as follows.

4.3.1.1 *EOM for Vehicle*

The vehicle transient kinematics in a fixed barrier impact are shown in Eq. (4.7). The vehicle transient velocity and displacement are

$$\ddot{x}_v = -\frac{F}{M_v} = -ESW, \quad \dot{x}_v = v_o - ESW\,t, \quad x_v = v_o t - \frac{1}{2}ESW\,t^2 \tag{4.7}$$

4.3.1.2 *EOM for Occupant*

An occupant in the passenger compartment has a restraint slack of δ and a restraint angular natural frequency of ω. The vehicle compartment is subjected to a constant excitation of ESW. The occupant transient kinematics [1] are shown in Eq. (4.8).

$$\begin{aligned}
&\ddot{x}_o = -ESW\,\{1 - C(p) + \omega t^* S(p)\}, \quad where \quad C(p)=Cosine(p), \quad S(p)=Sine(p)\\
&\dot{x}_o = \dot{x}_v + \frac{ESW}{\omega}[S(p) + \omega t^* C(p)]\\
&x_o = x_v + \delta + \frac{ESW}{\omega^2}[1 - C(p) + \omega t^* S(p)]\\
&\ddot{x}_o|_{\max} = -ESW\left[1 + \sqrt{1 + (\omega t^*)^2}\right]\\
&Where \quad p = \omega(t - t^*) \quad for \quad t \geq t^*\\
&\omega = \sqrt{\frac{K}{M_o}}, \quad t^* = \sqrt{\frac{2\delta}{ESW}} \;\ldots\; restraint\ contact\ time
\end{aligned} \tag{4.8}$$

4.3.2 Derivation of Ridedown Existence Criteria

Method I uses the occupant transient velocity and displacement relationships at the time of restraint contact. *Method II* uses the crash pulse relationships between the rigid barrier and sled tests.

4.3.2.1 *Method 1*

Taking advantage of the closed-form solutions, the formulas for the vehicle and occupant shown in Eqs. (4.7) and (4.8) are rearranged to yield the ridedown existence criteria shown by (4) of Eq. (4.9).

$$\begin{aligned}
&\because \quad \delta = v_o t^* - x_v = \frac{1}{2}ESW\,t^{*2},\\
&\therefore \quad t^* = \sqrt{\frac{2\delta}{ESW}} \quad \ldots\ldots\ldots\ldots \quad (1)\\
&also \quad v^* = v_o - \dot{x}_v = ESW\,t^*,\\
&\therefore \quad t^* = \frac{v^*}{ESW} \quad \ldots\ldots\ldots\ldots \quad (2)\\
&Square\ both\ sides\ of\ (1)\ and\ (2),\ and\ equate:\\
&(v^*)^2 = 2\delta\,(ESW) = 2\delta\left(\frac{v^2}{2c}\right)\\
&where\ all\ the\ variables\ including\ ESW\ are\ in\ consistent\ units:\\
&\therefore \quad \frac{v^*}{v_o} = \sqrt{\frac{\delta}{c}} \quad \ldots\ldots\ldots\ldots \quad (3)\\
&\because \quad v_o = ESW\,t_m, \quad and \quad v^* = ESW\,t^*\\
&\therefore \quad \frac{v^*}{v_o} = \frac{t^*}{t_m} = \sqrt{\frac{\delta}{c}} \quad \ldots\ldots\ldots\ldots \quad (4)
\end{aligned} \tag{4.9}$$

4.3.2.2 *Method II*

Using the kinematic relationships for the fixed barrier and sled impacts, where the common variable is the crash pulse, the ridedown existence criteria can also be derived. The variables used in the barrier impact formula are absolute quantities, while those in the sled impact formulas are relative quantities, such as the contact velocity and free travel space. By eliminating the common variable, the crash pulse, from the two sets of kinematic relationships, the ridedown existence criterion can be obtained. The derivation is shown in Eq. (4.10).

Formula (4) of Eq. (4.10) shows that the normalized contact velocity (ratio of occupant-interior surface contact velocity to the barrier impact velocity) is equal to the square root of the ratio of the free travel space to the dynamic crush of the vehicle. Fig. 4.13 depicts graphically the ridedown existence relationship where the normalized contact velocity, v^*/v_o, is less than one. Given a vehicle structure that yields a certain dynamic crush, the normalized contact velocity decreases as the free travel space or restraint slack decreases. Note that the relationship and plot apply also to the normalized contact time (ratio of contact time to the time of dynamic crush, t^*/t_m), as shown in (4) of Eq. (4.9)

d_o : *initial vehicle displacement* (= 0)
$\dot{\alpha}$: *occupant relative to vehicle velocity*
α : *occupant relative to vehicle displacement*

(*I*) *Vehicle Barrier Impact*:

$$a\ (ESW,\ Equivalent\ Square\ Wave) = \frac{v_o^2}{2c},\quad or$$

$$v_o = \sqrt{2ac} \quad \ldots\ldots\ldots\ldots \quad (1)$$

(*II*) *Sled Impact* (*Occupant Relative to Vehicle Kinematics*):

$$Let\quad \dot{\alpha} = \int a\,dt = at,\quad then\quad \alpha = \int \dot{\alpha}\,dt = \frac{a}{2}t^2 = \frac{a}{2}\left(\frac{\dot{\alpha}}{a}\right)^2 = \frac{\dot{\alpha}^2}{2a}$$

$$\dot{\alpha} = \sqrt{2a\alpha} \quad \ldots\ldots\ldots\ldots \quad (2)$$

Dividing both sides of (2) *by* (1) *yields*:

$$\frac{\dot{\alpha}}{v_o} = \sqrt{\frac{\alpha}{c}} \quad \ldots\ldots\ldots\ldots \quad (3) \qquad (4.10)$$

At the restraint contact time, $\alpha = \delta$ *and* $\dot{\alpha} = v^*$, *then*

$$\frac{v^*}{v_o} = \sqrt{\frac{\delta}{c}} \quad \ldots\ldots\ldots\ldots \quad (4)$$

The ridedown existence criterion is

$$\frac{v^*}{v_o} = \sqrt{\frac{\delta}{c}} < 1. \quad \ldots\ldots\ldots\ldots \quad (5)$$

$$\because\ ESW = 0.4\,\frac{v_o^2}{c},\quad where\ \ ESW: g;\ \ v_o: mph;\ \ c: in$$

Substituting $\dfrac{v_o}{\sqrt{c}} = \sqrt{\dfrac{ESW}{0.4}}$ *into* (4), *then*

$$v^* = 1.58\sqrt{\delta\, ESW} \quad \ldots\ldots\ldots \quad (6)$$

In order for ridedown to exist, the contact velocity, v*, must be smaller than the barrier impact velocity, v_o. The motion of the occupant can then be slowed down by the interior surface or restraint system during the vehicle deformation phase. The physical constraint needed to achieve this ridedown is having the interior space or restraint slack smaller than the vehicle dynamic crush. However, in the fixed barrier crashes, the dynamic crush of a truck is frequently smaller than that of cars. In order to

minimize the occupant impact severity, the restraint slack is frequently reduced by using the pretensioner (either pyrotechnical or mechanical driven) for both the lap belt buckle and the shoulder belt retractor.

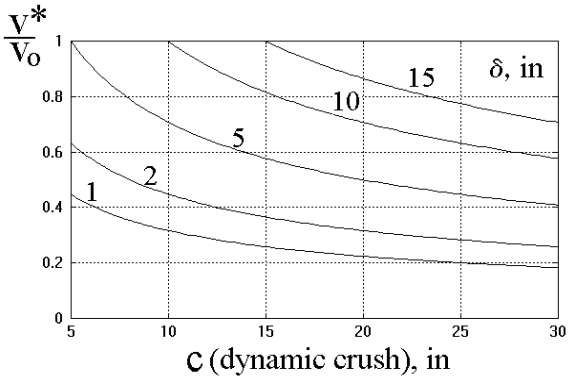

Fig. 4.13 Normalized Contact Velocity vs. Restraint Slack (δ) and Dynamic Crush (C)

4.3.3 Application of Ridedown Existence Criteria

The occupant-vehicle interior contact velocity can be estimated using the information on the vehicle crush and the occupant interior free travel space. The occupant relative contact velocity during a crash is a good indicator of the severity of an impact.

4.3.3.1 *Case Study – High Speed Crash*

A typical 30 mph rigid barrier test of a passenger car equipped with a driver side air bag would have a dynamic crush of 24 inches. For an unbelted driver, the interior free travel space between the torso and the fully deployed air bag is about 5 inches; using (4) of Eq. (4.10), the contact velocity computation is shown in Eq. (4.11). The contact velocity is about half of the barrier impact velocity.

$$v^* = v_o\sqrt{\frac{\delta}{c}} = 30\ mph\sqrt{\frac{5\ in}{24\ in}} = 30\ mph \times (0.46) \doteq 14\ mph \tag{4.11}$$

Therefore, the occupant would have impacted the fully-deployed air bag at a relative velocity of 14 mph. This contact velocity can also be computed using the following relationship in terms of occupant interior free travel space (δ, in) and equivalent square wave (ESW, g).

The units used in the computation of the relative contact velocity in Eq. (4.12) are the conventional units of g, mph, inches, and pounds.

$$\begin{aligned} &\textit{from}\quad v^* = v_o\sqrt{\frac{\delta}{c}} \quad \textit{and} \quad ESW = .4\,\frac{v_o^2}{c} \quad \textit{and} \\ &\textit{eliminating } v_o \textit{ and } c\textit{, one gets} \\ &v* = \sqrt{\frac{\delta\ ESW}{.4}} = 1.58\sqrt{\delta\ ESW} \ldots\ldots (1) \\ &\textit{For } \delta = 5\ in\textit{, and } ESW = .4\,\frac{v_o^2}{c} = .4\,\frac{(30\ mph)^2}{24\ in} = 15\ g \\ &\textit{then}\quad v* = 1.58\sqrt{(5\ in)(15\ g)} \doteq 14\ mph \end{aligned} \tag{4.12}$$

4.3.3.2 *Case Study – Low Speed Crash*

A mid-size vehicle was tested in a 14 mph rigid barrier condition. The vehicle responses are shown in Fig. 4.14, and the unbelted occupant responses with respect to the vehicle are shown in Fig. 4.15. Determine the occupant contact velocity and timing for the following two cases:

Case 1. No belt, no air bag, δ = 15 in => V*=_____mph, t*=_____ms

Case 2. No belt, w/ air bag, δ = 5 in => V*=_____mph, t*=_____ms

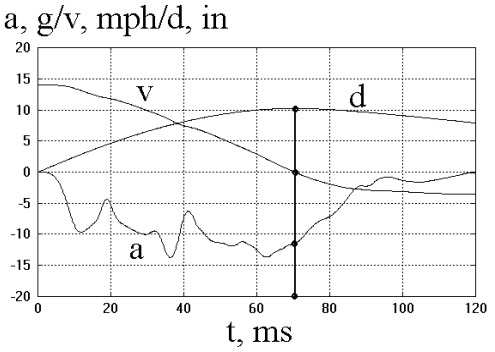

Fig. 4.14 Vehicle Kinematics in a 14 mph Rigid Barrier Test

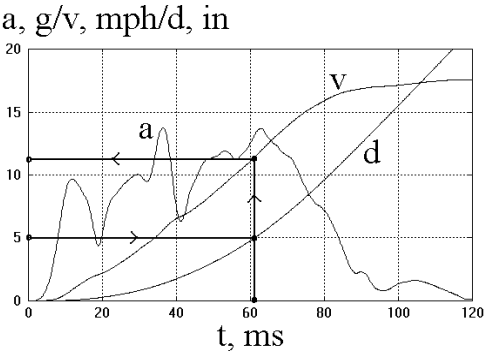

Fig. 4.15 Unbelted Occupant Kinematics in a 14 mph Rigid Barrier Test

4.3.4 Occupant Response Surface and Sensitivity

The response analysis of the simple vehicle model and the response sensitivity of the occupant to the vehicle and restraint parameters are presented. The major occupant response relationships are shown in Eq. (4.13) and the detailed derivations are listed in reference [1].

Definitions in Conventional Units:

a_o: *maximum occupant deceleration, g*

E: *ESW(Equivalent Square Wave) of vehicle, g*

C: *dynamic crush, in*

δ: *restraint slack, in*

t^*: *restraint contact time,* sec.

v^*: *restraint contact velocity, mph*

V_o: *fixed barrier impact speed, mph*

f : *restraint natural frequency, Hz*

γ: *dynamic amplification factor*

$$\gamma = 1+\sqrt{1+(2\pi f t^*)^2} \quad \ldots\ldots\ldots\ldots \quad (1)$$

$$\because \quad a_o = E\,\gamma \quad \ldots\ldots\ldots\ldots \quad (2) \qquad (4.13)$$

$$\therefore \quad a_o = E\,[1+\sqrt{1+(2\pi f t^*)^2}] \quad \ldots\ldots\ldots \quad (3)$$

$$E = .4\,\frac{V_o^2}{C} \quad \ldots\ldots\ldots\ldots\ldots\ldots \quad (4)$$

$$t^* = .072\sqrt{\frac{\delta}{E}} \quad \ldots\ldots\ldots\ldots\ldots\ldots \quad (5)$$

$$v^* = 1.58\sqrt{\delta E} \quad \ldots\ldots\ldots\ldots\ldots\ldots \quad (6)$$

$$\therefore \quad a_o = E + \sqrt{E^2+(0.286 f v^*)^2} \quad \ldots\ldots \quad (7)$$

Note: (7) *is based on the following in natural units*

$$v^* = E t^*, \quad \textit{and} \quad a_o = E + \sqrt{E^2 + (2\pi f v^*)^2}$$

4.3.4.1 *Restraint Design Optimization by Response Contour Plots*

Given a restraint natural frequency (e.g., 7 Hz), the occupant deceleration can be plotted in 3-D in terms of occupant restraint contact velocity (v*) and vehicle deceleration level (ESW) as shown in Fig. 4.16. To achieve a higher crash test rating, such as the NCAP (New Car Assessment Program), for the 35 mph frontal barrier testing, the occupant deceleration needs to be kept at around 40 g.

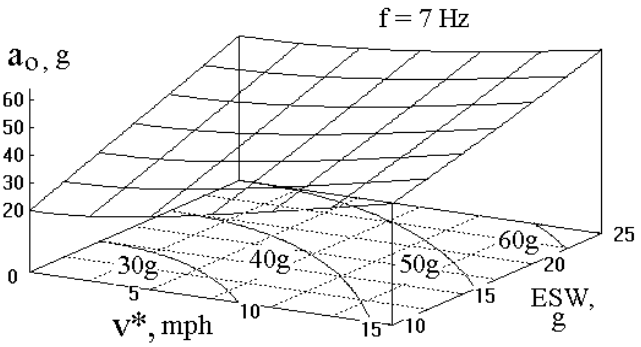

Fig. 4.16 Occupant Deceleration vs. Contact Velocity (v*) and ESW

From the constant surface contour plot shown in Fig. 4.17, one can form a window where the range of v* is between 0 mph and 10 mph, and the practical range of the truck ESW lies between 15 and 20g.

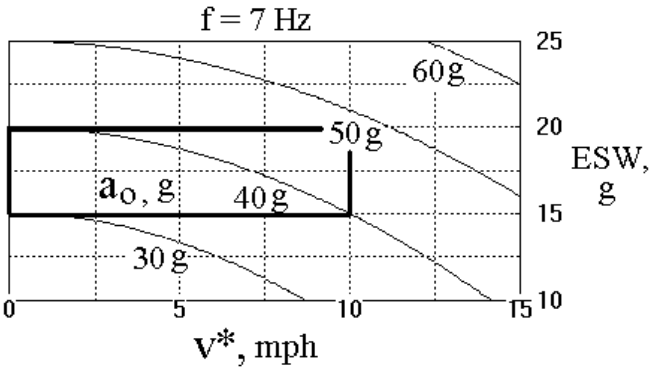

Fig. 4.17 Window of V* and ESW for Constant 40 g Occupant Deceleration

Note that Formula (6) of Eq. 4.13 can be rearranged such that the restraint slack, δ, can be computed to yield the desired contact velocity, v*, given the equivalent square wave, ESW, as shown in Fig. 4.18. The option of achieving the higher NCAP rating through the window constraints on the v* and ESW is to minimize the restraint slack. The range of restraint slack that would satisfy such a constraint is between 0.1 and 3 inches, as shown by the rectangle on the base of the plot in Fig. 4.18.

It is not unusual to have a belt pretensioner installed in a truck in order to achieve a higher crash rating. This is due to the fact that the ESW of a truck is relatively higher than that of a passenger car. Therefore, reducing the occupant deceleration by controlling and reducing the restraint slack to compensate for the higher vehicle ESW is certainly consistent with the relationship specified by the dynamic amplification factor.

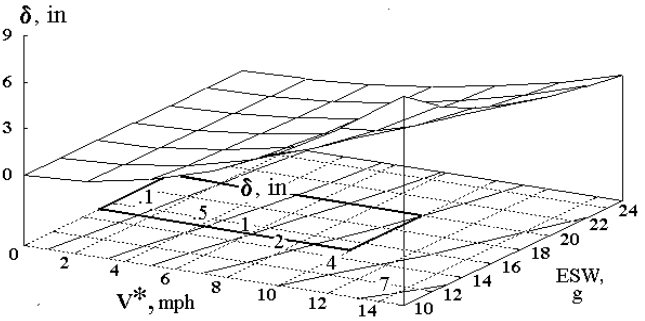

Fig. 4.18 Restraint Slack Constraint by v* and ESW

4.3.4.2 *Sensitivity of Occupant Response to ESW*

The sensitivity of the occupant response to the amount of vehicle crush and the vehicle equivalent square wave can be derived from the response formula for the occupant. From Eq. 4.13, the occupant deceleration (chest g) is a function of ESW and dynamic amplification factor, γ. By taking the partial derivative of the occupant deceleration with respect to ESW, the sensitivity of the occupant deceleration with respect to ESW is obtained, as shown in Eq. (4.14). It should be noted that the dynamic amplification factor, γ, is also a function of ESW. Therefore, the partial differentiation of occupant deceleration with respect to ESW is performed on the product of two terms, ESW and γ.

The sensitivity of occupant response to ESW, shown in Eq. (4.14), is a function of dynamic amplification factor. Since the dynamic amplification factor is a function of ESW and restraint slack, the sensitivity contour surface shown in Fig. 4.19 is plotted against these two variables. The sensitivity increases as the restraint slack increases. However, the sensitivity decreases as the ESW increases. For the special case where the restraint slack is reduced to zero, the sensitivity becomes a constant, which is 2 g/g. That is, for every one g increase in ESW, the occupant deceleration is increased by two g's. The typical range of sensitivity for vehicles in high speed barrier crashes is between 2.1 and 2.7. Fig. 4.20 shows the constant contour plot of the sensitivity as a function of ESW and restraint slack.

(1) ***Sensitivity of Chest G w.r.t. Equivalent Square Wave:***

$$\frac{\partial a_o}{\partial E} = \frac{\gamma^2}{2(\gamma - 1)} \qquad \textit{where} \quad \gamma\textit{: Dynamic Amplification Factor} \tag{4.14}$$

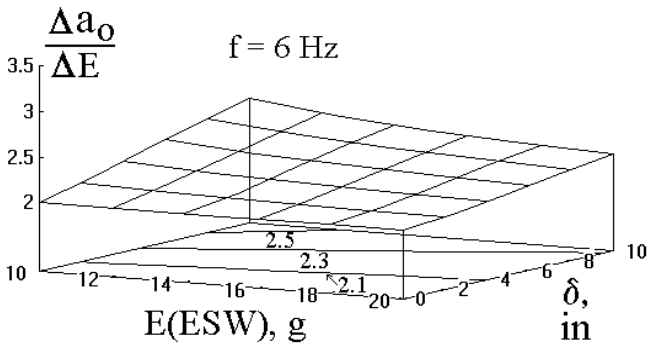

Fig. 4.19 Chest G Sensitivity vs. ESW and Slack (δ)

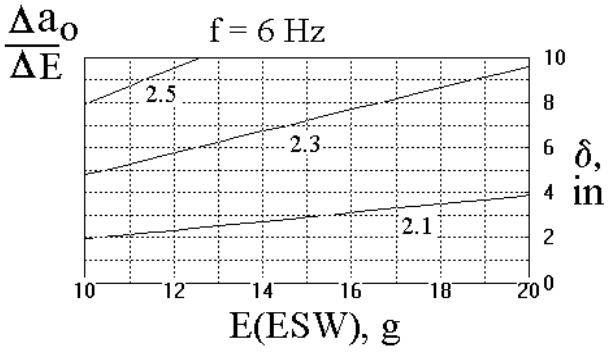

Fig. 4.20 Constant Chest G Sensitivity vs. ESW and δ

4.3.4.3 *Sensitivity of Occupant Response to Dynamic Crush*

Similarly, the sensitivity of the occupant deceleration with respect to dynamic crush can be derived. Shown in Eq. 4.15, the sensitivity is a function of the dynamic amplification factor and the centroid time, t_c, where t_c is equal to c/v_o.

(2) *Sensitivity of Chest G w.r.t. Dynamic Crush*:

$$\frac{\partial a_o}{\partial c} = \left[\frac{\partial a_o}{\partial E}\right]\left[\frac{\partial E}{\partial c}\right] = \left[\frac{\gamma^2}{2(\gamma-1)}\right]\left[-0.4\left(\frac{v_o}{c}\right)^2\right] \tag{4.15}$$

Fig. 4.21 shows the occupant deceleration sensitivity w.r.t. the dynamic crush. The sensitivity depends on the dynamic crush and restraint slack. Given a fixed barrier impact speed, restraint natural frequency, and a restraint slack, the sensitivity is higher when the dynamic crush is lower. This implies that the occupant deceleration sensitivity w.r.t. the dynamic crush is higher for the truck than for the car since the truck is stiffer than the car and the dynamic crush is less at a given speed. For the dynamic crush between 25 and 30 inches, the sensitivity is around −1.4 g/inch at 35 mph with slack of 5 inches and around −1.1 g/in at 31 mph with slack of 2 inches (see surface contour plots in Figs. 4.22 and 4.23).

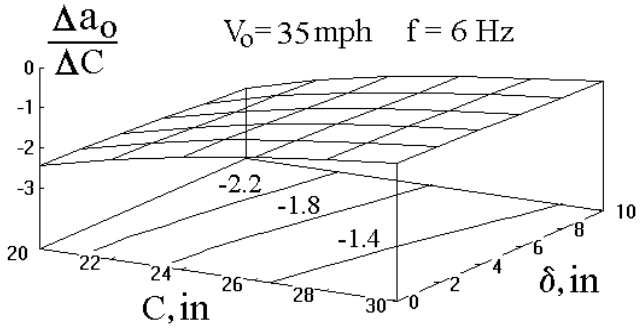

Fig. 4.21 Chest G Sensitivity vs. Dynamic Crush (C) and δ

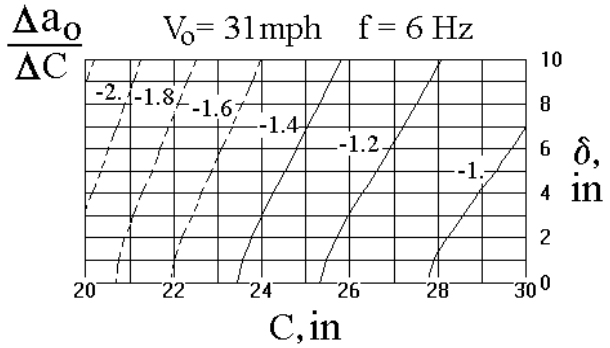

Fig. 4.22 Constant Chest G Sensitivity vs. C and δ (31 mph)

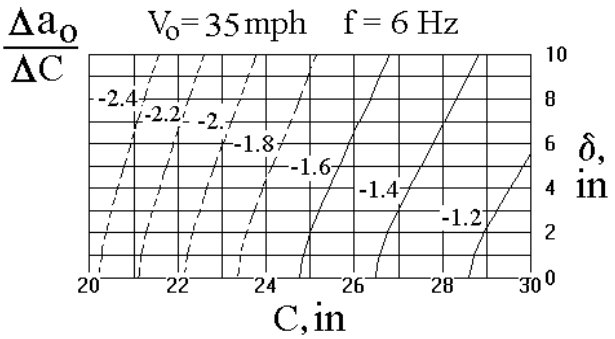

Fig. 4.23 Constant Chest G Sensitivity vs. C and δ (35 mph)

4.3.4.4 *Statistical Regression of Test Data and Model Responses*

Two sets of pre- and post-crash data of a SUV (sport utility vehicle) and a minivan were analyzed to predict the occupant responses using a linear regression model. The tests were all conducted at the NCAP (new car assessment program) speed of 35 mph.

I. SUV tests at NCAP 35 mph

In the linear regression analysis, the response is the chest deceleration and one of the major independent variables is dynamic crush. The associated coefficient for the dynamic crush is −1.37. This number is equivalent to the sensitivity coefficient derived from the physical model given in Eq. 4.10. Using the formulas in Eq. 4.13, the test data of a truck with 28 inches of dynamic crush, 6 Hz of restraint natural frequency, and 2 inches of restraint slack yield the values of ESW, t*, and γ shown in Eq. 4.16. The sensitivity coefficient is then computed in Eq. 4.15 and is equal to −1.28 g/in.

$$\begin{aligned} &\textit{for } v_o = 35 \textit{ mph}, \quad c = 28 \textit{ in}, \\ &\quad \delta = 2 \textit{ in, and } f = 6 \textit{ Hz}, \quad \textit{one gets} \\ &ESW = 17.5 \textit{ g}, \quad t^* = .024 \text{ sec}, \quad \textit{and } \gamma(DAF) = 2.35 \\ &\frac{\partial a_o}{\partial c} = \frac{\gamma^2}{2(\gamma-1)}\left[-.4\left(\frac{v_o}{c}\right)^2\right] = -1.28 \textit{ g/in} \end{aligned} \tag{4.16}$$

A regression analysis of a set of crash tests using SUV to rigid barrier impact at 35 mph is performed and has the relationship shown as follows.

Chest G = 79.1 - 1.37 * (Dynamic Crush) + ... + constant

According to the regression analysis, the change in chest deceleration with respect to that of dynamic crush is −1.37 g/in, which is very close to that derived by the model formula shown in Eq. 4.16. Even though the dynamic model is simple, the trend analysis based on the gross motion relationship appears to be in the right direction.

II. Minivan tests at 35 mph

In another study, a regression analysis was performed on the occupant response using a multi-body mathematical dynamic model. The input excitation to the model approximates the crash pulse of a minivan test at the NCAP speed of 35 mph. The ESW (equivalent square wave) is used as one of the independent variables and the corresponding regression coefficient is 2.49 as shown below.

Chest G = 2.49 * ESW + ...+ 41.9

The sensitivity coefficient of 2.49 g/g (chest g/unit of vehicle ESW in g) from the regression equation represents a typical value for the vehicle with a unitized body with a subframe supporting the power train. The minivans analyzed falls into this body style. The ESW for those vehicles with a unitized body is typically less than that of the frame vehicle. Shown in the upper left corner of the base of the 3-D plot in Fig. 4.20, the sensitivity coefficient of chest deceleration w.r.t. ESW is between 2.3 and 2.5. That is to say, for every 1 g increase in ESW, the chest deceleration increases by about 2.4 g. This sensitivity coefficient is related to the dynamic amplification factor, γ, as shown in Eq. 4.14.

4.3.4.5 *Response Prediction and Ridedown Efficiency*

I. Response Prediction

The model response prediction using ESW as input excitation is a first order response prediction. Given an ESW of 15 g, restraint slack of 5 inches, and an air bag restraint system natural frequency of 7 Hz, the restraint (air bag only) contact time, the occupant maximum deceleration, and corresponding timing are computed as follows:

Using the equations of motion for the vehicle and occupant shown in Eqs. (4.7) and (4.8), respectively, the transient acceleration, velocity, and displacement responses for both the vehicle and occupant can be computed and are shown in Figs. 4.24 to 4.26.

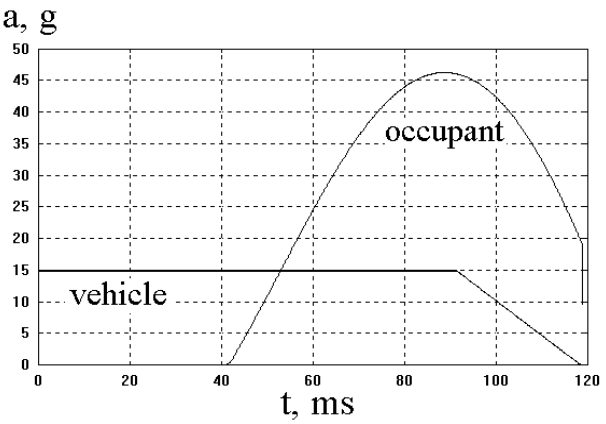

Fig. 4.24 Vehicle/Occupant Acceleration in a 30 mph Test (δ=5", f=7 Hz)

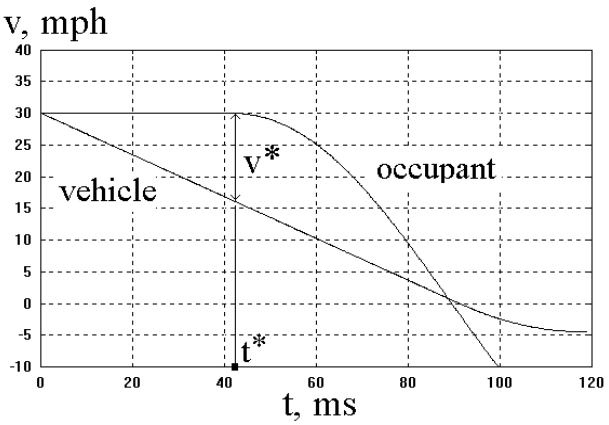

Fig. 4.25 Vehicle/Occupant Velocity

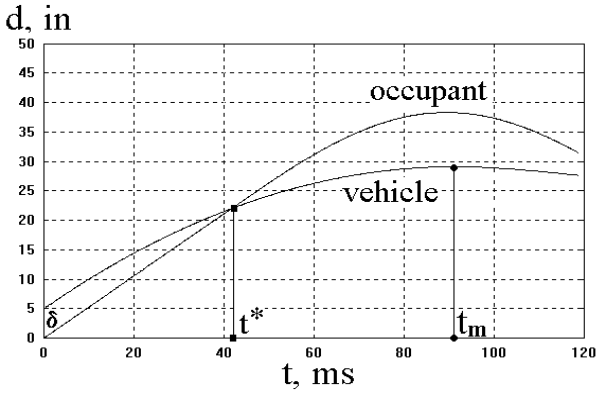

Fig. 4.26 Vehicle/Occupant Displacement

The velocity change is 30 mph in the vehicle deformation phase shown in Fig. 4.25, and a coefficient of restitution of 0.15 is used for the restitution phase. The maximum occupant deceleration occurs at 89 ms, 2 milliseconds before the vehicle reaches the dynamic crush at 91 ms.

Shown in Figs. 4.25 and 4.26 are the velocity and position plots of the vehicle and occupant. At time zero, the position of vehicle interior surface is 5 inches ahead of the occupant which is the occupant free travel space, δ. At t* of 42 ms, the relative displacement is zero where the restraint coupling phase starts. The relative contact velocity, v*, is about 14 mph. The vehicle dynamic crush is 24 (= 29 – 5) inches, and the rebound velocity is 4.5 mph (= 30 mph × 0.15). The maximum occupant stopping distance (the maximum restraint deformation) is about 9 (= 38 – 29) inches and occurred around 90 ms (see Fig. 4.26), just before the vehicle rebounds at 92 ms.

Fig. 4.27 shows the plane view of the occupant travel at three times. From t_o to t*, the occupant travels 5 inches while the air bag is being fully inflated. The occupant-restraint coupling phase starts at the restraint contact time, t* , and ends at the time of dynamic crush, t_m.

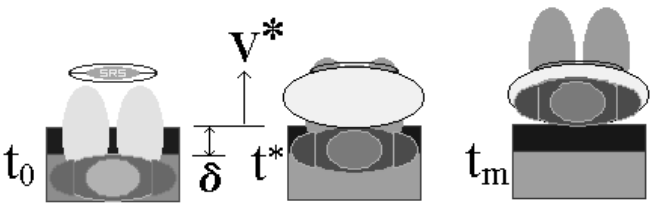

Fig. 4.27 Plane View of Occupant Interior Travel at 3 Times t_o, t^*, and t_m

II. Ridedown Efficiency

Since the occupant undergoes the ridedown during the restraint coupling phase, the initial occupant kinetic energy is diverted to one riding down along with the deforming vehicle structure, and the other deforming the restraint system. For the details on the computation of restraint and ridedown energy densities, the reader is referred to Section 1.10 in Chapter 1.

The closed-form formulas for the restraint and ridedown energy densities are shown in Eq. (4.18). Using the same input data which produces the vehicle responses in Figs. 4.24 to 4.26, the ridedown analysis is performed in Eq. (4.18). The late restraint contact time, t* = 42 ms, results in a low ridedown, high restraint energy densities, and high chest deceleration, 47 g. The dynamic amplification factor is $\gamma = 47/15 = 3.1$ which is higher than a typical value of 2.6.

Defines:
$e_{rd}|_{max}$: *maximum ridedown energy densitity (e.d.)*
$e_{rs}|_{max}$: *maximum restraint e.d., g−in*
v_o: *initial barrier impact speed, mph*
ESW: *equivalent square wave, g*
t^*: *restraint contact time, s*
t_m: *time of dynamic crush, s*
t_g: *time of* $a_o|_{max}$, *s*
ω: *restraint circular natural frequency* $(2\pi f)$, *radians*
$S(p)$: *sine*(p), $C(p)$: *cosine*(p), p: *angle in radian*
$p = \omega(t_m - t^*)$, *for* $t_m \geq t^*$
e: *occupant initial kinetic energy density, g−in*

(4.17)

$$e_{rd}|_{max} = 0.4 v_o^2 - (ESW)^2 \left[\frac{(t^*)^2}{2} + \frac{t^* S(p)}{\omega} - \frac{C(p)-1}{\omega^2} \right] \left(\frac{1}{386.4} \right) \quad \ldots \quad (1)$$

$$e_{rs}|_{max} = \left(\frac{ESW}{\omega} \right)^2 \left[1 + \frac{(\omega t^*)^2}{2} + \sqrt{1+(\omega t^*)^2} \right] \left(\frac{1}{386.4} \right) \quad \ldots\ldots\ldots \quad (2)$$

4.4 BASICS OF SPRING AND DAMPER DYNAMIC MODELING

Various models, ranging from one parameter to three parameters, are used in the analysis. The models consist of energy absorbing (EA) elements with masses connected to both ends. Since most engineering materials exhibit viscous and elastic characteristics, the EA can be represented by a Kelvin element, Maxwell element, or combinations of the two elements. Schematically, the masses in the models are connected by springs and/or dampers in various arrangements. The equations of motion (EOM) for most of the models have been solved explicitly with closed-form solutions. The applications of such a closed-form formulas are used for single vehicle and vehicle-vehicle impact analyses.

4.4.1 Spring and Damper Elements

Springs and dampers are the basic energy-absorbing components in a mechanical system. Fig. 4.28 shows the basic components of spring and damper and their combinations. The Kelvin element shown in (c) consists of spring and damper in parallel, while the Maxwell element in (d) has the two components in series. A gas MacPherson strut, a Kelvin element, used in a suspension system, is shown in Fig. 4.29. Note the construction of the Kelvin element, where both ends of the spring and damper are supported by the same reference points 1 (end plate) and 2 (cylinder), respectively.

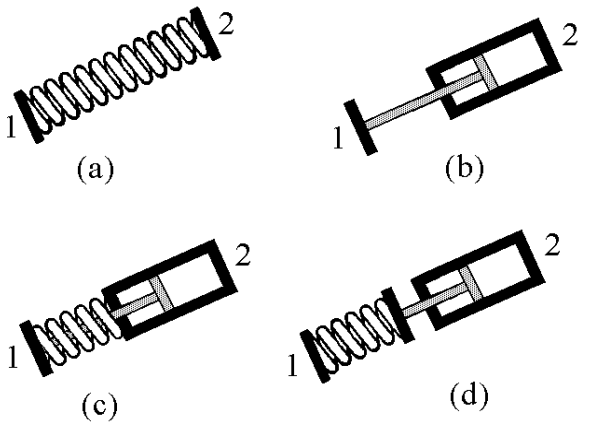

Fig. 4.28 (a) Spring, **(b)** Damper, **(c)** Kelvin, and **(d)** Maxwell Elements

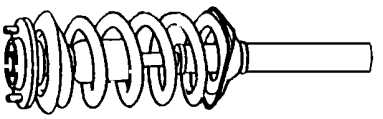

Fig. 4.29 A MacPherson Strut – A Kelvin Element

Schematic representations of the four elements are shown in Fig. 4.30. Each of the four elements has its own dynamic properties in terms of k, spring stiffness, and c, damping coefficient. Each element's function will be shown in the derivation of equation of motion for a specific spring and damper model.

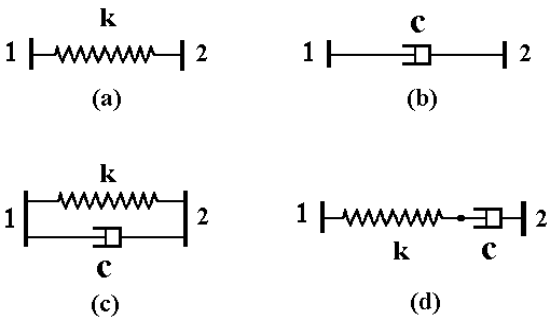

Fig. 4.30 Schematic Representation of Spring and Damper Elements

4.4.2 Properties of Viscoelastic Materials and Damping

All materials in an oscillatory systems exhibit viscoelastic behavior [2]. Some of the properties of viscoelastic materials are (1) strain increases with time (creep) when the applied stress is held constant, (2) stress decreases with time (relaxation) when the applied strain is held constant, (3) the effective stiffness depends on the strain rate, (4) energy loss occurs due to hysteresis, and (5) the coefficient of restitution is less than 1.

4.4.2.1 *Equivalent Viscous Damping*

Since all materials exhibit loss of energy in an oscillatory system, the equivalent viscous damping is defined in a model to describe such a behavior. The primary effect of damping is the removal of energy from a damped system. Such an energy loss results in the decay of amplitude of the free vibration in the system. In steady-state forced vibration (excitation), however, the loss of energy is replenished by energy supplied by the excitation.

There are different mechanisms which can induce damping in a system. These are internal molecular friction, viscous fluid resistance, and sliding friction. True damping in a system is a complex phenomenon. To provide the simplest form of describing such a phenomenon, a linear viscous damping is used.

Even with a minimal damping present in a dynamic system subjected to an impact and/or excitation, the damping effect on the transient (time) response can be significant. An analysis or design involving viscoelastic materials must consider the damping phenomenon, due to their effects on transient (time) response. In some applications, the transient response of the system subjected to a large impulsive loading is dominated by the damping phenomenon.

The ability of a component in transmitting an impulsive loading from the input to the output is termed transient transmissibility (TT) [3]. Crash performance of components such as body mounts located between the frame and body (cab or pickup box) of a truck can be studied using the Kelvin model (2-parameter model) and the standard solid model (3-parameter model). The number of parameters is referred to as the number of spring and/or damper elements.

4.4.3 2-Mass (Vehicle-to-Vehicle) Impact Model

An impact between two masses can be represented schematically, as in Fig. 4.31. Each of the two masses has a contact with a Kelvin element, a set of spring and damper in parallel. If the connection between the mass and the element is a rigid contact, the element may undergo tension and compression. If not, due to separation between the mass and element, the element can only be subjected to compression.

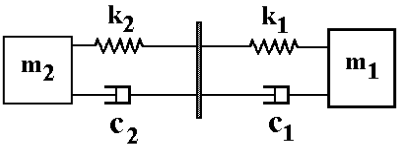

Fig. 4.31 Vehicle-to-Vehicle Impact Model – Two Kelvin Elements in Series

To simplify the analysis, the two sets of Kelvin elements can be combined into one resultant Kelvin element as shown in Fig. 4.32. The parametric relationship between the two individual Kelvin elements and the resultant Kelvin element can be obtained as follows.

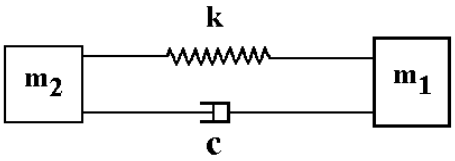

Fig. 4.32 Vehicle-to-Vehicle Impact Model
– A Kelvin Model

From the deformation (spring deflection) relationship, the total deformation of the combined spring k is equal to the sum of the deformations of the two individual springs (an additive deflection relationship). The spring force relationship can then be established as follows.

$$d = d_1 + d_2 \tag{4.18}$$

$$\frac{F_k}{k} = \frac{F_k}{k_1} = \frac{F_k}{k_2} \tag{4.19}$$

Similarly, by taking the time derivative of the deformation relationship, the deflection rates are also found to be additive for the dampers. Similarly, the damping force relationship is shown as follows.

$$\dot{d} = \dot{d}_1 + \dot{d}_2 \tag{4.20}$$

$$\frac{F_c}{c} = \frac{F_c}{c_1} = \frac{F_c}{c_2} \tag{4.21}$$

The final relationships for the spring stiffness and damping coefficients are then established.

$$k = \frac{k_1 k_2}{k_1 + k_2} \tag{4.22}$$

$$c = \frac{c_1 c_2}{c_1 + c_2} \tag{4.23}$$

Note that the total force, F, exerting on m_1 and m_2, is equal to the sum of forces exerted by the spring, k and damper, c.

$$F = F_k + F_c \tag{4.24}$$

4.4.4 Dynamic Equivalency Between Two-Mass and Effective Mass Systems

A two-mass system is shown in Fig. 4.33. Mass m_2 is impacted by m_1 at an initial relative speed (or closing speed) of V_{12} where $V_{12} = V_1 - V_2 = V_o$. The relative displacement α is the basis for the derivation of the response solution.

If one of the masses in the two-mass system is infinite, the system becomes a vehicle-to-barrier (VTB) model, as shown in Fig. 4.34. The only mass moving in this system is referred to as the effective mass, m_e. The relative motion of the mass with respect to the fixed barrier is the same as the absolute motion of the mass with respect to a fixed reference frame. In a system where there are multiple masses involved in an impact, the analysis can be simplified by using the relative motion and effective mass approaches. The relative displacement of the effective mass, m_e, is α.

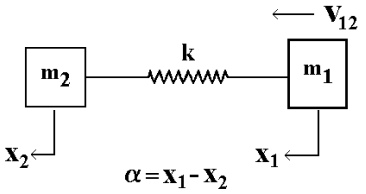

Fig. 4.33 A Two-Mass System

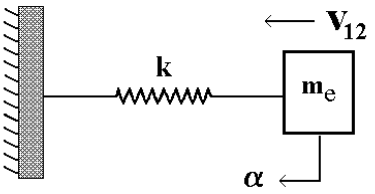

Fig. 4.34 An Effective-Mass System

The equations of motion of the two-mass system, the relative response variables, and the definitions of mass reduction factors and effective mass are covered. The dynamic responses of the two-mass system and one effective mass system are summarized in Eq. (4.25).

$$
\begin{aligned}
&\textit{TWO-MASS SYSTEM:}\quad \ddot{x}_1 = \gamma_1 \ddot{\alpha}, \qquad \ddot{x}_2 = -\gamma_2 \ddot{\alpha}, \quad \ldots\ldots \quad (1)\\
&\textit{where:}\quad \ddot{\alpha} = -v_{12}\,\omega_e \sin(\omega_e t) \quad \ldots\ldots\ldots\ldots\ldots\ldots \quad (2)\\
&\omega_e = \sqrt{\frac{k}{m_e}} \quad \ldots\ldots \textit{angular natural frequency} \quad \ldots\ldots \quad (3)\\
&\gamma_1 = \frac{m_2}{m_1 + m_2} \quad \ldots\ldots \#1\ \textit{mass reduction factor} \quad \ldots\ldots \quad (4)\\
&\gamma_2 = \frac{m_1}{m_1 + m_2} \quad \ldots\ldots \#2\ \textit{mass reduction factor} \quad \ldots\ldots \quad (5)\\
&m_e = \frac{m_1 m_2}{m_1 + m_2} \quad \ldots\ldots \textit{effective mass} \quad \ldots\ldots\ldots\ldots \quad (6)
\end{aligned}
\tag{4.25}
$$

Using the equations of motion and the relative motion relationship, the dynamic equivalency between the two-mass and effective-mass systems can be established. The absolute decelerations of the two masses in the two-mass system are then computed using the mass reduction factors. In a special case where mass m_2 is infinite, the effective mass shown in (6) of Eq. (4.25) then becomes m_1. The mass reduction factor for mass #1, γ_1, equals one, and that for mass #2, γ_2, equals zero.

In the effective mass system, the mass and spring stiffness are m_e and k, respectively. The impact speed remains the same as V_{12}. Therefore, the two systems become identical. Note that by using the mass reduction factor relationships shown in (4) and (5) of Eq. (4.25), the relative deceleration in the effective-mass system can be converted to the absolute decelerations of the two-mass system as shown in (1) of Eq. (4.25). Note that the relative deceleration of mass 1 to mass 2 is the same as the deceleration of the effective mass shown in (2) of Eq. (4.25). Also, the period T of the dynamic responses for both systems remains the same and equals $2\pi/\omega_e$ where ω_e is defined by (3) of Eq. (4.25).

4.5 VEHICLE TO BARRIER (VTB) IMPACT: SPRING-MASS MODEL

Since there is no damping in the spring-mass model being analyzed, the motion of the system is a non-decayed oscillatory one. The absolute displacements of the two masses are x_1 and x_2, and the relative impact velocity and displacement between the two masses are v_{12} and α, respectively. The motion of the spring-mass model is sinusoidal.

4.5.1 Model Formulation

The transient and major response relationships are shown by explicit formulas in Eq. (4.26) to (4.28). Given the rigid barrier impact velocity and model values of mass and spring, the dynamic

crush and the peak magnitude of the vehicle sinusoidal acceleration, A, can be computed. It can be shown that A is twice as large as the ESW (equivalent square wave) for the same vehicle.

Let us define:

C: dynamic crush
V: initial barrier impact velocity
A: peak sinusoidal deceleration magnitude of the effective mass
w: effective weight (or W)
k: effective spring stiffness (or K)
ω_e: circular natural frequency of the effective mass
f : vehicle structural natural frequency, Hz

TRANSIENT RESPONSES:

$$\alpha(t) = \frac{V}{\omega_e}\sin(\omega_e t), \quad \dot{\alpha}(t) = V\cos(\omega_e t), \quad \ddot{\alpha}(t) = -V\omega_e \sin(\omega_e t)$$

$$\alpha_m = \frac{V}{\omega_e} \quad \ldots\ldots\ldots \textit{maximum dynamic crush}$$

$$T_m = \frac{\pi}{2\omega_e} \quad \ldots\ldots\ldots \textit{time at } \alpha_m$$

(4.26)

Normalized Responses are: $\dfrac{\alpha(t)}{\frac{V}{\omega_e}}$; $\dfrac{\dot{\alpha}(t)}{V}$; $\dfrac{\ddot{\alpha}(t)}{V\omega_e}$

MAJOR RESPONSE FORMULAS (*in natural units*):

$$C = \frac{V}{\omega_e} \qquad (1)$$

$$V = C\omega_e \qquad (2)$$

$$A = V\omega_e = C\omega_e^2 \qquad (3)$$

(4.27)

Eliminating ω_e *between* (2) *and* (3) *yields*

$$A = \frac{V^2}{C} \qquad (4)$$

$$A = 2\pi f V \qquad (5)$$

MAJOR RESPONSE FORMULAS (*in conventional units*):
(*C*: *in*; *V*: *mph*; *A*, *g*; *w*: *lb*; *k*: *lb/in*; *f*: *Hz*)

$$C = 0.9V\sqrt{\frac{w}{k}} \qquad (1)$$

$$k = 0.8w\left(\frac{V}{C}\right)^2 \qquad (2)$$

$$k = 1.25w\left(\frac{A}{V}\right)^2 \qquad (3)$$

(4.28)

Equating (2) *to* (3), *then*

$$A = 0.8\frac{V^2}{C} = 2\,ESW \qquad (4)$$

$$A = 0.29fV \qquad (5)$$

Note that given the barrier impact speed of V and dynamic crush of C, the peak magnitude of sinusoidal acceleration, A, given by formula (4) of Eq. (4.27) is twice as large as the magnitude of the equivalent square wave (in conventional units of g, mph, and inches: ESW = 0.4 V^2/C).

4.5.2 Design and Trend Analysis

The parametric relationships between the major model dynamic responses and model parameters are shown in the following.

4.5.2.1 *Acceleration Function*

From the closed-form relationships, the trend of the peak vehicle deceleration in terms of weight and stiffness can be visualized from the surface plot shown in Fig. 4.35. The magnitude of peak deceleration decreases as the weight increases while the peak deceleration increases as the structural stiffness increases (note: 1 kips = 1 kilo-pounds = 1 klbs).

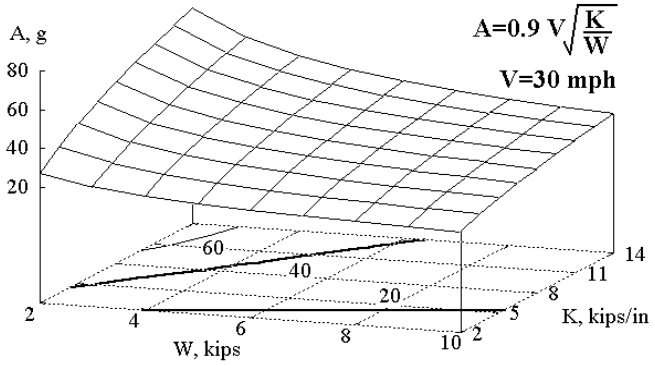

Fig. 4.35 3-D Surface Plot of Peak Acceleration of a Spring-Mass Model

4.5.2.2 *Dynamic Crush Function*

The trend of the dynamic crush, in terms of weight and stiffness, can be visualized in Fig. 4.36. Opposite to the trend of the peak acceleration, the dynamic crush increases as the weight increases, while the dynamic crush decreases as the structural stiffness increases. The opposite trend between the acceleration and dynamic crush can be explained by the relationship shown by formula (4) of Eq. (4.27) where the product of A and C equals to 0.8 V^2. For example, for V = 30 mph, C = 24 in of a vehicle in a barrier test, ESW = 0.4 V^2/C = 15 g, then A = 0.8 V^2/C = 30 g = 2 × ESW.

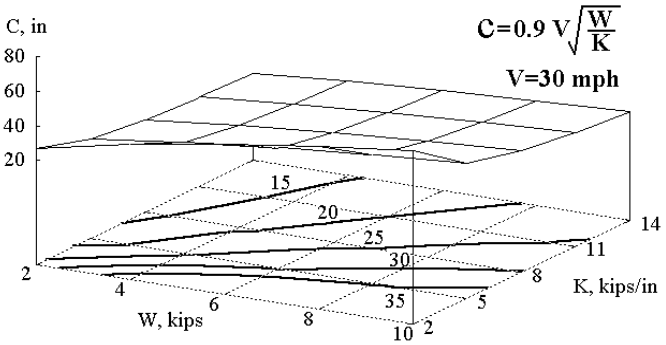

Fig. 4.36 3-D Surface Plot of Dynamic Crush as a Function of Weight and Stiffness

4.5.2.3 *Estimating Time of Dynamic Crush, T_m*

In a rigid barrier impact, where the vehicle structure is represented by a spring-mass system, the time of dynamic crush, T_m, can be estimated based on the period of the dynamic system. Since the dynamic crush occurs at the quarter of the period shown in Fig. 4.37, T_m can then be expressed as a function of the initial barrier impact speed, V, and dynamic crush, C, shown in Eq. (4.29).

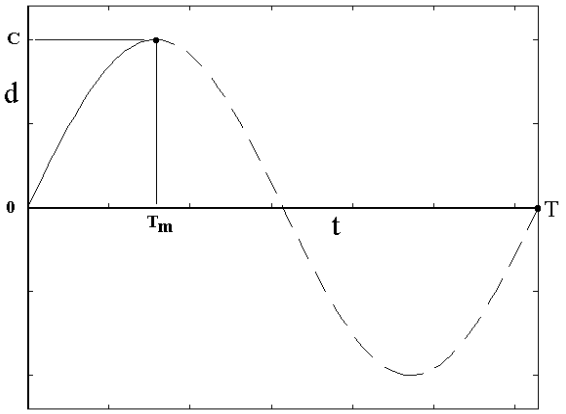

Fig. 4.37 Time of Dynamic Crush for a Spring-Mass System

$$\because \quad \omega_n = \frac{V}{C}, \quad and \quad T(period) = \frac{2\pi}{\omega_n}, \quad \therefore \quad T_m = \frac{T}{4} = \frac{\pi}{2\,\omega_n} = \frac{\pi\,C}{2\,V}$$
$$\because \quad T_c = \frac{C}{V}, \quad \therefore \quad T_c = \frac{2}{\pi} T_m = .64\,T_m \tag{4.29}$$

Therefore, for a simple (linear) spring-mass model, the output sinusoidal deceleration response (a quarter-cycle sine wave in the deformation phase) has a centroid time equal to 64% of the time of dynamic crush.

For computations using the conventional units of V in mph, C in inches, and T_m in milliseconds, the following formulas should be used:

In conventional units (mph, inches, milliseconds, lb, lb/in):

$$T_m = 28.4\,\frac{\pi\,C}{V} = 89\,(\frac{C}{V}), \qquad T_m = 89\left(\,.9\sqrt{\frac{W}{K}}\right) \doteq 80\sqrt{\frac{W}{K}} \tag{4.30}$$

Observing the parametric relationship shown in Eq. (4.30), T_m, the time of dynamic crush, is proportional to the characteristic length, C/V, but is only inversely proportional to the square root of specific stiffness, K/W. That is to say, the specific stiffness is not a strong factor by itself compared to characteristic length because of the square root. However, it will be shown in Chapter 5 that the damping factor plays an important role in controlling the time of dynamic crush in addition to K/W.

The trend of the time of dynamic crush in terms of weight (W) and stiffness (K) is shown by the 3-D plot in Fig. 4.38. The timing of the dynamic crush, T_m, increases as the weight increases, while the timing decreases as the structural stiffness increases.

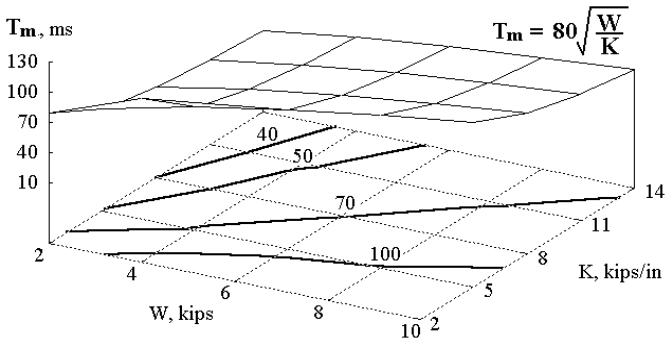

Fig. 4.38 T_m as a Function of Weight and Stiffness

4.5.2.4 *Response Properties as a Function of V and C*

Given a dynamic crush for the car and truck in a 35 mph barrier crush, four responses related to V and C, the characteristic length, specific stiffness, time of dynamic crush, and centroid time, can be obtained. These are shown in Table 4.1.

Table 4.1 Response Properties As A Function of V_o and C

Vehicle: V= 35 mph, fixed barrier	**C, in**	**C/V, in/mph**	**K/W, lb/in/lb**	**T_m, ms**	**T_c, ms**
	Dynamic Crush	Characteristic Length	Specific Stiffness $=0.8\ (V/C)^2$	Time at C =89 (C/V)	Centroid Time $=.64\ T_m$
Car	**35**	1.0	0.80	89	57
Truck	**28**	0.8	1.25	71	46

The computed characteristic length of the subject full-size vehicle falls within the typical range of 0.9 to 1.1. The characteristic length, expressed in time, is also equal to the centroid time T_c (time at the area centroid of the crash pulse in deformation phase), which is 57 ms [C/V = 35 in / (35*17.6 in/s) = 0.057 sec]. The relative centroid location with respect to T_m is then 57 ms/89 ms = 0.64. This confirms that the spring-mass model produces a quarter-sine acceleration response, where the relative centroid location is 0.64.

4.5.2.5 *Mass and Stiffness Ratios in Vehicle-to-Vehicle Impact*

Another useful relationship that can be derived from the above is the determination of the relative magnitude between the mass ratio and stiffness ratio of two vehicles in a collision. Knowing from Table 4.1 that the specific stiffness of the truck is greater than that of the car, it follows that the stiffness ratio of the truck (t) to car (c), r_K, will be greater than the mass ratio of the truck to car, r_M. The proof of this relationship is shown in Eq. (4.31).

$$
\begin{aligned}
&\textit{Since} \quad \frac{K_t}{M_t} > \frac{K_c}{M_c}, \quad \textit{and} \quad K>0, \quad M>0, \\
&\textit{after interchanging } K_c \textit{ and } M_t, \quad \textit{one gets} \\
&\qquad \frac{K_t}{K_c} > \frac{M_t}{M_c}, \quad \textit{or} \\
&\qquad r_K > r_M, \quad \textit{where} \\
&r_K : \textit{stiffness ratio of truck to car} \\
&r_M : \textit{mass ratio of truck to car}
\end{aligned}
\tag{4.31}
$$

The relationship between the stiffness and mass ratios shown in Eq. (4.31) provides a good basis for the determination of crash severity in a vehicle-to-vehicle impact.

4.5.3 Effect of Test Weight Change on Dynamic Responses

In the vehicle-to-rigid barrier test, the vehicle structural design may stay the same, but, due to differences in the optional contents and/or fastened payload, the test weight may differ substantially. Taking advantage of the closed-form formula, the sensitivity of the major dynamic responses with respect to the change in test weight can be derived. Using conventional units and the following definitions of variables:

W (or w):	vehicle test weight, lb
K (or k) :	stiffness, lb/in
V (or v) :	vehicle-to-rigid barrier impact speed, mph
C (or c) :	dynamic crush, in

$$
\begin{aligned}
\because \quad c &= .9v\sqrt{\frac{w}{k}} && (1) \\
\frac{\partial c}{\partial w} &= .45v\,\frac{1}{\sqrt{wk}} && (2) \\
k &= .8w\left(\frac{v}{c}\right)^2 && (3) \\
wk &= .8\left(\frac{wv}{c}\right)^2 \\
\textit{therefore} \quad \sqrt{wk} &\simeq .9\frac{wv}{c} && (4)
\end{aligned}
\tag{4.32}
$$

Substituting (4) into the sensitivity (2) of Eq. (4.32), (2) becomes

$$
\frac{\partial c}{\partial w} = .5\frac{c}{w} \tag{4.33}
$$

Case Study 1: Compute weight sensitivity on crush

A full-size passenger car was crashed in a 31 mph rigid barrier impact. The test weight was w = 4452 lb, and the dynamic crush was c = 31.5 in; compute the weight sensitivity of the dynamic crush.

Using Eq. (4.33), the change of the dynamic crush with respect to the change in the test weight is computed as follows:

$$\frac{\partial c}{\partial w} \simeq .5\,\frac{c}{w} = .5\,\frac{31.5}{4452} = 3.5\times10^{-3}\,\frac{in}{lb} = .35\,\frac{in}{100\,lb} \tag{4.34}$$

The change in the dynamic crush is therefore about 0.35 inches per each 100 pound increase in test weight. Since the characteristic length of the vehicle is 1.02 in/mph (31.5 in/31mph), the increase of 0.35 inches per 100 pounds weight increase is equivalent to that produced in a test with a speed increase of one-third of a mph on the original vehicle test weight.

In two 35 mph barrier crash tests, the same model trucks with different loadings were used. The decelerations at the rocker and B-pillar for both tests and their integrals are shown in Figs. 4.39 and 4.40, respectively.

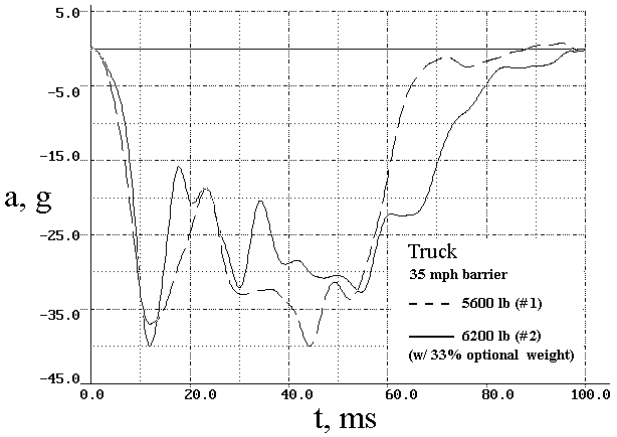

Fig. 4.39 Mass Effect on Vehicle Acceleration Response

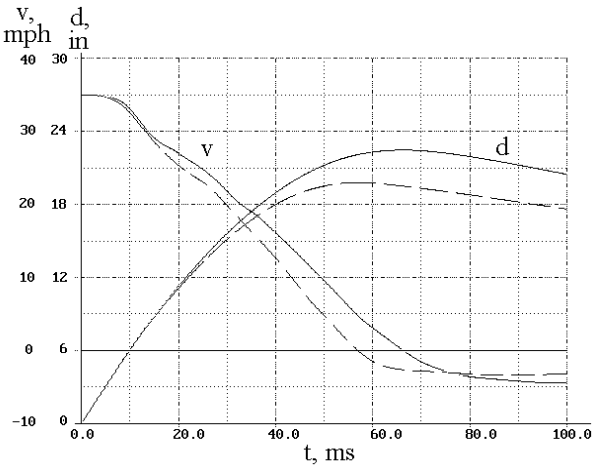

Fig. 4.40 Mass Effect on Vehicle Velocity and Displacement Responses

For the heavier truck (solid line), both dynamic crush and time of dynamic crush are larger than those for the lighter truck, as shown in Table 4.2. The relative response magnitudes of the acceleration and dynamic crush of the two vehicles are confirmed by the weight trend analysis plots shown in Figs.

4.35 and 4.36, respectively. Shown in Fig. 4.39, the impulses of the two vehicles between 0 to 20 ms are mainly due to the stiff front rail design and damping of the body mount. They are not considered the decelerations of the main body of the truck. It will be shown in Chapter 5 that the impulsive transient responses at the beginning of the crush are mainly controlled by the damping characteristics of the body mounts, positioned between the compartment (or cab) and frame. The steady state compartment responses, where the peak body deceleration occurs, are attributed mainly to and controlled by the spring stiffness of the system.

Table 4.2 Weight Effects on Major Vehicle Responses in 35 mph Rigid Barrier Tests

Truck Weight, lb	Transient State, A_t, g peak acceleration	Steady State A_P, g peak acceleration	C, in dynamic crush	T_m, ms time at C
6200 (heavier)	40	32.5 @ 53 ms	22.5	65
5600 (lighter)	37	40 @ 43	19.7	56

Case Study 2: Compute the truck stiffness in a low speed impact

A truck was tested in a perpendicular barrier condition with the following data:

V = 14 mph, A = 19 g (rocker panel at B-post), and w = 5800 lb

Determine the structural stiffness and the dynamic crush and show the transient dynamic responses.

$$\begin{aligned}
&\textit{Define:} \quad \frac{A}{V}\ (\textit{characteristic deceleration}) = \frac{19\ g}{14\ mph} = 1.36\,\frac{g}{mph} \\
&\textit{Compute:} \quad \frac{K}{W}\ (\textit{specific stiffness}) = 1.25\left(\frac{A}{V}\right)^2 = 2.312\,\frac{lb/in}{lb} \\
&\textit{therefore} \quad K = W\,x\,2.312 = 5800\,x\,2.312 = 13410\ lb/in \\
&\textit{Define:} \quad \frac{C}{V} = .9\sqrt{\frac{W}{K}} = .9\sqrt{\frac{1}{2.312}} = .592\,\frac{in}{mph} \\
&\textit{therefore} \quad C = V\,x\,.592 = 14\,x\,.592 = 8.3\ in
\end{aligned} \tag{4.35}$$

The computed dynamic crush C compares fairly well with the 8.4 inches obtained in the test film analysis.

Case Study 3: Compute the car stiffness in a low speed impact.

Two tests were conducted using a full-size sedan with a test weight of 4200 lbs. They were tested in 8 and 14 mph fixed barrier conditions with dynamic crushes of 6.9 and 12.2 inches, respectively. Determine the structural stiffness and the transient response of the car in the two test conditions.

Using the formulas for the spring-mass impact model, the transient responses and model parameters were calculated and compared to those from the tests (Table 4.3 and Figs. 4.41–4.43). The dynamic crushes of the model using the respective spring stiffnesses were identical to those from the tests. The model, which has only one structural parameter, stiffness, serves the purpose of predicting one boundary condition in the test, the dynamic crush. The times of dynamic crush between the model and test are different, since these timings were not constrained by the spring-mass model. The spring-mass model can be made to satisfy the time of dynamic crush of a test; however, the model dynamic crush will then not be constrained and may be different from that in the test.

Since the values of the computed model stiffness are about the same for the two tests at different speeds (see Table 4.3), this indicates that a linear system prevails for the test speed range of 8 to 14

mph. The model transient responses are therefore proportional to the speed, which are the characteristics of a linear system. For example, the ratios of the model peak deceleration, A (13.2 and 7.4 g), to the dynamic crush, C (12.2 and 6.9 in), at the 14 and 8 mph speeds are respectively equal to the speed ratio of 1.75. Since the principle of superposition holds for a linear system, the model responses at a 22 mph speed would be simply the sum of those responses at 8 and 14 mph (A = 13.2 + 7.4 = 20.6 g, and C = 12.2 + 6.9 = 19.1 in).

Table 4.3 Model and Test Vehicle Responses at 8 and 14 mph

Speed, mph	Car Weight, w, klbs	Dynamic Crush C, in @ T_m, ms		Model		
		Test	Model	k, klb/in	ω_e, rad/s [6/] (f, Hz)	A, g
8	4.2	6.9 @77	6.9 @ 84	4.47	20.30 (3.23)	7.4
14		12.2 @ 79	12.2 @ 78	4.54	20.44 (3.25)	13.2

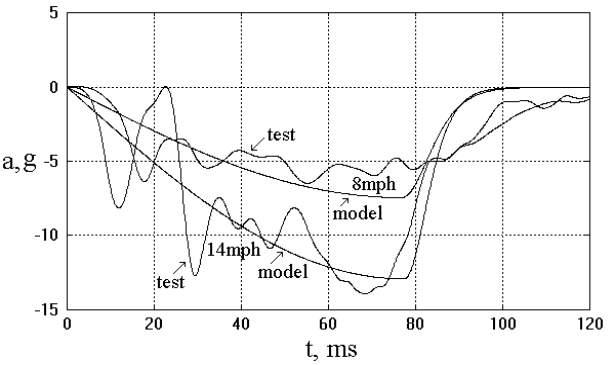

Fig. 4.41 a vs. t of a Full-Size Car in 8 and 14 mph Barrier Tests

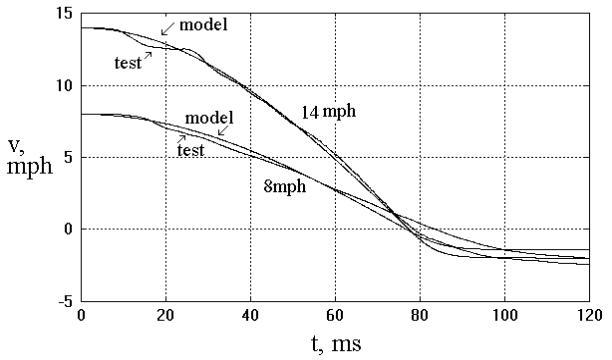

Fig. 4.42 v vs. t of a Full-Size Car in 8 and 14 mph Barrier Tests

---

[6/] $\omega_e = \sqrt{386.4\frac{k}{w}}$ rad / s, $f = \frac{\omega_e}{2\pi}$ Hz

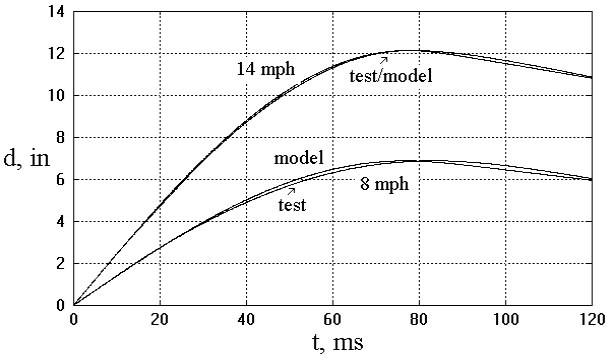

Fig. 4.43 d vs. t of a Full-Size Car in 8 and 14 mph Barrier Tests

4.6 SPRING-MASS OCCUPANT MODEL SUBJECTED TO EXCITATION

In the previous section, vehicle-to-barrier impact modeling was presented. In this section, the restrained occupant response in a sled test shown in Fig. 4.44 is presented.

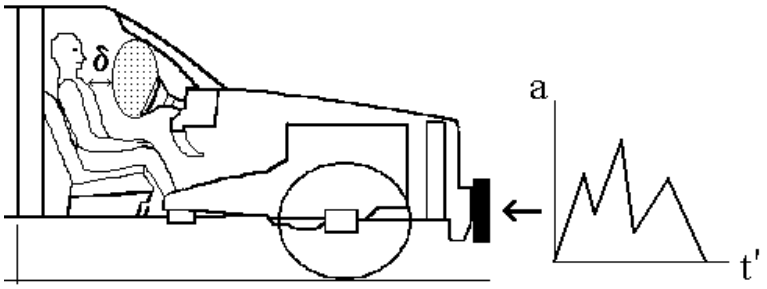

Fig. 4.44 An Occupant Model Subjected to An Excitation

In this section, the occupant restraint system is represented by a spring-mass model with a restraint slack, δ. A set of closed-form solutions for the model subjected to TESW and halfsine waves is derived. Since there is slack in the restraint system, the initial conditions of the occupant contacting the restraint need to be determined before the occupant response closed-form solutions can be derived. Fig. 4.45 shows the crash pulse excitation and the conditions at the time of restraint contact.

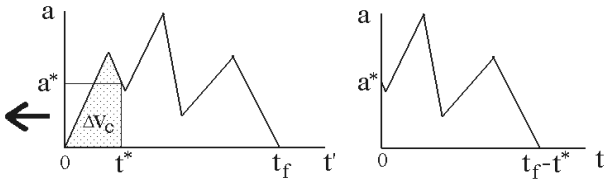

Fig. 4.45 Occupant Relative Kinematics at Restraint Contact Time

Using the relative motion approach, the equations of motion of an occupant in a fixed reference (w.r.t. the ground) and in a relative frame (w.r.t. the sled) are shown by expressions (1) and (3) in Eq. (4.36). The procedures for deriving the closed form solutions of the occupant responses due to a tipped equivalent square wave and a sinusoidal excitation are described in the next section.

4.6.1 Response Solutions due to TESW and Sinusoidal Excitation

A spring-mass model with restraint slack subjected to an TESW (tipped equivalent square wave) and sinusoidal excitations is shown in Fig. 4.46. The output responses of the model are derived in closed-form solutions. In general, the effect of the model parameters on the occupant responses can be described by a dynamic amplification factor (DAF).

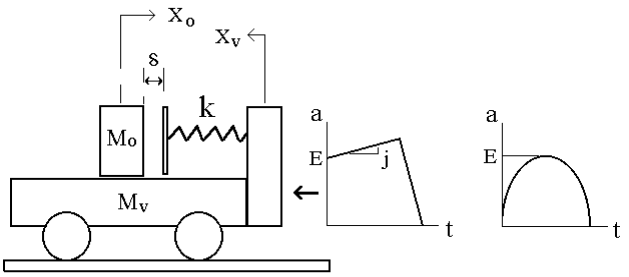

Fig. 4.46 A Sled Impact Model

A simple occupant restraint model has a restraint slack of δ and stiffness of k with an occupant mass of m. The initial conditions at the time of occupant restraint contact (the start of the restraint coupling phase) are shown as follows:

t: *time*
t_g: *time at* $a_o|_{max}$ (*measured from* t^*)
a_o: *occupant deceleration*
a_v: *sled excitation*
$\ddot{\alpha}$: *occupant decel relative to sled*
ω_e: *restraint natural frequency*$(=2\pi f_e)$
E^*: *sled decel at* t^*
E : *deceleration of TESW at* $t = 0$
t^*: *restraint contact time*
j: *slope of TESW*
v^*: *restraint contact velocity*

E.O.M.: $\Sigma F = ma$

$$K(X_v - X_o - \delta) + C(\dot{X}_v - \dot{X}_o) = M_o \ddot{X}_o \quad \ldots\ldots \quad (1) \tag{4.36}$$

where
X_v: *absolute displacement of vehicle* (*sled*)
X_o: *absolute displacement of occupant*
δ : *restraint system slack* (*a constant*)
Let α *be the relative displacement between* M_o *and* M_v

$$\alpha = X_v - X_o - \delta, \quad \dot{\alpha} = \dot{X}_v - \dot{X}_o - \dot{\delta} = \dot{X}_v - \dot{X}_o$$

$$\ddot{\alpha} = \ddot{X}_v - \ddot{X}_o \quad \ldots\ldots\ldots\ldots\ldots \quad (2)$$

from Eq.(2): $\ddot{X}_o = a_v - \ddot{\alpha}$

substituting into (1):

$$\ddot{\alpha} + \frac{C}{M_o}\dot{\alpha} + \frac{K}{M_o}\alpha = a_v \quad \ldots\ldots\ldots \quad (3)$$

4.6.1.1 *Model with TESW Excitation, (E + j t)*

Eq. (4.37) shows the equation of motion of a spring mass model subjected to a TESW excitation.

$$\ddot{\alpha}+\omega_e\alpha = -(E+jt) \tag{4.37}$$

Initial Conditions: The occupant kinematics at the time of restraint contact are shown as follows.

$$\begin{aligned} E^* &= E + jt^* \\ v^* &= Et^* + \frac{1}{2}j(t^*)^2 \\ \delta &= \frac{1}{2}E(t^*)^2 + \frac{1}{6}jt^{*3} \end{aligned} \tag{4.38}$$

Formula: The solutions to the equation of motion can be solved by the method of undetermined coefficients. The occupant transient response and maximum response formulas are shown in Eqs. (4.39) and (4.40), respectively.

$$\begin{aligned} &\textit{OCCUPANT TRANSIENT RESPONSE:} \\ &a_o = \ddot{\alpha} + a_v = p\sin(\omega_e t+\phi) + E^* + jt \quad \ldots\ldots\ldots \quad (1) \\ &\textit{where} \quad \phi = \tan^{-1}\left(\frac{-E^*}{v^*\omega_e - \frac{j}{\omega_e}}\right) \\ &p = \sqrt{(E*)^2 + \left(v^*\omega_e - \frac{j}{\omega_e}\right)^2} \end{aligned} \tag{4.39}$$

$$\begin{aligned} &\textit{OCCUPANT MAJOR RESPONSES:} \\ &a_o|_{\max} = \sqrt{E^{*2} + (v^*\omega_e)^2 - 2v^*j} + E^* + jt_g \quad \ldots\ldots\ldots \quad (2) \\ &t_g = \frac{\cos^{-1}\left(\frac{-j}{\omega_e p}\right) - \phi}{\omega_e} \end{aligned} \tag{4.40}$$

Special Case #1: For j (slope of TESW) = 0, then

$$\begin{aligned} E &= ESW\ (Equivalent\ Square\ Wave) \\ v* &= ESW\,t^*, \quad therefore \\ a_o|_{\max} &= ESW\left[1 + \sqrt{1+(2\pi f t^*)^2}\right] \end{aligned} \tag{4.41}$$

This closed-form solution for the maximum occupant deceleration has been derived [1]. The occupant model, having a restraint slack of δ and natural frequency of f, is subjected to a constant deceleration ESW.

Special Case #2: For δ (restraint slack) = 0

At time zero, occupant relative contact velocity equals zero. The maximum occupant acceleration equals the sum of two times the acceleration of the first TESW data point (E*) and the change in TESW acceleration between time zero and time when maximum occupant acceleration occurs. Using (2) of Eq. (4.40), the simplified occupant acceleration formula is obtained and shown in Eq. (4.42).

$$\because \quad v^* = 0, \quad E^* = P_o, \quad and \quad j t_g = \frac{P_1 - P_o}{t_m} t_g$$
$$\therefore \quad a_o|_{max} = 2E^* + j t_g \quad \ldots\ldots\ldots\ldots \quad (1) \tag{4.42}$$

Case Study:

Two crash pulses with the same velocity change in the deformation phase are used to excite an occupant model. One is a front-loaded and the other is a rear-loaded crash pulse. An occupant in a sled test is restrained with an air bag and 3-point belt with a pretensioner such that the restraint slack is about zero during the impact. Determine the occupant acceleration magnitudes due to the two distinctive crash pulses.

The solutions to the problems are shown in Table 4.4. The front-loaded crash pulse produces higher occupant acceleration than the rear-loaded one. The occupant without restraint slack is affected by the magnitude of the first point and slope of a TESW line-segment as shown in (1) of Eq. (4.42).

The front-loaded crash pulse may be beneficial in reducing the time for the occupant to reach and contact the restraint system and start the vehicle ridedown during the occupant-restraint coupling phase. However, the front-loaded pulse may yield a higher occupant response when the restraint slack is negligible. In the case of an even-loaded crash pulse, where the sled pulse is 17.5 g, the output acceleration is equal to 35 g, two times the constant sled pulse acceleration.

Table 4.4 Occupant Responses Due to TESW Pulses with δ = 0

Pulse Shape	TESW 1st & 2nd Points		t_m, ms	TESW Slope j, g/ms	Restraint Slack & Natural Freq		$a_o\|_{max}$, g @ t_g, ms
	P_o, g	P_1, g			δ, in	f, Hz	
Rear-Loaded	15	20	100	.05	0	7	33.7 @ 75
Front-Loaded	20	15	100	-.05	0	7	36.6 @69

The TESW sled pulses and transient occupant responses are shown in Fig. 4.47. As the TESW slope increases (more rear-loaded), the occupant peak acceleration decreases.

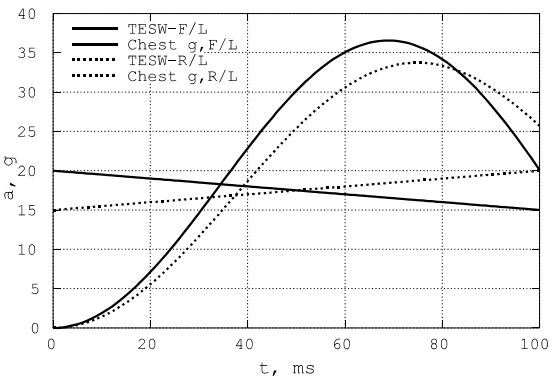

Fig. 4.47 Occupant Decelerations due to Front- and Rear-Loaded Pulse Excitation

4.6.1.2 *Sine Excitation (E sin ωt)*

The equation of motion of a spring mass model with a sinusoidal excitation is shown in Eq. (4.43). E is the peak magnitude of the sinusoidal acceleration.

$$\ddot{\alpha} + \omega_e \alpha = -E \sin(\omega t) \tag{4.43}$$

Initial Conditions: The occupant kinematics at the time of restraint contact are shown as follows.

$$E^* = E \sin(\omega t^*), \quad v^* = \frac{E}{\omega}\left[1 - \cos(\omega t^*)\right]$$
$$\text{and,} \quad \delta = \frac{E}{\omega}\left[t^* - \frac{\sin(\omega t^*)}{\omega}\right] \tag{4.44}$$

Response Formula: The solutions to the equation of motion which can be solved by the method of undetermined coefficients are shown in Eq. (4.45). The output acceleration consists of three components: complementary, particular parts of solution, and the magnitude of sinusoidal pulse, E.

$$\ddot{\alpha} + \omega_e^2 \alpha = -E \sin(\omega t), \quad \textit{the solution consists of:}$$
$$a_o = \ddot{\alpha}_c + \ddot{\alpha}_p - E \sin[\omega(t + t*)], \quad \textit{where}$$
$$\frac{\ddot{\alpha}_c}{E} = \left[\frac{\cos(\omega t*)}{1 - r_\omega^2} - 1\right]\frac{\sin(\omega_e t)}{r_\omega} + \frac{\sin(\omega t*)\cos(\omega_e t)}{1 - r_\omega^2}$$
$$\frac{\ddot{\alpha}_p}{E} = \frac{-r_w^2 \sin[\omega(t + t^*)]}{1 - r_\omega^2} \tag{4.45}$$
$$\textit{Here} \quad r_\omega = \frac{\omega}{\omega_e} = \frac{\textit{excitation frequency}}{\textit{restraint natural frequency}}$$
$$DAF = \frac{a_{o|\max}}{E}$$

Since each part of the solution contains the magnitude E, a transient DAF (dynamic amplification factor) for the sinusoidal excitation can be explicitly defined as DAF (t) = $a_o(t)$ / E. The maximum DAF, found by searching for the maximum occupant response, is equal to DAF = $a_o|_{max}$ / E.

Case Study 1: Occupant restraint system with a frequency ratio less than one

Given a restraint natural frequency, ω_e = 8 Hz, a 3-D contour surface plot of the DAF in terms of the frequency ratio, r_ω, and restraint contact time is shown in Fig. 4.48.

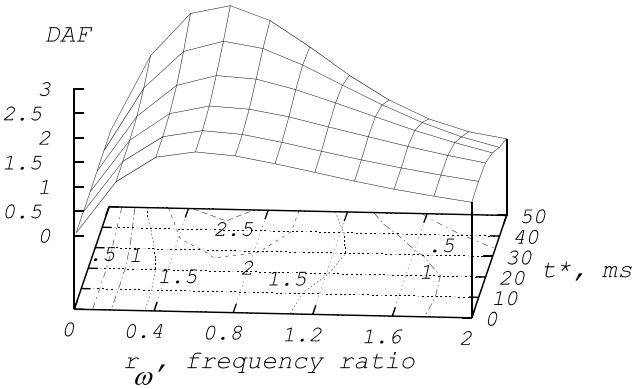

Fig. 4.48 DAF vs. Frequency Ratio and Contact Time

The excitation-to-restraint natural frequency ratio, r_ω, in the figure ranges from 0 to 2. The DAF(t), which is a function of time, is computed using the formula in Eq. (4.46) for the case where the restraint natural frequency is 8 Hz. The maximum occupant deceleration is then equal to the amplitude of the sine wave multiplied by the maximum dynamic amplification factor (DAF). The typical structural natural frequency of a passenger car in a rigid barrier impact is about 4 Hz. Therefore, given the value of the excitation to restraint natural frequency ratio, $r_\omega = 4/8 = .5$, the corresponding DAF ranges from about 1.7 to 2.5, depending on the restraint contact time, as shown in Fig. 4.48.

According to the surface plot shown in Fig. 4.48, the maximum DAF peaks when r_ω is between .4 and .6. The restraint system design with a natural frequency of 8 Hz and an excitation frequency of 4 Hz may not be an ideal combination since the frequency ratio is 4/8= .5. In studying the VOR (vehicle, occupant, and restraint) performance shown in Section 1.9.5, Chapter 1, the average restraint natural frequency in a 31 mph rigid barrier test is about 6 Hz. This would yield a frequency ratio of 4/6=.67 where the DAF is still on the high end.

According to the DAF surface contour plot, the DAF decreases noticeably when the frequency ratio is above 1. With a frequency ratio of 1, both excitation and restraint natural frequency are 4 Hz, and the DAF is about 1.5. It should be noted that the lower the restraint natural frequency, the softer the restraint is and the interior free travel space would have to be larger.

For each value of DAF, there exists a timing, t_g, where the maximum occupant acceleration, E*DAF, occurs. Fig. 4.49 shows a 3-D plot of t_g as a function of frequency ratio and restraint contact time.

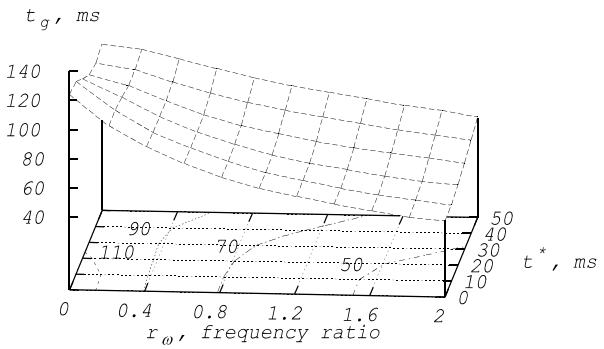

Fig. 4.49 Time at Maximum DAF (Restraint Freq.= 8 Hz)

Case Study 2: Body mount stranded cable with frequency ratio greater than one.

In a frame vehicle, the body mount mounted on the frame supports the cab or pickup box. During a crash, the cab tends to move forward relative to the frame due to the deformation of the mount assembly. To prevent the excessive deformation of the body mount, a piece of stranded steel cable is used to limit the deformation of the body mount to about 2.5 inches. In addition, the cable is used to produce an early impulsive loading on the passenger compartment. The early impulse yields a front loaded crash pulse which may improve the occupant ridedown efficiency, as discussed in Chapter 1.

The stranded cable is connected to the frame and rocker panel at both ends of the body mount. The installed cable has a slack of not more than one inch. Therefore, the cable will be under sudden dynamic loading when the body mount deforms more than one inch.

The loading conditions are described as follows. The excitation from the frame rail to the body mount is a halfsine with a 40 Hz excitation frequency (with a pulse duration of 12.5 ms) and a peak deceleration magnitude of 100 g. Determine whether the loading is sufficient to take up the slack. If it does, we would like to know the effect of the sudden cable loading on the deceleration of the cab.

From Chapter 2, Section 2.4.15, the displacement change due to halfsine loading is expressed as $\Delta d = 122.9\ A_p\ T^2$. Given $A_p = E = 100$ g, and T = .0125 seconds, then $\Delta d = 1.92$ inches. Therefore, the halfsine loading is more than enough to take up the slack of one inch and induce a dynamic loading on the cable.

To compute the dynamic amplification factor (DAF), the restraint contact time, t*, needs to be computed. Given $\delta = \Delta d = 1$ inch, t* can be computed from the displacement relationship shown in Eq. (4.44). A numerical method using a Newton-Raphson algorithm has been used, and it is found that t* = .0093 seconds (9.3 ms).

Using the DAF formulas shown in Eq. (4.45), the maximum DAF and the corresponding time have been obtained. The three parts of DAF, due to complementary, particular, and excitation (input) parts, are $DAF|_c = .199$, $DAF|_p = .822$, and $DAF|_e = -.771$. Therefore, the total DAF is equal to .251.

The dynamic loading on the cab due to the installed cable is then equal to 100 g x .251 = 25.1 g, which occurs at 21.5 ms.

Special Case: For $\delta = 0$, then t* = 0; a_o in Eq. (4.45) becomes

$$a|_{max} = -E\left[\frac{\sin\left(\frac{2\pi}{r_\omega + 1}\right)}{r_\omega - 1}\right] = -E\,[DAF] \quad \ldots\ (1)$$

t_g, the time when a is maximum, is

$$t_g = \frac{2\pi}{\omega + \omega_e} = \frac{1}{f + f_e} \quad \ldots\ (2) \qquad (4.46)$$

$$DAF = \frac{\sin\left(\frac{2\pi}{r_\omega + 1}\right)}{r_\omega - 1} \quad \ldots\ (3)$$

It is shown by (3) of Eq. (4.46) and Fig. 4.50 that the DAF is only a function of the excitation to natural frequency ratio when there is no restraint slack in the system. The timing, t_g, when the maximum output acceleration occurs, is equal to the inverse of the sum of the excitation and natural frequencies as shown by (2) of Eq. (4.46). For a typical passenger vehicle excitation frequency of 4 Hz and restraint natural frequency of 6 Hz, the peak occupant chest deceleration should therefore occur around 1/(6+4) = .1 seconds.

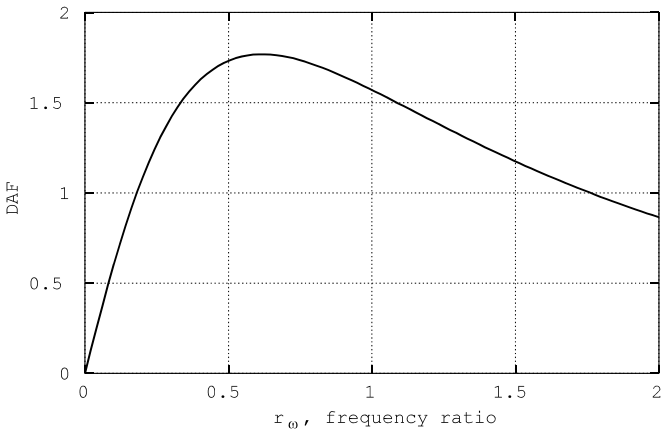

Fig. 4.50 DAF due to Sinusoidal Excitation ($\delta = 0$)

Case Study: A truck has f = 3 Hz (frequency of sinusoidal excitation to the cab or compartment), and E = 30 g (peak sinusoidal magnitude). The restraint system has no slack, and f_e = 7 Hz (the occupant restraint natural frequency). Then, the frequency ratio is r_ω = 3/7= .43. From Fig. 4.50, DAF = 1.67; therefore, the expected maximum occupant acceleration is 1.67*30 = 50 g, which occurs at 1/(3+7) = 0.1 sec (or 100 ms).

Excitation Frequency Ratio and Dynamic Loading

An impact is a dynamic loading if the DAF is greater than one and it is a static loading if the DAF is less than one. For the case of sinusoidal excitation to a spring-mass model without slack, the boundary between the static and dynamic loadings can be defined by the frequency ratio, the ratio of the sinusoidal excitation to system natural frequency.

As shown in Fig. 4.50, when the frequency is between 0.18 and 1.8, the system undergoes dynamic loading since the corresponding DAF is greater than one.

It is a common practice to use a pretensioner in the design of a restraint system for trucks. The purpose is to take up the restraint slack quickly and apply a limited pre-loading to the occupant to reduce chest deceleration. In this case, the restraint slack in the modeling can be assumed to be zero. The DAF reaches a maximum of about 1.75 when the frequency ratio is near 0.6. In order to minimize the occupant (output) acceleration, which is the product of the magnitude of the sinusoidal pulse and the DAF, the region in which the frequency ratio is near 0.6 should be avoided. This is especially true for a truck, since the peak sinusoidal magnitude is fairly high compared to that of a car.

4.6.2 Model Response due to Sinusoidal Displacement Excitation

A simple spring-mass model, shown in Fig. 4.51, excited by a displacement function can be used to model rigid barrier and/or sled test conditions. The base of the spring-mass system is driven by an eccentric wheel which generates a sinusoidal displacement. At time zero, the wheel is rotating at a constant velocity ω, and the initial velocity of mass m is v_o.

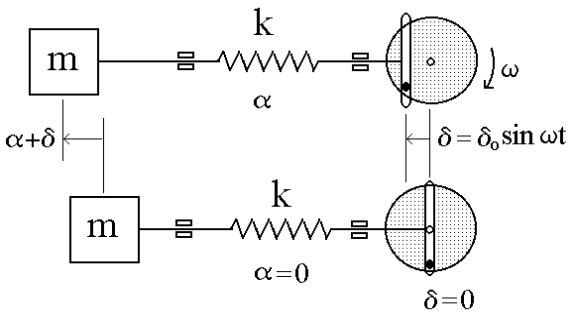

Fig. 4.51 Spring-Mass Model Under Impact and Sinusoidal Excitation

The equations of motion and their solutions are shown in the following pages. The solutions contain complementary and particular solutions. The complementary solution, defined by the free vibration, yields the transient part of the total solution, while the particular solution, defined by the force function, yields the steady state part of a total solution.

Since the system is linear, the acceleration of mass m due to the combination of impact and excitation is the sum of the individual accelerations due to the impact and excitation, respectively.

Definition of the System Variables and Excitation

Define:

δ: *displacement of pin A on disk*, δ_o: *displacement amplitude*

x: *absolute displacement of mass m*, α: *deflection of spring*,

ω: *angular excitation frequency of disk, radian*/sec,

ω_e: *natural frequency of the system*, r: *frequency ratio of* ω *to* ω_e (4.47)

$$x = \alpha + \delta = \alpha + \delta_o S\omega t\ , \qquad \therefore\ \ \alpha = x - \delta_o S\omega t$$

$$\dot{x} = \dot{\alpha} + \omega\delta_o C\omega t \qquad \ddot{x} = \ddot{\alpha} - \omega^2\delta_o S\omega t$$

where C: *Cosine function, and* $C\omega t = Cos(\omega t)$

S: *Sine function, and* $S\omega t = Sin(\omega t)$

Solutions to the Displacement and Acceleration Equations of Motion

E.O.M.: $\ddot{\alpha} + 2\zeta\,\omega_e\,\dot{\alpha} + \omega_e^2\,\alpha = -E\sin(\omega t)$

complementary solution (*transient due to free vibration*):

$$\alpha_c = C_1 S\omega_e t + C_2 C\omega_e t$$

$$\dot{\alpha}_c = \omega_e(C_1 C\omega_e t - C_2 S\omega_e t) \quad \ldots\ldots\ldots\ldots\ldots\ldots \quad (1)$$

$$\ddot{\alpha}_c = -\omega_e^2\alpha_c \qquad (4.48)$$

particular solution (*steady state due to forced vibration*):

$$\alpha_p = P_1 S\omega t + P_2 C\omega t$$

$$\dot{\alpha}_p = \omega(P_1 C\omega t - P_2 S\omega t) \quad \ldots\ldots\ldots\ldots\ldots\ldots \quad (2)$$

$$\ddot{\alpha}_p = -\omega^2\alpha_p$$

substitute the above into the EOM in α,
and equate the like terms:

$$S\omega t: -\omega^2 P_1 + \omega_e^2 P_1 = \omega^2\delta_o$$

$$C\omega t: -\omega^2 P_2 + \omega_e^2 P_2 = 0$$

$$\text{where}\ \ P_1 = \frac{r^2}{1-r^2}\delta_o\ ,\ \ P_2 = 0\ \text{and}\ \ r = \frac{\omega}{\omega_e} \quad \ldots\ldots \quad (3) \qquad (4.49)$$

$$\therefore\ \ \alpha_p = P_1 S\omega t$$

$$\alpha = \alpha_c + \alpha_p = C_1 S\omega_e t + C_2 C\omega_e t + P_1 S\omega t \quad \ldots\ldots\ldots \quad (4)$$

$$\dot{\alpha} = \dot{\alpha}_c + \dot{\alpha}_p = \omega_e(C_1 C\omega_e t - C_2 S\omega_e t) + P_1\omega C\omega t \quad \ldots\ldots \quad (5)$$

I.C. (*Initial Conditions*) *at* $t = 0$:

from (4): $\alpha = 0$, $C_2 = 0$; *from* (5): $\dot{\alpha} = v_0$, $v_0 = C_1\omega_e + P_1\omega$,

substituting p_1 *from* (3) *into* v_o, C_1 *becomes*

$$C_1 = \frac{v_o}{\omega_e} - \frac{r^3\delta_o}{1 - r^2} \quad \ldots\ldots\ldots\ldots \quad (6)$$

$$x = \alpha + \delta = \alpha_c + \alpha_p + \delta = C_1 S\omega_e t + (P_1 + \delta_o)S\omega t \qquad (4.50)$$

substituting P_1 *from* (3), C_1 *from* (6)
into x above, and simplifying, one gets

Displacement: $x = C_1 S\omega_e t + qS\omega t \quad \ldots\ldots\ldots\ldots\ldots \quad (7)$

$$\text{where}\ \ q = p_1 + \delta_o = \frac{\delta_o}{1 - r^2}$$

Deceleration: $\ddot{x} = -C_1\omega_e^2 S\omega_e t - q\omega^2 S\omega t \quad \ldots\ldots\ldots\ldots \quad (8)$

Based on the displacement and deceleration solutions given by (7) and (8) of Eq. (4.50), the solutions to the following three special cases can be derived and verified. Case (1), a translation problem, is for rigid barrier impact condition; Case (2), a rigid body rotation problem; and Case (3), an excitation problem where the initial impact velocity of the sled is zero. The DAF (dynamic amplification factor) is shown by (2) of Eq. (4.52). This is the same as formula (3) of Eq. (4.46), where the restraint slack is zero; the plot of DAF is shown in Fig. 4.50 in Section 4.6.1.2.

SPECIAL CASES:
Case (1): *Impact*: *Rigid Barrier Test*
since there is no excitation, $\delta_o = 0$ *and* $q = 0$, *then*

$$C_1 = \frac{v_o}{\omega_e} \quad \text{... dynamic crush,} \quad x = \frac{v_o}{\omega_e} S\omega t, \quad \text{and} \quad \ddot{x} = -v_o \omega_e S\omega_e t$$

Case (2): $v_o = 0$ *and* $r = 0$ *due to* (4.51)
$k = \infty$ (*spring is infinitively stiff*) *or* $\omega \ll \omega_e$

$$\therefore \quad r = \frac{\omega}{\omega_e} = 0, \quad \text{then} \quad C_1 = 0 \text{ and } q = \delta_o, \quad \text{then}$$

$$x = \delta_o S\omega t, \quad \ddot{x} = -\omega^2 \delta_o S\omega t$$

This is a rigid body dynamics in rotation.

Case (3) *Harmonic Excitation* (*a Halfsine*): *Sled Test*
Assuming the initial impact velocity is zero, then $v_o = 0$

$$C_1 = 0 - p_1 r = \frac{-r^3 \delta_o}{1 - r^2}, \quad \text{and} \quad q = \frac{\delta_o}{1 - r^2}$$

substituting into (7) *and* (8), *we get*

$$x = \frac{\delta_o}{1-r^2}(-r^3 S\omega_e t + S\omega t), \quad \ddot{x} = -\frac{\omega^2 \delta_o}{1-r^2}(-r S\omega_e t + S\omega t)$$

define $E = \omega^2 \delta_o$ . . . . *magnitude of sinusoidal acceleration*

$$\text{then} \quad \ddot{x} = \frac{-E}{1-r^2}(-r S\omega_e t + S\omega t) \quad \ldots\ldots\ldots\ldots\ldots\ldots \quad (1)$$

To determine t', *the time at maximum* $\ddot{x}$ *of mass m*:
set $\partial \ddot{x}/\partial t$ *to zero*:
$-r\omega_e C\omega_e t + \omega C\omega t = 0$, *since* $r\omega_e = \omega$, *then*
$-C\omega_e t + C\omega t = 0$, *or* $C\omega_e t = C\omega t$ (4.52)
The solution of the time at maxium $\ddot{x}$, t', *is solved using*
the trigonometric relationship: *Cosine*(x) = *Cosine*$(2\pi - x)$

$$\because \quad C\omega_e t' = C\omega t' = C(2\pi - \omega t'), \quad \therefore \quad \omega_e t' = 2\pi - \omega t', \quad \text{and}$$

to derive an expression for $\ddot{x}$ *at* $t = t'$:

$$S(\omega t') = S\left(\frac{2\pi\omega}{\omega_e + \omega}\right) = S\left(\frac{2\pi r}{1+r}\right) = S(2\pi - \omega_e t') = -S(\omega_e t')$$

Substituing $S(\omega t')$ *into* (1), *one gets*

$$\ddot{x} = \frac{-E}{1-r^2}\left[-rS\left(\frac{2\pi}{1+r}\right) + S\left(\frac{2\pi r}{1+r}\right)\right]$$

$$= \frac{E}{r^2 - 1}\left[-(r+1)\,S(\omega_e t)\right] = -E\left[\frac{S\left(\frac{2\pi}{r+1}\right)}{r-1}\right] = -E\,[DAF] \quad \ldots \quad (2)$$

4.7 VEHICLE-TO-VEHICLE (VTV) IMPACT: SPRING-MASS MODEL

In this section, the relative motion concept is applied to a vehicle-to-vehicle (VTV) impact analysis. First, the crash pulse approximation is performed and this is followed by the excitation on the occupant model described in Section 4.6. The same relative motion and dynamic amplification factor (DAF) concept is also applied to the vehicle-to-vehicle impact model, where the force deflection is elasto-plastic.

4.7.1 Crash Pulse Approximation by TESW and Sinusoidal Waves

Methods characterizing a test crash pulse using TESW (tipped equivalent square wave) and sinusoidal waves have been presented in Chapter 2. Using those two methods, two parameters satisfying two test boundary conditions can be specified for each of the approximations. For the TESW, the two parameters are p_o and p_1, the starting and ending decelerations at time zero, at time of dynamic crush. For the sinusoidal pulse, they are the structural natural frequency (or excitation frequency) and amplitude.

In the following analysis, only the sinusoidal wave approximation will be covered in detail. Since the procedures are the same, the analysis using the TESW is left for the readers as an exercise. However, the responses using TESW will be plotted and compared with those of the sinusoidal approximation and test pulses.

4.7.1.1 *Relative Motion Analysis (An Effective Mass System)*

In this section a vehicle-to-vehicle central impact involving a truck colliding with a car is used in the vehicle-to-vehicle compatibility analysis. Shown in Fig. 4.52 is a stationary mid-size passenger car with a test weight of 3000 lb struck by a truck of 4920 lb at 58 mph in a central impact. The subsequent test analysis evaluates the crash pulse approximation techniques using the concept of the effective mass system. The occupant-restraint model subjected to TESW and sinusoidal pulse excitations is then used to predict the occupant responses.

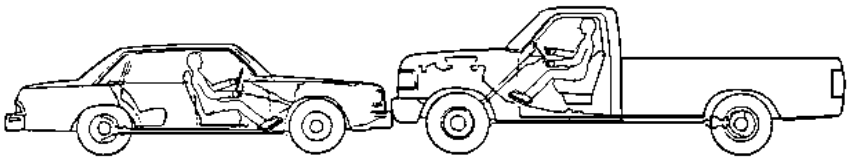

Fig. 4.52 A Truck-to-Car Central Impact

The crash test decelerations at the rocker panel on the B-pillar of the truck and car are shown in Fig. 4.53.

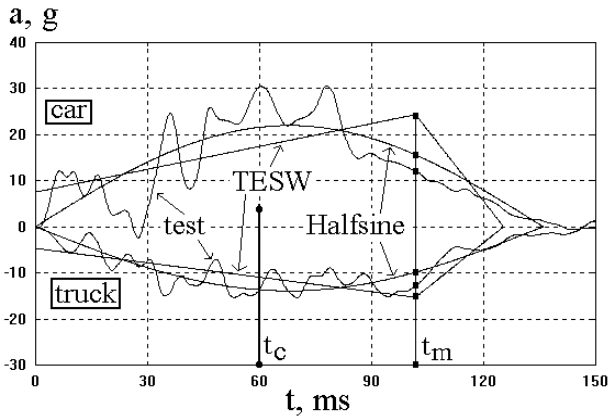

Fig. 4.53 Deceleration – A Two-Mass System

The relative truck-to-car deceleration can be obtained by subtracting the acceleration of the car from the deceleration of the truck; this is shown in Fig. 4.54. The relative deceleration of the two vehicles is then used to construct the TESW (tipped equivalent square wave) and sinusoidal approximated pulse. Based on the relative deceleration of the truck-to-car, as shown in Fig. 4.54, the steps needed to compute the parameters for the construction of the sinusoidal pulse are shown as follows.

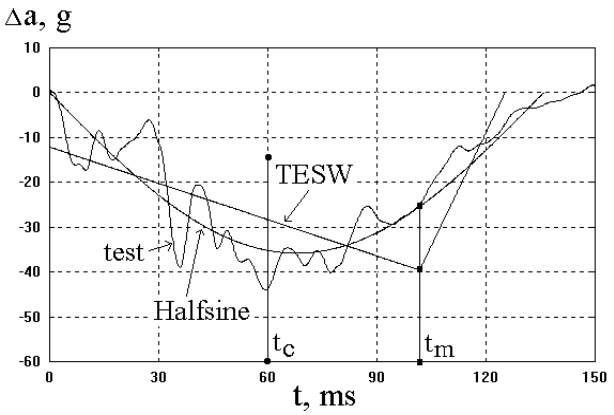

Fig. 4.54 Deceleration – An Effective Mass System

Construction Steps for the Sinusoidal Wave:

Given: The crash test data of a truck impacting on a stationary passenger car at 58 mph.

v (velocity change) = 58 mph = 85 ft/s,

C (relative displacement, dynamic crush, ft) = 61 in = 5.08 ft,

t_m (time at C)= .102 sec.

Construct the sinusoidal approximation to the relative deceleration of car to truck (shown in Fig. 4.54) using the following four steps:

I) computing natural frequency, f

Relative centroid location: $C/(vt_m)$= .586

find b: from the curve in Fig. 4.55, b = 2.3

then compute ω_n (= b / t_m) = 22.5 rad/s,

f = ω_n / (2π) = 3.6 Hz

Note: $\omega_n = \omega_e$

II) computing amplitude, A_p

Given: b = 2.3,

From Fig. 4.56, find $A_p/(v\omega_n)$ = .6,

then A_p=1148 ft/s^2 =35.6 g

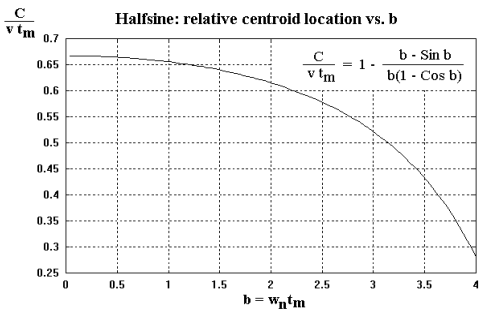

Fig. 4.55 Halfsine: Relative Centroid Location vs. b

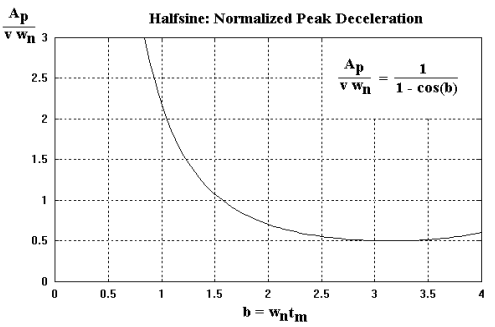

Fig. 4.56 Halfsine: Normalized Peak Deceleration

III) computing t_p, time at peak deceleration	**IV) computing A_m, deceleration at t_m**
Given: b = 2.3, From Fig. 4.57, find t_p/t_m = .68, then t_p = 69 ms	Given: b = 2.3, From Fig. 4.58, find A_m/A_p = .74, then A_m = 26 g

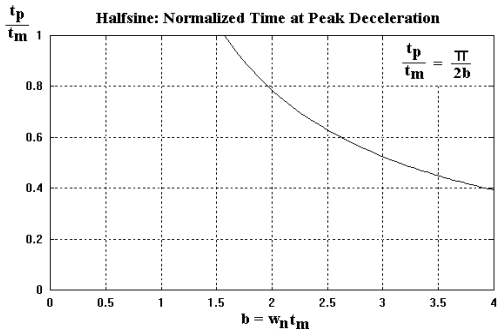

Fig. 4.57 Halfsine: Normalized Time at Peak Deceleration

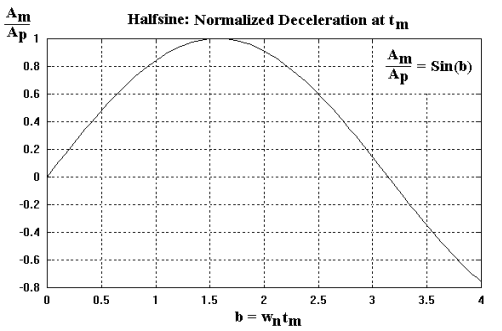

Fig. 4.58 Halfsine: Normalized Deceleration at t_m

4.7.1.2 *Individual Vehicle Response Analysis*

The peak magnitude of the sinusoidal pulse approximating the relative deceleration between the two vehicles is A_p = 35.6 g, as shown in Fig. 4.54. The computed frequency of the sinusoidal pulse is 3.6 Hz.

Using the concept of equivalency between the two-mass and one effective mass systems described in Section 4.4.4, the individual vehicle kinematic responses can then be computed. Let vehicle #1 be the car, and #2, the truck; then the mass reduction factors and the individual peak decelerations of the corresponding sinusoidal pulse are computed as follows.

$$r_m = \frac{m_1}{m_2} = \frac{3000}{4920} = .61 \qquad \gamma_1 = \frac{1}{1 + r_m} = .62, \quad then \quad \gamma_2 = .38$$
$$\ddot{x}_1 = \gamma_1 \ddot{\alpha} = .62 \times 35.6 = 22\ g, \quad and \quad \ddot{x}_2 = 13.6\ G \tag{4.53}$$

Since the individual crash pulse is equal to the relative deceleration multiplied by the respective mass reduction factor, the crash durations of the two vehicles are the same, as shown in Fig. 4.53. The approximated individual deceleration, velocity, and displacement, based on the sinusoidal crash pulse, match those of the test pulses fairly closely, as shown in Figs. 4.59 – 4.62.

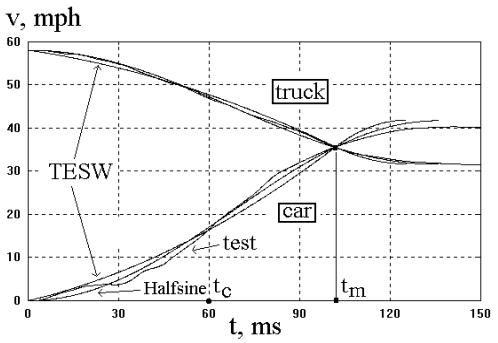

Fig. 4.59 Velocity – A Two-Mass System

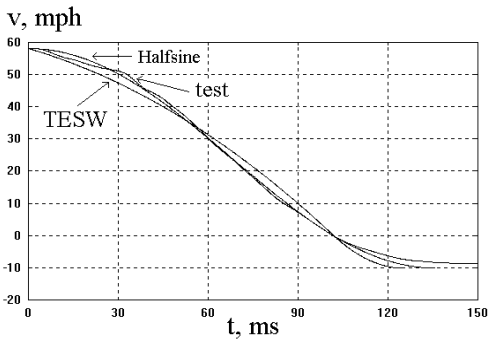

Fig. 4.60 Velocity – An Effective Mass System

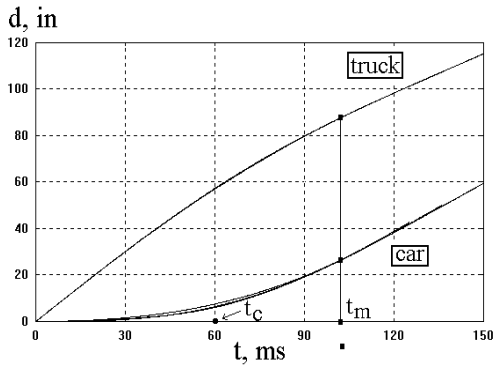

Fig. 4.61 Displacement – A Two-Mass System

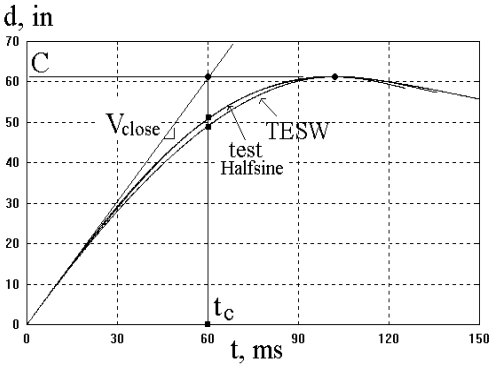

Fig. 4.62 Displacement – An Effective Mass System

4.7.2 Comparison of Sinusoidal Wave with Test Crash Pulse

Using the formulas for the sinusoidal approximation, the sinusoidal approximation can be derived. The details are described in Section 4.7.1.1 along with the formula and curves for computation. The parameters thus obtained are f = 3.6 Hz, A_p = 35.6 g, t_p = 69 ms, A_m = 26 g, and t_m = 102 ms. The sinusoidal pulse is overlapped with the crash test pulse and shown in Fig. 4.54. The sinusoidal pulse approximates the relative crash pulse up to t_m fairly well, especially the velocity and displacement comparisons shown in Figs. 4.60 and 4.62.

Note that no special unloading curve such as power curve unloading is used in the rebound phase of the sinusoidal pulse. The simple extension of the sinusoidal pulse from t_m is used as the unloading portion of the crash pulse. As noted in the velocity plot in Fig. 4.60, the separation velocity from the sinusoidal pulse is about 7.5 mph, not as much as 10 mph from the test pulse. The coefficient of restitution of this vehicle-to-vehicle test is about e = (10 mph/58 mph) × 100% = 17%. The percentage of the kinetic energy dissipated by the engaging structures of the two vehicles is about (1 - e^2) x 100% = 97%. Overall, the sinusoidal approximation to the crash pulse and its integrals is superior to TESW.

In the fixed barrier impact, the natural frequency of vehicle structure, f, is that of the impacting vehicle alone. However, in the vehicle-to-vehicle impact it is that of the engaging structures of the two vehicles. The crash pulses of the two vehicles have the same duration, because they have the same natural frequency. Shown in Eq. (4.23), the natural frequency of the engaging structure is proportional to the square root of the ratio of the effective spring stiffness to effective weight of the two vehicles.

In the next section, the concepts of the effective mass, effective stiffness, and mass reduction factors are defined. These concepts involving an effective mass are necessary in order to utilize the relative motion data of the two vehicles when computing parameters which approximate the crash pulse of the individual vehicle.

4.7.3 Truck and Car Occupant Responses due to Halfsine Excitation

In Section 4.6, the closed form formula for the occupant response due to the halfsine and TESW pulse excitation was presented. Using the halfsine as an excitation and a set of assumed restraint natural frequencies and restraint contact times from the test, the occupant transient response equation shown in Eq. (4.45) can be executed. The computation yields a chest deceleration of the occupant in the respective vehicle. After several trials, the final sets of the restraint parameters used to validate the occupant model for the truck and car are shown in Table 4.5.

Table 4.5 Model Parameters and Responses, for damping $\zeta = 0$, slack > 0

Vehicle	Structure		Restraint		Freq. Ratio	DAF	Chest g @ T_g, ms
	A_p, g @ T_p, ms	f, Hz	t*, ms	f_e, Hz	r=f/f_e		
#1, Truck	13.4 @ 69	3.6	40	8	0.45	2.22	30 @ 89
#2, Car	22.2 @ 69		33	6	0.51	1.93	43 @ 105

The test chest decelerations shown in Fig. 4.63 for the car and truck in the central impact did not start picking up until about 30 ms for the car occupant and about 40 ms for the truck occupant. Both the truck and car occupant response curves look more like a shifted and skewed haversine wave.

Overall, the occupant model subjected to the truck halfsine pulse approximates the test occupant response better than that of the car as shown in Fig. 4.63. This is because the test crash pulse of the truck, shown in Fig. 4.53, is better approximated by the halfsine wave than the crash pulse of the car.

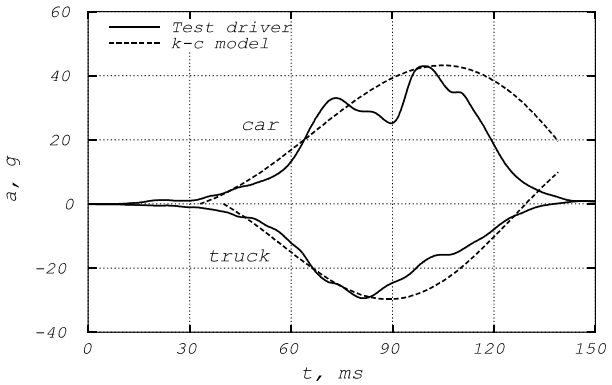

Fig. 4.63 Chest G from Test, and k-c Model w/ Halfsine Excitation ($\zeta = 0$, $\delta = 1.1$")

For comparison purposes, the restraint slack is set to zero. Assuming both vehicles were equipped with pretensioners, the occupant responses with the same restraint system (same restraint natural frequency) are shown in Table 4.6. Both the chest deceleration and the dynamic amplification factor drop significantly for the respective occupant.

Table 4.6 Model Parameters and Responses, for damping $\zeta = 0$, slack = 0

Vehicle	Structure		Restraint		Freq. Ratio	DAF	Chest g @ T_g, ms
	A_p, g @ T_p, ms	f, Hz	t*, ms	f_e, Hz	r=f/f_e		
#1, Truck	13.4 @ 69	3.6	0	8	0.45	1.69	23 @ 86
#2, Car	22.2 @ 69		0	6	0.51	1.74	39 @ 94

4.7.4 Elasto-plastic Modeling

In an impact, vehicle m_2 was struck by vehicle m_1 at a closing speed, v_{12}, of 10 mph. The weights of masses m_1 and m_2 were 1 and 2 klbs (kilo-pounds), respectively. Compute the transient deceleration, force, and deflection developed by the spring for the following two cases:

Case (1): The spring is elastic with a combined spring stiffness, k, of 2 klbs/in,

Case (2): The spring is elasto-plastic with an elastic range of 4 inches and spring stiffness of 2 klbs/in (see Fig. 4.64).

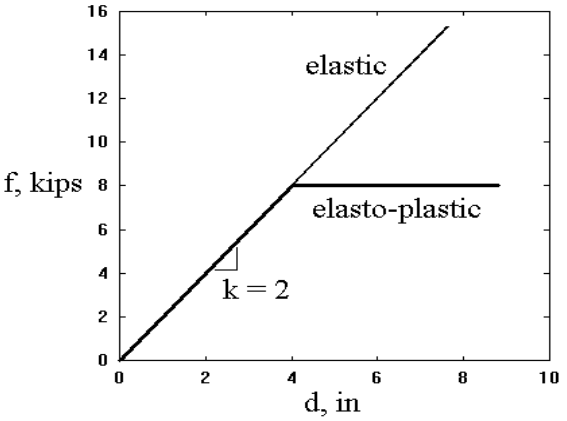

Fig. 4.64 F vs. D of Elasto-Plastic Spring

The force levels in the elastic and plastic deflection ranges are shown in Fig. 4.64. The plastic range starts from the end of the elastic range and has a constant force level of 8 klbs. The force deflection data shown are for the loading phase. The unloading stiffness in the unloading phase for both cases is assumed to be the same as the loading stiffness.

Case (1): The effective mass and angular natural frequency are computed in Eq. (4.54).

$$\begin{aligned} &\textit{Given } k = 2\,\frac{klbs}{in}, \quad w_1 = 1\,klb, \quad w_2 = 2\,klbs \\ &m_e = \frac{w_1 w_2}{w_1 + w_2}\,\frac{1}{g} = \frac{.667}{g} \\ &\omega_e = \sqrt{\frac{k}{m_e}} = \sqrt{\frac{2\,x\,386.4}{.667}} = 34\,rad/s \end{aligned} \tag{4.54}$$

Using the kinematic relationships between the effective mass and two-mass systems, the transient responses of the two masses are computed in Eq. (4.55).

$$\begin{aligned} &\textit{Motion of the effective mass:} \\ &\alpha(t) = \frac{v_o}{\omega_e}\sin(\omega_e t) = 5.2\sin(\omega_e t), \quad in \\ &\dot{\alpha}(t) = v_o\cos(\omega_e t) = 10\cos(\omega_e t), \quad mph \\ &\ddot{\alpha}(t) = -v_o\omega_e\sin(\omega_e t) = -15.6\sin(\omega_e t), \quad g \\ &\textit{Motion of the two mass system: The mass reduction factors are:} \\ &\gamma_1 = \frac{m_2}{m_1 + m_2} = .67, \quad \gamma_2 = \frac{m_1}{m_1 + m_2} = .33 \\ &\textit{The absolute accelerations of the two masses are:} \\ &\ddot{x}_1 = \gamma_1\,\ddot{\alpha} = -10.4\cos(34\,t), \quad g, \quad \ddot{x}_2 = -\gamma_2\,\ddot{\alpha} = 5.2\cos(34\,t), \quad g \end{aligned} \tag{4.55}$$

Case (2): The modeling of the transient responses of the two-mass system with elasto-plastic force deflection data has been executed by a general lumped-mass simulation model, CRUSH, introduced in Chapter 5. The transient force and deflection responses for the two cases were shown in Fig. 4.65.

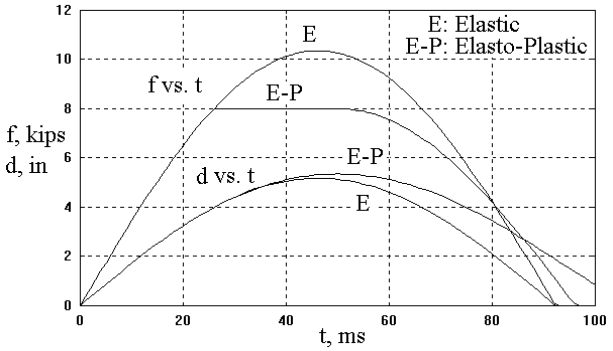

Fig. 4.65 Force/Deflection vs. Time of an Impact with Elastic and Elasto-Plastic Springs

In the elastic case, the maximum force and deflection occur at 45 ms; while in the elasto-plastic case, the maximum force of 8 klbs lasts from 26 to 50 ms due to constant force yielding, and maximum deflection occurs at the end of plastic deformation at 50 ms.

The final deflections for both cases can be verified by energy considerations, as shown in Eq. (4.56). The effective weight, W_e, of two masses of 1 and 2 klbs equals 0.67 klbs.

$$
\begin{aligned}
&\textit{Initial kinetic energy}\,(E,\ lb\text{-}in) = \textit{energy density}\,(e,\ g\text{-}in)\ x\ \textit{weight}\,(W_e,\ lb)\\
&\quad = .4\,V^2\ x\ W = .4\,(10mph)^2\ x\ 670\,lb = 26800\ lb\text{-}in\\
&E_e(\textit{elastic energy}) = \frac{k\,x^2}{2} = \frac{2000\,(4)^2}{2} = 16000\ lb\text{-}in\\
&\textit{For case}\ (1):\ \textit{Define}\ \ \Delta x_e\ :\ (\textit{additional elastic deformation}),\ \ \textit{then}\\
&\Delta E = E - E_e = \frac{1}{2}\,k\left[(4+\Delta x_e)^2 - 4\right] = 10800 \qquad (4.56)\\
&\textit{therefore}\ \ \Delta x_e = 1.2\ in,\ \ \textit{and}\ \ \textit{Total elastic deformation} = 4 + \Delta x_e = 5.2\ in\\
&\textit{For case}\ (2):\ \textit{Define}\ \ \Delta x_p\ :\ (\textit{additional plastic deformation}),\ \ \textit{then}\\
&\Delta E = E - E_e = 8000\,\Delta x_p = 10800,\ \ \textit{therefore}\ \ \Delta x_p = 1.4\ in,\ \ \textit{and}\\
&\textit{Total}\ (\textit{elastic}\ +\ \textit{plastic})\ \textit{deformation} = 4 + 1.4 = 5.4\ in
\end{aligned}
$$

The summaries of the transient responses for both cases are shown in Table 4.7. Among the responses in the two cases are the maximum force and maximum deformation (dynamic crush).

Table 4.7 Transient Responses for Elastic and Elasto-Plastic Cases

Case No.	Maximum Deformation, in @ ms	Maximum Force, klbs @ ms	Maximum Deceleration, g @ ms		
			effective mass, m_e (.667 klbs)	m_1 (1 klbs)	m_2 (2 klbs)
1. Elastic	5.2 @ 45	10.4 @ 45	-15.6 @ 45	-10.4 @ 45	5.2 @ 45
2. Elasto-Plastic	5.4 @ 50	8 @ 26-50	-12 @ 26-50	-8 @ 26-50	4 @ 26-50

Figs. 4.66 and 4.67 show the transient deceleration of each of the two masses and the effective mass for the cases with elastic and elasto-plastic springs. In both cases, the sum of the decelerations of the two masses, m_1 and m_2, equals the deceleration of the effective mass, m_e.

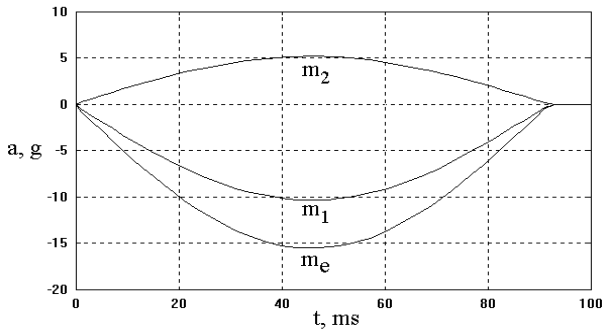

Fig. 4.66 Deceleration vs. Time of an Impact with Elastic Spring

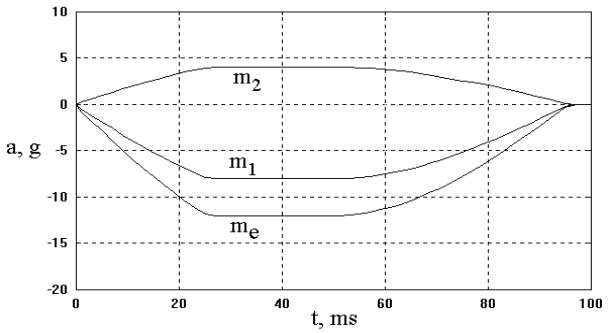

Fig. 4.67 Deceleration vs. Time of an Impact with Elasto-Plastic Spring

4.8 A MAXWELL MODEL

A system model consisting of a spring and damper in series is analyzed for its impact response characteristics. A two-parameter model, named Maxwell model in which the spring and damper are in series, provides a special response characteristics and is suitable for component relaxation and creep modeling and localized vehicle impact modeling.

Depending on the damping characteristics, the Maxwell model provides a wide range of timing where the maximum dynamic crush occurs. The timing at dynamic crush can be extended to infinity, at which the deflection approaches an asymptote. The damping coefficient at which the Maxwell model deflection becomes asymptotic is termed as transition damping coefficient. As far as the deflection is concerned, it reaches a point of no return when the system damping coefficient is less than the transition damping coefficient. It is suitable for modeling vehicle soft impacts such as for localized pole and offset collisions where the timing at dynamic crush is fairly long.

A special system with damper and mass only is analyzed first. Its dynamics is non-oscillatory in nature and the responses are characterized by an exponential decay function, as described in the following section.

4.8.1 A Damper-Mass System (without Oscillatory Motion)

Since the damper-mass system shown in Fig. 4.68 does not have a spring element, the motion is a decayed and non-oscillatory. As shown in Eq. (4.57), the characteristic equation has a zero and negative root which yield an exponential decay function.

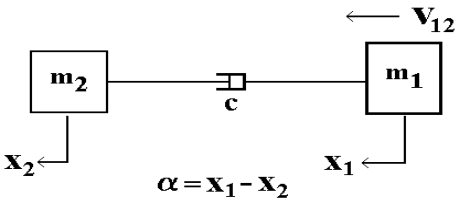

Fig. 4.68 A Damper-Mass System

The solutions with the impact velocity being the initial condition are shown in Eq. (4.57). The normalized responses are obtained by using the respective factors shown in Eq. (4.58). The time variable t can also be normalized by multiplying it by the factor c/m_e.

$$
\begin{aligned}
&\textit{The effective mass is:} \quad m_e = \frac{m_1 m_2}{m_1 + m_2} \\
&\textit{E.O.M.:} \quad m_e \ddot{\alpha} + c\dot{\alpha} = 0 \\
&\textit{Characteristic equation:} \quad s^2 + (c/m_e)\, s = 0 \\
&\qquad\qquad \textit{roots:} \quad s_1 = 0, \quad \textit{and} \quad s_2 = -c/m_e \\
&\textit{General solutions:} \quad \alpha = C_1 e^{s_1 t} + C_2 e^{s_2 t} = C_1 + C_2 e^{-(c/m_e)t}
\end{aligned}
\tag{4.57}
$$

$$
\begin{aligned}
&\textit{Initial conditions:} \quad \#1:\ \alpha(t{=}0) = 0, \quad \#2:\ \dot{\alpha}(t{=}0) = v_o \\
&\textit{Responses} \qquad\qquad\qquad \textit{Normalized Responses} \\
&\alpha = \left[v_o/(c/m_e)\right]\left(1 - e^{-(c/m_e)t}\right) \qquad y = \frac{\alpha}{\left[v_o/(c/m_e)\right]} = 1 - e^{-(c/m_e)t} \\
&\dot{\alpha} = v_o e^{-(c/m_e)t} \qquad\qquad \dot{y} = \frac{\dot{\alpha}}{v_o} = e^{-(c/m_e)t} \\
&\ddot{\alpha} = -v_o (c/m_e) e^{-(c/m_e)t} \qquad \ddot{y} = \frac{\ddot{\alpha}}{\left[v_o (c/m_e)\right]} = -e^{-(c/m_e)t}
\end{aligned}
\tag{4.58}
$$

Shown in Fig. 4.69 are the normalized responses versus the normalized time variable.

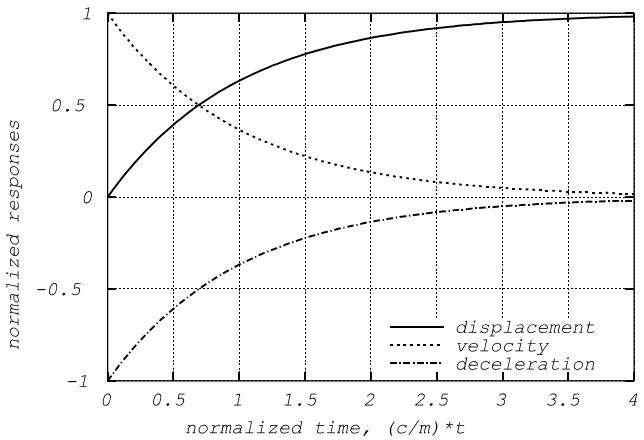

Fig. 4.69 Normalized Responses of a Damper-Mass System

The velocity response decreases from 1 to zero; so does the deceleration response in a negative sense. The displacement response, however, increases from zero to an asymptote. The asymptotic value of the displacement is equal to the displacement normalization factor, $v_o/(c/m_e)$.

4.8.2 The Maxwell Spring-Damper Model

The Maxwell element consists of spring and damper elements connected in series, as shown in Fig. 4.70. The element, massless and uni-axial, does not take into account the bending or torsion stiffness. The end points of the element can be attached to any bodies. The Maxwell model is suitable for modeling material responses that exhibit relaxation and creep, a time dependent phenomena. In vehicle impact modeling, it is suited for the localized impact where the vehicle effective stiffness is low.

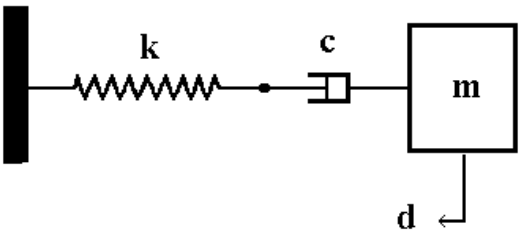

Fig. 4.70 A Maxwell Model

To study the dynamic interactions between the spring and damper, a mass m attached to the elements impacts on a rigid wall to simulate the vehicle-to-rigid barrier impact. For modeling a component test where the component weight is negligible compared to the impactor weight, the spring and damper elements then represent the component, such as a engine mount of a truck, and the mass represents the impactor in a laboratory test setup.

The equations of motion, derived for the damper deflection, d_c and total deflection, d, are shown in Eq. (4.59).

$$
\begin{aligned}
& f\,(force) = f_k = f_c = k\,d_k = c\,\dot{d}_c \\
& d\,(deflection) = d_k + d_c \\
& \therefore \quad \dot{d}_c = \frac{k}{c} d_k = \frac{k}{c}(d - d_c) \qquad (1) \\
& \ddot{d} = -\frac{f}{m} = -\frac{c\dot{d}_c}{m} \qquad (2)
\end{aligned}
\tag{4.59}
$$

Expressions (1) and (2) of Eq. (4.59) are the first and second order differential equations in d_c and d, respectively. Using numerical integration, d_c and d can be solved. Note that the deflections of spring and damper are additive in the Maxwell model, as are the deflection rates, as shown in Eq. (4.60).

$$
d = d_k + d_c \qquad \dot{d} = \dot{d}_k + \dot{d}_c \tag{4.60}
$$

4.8.3 Alternate Method: Zero Mass Between Maxwell Spring and Damper

In the previous section, the relationships between the total and individual deflection and deflection rate were used to derive the first and second order differential equations. In this section, an alternate method is used to derive a set of closed-form solution for a third order differential equation.

Since the mass m in the Maxwell model by itself does not describe the motion of a point between the spring and damper, it is proposed to put a small mass m′ between the spring and damper, as shown in Fig. 4.71. After deriving the two sets of second-order differential equations, they are simplified by letting mass m′ become zero. By using zero mass, the inertia effect between the spring and damper is neglected, and the system becomes a third order differential equation which can be solved explicitly.

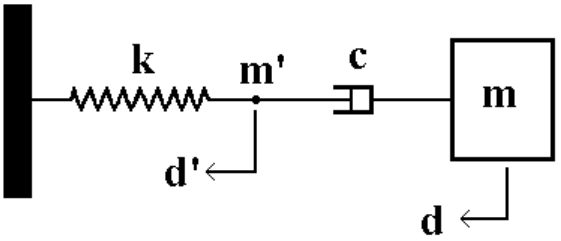

Fig. 4.71 Maxwell Model with Zero Mass

Define:

d: absolute displacement of mass m, d′: absolute displacement of mass m′

The equations of motions are:

$$m\ddot{d} = -c(\dot{d} - \dot{d}') \quad \ldots (1), \quad m'\ddot{d}' = c(\dot{d} - \dot{d}') - kd' \quad \ldots (2)$$

differentiating (1) *and* (2) *w.r.t. t, and letting* $m' = 0$:

$$m\dddot{d} = -c(\ddot{d} - \ddot{d}') \quad \ldots (3), \qquad 0 = c(\ddot{d} - \ddot{d}') - k\dot{d}' \quad \ldots (4)$$

summing up both sides of (3) *and* (4), *and rearranging*:

$$\dot{d}' = \frac{-m}{k}\dddot{d} \qquad \ldots\ldots\ldots\ldots \quad (5) \tag{4.61}$$

substituting (5) *into* (1), *and rearranging*:

$$\dddot{d} + \frac{k}{c}\ddot{d} + \frac{k}{m}\dot{d} = 0 \qquad \ldots\ldots\ldots (6)$$

From the third order differential equation shown by (6) above, the characteristic equation and the solutions are shown as follows.

$$s\left[s^2 + \frac{k}{c}s + \frac{k}{m}\right] = 0 \tag{4.62}$$

The roots of the third order characteristic equation are solved as follows:

In the Maxwell model, the impacting mass may not necessarily have a rebound. In this case,

I. when $\left(\frac{k}{c}\right)^2 > 4\frac{k}{m}$ *we obtain*:

$s_0 = 0$, *and two negative real roots,* s_1 *and* s_2 *where*:

$s_1 = a + b$ *and* $s_2 = a - b$. *Here*:

$$a = \frac{-k}{2c}, \quad \text{and} \quad b = \sqrt{\left(\frac{k}{2c}\right)^2 - \frac{k}{m}}$$

Note that $s_1 > s_2$ *or* $s_1 - s_2 > 0$ (4.63)

$$\alpha = d_o e^{-s_o t} + d_1 e^{-s_1 t} + d_2 e^{-s_2 t}, \quad \dot{\alpha} = -d_o s_o e^{-s_o t} - d_1 s_1 e^{-s_1 t} - d_2 s_2 e^{-s_2 t}$$

$$\ddot{\alpha} = d_o s_o^2 e^{-s_o t} + d_1 s_1^2 e^{-s_1 t} + d_2 s_2^2 e^{-s_2 t}$$

For the initial conditions at $t = 0$: $\alpha = 0$, $\dot{\alpha} = v$, *and* $\ddot{\alpha} = 0$,

the three constants are: $d_o = \frac{v(s_1 + s_2)}{s_1 s_2}$, $d_1 = \frac{v s_2}{s_1(s_1 - s_2)}$, $d_2 = \frac{-v s_1}{s_2(s_1 - s_2)}$

$$
\begin{aligned}
&\textit{II. when } \left(\frac{k}{c}\right)^2 < 4\frac{k}{m} \\
&s_0 = 0, \ \textit{and two complex roots, } s_1 \textit{ and } s_2\textit{:} \\
&s_1 = a + ib, \quad s_2 = a - ib, \quad \textit{where} \\
&\qquad a = \frac{-k}{2c}, \ \textit{and} \quad b = \sqrt{\frac{k}{m} - \left(\frac{k}{2c}\right)^2} \quad \ldots\ldots\ldots \quad (1) \\
&\alpha = d_o e^{s_o t} + e^{at}\left[d_1 S(bt) + d_2 C(bt)\right] \quad \ldots\ldots\ldots\ldots \quad (2) \\
&\dot{\alpha} = e^{at}\left[(ad_1 - bd_2) S(bt) + (bd_1 + ad_2) C(bt)\right] \\
&\ddot{\alpha} = e^{at}\left[\left[(a^2 - b^2)d_1 - 2ab\,d_2\right] S(bt) + \left[(a^2 - b^2)d_2 + 2ab\,d_1\right] C(bt)\right] \\
&\textit{For the initial conditions at } t = 0\textit{:} \ \ \alpha = 0, \ \ \dot{\alpha} = v, \textit{ and } \ddot{\alpha} = 0. \\
&\textit{The three constants are:} \ \ d_2 = \frac{2av}{a^2 + b^2}, \ \ d_1 = \frac{v - a d_2}{b}, \ \ d_o = -d_2
\end{aligned}
\tag{4.64}
$$

the displacement of the mass after impact increases with time and reaches an asymptotic value. The situation is similar to that when materials exhibit relaxation or creeping after a loading is applied. For this situation not to occur, there exists a minimum value of damping coefficient in the Maxwell model, named the transition damping coefficient, c*. For a damping coefficient, c, greater than c*, there exists a dynamic crush at a finite time. After reaching the dynamic crush, the mass of the system rebounds. An extreme case is when c becomes infinity; then the Maxwell model degenerates into a simple spring mass system. The value of c* is derived in the following section.

4.8.4 Transition and Infinite Damping Coefficients

The responses of the Maxwell models with two distinct damping coefficients are analyzed separately to get the response limit values. Knowing the response characteristics of the Maxwell model with the transition and infinite damping coefficients, one can better utilize and assess the model for its specific application.

4.8.4.1 *Transition Damping Coefficient, c** The response characteristics of the Maxwell model with the transition damping coefficient, c*, shown in Eq. (4.65) are covered in Section 4.8.5.

$$
\textit{when } \frac{k}{c} = 2\sqrt{\frac{k}{m}}, \ \ c^* = \frac{\sqrt{km}}{2}. \ \textit{For } c \le c^*, \ \textit{I.} \left(\frac{k}{c}\right)^2 > 4\frac{k}{m} \ \textit{is satisfied.} \tag{4.65}
$$

4.8.4.2 *Infinite Damping Coefficient, c=∞*

$$
\begin{aligned}
&\textit{For } c = \infty\textit{, then condition II. } \left(\frac{k}{c}\right)^2 < 4\frac{k}{m} \ \textit{ is satisfied :} \\
&\textit{From (1) in Eq. (4.64):} \\
&a = 0, \quad b = \omega, \quad \textit{and} \quad d_1 = \frac{v}{\omega}, \quad d_o = d_2 = 0 \\
&\textit{Substituting into (2) in Eq. (4.64), one gets} \quad \alpha = \frac{v}{\omega}\sin(\omega t) \\
&\textit{The lowest limits set by the Maxwell model are } c \textit{ and } t_m\textit{:} \\
&c \ (\textit{dynamic crush}) = \frac{v}{\omega} \\
&\textit{where} \quad t_m = \frac{t_c}{.64} = \frac{1}{.64}\frac{c}{v} \quad \textit{in natural units}
\end{aligned}
\tag{4.66}
$$

The relative displacement shown in Eq. (4.66) is the same as that of a simple spring-mass model. This is due to the fact that the damper with an infinite damping coefficient becomes a rigid device, and the Maxwell model degenerates into a simple spring-mass model.

4.8.5 Model Response Characteristics with Transition Damping Coefficient

The displacement response characteristics of the Maxwell model with transition damping coefficient, c*, are derived and compared with that of a simple spring-mass model. By doing this, one gains further insight into the model's limitations and capability for a softer impact, such as vehicle-to-pole or tree impact, or the vehicle-to-vehicle offset impact.

$$\textit{For } c = c* = \frac{\sqrt{k\,m}}{2}, \quad \textit{then from (1) of Eq. (4.64):}$$

$$a = -\omega, \quad b = 0, \quad \textit{where} \quad \omega = \sqrt{\frac{k}{m}} \quad \textit{circular natural frequency}$$

$$d_1 = -\frac{v}{b}, \quad d_2 = -2\frac{v}{\omega}, \quad \textit{and} \quad d_o = 2\frac{v}{\omega}$$

Substituting into (2) of Eq. (4.64), one gets:

$$\alpha = \frac{v}{\omega}\left[2 - \left(\omega\frac{\sin(b\,t)}{b} + 2\cos(b\,t)\right)e^{-\omega t}\right] \quad \ldots\ldots\ldots \quad (3) \qquad (4.67)$$

$$\textit{Since} \quad \lim_{b\to 0}\frac{\sin(b\,t)}{b} = t, \quad \textit{and} \quad \lim_{b\to 0}\cos(b\,t) = 1$$

$$(3)\ \textit{becomes:} \quad \alpha = \frac{v}{\omega}\left[2 - (\omega\,t + 2)\,e^{-\omega t}\right], \quad \textit{normalizing } \alpha \textit{ by } \frac{v}{\omega},$$

the dynamic crush of a spring-mass system:

$$\frac{\alpha}{v/\omega} = \left[2 - (\omega\,t + 2)\,e^{-\omega t}\right] \quad \ldots\ldots\ldots\ldots\ldots \quad (4)$$

Case Study 1:

Given the following data in a vehicle-to-rigid barrier impact:

V_o = 10 mph, W = 2000 lb, and c =300 lb-s/in.

Determine the transient responses of the mass and the kinematic interaction between the spring and damper for the three cases shown in Table 4.8.

Table 4.8 Maxwell Models with Different Spring Stiffness

Case # (stiffness)	k, lb/in	c, lb-s/in	c*, lb-s/in	Rebound
1 (stiff)	200,000 (stiff)	300	508.7	No
2 (regular)	30,000 (regular)		197.0	Yes
3 (soft)	3,000 (soft)		62.3	Yes

Using the first and second order differential equations (1) and (2) of Eq. (4.59), the individual responses of the spring and damper can be computed.

Shown in Fig. 4.72 are the decelerations for three different levels of spring stiffness. For case #1 with a stiff spring in the Maxwell model, the initial impulse has the largest magnitude among the three cases. The damping coefficient, c = 300 lb-s/in in case #1 of Table 4.8, is less than the transition damping coefficient, c* = 508.7 lb-s/in. The mass never rebounds, as shown by the deflection curve in Fig. 4.73. It reaches a point of no return and settles at an asymptotic deflection. Since the total deflection is the sum of the spring and damper deflections and since the spring is very stiff, the total deflection of the system is attributed to the damper deflection as shown in Fig. 4.73.

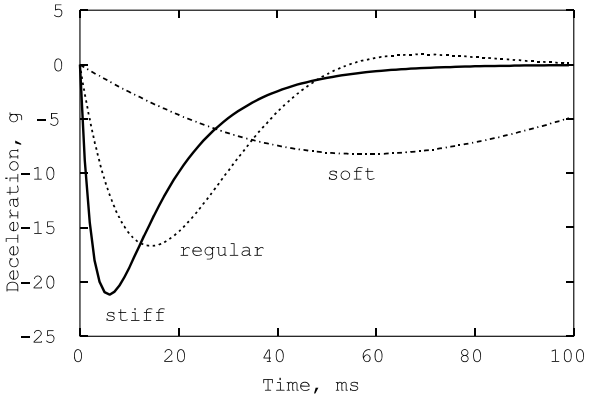

Fig. 4.72 Maxwell Model Accelerations with Damping and Various Stiffness

Figs. 4.73–4.75 show the transient displacement (deflection) of the Maxwell model with a given damping coefficient and three levels of spring stiffness. Again, the mass (total) displacement in each of the three displacement plots equals the sum of spring and damper displacement.

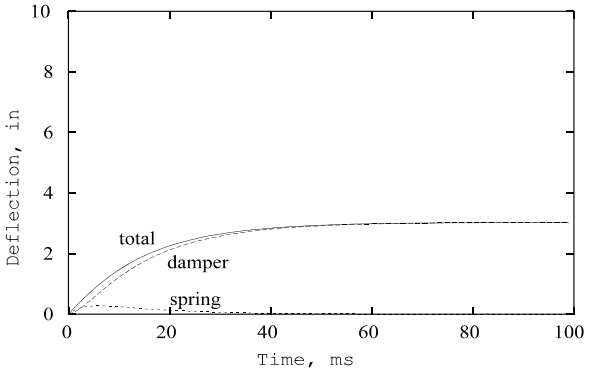

Fig. 4.73 Maxwell Model Deflection w/ Stiff Spring

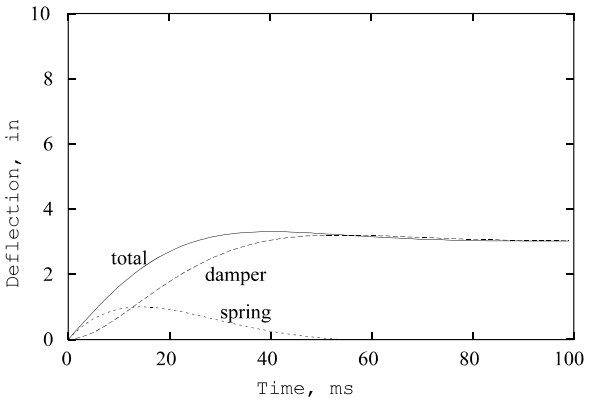

Fig. 4.74 Maxwell Model Deflection with Regular Spring

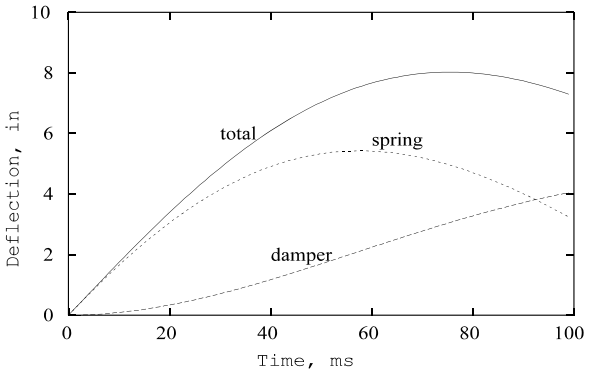

Fig. 4.75 Maxwell Model Deflection with Soft Spring

Figs. 4.76–4.78 show the transient velocity of the Maxwell model with a given damping coefficient and three levels of spring stiffness. Note that the mass (total) velocity in each of the three velocity plots equals the sum of spring and damper velocities.

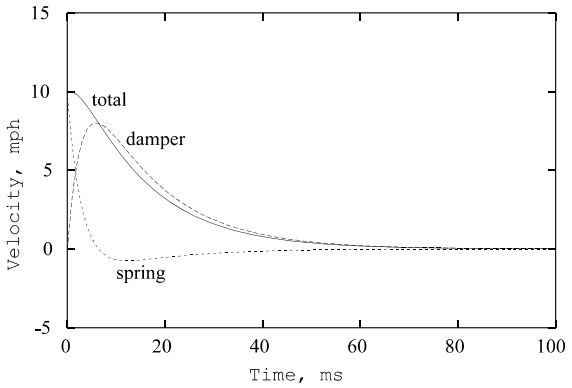

Fig. 4.76 Maxwell Model Velocity with Stiff Spring

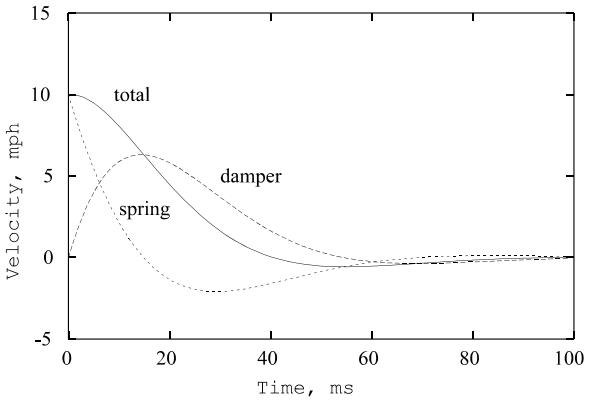

Fig. 4.77 Maxwell Model Velocity with Regular Spring

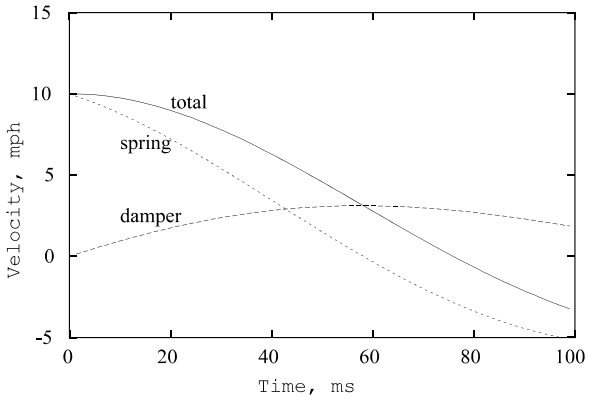

Fig. 4.78 Maxwell Model Velocity with Soft Spring

Case Study 2:

A full-size passenger car was tested at 21 mph, running into a fixed rigid pole at the front center location of the vehicle. Given are the test weight of 4500 lbs and a total pole penetration of 34 inches at 137 ms. Compute the transition damping coefficient and plot the normalized displacement of the Maxwell model with the transition damping coefficient.

Using the dynamic crush formula for a simple spring-mass model, the stiffness of the front structure engaged with the pole can be estimated and is shown in Eq. (4.68)

$$k = 0.8\,w\left(\frac{v}{c}\right)^2 = 0.8 \times 4500\,lb \times \left[\frac{21\,mph}{34\,in}\right]^2 = 1373\,\frac{lbs}{in}$$

$$\textit{The timing at dynamic crush, } T_m = 80\sqrt{\frac{w}{k}} = 144\ ms \tag{4.68}$$

$$\textit{For a Maxwell model: The transition damping coefficient is}$$

$$c* = \frac{\sqrt{k\,m}}{2} = \frac{1}{2}\sqrt{\frac{1373 \times 4500}{386.4}} = 63.2\,lb\text{-}sec^2/in$$

Thus, c* = 63.2 lb-sec^2/in is the minimum damping coefficient required in the Maxwell model which would yield a dynamic crush in a finite time.

Fig. 4.79 shows the normalized displacement response of a Maxwell model versus the angular displacement in radians, ωt. The expression of the normalized displacement is shown in Formula (2) of Eq. (4.67).

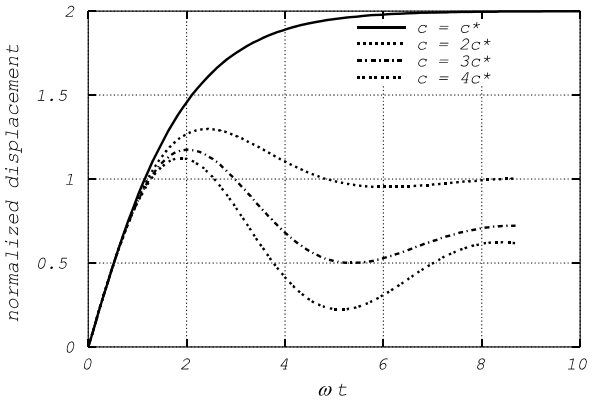

Fig. 4.79 Maxwell Model: Normalized Disp. vs. ωt

The solid curve in Fig. 4.79 is the normalized displacement response with c*, the transition damping coefficient. The asymptotic value of the normalized displacement with c* is two. The other three curves are the displacement responses of the model with damping coefficients ranging from two to four times the value of c*. As damping, c increases, the peak normalized displacement response becomes smaller than two. Finally, it approaches one as the damping coefficient becomes infinite, which is the displacement of a simple spring-mass model.

4.9 IMPACT ON KELVIN MODEL–VEHICLE OR COMPONENT

The Kelvin model described in Section 4.4.3 provides the basic configuration shown in Fig. 4.80 for the vehicle-to-vehicle (2-mass system), vehicle-to-barrier (one effective mass), and component impact modeling. Since most of the vehicle structures and components fall into the underdamped category, major efforts are focused on the underdamped system analysis and application.

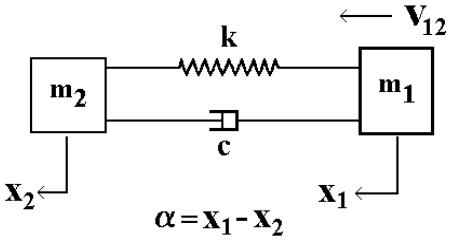

Fig. 4.80 A Kelvin Model

4.9.1 Transient and Major Responses of Kelvin Model

The equations of motion and general solutions of the Kelvin model in an impact are shown in Eq. (4.69) for the three systems: underdamped, critically damped, and overdamped.

$$
\begin{aligned}
&\textit{UNDERDAMPED SYSTEM: } (1>\zeta>0)\\
&\textit{EOM: } \ddot{\alpha}+2\zeta\omega_e\dot{\alpha}+\omega_e^2\alpha = 0, \quad \textit{where } \zeta=\frac{c}{2m\omega_e}\\
&\textit{characteristic equation: } s^2+2\zeta\omega_e s+\omega_e^2 = 0\\
&\textit{Define } \quad \beta=\sqrt{1-\zeta^2}, \quad \textit{roots: } s_1=a+ib, \quad s_2=a-ib\\
&\textit{where } a=-\zeta\omega_e \ , \ b=\beta\omega_e\\
&\textit{General solution: } \alpha=e^{at}\left[c_1\sin(bt)+c_2\cos(bt)\right]\\
&\\
&\textit{CRITICALLY DAMPED SYSTEM: } (\zeta=1)\\
&\textit{roots: } s_1=a+ib, \quad s_2=a-ib\\
&\because \zeta\to(\textit{approaches})\ 1, \quad \therefore bt=\sqrt{1-\zeta^2}\omega_e t\to 0, \quad \textit{and } s_1=s_2=a\\
&\textit{therefore } \quad \sin(bt)\to bt \ , \quad \cos(bt)\to 1\\
&\textit{General solution becomes: } \alpha = e^{at}[c_1+c_2 t]\\
&\textit{Note: For a characteristic equation}\\
&\textit{with n repeated roots, } s_1=s_2=\ldots=a\\
&\alpha=e^{at}[c_1+c_2 t+\ldots.+c_n t^{n-1}]\\
&\\
&\textit{OVERDAMPED SYSTEM: } (\zeta>1)\\
&\textit{Define } \quad \beta=\sqrt{\zeta^2-1}: \quad \textit{General solution: } \alpha=c_1e^{at}+c_2e^{at}\\
&\textit{where } a=(-\zeta+\beta)\omega<0, \quad b=(-\zeta-\beta)\omega_e<0\\
&\\
&\textit{I.C.: } \alpha(t=0)=0, \quad \dot{\alpha}(t=0)=v_0
\end{aligned}
\tag{4.69}
$$

In each damped system, there are two integration constants, c_1 and c_2 in the general solution. The constants are determined based on the initial conditions of the displacement and velocity at time zero.

The normalized response plots for the three systems are shown in Figs. 4.81–4.83, respectively. In obtaining the normalized responses, the factors used for normalization are those maximum response magnitudes of an undamped system. The factors are expressed in terms of the impact velocity, v_o, and undamped angular natural frequency of the system, ω_e. In addition, the time variable, t, is normalized by multiplying t by ω_e. Therefore, the normalized time variable, τ, equals ω_e t, which is an angular position.

The closed form solutions for the transient responses and major responses are presented in the following sections for the three damped systems.

4.9.1.1 *Underdamped System ($\zeta < 1$)*

The closed-form solutions for the transient responses of an underdamped system are shown in part (A) in Eq. (4.70) and that for the normalized transient responses of an underdamped system are shown in part (B) in Eq. (4.70). Since both response and time variables have been normalized, the relationship between the normalized response and the normalized time is only a function of damping factor, ζ, and is independent of undamped natural frequency, ω_e. Consequently, the shapes of the normalized response curves shown later in the case studies depend only on the damping factor of the system.

(4.70)

(A) Underdamped Transient Responses:

$$\alpha(t) = \frac{v_0 e^{-\zeta\omega_e t}}{\sqrt{1-\zeta^2}\,\omega_e}\sin\left(\sqrt{1-\zeta^2}\,\omega_e t\right)$$

$$\dot{\alpha}(t) = v_0 e^{-\zeta\omega_e t}\left[\cos\left(\sqrt{1-\zeta^2}\,\omega_e t\right) - \frac{\zeta}{\sqrt{1-\zeta^2}}\sin\left(\sqrt{1-\zeta^2}\,\omega_e t\right)\right]$$

$$\ddot{\alpha}(t) = v_0\,\omega_e\, e^{-\zeta\omega_e t}\left[-2\zeta\cos\left(\sqrt{1-\zeta^2}\,\omega_e t\right) + \frac{2\zeta^2-1}{\sqrt{1-\zeta^2}}\sin\left(\sqrt{1-\zeta^2}\,\omega_e t\right)\right]$$

(B) Underdamped Normalized Transient Responses:
Let us define the normalized factors:

$$\alpha|_{norm} = \frac{v_o}{\omega_e} \quad \ldots\ \textit{undamped maximum crush}$$

$$\ddot{\alpha}|_{norm} = v_o\omega_e \quad \ldots\ \textit{undamped maximum deceleration}$$

$$\tau = \omega_e t \quad \ldots\ \textit{angular position at t, then}$$

$$\frac{\alpha(t)}{\alpha_{norm}} = \frac{e^{-\zeta\tau}}{\sqrt{1-\zeta^2}}\sin\left(\sqrt{1-\zeta^2}\,\tau\right)$$

$$\frac{\dot{\alpha}(t)}{v_o} = e^{-\zeta\tau}\left[\cos\left(\sqrt{1-\zeta^2}\,\tau\right) - \frac{\zeta}{\sqrt{1-\zeta^2}}\sin\left(\sqrt{1-\zeta^2}\,\tau\right)\right]$$

$$\frac{\ddot{\alpha}(t)}{\ddot{\alpha}_{norm}} = e^{-\zeta\tau}\left[-2\zeta\cos\left(\sqrt{1-\zeta^2}\,\tau\right) + \frac{2\zeta^2-1}{\sqrt{1-\zeta^2}}\sin\left(\sqrt{1-\zeta^2}\,\tau\right)\right]$$

The major responses of the underdamped system, such as the dynamic crush which occurs at t_m and the rebound velocity (the maximum recoverable velocity) which occurs at t_r , are normalized and shown in Eq. (4.71).

Underdamped Major Responses:

Define: *normalized dynamic crush*: $\dfrac{\alpha_m}{(v_o/\omega_e)} = e^{-\zeta\tau_m}$

normalized centroid time: $\tau_c = t_c\,\omega_e$, *then* $\tau_c = \left(\dfrac{\alpha_m}{v_o}\right)\omega_e = e^{-\zeta\tau_m}$

τ_m: $t_m\omega_e$, *angular position at dynamic crush,*

τ_r: $t_r\omega_e$, *angular position at rebound velocity*

$$\tau_m = \frac{1}{\sqrt{1-\zeta^2}}\tan^{-1}\left(\frac{\sqrt{1-\zeta^2}}{\zeta}\right), \qquad \tau_r = 2\,\tau_m \tag{4.71}$$

normalized dynamic crush: $\dfrac{\alpha_m}{\alpha_{norm}} = e^{-\zeta\tau_m}$

normalized static crush (*at* τ_r): $\dfrac{\alpha_r}{\alpha_{norm}} = 2\,\zeta\, e^{-\zeta\tau_r}$

normalized rebound velocity: $\dfrac{\dot{\alpha}_r}{v_o} = -e^{-2\,\zeta\tau_m}$

At t_m, the time of dynamic crush, the corresponding velocity is zero. At t_r, the time of rebound velocity (or separation velocity), the corresponding deceleration is zero. Shown in Fig. 4.81 are the transient responses of an underdamped system with $\zeta = 0.2$. The major response timings are shown by the point symbols. Note that t_r is twice as long as t_m.

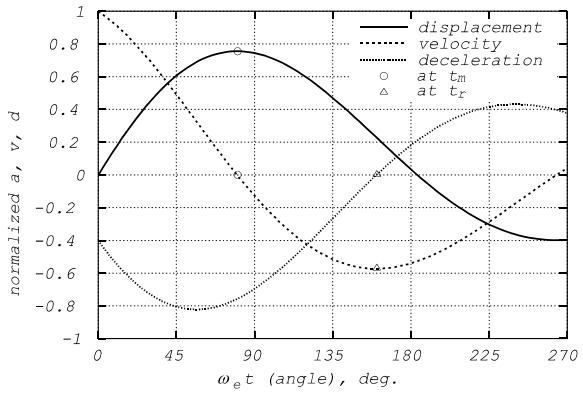

Fig. 4.81 Normalized Responses of an Underdamped System with ζ=0.2

For ζ = 0.2, the normalized dynamic crush is 0.756, and the corresponding normalized time (angular position) is 80.2°. The normalized separation velocity is −.57, which occurs at the angular position of 160.4° (2 times of 80.2°). At this time, the corresponding normalized static displacement is .229.

Since the coefficient of restitution (COR) is defined as the ratio of relative separation velocity to the relative approach velocity, the normalized separation velocity (with respect to the relative approach velocity of one) is therefore the same as COR, which is about 0.57.

It will be shown in the next section that COR is a function of the damping factor. Given a damping factor of 0.2, the corresponding COR is computed to be 0.57.

4.9.1.2 *Critically Damped System ($\zeta = 1$)*

The transient responses of a critically damped system are shown in Eq. (4.72). The timings, τ_m and τ_r, for the dynamic crush and separation velocity are shown in Eq. (4.73). τ_m and τ_r are equal to 1 and 2, respectively.

At t_m, the time at dynamic crush, the corresponding velocity is zero. At t_r, the time at rebound velocity (or separation velocity), the corresponding deceleration is zero. Shown in Fig. 4.82 are the transient responses of a critically damped system with $\zeta = 2$. The major response timings are shown by the point symbols.

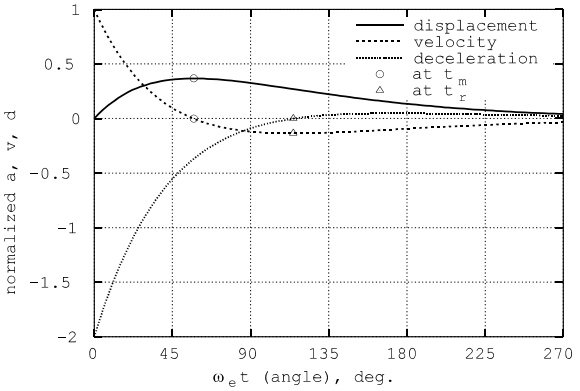

Fig. 4.82 Responses of a Critically Damped System with $\zeta=1$.

Critically Damped Transient Responses:

$$\alpha(t) = v_0\, t\, e^{-\omega_e t} \quad \ldots\ldots\ldots\ldots \quad (1)$$

$$\dot{\alpha}(t) = v_0 \left(1 - \omega_e t\right) e^{-\omega_e t} \quad \ldots\ldots\ldots \quad (2)$$

$$\ddot{\alpha}(t) = v_0\, \omega_e\, (\omega_e t - 2) e^{-\omega_e t} \quad \ldots\ldots \quad (3)$$

Let us define the normalized factors:

$$\alpha_{norm} = \frac{v_o}{\omega_e} \quad \ldots\ldots \textit{undamped maximum crush}$$

$$\ddot{\alpha}_{norm} = v_o \omega_e \quad \ldots \textit{undamped maximum deceleration} \qquad (4.72)$$

$$\tau = \omega_e t \quad \ldots\ldots \textit{angular position at } t, \quad \textit{then}$$

$$\frac{\alpha(t)}{\alpha_{norm}} = \tau\, e^{-\tau} \quad \ldots\ldots\ldots\ldots \quad (4)$$

$$\frac{\dot{\alpha}(t)}{v_o} = [1 - \tau]\, e^{-\tau} \quad \ldots\ldots\ldots\ldots \quad (5)$$

$$\frac{\ddot{\alpha}(t)}{\ddot{\alpha}_{norm}} = [\tau - 2]\, e^{-\tau} \quad \ldots\ldots\ldots \quad (6)$$

Critically Damped Major Responses: *let us define*:
τ_m: $t_m\omega_e$, *angular position at dynamic crush,*
τ_r: $t_r\omega_e$, *angular position at rebound velocity*
Differentiating (4) *of Eq.* (4.72) *w.r.t.* τ, *setting the differential to zero, one gets time of dynamic crush,* $\tau_m = 1$

$$\text{Normalized dynamic crush: } \frac{\alpha_m}{\alpha|_{norm}} = e^{-1} = .368 \text{ , and} \tag{4.73}$$

$$\text{Normalized centroid time : } \tau_c = t_c\,\omega_e, \text{ then, } \tau_r = 2\,\tau_m = 2$$

$$\text{Normalized static crush (at } \tau_r\text{): } \frac{\alpha_r}{\alpha|_{norm}} = 2\,e^{-2} = .27 \text{ , and}$$

$$\text{Normalized rebound velocity: } \frac{\dot{\alpha}_r}{v_o} = -e^{-2} = -.135$$

4.9.1.3 *Overdamped System ($\zeta > 1$)*

With the replacement of the trigonometry functions by the hyperbolic trigonometry functions shown in Table 4.9, the format of the closed-form solutions for the transient responses of an overdamped system are the same as those shown in Eq. (4.69) for the underdamped system.

Table 4.9 Trigonometry Functions used for the Under- and Overdamped Kelvin Models

System	Trigonometry Function	Sine	Cosine	ArcTangent
Underdamped	Normal	Sin	Cos	Tan^{-1}
Overdamped	Hyperbolic	Sinh	Cosh	$Tanh^{-1}$

Replacing the Sin (Sine function), Cos (Cosine function), and Tan^{-1} (Arctangent function) by the respective Sinh (Hyperbolic Sine function), Cosh (Hyperbolic Cosine function), and $Tanh^{-1}$ (Hyperbolic Arctangent function), the equations for the underdamped transient and normalized major responses become those for the overdamped system.

For an overdamped system with $\zeta = 2$, the normalized dynamic crush is .219, which occurs at the normalized time position of 43.6°. The normalized separation velocity is −.048 which occurs at the normalized separation time of 87.2° (2 times 43.6°). The corresponding static displacement is .191 as shown in Fig. 4.83.

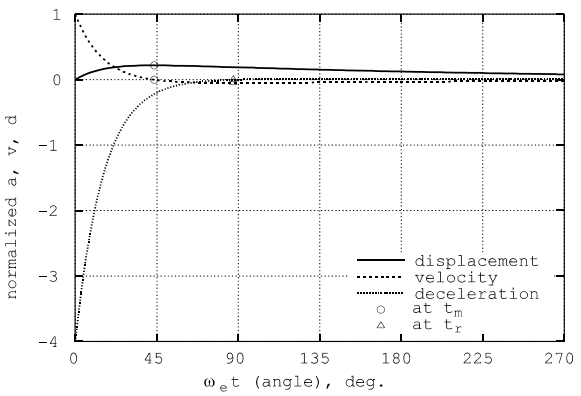

Fig. 4.83 Normalized Responses of an Overdamped System with ζ=2.

4.9.1.4 *Normalized Response Comparisons of Three Damping Systems*

The normalized response versus normalized time (angular position) curves for the three Kelvin model damping systems are compared for their response characteristics. The pulse shapes of the normalized curves depend on the damping factor only. Four levels of damping factor are used: spring only model with no damping, .2 (underdamped), 1. (critically damped), and 2. (overdamped).

Figs. 4.84–4.86 show the comparisons of the normalized displacement, velocity, and deceleration with different levels of damping factor: $\zeta = 0$ (k only), .2, 1., 2.

Note in Fig. 4.84, the peak magnitude of the normalized displacement decreases as the damping factor increases. The corresponding timing at the peak magnitude becomes shorter as the damping factor decreases.

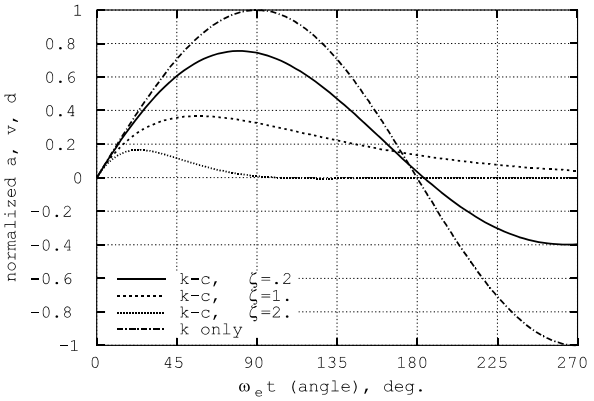

Fig. 4.84 Normalized Displacement vs. Time w/ Four Damping Levels

The normalized velocity curves with four damping levels are shown in Fig. 4.85. The normalized velocity starts from 1 at time zero to 0 at the time of dynamic crush. The velocity reaches a minimum value at the time of rebound velocity or separation velocity. Fig. 4.85 shows how the rebound velocity, the corresponding separation time, and time at dynamic crush (when the velocity is zero) change with the damping factor, ζ. For the undamped system with k (spring) only, the normalized rebound velocity is –1, therefore, the coefficient of restitution (e) is 1. While the normalized rebound velocity for the underdamped system with ζ=.2 is about –.57, therefore, e = .57. For a critically damped system with ζ=1, the normalized rebound velocity is found to be about –.13, therefore, e = .13. The analytical relationship between the coefficient of restitution (e or cor) and damping factor (ζ) of Kelvin's model is described in Section 4.9.4.

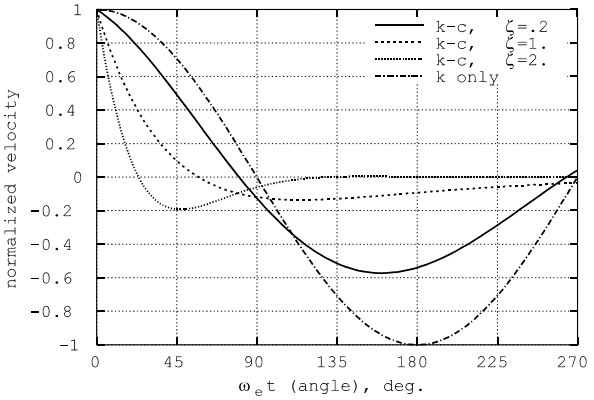

Fig. 4.85 Normalized Velocity vs. Time w/ Four Damping Levels

The normalized deceleration shown in Fig. 4.86 has a non-zero deceleration at time zero when the Kelvin system has a non-zero damping factor. As the damping factor increases, the non-zero initial deceleration increases, and the crash pulse become more front-loaded. The deceleration becomes zero at the time of separation velocity.

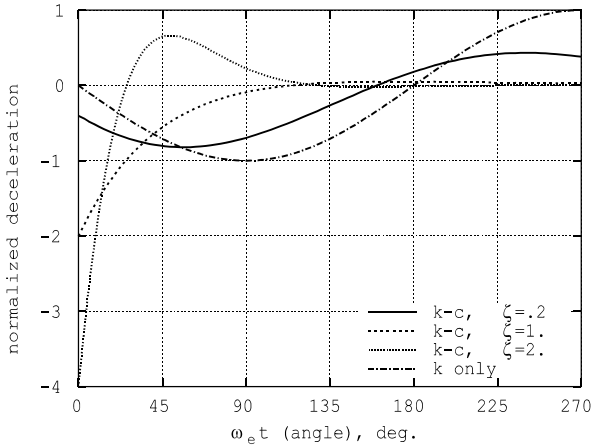

Fig. 4.86 Normalized Deceleration vs. Time with Four Damping Levels

4.9.2 Factors Affecting the Pulse Shape of System with Various Damping

The transient response formulas for the underdamped Kelvin model differ from those for the overdamped in the use of trigonometric and hyperbolic functions. There exists a similarity in a power series expansion between the trigonometric and hyperbolic functions as shown in Eq. (4.74).

$$\begin{aligned}
&\textit{Trigonometric}\ \ (\textit{all real values of } x): \quad \sin x = x - \frac{x^3}{3!} + \frac{x^5}{5!} - \frac{x^7}{7!} + \ldots \\
&\cos x = 1 - \frac{x^2}{2!} + \frac{x^4}{4!} - \frac{x^6}{6!} + \ldots, \quad \tan^{-1} x = x - \frac{x^3}{3} + \frac{x^5}{5} - \frac{x^7}{7} + \ldots \quad (x^2 < 1) \\
&\textit{Hyperbolic}: \quad \sinh x = x + \frac{x^3}{3!} + \frac{x^5}{5!} + \frac{x^7}{7!} + \ldots, \\
&\cosh x = 1 + \frac{x^2}{2!} + \frac{x^4}{4!} + \frac{x^6}{6!} + \ldots, \quad \tanh^{-1} x = x + \frac{x^3}{3} + \frac{x^5}{5} + \frac{x^7}{7} + \ldots
\end{aligned} \tag{4.74}$$

To visualize how the pulse shapes of the underdamped, critically damped, and overdamped Kelvin system are formed, the transient displacement equations shown in the previous sections are plotted without the use of the constant factors. A natural frequency of 13 Hz and damping factors of .75, 1., and 1.25 are used for the plotting.

Fig. 4.87 shows the pulse shape of the underdamped transient displacement α(t) of a Kelvin model. It is determined by the product of exponential decayed and sinusoidal function. The critically damped α(t) in Fig. 4.88 is determined by the product of exponential decayed and time function, $v_o t$. The overdamped α(t) shown in Fig. 4.89 equals the product of exponential decayed and hyperbolic sine functions.

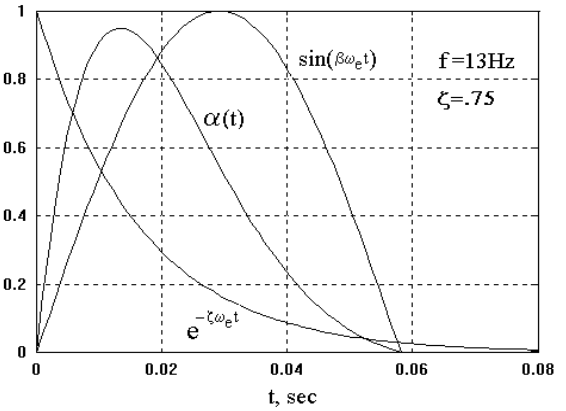

Fig. 4.87 Underdamped Transient Displacement

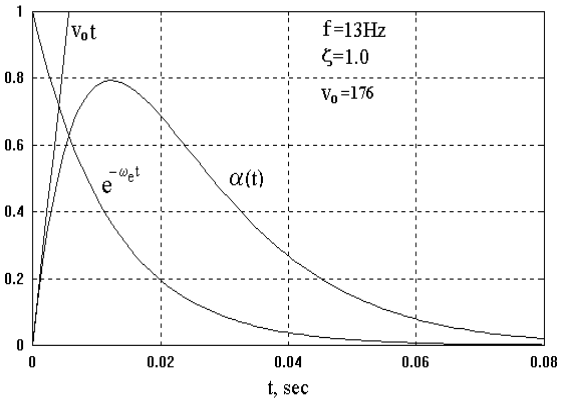

Fig. 4.88 Critically Damped Transient Displacement

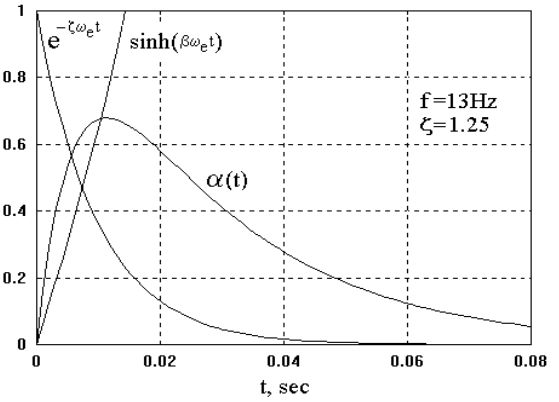

Fig. 4.89 Overrdamped Transient Displacement

The effect of damping on the peak magnitudes and timings of the transient displacements are shown in Fig. 4.90. Given an impact of a Kelvin system, damping tends to increase resistance to the body; therefore, the deformation is less. The timing of dynamic crush becomes shorter as damping increases. This is because the system becomes stiffer as damping increases in the Kelvin model.

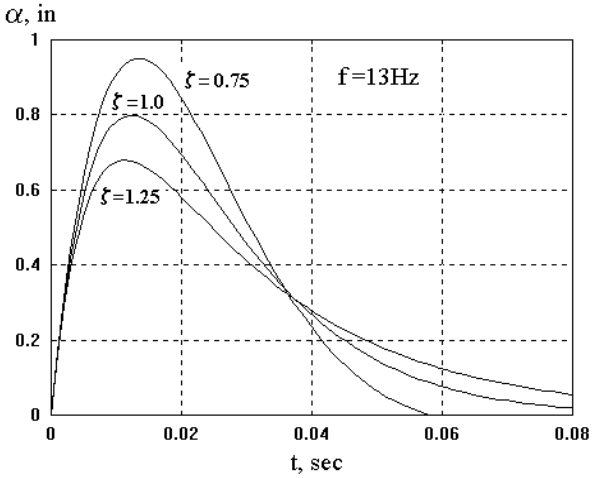

Fig. 4.90 Displ. vs. Time of a Kelvin Model with ζ

Since an exponentially decayed function is one of the two functions controlling the pulse shape of the Kelvin transient responses, one can use a power curve function to replace the exponentially decayed function, as shown in Eq. (4.75). A power curve function is represented by a binomial series, shown in Eq. (4.76).

$$e^{-x} = 1 - x + \frac{x^2}{2!} - \frac{x^3}{3!} + \frac{x^4}{4!} - \ldots \tag{4.75}$$

$$(1-x)^n = 1 - nx + \frac{n(n-1)x^2}{2!} - \frac{n(n-1)(n-2)x^3}{3!} + \ldots \text{ where } x^2 < 1 \tag{4.76}$$

For n = 5 and x = 10t where t ranges from 0 to .1$^-$ sec, the maximum of x is 1$^-$. The product of a time function and the power curve, expressed by $\alpha = ct\,(1\text{-}at)^b$, is termed an idealized power curve and is shown in Fig. 4.91. The idealized power curve has been used by Macmillan [4] to approximate a vehicle dynamic response.

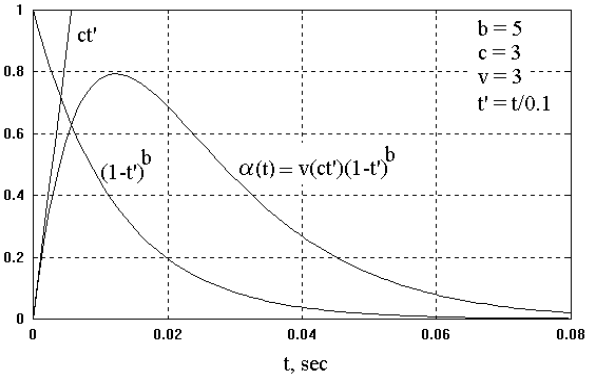

Fig. 4.91 Idealized Power Curve Transient Response

4.9.3 Hysteresis Loop

The normalized acceleration vs. the normalized displacement plot, shown in Fig. 4.92, is commonly referred to as a hysteresis loop. There are four curves shown in the plot, with damping factors (ζ) of 0.0, 0.2, 1., and 2.

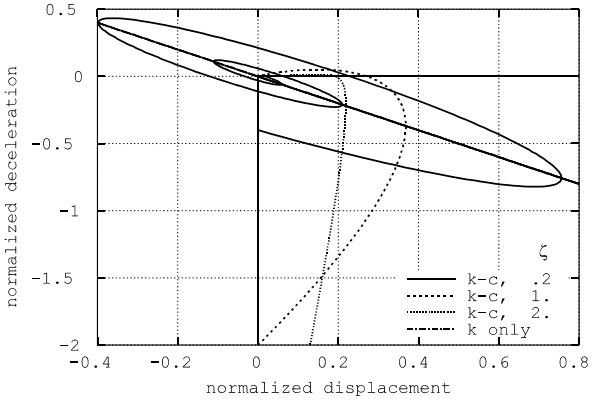

Fig. 4.92 Normalized Deceleration vs. Displacement with Various ζ

Note that in the plot of normalized responses, the shapes of the curves are controlled solely by the damping factor. The natural frequency does not have any influence on the shape and form of the hysteresis loop. This is because the normalized transient responses shown in part (B) of Eq. (4.70) are a function only of the damping factor.

Since the area enclosed by the curve shown in Fig. 4.92 is the hysteresis energy loss, the percentage of energy loss at any cyclic position can be estimated. For the cycle up to the dynamic crush (maximum normalized displacement) or up to the static crush (at the time of separation, where normalized acceleration is zero), the hysteresis energy loss can then be approximated.

Case Study 1: A Kelvin model is used to represent the structural property of a mid-size passenger car in a 14 mph barrier test. The test data are:
test weight, w = 3500 lb, dynamic crush, C = 10.1 inches at t_m = 76 ms, and v=14 mph.

The vehicle stiffness and damping coefficient have been computed (using the method described in Section 4.10) as shown in Eq. (4.77). They are k = 3099 lb/in and c = 66.8 lb-sec/in. Using the following formulas, the natural frequency and damping factor are found to be 2.94 Hz and .2, respectively.

$$
\begin{aligned}
&\textit{Calculate relative centroid location:}\\
&\frac{t_c}{t_m} = \frac{C/v}{t_m} = \frac{10.1in/(14\times 17.6in/s)}{.076s} = .54\\
&\textit{From Fig. 4.100 in Section 4.10, one gets } \zeta = .2 \textit{ for } t_c/t_m = .54\\
&\textit{From Fig. 4.101, one gets } ft_m = 222\ Hz\text{-}ms \textit{ for } \zeta = .2\\
&f = ft_m/t_m = 223/76 = 2.94\ Hz\\
&\textit{From Eq. (4.83) in Section 4.10.1:}\\
&\textit{Damping Coefficient:}\quad c = 0.033\,\zeta f w = 66.8\ \ lb\text{-}s/in\\
&\textit{Stiffness:}\qquad\qquad\ \ k = 0.102 f^2 w = 3099\ \ lb/in
\end{aligned}
\tag{4.77}
$$

Using the values of natural frequency and damping factor, the first half of the hysteresis loop is plotted using the transient deceleration and displacement equations shown in Eq. (4.70). The model initiation point is at (0 in,−4.7g) and the point at the end of elastic loading is (10.1 in,−9 g). Compared to the dotted test curve shown in Fig. 4.93, the model loading curve approximates the test curve well.

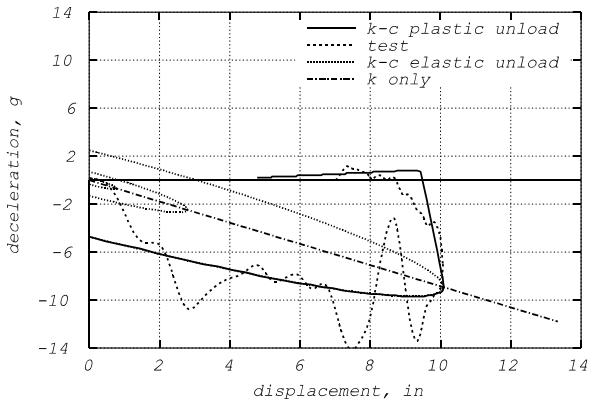

Fig. 4.93 Hysteresis Loops w/ Elastic and Plastic Unloading Compared w/ Test Data

Energy Absorption By The Spring and Damper

In the loading phase, energy absorptions by the spring and damper are shown in Eq. (4.78).

$$
\begin{aligned}
&E_k\text{: energy absorption by the spring only}\\
&E_k = \frac{1}{2}kx^2 = \frac{1}{2}(3099\ lb/in)(10.1\ in)^2 = 158{,}064\ lb\text{-}in\\
&E\text{: total kinetic energy}\\
&\text{Using conventional units of lb, mph, and in, then}\\
&\text{For } V_{mph} = 14\ mph,\ W = 3500\ lb\\
&\text{Then}\quad E = eW = (.4\,V_{mph}^2)(W, lb) = 274{,}400\ lb\text{-}in\\
&E_c\text{: energy absorption by damper}\\
&\text{therefore}\quad E_c = E - E_k = 116{,}336\ lb\text{-}in
\end{aligned}
\tag{4.78}
$$

Note that the energy absorption by the spring can also be checked by the hysteresis plot shown in Fig. 4.92. The computation is shown in Eq. (4.79) and the computed spring energy is very close to that of E_k in Eq. (4.78)

$$
\begin{aligned}
&\text{Area of triangle covered by the line for k only:}\\
&A \doteq \frac{1}{2}\times.75\times.75 = .28\ \text{units of energy density},\\
&\text{Each unit of energy density= product of normalized factors}\\
&\text{of deceleration and displacement} = (v_o\omega)\left(\frac{v_o}{\omega}\right)\\
&= v_o^2 = \left(14\,mph\times17.6\frac{in/s}{mph}\right)^2\times\frac{1g}{386.4\,in/s^2} = 157\ \frac{g\text{-}in}{unit}\\
&\text{Spring energy} = W\times A = 3500lb\times\left(.28\,units\times157\ \frac{g\text{-}in}{unit}\right) = 153{,}982\ lb\text{-}in
\end{aligned}
\tag{4.79}
$$

In the unloading phase, the spring returns the entire energy absorbed in the loading phase. However, part of this elastic unloading energy is absorbed again by the damper during the rebound phase. Since the spring and damper are under compression only during the loading, only the first quarter of the hysteresis loop is used.

The total hysteresis energy absorbed by the damper, therefore, is the total area enclosed by the first quarter hysteresis loop.

The test curve is also overlapped with the model curve. Since the test curve shows a quick plastic unloading, the Kelvin elastic unloading stiffness is modified to a plastic unloading. In this case, the unloading stiffness is set to 15 times the loading stiffness.

As far as the rebound kinematics, Fig. 4.94 shows the velocity versus position curve plots for cases with elastic unloading, plastic unloading, and the actual test curve. The test curves show that about 3% of the initial kinetic energy is due to the elastic return energy and the total energy dissipation is 97% of the initial kinetic energy. The Kelvin model with elastic loading and plastic unloading approximates the test responses reasonably well.

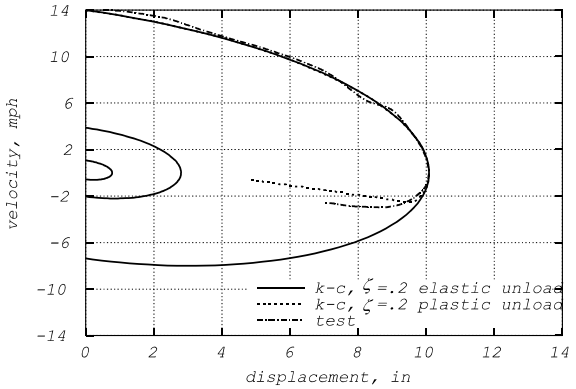

Fig. 4.94 v vs. d of Kelvin Model w/ Elastic and Plastic Unloading and Test

Case Study 2: In a component test of the body mount of a frame vehicle, an impactor of 400 lb strikes the body mount, which is held by a test fixture, at a speed 10 mph. The transient deformation curves are used to extract the stiffness and damping properties of the Kelvin model representing the body mount. Given a damping factor of .08, a mount natural frequency of 9 Hz, and the impact speed, the acceleration versus deflection responses can be computed using the closed form formula.

Shown in Fig. 4.95 are the model responses with test speeds of 5, 10, and 15 mph. Since elastic unloading is assumed in the model, the quick unloading observed in the test is due to the plastic unloading. It will be shown that the initial slope of the deceleration versus deflection curve is a function of the damping factor and natural frequency only. The impact speed controls only the magnitudes of the deceleration and deflection responses, but not the initial slope of the curve.

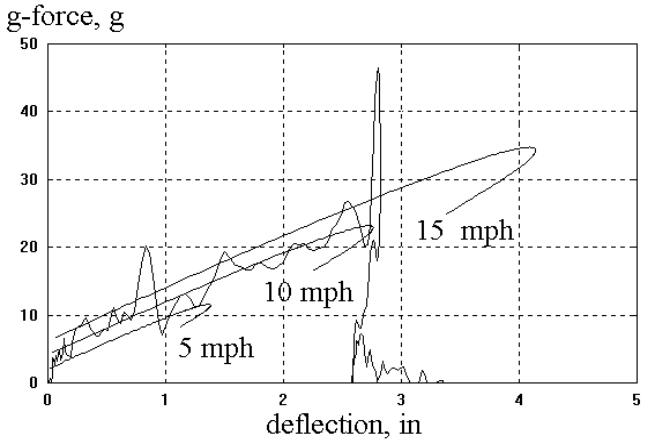

Fig. 4.95 g-d of an Engine Mount Model and Test at 10 mph (ζ=.08, f=9 Hz)

4.9.4 Coefficient of Restitution and Damping Factor (ζ)

In the impact of a dynamic system, the coefficient of restitution (cor) is defined as the ratio of relative separation velocity to the relative approach velocity. During the deformation phase, the relative approach velocity decreases from its initial value to zero due to the action of the deformation impulse, as shown in Fig. 4.96. At the time when the relative approach velocity is zero, the maximum dynamic crush occurs. The relative velocity in the rebound phase then increases negatively up to the final separation (or rebound) velocity, at which time the two masses separate from each other. At the separation time, there is no more restitution impulse acting on the masses, therefore, the relative acceleration at the separation time is zero. The relative velocity formula for the underdamped system ($0 \le \zeta \le 1$), derived in Section 4.9.1.1, can be used to derive the relationship between the coefficient of restitution and damping factor of the system. The relationship is shown as follows.

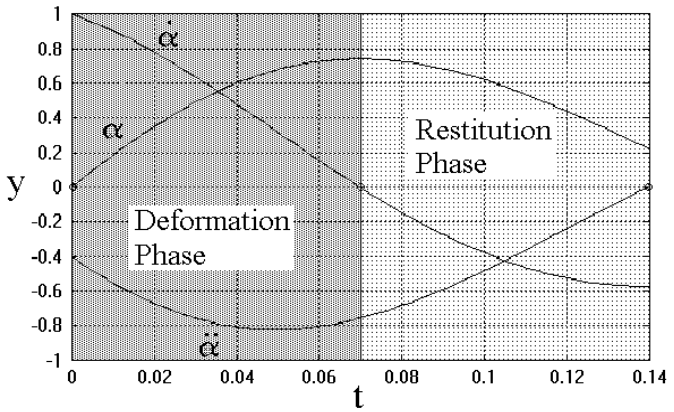

Fig. 4.96 Deformation and Restitution Phases of Kelvin Model with ζ=2, ω_e=20

At the time of separation, $t = t_f$, *the relative deceleration* $\ddot{\alpha} = 0$,

From Eq.(4.70): $2\zeta\cos(\sqrt{1-\zeta^2}\,\tau) + \dfrac{2\zeta^2-1}{\sqrt{1-\zeta^2}}\sin(\sqrt{1-\zeta^2}\,\tau) = 0$

Rearranging, $\tan(\sqrt{1-\zeta^2}\,\tau) = \dfrac{2\zeta\sqrt{1-\zeta^2}}{2\zeta^2-1}$

Using Pythagorean Theorem, one gets

$$\cos(\sqrt{1-\zeta^2}\,\tau) = 2\zeta^2 - 1 \quad \ldots\ldots\ldots\ldots\ldots \quad (1)$$

$$\therefore\ cor = \frac{\textit{relative separation velocity}}{\textit{relative approach velocity}} = \frac{\dot{\alpha}(t_f)}{v_0}$$

$$= e^{-\zeta\tau}\left[\cos(\sqrt{1-\zeta^2}\,\tau) - \frac{\zeta}{\sqrt{1-\zeta^2}}\sin(\sqrt{1-\zeta^2}\,\tau)\right] \quad \ldots\ldots\ldots \quad (2) \qquad (4.80)$$

Special Cases: 1. $\zeta = 0$ $\quad cor = 1$, $\quad$ 2. $\zeta = 1$ $\quad cor = -.135$

Substituting $\sin(\sqrt{1-\zeta^2}\,\tau) = 2\zeta\sqrt{1-\zeta^2}$
and simplifying the expressions, we get

$$cor = e^{-\left[\frac{\zeta}{\sqrt{1-\zeta^2}}\cos^{-1}(2\zeta^2-1)\right]} \quad \ldots\ldots\ldots\ldots\ldots\ldots \quad (3)$$

Special Cases:

(1) For $\zeta = 0$ (no damping), then cor = 1.
(1) For $\zeta = 1$ (critically damped), then cor = .135
(2) For $\zeta = \infty$ (highly overdamped), then cor=0

Graphically, the relationship between the coefficient of restitution and damping factor expressed by (3) of Eq. (4.80) is shown in Fig. 4.97.

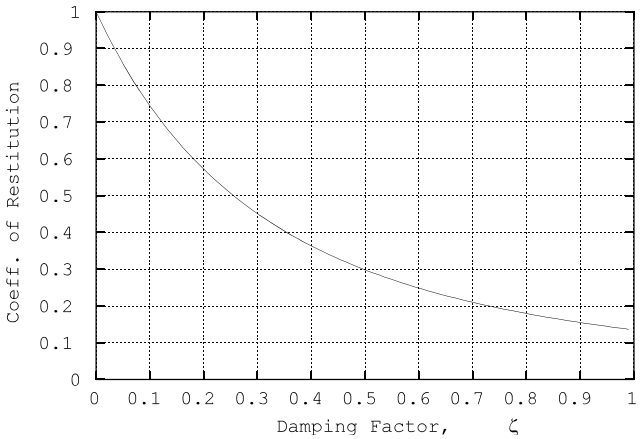

Fig. 4.97 Coefficient of Restitution as a Function of Damping Factor of a Kelvin Model

In the Kelvin model, the elastic loading and unloading stiffness of the spring are assumed to be the same. Consequently, the energy dissipation (hysteresis energy) during impact is attributed to damping only. The computed coefficient of restitution based on the elastic model is higher than that where plastic unloading occurs. In the case with plastic unloading, the unloading slope is larger than the loading slope.

4.9.5 Contact Duration

The contact duration, t_f (or separation time), of the two masses during impact includes the contact times in the deformation and restitution phases. At the end of contact just as the two masses separate from each other, the relative acceleration is zero and the relative separation velocity is the maximum recoverable velocity. The condition for zero relative acceleration at separation time is derived in Eq. (4.81) using (1) of Eq. (4.80) and t_f is derived in Eq. (4.81).

$$
\begin{aligned}
&\textit{since} \quad \sqrt{1-\zeta^2}\,\omega_e\, t_f = \cos^{-1}(2\zeta^2 - 1) \\
&\textit{therefore} \quad t_f = \frac{\cos^{-1}(2\zeta^2 - 1)}{\sqrt{1-\zeta^2}\,\omega_e} \quad \ldots (1) \\
&\quad \textit{where} \quad \omega_e : \textit{undamped natural frequency} \\
&\textit{special case:} \quad \zeta = 0 \\
&t_f = \frac{\cos^{-1}(-1)}{\omega_e} = \frac{\pi}{2\pi f} = \frac{1}{2f} \quad \ldots\ldots (2) \\
&\textit{compared to } T_m\textit{, time of dynamic crush, in Eq.}(4.27), \\
&t_f = 2T_m \qquad \ldots\ldots\ldots\ldots\ldots (3)
\end{aligned}
\tag{4.81}
$$

Case Study 3: A Kelvin Model (shown in Fig. 4.80) is used to simulate a component test. It is proposed to design the system such that the coefficient of restitution, e, is 0.5. Each of the two masses weighs 400 lbs; the spring stiffness k is 2 klb/in, and the closing speed is 15 mph. Using the effective mass approach, (1) compute the damping coefficient c, (2) draw the velocity profiles of the two masses, (3) show that the ratio of the relative separation velocity to the relative approach velocity equals e, the coefficient of restitution, and (4) determine the contact duration. [Ans.: $\zeta = .25$, f = 9.9 Hz, c = .0163 klb-s/in. The velocity plot is shown in Fig. 4.98].

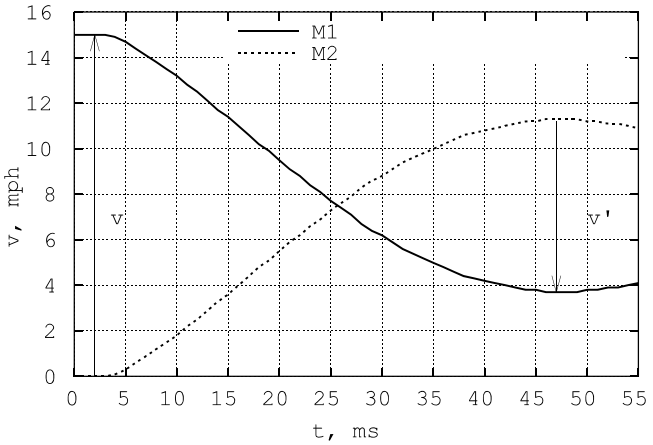

Fig. 4.98 Velocity Profiles for Case Study 3

4.10 DAMPING FACTOR AND NATURAL FREQUENCY FROM TESTS

In this section, the dynamic response or the crash pulse of a vehicle structure from a test is analyzed to obtain two parameters, damping factor, ζ, and structure natural frequency, f. The two unknown parameters of a vehicle structure, shown in Fig. 4.99, are solved using two closed form formulas for the dynamic crush and time at dynamic crush.

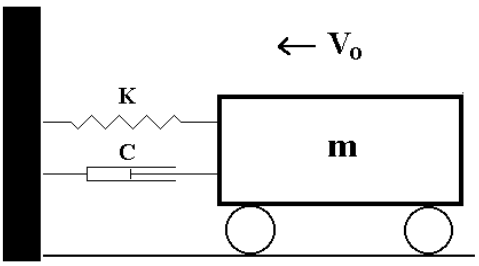

Fig. 4.99 A Vehicle Impact (Kelvin) Model

Let us define:
K: spring stiffness
C: damping coefficient
m: mass
τ_c : normalized time at centroid location [see Eq. (4.71)]
τ_m : normalized time of dynamic crush [see Eq. (4.71)]

Using the underdamped normalized response expressions for the dynamic crush and the corresponding time from Eq. (4.71), the derivation of the two unknowns is shown in Eq. (4.82).

$$\omega_e = \sqrt{\frac{K}{m}} \quad \ldots\ldots\ldots \quad \textit{angular frequency}$$

$$\zeta = \frac{C}{2m\omega_e} \quad \ldots\ldots\ldots \quad \textit{damping factor}$$

From Eq.(4.71) *for an underdamped system, we have*

$$\tau_c = e^{-\zeta\tau_m} \quad \ldots\ldots\ldots\ldots\ldots\ldots \quad (1)$$

$$\tau_m = \frac{1}{\sqrt{1-\zeta^2}} \tan^{-1}\frac{\sqrt{1-\zeta^2}}{\zeta} \quad \ldots\ldots\ldots\ldots \quad (2)$$

Substituting (2) *into* (1) *and dividing by* (2), *one gets* (4.82)

$$\frac{\tau_c}{\tau_m} = \frac{t_c}{t_m} = \frac{\sqrt{1-\zeta^2}}{\tan^{-1}\dfrac{\sqrt{1-\zeta^2}}{\zeta}} e^{\left[\frac{-\zeta}{\sqrt{1-\zeta^2}} \tan^{-1}\frac{\sqrt{1-\zeta^2}}{\zeta}\right]} \quad \ldots \quad (3)$$

$$\because \quad \tau_m = t_m(2\pi f), \qquad \textit{therefore}$$

$$f t_m = \frac{1}{2\pi\sqrt{1-\zeta^2}} \tan^{-1}\frac{\sqrt{1-\zeta^2}}{\zeta} \quad \ldots\ldots\ldots \quad (4)$$

Formulas (3) and (4) in Eq. (4.82) have been plotted and are shown in Figs. 4.100 and 4.101, respectively. Given the relative centroid location, one can find from the chart or the equation the damping factor. Similarly, one can find the value of f t_m from (4) of Eq. (4.82) or Fig. 4.101 from which f can be computed.

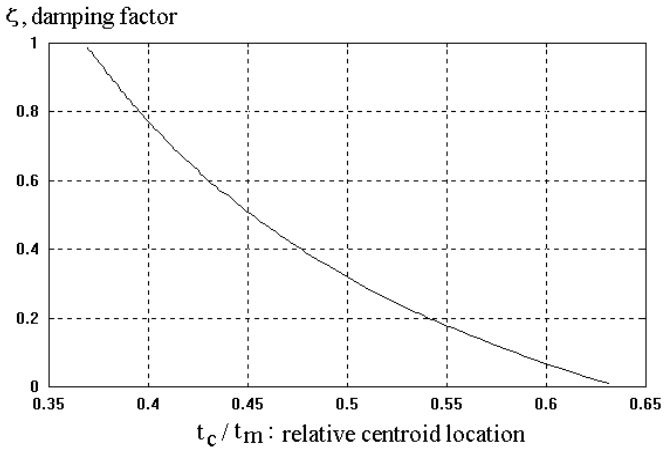

Fig. 4.100 Damping Factor as a Function of Relative Centroid Location

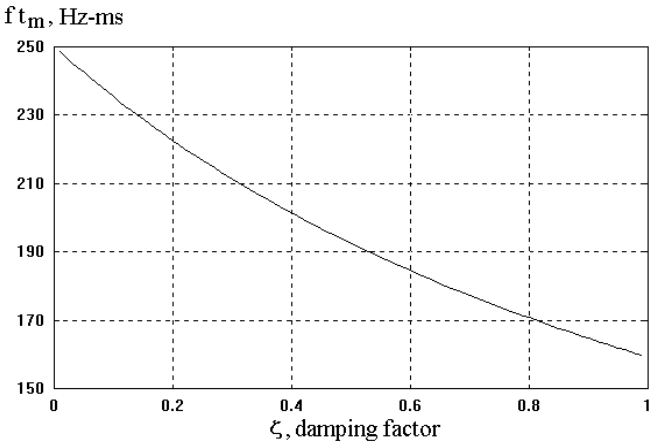

Fig. 4.101 Natural Frequency Multiplied by T_m vs. Damping Factor

4.10.1 Conversions of the Stiffness and Damping Coefficient

Using the impact test data of a vehicle or component, Fig. 4.100 and 4.101 define the damping factor (ζ) and natural frequency (f). Both ζ and f can be converted to the damping coefficient (c) and stiffness (k), provided the effective mass is known (as shown in Eq. (4.03)). The term specific damping coefficient is defined as the damping coefficient per unit weight and the specific stiffness per unit weight of a test object.

Define:
w: *weight, lb*
k: *stiffness, lb/in*
c: *damping coefficient, lb/(in/sec)*
ζ: *damping factor, and*
f: *natural frequency, Hz*

$$\textit{Specific damping coefficient}: \quad c' = \frac{c}{w} = 0.033\,\zeta f \quad \frac{g}{in/\text{sec}} \tag{4.83}$$

$$\textit{Specific stiffness}: \quad k' = \frac{k}{w} = 0.102 f^2 \quad \frac{g}{in}$$

$$\textit{Damping Coefficient}: \quad c = 0.033\,\zeta f w \quad . . \quad \frac{lb}{in/\text{sec}}$$

$$\textit{Stiffness}: \quad k = 0.102 f^2 w \quad . . \quad \frac{lb}{in}$$

4.10.2 Application to SUV and Sedan Frontal Structure Properties

The structural properties of one sport utility vehicle (SUV) and one mid-size sedan are to be studied using the Kelvin k-c model. Both vehicles were tested in 31 mph rigid barrier tests. The structural responses and properties of both vehicles are then compared.

Case Study 1: k-c Model for Truck. Find the stiffness and damping coefficient of an SUV which has the following frontal barrier test data.

$$
\begin{aligned}
&v_o = 31\ mph = 545.6\ in/s, \qquad c = 22\ in \\
&t_m = 73\ ms = .073\ \text{sec}, \qquad W = 4500\ lb \\
&m = \frac{W}{g} = \frac{4500\ lb}{386.4\ in/s^2} = 11.65\ \frac{lb\text{-}s^2}{in}
\end{aligned}
\tag{4.84}
$$

Determine the stiffness and damping coefficient of the frontal structure of the SUV.

Steps:

1. Compute the relative centroid location (t_c / t_m),
2. From ζ vs. t_c / t_m), find ζ,
3. From f t_m vs. ζ, find f t_m,
4. Given t_m, compute f.

The computation of the structural parameters is shown in Eq. (4.85).

$$
\begin{aligned}
&1:\ \frac{t_c}{t_m} = \frac{C}{t_m v_o} = \frac{22}{.073 \times 545.6} = .55 \\
&2:\ \textit{from the } \zeta \textit{ plot}: \quad \zeta = .185 \\
&3:\ \textit{from the } ft_m \textit{ plot}: \quad ft_m = 224\ Hz\text{-}ms \\
&4:\ f = \frac{224 Hz\text{-}ms}{73\ ms} = 3.07\ Hz \\
&\omega_e = 2\pi f = 19.3\ \frac{rad}{\text{sec}}, \quad 2m\omega_e = 450\ \frac{lb\text{-sec}}{in} \\
&\therefore\ k = m\omega_e^2 = 4339\ \frac{lb}{in}, \quad c = \zeta(2m\omega_e) = 83.2\ \frac{lb\text{-sec}}{in} \\
&\textit{NOTE: The damped natural frequency is} \\
&\omega_d = \omega_e\sqrt{1-\zeta^2} = 19.0\ \frac{rad}{\text{sec}}
\end{aligned}
\tag{4.85}
$$

Case Study 2: k Model for Truck. Find the stiffness only without damping in the model for the test condition. The determination of the stiffness of the structure is to satisfy the boundary condition of the dynamic crush only. The time of dynamic crush from the test is not controlled by the k model.

This is a special case where $\zeta = 0$. It is a spring mass model only. Since the spring mass model satisfies the boundary condition set by the dynamic crush of the test, the natural frequency is then computed from the given impact velocity and dynamic crush as shown in Eq. (4.86).

$$
\begin{aligned}
&\textit{For the spring-mass model:} \\
&\frac{t_c}{t_m} = \frac{2}{\pi} = .64, \quad t_m = \frac{t_c}{.64} = \frac{.0403}{.64} = .063\ \text{sec} \\
&\textit{Since}\ \ \omega_e = \frac{v_o}{c} = \frac{545.6}{22} = 24.8\ \frac{rad}{\text{sec}} \\
&f = \frac{\omega_e}{2\pi} = 3.95\ hz, \quad k = m\omega_e^2 = 7165\ \frac{lb}{in}
\end{aligned}
\tag{4.86}
$$

Since a spring-mass model does not have an additional resistance from the damper, the spring is stiffer than that in the spring-damper-mass model in order to satisfy the dynamic crush requirement. In addition, the time at dynamic crush for the spring-mass model is shorter than that in the spring-damper-mass model. This is due to the fact that the undamped natural frequency in Case Study 2 is higher than the damped natural frequency in Case Study 1.

Case Study 3: k-c Model for Sedan. A mid-size passenger car with a test weight (w) of 3500 lb was tested at a fixed barrier impact speed (v_o) of 31 mph. The sedan is a unitized body vehicle and the major damping contribution comes from the engine mounts and subframe body mounts which isolate the power train vibration. The transient responses of the vehicle are shown in thick solid curves in Fig. 4.102. The vehicle has a dynamic crush (C) of 27 inches at 87.4 ms (T_m) and has a rebound velocity (v′) of 5.92 mph.

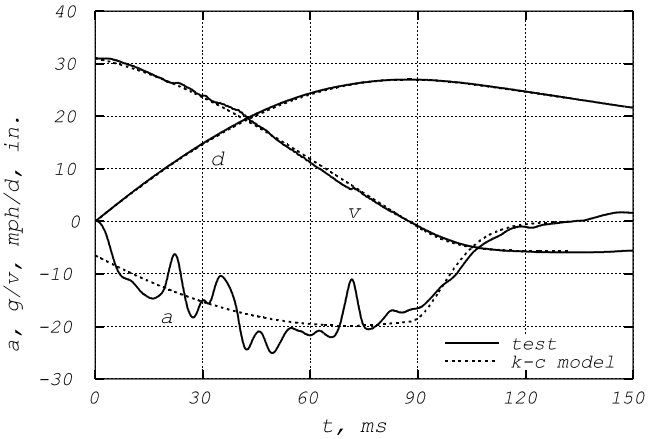

Fig. 4.102 k-c Model and Test Responses of a Mid-Size Sedan in a 31 mph Barrier Test

The structural parameters of the k-c model for the sedan have been computed and are shown in Table 4.10 along with those for the SUV described in Case Study 1.

Table 4.10 k-c Model Parameters for the SUV and Sedan

Vehicle	W, lb	t_c / t_m	ζ	f, Hz	k, lb/in	c, lb-s/in
#1, SUV	4500	.55	.185	3.07	4339	83.2
#2, Sedan	3500	.57	.139	2.63	2474	41.7

From the table, the structure natural frequency (f) and damping factor (ζ) are higher for the truck than for the car. Given the stiffness and mass of each vehicle shown in Table 4.10, the relationship between the mass ratio and stiffness ratio can then be computed.

$$r_m = \frac{m_1}{m_2} = \frac{4500}{3500} = 1.29, \quad r_k = \frac{k_1}{k_2} = \frac{4339}{2474} = 1.75$$
$$\textit{therefore} \qquad r_m < r_k \tag{4.87}$$

In the impact severity analysis of the vehicle-to-vehicle collision, the relative magnitude of the mass ratio and stiffness ratio determines the relative magnitudes of the velocity change (ΔV) and barrier equivalent velocity (BEV) of each vehicle involved in the collision.

4.11 EXCITATION OF THE KELVIN MODEL — OCCUPANT AND RESTRAINT

The spring-mass occupant model subjected to excitation was covered in Section 4.6. The model itself does not have a damper and therefore can only be used to control one vehicle parameter,

dynamic crush. The spring-mass model consists of the occupant mass, restraint characteristics, and restraint slack in addition to the forcing function. The closed form solutions for the occupant response and sensitivity functions are presented for the model subjected to the excitation of TESW (tipped equivalent square wave) and sinusoidal functions.

In this section, the Kelvin model with a spring, k, and damper, c, in parallel, and slack, δ, shown in Fig. 4.103, is subjected to a forcing function. The closed form solutions of the model subjected to TESW, halfsine, and haversine excitations are derived. The method of undetermined coefficients is used to solve for the particular solutions. The particular solution in displacement α is specified such that the derivative of α with respect to time yields the forcing function.

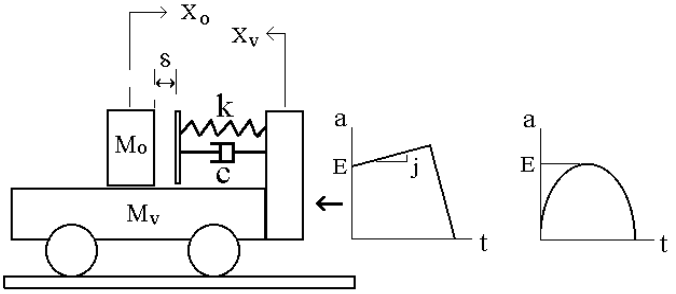

Fig. 4.103 A Kelvin Model with Slack, δ

The general solution to the second-order differential equation with the forcing function is then the summation of the homogeneous and particular solutions, as shown in Eq. (4.88). Since there exists a slack, restraint coupling does not start at time zero of the excitation pulse. The onset of the occupant acceleration starts at time t* when sled displacement reaches δ and the slack is taken out. Therefore, the time variable, t, applies to the time in the restraint coupling phase starting at t*. Based on the sled displacement, the second integral of the excitation pulse, t*, can then be computed. Note that the boundary conditions of the sled displacement and velocity at t* are used to derive the integration constants c_1 and c_2 which are used in Eq. (4.88). The boundary conditions at t* and the expressions for the integration constants c_1 and c_2 are shown in Tables 4.11 – 4.13 for the three pulses, respectively.

$$
\begin{aligned}
&\ddot{\alpha} + 2\zeta\omega_e\dot{\alpha} + \omega_e^2\alpha = \ddot{y}(t) \ldots \textit{a forcing function}\\
&\textit{General solution procedures:}\\
&\alpha = \alpha_c + \alpha_p, \quad \dot{\alpha} = \dot{\alpha}_c + \dot{\alpha}_p, \quad \ddot{\alpha} = \ddot{\alpha}_c + \ddot{\alpha}_p\\
&\alpha_c = e^{at}[c_1 S(bt) + c_2 C(bt)]\\
&\dot{\alpha}_c = e^{at}[d_1 S(bt) + d_2 C(bt)]\\
&\ddot{\alpha}_c = e^{at}[e_1 S(bt) + e_2 C(bt)]\\
&\textit{where}\\
&\quad S\text{: Sine function}\\
&\quad C\text{: Cosine function}\\
&\quad d_1 = ac_1 - bc_2\\
&\quad d_2 = bc_1 + ac_2\\
&\quad e_1 = ad_1 - bd_2\\
&\quad e_2 = bd_1 + ad_2\\
&\quad a = -\zeta\omega_e\\
&\quad b = \beta\omega_e\\
&\quad \beta = \sqrt{1-\zeta^2}
\end{aligned}
\tag{4.88}
$$

Table 4.11 Particular Solutions for TESW Excitation

TESW: $\ddot{y} = E + jt$, *where* j(*jerk*): *slope of tipped equivalent square wave*

Particular Solution	Parameter	Initial Condition at t*
$\alpha_p = p_0 t^2 + p_1 t + p_2$	$p_0 = 0$	$a* = E + jt^*$
$\dot{\alpha}_p = p_1$	$p_1 = \dfrac{j}{\omega_e^2}$	$v* = Et^* + \dfrac{1}{2} jt^{*2}$
$\ddot{\alpha}_p = 0$	$p_2 = \dfrac{1}{\omega_e^2}(E^* - \dfrac{2\zeta j}{\omega_e})$	$d* = \dfrac{t^{*2}}{6}(3E + jt^*)$
Integration constants: $c_2 = -p_2$, $c_1 = \dfrac{v^* + ap_2 - p_1}{b}$		

Table 4.12 Particular Solutions for a Sinusoidal Excitation

Sinusoidal: $\ddot{y}(t) = ES(\omega t)$

Particular Solution	Parameter	Initial Condition at t*
$\alpha_p = p_1 S(\omega t) + p_2 C(\omega t)$	$p_1 = \dfrac{r_{10} r_{11} + r_{12} r_{20}}{r_{11}^2 + r_{12}^2}$	$a^* = ES(\omega t^*)$
$\dot{\alpha}_p = p_1 \omega C(\omega t) - p_s \omega S(\omega t)$	$p_2 = \dfrac{r_{11} r_{20} - r_{10} r_{12}}{r_{11}^2 + r_{12}^2}$	$v^* = \dfrac{E[1 - C(\omega t^*)]}{\omega}$
$\ddot{\alpha}_p = -\omega^2 \alpha_p$	$r_{11} = 1 - r_\omega^2$	$d^* = \dfrac{E}{\omega}[t^* - \dfrac{S(\omega t^*)}{\omega}]$
	$r_\omega = \dfrac{\omega}{\omega_e}$, *frequency ratio*	
$r_{12} = 2\zeta r_\omega$	$r_{10} = \dfrac{EC(\omega t^*)}{\omega_e^2}$	$r_{20} = \dfrac{ES(\omega t^*)}{\omega_e^2}$
Integration constants: $c_2 = -p_2$, $c_1 = \dfrac{v^* + ap_2 - p_1}{b}$		

Table 4.13 Particular Solutions for a Haversine Excitation

Haversine: $\ddot{y}(t) = \frac{E}{2}[1 - C(\omega t)]$

Particular Solution	Parameter	Initial Condition at t*
$\alpha_p = p_0 + p_1 t + p_2 S(\omega t) + p_3 C(\omega t)$	$p_0 = \frac{E}{2\omega_e^2}$ $p_1 = 0$	$a^* = \frac{E}{2}[1 - C(\omega t^*)]$
$\dot{\alpha}_p = p_1 + p_2 \omega C(\omega t) - p_3 \omega S(\omega t)$	$p_2 = \frac{p_{21}}{p_{23}}$	$v^* = \frac{E}{2}[t - \frac{S(\omega t^*)}{\omega}]$
$\ddot{\alpha}_p = -p_2 \omega^2 S(\omega t) - p_3 \omega^2 C(\omega t)$	$p_3 = \frac{p_{31}}{p_{23}}$	$d^* = \frac{E}{2}[\frac{t^{*2}}{2} + \frac{C(\omega t)}{\omega^2} - \frac{1}{\omega^2}]$
$p_{21} = \frac{E}{2}[q_1 S(\omega t^*) - q_2 C(\omega t^*)]$	$p_{23} = [q_1^2 + q_2^2]\omega_e^2$	$p_{31} = \frac{-E}{2}[q_1 C(\omega t^*) + q_2 S(\omega t^*)]$
where $q_1 = 1 - r_\omega^2$, $q_2 = 2\zeta r_\omega$		
Integration constants: $c_2 = -(p_0 + p_1)$, $c_1 = \frac{v^* - a c_2 - p_1 - p_2 \omega}{b}$		

4.11.1 General Crash Pulse Excitation by Fourier Series

Using the crash pulse approximation method described in Section 2.4.1, Chapter 2, any crash pulse can be expressed by a Fourier equivalent wave (FEW), a Fourier series expansion in sinusoidal form. The fundamental frequency of the crash pulse can be determined either from its duration or from the angular natural frequency of a spring-mass model which equals the impact velocity divided by the dynamic crush. In addition to the excitation by the first harmonic, the occupant is also subjected to the excitations by the other multiple harmonics of the crash pulse. The overall occupant response is then the linear superposition of the series of occupant responses.

The closed form formula for the occupant response due to sinusoidal excitation can therefore be applied to the series of sinusoidal terms. Before applying the formula, the restraint contact time would have to be determined first. This is due to the fact that the formulas are applicable only in the occupant-restraint coupling phase. The restraint contact time t* occurs when the magnitude of the second integral of the crash pulse with zero initial velocity reaches the value of δ.

4.11.1.1 *Testing the Haversine Excitation*

To validate the concept of linear superposition, the responses of a restrained occupant subjected to a haversine excitation are computed in two ways: one by the closed-form formula shown in Table 4.13 and the other by the linear superposition of three sinusoidal harmonics in the FEW expression.

A restrained occupant with a restraint natural frequency of 7 Hz, a damping factor of 0.2, and a restraint slack of 2 inches is subjected to a haversine excitation. Eq. (4.89) shows the 5th order of FEW for the haversine excitation. The haversine has a duration of 200 ms with peak deceleration magnitude of 20 g. Note that there are only three sinusoidal waves (odd number harmonics) which make up the

haversine. The first, third, and fifth harmonics and the resultant haversine pulses are shown in Fig. 4.104. The fundamental frequency of the first harmonic is 2.5 Hz (period = 400 ms). The magnitude and the frequency of these three sinusoidal waves are shown in Eq. (4.89).

$$\textit{Haversine: } 5^{th} \textit{ order FEW (Fourier Equivalent Wave)}$$

$$A(t) = \sum_{i=1}^{5} a_i \sin(i\,\omega\, t) \qquad \textit{for} \quad \omega = 2.5\ Hz \tag{4.89}$$

i	1	2	3	4	5
$i\omega$	2.50	5.00	7.50	10.00	12.50
a_i	16.98	0.00	−3.39	0.00	−0.48

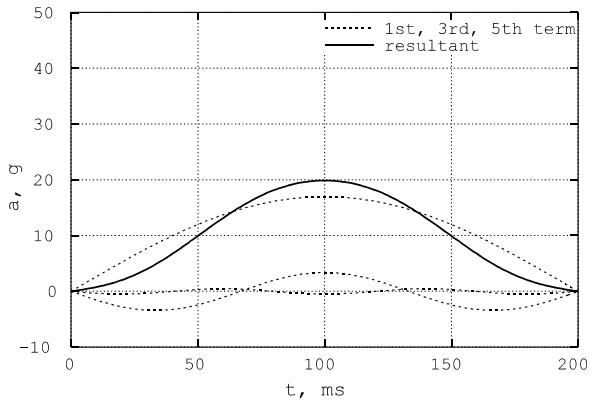

Fig. 4.104 Haversine Excitation and its Three Harmonics

The occupant responses attributed to the three harmonics are shown in Fig. 4.105. The resultant occupant response using the linear superposition of the three component responses is also shown in Fig. 4.105. This resultant occupant response is identical to the one obtained by the closed form formula shown in Table 4.13 for the haversine excitation.

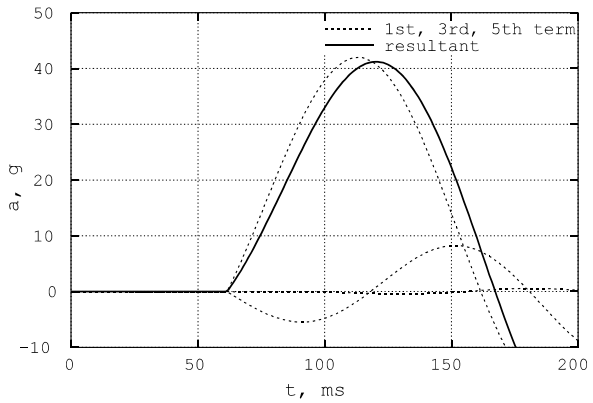

Fig. 4.105 Occupant Responses due to Three Harmonic Excitations

4.11.2 Effect of Restraint Damping Control on Occupant Response

In a vehicle-to-vehicle compatibility analysis, there are several factors normally considered by the researchers and engineers. They are the mass, stiffness, and geometry (MSG), which are all related to the physical parameters of the vehicles involved in the impact. In addition, this author has noticed two other important factors that need to be addressed. One factor is the engine (E) size and

location in the vehicle; these certainly would affect the shape of a crash pulse. Given a vehicle front end structure, the crash pulse may become more front-loaded if the engine is relocated further to the front and rear-loaded, if placed further rearward. The other factor is the occupant restraint system design, which is the subject of this section.

In the vehicle compatibility analysis presented in Section 4.7, the occupant is restrained by the three-point belt and air bag system. The occupant response is computed by using the closed form formula with the given data of restraint stiffness and slack only without damping. The baseline system for the car occupant (see Table 4.5 of Section 4.7.3) has a restraint natural frequency of 6 Hz, and a restraint slack of 1.1 inches, which corresponds to a restraint contact time of 33 ms.

In general, the damping coefficient and stiffness are the two restraint system parameters. It has been known that the vent holes located on the back of an air bag provide damping control during its deployment. Tuning the size of the vent holes and adjusting the mass flow rate can change the damping characteristics of the air bag system.

Assuming the new air bag and three-point belt system has a damping factor of 0.15, a new set of occupant responses can then be computed by using the closed form solution for the Kelvin model. Using Table 4.12 for the halfsine excitation on the k-c model, a new set of occupant response is then computed. The comparison of the occupant deceleration between the test, the baseline, and the new restraint system is shown in Fig. 4.106. The new system with $\zeta = 0.15$ has an occupant chest deceleration of 36 g @ 97 ms compared to the baseline system of 43 g @ 105 ms.

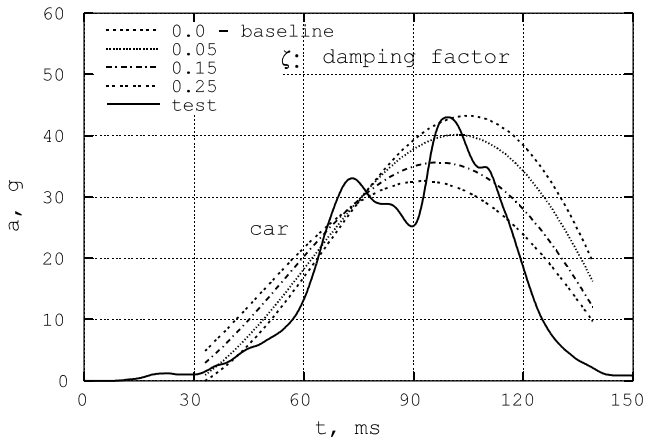

Fig. 4.106 Chest G from Test, and k-c Model w/ Halfsine Excitation ($\zeta > 0$, $\delta = 1.1$")

The effect of restraint damping control is significant. A restraint damping factor of 0.15 reduces the baseline occupant chest deceleration by 16%. Therefore, in a vehicle-to-vehicle compatibility analysis, it is more than just an MSGE (mass, stiffness, geometry, and engine) issue; it is the MSGER (MSGE plus Restraint) that needs to be considered as a whole.

4.12 REFERENCES

1. Huang, M., "An Analysis of the Vehicle-Occupant Impact Dynamics and its Application," SAE 830977, Passenger Car Meeting, Dearborn, Michigan, June 6–9, 1983.
2. Harker, R.J., "Generalized Methods of Vibration Analysis," John Wiley & Sons, 1982.
3. Huang, M., "On Body Mount Crash Characteristics," SAE paper No. 1999-01-3186, International Body Engineering Conference and Exposition, Detroit, Michigan, September 28–30, 1999. Also in Journal of Passenger Cars, SAE 1999 Transactions, Section 6, pp.3330–3342.
4. Macmillan, R.H., "Dynamics of Vehicle Collisions," Inderscience Enterprises Ltd., London, U.K., 1983.

CHAPTER 5

RESPONSE PREDICTION BY NUMERICAL METHODS

5.1 INTRODUCTION

The solution to a problem with an impact or excitation model having more than two masses and/or any number of non-linear energy absorbers becomes too complex to solve in a closed form. Then, numerical evaluation and integration techniques are necessary to solve for the dynamic responses.

Models such as the two non-isomorphic (with different structural configuration) hybrid or standard solid models, the combination of two hybrid models, and special cases with point masses will be treated first in closed-form. The purpose of the closed-form analysis is to investigate the dynamic responses of two dynamically equivalent hybrid models. In a multi-mass model, the unloading characteristics of a spring element is as important as the loading characteristics. The unloading of one mass in a model may produce loading of the neighboring masses, thereby, affecting the total system model responses.

Power curve loading and unloading simulation with hysteresis energy loss and permanent deformation will be covered. To help solve some dynamic models quickly, a lumped-parameter model, CRUSH II [1], coupled with animation, will be utilized. The force-deflection formulas of some simple structures are listed for ease of determining the spring stiffness for the modeling. Some lumped-parameter models for the full frontal, side, and frontal offset impacts are described. The basic concepts of splitting a simple spring-mass model for the frontal offset impact and the model validation are also presented.

5.2 HYBRID MODEL — A STANDARD SOLID MODEL

There are two types of hybrid models, Hybrid #1 and #2, shown in Figs. 5.1 and 5.2, respectively.

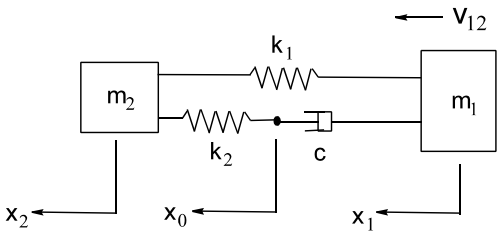

Fig. 5.1 Hybrid Model #1

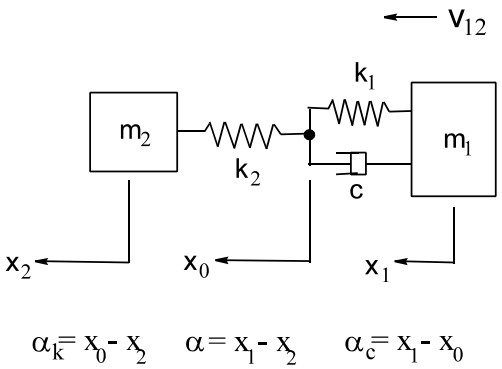

Fig. 5.2 Hybrid Model #2

A hybrid model is a combination of Maxwell and Kelvin models. It has three elements: two springs and one damper. These three elements are connected in such a way that the two hybrid models are structurally and functionally different (non-isomorphic). In impact analysis, each hybrid model has two mass systems with a closing speed of V_{12}. To simplify the two-mass system analysis, the concept of an effective mass system is introduced and utilized in the next section.

The hybrid model has been used in an impact dynamics study of the body mount in a body-on-frame vehicle [2], and the lateral impact modeling of the thorax of a driver in a car accident [3].

5.2.1 E.O.M. for Hybrid Model

Using the concept of an effective mass system and an approach similar to that used in deriving the equation of motions (E.O.M) for the Maxwell model shown in Section 4.8 of Chapter 4, the E.O.M. for the hybrid model can also be expressed in terms of one second order differential equation (D.E.) and one first order D.E. Similar to the Maxwell model, the E.O.M. for the hybrid model can be expressed in terms of one third order D.E. The corresponding characteristic equations for the two hybrid models are shown in (1) to (3) of Eq. (5.1), respectively.

$$\textit{Characteristic equation: } s^3 - ts^2 + us - v = 0 \quad \ldots\ldots\ldots\ldots\ldots \quad (1)$$

$$\textit{For Hybrid Model \#1: } t = \frac{-R\omega_e}{2\zeta}, \quad u = (1+R)\omega_e, \quad v = \frac{-R\omega_e^3}{2\zeta} \quad \ldots\ldots \quad (2)$$

$$\textit{For Hybrid Model \#2: } t = \frac{-(1+R)\omega_e}{2\zeta}, \quad u = R\omega_e^2, \quad v = \frac{-R\omega_e^3}{2\zeta} \quad \ldots\ldots \quad (3)$$

$$\omega_e = \sqrt{\frac{k_1}{m_e}} \quad \textit{undamped (angular) natural frequency}$$

$$\zeta\,(\textit{damping factor}) = \frac{c}{2m_e\omega_e} = \frac{\textit{damping coeff., } c}{\textit{critical } c,\ c_c}$$

$$m_e\,(\textit{effective mass}) = \frac{m_1 m_2}{m_1 + m_2}, \quad R = \frac{k_2}{k_1}$$

The three roots are: one real root β, *and a pair of complex conjugates,* $\epsilon + i\omega$ *and* $\epsilon - i\omega$. (5.1)

$$\textit{Here: } \epsilon = \frac{u + \frac{v}{\beta}}{2\beta}, \textit{ and } \omega = \sqrt{\left|\epsilon^2 + \frac{v}{\beta}\right|}$$

Note β, ϵ, *and* ω *are in radians/*sec.

Let $\dot{\alpha}$ *be relative velocity* $= v_1 - v_2 = v_{12}$,

Let $\Omega = \omega t, \quad C\Omega = \cos\omega t, \quad S\Omega = \sin\omega t$

$$\alpha = -pe^{-\beta t} + e^{-\epsilon t}(p\ C\Omega + q\ S\Omega) \quad \ldots\ldots\ldots\ldots\ldots\ldots \quad (4)$$

$$\dot{\alpha} = p\beta e^{-\beta t} + e^{-\epsilon t}[\omega(-p\,S\Omega + q\,C\Omega) - \epsilon(p\,C\Omega + q\,S\Omega) \quad \ldots\ldots\ldots \quad (5)$$

$$\ddot{\alpha} = -p\beta^2 e^{-\beta t} + e^{-\epsilon t}[(\epsilon^2 - \omega^2)(p\,C\Omega + q\,S\Omega) + 2\epsilon\omega(p\,S\Omega - q\,C\Omega)] \quad \ldots \quad (6)$$

$$\left.\frac{d\ddot{\alpha}}{d\alpha}\right|_{t=0} = \frac{p'(\beta^3 - \epsilon^3) - q'\omega^3 + 3\epsilon\omega(q'\epsilon + p'\omega)}{p'(\beta - \epsilon) + q'\omega} \quad \ldots\ldots\ldots\ldots \quad (7)$$

$$\textit{where } p' = \frac{-2\epsilon}{(\beta-\epsilon)^2 + \omega^2}, \quad q' = \frac{\beta^2 - \epsilon^2 + \omega^2}{\omega[(\beta-\epsilon)^2 + \omega^2]}, \quad p = p'v_{12}, \quad q = q'v_{12}$$

The two-mass system can be transformed into an one effective-mass system. Fig. 5.3(a) shows the hybrid #1 effective-mass system. In this model, there are two springs in contact with the rigid barrier. If one of the springs is moved to the other side of the mass while still in contact with the barrier (or ground), a new model arrangement is obtained, as shown in Fig. 5.3(b). Although the EA

arrangements in the two models look different, the models are functionally identical to each other. The underlying assumption is that the tension behavior of spring k_1 is the same as in compression.

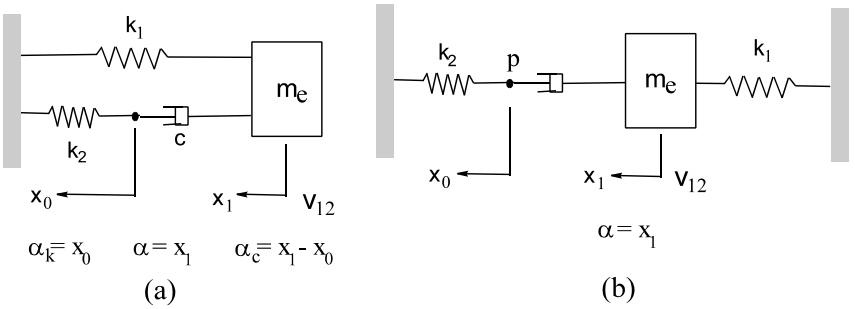

Fig. 5.3 Two Effective-Mass Systems (Hybrid Model #1)

5.2.2 Dynamic Response and Principles of Superposition

The dynamics of the Kelvin model has been described in Section 4.9 of Chapter 4. The Kelvin model with the spring and damper in parallel produces a non-zero deceleration at time zero. Consequently, the initial deceleration of the impactor, mass m_1, deviates from that in the test.

However, in the Kelvin model, the initial slope on the deceleration vs. displacement curve is only a function of the component parameters ω, and ζ and is independent of the impact speed. Note from (1) of Eq. (5.2), the sign of the initial slope of a vs. d changes when the damping factor ζ is more than 0.5. This change in slope direction has been shown in the hysteresis plot, Fig. 4.92 in Section 4.9.3.

$$\left.\frac{d\ddot{x}}{dx}\right|_{t=0} = \omega^2 (4\zeta^2 - 1) \ \ldots (1), \qquad \left.\frac{d\ddot{x}}{dt}\right|_{t=0} = v_o \left.\frac{d\ddot{x}}{dx}\right|_{t=0} \quad or \quad j = v_o k \ \ldots (2) \tag{5.2}$$

In Kelvin model, the initial slope of the deceleration vs displacement curve (k, a specific stiffness) multiplied by the initial velocity (v_o) is equal to the jerk (j, rate of change of deceleration) at time zero. This relationship $j = v_o k$ from Eq. (5.2) has been shown in Eq. (1.44) of Section 1.9.3.

Shown in Figs. 5.4 – 5.6 are the a vs. t, d vs. t, and a vs. d curves of the hybrid models for Type F body mount at the impact speeds of 5, 10, and 15 mph. Note that the initial slope for each of the three a vs. d curves in Fig. 5.6 is constant. It is independent of the impact speed and is solely determined by the component parameters expressed in (7) of Eq. (5.1). However, the impact speed changes the maximum magnitudes of the g-force and deflection, as shown in Fig. 5.6.

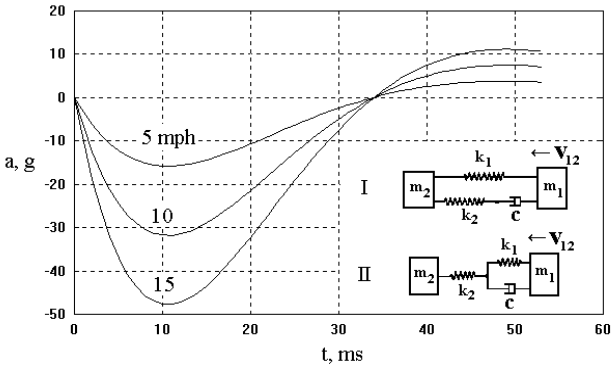

Fig. 5.4 a vs. t of Hybrid Models at Three Impact Speeds

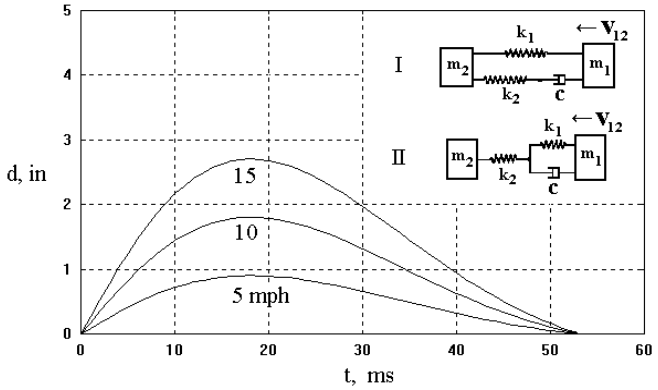

Fig. 5.5 d vs. t of Hybrid Models at Three Impact Speeds

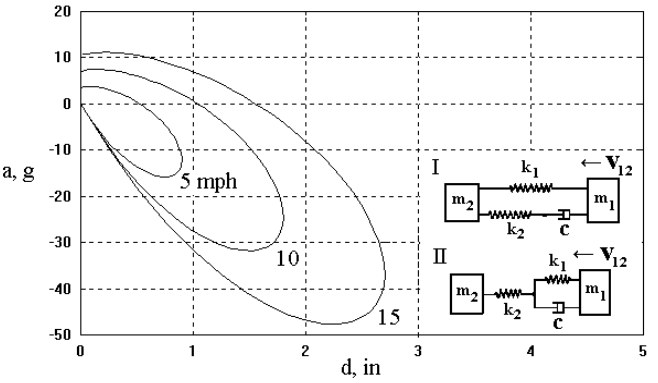

Fig. 5.6 a vs. d of Hybrid Models at Three Speeds

The fact that the impact speed does not change the initial slope on the a vs. d (g-force vs. deflection) curve does not suggest that the body mount is free of damping. This is because the initial slope has already been determined by the natural frequency and damping factor of the body mount.

The Hybrid model is a linear system; therefore, the principle of superposition applies. The transient displacement at 10 mph is simply equal to two times that at 5 mph as shown in Fig 5.5, while the transient displacement at 15 mph is equal to the sum of the displacements at 10 mph and 5 mph.

5.2.3 Combination of Two Hybrid Models

Similar to combining two Kelvin models for a vehicle-to-vehicle impact (see Section 4.4.3), one can also combine the EA′s (energy absorbers) of two hybrid models as shown in the upper figure in Fig. 5.7. The interface in the model, a point mass, has negligible weight. Based on the principle of superposition in combining two EA's into one EA, described in Section 4.4.3 of Chapter 4, two hybrid models in series can be simplified by joining them into one effective hybrid model as shown in the bottom of Fig. 5.7.

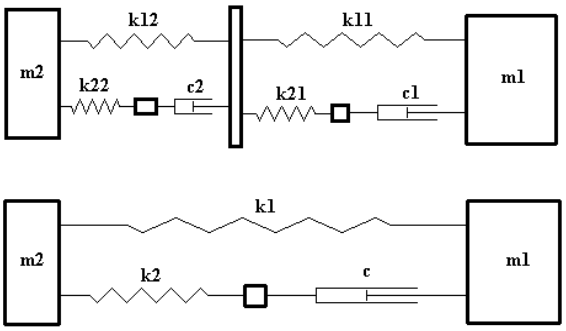

Fig. 5.7 Vehicle-to-Vehicle Impact Model: A Two-Hybrid Model

The EA parameters in the combined model are the effective spring and effective damper shown in Eq. (5.3).

$$K_1 = \frac{K_{11}\,k_{12}}{K_{11} + k_{12}}, \qquad K_2 = \frac{K_{21}\,k_{22}}{K_{21} + k_{22}}$$
$$\textit{and} \qquad c = \frac{c_1\,c_2}{c_1 + c_2} \tag{5.3}$$

Case Study: The weights of vehicles (masses) m1 and m2 are 6 and 3 klbs (kilo-pounds), respectively. The values of the individual and combined (or effective) parameters of the springs and damper in the two models are shown in Table 5.1.

Table 5.1 Parameters of the Two-Hybrid and One-Hybrid Models

Vehicle m2 structure (top left in Fig. 5.7)			Vehicle m1 structure (top right in Fig. 5.7)			Hybrid Model with Effective EAs		
k11, klb/in	k21, klb/in	c1, klb-s/in	k12, klb/in	k22, klb/in	c2, klb-s/in	K1, klb/in)	K2, klb/in	c, klb-s/in
6	12	.1	3	6	.08	2	4	.0444

The initial speed of m1 impacting on the stationary m2 is 60 mph. Note that for modeling purposes, the interfaces between two EAs are modeled by point masses with negligible weight (e.g., five pounds). The dynamic analysis is done by CRUSH II model simulation, and the output responses are animated and plotted. Shown in Fig. 5.8 are the decelerations of the two masses in two- and one-hybrid models. The deceleration curves of the two masses in the two-hybrid model are of the saw-tooth type. The saw-tooth responses are the high frequency noises, generated by the light weight interface connected by a stiff spring to the main body. In both models, the peak accelerations of m1 and m2 are −17 and 34 g for m1 and m2, respectively. These occur at the same time, at 45 ms.

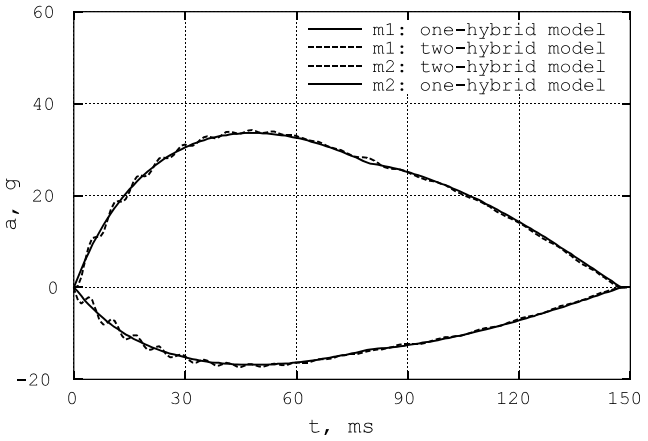

Fig. 5.8 Acceleration Responses of the Two Masses in the One- and Two-Hybrid Models

5.2.4 Dynamic Equivalency between Two Non-Isomorphic Hybrid Models

There are three EA′s (energy absorbers) in each of the two hybrid models shown in Figs. 5.1 and 5.2, respectively. By appending a subscript i to the existing parameters, the two sets of EA′s become unique for each model. The EA parameters are k_{1i}, k_{2i}, and c_i for hybrid model #i. Similarly, the coefficients in the characteristic equation shown in Eq. (5.4) are similarly assigned as t_i, u_i, and v_i for model #i.

To establish the dynamic equivalency between the two models, the three coefficients of hybrid model #1 are set equal to the corresponding coefficients of model #2 respectively. Since there are three constraint equations, the three EA parameters of one model can then be solved in terms of those of the other model.

$$\textit{Characteristic equation: } s^3 - ts^2 + us - v = 0$$

$$t_1 = t_2: \quad \frac{-R_1\,\omega_{e1}}{2\zeta_1} = \frac{-(1+R_2)\omega_{e2}}{2\zeta_2} \quad \ldots\ldots \quad (1)$$

$$u_1 = u_2: \quad (1+R_1)\omega_{e1}^2 = R_2\omega_{e2}^2 \quad \ldots\ldots\ldots \quad (2)$$

$$v_1 = v_2: \quad \frac{-R_1\,\omega_{e1}^3}{2\zeta_1} = \frac{-R_2\,\omega_{e2}^3}{2\zeta_2} \quad \ldots\ldots \quad (3)$$

Relationships between parameters, k_{1i}, k_{2i}, and c_i, i=1,2:

$$k_{12} = \left[\frac{1+R}{R}\right] k_{11} \quad \ldots\ldots\ldots\ldots\ldots\ldots \quad (4)$$

$$k_{22} = \left[1+R\right] K_{11} \quad \ldots\ldots\ldots\ldots\ldots\ldots \quad (5)$$

$$c_2 = \left[\frac{1+R}{R}\right]^2 c_1 \quad \ldots\ldots\ldots\ldots\ldots\ldots \quad (6)$$

$$\zeta_2 = \left[\frac{1+R}{R}\right]^{1.5} \zeta_1 \quad \ldots\ldots\ldots\ldots\ldots\ldots \quad (7)$$

(5.4)

$$\textit{where} \quad R = \frac{k_{21}}{k_{11}} = \frac{k_{22}}{k_{12}} = R_1 = R_2, \quad \zeta_i = \frac{c_i}{2\,m_e\,\omega_{ei}} = \frac{c_i}{2\,m_e\sqrt{\dfrac{k_{1i}}{m_e}}} = \frac{c_i}{2\sqrt{m_e\,k_{1i}}}$$

Therefore, given a set of values for the two springs and one damper parameters for hybrid model #1, one can compute the values of those for hybrid model #2. Formulas (4) to (6) of Eq. (5.4) are needed for the computation. It will be shown in the next section that dynamic equivalency between the two models applies to the kinematic, crush, and energy responses of the masses only. There are no equivalencies among the respective energy absorbers.

Case Study: Given the values of the following parameters of hybrid model #1:

k_{11} = 2 klb/in, k_{21} = 4 klb/in, c_1 = .0444 klb-sec/in, and
w_1 = 6 klb, w_2 = 3 klb, v_{close} = 60 mph

Determine the counterpart parameters for hybrid model #2 such that the dynamic responses of the two models are identical.

From Eq. (5.1), the effective weight and damping factor of hybrid model #1 are computed as shown in Eq. (5.5).

$$w_e = \frac{w_1 w_2}{w_1 + w2} = \frac{6\,x\,3}{6+3} = 2\ klb, \quad m_e = \frac{w_e}{g} = \frac{2}{386.4} = .0052\ klb\text{-}s^2/in$$

$$\zeta_1 = \frac{c_1}{2\sqrt{m_e k_{11}}} = \frac{.0444}{2\sqrt{.0052\,x\,2}} = .022, \quad \textit{and the total crush energy:} \qquad (5.5)$$

$$\Delta E \equiv .0334\, w_e\, v_{close}^2 = .0334\,(2\,klb)\,(60\,mph)^2 = 240\ klb\text{-}ft$$

Using Eq. (5.4), the parameters of hybrid model #2, k_{12}, k_{22}, and c_2, can be computed from those of hybrid model #1 and are shown in Eq. (5.6). Note that the spring stiffness ratio in the hybrid model #2, $k_{22}/k_{12} = 2$, is the same as that in model #1, k_{21}/k_{11}.

$$R = \frac{K_{21}}{k_{11}} = \frac{4}{2} = 2$$

$$k_{12} = \left[\frac{1+R}{R}\right] k_{11} = \frac{1+2}{2}\,2 = 3 \quad \ldots\ldots\ldots\ldots \quad (4)$$

$$k_{22} = [1+R]\,K_{11} = [1+2]2 = 6 \quad \ldots\ldots\ldots\ldots \quad (5) \qquad (5.6)$$

$$c_2 = \left[\frac{1+R}{R}\right]^2 c_1 = \left[\frac{1+2}{2}\right]^2 0.0444 = .0999 \quad \ldots\ldots \quad (6)$$

$$\zeta_2 = \left[\frac{1+R}{R}\right]^{1.5} \zeta_1 = \left[\frac{1+2}{2}\right]^{1.5} 0.022 = .04 \quad \ldots\ldots \quad (7)$$

The computed input data for hybrid model #2 are shown at the top of Fig. 5.9, and the original input data of model #1 are shown at the bottom of Fig. 5.9. Both models are effective mass models where the effective weight is 2 klb as computed in Eq. (5.5). The effective weight is moving at a speed of 60 mph to the left where the fixed rigid barrier is located. The total crush energy, the initial kinetic energy of the effective mass in the rigid barrier test, has been computed to be 240 klb-ft, as shown in Eq. (5.5).

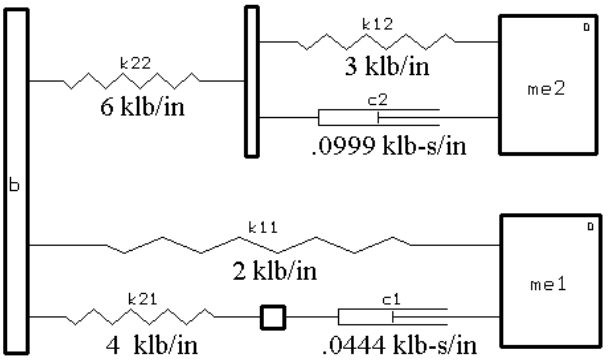

Fig. 5.9 Dynamic Equivalency of Hybrid #1 (bottom) and #2 (top) Models

5.2.4.1 *Dynamic Equivalency in Transient Kinematics and Crush Energy*

The effective mass deceleration vs. time curves of both hybrid models #1 and #2 are shown in Fig. 5.10. The peak accelerations of both models are equal, -51 g @ 46 ms, and both models have the same deceleration in the early portion of the rebound phase. The deceleration difference after 80 ms in the rebound phase is attributed to the way the EA(s) is in contact with the rigid barrier. Spring k22 in model #2 is in contact with the barrier (not rigidly attached to the barrier), while both springs k11 and k21 in model #1 are in contact with the barrier. Since at any given time, the spring contact forces in the two models may not be the same, the separation time and the deceleration may be different for the two models in that period.

In addition to acceleration, the two hybrid models are also dynamically equivalent in terms of transient velocity and displacement beyond the deformation phase, as shown in Fig. 5.10. The dynamic crush occurs at 68 ms where the velocity of the effective mass is zero.

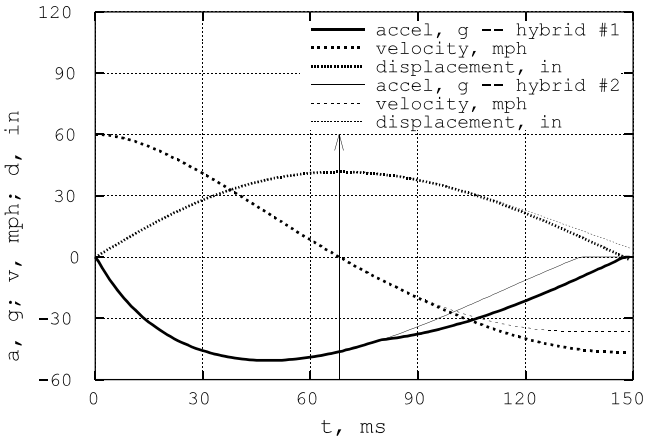

Fig. 5.10 Transient Kinematics of Hybrid Models #1 and #2

Beyond kinematics, the two hybrid models under dynamic equivalency conditions are also equivalent (identical) in terms of transient total crush energy. The total crush energy is the sum of the three individual crush energies due to springs #1 and #2 and the damper. Figs. 5.11 and 5.12 show the total and individual crush energies vs. time of the hybrid models #1 and #2, respectively. In both hybrid models, the transient individual crush energies due to two springs and one damper are different. However, the sums of the three energies of the two hybrid models are identical in the deformation

phase and in the early portion of the rebound phase. The maximum total crush energy is 240 klbs-ft at 68 ms, the time of dynamic crush. The maximum total crush energy can also be checked by the formula for the energy density, e, as shown in Eq. (5.7):

$$W_e = \frac{W_1 W_2}{W_1 + W_2} = 2000\ lbs$$
$$E = W_e e = W_e(lbs) \times 0.4\left[v(mph)\right]^2 \tag{5.7}$$
$$= 2000 \times 0.4\,[60]^2 = 2880\ klbs\text{-}in = 240\ klbs\text{-}ft$$

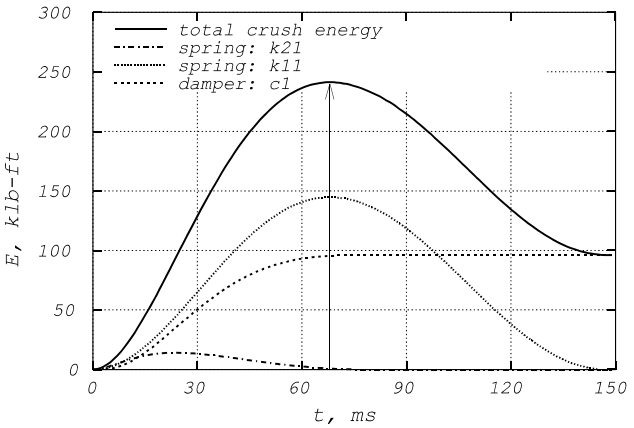

Fig. 5.11 Total and Individual Crush Energies vs. Time for Hybrid Model #1

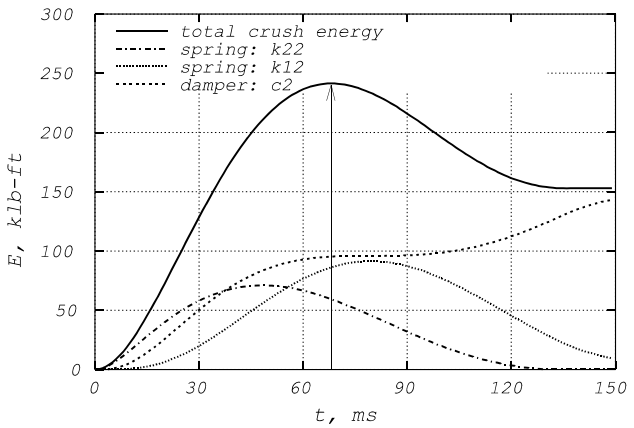

Fig. 5.12 Total and Individual Crush Energies vs. Time of Hybrid Model #2

5.3 TWO MASS-SPRING-DAMPER MODEL

A numerical method based on semi-closed-form solutions of a two mass-spring-damper (2-MSD) model (shown in Fig. 5.13) is presented. Applications of the model solutions to the vehicle pre-program and post-crash structural analyses are described. The model in these applications simulates a rigid barrier impact of a vehicle where m_1 and m_2 represent the frame rail (chassis) and passenger compartment masses, respectively. In other cases, m_1 may represent the vehicle structure with energy absorbers (spring and damper), and m_2, the torso with a restraint system of spring, k_2, and damper, c_2.

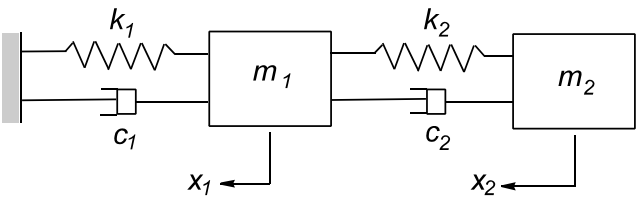

Fig. 5.13 A Two Mass-Spring-Damper Model

The method for solving the impact responses of the two masses is adapted from the method used in the free vibration analysis of a two-degree of freedom damped system [4]. The equations of motion (EOM) of the 2-MSD are shown in Eq. (5.8).

$$
\begin{aligned}
&m_1\ddot{x}_1 = -k_1x_1 - k_2(x_1-x_2) - c_1\dot{x}_1 - c_2(\dot{x}_1-\dot{x}_2)\\
&m_2\ddot{x}_2 = k_2(x_1-x_2) + c_2(\dot{x}_1-\dot{x}_2)\\
&m_1\ddot{x}_1 + (c_1+c_2)\dot{x}_1 + (k_1+k_2)x_1 - c_2\dot{x}_2 - k_2x_2 = 0 \quad .. \quad (1)\\
&c_2\dot{x}_1 - k_2x_1 + m_2\ddot{x}_2 + c_2\dot{x}_2 + k_2x_2 = 0 \quad ..... \quad (2)
\end{aligned}
\tag{5.8}
$$

Since an exponential function of t, e^{st}, returns to the same form in all derivatives, it therefore satisfies the differential equations (1) and (2) of Eq. (5.8). The solution for x_1 and x_2 is shown by (3) of Eq. (5.9). Note that s is a complex root in general, as are C_i, R_i, S_i, as shown by (4) of Eq. (5.9).

$$
\begin{aligned}
&x_i = C_ie^{st} \quad \text{where} \quad i = 1,2 \quad ..... \quad (3)\\
&\text{where } C_i \text{ and } s \text{ may be complex numbers,}\\
&\text{substituting into (1) and (2), one gets}\\
&R_1C_1 - R_2C_2 = 0, \quad -S_1C_1 + S_2C_2 = 0\\
&\text{where} \quad R_1 = m_1s^2 + (c_1+c_2)s + (k_1+k_2), \quad R_2 = c_2s + k_2\\
&\qquad S_1 = c_2s + k_2, \qquad S_2 = m_2s^2 + c_2s + k_2\\
&\because \quad \frac{C_2}{C_1} = \frac{R_1}{R_2} = \frac{S_1}{S_2}, \qquad \therefore \quad R_1S_2 - R_2S_1 = 0 \quad .... \quad (4)
\end{aligned}
\tag{5.9}
$$

5.3.1 Solutions of the Characteristic Equation

After substituting R_1, R_2, S_1, and S_2 into (3) of Eq. (5.9), a characteristic equation (a 4th order polynomial) is obtained as shown in Eq. (5.10).

$$
\begin{aligned}
&s^4 + ts^3 + us^2 + vs + w = 0\\
&\text{where} \quad t = \frac{m_1c_2+m_2(c_1+c_2)}{m_1m_2}, \qquad u = \frac{m_1k_2+m_2(k_1+k_2)+c_1c_2}{m_1m_2}\\
&\qquad v = \frac{k_1c_2+k_2c_1}{m_1m_2}, \qquad w = \frac{k_1k_2}{m_1m_2}
\end{aligned}
\tag{5.10}
$$

Since all the physical parameters, mass, damping, and stiffness, are positive, the coefficients in the polynomial characteristic equation are also positive. The alternate name for such a polynomial is a posinomial. For a posinomial, there can be no positive roots. The three possible combinations of the four roots are shown as follows.

Case 1: Two pairs of complex conjugates,
Case 2: One pair of complex conjugate and two real and negative roots, and
Case 3: Four real and negative roots.

The solutions to the three cases are described as follows.

Case 1: Two pairs of complex conjugates

The system in this case has moderate damping. The rate of decay is defined by p_1, the real part of the root, and the frequency of vibration is specified by q_1, the imaginary part.

$$\begin{aligned} &\textit{Two pairs of complex conjugates are:} \\ &(1):\ s_1 = -p_1 + iq_1, \qquad s_2 = -p_1 - iq_1 \\ &(2):\ s_3 = -p_2 + iq_2, \qquad s_4 = -p_2 - iq_2 \end{aligned} \tag{5.11}$$

where p_1, p_2, q_1, and q_2 are all positive. s_1 and s_2 are the first pair of complex conjugates, and s_3 and s_4, the second pair. The two roots s_1 and s_2 in the first pair will yield the solutions x_{11} and x_{21}, where the first subscript refers to the mass index and the second subscript the pair number of the complex conjugate:

(I) Displacement components x_{11} and x_{21} due to s_1 and s_2, respectively

$$\begin{aligned} &\textit{mass } 1{:}\ x_{11} = A_{11}e^{-p_1 t}\sin(q_1 t+\phi_{11}), \quad \textit{mass } 2{:}\ x_{21} = A_{21}e^{-p_1 t}\sin(q_1 t+\phi_{21}) \\ &\textit{where} \quad A_{11}\sin\phi_{11} = C_{11} + C_{12} \quad \textit{and} \quad A_{11}C\phi_{11} = (C_{11} - C_{12})i \end{aligned} \tag{5.12}$$

The ratios of complex numbers C_{21}/C_{11} and C_{22}/C_{12} can be obtained by substituting s_1 and s_2 into the characteristic equation, respectively. The ratio of amplitudes A_{21}/A_{11} can thus be obtained, and the phase angle relationship between Φ_{21} and Φ_{11} can be related as shown in Eq. (5.13).

$$\begin{aligned} &\frac{C_{21}}{C_{11}} = \frac{S_{11}}{S_{21}} = \frac{c_2 s_1 + k_2}{m_2 s_1^2 + c_2 s_1 + k_2} = e + fi, \qquad \frac{C_{22}}{C_{12}} = e - fi \\ &\because\ A_{11}^2 = (A_{11}S\phi_{11})^2 + (A_{11}C\phi_{11})^2 = 4C_{11}C_{12}, \qquad \therefore\ A_{21}^2 = 4C_{21}C_{22} \\ &\textit{then} \quad \frac{A_{21}}{A_{11}} = \sqrt{\frac{C_{21}C_{22}}{C_{11}C_{12}}} = \sqrt{e^2+f^2}, \qquad \tan\phi_{21} = \frac{\dfrac{f}{e} + \tan\phi_{11}}{1 - \left(\dfrac{f}{e}\right)\tan\phi_{11}} \end{aligned} \tag{5.13}$$

(II) Displacement components x_{12} and x_{22} due to s_3 and s_4, respectively

Similarly, using the same approach as in (I), the ratio of amplitudes A_{22} to A_{12} and the phase angle relationship between Φ_{22} and Φ_{12} can also be obtained. They are shown in Eq. (5.14).

$$\frac{C_{23}}{C_{13}} = g + hi, \qquad \frac{C_{24}}{C_{14}} = g - hi, \quad \textit{and}$$

$$\frac{A_{22}}{A_{12}} = \sqrt{g^2+h^2}, \quad \textit{and} \quad \tan\phi_{22} = \frac{\frac{h}{g} + \tan\phi_{12}}{1 - \left(\frac{h}{g}\right)\tan\phi_{12}} \tag{5.14}$$

(III) General Solution

A set of simultaneous equations is formulated based on the displacement and velocity expressions and the initial conditions as shown in Eq. (5.15).

$$\begin{aligned}
&\textit{Displacement:}\quad x_i = \sum_{j=1}^{2} x_{ij} = A_{i1}e^{-p_1 t}S(q_1 t + \phi_{i1}) + A_{i2}e^{-p_2 t}S(q_2 t + \phi_{i2}) \\
&\textit{Velocity:}\quad \dot{x}_i = A_{i1}e^{-p_1 t}[q_1 C(q_1 t + \phi_{i1}) - p_1 S(q_1 t + \phi_{i1})] + \\
&\qquad\qquad A_{i2}e^{-p_2 t}[q_2 C(q_2 t + \phi_{i2}) - p_2 S(q_2 t + \phi_{i2})], \quad \textit{where } i = 1, 2 \\
&\textit{at } t = 0, \quad x_1 = 0, \quad x_2 = 0, \quad \textit{and} \quad \dot{x}_1 = v_0, \quad \dot{x}_2 = v_0 \\
&\textit{A set of displacement and velocity equations is obtained:} \\
&A_{11}S\phi_{11} + A_{12}S\phi_{12} = 0 \quad \ldots\ldots\ldots\ldots\ldots\ldots \quad (1) \\
&A_{21}S\phi_{21} + A_{22}S\phi_{22} = 0 \quad \ldots\ldots\ldots\ldots\ldots\ldots \quad (2) \\
&A_{11}[q_1 C\phi_{11} - p_1 S\phi_{11}] + A_{12}[q_2 C\phi_{12} - p_2 S\phi_{12}] = v_0 \quad \ldots \quad (3) \\
&A_{21}[q_1 C\phi_{21} - p_1 S\phi_{21}] + A_{22}[q_2 C\phi_{22} - p_2 S\phi_{22}] = v_0 \quad \ldots \quad (4)
\end{aligned} \tag{5.15}$$

Note that A_{21}, A_{22}, ϕ_{21}, and ϕ_{22} are related to A_{11}, A_{12}, ϕ_{11}, and ϕ_{12}, respectively, by the relationships shown in the derivation before. Thus, the general displacement equations are completely defined after solving the four unknowns in the four non-linear equations. Note that this system has a moderate value of damping.

Case 2: One pair of complex conjugate and two real and negative roots

The rate of decay is defined by p_1, the real part of the root, and the frequency of vibration, by q_1 imaginary part. If the damping in the system is slight, the values of p_1 and p_2 will be small, and q_1 and q_2 will approximate the values of ω_1 and ω_2, the frequencies of the system without damping.

The solutions of the 4th order posinomial yield four roots where the coefficients p_1, q_1, σ_3, and σ_4 are all positive. The general displacement solutions are shown in Eq. (5.16).

$$\begin{aligned}
&\textit{First pair of complex conjugates:} \\
&s_1 = -p_1 + iq_1, \qquad s_2 = -p_1 - iq_1 \\
&\textit{Two real and negative roots:} \\
&s_3 = -\sigma_3, \qquad\qquad s_4 = -\sigma_4 \\
&x_i = A_{i1}e^{-pt}S(qt + \phi_{i1}) + C_{i3}e^{-\sigma_3 t} + C_{i4}e^{-\sigma_4 t}, \quad \textit{where} \quad i = 1, 2 \\
&\textit{From} \quad \frac{C_2}{C_1} = \frac{S_1}{S_2}, \quad \textit{then} \quad \frac{C_{23}}{C_{13}} = \frac{S_{13}}{S_{23}} = \frac{-c_2\sigma_3 + k_2}{m_2\sigma_3^2 - c_2\sigma_3 + k_2}
\end{aligned} \tag{5.16}$$

Case 3: Four real and negative roots

The system has a large damping. When it is disturbed, the system will settle to its equilibrium configuration without oscillation. The solutions of the 4th order posinomial yield

$$\begin{aligned} &\textit{Four real and negative roots:} \\ &s_k = -\sigma_k \quad \textit{where} \quad \sigma_k > 0, \quad k = 1, 2, 3, \textit{and } 4. \\ &x_i = C_{i1}e^{s_1 t} + C_{i2}e^{s_2 t} + C_{i3}e^{s_3 t} + C_{i4}e^{s_4 t}, \quad i = 1, 2 \end{aligned} \tag{5.17}$$

There are four unknowns C_{11}, C_{12}, C_{13}, and C_{14} in four equations. C_{21}, C_{22}, C_{23}, and C_{24} are related to C_{11}, C_{12}, C_{13}, and C_{14}, respectively, by relationships similar to those shown in the derivation for Case 2.

5.3.2 Vehicle Displacement Responses in Fixed Barrier Impact

A vehicle in a 31 mph fixed barrier impact is modeled by m_1= 1 klb (kilo-pound), m_2 = 2 klb, k_1 = 6.28 klb/in, k_2 = 3.96 klb/in, c_1 = .076 klb-sec/in, c_2 = .056 klb-sec/in.

The characteristic equation and the four roots are shown in Eq. (5.18).

$$\begin{aligned} &s^4 + 62.1\, s^3 + 5043.2\, s^2 + 48974\, s + 1856910 = 0 \\ &\textit{Two pairs of complex conjugates are:} \\ &\textit{I.} \quad s_1 = -p_1 + iq_1, \quad s_2 = -p_1 - iq_1, \quad \textit{where} \quad p_1 = 2.86, \quad q_1 = 20.61 \\ &\textit{II.} \quad s_3 = -p_2 + iq_2, \quad s_4 = -p_2 - iq_2, \quad \textit{where} \quad p_2 = 28.21, \quad q_2 = 59.09 \end{aligned} \tag{5.18}$$

Since the roots are two pairs of complex conjugates, the procedures used to solve for Case I in Section 5.3.1 are followed. The numerical solutions are computed and shown for comparison.

$$\begin{aligned} &(I)\ \textit{For roots } s_1 \textit{ and } s_2\textit{:} \\ &\frac{C_{21}}{C_{11}} = 2.3 + .06\, i\,, \qquad \frac{C_{22}}{C_{12}} = 2.3 - .06\, i = e - f\, i \\ &\frac{A_{21}}{A_{11}} = \sqrt{e^2+f^2} = 2.3, \quad \textit{and} \quad \tan\phi_{21} = \frac{.026 + \tan\phi_{11}}{1 - .026\tan\phi_{11}} \\ &(II)\ \textit{For roots } s_3 \textit{ and } s_4\textit{:} \\ &\frac{C_{23}}{C_{13}} = -.224 - .016\, i\,, \quad \textit{and} \quad \frac{C_{24}}{C_{14}} = -.224 + .016\, i \\ &\frac{A_{22}}{A_{12}} = -.225\,, \quad \textit{and} \quad \tan\phi_{22} = \frac{.073 + \tan\phi_{12}}{1 - .073\tan\phi_{12}} \end{aligned} \tag{5.19}$$

Closed-Form Displacement Equations and Plots:

The four unknowns A_{11}, A_{12}, ϕ_{11}, and ϕ_{12} shown in Eq. (5.19) can therefore be solved using a numerical approach. The results are shown in Tables 5.2 and 5.3.

Table 5.2 Damping and Frequency Terms

k	1	2
p_k	2.87	28.21
q_k	20.61 rad/s (3.3 Hz)	59.09 rad/s (9.4 Hz)

Table 5.3 Amplitude and Phase Angle Terms

i	A_{i1}	A_{i2}	ϕ_{i1}, rad	ϕ_{i2}, rad
1	12.76	4.89	-.021	.056
2	29.37	-1.1	.005	.129

The closed-form displacement equation for mass i is shown in Eq. (5.20)

$$x_i = x_{i1} + x_{i2} = A_{i1}e^{-p_1 t}S(q_1 t+\phi_{i1}) + A_{i2}e^{-p_2 t}S(q_2 t+\phi_{i2}) \tag{5.20}$$

The transient displacement responses of the two masses and their displacement components are plotted in Fig.5.14–5.16.

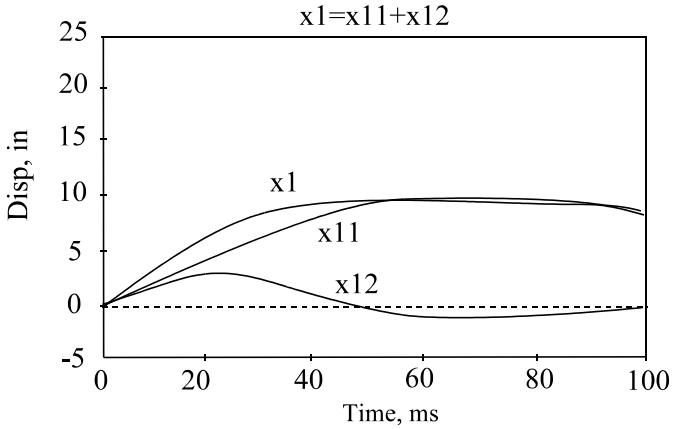

Fig. 5.14 Mass 1 Displacement Components

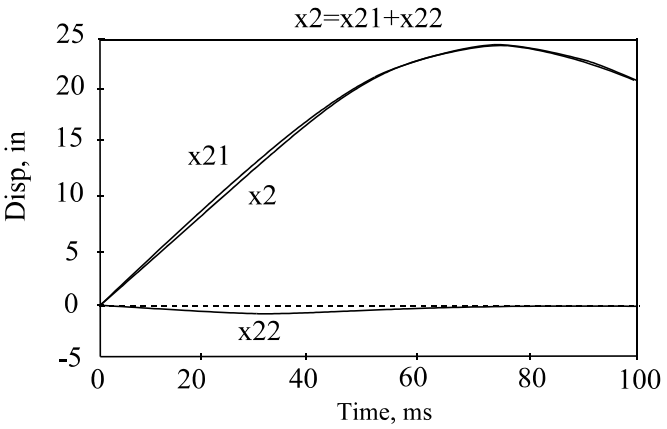

Fig. 5.15 Mass 2 Displacement Components

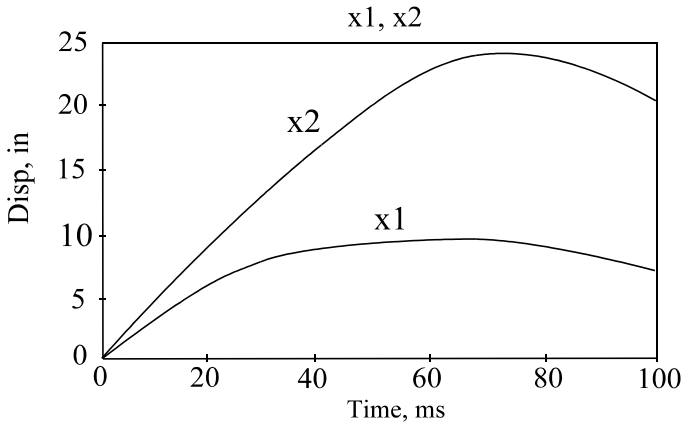

Fig. 5.16 Total Displacements of Mass 1 and Mass 2

5.3.3 Application in Pre-Program Vehicle Structural Analysis

In the early development stage of a prototype, the vehicle crush requirements, such as dynamic crush and timing, are defined. Using the derived closed-form displacement equations and a searching technique called "Imbedded Random Search" (IRS) (described in Section 5.5.1), the spring stiffness and damping coefficients in the two mass-spring-damper model can be estimated for crash analysis.

Case A: In a 31 mph fixed barrier impact, the maximum displacements of the fore-frame and aft-frame of a vehicle are specified to be 10 and 24 inches, respectively, and the corresponding timings are 50 and 60 ms. The total vehicle weight is 3 klbs with the fore-frame weighing 1 klb and the aft-frame 2 klbs. Task: Estimate the structural parameters in terms of the stiffness and damping coefficients for the two structural members.

The objective function in the imbedded random searching technique is to minimize the differences between the desired and model peak displacements and the times of these displacements.

The final model displacement equations are found to be

$$x_i = x_{i1} + x_{i2} = A_{i1}e^{-p_1 t}S(q_1 t+\phi_{i1}) + A_{i2}e^{-p_2 t}S(q_2 t+\phi_{i2}), \quad where\ i = 1,\ 2. \tag{5.21}$$

The computed amplitudes, phase angles, and damping and frequency terms are shown in Tables 5.4 and 5.5.

Table 5.4 Computed Amplitudes and Phase Angles

i	A_{i1}	A_{i2}	ϕ_{i1}, rad	ϕ_{i2}, rad
1	12.44	4.50	-.037	.104
2	28.01	-1.05	.009	.236

Table 5.5 Damping and Frequency Terms

k	1	2
p_k	2.41	23.68
q_k	21.63 rad/s (3.4 Hz)	64.14 rad/s (10.2 Hz)

Table 5.6 summarizes the input data requirements, the computed model parameters, the model displacement, and the time responses. The model displacement responses compare favorably with the input requirements although the corresponding times are slightly longer than desired (see Fig. 5.19).

Table 5.6 Input, Computed Structural Parameters, and Output

i	m_i, klb	x_i, in	t_i, ms	k_i, klb/in	c_i, klb-s/in	Model x_i, in	Model t_i, ms
1	1	10	50	6.77	.057	9.6	75
2	2	24	60	4.38	.052	23.9	67

Case B: Referring to Case A, it was decided to shorten the front end crush space by limiting the aft-frame maximum displacement to be 20 inches. The fore-frame displacement, timings, and weights are kept the same. Estimate the difference in structural parameters between Case A and Case B. Do the structural parameter differences in both cases agree with engineering judgement?

The parameters for the displacement equations of the two masses are shown in Tables 5.7 and 5.8.

Table 5.7 Computed Amplitudes and Phase Angles

i	A_{i1}	A_{i2}	ϕ_{i1}, rad	ϕ_{i2}, rad
1	11.89	3.06	-.044	.172
2	22.70	-0.85	.012	.337

Table 5.8 Damping and Frequency Terms

k	1	2
p_k	2.41	26.54
q_k	26.59 rad/s (4.2 Hz)	80.30 rad/s (12.8 Hz)

Table 5.9 summarizes the input data requirements, the computed model parameters, the model displacements, and the time responses. The model displacement responses compare favorably with these input requirements as shown in Fig. 5.17.

Table 5.9 Input Requirements, Computed Structural Parameters, and Output Responses

i	m_i, klb	x_i, in	t_i, ms	k_i, klb/in	c_i, klb-s/in	Model x_i, in	Model t_i, ms
1	1	10	50	8.91	.045	9.7	62
2	2	20	60	7.67	.070	20.0	55

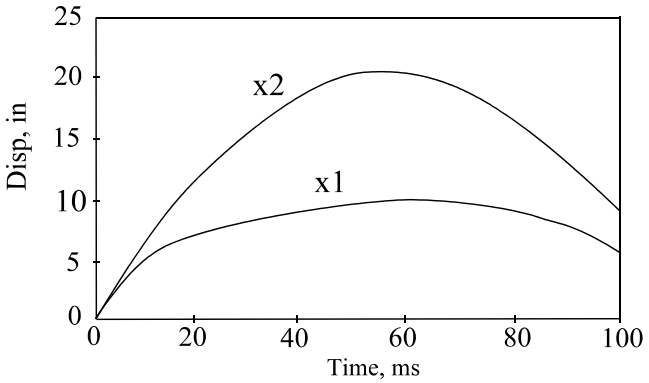

Fig. 5.17 Fore- and Aft-Frame Displacement in a Pre-Program Vehicle

The stiffnesses of the fore-frame and aft-frames in Case B are larger than those in Case A. The damping coefficients in Case B are not much different from those in Case A. In order to decrease the aft-frame crush from 24 to 20 inches, an increase of k_2 from 4.38 to 7.67 klb/in agrees with engineering judgement. In order to keep the fore-frame from crushing even more due to the stiffer aft-frame, the fore-frame stiffness, k_1, also has to be increased (from 6.77 to 8.91 klb/in). The computed structural parameters for both Cases A and B are considered to be reasonable.

5.3.4 Application in Post-Crash Structural Analysis

Given two sets of accelerometer data in a crash test, the structural parameters defining the components between the two accelerometer locations can be computed. In a frontal impact, for example, the accelerometer data can be taken from the A- and B-pillar locations. Boundary conditions, such as the maximum displacements and the corresponding times at the two locations, can be satisfied by the computed parameters.

Case C: In a 35 mph fixed barrier test, the maximum displacements of the fore-frame (at the A-pillar) and the aft-frame (Rocker at the B-Pillar) of a medium size pick-up truck are 23 and 24.6 inches, and the corresponding times are 78.4 and 75.6 ms, respectively. The total vehicle weight is 5 klbs. The fore-frame has a weight of 3 klbs and the aft-frame 2 klbs. Estimate the structural parameters in terms of the stiffness and damping coefficients for the two structural members. Note that the body mount at the A-pillar stays intact during the crash.

Using the imbedded random searching technique for this problem, one can develop a set of parameters that would satisfy the design requirements. The objective is to minimize the sum of errors due to difference between the desired and model peak displacements and the difference between the timings of these displacement.

The final model displacement equations are found and shown in Eq. (5.22).

$$x_i = A_{i1} e^{-pt} S(qt + \phi_{i1}) + C_{i3} e^{-\sigma_3 t} + C_{i4} e^{-\sigma_4 t}, \quad where \quad i=1,2$$
$$and \quad p = 5.38, \quad q = 16.08 \; rad/s \; (2.56 \; Hz)$$
$$\sigma_3 = -45.35, \quad \sigma_4 = -261.83 \tag{5.22}$$

The computed amplitudes, phase angles, and coefficients C_{i3} and C_{i4} are shown in Table 5.10.

Table 5.10 The Computed Four Unknowns A_{i1}, ϕ_{i1}, and C_{i3} and C_{i4}

i	A_{i1}	ϕ_{i1}, rad	C_{i3}	C_{i4}
1	37.65	0.0	.23	−.08
2	39.31	0.0	−.29	.11

The "optimal" k and c computed using the formulas described in Section 5.3.3 and in the IRS technique are shown in Table 5.11. To check the accuracy of the displacement equations, such as that shown in Eq. (5.16), numerical integration is used to solve the equations of motion. The displacement from the numerical integration is also shown in the table. Since displacement responses from the two methods are practically identical, the formulas described in this section are considered validated.

Table 5.11 shows the values of stiffness for the two structural members (sections). Since the relative displacement between the A- and B-pillars is only 1.6 inches (= 24.6 − 23), the structure in between which consists of frame section and floor pan should be fairly stiff. This is evidenced from the fact that k_2 is very large, as shown in the table.

Table 5.11 Input Data, Computed Structural Parameters, and Output Responses

i	m_i, klb	x_i, in	t_i, ms	k_i, klb/in	c_i, klb-s/in	Numerical EOM x_i @ t_i	Formula x_i @ t_i
1	3	23	78.4	3.78	.142	23.3 @ 78	23.5 @ 78
2	2	24.6	75.6	36.28	.931	24.4 @ 77	24.6 @ 77

In addition to the stiffness, the damping coefficient for section 2 is also very large compared to that of section 1. This is because there are body mounts located at the A-pillar between the body panel and the frame. The body mount, shown in Fig. 3.26 of Chapter 3, consists of Butyl, a man-made rubber with high damping.

In the next section, a set of closed-form formulas is developed for the undamped natural frequencies of the two mass-spring-damper model. The natural frequencies of the two masses computed in the current section are then checked for accuracy.

5.4 NATURAL FREQUENCIES IN TWO–MASS SYSTEM

A two mass-spring-damper system, as shown in Fig. 5.13, has two modes of vibration with two undamped natural frequencies. The motion of each mass is the superposition of the two modes of vibration. When one of the masses in the system resonates due to a change in excitation condition, it vibrates strongly about its own natural frequency.

In a vehicle-to-rigid object impact, the structural response is higher and impact duration is longer than those in a soft impact such as vehicle offset or side impact. In soft impact, the main component

is characterized by a lower response magnitude with a lower natural frequency. In a given impact mode, such as a truck in a rigid barrier test, the frame response exhibits higher frequency content than the body as shown in Fig. 2.44 of Section 2.4.6.1.

To further investigate the intrinsic parametric relationships in the two-mass system, the natural frequency relationship used in the vehicle suspension and handling dynamics [5] is utilized. In this vehicle dynamic study, components, such as an unsprung mass (control arm and suspension) or a sprung mass (vehicle chassis), are evaluated for ride comfort in terms of their natural frequencies.

If the two-mass model (shown in Fig. 5.13) were placed in an upright position with m_1 representing the mass of the tire at the bottom, and the sprung mass, m_2 representing the vehicle body, on the top, k_1 would represent the tire spring rate and k_2 the suspension compliance.

5.4.1 Formulas for the Natural Frequencies

Formulas (1) and (2) of Eq. 5.23 show the natural frequencies of mass 1 and mass 2 in a 2 mass-spring-damper system, respectively [5]. The formulas are expressed in terms of x, a dynamic coupling factor which is a function of mass ratio and stiffness ratios of the two-mass system.

Natural frequencies for m_1 and m_2 are f_1 and f_2, respectively:

$$f_1 = \frac{1}{2\pi}\sqrt{\frac{k_1 + \dfrac{k_2}{1-x}}{w_1}\,g} \quad \ldots\ldots\ldots\ldots\ldots\ldots \quad (1)$$

$$f_2 = \frac{1}{2\pi}\sqrt{\frac{k_e}{w_2}\,g} \quad \ldots\ldots\ldots\ldots\ldots\ldots\ldots\ldots \quad (2) \qquad (5.23)$$

$$\text{where} \quad k_e = \frac{k_2 k_1 (1-x)}{k_2 + k_1 (1-x)} \quad \ldots\ldots\ldots\ldots\ldots \quad (3)$$

x is the solution to the following:

$$\frac{k_2}{x} = \frac{m_2}{m_1}\left(k_1 + \frac{k_2}{1-x}\right) \quad \ldots\ldots\ldots\ldots\ldots\ldots \quad (4)$$

where x: *a dynamic coupling factor*

Formula (4) can be rearranged such that x is expressed in terms of the mass ratio and stiffness ratio, as shown by formula (6) of Eq. (5.24).

$$\text{Define} \quad r_m = \frac{m_1}{m_2} \quad \text{and} \quad r_k = \frac{k_1}{k_2} \quad \ldots\ldots\ldots \quad (5)$$

Rearranging the equation for x:

$$\frac{k_2}{x} = \frac{m_2}{m_1}\left(k_1 + \frac{k_2}{1-x}\right) \qquad (5.24)$$

$$\text{then} \quad r_k x^2 - (1 + r_m + r_k)\,x + r_m = 0,$$

since $0 \le x \le 1$, *choose one of the two roots*:

$$x = \frac{(1 + r_m + r_k) - \sqrt{(1 + r_m + r_k)^2 - 4 r_m r_k}}{2 r_k} \quad \ldots\ldots\ldots \quad (6)$$

Fig. 5.18 shows a 3-D plot of the dynamic coupling factor in terms of mass ratio and stiffness ratio. As the mass of the coupling mass, m_1, increases, the mass ratio ($R_m=m_1/m_2$) increases; therefore, dynamic coupling factor increases. When the coupling mass decreases to zero, the dynamic coupling factor becomes zero.

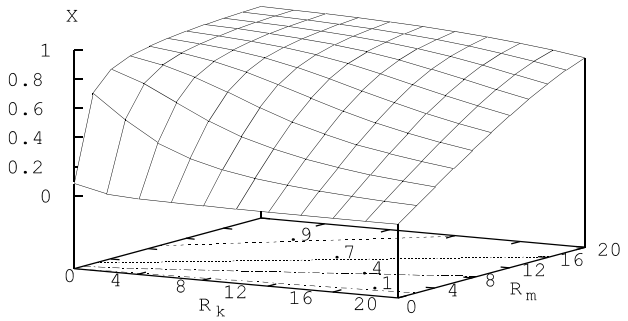

Fig. 5.18 A 3-D Plot of Dynamic Coupling Factor

5.4.1.1 *Decoupling of a Two-Mass System*

Case Study (Exercise): For the following two special cases, the two masses in the two-mass system shown in Fig. 5.13 are decoupled and degenerated into an effective mass system. (1) Sketch the effective mass diagram and express the natural frequency, (2) Compare the natural frequency with that from (6) of Eq. (5.24) for each of the two cases.

Case 1: Mass 1 is a point mass with $m_1 = 0$, and $r_m = 0$.

From (3) of Eq. (5.23), x = 0., and the effective spring rate, $k_e = k_1 k_2 /(k_1 + k_2)$. The natural frequency of mass 2, shown by (2) of Eq. (5.23), is due to mass 2 and the two springs in series.

Case 2: Mass 2 is infinite, then $m_2 = \infty$, $r_m = 0$, and x = 0.

The natural frequency of mass 1, shown by (1) of Eq. (5.23), is due to mass 1 and the two springs in parallel. The two springs, k_1 and k_2, are connected by the suspended mass m_1 and the ground (the fixed rigid barrier).

Solution Steps: Given the mass and stiffness ratios of the two mass system, the value of x can be determined from (6) of Eq. (5.24). The natural frequencies of masses m_1 and m_2 can then be computed using (1) and (2) of Eq. (5.23).

5.4.2 Natural Frequency Ratio and Stiffness Computation

Given an impact test result, the natural frequency of each of the two masses can be determined from the deceleration and relative displacement data; the natural frequency ratio can also be determined. In addition, if the mass ratio is also given, the stiffness of each of the two spring elements can also be computed.

To define the frequency ratio in terms of x, r_k, and r_m, the frequency expression for f_1 in (7) is divided by that in (8) of Eq. (5.25) and rearranged, as shown in (9) of Eq. (5.25).

Deriving the natural frequency ratio, $r_f = \dfrac{f_1}{f_2}$, *where*

$$f_1 = \frac{1}{2\pi}\sqrt{\frac{k_1}{m_1}\left[1 + \frac{1}{r_k(1-x)}\right]} \quad \ldots\ldots \quad (7)$$

$$f_2 = \frac{1}{2\pi}\sqrt{\frac{k_2}{m_2}\left[\frac{r_k(1-x)}{1 + r_k(1-x)}\right]} \quad \ldots\ldots \quad (8) \qquad (5.25)$$

dividing (7) *by* (8), *it becomes*

$$\frac{f_1}{f_2} = \sqrt{\frac{r_k}{r_m}\left[\frac{1 + r_k(1-x)}{r_k(1-x)}\right]} \quad \ldots\ldots \quad (9)$$

5.4.3 Add-On or Splitting of a Spring-Mass Model

A simple spring-mass model in an impact yields a sinusoidal response. Such a model is useful in modeling a vehicle compartment response in a fixed barrier impact. However, it may not be suitable for modeling non-perpendicular barrier crashes such as vehicle pole (or tree) and offset tests. In these softer crashes, the crash pulse looks more like a haversine, having a softer pulse in the beginning followed by a stiffer pulse.

By doubling or splitting a spring-mass model, the output responses become the superposition of two modes of vibrations. There exist two natural frequencies in the new system: one is larger and the other is smaller than the original natural frequency of the simple spring mass model. The mass with the smaller natural frequency has a longer crash duration and a pulse shape of haversine.

5.4.3.1 *Doubled-Up of a Spring-Mass Model*

A single spring-mass system with m and k has a natural frequency f, of 1Hz, as shown in Fig. 5.19(a). Assume an additional (identical) set is added in series to the first one, as shown in Fig. 5.19 (b). We propose to find the natural frequency of each of the two masses in the doubled spring-mass system.

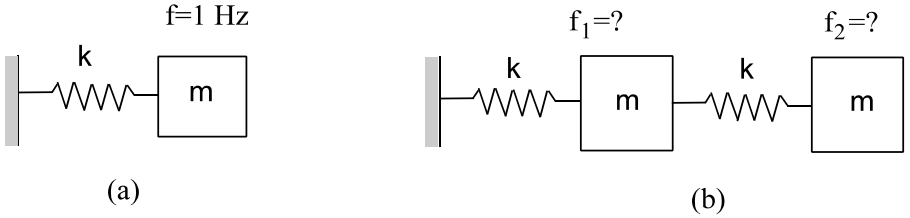

Fig. 5.19 Natural Frequencies of a Double-Up Spring-Mass System

The mass ratio and stiffness ratio are equal to one. The computation of the coupling factor x and the two natural frequencies in the two-mass system are shown in Eq. (5.26). The natural frequency of the inner mass, m_1, becomes higher and equals 1.62 Hz; while that of outer mass, m_2, becomes lower and equals 0.62 Hz.

Since $r_m = 1$, *and* $r_k = 1$, *then*

$$x = \frac{(1 + r_m + r_k) - \sqrt{(1 + r_m + r_k)^2 - 4 r_m r_K}}{2 r_k} = \frac{3 - \sqrt{9 - 4}}{2} = 0.382$$

For system 1 (k_1 *and* m_1) *alone*:

$$\because \quad f_1' = \frac{1}{2\pi}\sqrt{\frac{k_1}{m_1}} = 1\,Hz, \quad \therefore \quad \frac{k_1}{m_1} = (2\pi)^2$$

Substituting into (7) *of Eq.*(5.25): (5.26)

$$f_1 = \sqrt{1 + \frac{1}{r_k(1 - x)}} = \sqrt{1 + \frac{1}{1\,(1 - .382)}} = 1.62\ Hz$$

Similarly, for system 2 (k_2 *and* m_2) *alone*:

$f_2' = 1$ *Hz, from* (8) *of Eq.*(5.25):

$$f_2 = \sqrt{\frac{r_k(1 - x)}{1 + r_k(1 - x)}} = \sqrt{\frac{.618}{1 + .618}} = 0.62\ Hz$$

5.4.3.2 *Splitting of a Spring-Mass Model*

In the simple spring-mass model shown in Fig. 5.20(a), assume the whole mass is split into two masses, and the spring is resized to have a different stiffness, as shown in Fig. 5.20. Combination (b) has k and m/3 as the first subsystem, and k and 2m/3 as the second connected in series; combination (c) has k/2 and m/2 as the first and second subsystems; and combination (d) has 2k and m/2 as the first and second subsystems. What are the two natural frequencies of the two masses in each of the three combinations? [Ans: (b) $f_1 = 2.62$ Hz, $f_2 = .81$ Hz, (c) $f_1 = 1.62$ Hz, $f_2 = .62$ Hz, and (d) $f_1 = 3.24$ Hz, $f_2 = 1.24$ Hz]

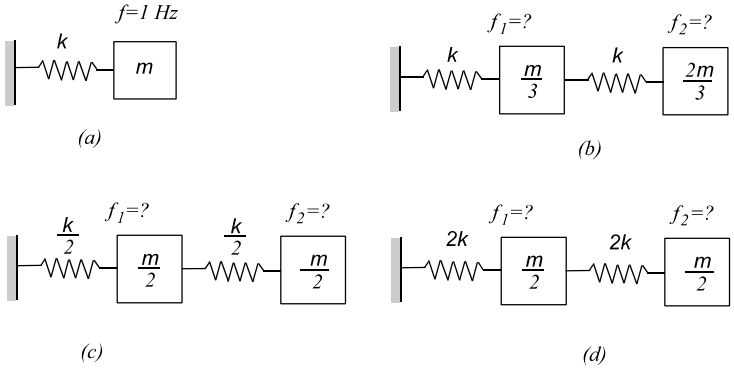

Fig. 5.20 Natural Frequencies of a Split Spring-Mass System

In Case A of Section 5.3.3, the mass and stiffness input data shown in Table 5.9 have the following ratios: $r_m = w_1/w_2 = ½ = .5$ and $r_k = k_1/k_2 = 6.77/4.38 = 1.55$. From Eq. (5.24), the dynamic coupling factor x is computed and is equal to .181. Using Eq. (5.25) for the two-mass system, the natural frequencies are found to be equal to 3.46 and 10.89 Hz. Compared with the values of 3.4 and 10.2 Hz in Table 5.6, obtained from the two mass-spring-damper model computation in Section 5.3.3, the two approaches agree fairly well. Table 5.12 summarizes the input data and the natural frequencies computed by different methods.

Table 5.12 Input, Computed Structural Parameters and Output of 2-Mass System

i	m_i, klb	x_i, in	t_i, ms	k_i, klb/in	c_i, klb-s/in	Table 5.5, q_i, rad/sec (**Hz**)	Eq. (5.25), f_i, **Hz**
1	1	10	50	6.77	.057	21.6 (**3.4**)	**3.46**
2	2	24	60	4.38	.052	64.1 (**10.2**)	**10.89**

The CRUSH II model is set up to simulate the rigid barrier impact of the two-mass system with the input data shown in Table 5.12. The rigid barrier impact velocity is 31 mph. The transient displacement responses up to 1000 ms for the frame (#1) and the body (#2) are shown in Fig. 5.21. This numerical approach using CRUSH II to simulate the multiple-mass impact is also used to confirm the accuracy of the closed-form solutions for the two-mass system derived in Section 5.3.

In the model where both masses are moving toward the barrier at 31 mph (to the left shown in Fig. 5.13), the frequencies of displacement responses for both masses are about the same, around 3.4 Hz (3.4 cycles/1000 ms). This is evident from Tables 5.4 and 5.5 where the large amplitude (A_{i1}) and low damping (p_1) of the first mode of vibration dominate the responses of the two masses. The frequency of the first mode of vibration is 3.4 Hz, which is the natural frequency of mass #2.

In order to have mass #1 vibrate at its own natural frequency, a different impact condition would have to be imposed. Assuming that the initial velocity of mass #1 is 31 mph to the right (for the purpose of creating frame resonance at higher frequency) and that of mass #2 is 31 mph to the left, the response frequencies of both masses, shown in Fig. 5.22, are at their own natural frequencies, 3.4 Hz for mass #2 and 10.8 Hz for mass #1. These two natural frequencies agree with those computed and shown in Table 5.5.

Case Study (Exercise): Using the data shown in Table 5.12 for a two-mass system and formula (9) of Eq. (5.25), compute the natural frequency ratio of the system. How is the ratio compared with those obtained from Table 5.5 and CRUSH II?

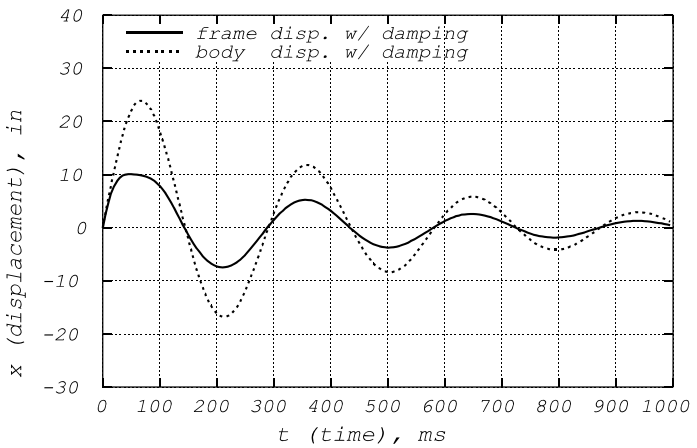

Fig. 5.21 Truck Model Responses Dominated by 1st Mode of Vibration

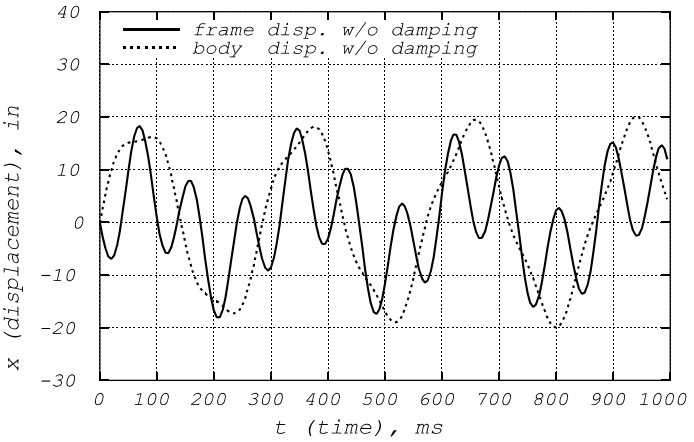

Fig. 5.22 Truck Model Responses Dominated by 2nd Mode of Vibration

5.5 NUMERICAL SEARCHING TECHNIQUES

Techniques used in searching for an optimal solution which satisfies an objective function are briefly presented. These are used to obtain the "best" responses of a dynamic model. The techniques include imbedded random searching (IRS) [6] and the Newton-Raphson algorithm.

5.5.1 Imbedded Random Search (IRS)

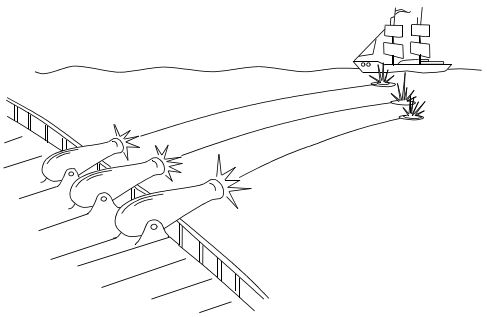

Fig. 5.23 Firing Cannons to a Target

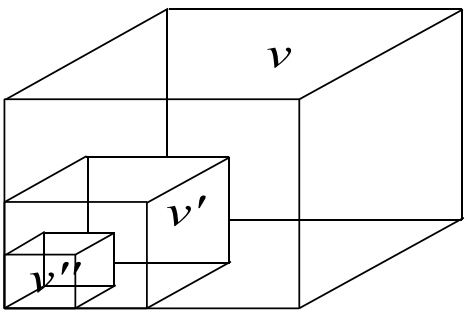

Fig. 5.24 Imbedded Random Search

Just like firing cannons at a target ship, shown in Fig. 5.23, random number searching technique is a probability event. After n number of drawings (events), the probability, P, of having at least one event being on the target (zone v', in the first trial shown in Fig 5.24, is called the optimal zone) is

$$P = 1 - (1-a)^n \qquad \text{where} \quad a = \frac{v'}{v} \tag{5.27}$$

where a: probability of hitting the target v' in the design space V or a volume ratio
n: number of random drawings (shootings) in the design space

Rearranging the equation for P, and taking natural logarithms on both sides of the equation, it becomes

$$\ln(1-P) = n\ln(1-a) \quad or \quad n = \frac{\ln(1-p)}{\ln(1-a)} \tag{5.28}$$

Example: For a confidence level of 99%, and a volume ratio of .1, P = .99, and a = .1, then

$$n = \frac{\ln(1-.99)}{\ln(1-.1)} = \frac{-4.6052}{-1.054} = 44 \tag{5.29}$$

Note that if the design space V is a 3-dimensional unit cube (with 3 design variables) where the volume is equal to one, the resolution of each side of the target cube can be computed as follows

$$a = \frac{v'}{V} = \frac{s'^3}{S^3} = .1 \tag{5.30}$$

where s' and S are the length of each side of cube v' and V, respectively. Since S = 1 for the original unit cube, then

$$s' = a^{\frac{1}{3}} = (.1)^{\frac{1}{3}} = .464 \tag{5.31}$$

The above computation is for the first pass of the searching process. If the same process is repeated, then after N passes, the final confidence level becomes P_{final} shown in Eq. (5.32).

$$\begin{aligned} &P_{final} = P^N \qquad and \quad v'_{final} = a^N V \\ &s'_{final} = (a^N)^{1/3} S = (a^N)^{1/3} \end{aligned} \tag{5.32}$$

In this parametric optimization problem, there are three design variables (the design variable space is a cube). Given the volume ratio, a = .1, and the confidence level, P = .99 in each pass, from Eq. (5.29), the number of random searching runs in one pass equals 44.

The total number of trials after three passes is equal to 3 × 44 = 132 with a 97% confidence level that the solution is in the optimal zone and the resolution of the final design variable is one tenth of the design range of the original variable. If an exhaustive search (a brute force approach) had been used, it would have taken 10 × 10 ×10 = 1000 trials to get to the same variable resolution but with 100% confidence.

$$\begin{aligned} &In\ each\ pass:\ a = .1, \quad P=.99, \quad then \quad n = 44 \\ &For \quad N\ (no.\ of\ passes) = 3,\ then \\ &P_{final} = P^N = (.99)^3 = .97, \quad S'_{final} = (a^3)^{\frac{1}{3}} = a = .1 \end{aligned} \tag{5.33}$$

The above random searching technique can also be applied to a design space other than a cube with three design variables. For a design space of d-dimension (with d variables), the resolution of each variable after each pass is then

$$a = \frac{v'}{V} = \frac{s'^d}{S^d}, \quad or \quad s' = a^{1/d} S \tag{5.34}$$

and the final resolution of each variable is

$$s'_{final} = (a^N)^{1/d} S = (a^N)^{1/d} \tag{5.35}$$

where d: number of design variables in space (or d-dimensional hypercube).

5.5.2 Newton-Raphson Search Algorithm

The solution of F, F*, which satisfies a function f(F) = 0 can be obtained by a method using the Newton-Raphson algorithm described in Eq. (5.36) and shown in Fig. 5.25. The slope of the curve at point F_i is f '(F_i). F_i is the value of the independent variable at iteration i. The iteration process continues until F_i and F_{i+1} converge to the solution of the function in which f(F_{i+1}) approaches zero. The error function ϵ shown in Eq. (5.37) can also be used to check for the numerical convergence.

$$f' = \frac{f(F_i) - f(F_{i+1})}{F_i - F_{i+1}} \quad \text{. . . . . (1)}$$

$$\text{let } f(F_{i+1}) = 0., \quad \text{then } F_{i+1} = F_i - \frac{f(F_i)}{f'} \quad \text{. . . . (2)} \tag{5.36}$$

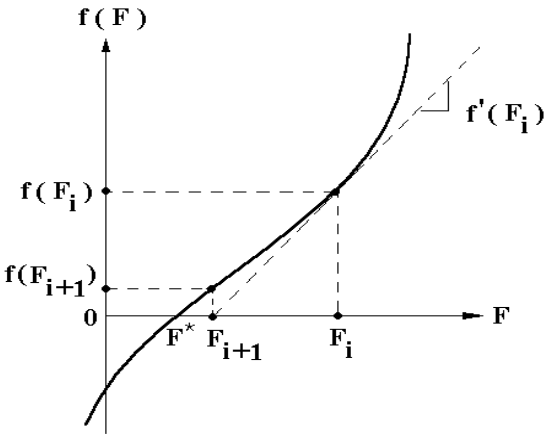

Fig. 5.25 Newton-Raphson Iterative Method

$$\varepsilon = |(F_{i+1} - F_i)| / F_i \le 0.001 \quad \text{. . . . . (3)} \tag{5.37}$$

Note that the computation of F* usually takes no more than three iterations if the relative error, ϵ, is set at 0.001. The algorithm converges rapidly during the loading phase simulation, and the initial value of F_i at any given time step should be the F* from the previous time step.

5.6 LOADING AND UNLOADING SIMULATION

Fig. 5.26 shows the loading and unloading curves for the struck (#1) and striking (#2) vehicles. The loading phase is defined by a power curve, $F=kD^n$, and the unloading by a constant slope. In the dynamic simulation during the loading phase, an efficient numerical technique using the Newton-Raphson method is used to compute the individual deflections of the two non-linear springs (EA), and during the unloading phase, the relative deformations of the two EA′s and the corresponding unloading force are explicitly computed.

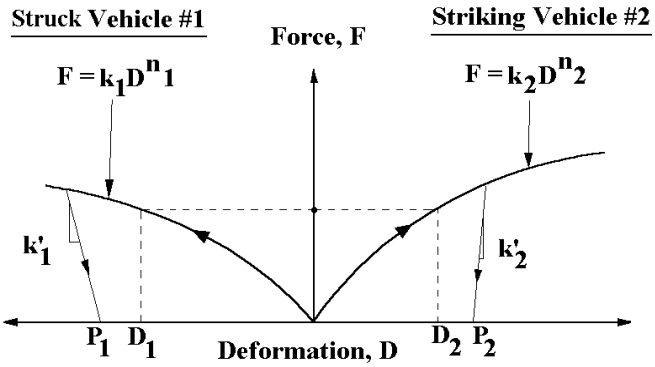

Fig. 5.26 Loading and Unloading Phases of Two Vehicles

5.6.1 Loading Phase Simulation

In general, there are two non-linear springs involved in the force-deflection computation. An interactive scheme using the Newton-Raphson algorithm is used. This is described as follows.

Given a total deflection of the two springs obtained from the numerical integration at each time step, the method computes the force and individual deflection, as shown in Eq. (5.38).

$$
\begin{aligned}
&\textit{Given: } D_t \ (\textit{Total deformation} = D_1 + D_2), \quad k_i,\ n_i,\ i = 1,\ 2 \\
&\textit{Find: } \quad F,\ D_1,\ \textit{and}\ D_2 \\
&\textit{Let } \alpha = \frac{1}{n_1}\ ,\ \beta = \frac{1}{n_2}\ ,\ \textit{then:} \\
&D_t = D_1 + D_2 = \left(\frac{F}{k_1}\right)^{\alpha} + \left(\frac{F}{k_2}\right)^{\beta} \quad \ldots\ldots\ldots\ldots \quad (1) \\
&\textit{To solve for } F \textit{ which satisfies relationship } (1), \\
&\textit{Let } \quad f = \left(\frac{F}{k_1}\right)^{\alpha} + \left(\frac{F}{k_2}\right)^{\beta} - D_t = 0 \quad \ldots\ldots\ldots\ldots \quad (2) \\
&\textit{Hence: } \quad f' = \frac{df}{dF} = \alpha\frac{F^{\alpha-1}}{k_1^{\alpha}} + \beta\frac{F^{\beta-1}}{k_2^{\beta}} \quad \ldots\ldots\ldots \quad (3)
\end{aligned}
\tag{5.38}
$$

The solution of F, F*, which satisfies (2) of Eq. (5.38) can be obtained by applying the Newton-Raphson algorithm.

5.6.2 Unloading Phase Simulation

The initial conditions of the unloading phase simulation are the final conditions of the loading phase simulation. The force and the individual deflections of the two springs depend on the total deflection and unloading stiffnesses of the two springs. The method to execute the unloading phase simulation is described in Fig. 5.27 and Eq. (5.39).

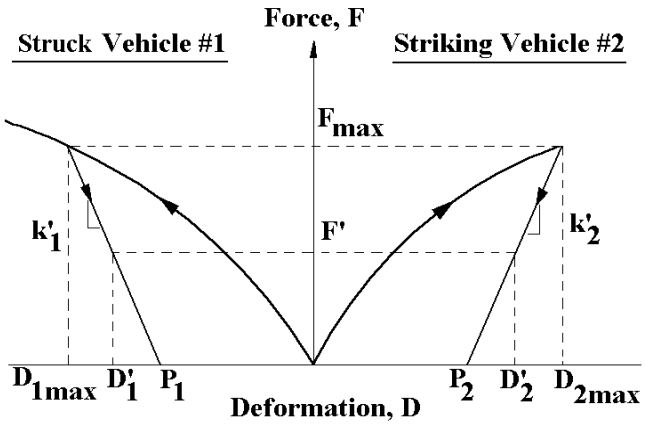

Fig. 5.27 Force-Deflection Computation in the Unloading Phase

F_{max} : *Maximum force developed in the loading phase*
D_{imax} : *Maximum deflection of the non-linear spring i*
k_1', k_2' : *Unloading stiffness of the two springs*
F' : *Unloading force*
D_1', D_2' : *Individual unloading deflections of the two springs*
P_1, P_2 : *Permanent deformations of the two springs*

$$\begin{aligned}
&\textit{Since } k_i' = F_{max}/(D_{imax} - P_i), \textit{ and} \\
&\qquad P_i = D_{imax} - F_{max}/k_i' \\
&\textit{Given: } D_t \textit{ (Total deformation } = D_1' + D_2'), \quad k_i', \; i = 1, 2 \\
&\textit{Find: } \quad F', D_1', \textit{ and } D_2' \textit{ (three unknowns).} \\
&\textit{Three equations are:} \\
&\quad (D_1' - P_1)k_1' = F', \\
&\quad (D_2' - P_2)k_2 = F', \quad \textit{and} \\
&\quad D_1' + D_2' = D_t \\
&\textit{and the solutions are:} \\
&\quad D_2' = [k_1'/(k_1' + k_2')][(k_2'/k_1')P_2 - P_1 + D_t], \\
&\quad D_1' = D_t - D_2' \\
&\quad F' = (D_1' - P_1)k_1'
\end{aligned} \tag{5.39}$$

5.6.3 Model with Power Curve Loading and Unloading

Fig. 5.28 shows the general loading, reloading, and unloading power curves. The start-loading point is at x_i, the start-unloading point is at point U, and the reloading-point is at point x_r. Unloading starts at the end of loading. The unloading power curve is defined by the two parameters k′ and n′. Given the specified hysteresis energy, E_h, and permanent deformation, x_p, the two unloading parameters are derived in closed-form and shown in Eq. (5.40). It is also shown that under the specified loading and unloading conditions, the unloading power n′ is always greater than the loading power n.

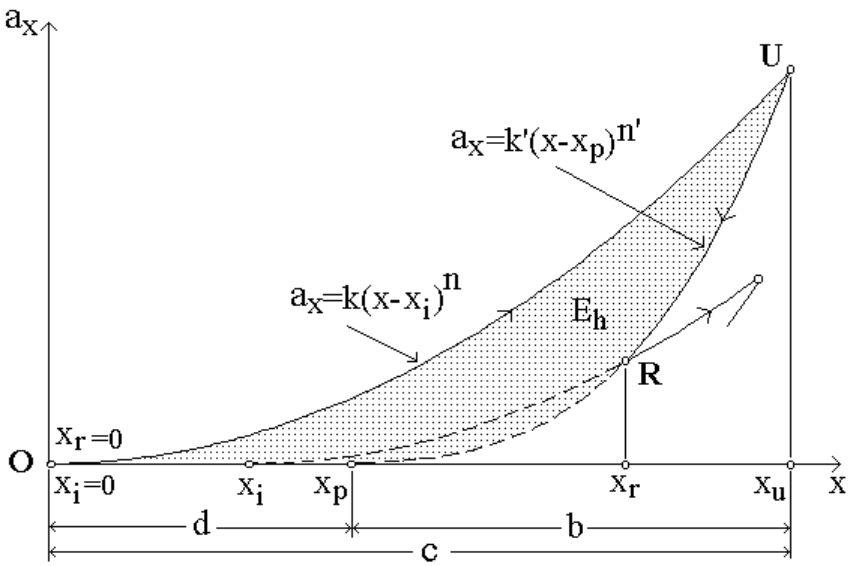

Fig. 5.28 Parametric Relationships in Loading/Unloading Cycles

Variable Definitions in the Loading and Unloading Cycles

Loading: $a_x = k(x-x_i)^n$

Unloading: $a_x = k'(x-x_p)^{n'}$, where

a_x : acceleration function at x
x :displacement or velocity for spring damper
x_i : x location of starting loading or reloading cycle
x_p : x location of permanent deformation or deformation rate

At the point of unloading, U,
a_{max} (loading) = a'_{max} (unloading),
Let E_h be the hysteresis energy in the loading/unloading cycle; then
$E_h = E_L$ (loading energy) – E_u (unloading energy).

$$E_L = \int_{x_i}^{x_u} a\,dx = \int_{x_i}^{x_u} k(x-x_i)^n dx = \frac{k}{n+1}(x-x_i)^{n+1}\Big|_{x_i}^{x_u} = \frac{k}{n+1}c^{n+1}$$

$$\text{Similarly, } E_u = \int_{x_p}^{x_u} a'dx = \int_{x_p}^{x_u} k'(x-x_p)^{n'}dx = \frac{k'}{n'+1}b^{n'+1}$$

$$\text{where } c = x_u - x_i, \quad b = x_u - x_p = (x_u - x_i) - (x_p - x_i) = c - d$$

$$\text{Define } p(\text{permanent deformation/rate factor}) = \frac{d}{c} \quad \ldots\ldots\ldots \quad (1)$$

$$\text{and } h(\text{hysteresis energy factor}) = \frac{E_h}{E_L},$$

$$\text{then } h = 1 - \frac{E_u}{E_L} = 1 - \frac{k'(n+1)b^{n'+1}}{k(n'+1)c^{n+1}} \quad \ldots\ldots\ldots\ldots\ldots\ldots \quad (2) \qquad (5.40)$$

$$\text{thus, at point } u\text{: } kc^n = k'b^{n'}, \ \therefore\ kc^n b = k'b^{n'+1}, \ \text{then}$$

$$\frac{k'b^{n'+1}}{kc^{n+1}} = \frac{kc^n b}{kc^{n+1}} = \frac{b}{c} = \frac{c-d}{c} = 1-p$$

$$\text{Substituting into (1), and it becomes}$$

$$h = 1\,\frac{n+1}{n'+1}(1-p) \quad \ldots\ldots\ldots\ldots\ldots\ldots\ldots\ldots \quad (3)$$

$$\text{Special Case: For a perfectly elastic component, } x_p = x_i, \text{ then}$$

$$p = \frac{d}{c} = \frac{x_p - x_i}{c} = 0, \quad \text{and} \quad h = 1 - \frac{n+1}{n'+1}(1-0) = \frac{n'-n}{n'+1},$$

$$\text{Now, since } h \geq 0, \quad n' \geq n$$

Reloading starts at the end of unloading. During reloading, the system may unload at any moment. The unloading curve is not only a function of k′ and n′, it is also a function of x_i, the x location of starting loading or reloading cycle, as shown in Fig. 5.28.

5.6.3.1 *Unloading Parameters k', n', and x_i in Reloading Cycle*

The derivation of the unloading parameters are described in Eq. (5.41).

$$\text{I. Given: } p \text{ and } h \text{ factors, and loading parameters } k \text{ and } n,$$
$$\text{Find: unloading parameters, } k' \text{ and } n'$$

$$\text{Since at point of unloading, } kc^n = k'b^{n'}, \quad k' = \frac{c^n}{b^{n'}}k \quad \ldots\ldots \quad (4)$$

$$\text{Since } h = 1 - \frac{n+1}{n'+1}(1-p), \quad n' = \frac{1-p}{1-h}(1+n) - 1 \quad \ldots\ldots\ldots\ldots \quad (5)$$

$$\text{II. Given: reloading point } (x_r, a_r), \text{ loading parameters } k \text{ and } n, \qquad (5.41)$$
$$\text{Find : expression of } x_i$$

$$\text{At } x_i = 0, \ a_x = 0; \ \text{at } x_r \text{ reloading point, } a_r = k(x_r - x_i)^n,$$

$$\text{therefore, } x_i = x_r - \left(\frac{a_r}{k}\right)^{\frac{1}{n}} \quad \ldots\ldots\ldots\ldots\ldots\ldots\ldots\ldots \quad (6)$$

For a spring-damper model with power curve loading and unloading characteristics, the numerical simulation follows the flow charts shown in Table 5.13. There are two flow charts. The one on the top shows the numerical integration procedures. The one on the bottom computes the deceleration (force) due to loading or unloading by the spring and damper.

Table 5.13 Power Curve Loading and Unloading Flow Chart

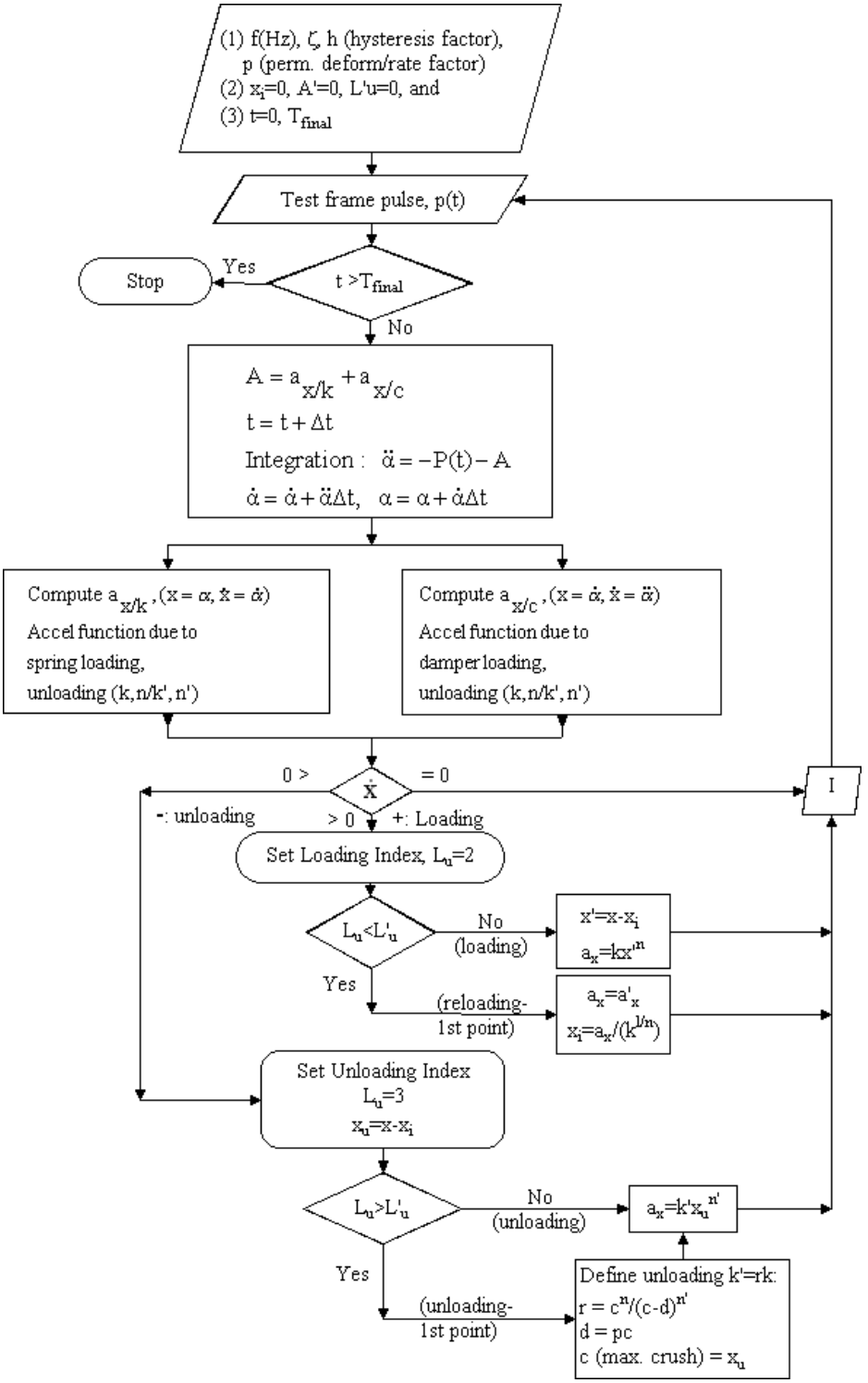

A Kelvin model with non-linear stiffness and damping is used to simulate the dynamic characteristics of a body mount on a frame vehicle. The frame pulse from a truck-to-a-fixed-barrier test at 35 mph is used to excite the model. The predicted model body (output) pulse is then compared with the body accelerometer data from the test. By optimizing the stiffness and damping, a 'best' model is then found, where the output pulse matches that from the test. Fig. 5.29 compares the test body crash pulse with that from the optimized models with and without damping. It is clearly shown that a model without damping is not adequate to simulate the impulsive response which occurs in the early part of the body crash pulse. The body impulsive response is the result of the frame impulsive loading being transmitted by the body mount.

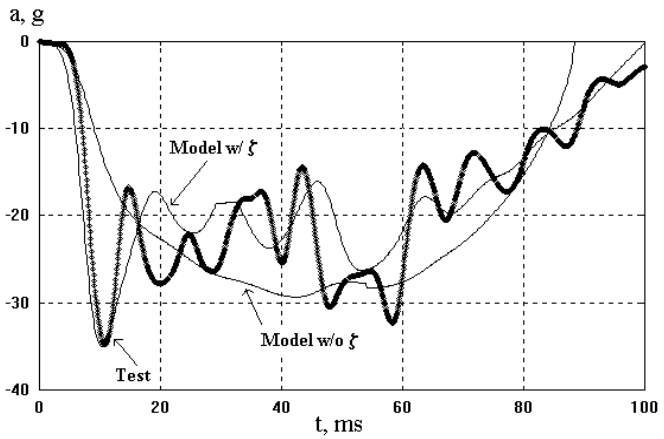

Fig. 5.29 Test Body and Optimal Model Responses w/ and w/o Damping in a 35 mph Test

5.6.3.2 *Deceleration Contributions of Spring and Damper*

To further analyze the contribution of the spring and damper to the overall model body response, the deceleration contributions of the spring and damper are denoted as a_k and a_c, respectively. Since a_k is controlled by the deflection and a_c by the deflection rate, both the transient deflection, Δd, and the deflection rate, Δv, are shown in Fig. 5.30. It is clearly shown that the first peak of the body pulse is dominated by a_c, which is controlled by Δv. Note that the first damper unloading occurs very early, at around 10 ms, when Δv decreases after reaching the peak. Subsequent re-loading occurs when Δv increases at around 20 ms.

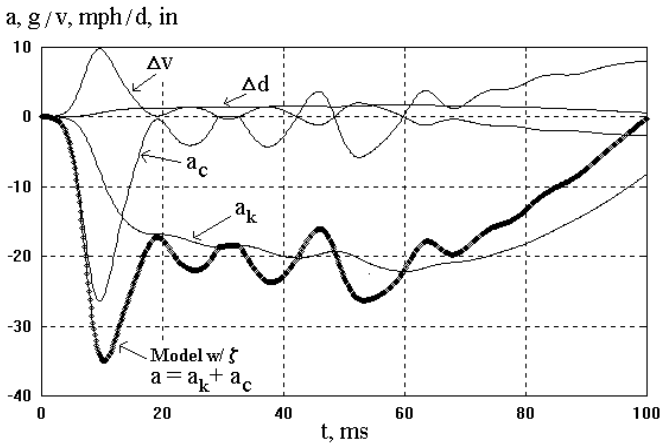

Fig. 5.30 Spring and Damper Contributions in Model Body Response.

Note that loading occurs while Δv is increasing, until it starts decreasing. At 10 ms, Δv reaches a maximum velocity of 10 mph, which is the end of the damper loading. Damper unloading lasts till about 19 ms, then reloading starts. Since Δv keeps decreasing, contribution of damper to the output acceleration becomes minimal. However, in the steady state period after the transient response, the spring contributes more than the damper to the output deceleration, a, due to the ever-increasing deflection.

Fig. 5.31shows the test frame pulse of another 35 mph truck to barrier test which is the input excitation to the Kelvin model for the body mount. The magnitude of the test frame impulsive loading is about 138 g, and that of the test and model body impulsive response is about 53 g. The output response of the power curve model matches quite well the test responses in both the transient and steady state domains, as shown by the body test and model curves in Fig. 5.31.

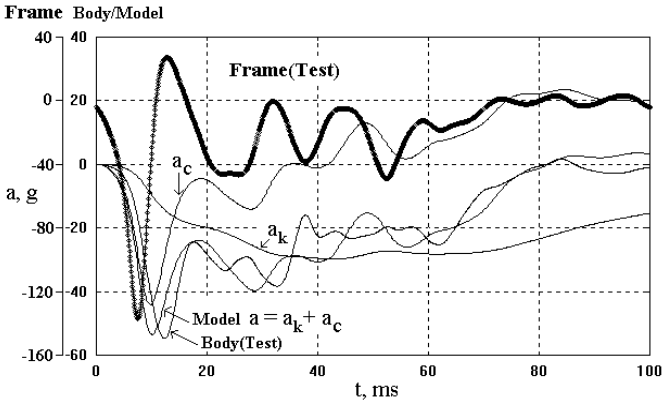

Fig. 5.31 Body Responses for the Truck Test and Power-Curve Model

5.7 A LUMPED-PARAMETER MODEL — CRUSH II

A system can be modeled by a lumped mass model with an infinite number of natural frequencies. The motion of a system can be studied by the summation of many subsystems with different natural frequencies. These subsystems, which generate the high frequency noise, can be excluded from system modeling.

CRUSH II (Crash Reconstruction Using Static History) is a one-dimensional mathematical model used to simulate the impact dynamics of objects or masses connected by springs and dampers. Since it uses connecting masses, it is frequently referred to as a lumped-mass model (or lumped-parameter model), and the spring and dampers are referred to as energy absorbers (EA). The original version of the software was developed under a contract with the U.S. Department of Transportation [1]. It was used to perform a computer simulation of collinear car-to-car and car-to-barrier collisions.

5.7.1 Simple Structure Force-Deflection Table

The operation of CRUSH II requires the use of quasi-static force-deflection data. In a component test laboratory, a testing device called Crusher can be used to generate the quasi-static force-deflection data. The components to be crushed are placed between the reaction fixtures and load plates. As the ram is extended, generally in steps of 0.3 inches, force measurements are recorded.

In the elastic range, stiffness (K) is the slope of the force-deflection curve. K is equal to AE/L, as shown in the load vs. elongation plot of Fig. 5.32. E is Young's Modulus, the slope of the stress-strain curve in Fig. 5.32; A, the cross sectional area; and L, the length of the material.

The stress-strain curves of ductile and brittle materials are shown in Figs 5.33 and 5.34, respectively. In contrast to ductile materials, the brittle materials do not have a yield point on its stress-strain curve. The last point on the curve is the fracture point.

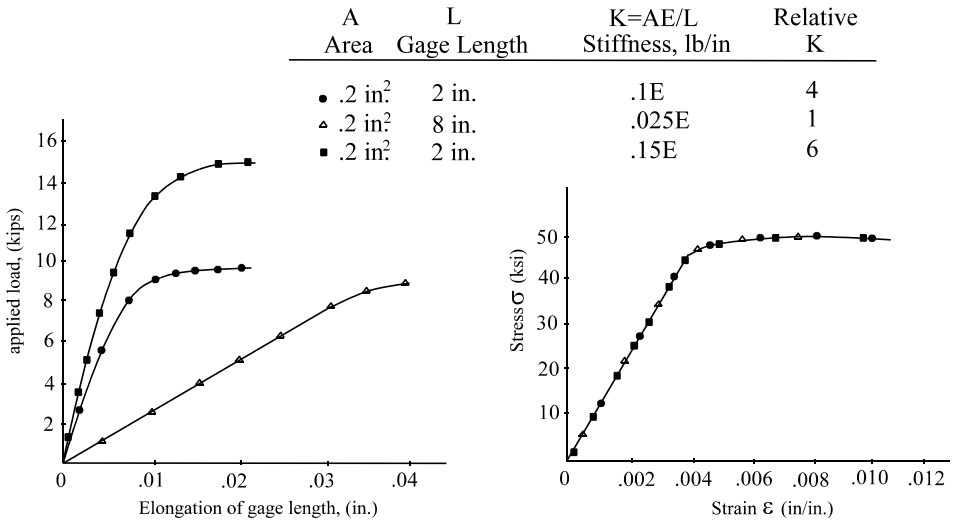

Fig. 5.32 Relationship between Force-Deflection and Stress-Strain Curves

The elastic stiffness of a structure under a specific loading can be obtained from a deflection formula. The stiffness of the structure in the direction of applied load is the ratio of the applied load to the deflection in the loading direction. The deflection of a structure at a given point can be derived by the strain energy method using Castigliano's Theorem [7]. Fifteen simple structures are shown in Table 5.14 and the deflection formulas for the structures are shown. Note that most of the deflection due to axial and shear forces are neglected. In the formulas, E denotes Young's modulus, G, the modulus of rigidity, and I, the moment of inertia of the cross section of the structure member.

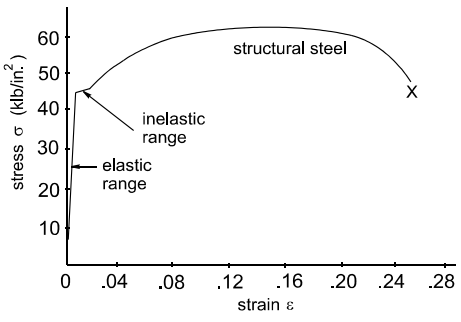

Fig. 5.33 σ vs. ϵ for Structural Steel

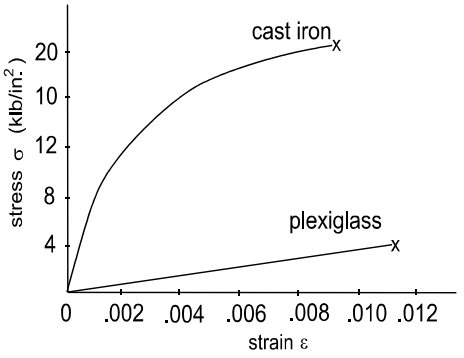

Fig. 5.34 σ vs. ϵ for Brittle Materials

5.7.2 Push Bumper Force-Deflection Data

A push bumper mounted on the front bumper of a police car requires a certain stiffness to perform its task. Fig. 5.35 is a sketch of the push bumper. A properly designed push bumper should not affect air bag crash sensor performance in a frontal collision. The proper design of push bumper needs to consider the effective stiffness of the push bumper and the attached front end of the vehicle, and its effect on the occupant kinematics and sensor performance in a test.

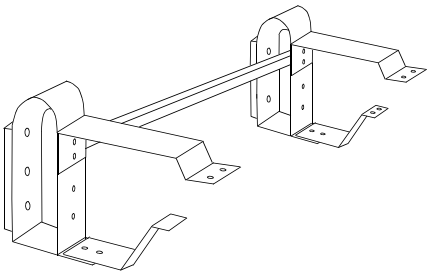

Fig. 5.35 Police Car Push Bumper

The stiffness of the push bumper, based on the stiffness formulas of various structures shown in Table 5.14, is computed in this section. The force-deflection data from the quasi-static component test is shown in Fig. 5.36. The slope of the straight line approximating the test curve is k=18 klbs/in.

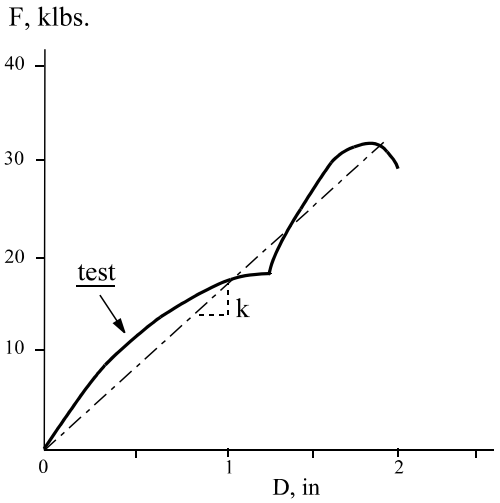

Fig. 5.36 Push Bumper Force vs. Deflection

The push bumper is modeled as a half circular spring with a beam supported by free and fixed ends, as shown in Fig. 5.37. Assuming a concentrated load acting at the midpoint of the push bumper, the combined force-deflection can be estimated by formulas #8 and #15 in Table 5.14. The computation is shown in Eq. (5.42).

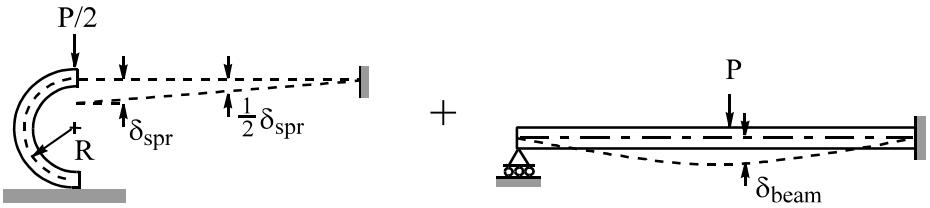

Fig. 5.37 Beam and Spring Modeling of Push Bumper

Table 5.14 Deflection and Stiffness of Structural Members

1

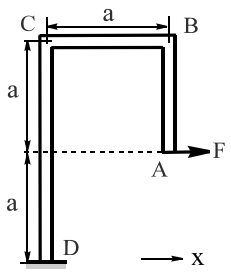

$$x_A = \frac{2Fa^3}{EI}$$

2

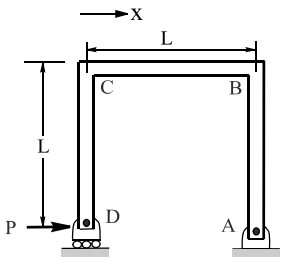

$$x_D = \frac{5PL^3}{3EI}$$

3

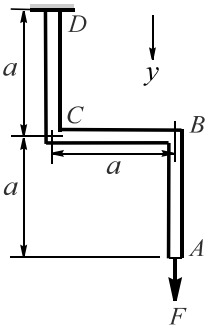

$$y_A = \frac{2Fa^3}{EI}$$

4

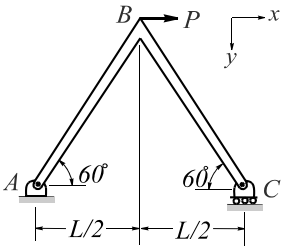

$$x_B = \frac{PL^3}{8EI}$$

$$y_B = \frac{\sqrt{3}PL^3}{24EI}$$

5

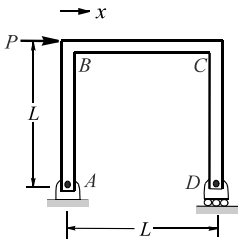

$$x_D = \frac{5PL^3}{6EI}$$

$$\theta_D = \frac{PL^2}{6EI}$$

6

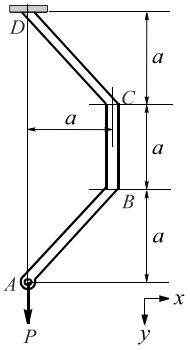

$$x_A = \left(\frac{2\sqrt{2}}{3} + 1\right)\frac{Pa^3}{EI}$$

$$y_A = \frac{3(1+\sqrt{2})Pa^3}{2EI}$$

7

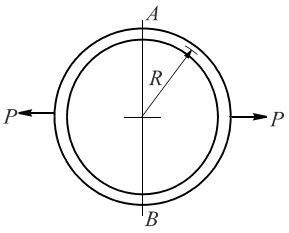

$$\Delta AB(decrease) = \left(\frac{2}{\pi} - \frac{1}{2}\right)\frac{PR^3}{EI}$$

8

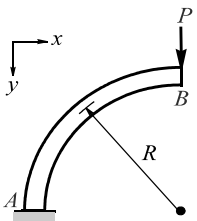

$$x_B = \frac{PR^3}{2EI}$$

$$y_B = \frac{\pi PR^3}{4EI}$$

Table 5.14 Deflection and Stiffness of Structural Members (Continued)

9

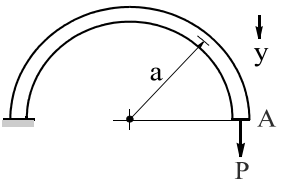

$$y_A = \left(\frac{1}{EI} + \frac{3}{GJ} \right) \frac{\pi P a^3}{2}$$

10

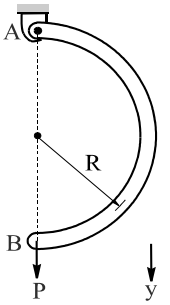

$$y_B = \frac{\pi P R^3}{2EI}$$

11

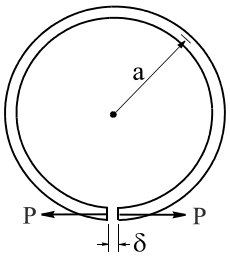

$$P = \frac{\delta EI}{3\pi a^3}$$

12

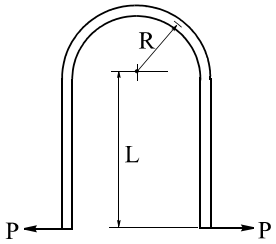

$$x_{p-p} = \frac{PL^3}{EI}\left[\frac{2}{3} + \pi \frac{R}{L} + 4\frac{R^2}{L^2} + \frac{\pi}{2}\frac{R^3}{L^3} \right]$$

Cantilever 13

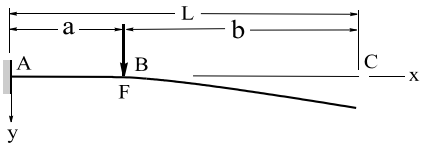

$$K = \frac{3EI}{L^3}\left(\frac{L}{a} \right)^3$$

at free end: $\frac{L}{a} = 1,\ K = \frac{3EI}{L^3}$

Fixed Supports 14

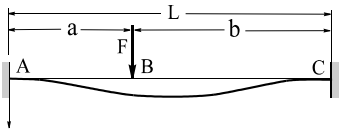

$$K = \frac{3EI}{L^3}\left[\frac{1}{\frac{a}{L}\left(1 - \frac{a}{L} \right)} \right]^3$$

At center: $\frac{a}{L} = \frac{1}{2},\ K = \frac{192EI}{L^3}$

15

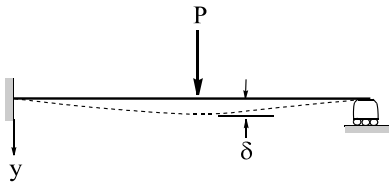

$$k = \frac{P}{\delta} = \frac{768EI}{7L^3}$$

$$\delta = \frac{1}{2}\delta_{spr} + \delta_{beam} \quad \ldots\ldots\ldots\ldots \quad (1)$$

$$= \frac{1}{2}\left[\frac{\pi(\frac{P}{2})R^3}{2EI}\right] + \frac{7PL^3}{768EI} = \frac{P}{EI}\left[\frac{\pi R^3}{8} + \frac{7L^3}{768}\right]$$

$$\therefore \quad k = \frac{P}{\delta} = \frac{EI}{\frac{\pi R^3}{8} + \frac{7L^3}{768}} \quad \ldots\ldots\ldots \quad (2) \qquad (5.42)$$

$$For \quad E\ (steel) = 30\times10^6\ psi, \quad I = \frac{bt^3}{12} = .011\ in^4$$

$$where \quad b = 2.5'' \quad and \quad t = \frac{3}{8}'' = .375'', \quad R = 1.5'', \quad L = 12''$$

$$then \quad k = \frac{30\times10^6\times.011}{1.325 + 15.75} = 19{,}327\ lb/in$$

$$(compared\ to\ test \approx 18{,}000\ lb/in)$$

The computed push bumper stiffness in the direction perpendicular to the face plate is about 19 klbs/in. This analytical estimate is fairly close to that obtained from the component test, 18 klbs/in.

5.7.3 Basic Operation of EA Types

In addition to the use of quasi-static force-deflection data for the structural components in the model, there are eight types of EA and five types of CV (velocity sensitive) factors to choose from for each of the components used in the model. The EA type specifies how the loading and unloading are simulated and the CV type specifies the type of material strain rate effects [8,9] to be used for that EA.

The EA Type 4 allows the user to input discrete force-deflection (F-D) data points for a structural component. In addition to the loading portion of the data set, it permits the unloading and reloading along the same slope, k_u. If the unloading is driven lower, such that it intercepts the second unloading slope, k_u', the unloading then follows this new path, as shown in Fig. 5.38. During the unloading along k_u', if it encounters reloading, it would then create a new reloading path with the same slope as k_u.

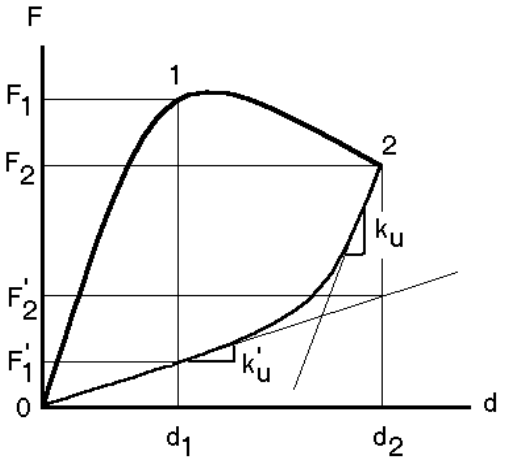

Fig. 5.38 Force-Deflection Data with Unloading Properties

The EA Type 4 was created to model the material property in which the corresponding permanent deformation and hysteresis energy can be specified. This is done by the use of two unloading slopes k_u and k_u', as shown in Fig. 5.38.

Even though k_u' is specified for the unloading of a certain structural component, it does not guarantee that the deformed material will return to its initial undeformed state. The material specified for compression (or tension) alone will not return to its undeformed state unless it has enough elastic energy returned in the restitution phase (area of the force-deflection under the unloading curve) and/or is forced to return to its initial position by the neighboring component(s) connected to it.

The data format used to specify the discrete force-deflection data points for the EA Type 4 is shown as follows: Given a data point 2 with (d_2, F_2) and a corresponding unloading force level F_2', the second unloading slope, k_u', is then equal to F_2'/d_2. The unloading force levels of the other data points can then be computed by simply multiplying k_u' by the corresponding deflection.

Pt.	**d**	**F_{load}**	**F'_{unload}**
0	0	0	0
1	d_1	F_1	F_1'
2	d_2	F_2	F_2

k_u: initial unloading or subsequent reloading stiffness for the EA Type 4 with F-D tabular input.

k_u': the second unloading slope, equal to F_2'/d_2.

In a special case, k_u' equals zero. Then, the intercept of the unloading slope k_u on the zero force level is the permanent deformation, d_p , as shown in Fig. 5.39.

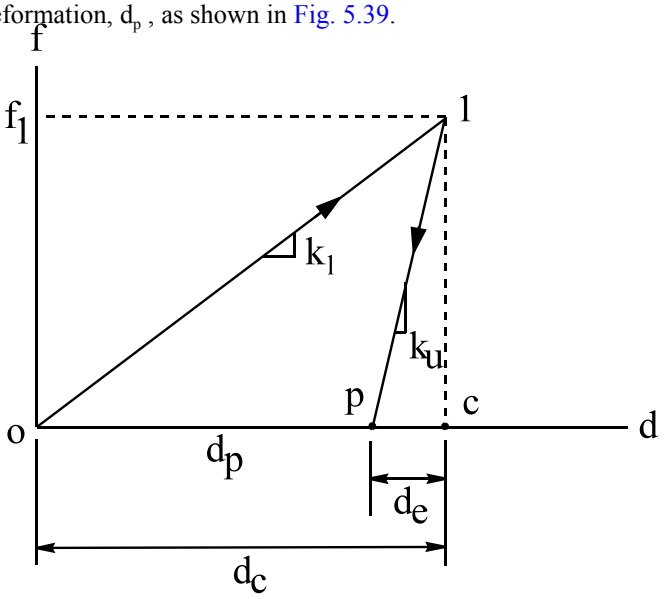

Fig. 5.39 Loading and Unloading Events

Pt.	d	F_{load}	F'_{unload}
0	0	0	0
1	d_1	F_1	$F_1'=0$

Type 4:

k_u: initial unloading or reloading stiffness specified in EA Type 4 F-D tabular input

Type 3: k_L, k_u: loading and unloading stiffnesses, specified in EA Type 3 F-D tabular input

5.7.4 Basic Operation of CV Factor (Velocity Sensitive Factor)

The velocity sensitivity (CV) factors provide an important link in converting the crusher static force-deflection data to dynamic. Strain-rate has an important effect on the dynamic response of structural members. Various equations have been formulated to express the strain-rate effect. At crush rates of 30 mph, CV factors applied to the static force to obtain the dynamic force range from 1.3 to 1.5 for heavy frame type sections. The effect is less important for light elements such as sheet metal. The strengths of highly elastic rubber mounts seem to be independent of the strain-rate. There are five CV factors built into the CRUSH II model. As an example, CV Factor 3 is based on material properties and test strain rate effects caused by the quasi-static Crusher test[1]. Eq. (5.43) shows the CV factors based on the following formula for hot-rolled steel with various percentages of carbon content.

$$CV = A + KR \times \log_e\left(\frac{CR}{SCR}\right) \tag{5.43}$$

where A: a constant, usually 1.0
KR: a material factor (See Table 5.15)
CR: the absolute value of instantaneous crush rate
SCR: the crush rate of the test specimen, usually .03333 in/sec

Table 5.15 Some KR Values for Various Materials

Material		KR
Hot-Rolled Steel % Carbon	0.10 %	.087
	0.47 %	.0456
	0.82 %	.0363
Hard-Roll 1010		.0413
Aluminum-6061		.0
Fiberglass		.1178

The CRUSH II model will not permit a crush rate less than SCR. If the crush rate becomes less than SCR, it will be set equal to SCR.

5.7.5 Coefficient of Restitution, Static, and Dynamic Crush Relationship

It will be shown that the coefficient of restitution is equal to the square root of the ratio of elastic rebound displacement to the dynamic crush. This relationship is identical to that of a ball released at rest from a height of h. Assuming that the maximum height that the ball rebounds to is h'. Then h corresponds to dynamic crush, and h' corresponds to the elastic rebound displacement.

The derivation for such a relationship is shown in Eq. (5.44). It is also shown that the ratio of linear loading stiffness to unloading stiffness is equal to the coefficient of restitution squared. If unloading is perfectly plastic, and the unloading stiffness is infinite, the coefficient of restitution becomes zero.

Let us define (see Fig. 5.41):
f_1: force at d_c
d_c: dynamic crush
k_l: loading stiffness
k_u: unloading stiffness
d_p: permanent deformation
d_e: elastic rebound displacement (=d_c-d_p)
ΔE: total crush energy absorbed at c
$\Delta E'$: elastic energy recovered
v: vehicle rigid barrier impact speed
v': rebound velocity in rigid barrier test
e: coefficient of restitution

Define force at d_c: $f_1 = k_L \cdot d_c = k_u \cdot d_e$ . . . . . (1)

Rearranging (1): $\frac{d_e}{d_c} = \frac{k_L}{k_u}$ . . . . . (2)

Crush energy absorbed at d_c: $\Delta E = \frac{1}{2} k_L d_c^2 = \frac{1}{2} m v^2$ . . . (3)

Rebound energy: $\Delta E' = \frac{1}{2} k_u d_e^2 = \frac{1}{2} m v'^2$ . . . (4)

Dividing (4) *by* (3): $\frac{\Delta E'}{\Delta E} = \left(\frac{v'}{v}\right)^2 = e^2$ . . . . . (5)

$$\frac{\Delta E'}{\Delta E} = \frac{k_u d_e^2}{k_L d_c^2} \quad \text{. . . . . (6)} \tag{5.44}$$

Substituting (5) *and* (2) *into* (6):

$e^2 = \frac{k_L}{k_u}$ . . . . . (7)

$k_u = \frac{k_L}{e^2}$ . . . . . (8)

$e = \sqrt{\frac{d_e}{d_c}}$ . . . . . (9)

5.7.5.1 1-*mass Model with Elasto-Plastic Spring*

A vehicle impacting a fixed barrier is modeled by a spring-mass model. The loading is assumed to be elastic with three unloading scenarios. The test data are shown as follows:
V (initial velocity) = 14 mph, W (weight) = 3,000 pounds, C (dynamic crush) = 7 inches

The linear stiffness, K, in the loading phase can be estimated by the following formula (presented in Section 4.5.2 of Chapter 4):

$$k = .8w\left(\frac{v}{c}\right)^2 = .8(3\ klb)\left(\frac{14\ mph}{7\ in}\right)^2 = 9.6\ \frac{klb}{in} \tag{5.45}$$

There are three unloading scenarios to be covered, and the coefficient of restitution, e, is shown for each of the following unloading scenario:
(A) E: Elastic (e = 1.0), (B) EP: Elasto-Plastic (e = 0.283), (C) P: Plastic (e = 0.0)

The loading and unloading input parameters and the outputs in terms of permanent deformation and energy dissipation are shown in Table 5.16.

Table 5.16 Summary of the Spring-Mass Impact Models

	(A) Elastic	(B) Elasto-Plastic	(C) Plastic
K_l, Klb/in	9.6	9.6	9.6
K_u, Klb/in	9.6	19.2	960
K_u', klb/in *	0	0.667	0
e, coefficient of restitution	1.0	0.283	0.0
e^2, % elastic rebound	100	8	0
$(1-e^2)$, % kinetic energy dissipated	0	92	100

* Note: Second unloading with slope of K_u' functions only when the EA is in tension and compression mode.

The force-deflection relationships for the three cases are shown in Fig. 5.40. The area enclosed in the triangular-like force-deflection curve is the energy dissipated. The motion response of the mass in the model where the EA has more plastic behavior tends to 'stick' with the barrier longer than the response for the more elastic model.

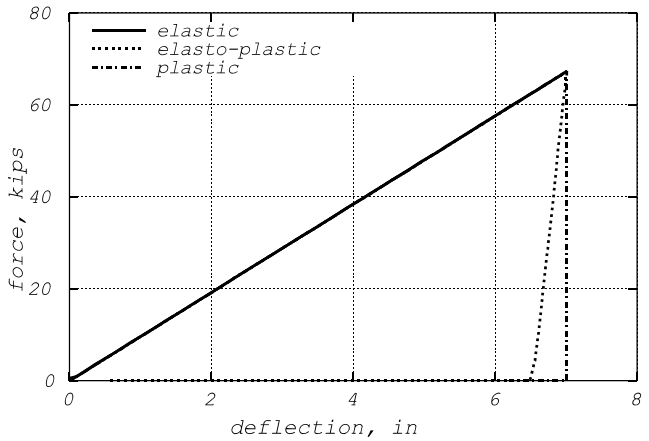

Fig. 5.40 Force-Deflection Responses of Three Models with Elastic and/or Plastic EA

Case Study (Exercise): A mid-size passenger car with a test weight (w) of 3500 lb was tested at a fixed barrier impact speed (v_o) of 31 mph. The kinematics of the vehicle is shown in Fig. 5.41. It has a dynamic crush (C) of 27 inches at 87.4 ms (T_m) and has a rebound velocity (v') of 5.92 mph, as shown in the figure.

(I.a) Determine the (linear) spring stiffness, k1, alone in the model shown in Fig. 5.42, such that the dynamic crush in the test will be matched. How does the model time of dynamic crush, T_m, compare to that in the test? What is the separation velocity (or the rebound velocity at the time of vehicle separating from the rigid barrier)? How does the cor (coefficient of restitution = relative separation velocity / relative approach velocity) for the model compare to that in the test?

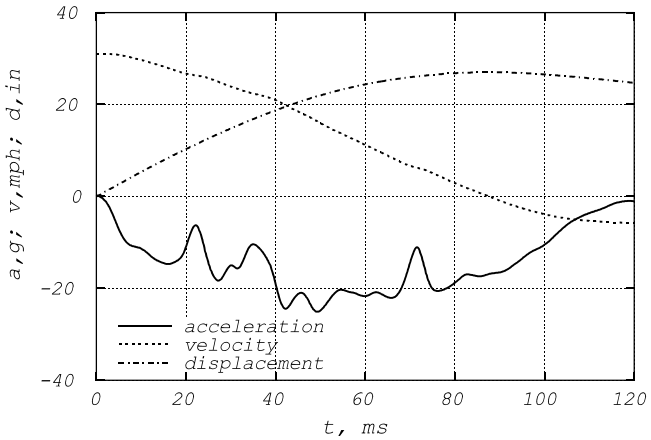

Fig. 5.41 The Kinematics of a Mid-Size Car for a 31 MPH Barrier Impact

(I.b) Determine the spring stiffness, k1, and damping coefficient, c1, that would match the dynamic crush and its timing T_m. The same spring stiffness in the EA type 4 is used for loading and unloading. What are the rebound velocity (or the separation of the vehicle from the rigid barrier) and coefficient of restitution (cor)?

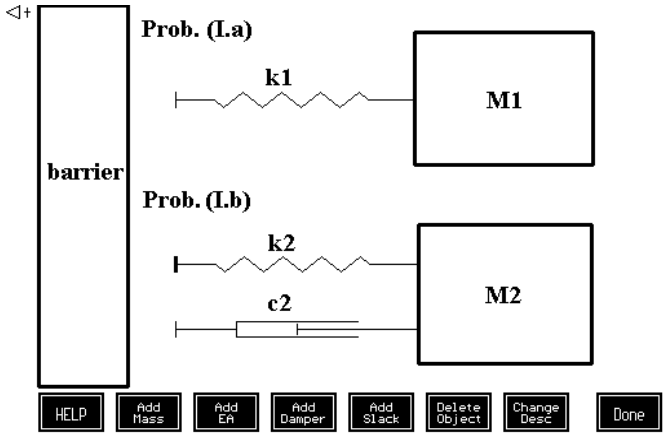

Fig. 5.42 A Model with an Elasto-Plastic Spring

5.8 SIDE-IMPACT AND FRONTAL OFFSET MODELS

Unlike the full frontal rigid barrier test where the loading is distributed across the width of the vehicle, vehicle offset and side impact tests are of localized impact where the loading is concentrated. In a high speed localized impact, the major concern to occupant protection is not the crash pulse severity, but the large magnitude of intrusion into the passenger compartment which directly impacts on the occupant. The crash pulse excitation in the passenger compartment does not result in a major injury potential as compared to that caused by intrusion in a high speed localized impact.

The concept of effective mass and stiffness in frontal offset impact is explored. The concept and methods are equally applicable to front and rear offset impact analysis.

5.8.1 Side Impact Model

The typical side impact configurations are T-Type and L-Type configurations, as shown in Figs. 5.43 and 5.44, respectively. In the T-type side impact, the impactor (striking vehicle) strikes along the front seat occupant location; while in L-type impact, the area in front of the occupant location gets directly hit and the vehicle compartment moves and carries the door and occupant with it.

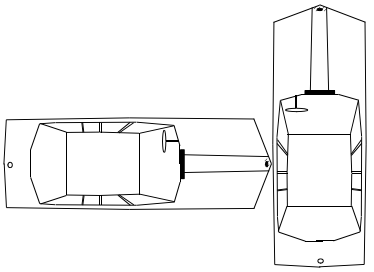

Fig. 5.43 T-Type Side Impact

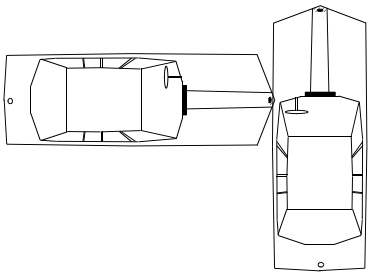

Fig. 5.44 L-Type Side Impact

The lumped-mass models for the T- and L-type side impacts [10-11] are shown in Figs. 5.45 and 5.46, respectively.

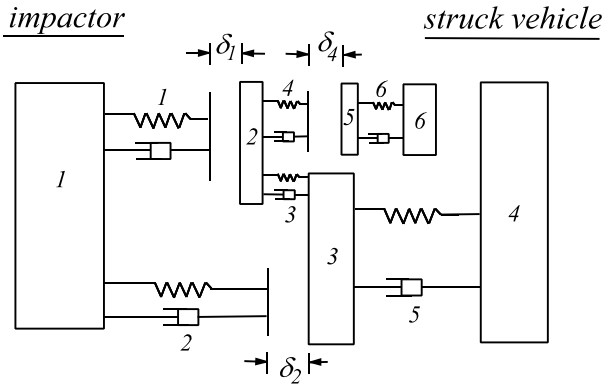

Fig. 5.45 T-Type Side Impact Model

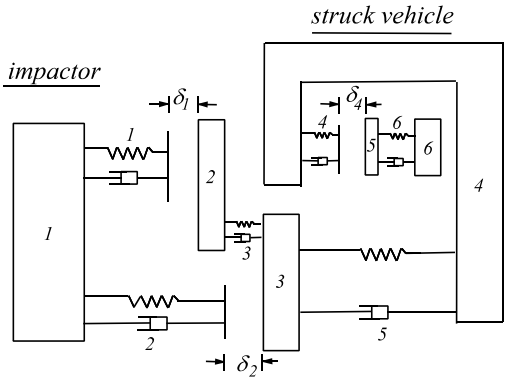

Fig. 5.46 L-Type Side Impact Model

The names of the six masses and six EAs defining each of the two side impact models are shown in Table 5.17. Note that each EA consists of spring and damper, a Kelvin element.

Table 5.17 List of Parameters for Side Impact Models (M: Mass, EA: Energy Absorber)

M1: Impactor	EA1: Impactor Front End
M2: Door (Fender or Quarter Panel in L-Type)	EA2: Impactor to Sill
M3: Sill, A and B Pillars	EA3: Door to Sill (Side Panel to Sill in L-Type)
M4: Struck Vehicle	EA4: Door Pad (Bolster)
M5: Rib Cage	EA5: Sill to Struck Vehicle Compartment
M6: Torso	EA6: Torso to Rib Cage
	δ4: Torso to Pad Clearance

The impactor, after crushing the door panel, picks up the door sill, floor pan, rocker panel and/or B-pillar. Before the crushed door moves along with the major vehicle structure as one big mass, it impacts on the occupant with an impulsive loading. Thereafter, the door moves together with the rest of the vehicle structural components at a common velocity as shown in Fig. 5.47. Meantime, the occupant separates from the door contact at a velocity higher than the common velocity of the door and vehicle.

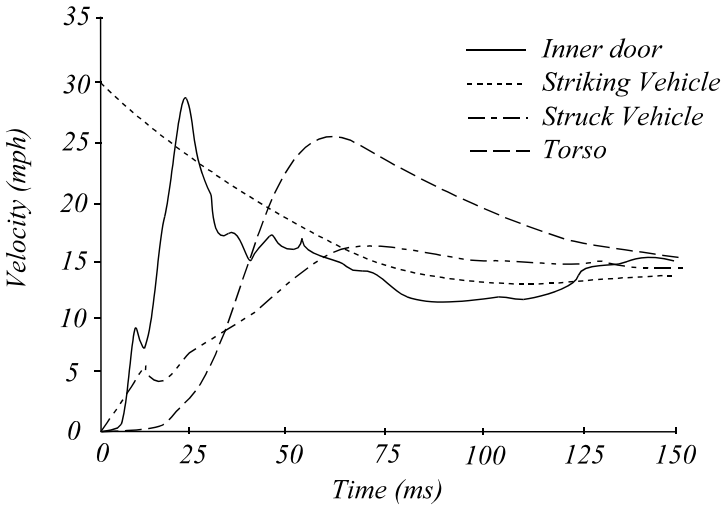

Fig. 5.47 Velocity Profiles of Impactor, Side Struck Vehicle, Crushed Door, and Torso

Fig. 5.47 shows the typical vehicle and occupant velocity profiles in a T-type impact at 30 mph [12]. The impactor, after crushing the door panel, picks up the door sill, floor pan, rocker panel and/or B-pillar. Before the crushed door moves along with the major vehicle structure as one big mass, it impacts on the occupant with an impulsive loading. Thereafter, the door moves together with the rest of the vehicle structural components at a common velocity as shown in Fig. 5.47.

Meantime, the occupant rebounds after contacting the door at a peak velocity (about 25 mph) higher than the common velocity of the door and vehicle (about 15 mph).

5.8.2 Frontal Offset Impact

In a vehicle-to-vehicle (or fixed rigid or fixed deformable barrier) frontal offset impact, due to the smaller contact area, the effective stiffness of the vehicle front end structure is reduced from that in a full frontal impact. The effective mass is also less than the mass of the full vehicle. The basic concept of splitting a spring mass model and the methods of evaluating the effective mass and stiffness are presented below.

5.8.2.1 *Basic Concepts in Offset Impact Modeling*

In modeling a frontal rigid barrier impact, a simple spring-mass model is used, as shown in Fig. 5.48. The total spring stiffness, k, is assumed to be evenly distributed across the front end of the vehicle, and M is the mass of the vehicle. The stiffness and mass distribution of the vehicle in the lateral direction is assumed to be that shown in Fig. 5.49. The outer springs on both sides represent the frame rails, which are stiffer than those in the inner position, 0.3 k versus 0.2 k.

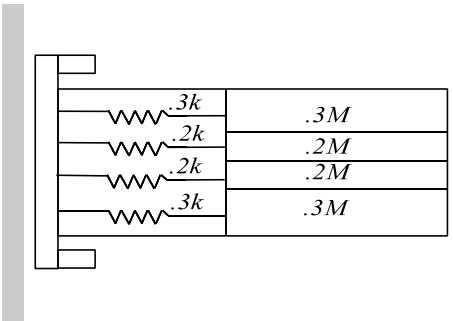

Fig. 5.48 A Frontal Distributed Vehicle Model

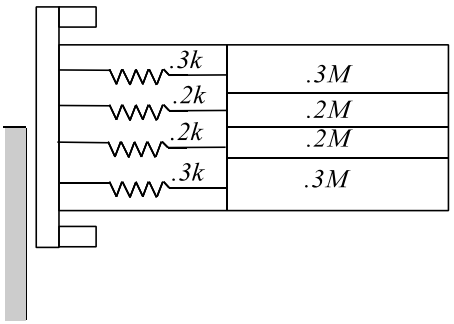

Fig. 5.49 An Offset Distributed Vehicle Model

In a 50% offset barrier test, 50% of the vehicle frontal area sustains a direct impact. However, there is other induced (or indirect) damage due to the presence of shearing forces, bending, and buckling loads transmitted through structural members from the impacting side to the non-impacting side. Assuming that 3/4 of the frontal springs account for the offset resistance, the effective spring stiffness is then added up to 70% of the spring stiffness (0.7k out of 1k).

Similarly, for the effective mass distribution, even though only half of the total mass is on the impacting side, the effective mass in the offset impact is greater than half but less than the entire mass of the vehicle. Assume the mass distribution in the lateral direction is as shown in Fig. 5.49 and the effective mass covers 3/4 of the area, which accounts for 0.7 M.

The non-impacting section of the area has a mass of 0.3 M, which is connected to the area in the impacting side. The mass of 0.3 M can then be separated and attached to the mass of 0.7 M in a series by a very stiff spring. Fig. 5.50 shows the distribution of the mass and stiffness contributing to the effective mass and stiffness. The final 2-mass offset model with the effective mass and stiffness is shown in Fig. 5.51.

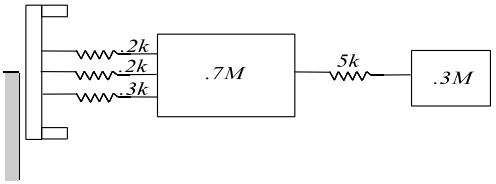

Fig. 5.50 An Effective Spring-Mass Offset Model

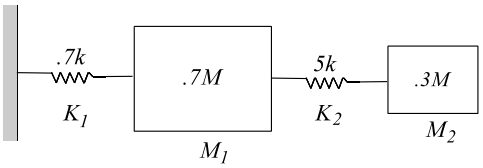

Fig. 5.51 A Simplified Offset Model

Using a one dimensional model for offset simulation requires certain model adjustments to account for the nature of a softer impact such as lower deceleration and longer duration. In a study made by Fileta [13], the use of an effective mass and spring in an offset model is justified. The study compares the test results of two identical mid-size cars which were tested at 35 mph in full frontal barrier and 50% offset rigid barrier tests. In the 50% offset test, 50% of the frontal area of the vehicle contacted a fixed rigid barrier. In the following section, the test results of full barrier and offset barrier tests are analyzed, followed by the modeling of the full barrier and offset impacts. The strategy of obtaining the optimal vehicle structure to meet the design targets of minimum vehicle intrusion and peak deceleration magnitude models in the full barrier and offset tests is presented.

5.8.2.2 *Full Barrier and Frontal Offset Test Results*

The transient acceleration responses of the full rigid barrier and 50% offset tests are shown in Fig. 5.52. As noted, the transient deceleration curve for the rigid barrier test has the shape of a halfsine pulse, while for the offset test, a haversine. Having the haversine pulse shape is an indication that the offset model needs two masses, yielding two modes of vibration. Looking at the velocity vs. displacement curves for both full frontal and 50% offset tests, as shown in Fig. 5.53, the velocity change and energy relationships can be obtained.

In the full barrier test, the dynamic crush is 32 inches, which occurs at 92 ms shown in Fig. 5.54, and the total absorbed energy is 100% of the initial kinetic energy. In the offset test the corresponding timing is 59 ms at a crush of 32 inches. The offset vehicle is still moving at a velocity of 23 mph or 65% of the initial impact velocity. Therefore, the percentage of initial kinetic energy in crushing the second part of the offset crush (40 – 32 = 8 inches) is 43% (square of 65%).

Since there is a large structural deformation involved in the offset crush, intrusions at the floor pan, firewall, and toe board may be detrimental to the occupant. In the impacting side, due to excessive frame deformation in both longitudinal and lateral directions, the front wheel may be pushed back. Once the deformation is larger than the available crush space in the front end, compartment

intrusion occurs. The toe board intrusion along the driver longitudinal direction may cause a high HIC at the head due to torso rotation and large injury numbers at the lower extremities of the occupants.

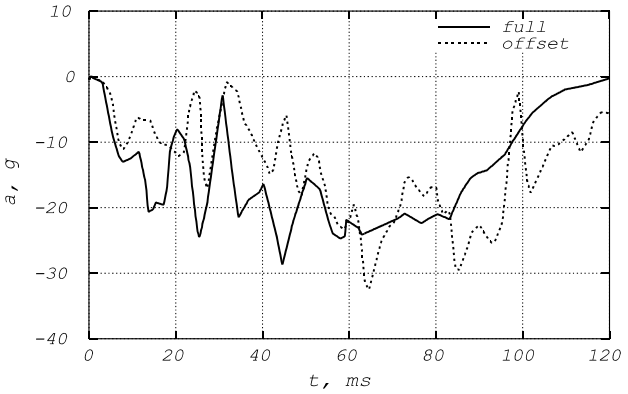

Fig. 5.52 Transient Decelerations of a Sedan in Full Frontal and 50% Offset Tests

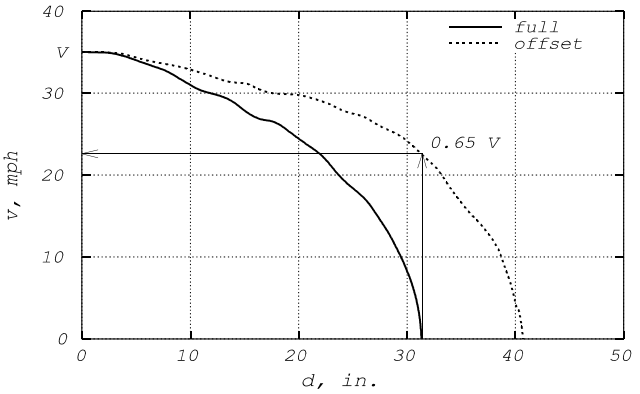

Fig. 5.53 Velocity vs. Displacements of a Sedan in Full Frontal and 50% Offset Tests

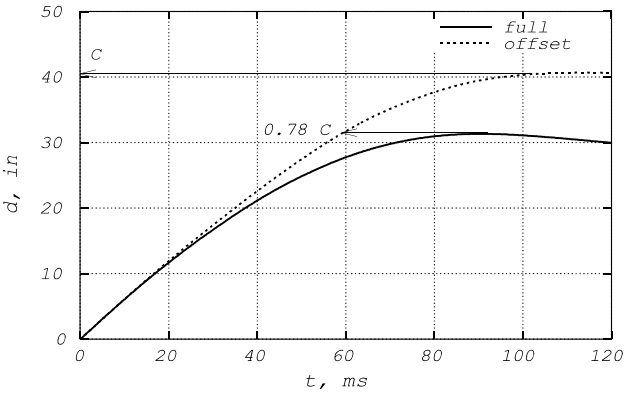

Fig. 5.54 Transient Displacements of a Sedan in Full Frontal and 50% Offset Tests

5.8.2.3 *Modeling the Full Barrier and Frontal Offset Tests*

The full barrier and offset models are analyzed and compared to the crash test results. Given a dynamic crush of 32 inches as shown in Fig. 5.54 for the full barrier test and the formula derived in Eq. (4.26), Chapter 4, the model stiffness for w = 4000 lbs can then be computed as follows.

$$k = 0.8\,w\left(\frac{v}{c}\right)^2 = 0.8\,(4000\ lb)\left(\frac{35\ mph}{32\ in}\right) = 3830\ lb/in \tag{5.46}$$

The offset model shown in Fig. 5.51 has the following parameters:

$k_1 = 0.7k = 2680$ lb/in, $m_1 = 0.7w = 2800$ lb
$k_2 = 5k = 19150$ lb/in $m_2 = 0.3w = 1200$ lb

Both simulations of the one mass-spring full barrier and two mass-spring offset models are carried out by CRUSH II. The transient displacements are compared for the model and test for the full frontal barrier and frontal offset tests shown in Fig. 5.55. Both the dynamic crush and time of dynamic crush agree fairly well for the model and the test, especially for the offset test. Note that one more parameter, such as a damping coefficient, should be added to improve the simulation accuracy of the one mass-spring full barrier model.

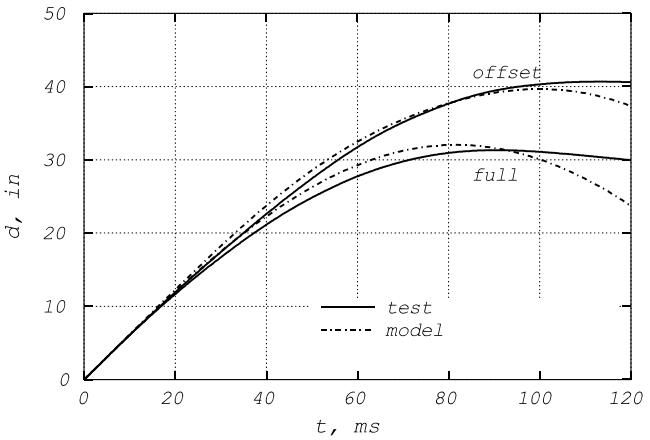

Fig. 5.55 Model and Test Displacements for the Full and Offset Barrier Impacts

5.8.2.4 *Optimal Vehicle Structure for Both Full Frontal and Offset Tests*

Since the effective structure stiffness in the frontal offset test is smaller than in the full frontal rigid barrier test, large deformation occurs in the offset test vehicle where the crush energy input is the same as that in the full frontal test. Therefore one of the goals in the offset testing is to reduce the intrusion of the toe board and dash panel area underneath the instrument panel. This can be achieved for example by using a stiffener inside the frame rail section and/or redesigning the architectural style of the load-bearing structures. A frame geometry with a wishbone or a tuning fork shape helps distribute the concentrated loading and prevents frame from buckling in the lateral direction.

However, the re-enforced structure, prompted by the idea of reducing the deformation in the offset test, may become too stiff in the high speed fixed barrier testing. The occupant deceleration may exceed the requirement set forth by the FMVSS 208 for the occupant protection. Therefore, an optimal vehicle structure needs to consider the intrusion and the vehicle peak deceleration in both full frontal and offset testing.

Using the vehicle weight and stiffness data shown in Section 5.8.2.3 for both the frontal and offset tests, the intrusion and vehicle peak deceleration can be computed for the impact speed of 35 mph.

To simplify the offset analysis using the 2-mass model shown in Fig. 5.51, the stiffness of spring #2 is assumed to be infinite. Therefore, using the formulas for the simple spring-mass model, the vehicle peak deceleration and dynamic crush can be computed as shown in Eq. (5.47). Assuming the vehicle has an available crush space of 28 inches, the intrusion is then equal to dynamic crush minus the available crush space. Note that there is no intrusion if the dynamic crush is less than or equal to the available crush space.

$$
\begin{aligned}
&\textit{Vehicle peak deceleration:}\quad A = v\,\omega,\\
&\textit{Vehicle dynamic crush:}\quad C = \frac{v}{\omega},\quad \textit{For } v = 35\ \textit{mph},\\
&W = 4000\ \textit{lbs},\quad \textit{where}\quad \omega = \sqrt{\frac{k}{m}}\\
&(I)\ \textit{vehicle full barrier test},\quad \textit{baseline } k = 3830\ \textit{lb/in}\\
&\qquad A(g) = 0.5\sqrt{k},\qquad C(in) = \frac{1992}{\sqrt{k}}\\
&(II)\ \textit{vehicle 50\% offset test},\quad \textit{baseline } k = 2680\ \textit{lb/in}\\
&\qquad A(g) = 0.42\sqrt{k},\qquad C(in) = \frac{2381}{\sqrt{k}}
\end{aligned}
\tag{5.47}
$$

The vehicle peak deceleration and intrusion (= C – 28") are shown in Fig. 5.56 as functions of structure stiffness. The baseline stiffness of 3830 lb/in in the full barrier test yields an intrusion of 4 inches and vehicle peak deceleration of 31 g. Shown in the plot, the vehicle peak deceleration in the full barrier test is higher than that in the offset test, and the intrusion in the offset test is always higher than that in the full barrier test. The worst-case vehicle as far as the peak vehicle deceleration is the one that is too stiff, and the worst case as far as the intrusion is the one that is too soft.

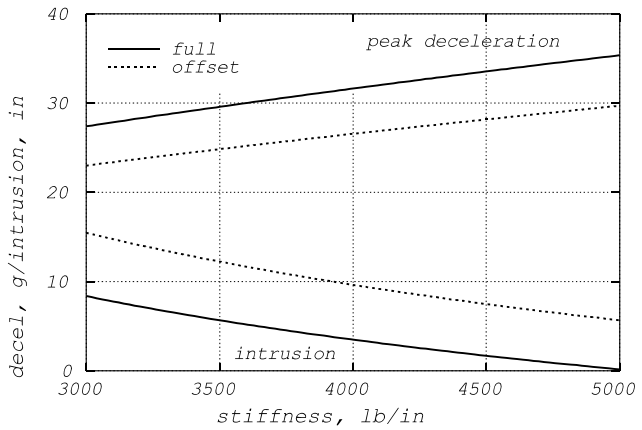

Fig. 5.56 Vehicle Deceleration and Intrusion in Full and Offset Barrier Tests (35mph)

The selection of the optimal vehicle structure therefore is based on the set of vehicle responses, the peak deceleration in the full barrier test, and the intrusion in the offset test that provides the best overall occupant responses.

5.8.2.5 *An Offset Lumped-Mass Model*

To better model the intrusion response and vehicle crash pulse in an offset test, a 12-mass 20-EA lumped-parameter model similar to the one proposed by Cheva, etc [14] is shown in Fig. 5.57. The

names of the masses and EAs are listed in Table 5.18. Note that the cross member and/or steel plate connecting the left and right sides of the vehicle are simulated by an energy absorber, EA(or E shown in Table 5.18)#2. Therefore, even though the offset impact loading is on one side of the vehicle, the induced damage and loading on the other side is simulated by EA #2.

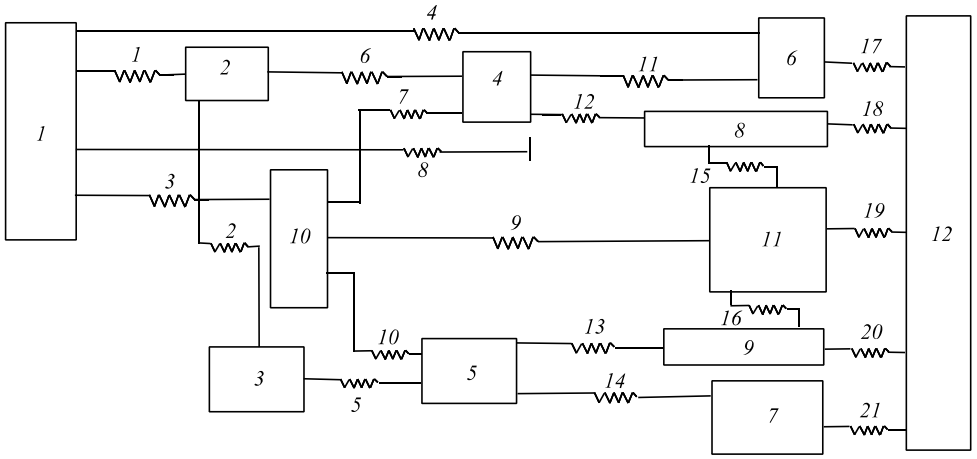

Fig. 5.57 A 12-Mass 20-EA Offset Impact Model

Table 5.18 List of Parameters for An Offset Impact Model (M: Mass, E: Energy Absorber)

M1: Barrier	M8: R. Engine Cradle	E1: Crush Can	E9: Engine Intake Manifold
M2: R. Bumper	M9: L. Engine Cradle	E2: Bumper Beam	E10: L. Lower Radiator Bracket
M3: L. Bumper	M10: Radiator	E3: Radiator Bracket	E11, E14: R & L Frame Rails
M4: R. Towhook	M11: Engine	E4: R. Shotgun Fender	E12, E13: R & L Subframe Mount
M5: L. Towhook	M12: Compartment	E5, E6: L & R Cross Members	E17, E21: R & L Rear Frame Rails
M6: R. Shotgun		E7: R. Lower Radiator Bracket	E19: Engine/Powertrain
M7: L. Shotgun		E8: First Cross Member Center	E18, E20: R & L Cradle Support

5.9 REFERENCES

1. Battelle Columbus Laboratories, "Development of a Computer Simulation Program for Collinear Car/Car and Car/Barrier Collisions," Prepared for DOT Contract No. FH-11-7550. Also ASME Paper 73-ICT-34 by J.T. Herridge and R.K. Mitchel.
2. Huang, M., "On Body Mount Crash Characteristics," SAE paper No. 1999-01-3186, International Body Engineering Conference and Exposition, Detroit, Michigan, September 28-30, 1999. Also in Journal of Passenger Cars, SAE 1999 Transactions, Section 6, pp.3330-3342.
3. Langdon, M.G., "Modeling the Lateral Impact of the Thorax in Car Side Impact Accident," pp. 114-124," Tenth International Technical Conference on Experimental Safety Vehicle, Oxford, England, July 1-4, 1985.

4. Vierck, R.K., “Vibration Analysis,” International Text Book Company, 1967.
5. Bastow, Donald, “Car Suspension and Handling,” Pentech Press, London and Society of Automotive Engineers, Inc., Warrendale, USA.
6. Carnahan, B. and Wilkes, J.O., “Numerical Methods, Optimization Techniques and Simulation for Engineers,” The University of Michigan Engineering Summer Conference, Ann Arbor, Michigan, August, 1970.
7. Beer, F. and Johnston, R., “Mechanics of Materials,” Second Edition, McGraw Hill, Inc., 1992.
8. Zaouk, A. Bedewi, N.E., Kan, C.D. and Marzougui, D., “Validation of a Non-linear Finite Element Vehicle Model using Multiple Impact Data,” pp. 91-106, AMD-Vol. 218, Crashworthiness and Occupant Protection in Transportation Systems, ASME, 1996.
(George Washington Univ., Crash Analysis Center .. Energy absorption by components)
9. Davies, R.G. and Magee, C.L., "The Effect of Strain-Rate Upon the Deformation of Materials, I - Tensile Behavior," Ford Scientific Research Report, SR-73-114, Oct. 4, 1973.
10. Henson, S.E., Huang, M., Hultman, R.W., Parekh, I.S., Grush, E.S., Pike, J.A., “Testing the Side Impact Tests: Method and Some Initial Results,” pp.667-715, Tenth International Technical Conference on Experimental Safety Vehicles, Oxford, England, July 1-4, 1985.
11. Struble, D., Piganell, T., “An Improved Integrated Simulation Model for Side Impact Countermeasure Design,” SAE Paper #920355, SP-906, Analytical Modeling and Occupant Protection Technologies, Society of Automotive Engineers Congress, February, 1996.
12. King, A.I., “Occupant Kinematics and Impact Biomechanics,” pp.3-21, Crashworthiness of Transportation Systems, Structural Impact and Occupant Protection,” NATO Advanced Science Institutes Series, Series E: Applied Sciences - Vol. 332..
13. Fileta, B.and X. Liu, “Predicting Vehicle Crash Performance in Offset Barrier Impact,” pp. 1-23, AMD-V. 218, Crashworthiness & Occupant Protection in Transportation Systems, ASME, 1996.
14. Cheva, W, Yasuki, T., Gupta, V., and Mendis, K., “Vehicle Development for Frontal/Offset Crash Using Lumped Parameter Modeling,” SAE Paper #960437, SP-1139, Vehicle Safety Technology, Society of Automotive Engineers, International Congress, February, 1996.
15. Chatfield, D.A. and Rote, R.R., “Strain Rate Effects on the Properties of High Strength, Low Alloy Steels,” SAE Paper No.740177

CHAPTER 6

IMPULSE, MOMENTUM, AND ENERGY

6.1 INTRODUCTION

In Chapters 4 and 5, efforts were directed toward analyzing the transient response and parametric relationships of a dynamic system under impact and/or excitation conditions. The basis for modeling such a dynamic system is Newton's Second Law. In this chapter, the principle of impulse and momentum and the principle of energy derived from Newton's Second Law are utilized to solve impulsive loading problems. The solutions to such dynamic problems do not directly involve the time variable.

On the subject of impulse and momentum, the basic principles are reviewed first. This is followed by the application of the CG (center of gravity) motion theorem in an analysis of multiple vehicle collisions and the circle of constant acceleration (COCA) for the g-loading of vehicles. Impulsive loading can be concentrated or distributed. The distributed loading can be analyzed because the superposition method is applicable to linear systems. Specific design analysis, such as the selection of a location for an air bag crash sensor, is presented.

In the analysis of vehicle/occupant collisions without using time as a reference variable, it is imperative that both principles be used. This is because collisions between multiple objects involve energy loss, and the principle of impulse and momentum provides information about the kinetic and the absorbed structural energies being transferred. In modeling component tests, the parametric relationships among the effective weight of the energy absorber, the mass ratio, and the coefficient of the restitution are presented.

Methods of determining vehicle inertia properties, such as the CG height and moment of inertia of a vehicle, are covered. The formulations of critical sliding velocity (CSV), rollover dynamics, and detection of an incipient rollover using a simple vehicle model are introduced.

Extending the local coordinate based COCA method, a vector operation in a global coordinate system is used to analyze the acceleration response at any location in a vehicle subjected to eccentric loading. The steps used to construct a vector diagram to analyze the loading distribution in the vehicle are described. The outcome of the eccentric loading analysis helps identifying where the largest loading occurs so that counter-measures can be taken. The vector method is also presented to determine the roll over kinematics including the geometric conditions for a vehicle to stop rolling after one side of vehicle hitting on the ground.

6.2 BACKGROUND

Before presenting applications of the principles of impulse and momentum, definitions of these important dynamic variables will be made:

Momentum is a vector quantity pertaining to the motion of an object; its magnitude is the mass of the object times its speed, and its direction is the direction of motion. The units of momentum are mass times speed [kg · m/s]. The symbol usually used for momentum is "p".

Impulse is a vector quantity pertaining to a force; it is the integral of the force over a specified period of time. Usually, the time period is very short, as in the impact occurring during a crash. The units are the same as for momentum. The symbol for impulse is usually an " I ".

The effect of an impulse on a body is a change in the momentum (a vector quantity) of the body: $\Delta p = I$. Then, for the momentum before and after an impulse, one can write:

$$\vec{p}_B + \vec{I} = \vec{p}_A \tag{6.1}$$

6.2.1 Impulse and Momentum for a Single Particle

For a body acted on by several forces, as shown in Fig. 6.1, the forces can be summed vectorially, giving one resultant force. This produces an acceleration in the direction of the resultant force. Then, using Newton's Second Law:

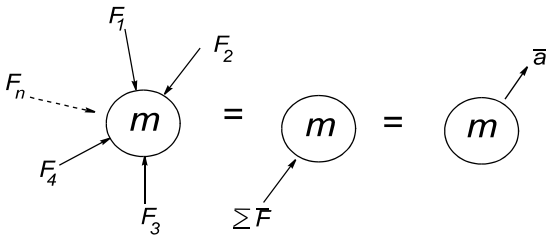

Fig. 6.1 Resultant Force and Acceleration

$$\Sigma\vec{F}_i = m\,\vec{a} = m\frac{d\vec{v}}{dt}. \quad \textit{Multiplying through by } dt \textit{ yields } \Sigma\vec{F}_i dt = m\,d\vec{v}.$$
$$\textit{Integrating: } \Sigma\int_{t_1}^{t_2}\vec{F}_i dt = m\int_{v_1}^{v_2} d\vec{v} = m\vec{v}_2 - m\vec{v}_1, \textit{ where } \vec{v}_i \textit{ is the velocity at } t_i. \tag{6.2}$$

For a single particle, with an impulse acting on it, we have : $p_1 + I = p_2$. This also can be stated as :

$$m\vec{v}_1 + \Sigma\int_{t_1}^{t_2}\vec{F}_i dt = m\vec{v}_2 \tag{6.3}$$

Graphically, this equation can be depicted as shown below:

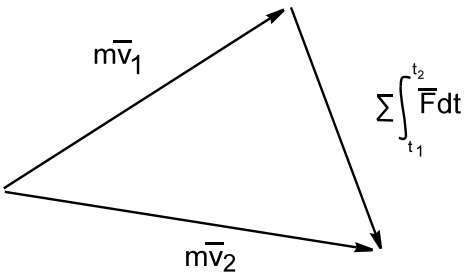

Fig. 6.2 Vector Addition of Momentum and Impulse

Case Study: Batting A Baseball.

A baseball player sees a ball thrown at him horizontally. He intends to hit the ball in such a way that the ball will take off at an angle of 40° and at a speed of 120 ft/sec, as shown in Fig. 6.3. The given information is as follows.

weight of the ball (W) = 4 oz
incoming speed (v_1) = 80 ft/sec
outgoing speed (v_2) = 120 ft/sec
ball-bat contact duration (Δt) = .015 sec

Determine the upward angle α that he has to swing the bat and what the impulse force F should be to achieve the desired outcome.

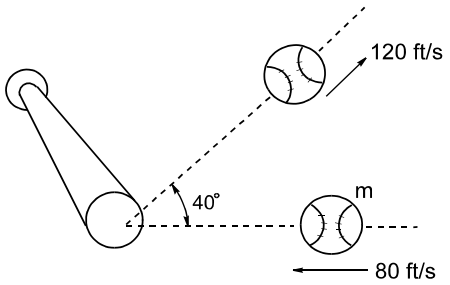

Fig. 6.3 Batting a Baseball

Using the principle of impulse and momentum, one gets a vector relationship.

$$m\mathbf{v}_1 + \int_{t_1}^{t_2} \mathbf{F}\,dt = m\mathbf{v}_2, \quad or \quad m\mathbf{v}_1 + \mathbf{F}\Delta t = m\mathbf{v}_2 \tag{6.4}$$

The triangle which defines the vector relationships is shown in Fig. 6.4. Since the initial and final momentum vectors are given, the two unknowns are the magnitude of the force and angle α. Assuming the force is constant, the magnitude of the impulse can then be measured from the plot or computed by using Eq. (6.4):

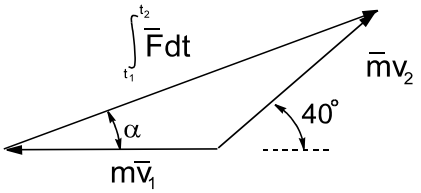

Fig. 6.4 Vector Operation of Batting a Baseball

$$m v_1 + m v_2 \cos(40^o) = F\Delta t \cos(\alpha) \qquad (1)$$

$$m v_2 \sin(40^o) = F\Delta t \sin(\alpha) \qquad (2)$$

Dividing (2) *by* (1) *gives*

$$\tan(\alpha) = \frac{v_2 \sin(40^o)}{v_1 + v_2 \cos(40^o)}, \quad then \quad \alpha = 24.2^o \tag{6.5}$$

$$From\ (2): \quad a = \frac{F}{m} = \frac{v_2 \sin(40^o)}{\Delta t \sin(\alpha)} = 12545\ ft/\sec^2 = 390\ g$$

$$Therefore \quad F = ma = W(lb) \times a(g) = \frac{1}{4} lb \times 390 = 97.4\ lb$$

Note on statistics:

1. An official major league baseball weighs 5.25 ounces and is sewn with 116 stitches. The coefficient of restitution of the ball, striking a board made of white ash at a speed of 85 ft/s, is 0.546 ± 3.2%. The percent of kinetic energy loss due to impact is (1 - e^2) x 100% = 70.2 %.

For average major league players:

2. Ball speed = 90 mph = 132 ft/s
3. Duration of flight = distance/time = 54 ft / 132 ft/s = .41 sec
4. Time taken swinging bat (until contact with ball) = .28 sec
5. Time available for decision to swing or not = .13 sec

Since it takes two-thirds of the flight time of the ball to swing a bat, there is very little time left to make a decision.

6.2.2 Impulse and Momentum for a System of Particles

For a system of particles, a similar expression can be stated, except that the velocities are replaced by the velocity of the center of mass of the particles. The center of mass is a point in the system which will be defined later.

There are both internal and external forces acting on each particle in the system as shown in Fig. 6.5. Internal forces are those exerted by other particles in the system. External forces are those produced by elements not part of the system (e.g., for a vehicle, the external forces are the force of gravity, frictional forces arising from tires contacting the road, impact forces due to a collision with an obstacle, etc.).

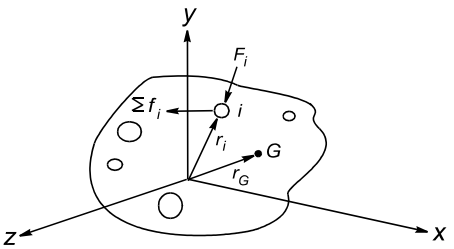

Fig. 6.5 External and Internal Forces Acting on a Rigid Body

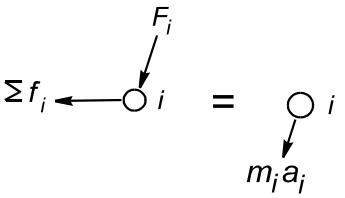

Fig. 6.6 External and Internal Forces Acting on Particle i

The equation of motion for particle i in the system shown in Fig. 6.6 is:

$$\vec{F}_i + \sum_j \vec{f}_{ij} = m_i \vec{a}_i \tag{6.6}$$

The sum over j is for the internal forces associated with other particles. Summing up over all particles in the system gives:

$$\Sigma F_i = \Sigma m_i a_i \tag{6.7}$$

Note that as a result of Newton's Third Law, the internal forces all cancel out, since for every internal force given by (i, j) there is an internal force with subscript (j, i) that is of equal magnitude but in the opposite direction.

6.3 CENTER OF GRAVITY AND MOTION THEOREM

By recognizing the relationship between the formula for the coordinates of the center of mass (CM or center of gravity, CG) and the CG motion of a system of particles, the solution to some difficult accident reconstruction problems can be undertaken with ease. This is due to the fact that if the external impulse to a system of particles is negligible; the CG motion of the system with and without collision is the same.

6.3.1 Location and Motion of Center of Mass

In the following, the terms "center of mass" (CM) and "center of gravity" (CG) will be used interchangeably.

The vector position of the center of mass is given by:

$$
\begin{aligned}
&M\vec{r}_G = \sum_i^n m_i\vec{r}_i \quad \ldots . \quad CG\ formula, \quad where \\
&M\ is\ a\ single\ fictitious\ particle, \qquad M = \sum_i^n m_i \\
&\vec{r}_G = x_G\vec{i} + y_G\vec{j} + z_G\vec{k} \quad (position\ vector\ of\ CG) \\
&\vec{r}_i = x_i\vec{i} + y_i\vec{j} + z_i\vec{k} \quad (position\ vector\ of\ particle\ i) \\
&where\ \vec{i},\vec{j},\vec{k}, are\ unit\ vectors\ along\ x,\ y,\ z,\ respectively.
\end{aligned}
\tag{6.8}
$$

Substituting these expressions of the position vectors into the CG (center of gravity) formula, one gets for the components of the position vector of the CG:

$$
\vec{i}\ term:\ x_G = \frac{\Sigma m_i x_i}{M}; \quad \vec{j}\ term:\ y_G = \frac{\Sigma m_i y_i}{M}; \quad \vec{k}\ term:\ z_G = \frac{\Sigma m_i z_i}{M} \tag{6.9}
$$

Differentiating the CG formula shown in Eq.(6.8) twice yields its velocity and acceleration:

$$
\begin{aligned}
&M\vec{v}_G = \Sigma m_i\vec{v}_i \quad \ldots\ldots\ldots\ldots \quad (1) \\
&M\vec{a}_G = \Sigma m_i\vec{a}_i = \Sigma m_i\frac{d\vec{v}_i}{dt} \quad \ldots\ldots \quad (2)
\end{aligned}
\tag{6.10}
$$

The acceleration equation, (2) of Eq.(6.10), can be written as:

$$
\begin{aligned}
&\Sigma\vec{F}\,dt = \Sigma m_i d\vec{v}_i, \\
&integrating\ from\ t_1\ to\ t_2\ yields:\ \Sigma\int_{t_1}^{t_2}\vec{F}\,dt = \Sigma m_i\int_{t_1}^{t_2}d\vec{v}_i = \left[\Sigma m_i\vec{v}_i\right]_{t_1}^{t_2}, \\
&substituting\ M\vec{v}_G\ for\ \Sigma m_i\vec{v}_i\ yields:\ M\vec{v}_G|_{t_1} + \Sigma\int_{t_1}^{t_2}\vec{F}\,dt = M\vec{v}_G|_{t_2}
\end{aligned}
\tag{6.11}
$$

In words, this states that the final momentum is equal to the initial momentum plus the sum of all the impulses. Note that each term is a vector quantity. Graphically, this equation can be presented by the vector operation shown in Fig. 6.7.

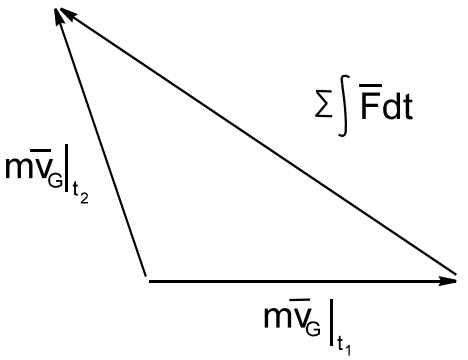

Fig. 6.7 Vector Operation of Linear Impulse and Momentum Changes

When the sum of all impulses is zero, we get the classical conservation of momentum law: (1) of Eq. (6.12) is in terms of the center of mass, and (2) is in terms of a system of n particles:

$$m\bar{v}_G|_{t_1} = m\bar{v}_G|_{t_2} \quad \ldots . \quad (1), \qquad \sum_{i=1}^{n} m_i \vec{v}_i|_{t_1} = \sum_{i=1}^{n} m_i \vec{v}_i|_{t_2} \quad \ldots \quad (2) \tag{6.12}$$

6.3.2 Conservation of Momentum and CG Formula

Assuming a collision of a system of particles is totally inelastic and the external frictional impulse is negligible, then the movement of the center of mass of the system of particles after collision is the same as that without collision.

If there is an inelastic impact between m_1 and m_2, then the distance traveled by both particles in a given time t is equal to $v_c t$, as shown in Fig. 6.8. If there were no collision, the two particles would simply pass by each other and travel in time t a distance of $v_1 t$ and $v_2 t$, respectively. It will be shown that the center of mass of the two particles in free travel at any given time t is at the same location as when the two particles travel together.

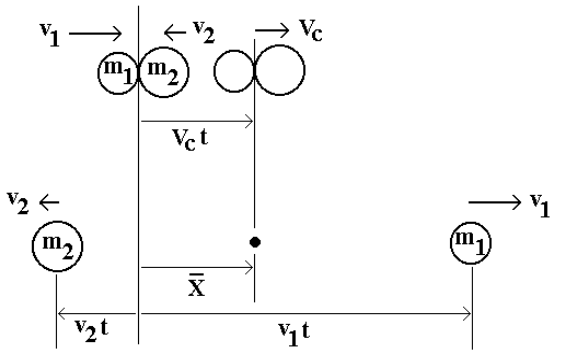

Fig. 6.8 CG Motion of Two Particles

Since the initial momentum of the particles is the same as that at the time of common velocity, we have the momentum relationship shown in Eq. (6.13).

$$\sum_{i=1}^{2} m_i v_i = (\sum_{i=1}^{2} m_i) v_c, \quad \textit{where}$$
$$m_i\textit{: mass of particle } i, \quad v_i\textit{: velocity of } m_i$$
$$v_c\textit{: common velocity of total mass} \tag{6.13}$$

I. One-Dimensional Analysis

(a) Conservation of Momentum (before and after collision)

The common velocity of the two particles after impact can be derived as shown in Eq. (6.14).

$$v_c \ (\textit{common velocity}) = \frac{m_1 v_1 - m_2 v_2}{m_1 + m_2} \tag{6.14}$$

(b) Without Collision (CG location at time t)

The x coordinate of the CG position of a system of particles at time t is shown in Eq. (6.15). In the derivation, the position of each particle is equal to its speed multiplied by the time elapsed.

$$x = \frac{\sum_{i=1}^{2} m_i x_i}{\sum_{i=1}^{2} m_i} = \frac{m_1(v_1 t) - m_2(v_2 t)}{m_1 + m_2} = \frac{m_1 v_1 - m_2 v_2}{m_1 + m_2} t = v_c t \qquad (6.15)$$

Note expression for v_c above is the same as that in Eq. (6.14).

Eq. (6.15) shows that the displacement of the CG of a system of particles with collision is the same as that without a collision.

II. Multi-Dimensional (Vector) Analysis

The position vector relationship between the particles and the CG of the system of particles is shown in (1) of Eq. (6.16). After differentiating the position vector formula, one gets the relationship shown in (2) of Eq. (6.16) which is the conservation of momentum for a system of two particles.

$$\sum_{i=1}^{2} m_i \vec{r}_i = (\sum_{i=1}^{2} m_i)\vec{r}_c \quad \ldots\ldots\ldots\ldots\ldots\ldots \quad (1)$$

where $\vec{r}_i$: *position vector of mass* m_i

$\vec{r}_c$: *position vector of the CG* (6.16)

Differentiate (1) *with respect to* (*w.r.t.*) *time*:

$$\sum_{i=1}^{2} m_i \frac{d\vec{r}_i}{dt} = \sum_{i=1}^{2} m_i \frac{d\vec{r}_c}{dt}, \quad \text{then} \quad \sum_{i=1}^{2} m_i \vec{v}_i = (\sum_{i=1}^{2} m_i)\vec{v}_c \quad \ldots\ldots \quad (2)$$

6.3.3 CG Motion Theorem

Theorem: *In the absence of any external forces, the center of mass of a system of particles will move in a straight line at a constant speed. Any collisions between the particles, elastic or inelastic, will have no effect on this motion.*

Proof: The position vector of the center of mass is defined as follows:

Position vector of CG or center of mass is: $\vec{r}_c = \vec{r}_G = \vec{r}_{CM}$

$$M\vec{r}_{CM} = m_1\vec{r}_1 + m_2\vec{r}_2 + \cdots + m_n\vec{r}_n, \quad \text{where } M = m_1 + m_2 + \cdots + m_n = \sum_{i=1}^{n} m_i$$

Differentiating with respect to time yields:

$$M\frac{d\vec{r}_{CM}}{dt} = m_1\frac{d\vec{r}_1}{dt} + m_2\frac{d\vec{r}_2}{dt} + \cdots + m_n\frac{d\vec{r}_n}{dt} \qquad (6.17)$$

Each term on the right is the momentum of a particle so:

$$M\frac{d\vec{r}_{CM}}{dt} = \vec{p}_1 + \vec{p}_2 + \cdots + \vec{p}_n = \sum_{i=1}^{n} \vec{p}_i$$

The total momentum of the system is equal to the product of the total mass and the velocity of the center of mass. This can be called the momentum of the center of mass. Keep in mind that the center of mass is not a mass but a point. It is possible that a real mass doesn't even exist at the point!

Taking the next derivative:

$$M\frac{d^2\vec{r}_{CM}}{dt^2} = m_1\frac{d^2\vec{r}_1}{dt^2} + m_2\frac{d^2\vec{r}_2}{dt^2} + \cdots + m_n\frac{d^2\vec{r}_n}{dt^2} \qquad (6.18)$$

Now applying Newton's Second Law to each term on the right:

$$m_i \frac{d^2 \vec{r}_i}{dt^2} = \sum_{k=1}^{m} \vec{F}_{ik} + \sum_{j=1}^{n} \vec{f}_{ij} = \vec{F}_i + \vec{f}_i \tag{6.19}$$

F_i is the net external force acting on particle i and f_i is the net internal force acting on it. Summing over all particles gives:

$$M \frac{d^2 \vec{r}_{CM}}{dt^2} = \sum_{i=1}^{n} \vec{F}_i + \sum_i \sum_j \vec{f}_{ij} \tag{6.20}$$

The f_{ij}'s are internal forces and, based on Newton's Third Law, for each of these there is an equal and opposite reaction force acting on another particle. This includes any forces developed in a collision between any two or more particles in the system. In summing over i and j, all of these forces cancel out, leaving no net internal force.

Thus, dropping the sum involving the internal forces, one gets:

$$M \frac{d^2 \vec{r}_{CM}}{dt^2} = \sum_{i=1}^{n} \vec{F}_i \tag{6.21}$$

In the case wherein there are no external forces, one gets:

$$M \frac{d^2 \vec{r}_{CM}}{dt^2} = 0 \tag{6.22}$$

Solving this differential equation leads to:

$$\vec{r}_{CM} = \vec{r}_{CM}(0) + \vec{v}_{CM}(0)\, t \tag{6.23}$$

This is the equation of a straight line whose coefficient is a constant speed. Thus:

In the absence of external forces, the center of mass of a system of particles will move in a straight line at constant speed, independently of any collisions of the particles with each other.

Case Study 1: CG of Two Vehicles With and Without Collision. Two vehicles having masses m_1 and m_2 are traveling on a horizontal icy surface with velocities of v_1 and v_2 , respectively. Assume that they collide and after the collision, their separation velocities are v_1' and v_2' , respectively. Show that the velocities of the center of the mass (CM or CG) before and after collision are equal.

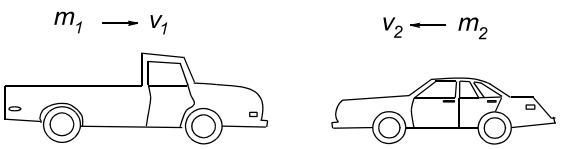

Fig. 6.9 Two Vehicles with and without Collision

Momentum before impact = Momentum after impact

$$m v_1 + m_2 v_2 = m_1 v_1' + m_2 v_2'$$

Position and velocity vectors of CG before impact are:

$$\vec{r} = \frac{m_1 x_1 + m_2 x_2}{m_1 + m_2}, \quad \frac{d\vec{r}}{dt} = \frac{m_1 v_1 + m_2 v_2}{m_1 + m_2}$$

velocity vector of CG after impact (6.24)

$$\frac{d\vec{r}'}{dt} = \frac{m_1 v_1' + m_2 v_2'}{m_1 + m_2}$$

Since the frictional impulse is negligible:

$$m_1 v_1 + m_2 v_2 = m_1 v_1' + m_2 v_2' \quad or \quad \frac{d\vec{r}}{dt} = \frac{d\vec{r}'}{dt}$$

$\therefore$ *Velocities of CG before and after collision are equal.*

Case Study 2: CG Motion of Two Cars With And Without Collision. The following problem is an exercise for students: The reference values of the mass and velocity of vehicle #2 are $m_2 = 1$ and $v_2 = 1$, respectively. The values of those for the subject vehicle #1 are relative to #1 and are to be filled in.

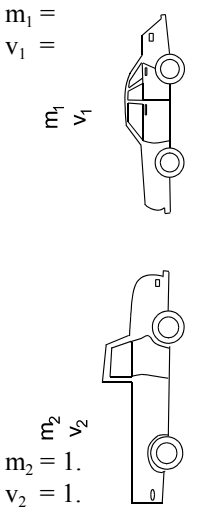

Fig. 6.10 Car & Truck Head-On

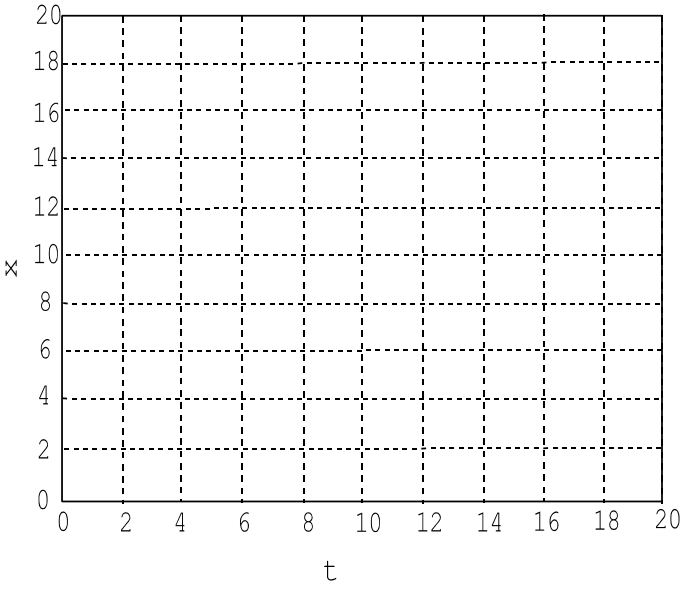

Fig. 6.11 Displacement (Travel) versus Time

(1) Write down below the values of m_1 and v_1 from the vehicle-to-vehicle crash experiment.
(2) On the x vs. t (displacement vs. time) plot, draw a line segment from the lower left corner (0,0) to the right border where the slope is velocity v_2. Similarly, draw another line segment from the upper left corner (0,20) to the right border for the velocity v_1.
(3) From the intersection of the two line segments, draw another line segment where the slope is the common velocity of the two vehicles, v_c, which is defined as follows:

$$v_c = \frac{m_1 v_1 + m_2 v_2}{m_1 + m_2} \tag{6.25}$$

(4) Extending the common velocity line segment to the left and right borders, one gets a line of C.M. (or CG) motion of the two vehicles before and after the inelastic impact where no vehicle separation occurs.
(5) To verify the line of CG motion, compute the CG location of the two vehicles at any point in time using the following CG position formula.

$$x_{CG} = \frac{m_1 x_1 + m_2 x_2}{m_1 + m_2} \tag{6.26}$$

where x_1 and x_2 are the x positions of the two vehicles measured along x from (0,0) at any point in time. Check whether x_{CG} falls right on the common velocity line segment, and what does Eq. (6.26) become after being differentiated w.r.t. time? Why ?

Case Study 3: Collision at Intersection. Car A and Cruiser B of equal mass collide at a right angle at the intersection of two icy roads. The cars become entangled and move off together with a common velocity v_c in the direction shown. If the Cruiser B was traveling 30 mph at the instant of impact, compute the corresponding velocity of car A just prior to the collision. [Ans.: v_A=52 mph]

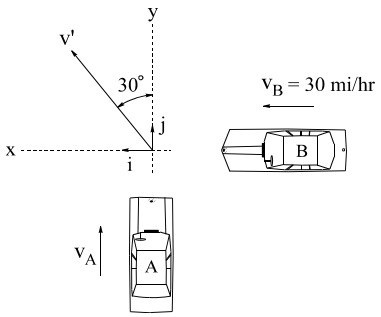

Fig. 6.12 Intersection Collision

6.3.4 Use of CG Motion Theorem in a Three−Car Collision Analysis

Car A was a police car traveling east at 60 mph; it was hit by car B, which was going south at a high speed. The collision occurred at the middle of an intersection (the origin in the accompanying diagram). The pavement was wet and the two cars slid together and collided with another police car (car C). Car C was traveling north at 45 mph. The three cars stuck together and skidded into a wall and came to a stop at point D in the figure. Point D was 42 feet east and 46.5 feet south of the intersection.

Cars A and C weighed 3000 lbs and car B weighed 3600 lbs. Car C was 63 feet south of the intersection when the first collision occurred. Car C was determined to be 20 feet to the right of the intersection before and during its collision with car A and B.

Determine the speed of car B, v_B, and the time elapsed from the time of the first collision to the stop at point D. Neglect any forces exerted on the cars by the wet pavement.

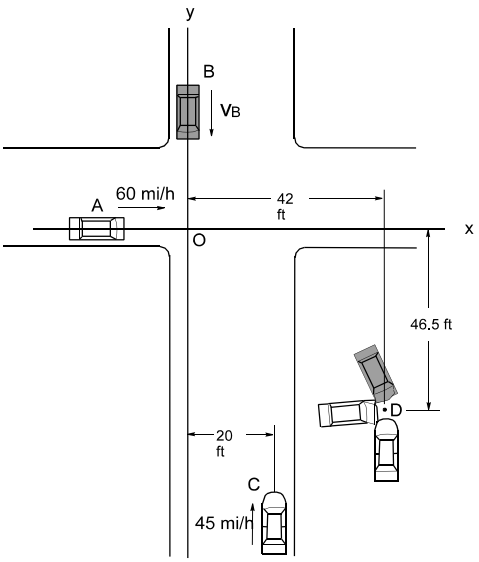

Fig. 6.13 Three-Car Collision

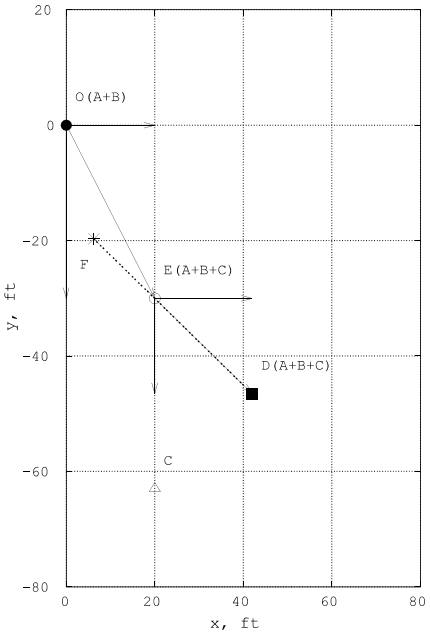

Fig. 6.14 Three-Car Collision Trajectory

Method 1: *Simple Solution Using CG Motion Theorem*

Note: A slug is the mass of an object weighing 32.2 pounds. The velocities for cars A and C are positive numbers, since they are headed along the positive x and y axes. Since car B is headed south (i.e., in the negative y direction), v_B is a negative number.

The initial conditions and parameters for the three cars are:

Masses (slugs):	$m_A = 93.2$	$m_B = 111.8$	$m_C = 93.2$
Velocities:	$v_A = 88.0$ ft/sec (east)	$v_B = ?$ (south)	$v_C = 66.0$ ft/sec (north)

Collision of A and B is assumed to occur at the origin of the coordinate system. Time zero is taken to be the time of the incipient first collision. Car C is approaching the intersection from the south.

Since the collisions of the three cars took place on the icy pavements, the frictional impulse transmitted through the tires to a system of three cars is negligible. Therefore, the CG formula can be used to solve the problem where the conservation of momentum applies. The motion of the CG of the system of three cars is therefore not affected by the collisions.

The position vectors of the three cars are given by:

$$\begin{aligned}\vec{r}_A &= \vec{v}_A t = (88t)\,\vec{i} \\ \vec{r}_B &= \vec{v}_B t = -v_B t\,\vec{j} \\ \vec{r}_C &= \vec{r}_C(0) + \vec{v}_C t = (20.0\vec{i} - 63.0\vec{j}) + (66.0t)\,\vec{j}\end{aligned} \tag{6.27}$$

The motion of the center of mass is shown by Eq. (6.28) where M is the sum of the masses.

$$(m_A + m_B + m_C)\vec{r}_G = M\vec{r}_G = m_A\vec{r}_A + m_B\vec{r}_B + m_C\vec{r}_C \tag{6.28}$$

Since all external forces are assumed to be zero, the conservation equations provide that the center of mass of the system (all three cars) will move in a straight line, independently of any and all collisions, i.e., whether or not there are any collisions. Substituting the above equations for the position vectors for the three cars, we get:

$$\begin{aligned} &\textit{Along the } x\textit{-axis:} \quad M x_G|_t = m_A(88t) + m_C(20) \\ &\textit{Along the } y\textit{-axis:} \quad M y_G|_t = m_B(-v_B t) + m_C(-63 + 66t) \end{aligned} \tag{6.29}$$

At time zero, the center of mass of the three cars is at a point called F, as shown in Fig. 6.14. The coordinates of point F are x = (m_C/M) (20.0) = 6.25 feet and y = −(m_C /M) (63) = −19.7 feet. The entire CG path is FED where the three cars move. At time T, the three cars, stuck together due to two inelastic collisions, stopped.

Assuming *no* collisions, in the time T, the three cars would have moved distances based on their original velocities. The center of mass, known to be at point D, would then satisfy the following equations:

$$\begin{aligned} &\textit{Along the } x\textit{-axis:} \quad M(42.0) = m_A(88.0T) + m_C(20.0) \\ &\textit{Along the } y\textit{-axis:} \quad M(-46.5) = m_B(-v_B T) - m_C(63.0) + m_C(66T) \end{aligned} \tag{6.30}$$

Solving the first of these equations for T yields T = 1.3 seconds. Then, using this value of T, the second equation can be solved for v_B , yielding v_B = 110 feet/second. Then, the speed of car B is 110 feet/second or 75 MPH.

According to the CG motion theorem presented in Section 6.3.3, the CG of the three vehicles moves in a straight line (FED) as shown in Fig. 6.14 at constant speed. The constant speed will be computed using the following method for the detailed analysis.

Method II: *In-Depth Analysis Using Momentum and Displacement Relationships*

In this approach, the first collision, between cars A and B, is analyzed. Then, the resultant velocity is used as inputs for the second collision, between cars (A and B) and C. The trajectory shown in Fig. 6.14 depicts the sequence of the two collisions. Cars A and B collided at point O, then moved together to point E where car C hit both cars, A and B. Then, the three cars tangled up, moved together, and stopped at point D after hitting a fixed object at that point.

Only the relative weights of the cars matter; so their masses will be simplified in the following such that the masses are given by: A = 1.0, B = 1.2, C = 1.0 (Dividing each mass by 93.2 slugs).

(A) Cars A and B collide at time zero. The momentum is the same before and after collision:

$$\begin{aligned} &A\,\vec{v}_A + B\,\vec{v}_B = (A+B)\,\vec{v}' \\ &\textit{where } \vec{v}' \textit{ is the common velocity after collision} \end{aligned} \tag{6.31}$$

This equation yields two component equations, one for x and one for y. Solving for the velocity components, one gets the two velocity components:

$$\begin{aligned} &\textit{Along } x\textit{:} \quad 1(88) = 2.2 v_X' \qquad \textit{Along } y\textit{:} \quad 1.2 v_B = 2.2 v_Y' \\ &\qquad\qquad v_X' = 40.0 \qquad\qquad\qquad\qquad v_Y' = 0.545 v_B \end{aligned} \tag{6.32}$$

The time for cars A and B, moving together, to reach the second collision point (colliding with car C) can be obtained by equating the distance ($v_X' t_C$) to the distance traversed along x (20.0 feet). This can be solved for time:

$$v_X' t_C = 20.0 \quad \textit{or} \quad t_C = 20.0/40.0 = 0.50 \textit{ seconds} \tag{6.33}$$

(B) At this time car C (with velocity v_C = 66.0 ft/sec) collides with A and B and all three move off together, as one mass. Again, the momentum before and after collision is the same:

$$2.2\vec{v}' + 1.0\vec{v}_C = 3.2 v'' \quad (v'' \textit{ is the velocity after collision}) \tag{6.34}$$

Resolving into components yields:

$$\begin{aligned} &\textit{Along } x\text{:} \quad 2.2\,v_X' \;=\; 3.2\,v_X'' \\ &\textit{Along } y\text{:} \quad 2.2\,v_Y' \;+\; 1.0(66.0) \;=\; 3.2\,v_Y'' \end{aligned} \tag{6.35}$$

Using the values for v_X' and v_Y' determined earlier, these equations in v_X'' and v_Y'' yield:

$$\begin{aligned} v_X'' &= \frac{2.2(40)}{3.2} = \frac{88.0}{3.2} = 27.5 \\ v_Y'' &= \frac{2.2(0.545)v_B + 66.0}{3.2} = (0.375\,v_B + 20.6) \end{aligned} \tag{6.36}$$

The speed of the three cars, stuck together, in the direction of the x axis times the traversal time from point E to D equals the x component of the distance from E to D. Then:

$$t_{ED} = (x_E - x_D)/v_X'' = 22.0/27.5 = 0.80 \tag{6.37}$$

The total time from the origin to point D is then 0.50 + 0.80 = 1.3 seconds, so T = 1.3 seconds.

The y components of the paths from the origin to E and then from E to D should add up to the given vertical distance of 46.5 feet. Now, we can state that the changes in distance in x and y will be in proportion to the velocity components along x and y. Thus:

$$\begin{aligned} &\textit{Letting } \Delta x' = \textit{Lateral distance from origin to point E} \\ &\quad \textit{and } \Delta y' = \textit{Vertical distance from origin to point E} \\ &\textit{Then:} \quad \Delta y' = \Delta x' \frac{v_Y'}{v_X'} = 20.0 \frac{0.545\,v_B}{40.0} = 0.273\,v_B \end{aligned} \tag{6.38}$$

Following the y component from E to D, with a distance along x of 22.0 feet:

$$\begin{aligned} &\textit{Letting} \quad \Delta x'' = \textit{Lateral distance from E to point D} \\ &\textit{and} \qquad \Delta y'' = \textit{Vertical distance from E to point D} \\ &\textit{Then:} \quad \Delta y'' = \Delta x'' \frac{v_Y''}{v_X''} = 22.0 \frac{0.375\,v_B + 20.6}{27.5} = 0.30\,v_B + 16.5 \end{aligned} \tag{6.39}$$

Now $\Delta y' + \Delta y''$ = Distance from origin to point D in y direction, so:

$$\begin{aligned} &0.273\,v_B + (0.30\,v_B + 16.5) = -46.5 \\ &\textit{Solving for } v_B \textit{ gives:} \quad v_B = \frac{-63.0}{0.57} = -110 \end{aligned} \tag{6.40}$$

Thus, the initial speed of car B is 110 feet/second or 75 MPH, which agrees with the result of the first method.

(C) There are two separate collision events involved in this three car collisions. Utilizing the velocity and displacement relationships at the major events, the kinematic parameters are computed and shown in Table 6.1.

Table 6.1 Summary of Results of 3-Car Collision

Event	v′, ft/sec O – E (O – C′)	v″, ft/sec E – D (C′ – D)	displacement changes, ft		Δt, sec
			O –E	E – D	
O-E	$v_x' = 40$ $v_y' = 60$		$\Delta x' = 20$ $\Delta y' = 30$		0.5
E-D		$v_x'' = 27.50$ $v_y'' = 20.53$ $v'' = 34.30$		$\Delta x'' = 22.0$ $\Delta y'' = 16.5$ $\Delta d'' = 27.5$	0.8

The summary data can be confirmed by the drawing shown in Fig.6.15. The trajectory of the CG of the three cars if there were no collision is shown by three locations: (1) F, center of gravity of the three cars, located at A, B, and C at time zero, (2) E, center of gravity of the three cars located at A′, B′, and C′ at time $t_C = 0.5$ sec, and (3) D, center of gravity of the three cars located at A″, B″, and C″ at the final time, 1.3 sec. Location E coincides with the location where the three cars first collided, point C′. Afterwards, the three cars moved together until stopped at point D.

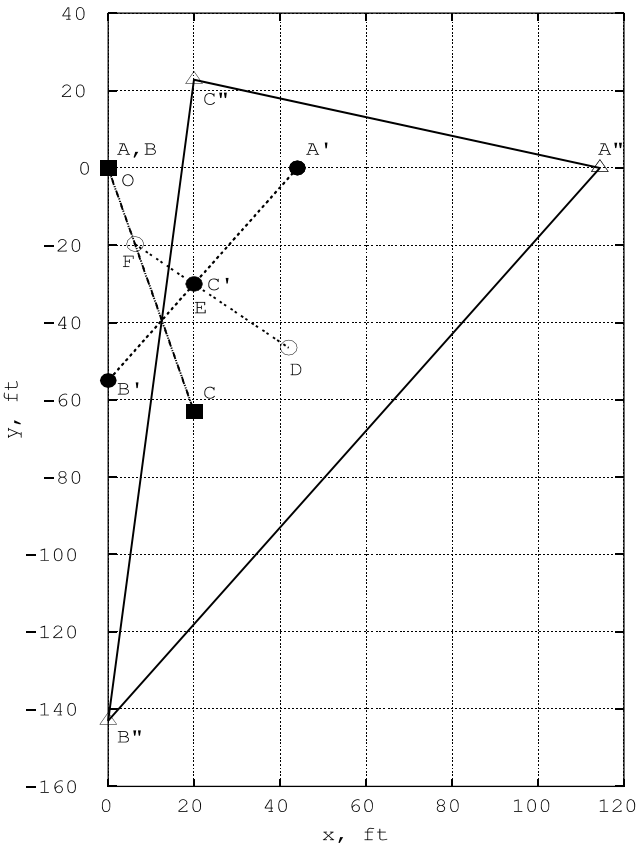

Fig. 6.15 Three-Car Collision Trajectory and CG Locations

According to the CG Motion Theorem, the CG of the three cars would move in a straight line at constant speed. The straight line shown in Fig. 6.15 is FED. The constant speed of the CG along FED can be computed as follows: $|FD| / \Delta t = 44.7/1.3 = 34.4$ ft/s. The constant speed of the CG of the three vehicles can also be computed from each of the two phases of collisions: the first phase from F to E has a constant speed of $|FE| / \Delta t_1 = 17.2$ ft / .5 s = 34.4 ft/s, and the second phase from E to D has a constant speed of $|ED| / \Delta t_2 = 27.5$ ft / .8 s = 34.4 ft/s. The constant speed of the CG of the three vehicles is the common speed of all the three vehicles involved in the collision.

6.4 IMPULSE AND CIRCLE OF CONSTANT ACCELERATION

Here we will analyze the motion of a plane (two-dimensional) rigid body acted upon by an impulsive force which lies in the plane, as shown in Fig. 6.16. The objective of this study is to analyze the instantaneous motion of the body (up to the moment at which the impulse ends). In general, the body will suffer both linear and angular accelerations, both lying in the plane of the body, during the impulse.

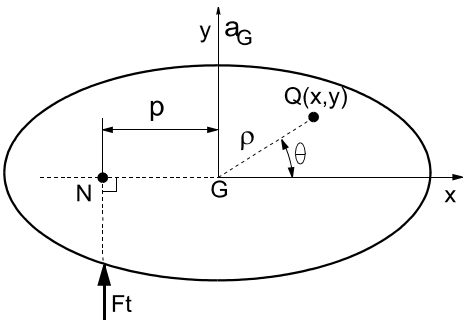

Fig. 6.16 An Impulse Acting on a Rigid Body

Due to the force, each point on the body will acquire an acceleration. The following analysis will be used to (1) derive the equations of motion of the body, (2) show that certain sets of points on the body will have the same magnitude of acceleration, and (3) obtain the equations defining these sets of points. In all cases, the sets will be found to be in the form of circles or arcs of circles, as shown in Fig. 6.17, thus the term "Circle Of Constant Acceleration." This term will be abbreviated in this analysis as COCA.

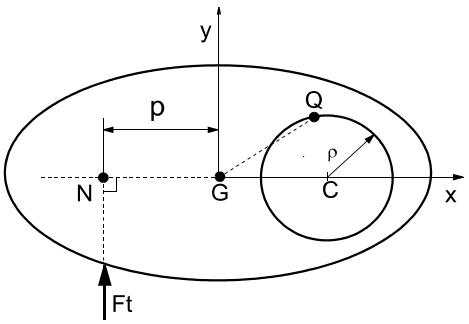

Fig. 6.17 A Point Q on a COCA

Note that once the impulse is terminated, the body will have a constant linear speed along the y-axis plus a constant angular speed about the center of mass.

Definitions of Terms:

The following terms will be used in the derivation of COCA:

m = Mass of body

G = Center of mass of the body (or center of gravity), located at the origin of the coordinate system

T = Duration of impulse

F(t) = Force (acting in the +Y direction, from $t_0 = 0$ to $t_1 = T$)

$\int F(t) \cdot dt$ = Impulse

p = Momentum arm of F about center of mass (perpendicular distance from G to the line of force)

M = Moment, which is to the force times the moment arm [$M(t) = p \times F(t)$]

Q = Any given point on body, defined by polar coordinates r and θ and by Cartesian coordinates x and y.

N= Point along line of force which lies on x-axis.

It will be assumed that the center of mass, G, is located at the origin of the coordinate system and that the body is oriented such that the impulsive force is parallel to the y-axis (see Fig. 6.18).

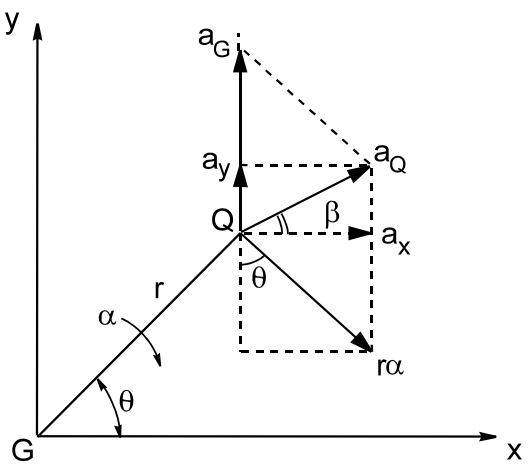

Fig. 6.18 Acceleration Components at Point Q

6.4.1 Derivation of Acceleration at Point Q

We wish to find the acceleration of an arbitrary point, Q, in the body due to the impulse and to determine the circles of constant acceleration. It is assumed that the duration is very short, such that all points on the body suffer negligible displacement during this time. The acceleration of Q in this case can be stated as follows:

$$\vec{a}_Q = \vec{a}_G + \vec{r} \cdot \vec{\alpha} \tag{6.41}$$

where a_G is the acceleration of the center of mass, r is the radial distance from G to Q, and α is the angular acceleration of Q.

The moment M_G about the center of mass G is given by:

$$\vec{M}_G = I_G \cdot \vec{\alpha} \tag{6.42}$$

where I_G is the moment of inertia of the body about the center of mass G. Setting I_G equal to mk^2, where k is the radius of gyration about G, and letting the moment be equal to F·p (Force times the moment arm) yields:

$$F \cdot p = mk^2 \cdot \alpha \tag{6.43}$$

Also, since the force is parallel to the y-axis, the force equation in the y direction can be written as: $m \cdot a_G = F$. Then, substituting for F in the preceding equation, one obtains:

$$\alpha = \frac{F \cdot p}{m \cdot k^2} = \frac{a_G \cdot p}{k^2} \tag{6.44}$$

Using the well-known relationships between Cartesian and polar coordinates, we get for the x and y components of acceleration:

$$\begin{aligned} a_x &= \alpha r \sin\theta = \frac{p a_G}{k^2} r \sin\theta \\ a_y &= a_G - \alpha r \cos\theta = a_G \left[1 - \frac{p}{k^2} r \cos\theta \right] \\ &\textit{Using the relationship:}\quad a_Q^2 = a_x^2 + a_y^2 \\ &\textit{yields}\quad a_Q^2 = a_G^2 \left[1 + \left(\frac{pr}{k^2} \right)^2 - 2 \frac{p}{k^2} r \cos\theta \right] \end{aligned} \tag{6.45}$$

Here, a_Q is the magnitude of the acceleration of point Q due to the impulse. The force F contributes to this acceleration through (1) its effect on the translational motion of the center of mass and (2) its effect on the angular motion of the body about the center of mass. Note that if p is set to zero (i.e., the force acts through the center of mass), all points Q have the same acceleration, namely, a_G.

Special Case

If Q lies at the intersection of the line of force, F, and the x-axis, then the value of r becomes equal to p and the angle θ becomes 180°. Shown in Fig. 6.19, points N and Q then coincide. Acceleration a_Q in Eq. (6.45) is then simplified to that shown in Eq. (6.46).

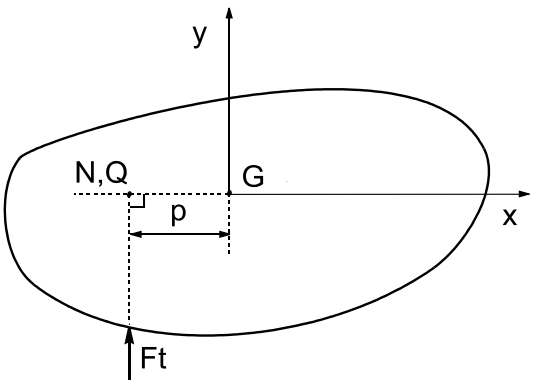

Fig. 6.19 Special Case when N and Q Coincides.

$$a_Q^2 = a_G^2\left[1 + (\frac{p^2}{k^2})^2 + 2\frac{p^2}{k^2}\right] = a_G^2\left[1 + (\frac{p}{k})^2\right]^2$$

$$a_Q = a_G\left[1 + (\frac{p}{k})^2\right], \quad a_G = a_Q\left[\frac{k^2}{k^2 + p^2}\right] \quad \ldots . \quad (1) \tag{6.46}$$

A term 'mass reduction factor' of a rigid body at point Q can be defined as follows:

$$\gamma = \frac{k^2}{k^2 + p^2} \tag{6.47}$$

Note that in any offset impact, γ is less than one, and $1/\gamma$ is greater than one. Then the acceleration at point Q is $1/\gamma$ times greater than that at G, the center of mass. The effect of the offset impact on the acceleration at point Q is equivalent to the reduction of mass by $1/\gamma$ times in the direction of impact. Thus, at point Q, the effective mass is reduced by $1/\gamma$ and the acceleration is increased by $1/\gamma$.

As an example, a mid-size light truck has a yaw radius of gyration, k, of 66 inches and a frontal width of 80 inches. The offset distance, p, of a truck in a 40% offset barrier test, described in Section 5.8.2 of Chapter 5, is equal to 20 inches. From Eq. (6.47), the mass reduction factor is $\gamma = 0.92$. Since $1/\gamma = 1.09$, the acceleration at the impacting side of the truck will be about 9 % higher than that at the CG of the truck.

6.4.2 Circle of Constant Acceleration (COCA)

Considering the set of points for which the magnitude of acceleration, a_Q, is the same, we have, from Eq. (6.45):

$$a_Q^2 = a_G^2\left[1 + \left(\frac{rp}{k^2}\right)^2 - 2\frac{rp}{k^2}\cos\theta\right] \tag{6.48}$$

Substituting x for [r cos θ], and $x^2 + y^2$] for r^2 yields:

$$c^2 = \left[1 + (x^2 + y^2)\left(\frac{p}{k^2}\right)^2 - 2x\frac{p}{k^2}\right]$$

$$\textit{where} \quad c = \frac{a_Q}{a_G} \tag{6.49}$$

Multiplying both sides of Eq. (6.49) by $(k^2/p)^2$ and rearranging terms yields:

$$\left(x - \frac{k^2}{p}\right)^2 + y^2 = \left(c\frac{k^2}{p}\right)^2 \quad \ldots\ldots\ldots\ldots\ldots\ldots (1)$$

This is the equation of a circle:

$$(x - x_c)^2 + y^2 = \rho^2 \quad \ldots\ldots\ldots\ldots\ldots\ldots\ldots (2)$$

where

$$x_c \text{ (x coordinate of center of circle)} = GC = \frac{k^2}{p} \quad .. \quad (3)$$

$$\rho \text{ (radius of circle)} = c\frac{k^2}{p}, \quad \ldots\ldots\ldots\ldots\ldots (4)$$

Substituting (3) *into* (4): $\rho = c \cdot GC \quad \ldots\ldots\ldots\ldots (5)$ (6.50)

Formula (1) of Eq. (6.50) is the equation of a circle with its center lying on the x-axis and at a distance GC = k^2/p from the center of mass; the radius of the circle is ρ = c GC, as shown in (5) of Eq.(6.50). Thus, for a given force, F (independent of the duration of the impulse), and a given moment arm, p, the moment is equal to M = F p. It will be shown in the following that the acceleration at Q, a_Q, does not depend on the force, per se, nor the moment arm, per se, but on their product, i.e., the moment M.

$$a_Q = c\,a_G = \left(\frac{\rho}{GC}\right)a_G = \left(\frac{\rho\,p}{k^2}\right)a_G \quad \ldots\ldots\ldots\ldots\ldots\ldots \quad (1)$$

$$\textit{since}\quad a_G = \frac{F}{m}, \quad \textit{and}\quad M = F\,p, \quad (1)\ \textit{becomes} \tag{6.51}$$

$$a_Q = \frac{\rho\,M}{k^2\,m} \quad \ldots\ldots\ldots\ldots\ldots\ldots\ldots\ldots \quad (2)$$

While the impulse is acting, an impulsive force imparts accelerations to all points of a plane body such that sets of points along a circular arc will have the same magnitude of acceleration. The directions of the accelerations at these points will lie along the arcs. The arcs are defined by a circle whose radius and center are given by:

$$\left(x - \frac{k^2}{p}\right)^2 + y^2 = \rho^2 \quad \ldots\ldots\ldots\ldots\ldots\ldots \quad (1)$$

From (2) *in Eq.* (6.51):

$$\rho = \frac{m\,k^2\,a_Q}{M} = \frac{I_G\,a_Q}{M} \quad \ldots\ldots\ldots\ldots\ldots\ldots \quad (2) \tag{6.52}$$

where I_G: (*mass moment of inertia about C.G.*) = $m\,k^2$

The direction of acceleration of each point is tangent to the arc of the circle at that point, as will be shown in Section 6.4.5. The net effect is an instantaneous rotation of the body about the point which is the center of the circle. The acceleration at the center of the circle, C, is equal to zero, i.e., there is no acceleration. The position of this point is (GC,0) or (k^2/p, 0).

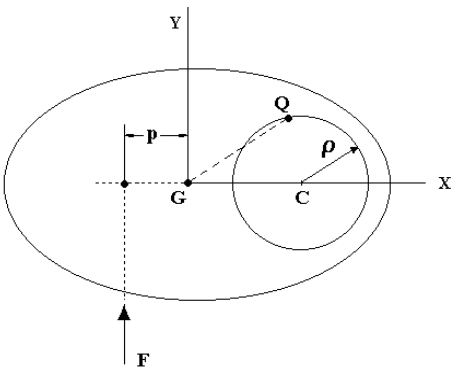

Fig. 6.20 Relationship between Impact Point and Location of COCA

6.4.3 Construction of COCA Given the Acceleration Ratio, c

The steps needed to construct the circle of constant acceleration (COCA) given the acceleration ratio, c, are shown below.

1) Define the center of circle, C, by computing the center offset distance of GC = k^2/p, and the radius of the circle ρ = c GC

2) Define the range of the x coordinate of point Q, from x_{min} (=GC - ρ) to x_{max} (=GC + ρ) as shown in Fig. 6.21.

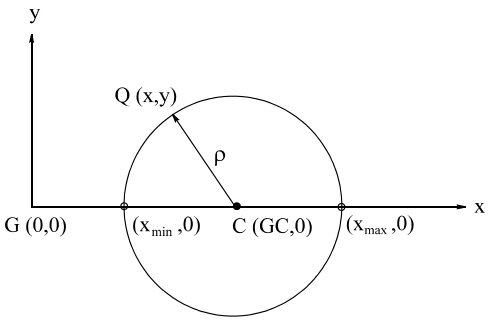

Fig. 6.21 Range of x coordinate of point Q

3) Specify the x coordinate of point Q starting from X_{min}, and compute the y coordinate of point Q using the following Pythagorean relationship:

$$y = \sqrt{\rho^2 - (GC-x)^2} \tag{6.53}$$

4) Plot the point Q with the x and y coordinates.
5) Repeat steps 3 and 4 until x_{max} is reached.

6.4.4 COCA Case Studies

Four case studies are presented in the following to determine the acceleration of a point in an object and to construct the COCA given an impulsive loading acting on the object. The four case studies are a slender rod, the moment of inertia of a uniform thin rectangular ring (frame), an impulse to the ring, and a COCA with an acceleration ratio, c.

Case Study 1: Slender Rod

A uniform slender rod is assumed to be impacted at one end in a direction normal to the rod, as shown in Fig. 6.22. It is desired to find a point, Q, on the rod such that the instantaneous acceleration is zero, i.e., where $a_Q = 0.0$. In the preceding section, it was shown that the acceleration at the center of a COCA is zero. Therefore, a point C on the x-axis at a distance k^2/p from G is the desired point. The length of the rod is L; so the impact point is L/2 units from G.

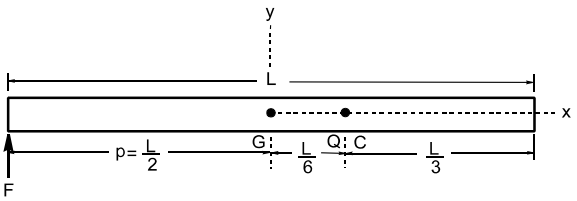

Fig. 6.22 A Slender Rod

The radius of gyration, k, is given by: $I_G = (1/12)mL^2 = mk^2$. Solving this for k^2:

$$k^2 = (1/12)L^2, \quad GC = k^2/p = (1/12)L^2/(L/2) = L/6 \tag{6.54}$$

A check can be made using Eq. (6.48). Here, r = L/6 , θ = 0° , $k^2 = (1/12)L^2$, and p = L/2.

$$a_Q^2 = a_G^2\left[1 + \left(\frac{pr}{k^2}\right)^2 - 2\left(\frac{pr}{k^2}\right)\cos\theta\right] \quad \ldots\ldots\ldots \quad (1)$$

$$a_Q^2 = a_G^2\left[1 + \left(\frac{(L/2)(L/6)}{(1/12)L^2}\right)^2 - 2\left(\frac{(L/2)(L/6)}{(1/12)L^2}\right)(1.0)\right] \qquad (6.55)$$

$$a_Q^2 = a_G^2[1.0 + 1.0 - 2.0] = 0.0$$

Case Study 2: Uniform Thin Rectangular Ring

This ring approximates a vehicle structure in a two-dimensional simplification (suppressing the z-dimension). The ring can be thought of as representing the main frame structure of a truck. The x-y plane represents the roadway. An impact is delivered to the body as shown in Fig. 6.23 at a distance p to the left of the y-axis.

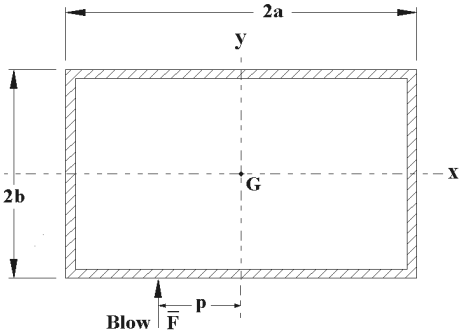

Fig. 6.23 A Rectangular Ring

First, we want to determine the value of the radius of gyration, k, for the moment of inertia about the z-axis. To obtain this moment, we will find the moments of inertia about the x-axis and the y-axis and then use the well-known theorem: $I_z = I_x + I_y$ plus the formula for a centered thin rod, given by I(thin rod, axis at center) = (1/12) mL^2. Let d be the mass per unit length of the ring.

$I_x = I_{xH}$(two horizontal segments) + I_{yV}(two vertical segments)
$I_{xH} = 2d\,(2a)\,b^2$ $\quad$ $I_{yV} = 2d(2b)(1/12)\,(2b)^2$
Combining the two terms yields: $I_x = m\,[(b^2) / (a + b)]\cdot[a + (1/3)b]$
In a similar manner we get: $I_y = m\,[(a^2) / (a + b)]\cdot[b + (1/3)a]$
Adding these two results gives $I_z = (m/3)\cdot[a + b]^2$
Setting $mk^2 = (m/3)\cdot[a + b]^2$ yields the result: $\quad k^2 = (1/3)\cdot[a + b]^2$

Case Study 3: Impulse to Ring

As an example, let us assume a ring with a = 2b and an impulse parallel to the y-axis and to the left of the center of mass (which is located at the origin). We can assign values to the moment arm, p, and ascertain the COCA for the ring.

First, let us obtain the value of k. From the preceding section, we have found that $k^2 = (a + b)^2/3$; then, using a = 2b, we get $k^2 = (3b)^2/3 = 3b^2$.

Case 1: Let p = 2b (force applied at the far end of the ring). Then, the x coordinate of the center of the circle is given by GC = $k^2/p = 3\,b^2\,/2\,b = 1.5b$. The y coordinate is, of course, y = 0.0.
The radius of the circle, COCA, is given by ρ = c (GC).
For c = 0.5 we obtain: ρ = c GC = (0.5) (1.5 b) = 0.75 b. This result is shown in Fig. 6.24.

Results for Case 1: Here a = 2 b and c = 0.5

$a_Q = 0.5\ a_P$ (c=0.5)

p = 2 b, then

GC = 1.5 b

$\rho = 0.75$ b (= c GC)

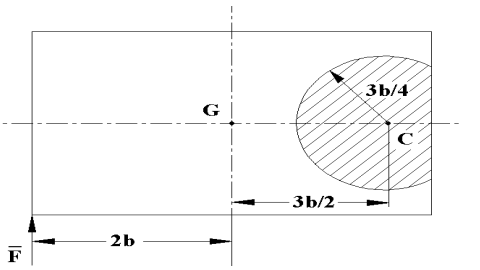

Fig. 6.24 Size and Location of COCA and Impulsive Loading (c=.5, p = 2b)

$a_Q = 0.5\ a_G$

Similarly, for

p = b, then

GC = 3 b

$\rho = 1.5$ b

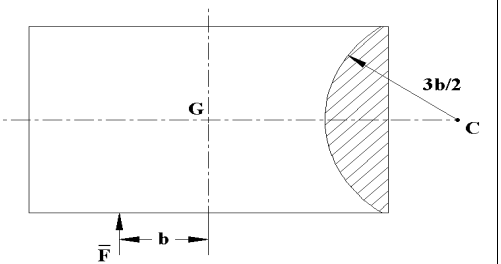

Fig. 6.25 Size and Location of COCA and Impulsive Loading (c=.5, p = b)

Case Study 4: COCA with Various Acceleration Ratios

Using the ring defined by a = 2b, the x coordinate of the center and radius of COCA for a given acceleration ratio, c, can then be computed.

Case 1:
Let p = 2b (Force applied at end of rail)
GC = $k^2/p = 3\ b^2 / 2\ b = 1.5b$
The y coordinate of the center is y = 0.
(The center is near the right hand rail)
Let $c = a_Q / a_G$

c	ρ
0.5	0.75 b
1.	1.50 b
2.0	3.00 b

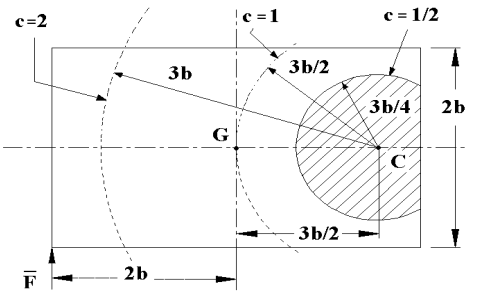

Fig. 6.26 Size and Location of COCA and Impulsive Loading (c=.5,1.,2., p = 2b)

Case 2:
Let p = b (Force applied at half way between center and end of rail)
GC = $k^2/p = 3\ b^2 / b = 3b$.
The y coordinate of the center is y = 0.
(The center is beyond the right hand rail)
Let $c = a_Q / a_G$

c	ρ
0.5	1.50 b
1.0	3.00 b
2.0	6.00 b

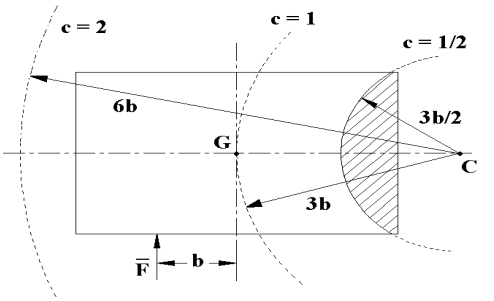

Fig. 6.27 Size and Location of COCA and Impulsive Loading (c=.5,1.,2., p = b)

6.4.5 Determination of the Direction of Acceleration, a_Q

The direction of acceleration, a_Q, shown in Fig. 6.28, is perpendicular to the radius of the circle. It is also tangent to the COCA at point Q. The proof is given in Eq. (6.56).

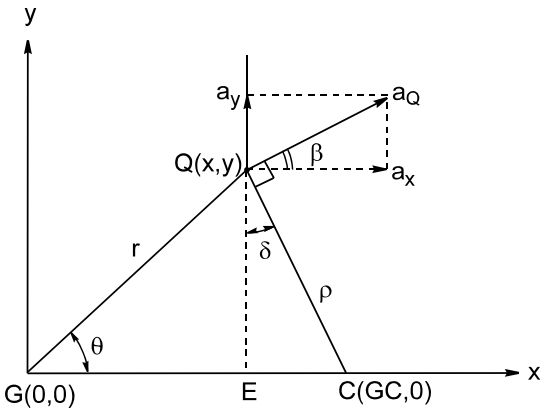

Fig. 6.28 Direction of Acceleration, a_Q

Let β *be the horizontal angle of* a_Q, *then* $\tan\beta = \dfrac{a_y}{a_x}$ . . . . . (1)

Substituting for a_x, a_y *from Eq.* (6.45)

and using $\dfrac{k^2}{p} = GC$, $x = r\cos(\theta)$, $y = r\sin(\theta)$ *in* (1) *yields*: (6.56)

$\tan\beta = \dfrac{GC - x}{y}$, *and since* $\tan\delta = \dfrac{GC - x}{y}$, $\beta = \delta$.

Since a_x *is perpendicular to QE,* a_Q *is also perpendicular to QC, the radius of the circle.*

6.4.6 COCA Evaluation of Impact Severity

The impact severity of a vehicle subjected to side, frontal, and offset impulsive loadings can be examined by the use of COCA. Under the same impulsive loading to the vehicle, different locations in the vehicle would bear different acceleration magnitudes and different acceleration directions. By plotting the acceleration magnitudes and directions, it becomes easy to compare the impact severity at any point on the vehicle.

Since the COCA method is based on the analysis of a linear system subjected to a concentrated load, it is applicable to distributed loading using the superposition technique. Therefore, offset impact severity can be analyzed by the COCA method.

In developing an air bag crash sensor system, judging the impact severity at any point on the vehicle can be expedited by examining the COCA for the magnitude and direction.

Fig. 6.29 shows a vehicle subjected to a concentrated loading at the right front corner similar to the tree impact accident described in Section 1.8 of Chapter 1. There are three COCA's with acceleration ratios (c) of 0.7, 1.0, and 1.3. The outer circle, having a c of 1.3, passes through point N on the right side of the vehicle, and the inner circle, having a c of 0.7, passes through a point opposite to N on the left side. The middle circle, having a c of 1.0, simply passes through the CG of the vehicle. Note that from the similar triangles, the ratio of acceleration at point N to that at CG is equal to the ratio of the distance from N to C (center of circle where acceleration equals zero) to the distance from G (CG) to C as shown in Fig. 6.29.

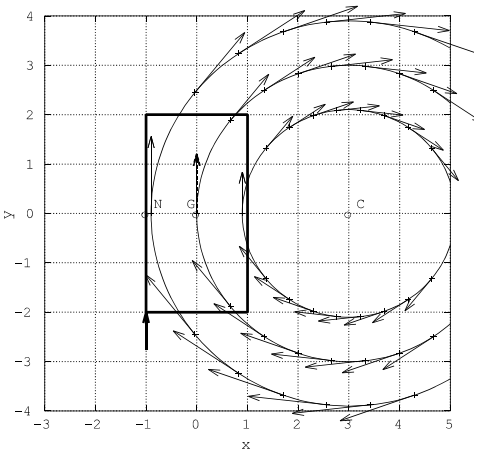

Fig. 6.29 Right Front Impact and COCA with c=0.7, 1, and 1.3 (k^2=3, p=1)

Even though the impact velocity (based on the flight recorder data) is low, the crash sensor located in the right hand side (on the same side as the impulsive loading) near point N in Fig. 6.29 was activated. This is evident from the outer COCA plot which shows that the acceleration at point N is relatively high, 30 % higher than that at the CG and 2 times higher than that at the opposite side.

If the crash sensor were located on the opposite side of the impulsive loading, the acceleration at the sensor location would be low relative to that of the CG, and the crash sensor might not be activated. This type of accident scenario does happen and has been observed in a real world accident.

An L-type left front side impact and COCA's with acceleration ratios of 0.5, 1.0, and 2.0 are shown in Fig. 6.30. The procedures needed to draw the respective COCA's are presented in the following section. At point N, located at a distance NC from the center of the circle and on the same side as the loading, the acceleration is twice that at the CG. Note that the direction of acceleration at point N is parallel to that of the impulsive loading.

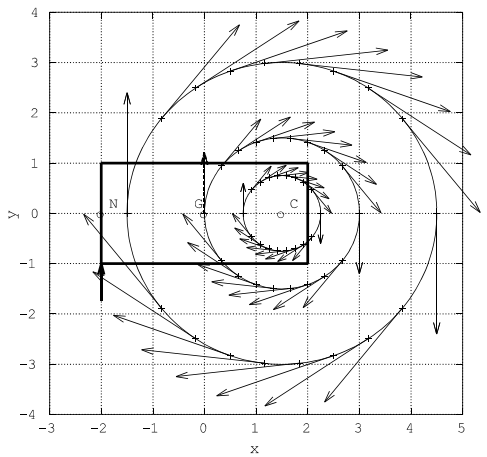

Fig. 6.30 L-Type Side Impact and COCA with c=0.5, 1, and 2 (k^2=3, p=2)

6.4.7 Given the Coordinates of Point Q, Find the Acceleration Ratio c

Given the radius of gyration squared, k^2, the offset distance, p, and the coordinates of point Q (x_Q, y_Q), the steps needed to compute the acceleration ratio, c, and the COCA's are shown as follows:

1) Compute the following:

$$GC = \frac{k^2}{p}, \qquad \theta = \tan^{-1}\frac{y_Q}{x_Q}$$
$$r_Q = \sqrt{x_Q^2 + y_Q^2}, \qquad \rho = \sqrt{(GC - x_Q)^2 + y_Q^2} \tag{6.57}$$

2) Compute the acceleration ratio, c

$$c = \frac{a_Q}{a_G} = \frac{\rho}{GC} \tag{6.58}$$

3) Specify the x and y coordinates of point Q starting from x_{min} as shown in Fig, 6.21, and compute y coordinate of point Q using the following Pythagorean relationship:

$$y = \sqrt{\rho^2 - (GC - x)^2} \tag{6.59}$$

Define the range of the x coordinate of point Q that is from x_{min} (= GC - ρ) to x_{max} (= GC + ρ).

4) Plot the point Q using the x and y coordinates (starting from x_{min}).

5) Compute β (horizontal angle) of a_Q shown in Eq. (6.56) and plot the acceleration of a_Q.

6) Repeat steps 3 and 5 until x_{max} is reached.

Shown in Fig. 6.31 is a sketch of an L-type side impact where the coordinates of the right rear seat, Q_1 (1.0,0.5), and right front seat, Q_2 (-1.0,0.5), are given. To construct the COCA passing through each one of the two points, the procedures described in this section are followed. The acceleration ratio, c, equals ρ/GC and the direction of the acceleration, tangent to the circle at the respective point Q, is shown in the drawing. The magnitude of acceleration on the Q_1 circle is about 3.7 times (Q_2C/Q_1C) smaller than that on the Q_2 circle.

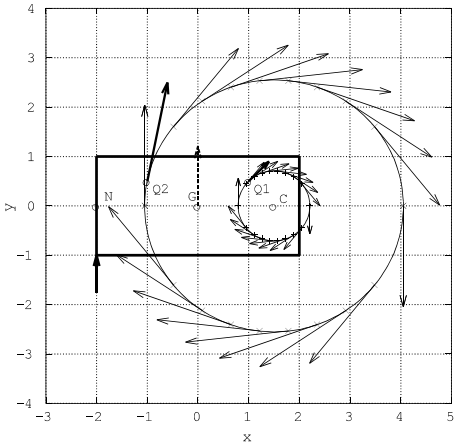

Fig. 6.31 L-Type Side Impact and COCA with Q_1(1, .5) and Q_2(-1, .5)

6.4.8 Distributed Loading by Superposition

From Eq. (6.46), the acceleration at point Q is a linear function of the acceleration at point G. By the principle of superposition, the distributed loading then becomes a linear combination of the concentrated loadings.

Fig. 6.32 and Fig. 6.33 show the impulsive loadings acting at the right front and right near-center of the vehicle. For each impulsive loading, two COCA's, passing through points Q_1 and Q_2 at the left and right sides of the vehicle, are shown.

The resultant of the right front and right near-center loadings is shown in Fig. 6.34. Two COCA's due to the resultant loading are shown passing through points Q_1 and Q_2, at the left and right sides of the vehicle.

Fig. 6.35 shows a distributed loading consisting of the two individual impulsive loadings. The resultant loading is shown in the middle of the two. The resultant output accelerations at points Q_1 and Q_2 are seen to be the resultants of the two output component accelerations at points Q_1 and Q_2, respectively.

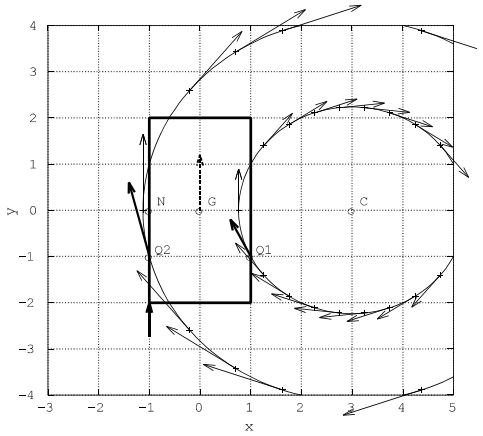

Fig. 6.32 Right Front Impact and COCA with $Q_1(1, -1)$ and $Q_2(-1, -1)$

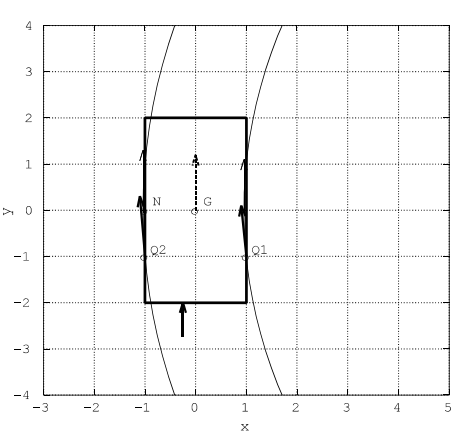

Fig. 6.33 Left Near-Center Impact and COCA with $Q_1(1, -1)$ and $Q_2(-1, -1)$

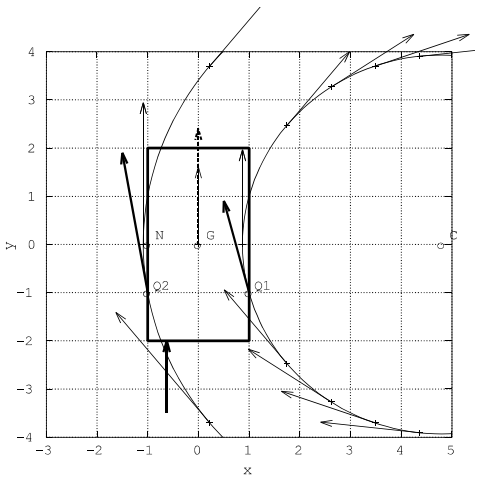

Fig. 6.34 Right Front Impact with Resultant Force of Right Front and Front Center

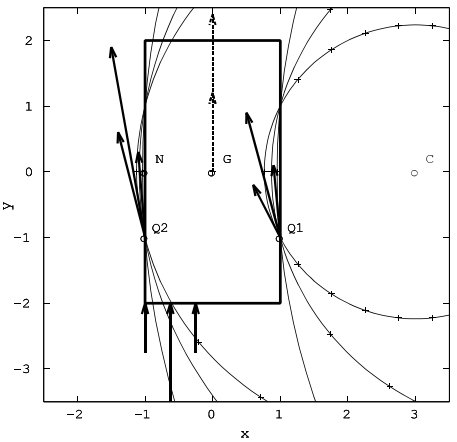

Fig. 6.35 Right Front Distributed Impact ($p=p_1+p_2$) and COCA

6.5 PRINCIPLE OF WORK AND ENERGY

The principle of work and energy is obtainable from Newton's Second Law. Its derivation and relationship to the kinetic energy, elastic, and gravitational potential energy, and the work done by external forces (shown in Fig. 6.36), including the frictional force, are shown in Eq. (6.60). It should be noted that the normal force ΣF_n along direction n is perpendicular to the path. The normal force does no work since it does not produce any displacement of the mass along n.

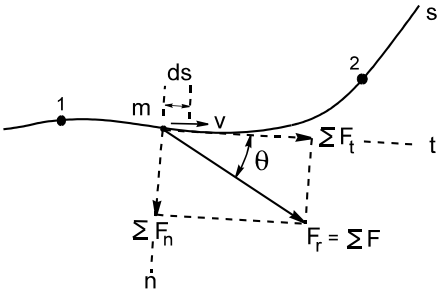

Fig. 6.36 Work by a Force

$$
\begin{aligned}
&n\,(normal): \quad \sum F_n \quad \textit{does no work} \\
&t\,(tangential): \sum F_t = ma_t, \quad \sum F\cos\theta = ma_t, \quad \textit{where } a_t = v\frac{dv}{ds} \\
&\textit{Then}: \quad \sum F\cos\theta\, ds = mv\, dv \\
&\sum \int_{s1}^{s2} F\cos\theta\, ds = \int_{v1}^{v2} mv\, dv = \frac{1}{2}mv_2^2 - \frac{1}{2}mv_1^2 \qquad (6.60) \\
&\textit{Let} \quad T_i = \frac{1}{2}mv_i^2 \;\ldots\; \textit{Kinetic energy at position } i \\
&\textstyle\sum U_{1\text{-}2}: \textit{ work done by all the forces from position 1 to 2} \\
&\textstyle\sum U_{1\text{-}2} = T_2 - T_1, \quad \textit{or} \quad T_1 + \sum U_{1\text{-}2} = T_2 \quad \ldots\ldots\ (1)
\end{aligned}
$$

$$
\begin{aligned}
&\textit{Generalizing} \quad \textstyle\sum U_{1\text{-}2} = W_f + E_g + E_e + E_f, \quad \textit{where} \\
&\qquad W_f\textit{: work done by external force} \\
&\qquad \Delta E_g\textit{: gravitational potential energy change} \\
&\qquad \Delta E_e\textit{: Elastic potential energy change} \\
&\qquad E_f\textit{: frictional energy loss} \qquad (6.61) \\
&\textit{Note: Use appropriate signs for the work and energy components} \\
&\qquad \textit{If } W_f \textit{ and } E_f \textit{ are absent, then} \\
&\qquad \Sigma U_{1\text{-}2} = U_1 - U_2 = \Delta E_g + \Delta E_e \\
&\qquad T_1 + \Sigma U_{1\text{-}2} = T_1 + U_1 - U_2 = T_2 \\
&\qquad \textit{or} \quad T_1 + U_1 = T_2 + U_2 \;\ldots\ldots\ldots\ldots\ldots\ (1)
\end{aligned}
$$

The relationship shown by formula (1) of Eq. (6.61) is referred to as the conservation of energy. There is no energy loss between events 1 and 2. Therefore, the energy at the i^{th} position, $T_i + U_i$, is conserved.

6.5.1 Applications using Principle of Impulse, Momentum, and Energy

Case Study 1: Calculate the stopping distance, x_s, of a car skidding to a stop, with an initial velocity of v on a pavement with a kinetic coefficient of friction, μ.

Between positions 1 and 2, there are no changes in elastic and gravitational energies and no work done by the external forces. Therefore, applying the energy formula (1) of Eq. (6.60) yields the relationship between the kinetic energy and energy lost due to frictional force. The computations are shown in Eq. (6.62).

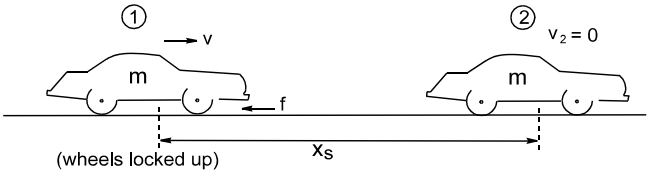

Fig. 6.37 Vehicle Skidding to Stop

$$T_1 = \frac{1}{2}mv^2 \qquad \Sigma U_{1\text{-}2} = -f \cdot x_s = -(\mu mg) \cdot x_s \quad \textit{where}$$

$$T_2 = \frac{1}{2}mv_2^2 = 0 \qquad f\textit{: maximum kinetic frictional force}$$

$$\therefore \quad \frac{1}{2}mv^2 - \mu mgx_s = 0, \quad x_s = \frac{v^2}{2\mu g} \tag{6.62}$$

$$\textit{For} \quad v = 100\,km/h, \quad m = 1000\,kg, \quad \mu = .5$$

$$\textit{one gets} \quad x_s = 78.7\ m$$

$$\textit{NOTE for the conventional units: } v\textit{: mph }, x_s\textit{: ft,}$$

$$x_s = \frac{1}{\mu}\left(\frac{v}{5.5}\right)^2 \quad \textit{or} \quad v = 5.5\sqrt{\mu x_s}$$

Case Study 2: Shown in Fig. 6.38 are two cars, A and B, each having a weight of 4000 lb, that collide on an icy pavement at an intersection. The direction of motion of each car after collision is determined from the snow tracks. The driver in car A states that he was going at the posted speed of 30 mph just before the collision; he applied the brakes and his car skidded 10 feet in the direction shown. Determine the speed of car B just before the collision. The kinetic coefficient of friction is assumed to be 0.15.

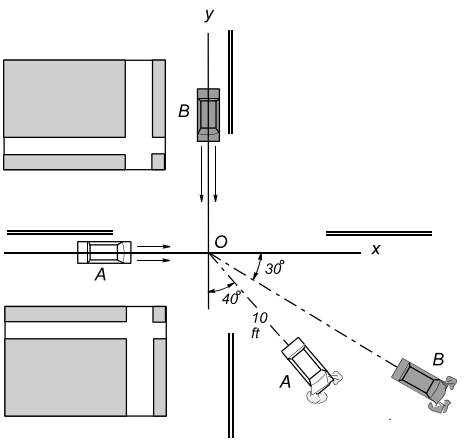

Fig. 6.38 Collision at an Intersection

Defining events: $0 \rightarrow 1$: collision, $1 \rightarrow 2$: skidding

v_{A0} (velocity of car A before collision) = 30 mph = 40 ft/s

v_{A1} : separation velocity of car A after collision

v_{B0} (velocity of car B before collision)

v_{B1} : separation velocity of car B after collision

In accident reconstruction, the skidding information from event 1 to 2 is utilized in the energy formula to compute the separation velocity of car A, v_{A1}, as shown in Eq. (6.63). Since the collision occurs on the icy surface, the external impulse to the system of two cars is negligible. Therefore, applying the conservation of momentum from event 0 to 1, the velocity of car B, v_{B0}, before impact can then be computed.

$$
\begin{aligned}
&\textit{Masses of cars A and B are: } m_A = m_B = \frac{4000\,lb}{32.2\,ft/s} = 124\,slugs \\
&A\,(\textit{Energy}): \quad 1 \rightarrow 2\,(\textit{skidding phase}): \quad T_1 + \Sigma U_{1-2} = T_2\,, \\
&\quad \frac{1}{2}(124)v_{A1}^2 - 4000\,(.15)(10) = 0, \\
&\quad \therefore \quad v_{A1} = 9.84\,ft/s = 6.71\,mph \\
&A \text{ and } B\,(\textit{Momentum}): \quad 0 \rightarrow 1\,(\textit{collision phase}): \\
&\quad x: \; 124(44) + 0 = 124(9.84\sin 40°) + 124(v_{B1}\cos 30°) \\
&\quad \therefore \quad v_{B1} = 43.5\,ft/s \\
&\quad y: \; 0 + 124(v_{B0}) = 124(9.84\cos 40°) + 124(43.5\sin 30°) \\
&\quad \therefore \quad v_{B0} = 29.3\,ft/s = 20\,mph
\end{aligned}
\tag{6.63}
$$

Case Study 3: Vehicle-to-Barrier (VTB) Impact

Using the principle of work and energy, derive the relationship between the dynamic crush, barrier impact speed, and the circular natural frequency of the vehicle system.

Just before the vehicle contacts the rigid barrier, its velocity is v_0 , as shown in position 1 of Fig. 6.39. During the collision (from position 1 to position 2), there are no changes in the gravitational potential energy and no frictional energy loss. The conservation of energy applies to the system, which involves only the kinetic energy and the elastic potential energy. Note that at position 2, the vehicle stops momentarily against the rigid barrier before it rebounds.

The parametric relationships for the VTB impact, shown in Eq.(6.64), are special cases of those derived in Section 4.9.1.1 of Chapter 4 for the underdamped Kelvin model.

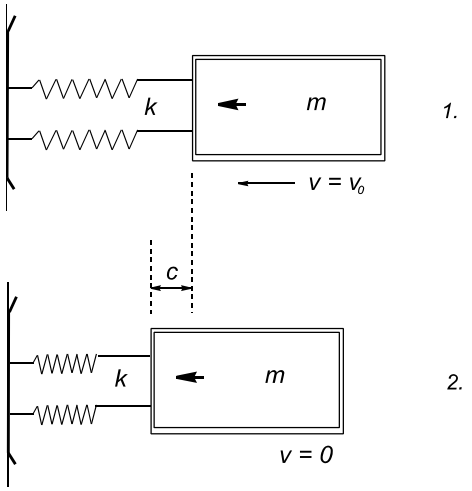

Fig. 6.39 A Spring-Mass Impact Model

The parametric relationships shown in (1) and (2) of Eq. (6.64) are the same as those derived by Newton's Second Law, shown in Section 4.5.1 of Chapter 4.

$$
\begin{aligned}
&T_1 + U = T_2 + U_2, \quad \frac{1}{2}mv_0^2 + 0 = 0 + \frac{1}{2}kc^2 \\
&\textit{therefore} \quad v_0 = \sqrt{\frac{k}{m}}\,c, \quad \textit{Let } \omega_n = \sqrt{\frac{k}{m}} \quad \ldots \quad \textit{natural frequency} \\
&\therefore \quad v_0 = c\omega_n \quad \ldots\ldots\ldots\ldots\ldots\ldots \quad (1) \\
&\textit{Now} \quad F = kc \quad (F\text{: peak force at } c, \textit{ dynamic crush}) \\
&\therefore \quad \frac{1}{2}mv_0^2 = \frac{1}{2}kc^2 = \frac{1}{2}Fc, \quad \textit{or} \quad mv_0^2 = Fc \\
&\therefore \quad a \ (\textit{peak accel.}) = \frac{F}{m} = \frac{v_0^2}{c} = v_0\omega_n \quad \ldots\ldots \quad (2)
\end{aligned}
\tag{6.64}
$$

6.5.2 Drop Test and Impact Using a Spring Having Finite Weight

The effects of the weight of a spring in drop tests and horizontal impacts on the major dynamic responses are examined in this section.

6.5.2.1 *Drop Test on a Weightless Spring*

A block is released from rest at a height of h above a vertical weightless spring having a spring constant of k, as shown in Fig. 6.40. Derive a formula for the maximum deformation of the spring.

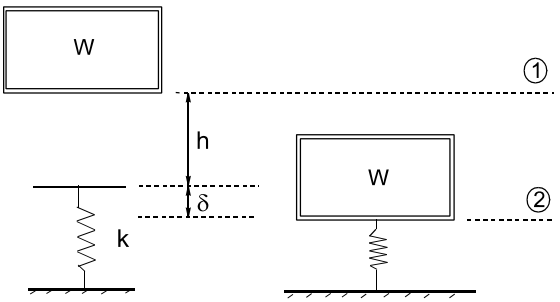

Fig. 6.40 A Drop Test on a Weightless Spring

This problem can be solved by the application of the law of conservation of energy to the system. We will obtain the kinetic and potential energy at the start, when the block is at rest above the spring, and at the end, when the block is at its lowest point. Dissipative forces will be excluded from consideration. This yields the following equations:

$$
\begin{aligned}
&\textit{Block weight}: W, \quad \textit{Height}: h, \quad \textit{Spring constant}: k \\
&\textit{At the start (position 1):} \\
&\quad \textit{Kinetic Energy}, \quad T_1 = 0.0 \quad (\textit{Block at rest, before falling}) \\
&\quad \textit{Potential Energy}, \quad U_1 = 0.0 \quad (\textit{Assumed zero potential level}) \\
&\textit{At the bottom (position 2):} \\
&\quad \textit{Kinetic energy}: \quad T_2 = 0.0 \quad (\textit{Block reaches zero speed}) \\
&\quad \textit{Potential Energy}: \quad U_2 = -W(h + \delta) + \frac{k}{2}\delta^2
\end{aligned}
\tag{6.65}
$$

Equating the total energy at the start and end (potential and kinetic) yields:

$$T_1 + U_1 = T_2 + U_2$$
$$0.0 + 0.0 = 0.0 - W\cdot(\delta + h) + \frac{k}{2}\delta^2 \tag{6.66}$$

which is a quadratic in δ and can be rearranged as follows:

$$\delta^2 - \frac{2\cdot W}{k}\delta - \frac{2\cdot W}{k}h = 0.0$$
$$\textit{Define the static deflection of the spring: } \delta_s = \frac{W}{k}$$
$$\textit{Substituting gives: } \delta^2 - 2\delta_s\delta - 2\delta_s h = 0.0, \textit{ yielding:} \tag{6.67}$$
$$\delta = \delta_s\left[1 + \sqrt{1 + \left(2\frac{h}{\delta_s}\right)}\right]$$

Given the values of W = 5 lbs, h = 3.0 feet and k = 20 lbs/ft, δ_S = 5/20 = 0.25 ft. Substituting this in the above equation gives for the maximum deformation δ = 1.5 feet or 6 δ_S.

6.5.2.2 *Drop Test Using a Spring Having Finite Weight*

Let us repeat the drop test, but now assume that the bar has appreciable mass, W_b, as shown in Fig. 6.41. The uniform bar-mass model is represented by a spring-mass model shown in Fig. 6.42. The spring mass is uniformly distributed along the length of the spring and has a finite weight, W_s = W_b .

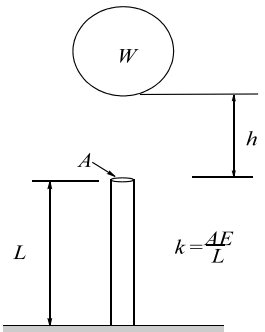

Fig. 6.41 Vertical Bar in Drop Test

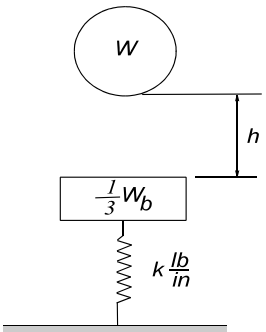

Fig. 6.42 Equivalent Spring in Drop Test

First, it should be noted that the spring mass will contribute to the kinetic energy during deflection of the spring, since each differential element of mass along the length will move downward with some kinetic energy during the deflection. This will decrease the potential energy of the system. The uppermost element of mass will move the same amount as the block, since it is immediately below it. The next element will move slightly less, etc. The lowest element will not move at all, since it is contiguous with the base of the spring.

Second, the block, upon falling through a height and gaining speed, now impacts another mass (the spring) and the change in speed upon impacting the spring needs to be ascertained using the principle of conservation of momentum [1].

The derivation of the equations involved in this process is covered in an article by Spotts [2]. Spotts develops an equivalent mass of the spring, accounting for the different amounts of movement of the mass elements in the spring during deflection. This equivalent mass is 1/3 of the spring mass and it is then assumed that the spring has no mass and an "effective" mass is mounted on top of the spring as a lumped mass. That is, the original spring is replaced by a weightless spring and on top of this spring is attached a block having 1/3 the original weight of the spring.

First, the speed of the block at the point of contacting the spring, v_h, must be determined. This is obtained in the same manner as above, equating the total energy at the start (at height h) and at the end (when contacting the spring):

$$0.0 + 0.0 = -Wh + \frac{W}{g}\frac{v_h^2}{2}$$
$$\textit{This yields:}\quad v_h = \sqrt{2gh} \tag{6.68}$$

Next, apply the conservation of momentum to the system of block and lumped mass at the time the two make contact. The spring weight will be defined as W_S . It will be assumed that the impact is totally inelastic (e = 0). The two masses then move as one at a common velocity of v_S:

$$\frac{W}{g}\cdot v_h = \left(\frac{W}{g} + \frac{W_S}{3g}\right)v_S. \quad \textit{Solving for } v_S \textit{ yields:}$$
$$v_S = \frac{W}{W + W_S/3}v_h \tag{6.69}$$

The kinetic energy of the combined masses will now be:

$$K.E. = \frac{(W + W_S/3)}{2g}v_S^2 = \frac{(W + W_S/3)}{2g}\frac{W^2}{(W + W_S/3)^2}(2gh) = \frac{W}{(W + W_S/3)}(Wh) \tag{6.70}$$

Note that the kinetic energy is less than that just prior to collision (Wh). This is a necessary result whenever there is an inelastic collision, where a portion of the energy is lost to heat and deformation.

The maximum deflection of the spring, δ, can now be determined by equating the total energy at the top of the spring and at the point where the masses come to a stop at a distance δ down from the top:

$$\textit{At the top:}\quad \textit{Kinetic Energy} = \frac{W}{(W + W_S/3)}(W\cdot h)$$
$$\textit{Potential Energy} = 0.0 \quad (\textit{Assumed zero potential level})$$
$$\textit{At the bottom: Kinetic Energy} = 0.0 \quad (\textit{Block reaches zero speed}) \tag{6.71}$$
$$\textit{Potential Energy:} = -(W + W_S/3)\cdot\delta + \frac{k}{2}\delta^2$$

Equating the energies:

$$0.0 + \frac{W^2}{(W + W_S/3)}\cdot h = -(W + W_S/3)\,\delta + \frac{k}{2}\delta^2 \tag{6.72}$$

This, again, is a quadratic in δ and can be solved in the same manner as before. The result is:

$$\delta = \delta_S\left[1 + \sqrt{1 + \frac{2h}{\delta_{SS}}}\right] \tag{6.73}$$

where δ_S is the static deflection of the spring produced by the block, W ($\delta_S = W/k$), and δ_{SS} is the static deflection produced by the combined weights W and $W_S/3$.

$$\delta_{SS} = \frac{W + W_S/3}{k} \tag{6.74}$$

Eq. (6.73) differs from the case without spring mass only in that the term in the denominator, δ_{ss}, appears in place of the term δ_S . Since the combined mass will give a greater deflection, this term is larger than δ_S and, hence, the maximum deflection, δ ,will be smaller for the case with spring weight.

Using the data supplied (W = 5 lb, W_s = 9 lb, and K = 20 lb/in, h = 3 ft), we obtain

$$\begin{aligned} &\delta_S = 5/20 = 0.25 ft \\ &\delta_{SS} = (5 + 9/3)/20 = 0.4 \\ &\delta = 0.25(1 + \sqrt{1 + 2 \cdot 3/0.4}) = 0.25(5) = 1.25 = 5\delta_S \end{aligned} \tag{6.75}$$

The deformation with a nonzero spring weight is seen to be less than that without any spring weight: 1.25 ft versus 1.50 ft. This is expected since a portion of the block initial kinetic energy is converted to heat, energy that would have otherwise been used to deform the spring.

The formula for the dynamic deflection, δ, can be rearranged as follows:

$$\begin{aligned} &since \quad \delta_{SS} = \frac{W + W_S/3}{k}, \quad and \quad \delta_S = \frac{W}{k}, \; then \quad \delta_{SS} = \left(1 + \frac{1}{3}\frac{W_S}{W}\right)\delta_S, \\ &and \quad \delta \; becomes \; \delta = \delta_S\left[1 + \sqrt{1 + \frac{2h}{\delta_S}\frac{1}{\left(1 + \frac{1}{3}\frac{W_S}{W}\right)}}\right] = \delta_S[DAF] \end{aligned} \tag{6.76}$$

The expression in the bracket is referred to as the dynamic amplification factor [DAF]. The minimum value of DAF is two which occurs when h = 0. Although the drop height is zero, however, due to sudden dynamic loading, the dynamic deflection is equal to two times the static deflection.

G-Force Loading Due to Impact

The maximum deceleration, a, due to the impact occurs at the maximum deflection, δ.

$$\begin{aligned} &Since \; \delta = \delta_S[DAF], \quad \ldots\ldots\ldots \quad (1) \\ &and \quad \delta_S = \frac{W}{k} = \frac{m}{k}g, \\ &Substituting \; \delta_S \; into \; (1) \; and \; rearrange, \; we \; get \\ &\frac{\delta k}{m} = [DAF]\, g, \\ &but \quad \frac{\delta k}{m} = \frac{f}{m} = a, \quad therefore \\ &acceleration \; loading: \quad a = [DAF]\, g \end{aligned} \tag{6.77}$$

6.5.2.3 *Horizontal Impact on a Bar/Spring*

The initial horizontal impact velocity of the weight on the bar is v_a, as shown in Fig.6.43. After impact, the combined impactor weight and the effective bar (or spring) weight move at the common velocity of v_S (see the spirng equivalent of the bar shown in Fig. 6.44). The maximum deflection can then be computed:

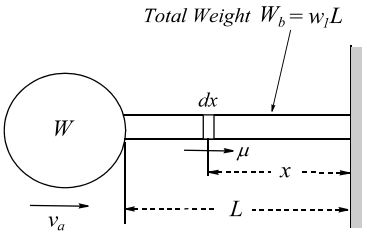

Fig. 6.43 A Bar Struck By a Weight

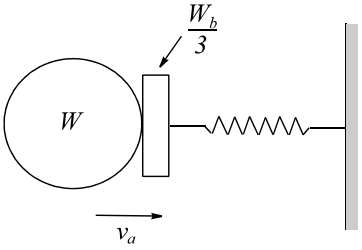

Fig. 6.44 Spring Equivalent of a Struck Bar

Kinetic energy upon impact: $K.E. = \frac{1}{2}(W + W_S/3)\, v_S^2$, *and* $v_S = \frac{W}{W + W_S/3}\, v_a$

Potential energy due to spring compression is $P.E. = \frac{1}{2} k \delta^2$,

since $K.E. = P.E.$, *one gets* $\delta = \frac{1}{\left(1 + \frac{1}{3}\frac{W_S}{W}\right)} \frac{v_a}{\omega}$, *where* $\omega = \sqrt{\frac{k}{W} g}$ (6.78)

and $\frac{v_a}{\omega}$ *is the dynamic crush of the system with a weightless spring.*

6.5.2.4 *Vertical Impact on a Beam/Spring*

It can also be shown that in a vertical drop test where a block impacts on a horizontal free-supported beam, the effective spring weight is 17/35 of the weight of the bar (Figs. 6.45 and 6.46). Compared to the impact on the vertical bar (or spring), a smaller portion of the initial kinetic energy is converted to deform the horizontal beam.

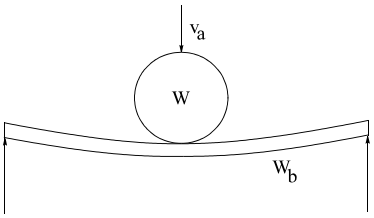

Fig. 6.45 Impact on a Horizontal Beam

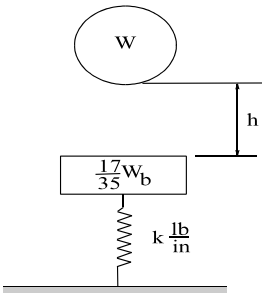

Fig. 6.46 Spring Equivalent of a Struck Horizontal Bar

6.5.3 Rebound Criterion in a Two-Mass Impact

Two test setups, shown in Figs. 6.47 and 6.48, are used to analyze the separation kinematics between the impactor and component. In both cases, one vertical and the other horizontal, we will derive the relationship between the mass ratio and coefficient of restitution such that immediately after separation, both objects move in the same direction.

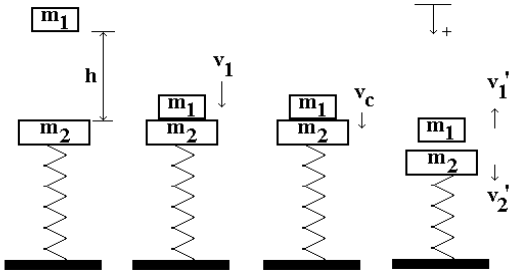

Fig. 6.47 A Drop Tower Test

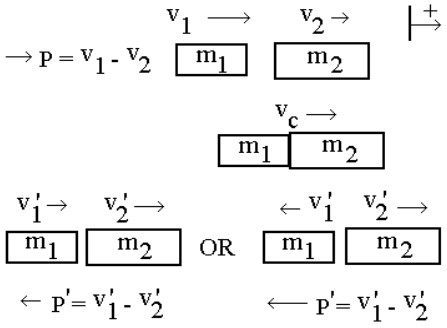

Fig. 6.48 Two Car Collision and Separation

The drop height of an impactor, m_1, is h, as shown in Fig. 6.47. The horizontal impact velocity is v_1, as shown in Fig. 6.48. e is defined as the coefficient of restitution (COR).
Find: the separation velocity, v_1', of m_1 after impact and with the condition of not rebounding.
Let v_1: initial impact velocity
v_c: common velocity of m_1 and m_2 after contact
v_1', v_2': rebound velocities of m_1 and m_2, respectively

$$\textit{Momentum:} \quad m_1\bar{v}_1 = (m_1+m_2)\bar{v}_c$$

$$\therefore \quad v_c = \frac{m_1}{m_1+m_2}v_1 = \frac{r_m}{1+r_m}v_1 \qquad \ldots\ldots\ldots\ldots \quad (1)$$

$$\textit{where } v_1 = \sqrt{2gh} \qquad \textit{and} \qquad r_m = \frac{m_1}{m_2}$$

$$\textit{c.o.r.} \qquad e = \frac{\bar{v}_1'-\bar{v}_c}{\bar{v}_c-\bar{v}_1} = \frac{v_1'-v_c}{v_c-v_1} \qquad (6.79)$$

$$\textit{therefore} \quad v_1' = v_c + e(v_c-v_1) \qquad \ldots\ldots\ldots\ldots \quad (2)$$

$$(1) \rightarrow (2) \textit{ and rearrange}: \quad \frac{v_1'}{v_1} = \frac{r_m-e}{1+r_m} \qquad \ldots\ldots \quad (3)$$

$$\textit{For a rebounding } m_1, \quad \frac{v_1'}{v_1} < 0 \quad \textit{or} \quad r_m < e \qquad \ldots (4)$$

$$\textit{For } m_1 \textit{ not rebounding backward}: \quad r_m \geq e \qquad \ldots\ldots \quad (5)$$

The separation velocity ratio shown in (3) of Eq. (6.79) is plotted and shown in Fig. 6.49. The shaded section in the plot is bounded by both the mass ratio and coefficient of restitution ranging from 0 to 1. In this shaded section, the separation velocity ratio is negative.

Case Study(exercise) In the example in Section 6.5.2.2 on the "Drop Test Using a Spring Having Finite Weight," we assumed that the striking mass, W, would stick with the struck mass, W_S, until the time that both masses reach the maximum deformation, δ. To ensure that the striking mass does not rebound upward at the time of separation, what is the maximum e (coefficient of restitution) allowed between the two masses? [Ans.: $e \leq 3W/W_S$]

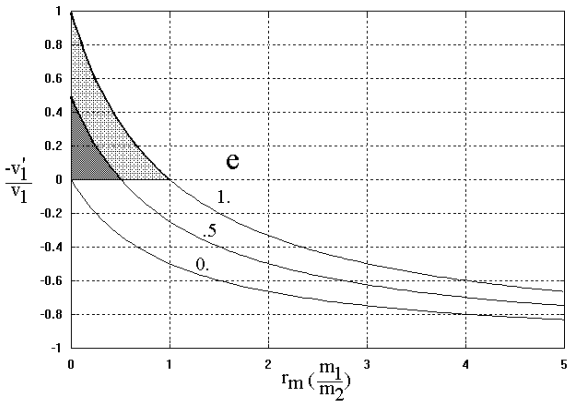

Fig. 6.49 Two-Particle Impact Rebound Condition

6.5.4 Separation Kinematics in a Multi-Mass Impact

In laboratory component impact tests, such as those of windshield breakage or body mounts, it is imperative to be able to reproduce the transient decelerations observed in actual crash tests. However, unwanted signals often appear in the component tests. As an example, repetitive loading due to multiple impacts between the striking object (impactor) and the struck object often produces an additional signal following that due to the first impact.

The problem of repetitive loading is often caused by a mismatch of the coefficients of restitution (COR) and the mass ratios among the impactor, test component, and supporting fixture. To control the repetitive loading on an object, the separation kinematics of that object has to be understood first. The relative values of the mass ratios and the COR values can then be adjusted to minimize any repetitive loading signals that may occur.

In the case of a vehicle collision, repetitive loading due to multiple impacts can cause additional injury to an occupant in an accident. As an example, let us assume that a car (Car #2), right behind another car (Car #3), which is stopped at an intersection, is rear-ended by a third car (Car #1) as shown in Fig. 6.50. Depending on the weights of the cars and the coefficients of restitution of the structures that are engaged, the driver in Car #2, the middle one of the three cars, may suffer a more severe neck injury due to double whiplashes. Assume that the masses of the three vehicles are the same (M = 1, 1, 1), the COR's between #1 and #2 and between #2 and #3 are the same, 0.15, and the initial impact speed of Car #1 is 35 mph.

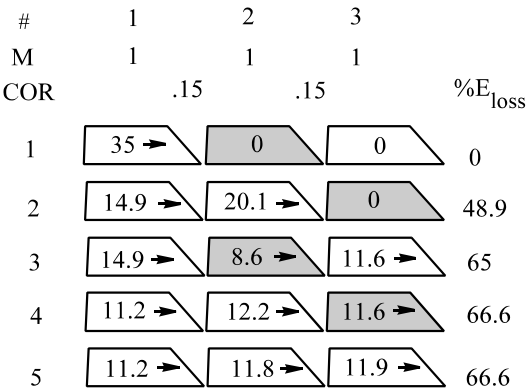

Fig. 6.50 Middle Car Rear-Ended Twice

Before performing the computation of the separation kinematics, let us examine what happens to the middle car, Car #2. The first whiplash occurs in the first impact, when it is rear-ended by Car #1 at a speed of 35 mph. In this impact, the velocity change of Car #2 is 20.1 mph. The percentage of initial kinetic energy dissipated by the structure is 48.9 % (shown on the right side of plot) at the end of the first impact. In the second impact, Car #2 hits Car #3 at a speed of 20.1 mph. Since Car #2 is slowed down to 8.6 mph, which is the separation velocity of Car #2 after the second impact, it gets rear-ended a second time by Car #1, which is traveling at 14.9 mph. The second rear-ended velocity change of car #2 is 3.6 mph (= 12.2 – 8.6). Following this third impact, Car #2 picks up speed and hits Car #3 again. This fourth impact is the last one. Afterwards, the car in the front (Car #3) is moving away from Car #2 and Car #2 moves away from Car #1. In this example, a total of four collisions occur and the drivers in Car #2 and #3 both receive double whiplashes.

6.5.4.1 *Separation Kinematics in a 3-Vehicle Collision*

The separation kinematics of the cars involved can be solved by successively applying the equations for momentum and the coefficient of restitution at the times of impact and separation for each of the impacts. Eq. (6.80) shows the derivation and the relationship between the two coefficients of restitution such that at least the middle car receives double whiplashes.

$$\textit{Momentum: } m_1\bar{v}_1 = m_1\bar{v}_1' + m_2\bar{v}_2' \quad \ldots\ldots\ldots\ldots \quad (1)$$

$$\textit{COR: } \quad e_1 = \frac{\bar{v}_1' - \bar{v}_2'}{\bar{v}_2 - \bar{v}_1} \quad \ldots\ldots\ldots\ldots\ldots\ldots \quad (2)$$

$$\textit{Defining } \quad r_1 = \frac{m_1}{m_2}, \quad r_2 = \frac{m_2}{m_3}$$

For the first impact, between m_1 *and* m_2:

$$v_1' = \frac{r_1 - e_1}{1 + r_1} v_1, \quad v_2' = \frac{r_1(1 + e_1)}{1 + r_1} v_1 \quad \ldots\ldots\ldots\ldots \quad (3) \qquad (6.80)$$

Similarly, for the second impact, between m_2 *and* m_3:

$$v_2'' = \frac{r_2 - e_2}{1 + r_2} v_2', \quad v_3'' = \frac{r_2(1 + e_2)}{1 + r_2} v_2' \quad \ldots\ldots\ldots\ldots \quad (4)$$

For Car #2 to be rear-ended twice: $v_1' \geq v_2''$

$$\textit{Rearranging one gets } \quad e_2 > r_2 - \left(\frac{r_1 - e_1}{1 + e_1}\right)\left(\frac{1 + r_2}{r_1}\right) \quad \ldots\ldots \quad (5)$$

Equation (5) shown in the Eq. (6.80) specifies the relationship between the two coefficients of restitution such that second car is subjected to multiple rear impacts. Note that this condition does not depend on the impact speed.

For the data shown in Fig. 6.50, the two mass ratios are equal to one, and the two COR's are 0.15; substituting these numbers into (5) of Eq. (6.80), one gets $0.15 > -0.48$. Therefore, the condition for the middle car subjected to multiple rear impacts, as shown in Fig. 6.50, is satisfied. However, if the middle car is twice as heavy as each of the other two cars, then r_1 becomes 0.5, and r_2 becomes 2. Computing the values of both sides of (5) of Eq. (6.80), it is found $0.15 \not> 0.78$. Since the multiple impact condition is not met, car #2 receives only one rear impact as shown in Fig. 6.51. The only one rear-ended velocity change of car #2 is 13.4 mph, smaller than 20.1 mph shown before in Fig. 6.50. The percentage of initial kinetic energy loss ($\%E_{loss}$) by the structure is 65.2% (on the right column of the plot) at the end of the second impact event. This points out the advantage of driving a larger car, as the driver in such a car is subjected to one whiplash only in the case described above.

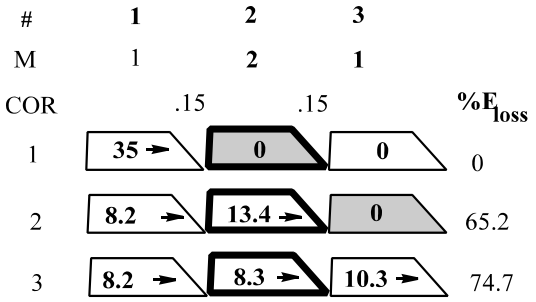

Fig. 6.51 Middle Car (with larger weight) Rear-Ended Once

The middle car does not have to be very heavy to receive only one rear impact. If the section of the structure engaging in the impact between cars #1 and #2 is such that it has a COR of .55, the middle car would be subjected to only one rear impact as shown in Fig.6.52. This is because when $r_1 = r_2 = 1$ and $e_2 = .15$, the maximum value of e_1 for Car #2 to have multiple rear impacts can be derived by using the condition shown in (5) of Eq. (6.80). The condition is $e_1 < 0.4$. Therefore, a value of $e_1 = .55$, not satisfying the limit condition, would insure that Car #2 would have only one rear impact. The velocity change of Car #2 is 27.1 mph, higher than the previous two cases. This is because the percentage of initial kinetic energy dissipated by the structure is only 34.9% (on the right side of plot) at the end of second impact.

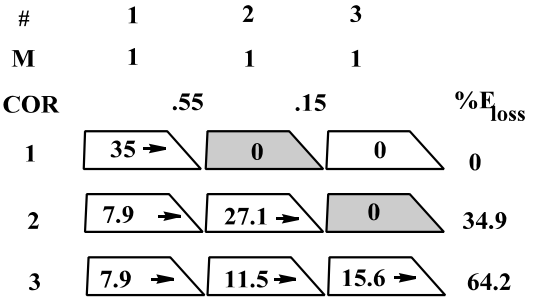

Fig. 6.52 Middle Car (with High Rear COR) Rear-Ended Once

6.5.5 COR, Times of Dynamic Crush, and Separation Time

A simple analytical relationship based on the relative separation velocity and relative approach velocity can be derived for the coefficient of restitution, e. Given two timings obtained from a crash test, t_m and t_f, e can then be computed.

Let define

a:	Constant deceleration or ASW (Average Square Wave)
v:	Velocity change up to t_m
t_m:	Time of (maximum) dynamic crush
t_f:	Final separation time
e:	Coefficient of restitution

Either in the vehicle-to-(fixed rigid) barrier (VTB) test or in the vehicle-to-vehicle (VTV) test, the relative acceleration of the two objects in the deformation phase can be approximated by an average square wave as shown in Fig. 6.53. The area under the square wave is the relative approach velocity. The vehicle deceleration in the restitution phase is approximated by a triangle, and the area is the rebound or relative separation velocity. Eq. (6.81) shows the derivation and relationship between the three parameters, t_m, t_f, and e.

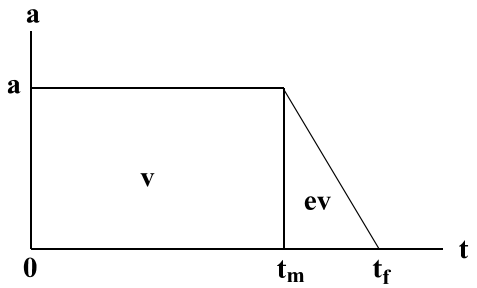

Fig. 6.53 Velocity Changes in the Deformation and Rebound Phases

$$v = a\,t_m \quad \ldots\ldots\ldots\ldots (1), \qquad e\,v = \frac{(t_f - t_m)a}{2} \quad \ldots\ldots\ldots (2),$$

$$\frac{(2)}{(1)}: \quad e = \frac{(t_f - t_m)}{2\,t_m} \quad \ldots\ldots (3), \qquad t_f = t_m(1 + 2e) \quad \ldots\ldots\ldots (4) \tag{6.81}$$

Using available crash test results for cars and trucks in rigid barrier and vehicle-to-vehicle crashes, a summary of the two timings and the coefficients of restitution are shown in Table 6.2.

Table 6.2 Relationship Between t_f, t_m, and e

Crash Mode	e	$t_f/t_m = 1+2e$	t_f/t_m from Crash Tests	t_m, ms, from Crash Tests
Vehicle-to-Barrier	.15	1.3	1.3 to 1.5	80 to 100
Vehicle-to-Vehicle in line	.10	1.2	1.2 to 1.4	100 to 140

6.5.6 Coefficient of Restitution and Stiffness in Vehicle Crashes

This section deals with the determination of *e*, the coefficient of restitution, for a two-car collision using car-barrier data. A study made by Prasad [3] investigated the coefficient of restitution for vehicle structures and its application in estimating velocity changes in vehicle collisions.

The coefficient of restitution, *e*, for a two-car central collision can be obtained using data from car-barrier collisions. The value obtained will be an approximation since it assumes that the amount of energy each car loses is the same in both the car-to-car and the barrier collisions. The values of *k*, the slope of the force-deflection curve for each barrier crash, must also be known.

First, let us obtain a measure of the lost energy in a barrier crash as it relates to *e*. The definition of *e* is:

$$e = \frac{\textit{Relative separation speed}}{\textit{Relative approach speed}} = \frac{(v_2' - v_1')}{(v_1 - v_2)} \tag{6.82}$$

Here, a fixed reference system is assumed (relative to the earth). Then, the car to the left has an initial speed of v_1; after the collision, its speed is v_1'. The other car, or barrier if one is used, has a speed of v_2 and then v_2', as shown in Fig. 6.48.

Note that *e* is invariant to the reference system used, as long as the system is moving at a constant speed. If one uses a system moving at a speed w with respect to the fixed system, each velocity term in the equation would be less by the amount w. Since each relative speed will have two w's, one positive and one negative, these would cancel, leaving the relative speed unchanged. Thus, *e* will stay the same for any reference moving at a constant speed.

As has been shown earlier, at some time during the collision, the two cars will have the same speed, called the common speed, v_c. At this point, the maximum deformation between two cars occurs and it is at the end of deformation phase (or loading phase). Beyond this point, the two cars will start to unload and separate, releasing any elastic rebound (potential) energy until the two cars are totally apart from each other.

For a car-fixed barrier collision, assuming a coordinate system at rest with respect to the barrier, we see that v_2 is zero and v_2' will also be zero (since the mass of the barrier is assumed to be infinite). Then:

$$v_1' = -ev_1 \quad \textit{so:} \quad \frac{m_1}{2}(v_1')^2 = e^2\left(\frac{m_1}{2}v_1^2\right) \quad \textit{or, in words:}$$
$$\textit{Kinetic energy (after,)} = e^2 \times \textit{Kinetic energy (before)} \tag{6.83}$$

If *e* equals 1.0, the kinetic energy after collision equals that before; i.e., there is no loss. If *e* equals 0.0, the kinetic energy after collision is zero; i.e., the car is at rest, resting against the barrier. Also, the initial kinetic energy is equal to the stored (i.e., available or elastic rebound) energy obtained during the collision.

Now, consider a two-car central collision, with a moving reference system which moves at the common velocity, v_C. At the time the speeds of the two cars are equal, their speed will be the common speed. In the common speed reference system used, their speeds will be zero. After separation, their speeds will be v_1' and v_2'. Applying the conservation of momentum in this reference system:

$$0 = M_1(v_1' - v_C) + M_2(v_2' - v_C) \quad \textit{then:} \ (v_2' - v_C) = -\frac{M_1}{M_2}(v_1' - v_C) \tag{6.84}$$

The kinetic energy after separation will be equal to the rebound energy, i.e., the energy released by each car during the unloading (or restitution) phase. This rebound energy is retrievable upon separation of the two cars. As was noted earlier, this energy in the case of a car-barrier collision is $e^2 \times$ (Initial kinetic energy). Assuming the rebound energy in each car in the case of a car-to-car collision is equal to that obtained when the car collides with a fixed barrier, we can equate the rebound energy in the car-barrier crash and the final kinetic energy in the car-to-car crash. Then:

$$e_1^2 \Delta E_1 + e_2^2 \Delta E_2 = \frac{M_1}{2}(v_1' - v_C)^2 + \frac{M_2}{2}(v_2' - v_C)^2 \tag{6.85}$$

The values of ΔE_1 and ΔE_2 can be obtained from Eqs. (7.34) and (7.35) in Section 7.4 of Chapter 7 on central collisions:

$$\Delta E_1 = \frac{M_1 M_2}{2(M_1 + M_2)}\left(\frac{k_2}{k_1 + k_2}\right)(v_1 + v_2)^2$$
$$\Delta E_2 = \frac{M_1 M_2}{2(M_1 + M_2)}\left(\frac{k_1}{k_1 + k_2}\right)(v_1 + v_2)^2 \tag{6.86}$$

Substituting ΔE_1 and ΔE_2 in Eq. (6.86) into Eq. (6.85), one gets:

$$(v_1' - v_C) = \frac{M_2}{M_1 + M_2}(v_1 + v_2)\sqrt{\frac{e_1^2 k_2 + e_2^2 k_1}{k_1 + k_2}}$$
$$(v_2' - v_C) = \frac{M_1}{M_1 + M_2}(v_1 + v_2)\sqrt{\frac{e_1^2 k_2 + e_2^2 k_1}{k_1 + k_2}} \tag{6.87}$$

Note that these expressions differ only by the mass term in the numerator. Now, substituting the velocity terms in the equation for e in Eq. (6.82), it becomes:

$$e = \sqrt{\frac{e_1^2 k_2 + e_2^2 k_1}{k_1 + k_2}} \tag{6.88}$$

Here, e is the equivalent coefficient of restitution (combined COR) for the two-car crash but expressed using the e values and the force-deflection constants, k_i, for two car-barrier crashes. Note that when k_2 is extremely large (such as for a barrier), the value of the equivalent e becomes e_1, as it should (car-barrier case). Also, if the e's are equal and the k's are equal, then the value of e becomes the same as the e for either car.

The above equation can be normalized to the coefficient of restitution of either car, say car 2. Dividing through by e_2 gives the following normalized equation:

$$\frac{e}{e_2} = \sqrt{\frac{\left(\frac{e_1}{e_2}\right)^2 + \frac{k_1}{k_2}}{1 + \frac{k_1}{k_2}}} \tag{6.89}$$

One might ask what the advantage is for determining e in this fashion since two separate car-barrier crashes are necessary to obtain the needed values of e and k. The advantage accrues when one has a fleet of vehicles and wishes the e value for all pairs. For example, for a fleet of four cars (A, B, C, D), six crashes would be needed (AB, AC, AD, BC, BD, CD) and a total of twelve cars would be crashed. Using the approximation formula above, only four car-barrier crashes would be needed and only four cars would be crashed. This represents a considerable saving in cost, effort, and time! Note that for larger fleet sizes, the advantage grows very markedly.

A 3-D plot of (e/e_2) versus (k_1/k_2) and (e_1/e_2) is presented in Fig. 6.54. Given a stiffness ratio k_1/k_2, the combined normalized COR ratio e/e_2 of two vehicles increases as the ratio of e_1/e_2 increases; while depending on the whether the individual COR ratio is greater or less than one, the stiffness ratio yields a different effect on the combined COR ratio. Note that when $e_1/e_2 = k_1/k_2 = 1$, then $e/e_2 = 1$.

As shown by the surface contour in Fig. 6.54, when the COR of vehicle 1 (e.g., $e_1 = e_{truck} \approx .14$) is less than that of vehicle 2 (e.g., $e_2 = e_{car} \approx .17$), the stiffness ratio k_1/k_2 of truck-to-car is about 2,

the combined COR ratio computed from Eq. (6.89) is $e/e_2 = .95$, and $e = .95 \times .17 = .16$. The value of the combined COR, e, is less than that of e_2. This is because the individual COR ratio, e_1/e_2, is less than one, the stiffness ratio is greater than one, and, therefore, the combined COR ratio is less than one.

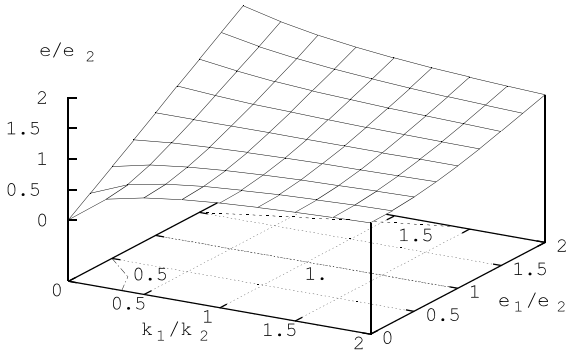

Fig. 6.54 Normalized e/e_2 as a Function of k_1/k_2 , e_1/e_2

6.6 VEHICLE INERTIA PROPERTIES AND CRITICAL SLIDING VELOCITY

Three methods of determining the vehicle CG heights and two methods of computing the vehicle moments of inertia in roll and in yaw are presented in Sections 6.6.1–6.6.3. In the derivations of these formulas and in the laboratory test measurements, the vehicle is assumed to be a rigid block which does not have compliance. Therefore, in performing the test in a laboratory, care should be given such that there are no significant errors introduced due to a change in vehicle geometry (e.g., due to suspension compliance).

With the intention of defining a measure that would correlate with the rollover propensity of a vehicle in an accident, NHTSA (National Highway Traffic Accident Administration) put forth a laboratory test procedure to evaluate the critical sliding velocity (CSV). CSV is defined as the minimum lateral velocity of a vehicle required to initiate a quarter turn rollover in a tripping condition. The derivation and application of the CSV are covered in Section 6.6.4.

6.6.1 CG Height Determination

Three methods of determining the CG height of a vehicle are presented. These methods are based on the assumption that the vehicle is a rigid body, where the vehicle's shape and form do not change when tilted about the y-axis, as shown in Fig. 6.55. The methods, based on rigid body static equilibrium, generally yield an accurate CG height estimate, if the rotation angle is small.

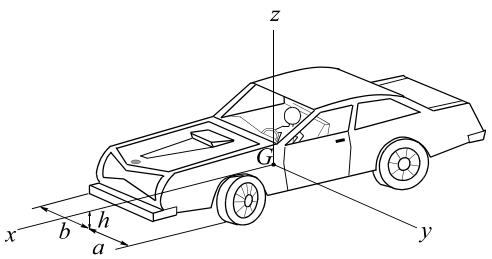

Fig. 6.55 Vehicle CG Location

Method 1:

Figs. 6.56 and 6.57 show the setup for the CG height measurement. First, the vehicle is positioned horizontally on a platform which is supported by a knife edge at the previously obtained horizontal CG location of the vehicle. The vehicle is then tilted at a small angle θ; a force, F, is applied at the rear bumper area such that the vehicle is in equilibrium at the tilted position. The derivation of the CG formula is given in Eq. (6.90).

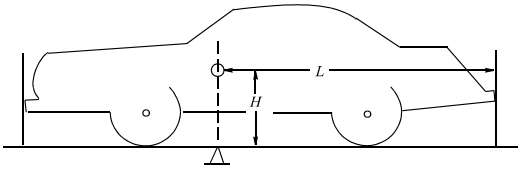

Fig. 6.56 Vehicle in Horizontal Equilibrium

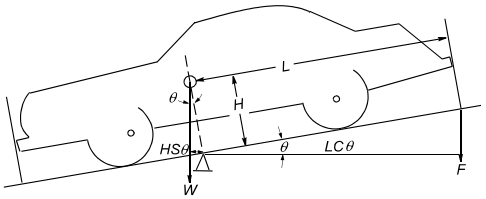

Fig. 6.57 Vehicle in Inclined Equilibrium

$$\Sigma M_{knife\ edge} = 0, \quad then \quad WH\sin\theta = FL\cos\theta$$
$$therefore \quad \frac{H}{L} = \frac{F}{W}\frac{1}{\tan\theta} \quad \ldots\ldots\ldots\ldots \quad (1) \qquad (6.90)$$

Method 2:

The rear axle of a vehicle on a horizontal surface is lifted up to a height of h1 from the ground as shown in Fig. 6.58. The load transfer to the front axle W3-W1 is measured. The CG height H can then be obtained as shown in Eq. (6.91).

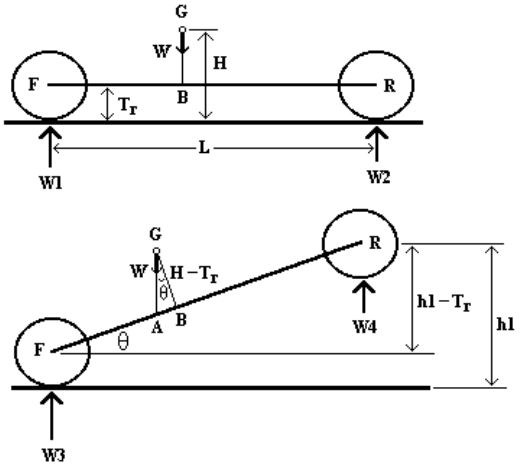

Fig. 6.58 Method 2: CG Height Measurement

$$\Sigma M_F = 0, \quad -W\,\overline{FB} + W2\,L = 0, \quad \therefore \quad \overline{FB} = \frac{W2}{W}L$$

$$\Sigma M_A = 0, \quad -W3(\overline{FA}\cos\theta) + W4(L-\overline{FA})\cos\theta = 0$$

$$\overline{FA} = \frac{W4}{W3+W4}L = \frac{W4}{W}L, \quad \overline{FB}-\overline{FA} = (W2-W4)\frac{L}{W} = (W3-W1)\frac{L}{W}$$

$$Since\ \tan\theta = \frac{h1-T_r}{\sqrt{L^2-(h1-T_r)^2}} = \frac{\overline{FB}-\overline{FA}}{H-T_r}, \quad H = T_r + \frac{\overline{FB}-\overline{FA}}{\tan\theta}\ \ and \tag{6.91}$$

$$H = T_r + \frac{(W3-W1)L\sqrt{L^2-(h1-T_r)^2}}{W(h1-T_r)} \quad \ldots\ldots \quad (2)$$

Method 3: The setup in this method, shown in Fig. 6.59, is similar to that used in Method 2. However, different measurements are taken, which makes the computation of the CG height easier.

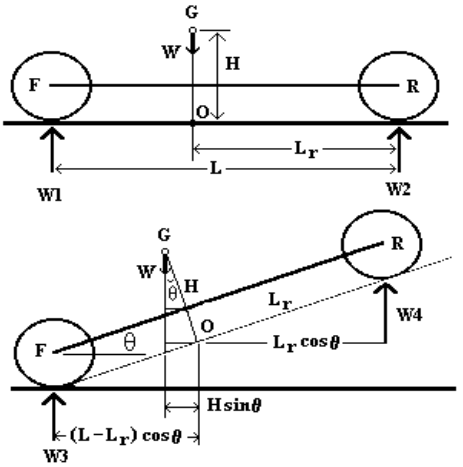

Fig. 6.59 Method 3: CG Height Measurement

$$L_r' = L_r - R\theta \quad (correcting\ for\ contact\ point)$$

$$where\ R\ is\ the\ tire\ radius.$$

$$\Sigma M = 0: \quad W(H\sin\theta) + W_4(L_r'\cos\theta) - W_3(L - L_r')\cos\theta = 0$$

$$Substituting\ W_4 = W - W_3\ into\ the\ equation\ above\ yields: \tag{6.92}$$

$$H = \frac{W_3 L - W L_r'}{W\tan\theta} \quad \ldots\ldots\ldots\ldots \quad (3)$$

$$Note: For\ small\ \theta, \quad L_r' \approx L_r$$

6.6.2 Moment of Inertia Using Trifilar Pendulum Method

An interesting application of the principle of work and energy is the determination of the moment of inertia of an object, e.g., the yaw moment of inertia of a car, using the Trifilar Pendulum Method.

This method uses a circular platform which is suspended by three long vertical wires shown in Fig. 6.60. The object to be tested is mounted on the platform and the platform is then rotated about a central vertical axis. The resultant motion is analyzed to determine the moment of inertia of the object.

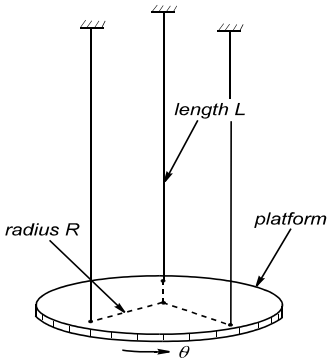

Fig. 6.60 A Trifilar Pendulum Method

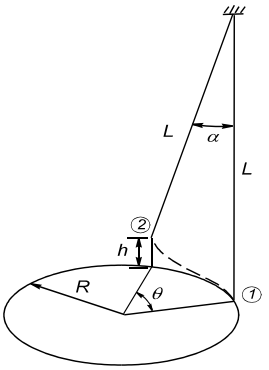

Fig. 6.61 Rotation of Trifilar Platform

As shown in Fig. 6.61, the platform is rotated about its central axis; the lower end of each supporting wire also rotates but the upper end of the wire remains fixed. Thus, the wire is no longer vertical. Since its length is fixed, the lower end of the wire is necessarily raised to a higher level, which in turn raises the platform the same amount. This raising process increases the gravitational potential energy of the platform and object; work has been done on the system to raise it; the energy has been stored as gravitational potential energy.

Now, if the platform is released, it rotates back toward its original position and beyond, first picking up kinetic energy on the way and then losing it at the far end of its travel. A cyclic motion ensues in which the platform rotates back and forth in a cyclic motion. The period of the cyclic motion can be correlated to the moment of inertia of the object, thus yielding a method of determining the moment of inertia of the system.

The first step in the analysis is to determine the height that the platform (and object) is raised as a function of the angle of its rotation. (Note: In the following, small angle approximations will be used.) Assume the angle of rotation is θ. Then, the distance the lower end of a wire is moved sideways is R θ. Here, R is the radial distance from the center of the platform to the lower end of the wire. The wire also moves upward a small amount, h, due to the constraint of constant wire length. The angle swept out by the wire as it moves sideways, from its vertex at the top of the wire, is α=(Rθ)/L, where L is the fixed length of the wire.

The original vertical length of the wire, L, minus its projected vertical length, once rotated, is equal to the height raised (see the arc between positions 1 and 2, and h in Fig. 6.61):

$$
\begin{aligned}
&h = L - L\cos(\alpha), \quad \textit{For small angle } \alpha, \\
&\cos(\alpha) \textit{ can be approximated by } \cos(\alpha) = 1 - \frac{\alpha^2}{2} \\
&\textit{Then:} \quad h = L - L(1 - \alpha^2/2) = \frac{L\alpha^2}{2} \\
&\textit{Substituting for } \alpha \textit{ yields an equation for} \\
&\textit{the height versus the angle of rotation:} \\
&h = \frac{R^2\theta^2}{2L}. \quad \textit{Note that} \quad h \propto \theta^2
\end{aligned}
\tag{6.93}
$$

The potential energy of the platform system, V, assuming the zero potential height is taken to be at the lowest position of the platform, is given by the product of weight and height:

$$V = Wh = W\left(\frac{R^2\theta^2}{2L}\right) \qquad \textit{Where } W \textit{ is the weight of the platform and object.} \tag{6.94}$$

The kinetic energy of the platform and object system, T, is given by:

$$T = (I_p + I_o)\frac{\dot{\theta}^2}{2}, \quad \textit{where}$$
$$I_p = \textit{Moment of inertia of platform (about central axis)} \tag{6.95}$$
$$I_o = \textit{Moment of inertia of object (about central axis)}$$

The centers of mass of both platform and object are assumed to be located on the central axis.

Now, applying Lagrange's equations to the system, we first calculate the Lagrangian function, L, shown by (1) of Eq. (6.96). This involves only one variable, θ; so the Lagrange equation to be used is shown by (2) of Eq. (6.96).

$$L = T - V = (I_p + I_o)\frac{\dot{\theta}^2}{2} - W\frac{R^2\theta^2}{2L} \quad \ldots\ldots\ldots \quad (1)$$
$$\frac{d}{dt}\left(\frac{\partial L}{\partial \dot{\theta}}\right) - \frac{\partial L}{\partial \theta} = 0 \quad \ldots\ldots\ldots\ldots\ldots\ldots \quad (2) \tag{6.96}$$

The Lagrange equation yields an equation of motion of the form:

$$(I_p + I_o)\ddot{\theta} + \left(\frac{WR^2}{L}\right)\theta = 0 \tag{6.97}$$

This is the equation of motion for the classical linear oscillator, with no damping, whose motion can be expressed as a cyclic function. Assuming initial conditions where the platform is rotated to its maximum angle and its speed is zero (at time zero), one gets:

$$\theta = \theta_{max}\cos(\omega t) \qquad \textit{where } \omega = \sqrt{\frac{WR^2}{(I_p + I_o)L}} \tag{6.98}$$

Here, ω = the angular speed of rotation of the system, and
Γ = the period of a cycle (= 2 π / ω)

we can substitute Γ in for ω and solve for the moments of inertia as a function of the period:

$$(I_p + I_o) = \left(\frac{\Gamma R}{2\pi}\right)^2 \frac{W}{L} \tag{6.99}$$

Thus, by measuring the period of oscillatory motion (using a number of cycles for increased accuracy) one can obtain the combined moment of inertia. Then, repeating the experiment with only the platform in place, its moment of inertia can be obtained and subtracted out from the combined moment, yielding the moment of inertia of the object alone. Alternatively, if the platform is of a simple shape, one can use a formula to subtract out its moment. For example, the moment of inertia of a disk about its central axis is simply one-half its mass times its radius squared. As a final result, one gets:

$$I_o = \left(\frac{\Gamma R}{2\pi}\right)^2 \frac{W}{L} - I_p \tag{6.100}$$

Notes: The term R in the formula is the distance from the center of the platform to the wire attachment point, which may be less than the radius of the disk. The weight, W, is the combined weight of the platform and object. When testing the platform alone, the weight to be used in the formula is only the platform weight. Although damping exists in this system, it is very weak and can be neglected.

6.6.3 Moment of Inertia Using Swinging Pendulum Method

A platform pendulum pinned at a fixed point as shown in Fig. 6.62 is made to swing back and forth through a small angle. This setup can be used to obtain the moment of inertia of an object about an axis perpendicular to the plane of motion through the CG of the object.

Assume the platform AB has an empty weight of W_1 with the CG at point G_1, and a period of τ_1. A car having a weight of W_2 with the CG at point G_2 is placed on the platform. We propose to determine the moment of inertia of the car about an axis passing through G_2.

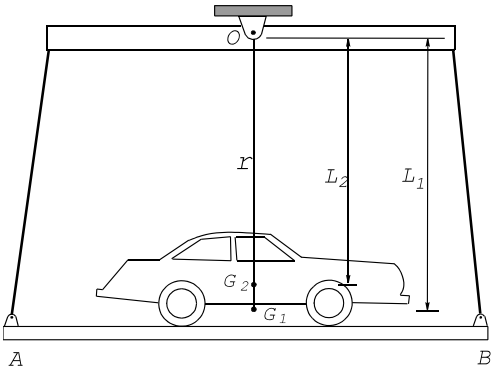

Fig. 6.62 A Pendulum Platform and a Car

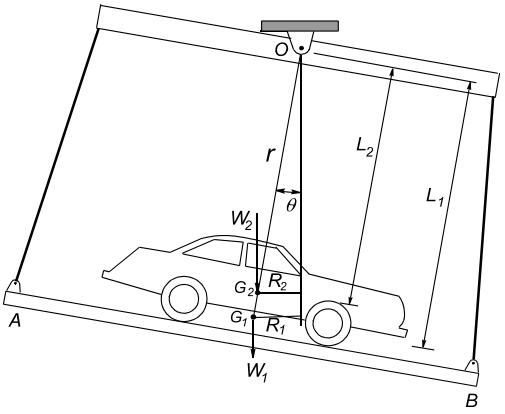

Fig. 6.63 A Swinging Platform and a Car

From vibration analysis, the circular angular frequency and the period of oscillation of an arbitrarily shaped body pinned at a fixed point O can be derived as shown in Eq. (6.101).

$$
\begin{aligned}
&\textit{Equation of Motion for small oscillation:}\\
&\Sigma M_o = I_o \alpha = I_o \ddot{\theta}, \quad \textit{where } \Sigma M_o = -W r \sin\theta = -W r \theta\\
&\textit{therefore} \quad \ddot{\theta} + \frac{Wr}{I_o}\theta = 0 \qquad (1)\\
&\omega = \sqrt{\frac{Wr}{I_o}}, \quad \textit{and} \quad \tau = 2\pi\sqrt{\frac{I_o}{Wr}} \qquad (2)\\
&\textit{where:}\\
&\omega \ : \textit{circular angular frequency}\\
&\tau \ : \textit{period of oscillation}\\
&W \ : \textit{weight of the object}\\
&r \ : \textit{distance between } O \textit{ and } G_2\textit{, C.G. of the object}\\
&I_o \ : \textit{moment of inertia about the fixed point } O.
\end{aligned}
\qquad (6.101)
$$

Applying formula (2) of Eq. (6.101) to the following Case (1) and Case (2), one get the respective moment of inertia about the fixed point O. The moment of inertia of the car about its own CG (pitch moment of inertia) can then be computed as shown in (5) and (6) of Eq. (6.102).

Moment of Inertia about the fixed point O:

Case (1) *car and platform*: $$I_0 = \left(\frac{\tau}{2\pi}\right)^2 \left(W_1 L_1 + W_2 L_2\right) \quad \ldots\ldots\ldots \quad (3)$$

Case (2) *platform only*: $$I_1 = \left(\frac{\tau_1}{2\pi}\right)^2 (W_1 L_1) \quad \ldots\ldots\ldots\ldots \quad (4)$$

Case (3) *car only*: $$I_2 = I_0 - I_1 \quad \ldots\ldots\ldots\ldots\ldots\ldots \quad (5)$$

(6.102)

Moment of Inertia of car about G_2 (*C.G. of the car*):

$$I_{G_2} = I_2 - \left(\frac{W_2}{g}\right) L_2^2 \quad \ldots\ldots\ldots\ldots\ldots\ldots\ldots\ldots\ldots\ldots \quad (6)$$

6.6.4 Critical Sliding Velocity (CSV)

As part of FMVSS 208 (or SAE J2114) on the rollover test procedures for occupant protection, a vehicle supported on an inclined sled of 23° is tested at 30 mph tripped rollover. The purpose is to provide containment for an occupant who would otherwise be ejected during rollover. CSV is a measure of the minimum lateral velocity of a vehicle needed to initiate a quarter turn rollover when the vehicle is tripped in the lateral direction. The determination of CSV is based on a tripping action that produces a rollover just sufficient to bring the center of gravity of the vehicle (CG) to its highest point.

The derivation of CSV formulas, parametric trend analysis, and the computation procedures are presented in the following sections.

6.6.4.1 *Derivation of CSV Formulas*

A basic assumption used in the modeling is that the vehicle consists of a solid block with no tires, suspension, etc. The needed velocity is obtained by sliding the vehicle laterally down a tilted table to a stop which initiates the rollover action.

Fig.6.64 shows the nature of the sliding, impacting process. Point B is the pivot point, at which the sliding motion ceases and rollover ensues. The lateral velocity is transformed into angular velocity (roll) which raises the center of gravity. CSV is that velocity which will just roll the CG to its highest point (where the CG is directly above the pivot point, B). The vehicle can then drop onto its side on the pavement. For a vehicle rolling over on a level pavement, this would constitute a rollover of a one-quarter turn.

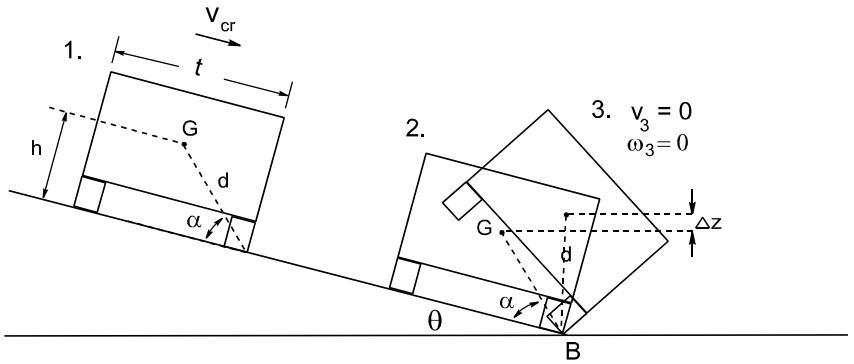

Fig. 6.64 A Vehicle Sliding On A Tilt Table for Rollover Test

Parameter List (Units are slugs, inches, degrees, seconds) :

B	= Trip point, where roll begins	G	= Position of center of gravity
t	= Track width	h	= CG height (from tilt table)
d	= Distance, CG to tire contact point	α	= Angle between line d and table
v_{cr}	= Velocity along table, when reaching point B	θ	= Tilt table angle
I_G	= Roll moment of inertia about CG axis	k	= Radius of gyration in roll ($I_G = mk^2$)
ω	= Angular velocity (about point B)	z	= CG height (from pavement)
m	= Mass of vehicle	L	= Angular momentum about B axis
CSV= Critical Sliding Velocity = V_{cr}		I_B	= Moment of Inertia about B axis

In order to relate the CSV to the amount of roll, we must first ascertain the angular speed of the vehicle around point B following the impact at that point. Applying the principle of momentum and impulse to the system before and after impact(from event 1 to event 2 in the figure) with the trip point, one obtains:

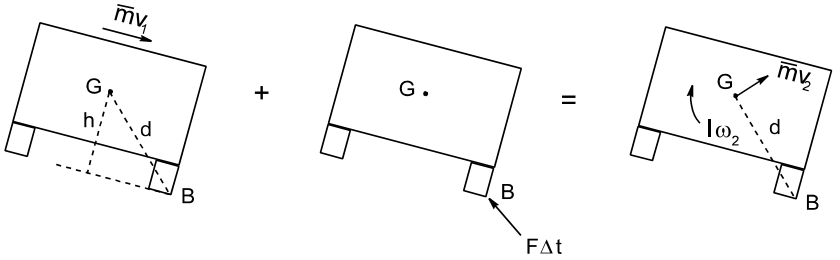

Fig. 6.65 Vehicle Impulse and Momentum at Impact (event 1 – event 2)

$$L\ (Before)\ +\ Angular\ impulse\ =\ L\ (After) \tag{6.103}$$

The angular momentum before impact with the trip point is given by the product of the mass of the vehicle, m, its velocity, v, and the height of the CG above the table, h:

$$L\ (before\ impact)\ =\ m\,v\,h \tag{6.104}$$

The angular momentum after impact is given by the product of the moment of inertia about an axis through point B and the angular velocity, ω.

$$L\ (after\ impact)\ =\ I_B\,\omega \tag{6.105}$$

During the impact process, the impact forces are all through point B and, thus, have no moment arms. There is a moment due to the weight acting through a moment arm of (t/2) cos θ, but its magnitude is small so its contribution can be ignored.

Equating the momentum before and after and solving for v_{cr} gives:

$$v_{cr} = I_B \frac{\omega}{m\,h} \tag{6.106}$$

Using the parallel-axis theorem for moments of inertia we get:

$$I_B = I_G + m\,d^2 = m\,k^2 + m\,d^2, \quad Note:\ d = \sqrt{h^2 + \left(\frac{t}{2}\right)^2}$$
$$Substituting\ into\ Eq.\ (6.106)\ gives:\quad v_{cr} = \frac{(k^2 + d^2)}{h}\,\omega \tag{6.107}$$

This gives the needed relationship between the initial lateral velocity and the subsequent roll angular velocity.

Next, we must determine the magnitude of ω needed to just raise the CG to its maximum height, where it is directly above the trip point. For this, we will use the principle of conservation of energy, equating the total energy just after impact, when the vehicle starts to roll, and at the time when the CG has reached its maximum height. At that time, the angular velocity should be zero, such that the vehicle is in an unstable equilibrium position, balanced at the peak, and could fall down to the pavement on its side, or fall back onto its wheels.

Taking the zero potential level to be at the height of the CG at the time of impact, the energy at the outset, just after impact, is purely kinetic energy and is equal to:

$$E_1 = \frac{I_B}{2}\omega^2 = \frac{m}{2}\left(k^2 + d^2\right)\omega^2 \tag{6.108}$$

As the body rotates it reaches a point wherein the CG is directly above point B. At this time, we want the angular velocity to become zero. Then, there is no kinetic energy and all the energy is potential energy. The change in height of the CG, Δz, determines this energy:

$$E_2 = m\,g\,\Delta z \tag{6.109}$$

The magnitude of Δz can be ascertained as follows. At its peak position, the CG is d units directly above point B. At the start of rotation, using trigonometry, z is given by z = d sin (θ + α). The difference is:

$$\Delta z = d\left[1 - \sin(\theta + \alpha)\right], \quad and \quad E_2 = m\,g\,d\left[1 - \sin(\theta + \alpha)\right] \tag{6.110}$$

Equating energies and solving for ω gives:

$$\omega = \sqrt{\frac{2\,g\,d\left[1 - \sin(\theta + \alpha)\right]}{k^2 + d^2}} \tag{6.111}$$

Substituting this back into the equation for v_{cr} yields for the CSV:

$$CSV = \left(\frac{1}{h}\right)\sqrt{2\,g\,d\,(k^2 + d^2)\left[1 - \sin(\theta + \alpha)\right]}$$
$$where \quad d = \sqrt{h^2 + \left(\frac{t}{2}\right)^2}, \quad and \tag{6.112}$$
$$\alpha = \tan^{-1}\frac{2\,h}{t} = \sin^{-1}\frac{h}{d}$$

6.6.4.2 *Normalized CSV Equation and Applications*

The formula for CSV can be expressed in terms of a normalizing velocity, the square root of 2gh, as shown in the following equation:

$$\textit{Define: Stability index: } \sigma = \frac{t/2}{h}, \quad \textit{Radius of gyration index: } \beta = \frac{k}{t/2}$$

$$\textit{then, } \frac{CSV}{\sqrt{2gh}} = \sigma \sqrt{\sqrt{1+\sigma^2}\left(\frac{1+\sigma^2}{\sigma^2}+\beta^2\right)\left[1-\sin\left(\tan^{-1}\frac{1}{\sigma}+\theta\right)\right]} \tag{6.113}$$

Special case: $\theta = 0.0°$ (Tilt table level with floor or pavement). In this case we have:

$$CSV = \left(\frac{1}{h}\right)\sqrt{2g\,(k^2+d^2)\,(d-h)} \tag{6.114}$$

Substituting for $(k^2 + d^2)$ and for d gives the CSV formula as used by the NHTSA [NHTSA's Technical Assessment Paper, 1991, pp.4–35].

The formula above can also be written as follows:

$$CSV = \sqrt{\frac{2gI_B}{mh^2}\left[\sqrt{h^2+\left(\frac{t}{2}\right)^2}-h\right]} \tag{6.115}$$

$$\textit{where} \quad I_B = I_G + md^2,$$

$$I_G\textit{: roll moment of inertia about CG}$$

Given a track width of a vehicle, the effect of the CG height and roll radius of gyration on the CSV can be visualized by plotting Eq. (6.114). The 3-D surface plot shown in Fig. 6.66 reveals the following trends: (1) As the CG height (h) increases, CSV decreases, and the vehicle is more vulnerable to rollover; (2) As the roll radius of gyration (k) increases, CSV also increases, and the vehicle becomes more resistant to rollover. Within the practical range of the radius of gyration, the effect of the radius of gyration on the CSV is not as drastic as the CG height.

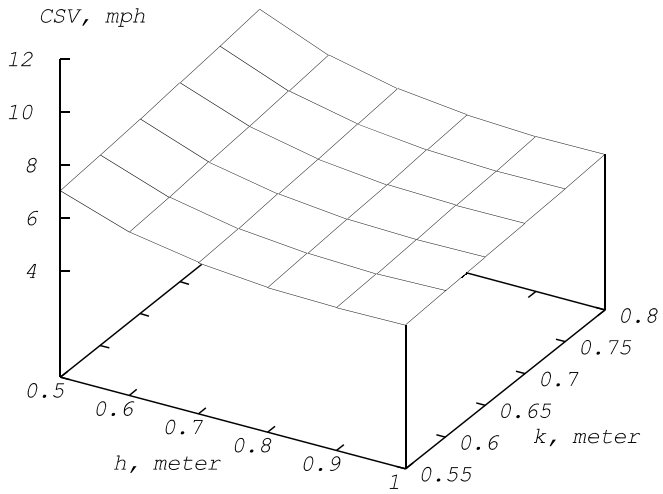

Fig. 6.66 Sensitivity of Critical Sliding Velocity (θ=0°, t=1.72 m)

The effect of stability index, σ, and radius of gyration index, β, on the CSV is shown in Fig. 6.67. The plot, based on Eq. (6.113), shows that normalized CSV increases while either stability index ($\sigma = t / 2h$) or radius of gyration index ($\beta = 2k / t$) increases. However, normalized CSV is more sensitive to the change of stability index than that of radius of gyration index.

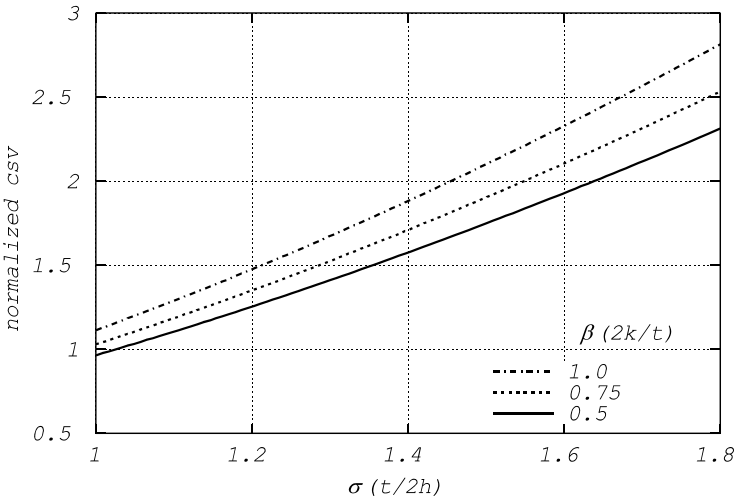

Fig. 6.67 Normalized CSV as a Function of σ and β

Case Study (exercise): For $\theta = 0^o$, compute the CSV (V_{cr}) for the following two frame vehicles by filling out the table below. The weight and wheelbase for Bronco II are 3430 lbs and 94 in, for F-150 are 4310 lbs and 133 in, respectively (Note: roll moment of inertia about CG, I_G, for Bronco II and F-150 are 460 ft-lb-sec^2 (624 kg-m^2) and 560 ft-lb-sec^2 (759 kg-m^2), respectively. Data source: Failure Analysis Associates [4]).

Table 6.3 Estimating CSV's of Two Trucks (SUV B and Truck F)

	SUV B (Bronco II)	Truck F (F-150)
k: radius of gyration, in	25.0	25.0
$\sigma = t/(2h)$: stability index	1.03	1.17
h: CG height, in	27.5	27.5
t: track width, in		
$\beta = 2k/t$: radius of gyration index, in		
$\frac{v_{cr}}{\sqrt{2gh}}$ (*normalized* v_{cr})		
V_{cr} (mph)		

6.7 ROLLOVER CRASHES

Among the various modes of vehicle crashes, rollover crashes are often very severe and threatening events that involve automotive vehicles. Rollover occurs as a result of complex interactions among the driver, the vehicle, and the environment. It may be precipitated from one or a combination of factors. Rollover may be initiated on a flat and level road surface such as when making a steady turn. Once the lateral acceleration acting on a vehicle exceeds rollover threshold for that vehicle, the wheels on one side of the vehicle lift up from the road surface, and the vehicle begins a rollover process. Rollover may also occur after a vehicle slides sideway and hits a curb. In this situation, the vehicle acquires a large angular velocity due to the sudden stopping of the sliding vehicle upon hitting the curb.

In this section, the fundamentals of vehicle rollover dynamics, including rollover detection methodology, are introduced. Other factors such as handling, suspension, and tire properties, the vehicle geometry including wheelbase, the driver, and the complex road conditions are beyond the scope of this text.

6.7.1 Rollover Dynamics of a Rigid Vehicle in a Steady Turn

A vehicle cruising at a speed of v is negotiating a steady left turn on a level surface road. The radius of the circle of the turn is r. The coefficient of friction between the tire and road surface is μ. The CG height and track width of the vehicle are h and t, respectively.

We propose to determine the vehicle roll dynamic relationship and to derive the condition at which the inside wheels of the vehicle would start lifting up from the road surface. This is a condition termed rollover threshold [5].

Shown in Fig. 6.68 is the rear view of a vehicle making a steady left turn on a level surface road. Since the turn is steady and there is no abrupt change in roll angle, there is no roll acceleration. The only acceleration acting on the CG location of the vehicle is the centripetal acceleration which is directed toward the center of the circle. This centripetal acceleration, a, also termed lateral acceleration [5], is generated due to the change of the direction of vehicle velocity while turning. The magnitude of the lateral acceleration is equal to v^2/r, where v is the speed of the vehicle, and r is the radius of the circle that the vehicle is negotiating.

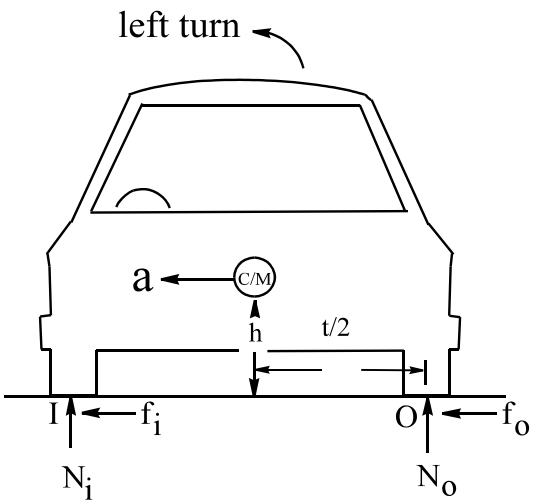

Fig. 6.68 Dynamic Equilirium of a Vehicle in a Steady Left Turn

The dynamic equilibrium of the vehicle and its parametric relationships in a steady turn is shown in Eq. (6.116).

$$
\begin{aligned}
&\textit{At rollover threshold, reactions at i, the inside tire center}\\
&\textit{contact point, are } N_i = 0, \quad \textit{and } f_i = 0.\\
&\sum F_y = m a_y = 0, \quad \textit{therefore, } N_o = W \quad \ldots\ldots\ldots \quad (1)\\
&\sum F_x = m a_x = m a \quad \textit{where}\\
&\quad f_o = \textit{maximum available friction} = \mu N_o = \mu W = \mu m g\\
&\quad f_o = m a, \qquad \textit{therefore } a = \mu g \quad \ldots\ldots\ldots \quad (2)\\
&\sum M_o = m a h, \quad m g \frac{t}{2} = m a h, \quad \therefore \quad \frac{a}{g} = \frac{t}{2h} \quad \ldots\ldots \quad (3)
\end{aligned}
\tag{6.116}
$$

From (2) of Eq.(6.116), to prevent the vehicle from skidding outward, the coefficient of friction must be equal to or greater than the lateral acceleration, $\mu \geq a/g$. From (3) of Eq.(6.116), to exceed the rollover threshold, the lateral acceleration must be greater than t/(2h). t/(2h), termed the stability index, is defined as half of the track width divided by the CG height. Therefore, to reach or exceed the rollover threshold, the following conditions must be satisfied.

$$\mu \geq \frac{a}{g} \geq \frac{t}{2h} \tag{6.117}$$

After the vehicle exceeds the rollover threshold, the vehicle lateral attitude is changed from the horizontal to a position with a roll angle θ, as shown in Fig. 6.69.

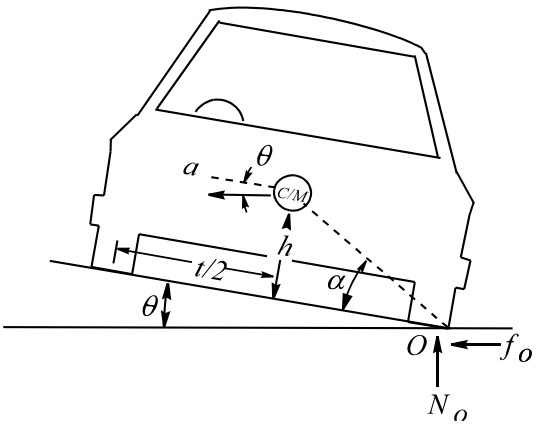

Fig. 6.69 Vehicle Rollover Attitude at a Roll Angle θ

In this orientation, the lateral acceleration needed for dynamic equilibrium decreases from the previous position having a smaller roll angle. This relationship is shown in Eq.(6.118).

$$
\begin{aligned}
&\sum M_o = m a \left(h \cos\theta + \frac{t}{2} \sin\theta \right) \quad \ldots\ldots\ldots\ldots \quad (1)\\
&\frac{t}{2} m g \cos\theta - h m g \sin\theta = m a \left(h \cos\theta + \frac{t}{2} \sin\theta \right)\\
&\textit{Dividing both sides by } m g \cos\theta\, h, \textit{ this becomes}\\
&\frac{t}{2h} - \tan\theta = \frac{a}{g} \left(1 + \tan\theta \frac{t}{2h} \right) \quad \ldots\ldots\ldots\ldots \quad (2)\\
&\textit{for } \theta \approx 0, \textit{ then } \tan\theta \approx 0, \textit{ one gets} \quad \frac{a}{g} = \frac{t}{2h}\\
&\textit{for } a = 0, \textit{ then } \theta = \tan^{-1} \frac{t}{2h}
\end{aligned}
\tag{6.118}
$$

Formula (2) of Eq.(6.118) with a stability index t/2h = 1.2, is plotted in Fig. 6.70. When the roll angle θ is zero, the lateral acceleration required for incipient rollover is a = 1.2 g; for θ = 25°, a = .47 g; and for θ = $\tan^{-1}$(t/2h) =50°, the CG is directly above the trip point, a = 0, no lateral acceleration is needed for the incipient rollover.

6.7.2 Rollover Detection and Threshold Criterion of a Rigid Vehicle

A vehicle supported by a tilt table with an inclination of θ°, hitting a trip point B (or a curb) at the critical sliding velocity, has been shown in Fig. 6.64. Immediately after the curb impact, the relationship between the initial roll angular velocity (or roll rate of the vehicle), ω, the tilt table angle, θ, the vehicle CG height, and track width shown in Eq. (6.111) is rewritten as follows.

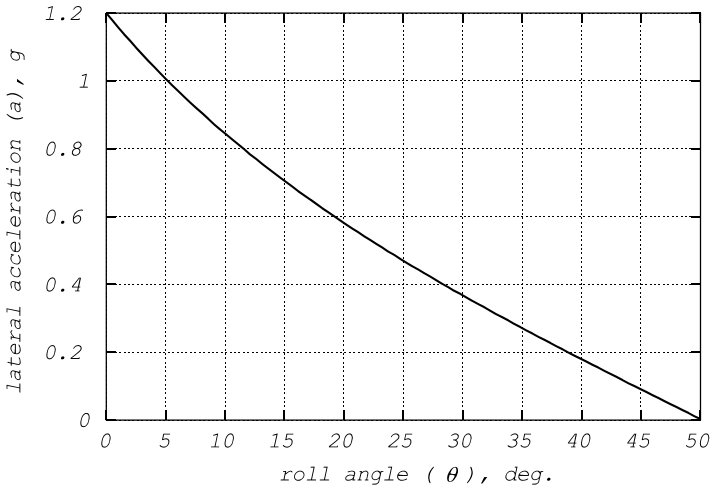

Fig. 6.70 Required Lateral Acceleration for Roll Dynamic Equilibrium at a Roll Angle θ

$$\omega = \sqrt{\frac{2gd[1 - \sin(\theta + \alpha)]}{k^2 + d^2}}$$
$$\alpha = \tan^{-1}\frac{2h}{t} \qquad (6.119)$$

Since the roll rate, ω, shown in Eq. (6.119), is just large enough to raise the vehicle CG from the angle, θ (roll angle of the vehicle), to a point directly above the curb, the formula can be used as a rollover threshold criterion. The rollover threshold for a given vehicle is checked against the transient roll dynamic for rollover detection. The detection of an incipient rollover is one of the rollover threshold criteria used to decide the activation of a safety restraint such as side curtain air bag. Other rollover criteria include the velocity change and magnitude of acceleration at certain vehicle locations.

The data for the two trucks B and F shown in Table 6.3 of Section 6.6.4.2 are used to show the relationship between the roll rate and roll angle. The upper two curves in Fig. 6.71 show that as the roll angle, θ, increases, the corresponding roll rate, ω, decreases, as indicated by Eq. (6.119). When the CG is right above the trip point, the roll rate required for the impending rollover is zero, and the roll angle, θ, complement to the angle α (see Fig. 6.64), is equal to the arctangent of the stability index, σ. As an example, for truck F, the stability index is 1.17, the roll angle at zero roll rate is therefore equal to 90° – $\tan^{-1}$(1/1.17) = 50°. This special angle agrees with that shown in Fig. 6.71.

The corresponding relationships between the CSV and the tilt table angle for the two frame vehicles shown in the lower two curves of Fig. 6.71 also follow the same trend: as the tilt table angle increases, the CSV decreases. As the tilt table angle drops to zero degrees, the CSV rises to about 10 mph.

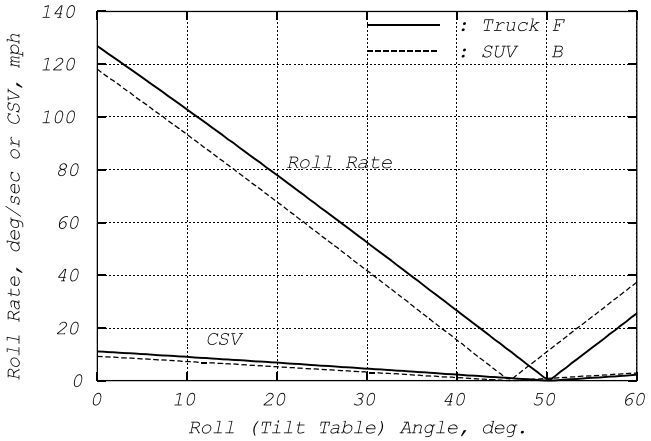

Fig. 6.71 Roll Rate and CSV vs. Roll Angle for Truck F and SUV B.

6.7.3 Transient Rollover Dynamics of a Rigid Vehicle

Upon a lateral impact of a vehicle with a curb, as shown in Fig. 6.72, the vehicle experiences an angular acceleration due to a sudden change in roll rate (roll angular velocity). The equation of motion for θ, shown in (1) of Eq. (6.121), is the basis for the transient rollover dynamics of the vehicle shown in Fig. 6.72. Based on the analysis for the critical sliding velocity given in Eq. (6.108) of Section 6.6.4.1, the initial angular velocity, in terms of the initial impact velocity, is used as the initial condition for integrating the angular acceleration equation shown in (3) of Eq. (6.120).

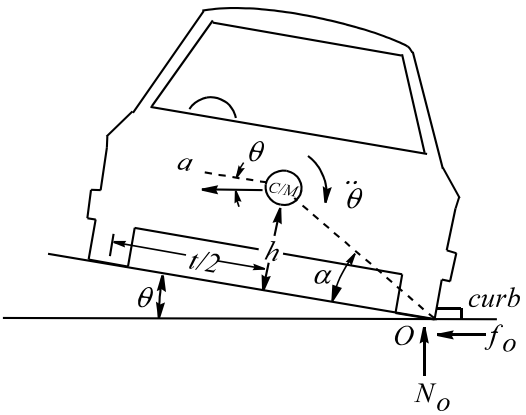

Fig. 6.72 Vehicle Rollover due to Curb Impact

Define the following:
M_o: *moments about O*
$I_o = m(k^2 + d^2) = mk_o^2$
a: *lateral acceleration, g*
$\ddot{\theta}$: *angular acceleration, rad/s*^{2}
k: *roll radius of gyration about CG*
k_o: *roll radius of gyration about point O*
I_o: *roll moment of inertia about point O*
d: *distance from CG to point O*

$$\sum M_o = I_o \ddot{\theta} \quad \ldots\ldots\ldots\ldots\ldots\ldots \quad (1)$$

$$mad\sin(\alpha+\theta) - mgd\cos(\alpha+\theta) = I_o\ddot{\theta} \quad \ldots\ldots\ldots \quad (2)$$

$$\ddot{\theta} = \left[\frac{a\sin(\alpha+\theta) - g\cos(\alpha+\theta)}{k_o^2}\right] d \quad \ldots\ldots\ldots \quad (3)$$

Initial Condition at t =0: $\theta(t=0) = 0.$, $\dot{\theta}(t=0) = \frac{h}{k_o^2} v_o$ (6.120)

6.7.3.1 *Transient Rollover Without Lateral Acceleration*

The dimensions and inertial properties of the SUV B shown in Table 6.3 of Section 6.6.4.2 are used in (3) of Eq. (6.120) for numerical integration. The roll rate and roll angle transient responses can then be computed for three impact speeds of 8, 10, and 12 mph. In this example, the lateral acceleration, a, is assumed to be zero. Lateral acceleration occurs when a vehicle is negotiating a steady turn. Without the lateral acceleration, the model is the same as that where the vehicle slides on a tilt table and trips at a curb. Using the SUV B data, the plots of the transient roll angle responses for the three impact speeds are shown in Fig. 6.73. In the 8 mph curb impact, SUV B rolls from horizontal surface to a maximum roll angle of 22° and then comes back down. Since the maximum roll angle, α, at 8 mph is far from the 44° for which the vehicle CG is above the trip point, the truck does not rollover. In the 10 and 12 mph cases, the truck rolls over, and the time at which the angle is 44° is 670 ms and 400 ms for the 10 and 12 mph tests, respectively.

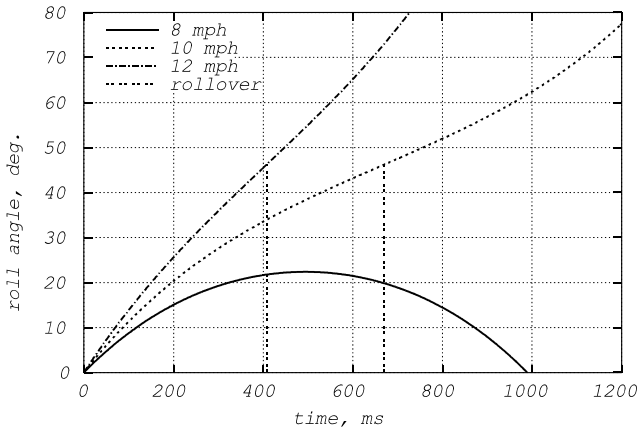

Fig. 6.73 Roll Angle vs. Time for SUV B at Trip Speeds of 8, 10, and 12 mph

The roll rate versus roll angle for SUV B in the three impact tests is shown in Fig. 6.74. The sensor activation threshold window is nearly a straight line, plotted by Eq. (6.119). Any rollover test with the roll rate versus roll angle curve in the section above the window is a test in which the side and curtain air bag activation is warranted. Since the vehicle body and chassis are assumed to be rigid and there is no compliance in the suspension system, the magnitude of roll rate is finite even at time zero when tire just impacts the curb.

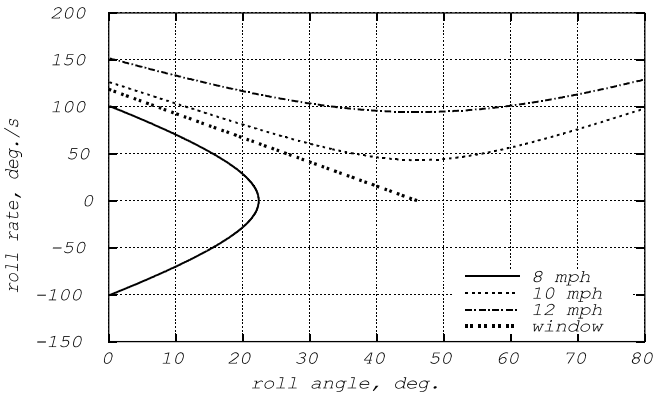

Fig. 6.74 Roll Rate vs. Roll Angle for SUV B at Trip Speeds of 8, 10, and 12 mph

6.7.3.2 *Transient Rollover With Lateral Acceleration*

When a skidding vehicle impacts a curb, the lateral acceleration plays an important role in the transient rollover kinematics. In Section 6.7.3.1, with the sliding vehicle hitting a curb at 8 mph, the maximum roll angle is 22° at 500 ms, as shown in Fig. 6.73. However, when the same vehicle is skidding at the same speed of 8 mph but with the lateral acceleration of only 0.15 g, it reaches 22° at 300 ms, 200 ms earlier than that without the lateral acceleration as shown by the dotted curve in Fig. 6.75. At 1050 ms, the vehicle CG is above the tripped point and has a roll angle of 46°. At this roll angle, the vehicle is still rotating at a roll rate of 40° per second. Since the roll rate vs. roll angle curve passes through the threshold window as shown in Fig. 6.76, the 8 mph test with lateral acceleration becomes a case where the activation of the rollover restraint system is warranted.

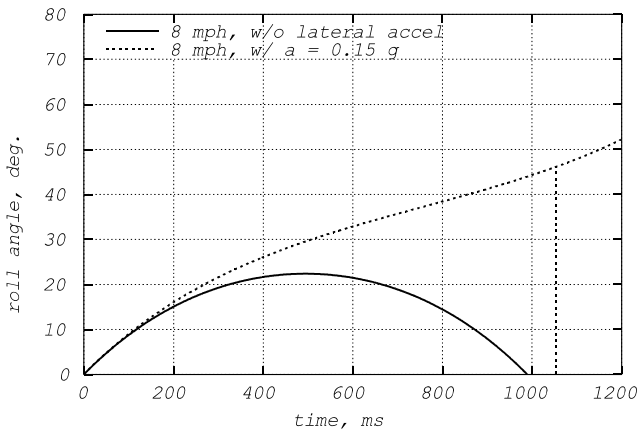

Fig. 6.75 Roll Angle vs. Time for SUV B w/ & w/o Lateral Accel., 0.15 g at 8 mph

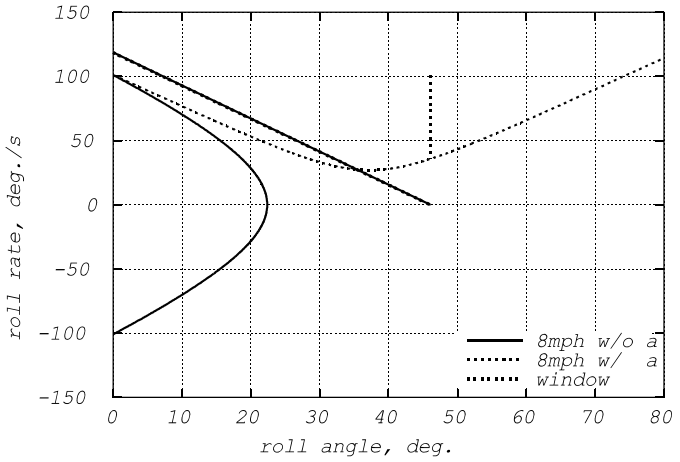

Fig. 6.76 Roll Rate vs. Angle of SUV B w/ & w/o Lateral Accel., 0.15 g at 8 mph

Formula (3) of Eq. (6.120) can be simplified for the special case when the tilt table angle is zero. Since d sin(α) = y (vertical distance between the impulsive loading point F and the CG), and d cos(α) = x (horizontal distance between the application points of F and CG), shown in the rolling and pitching configurations in Figs. 6.77 and 6.78, a simplified formula for the angular acceleration can be obtained as shown in Eq. (6.121).

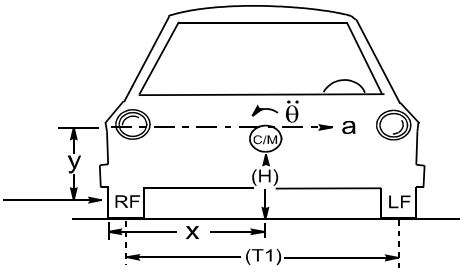

Fig. 6.77 Initial Angular Acceleration in Rolling

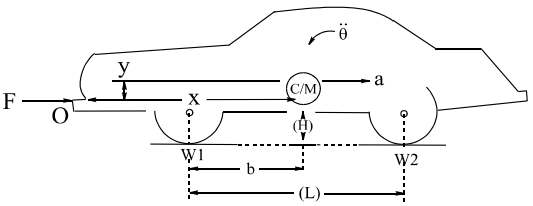

Fig. 6.78 Initial Angular Acceleration in Pitching

$$\ddot{\theta} = \frac{ay - gx}{k_o^2} \tag{6.121}$$

When the car shown in Fig. 6.77 is making a left turn (with the center of the turn circle on the driver side), the inner wheels tend to lift up if the numerator in Eq. (6.121) is positive, or ay > gx. The larger the difference, the larger the angular acceleration in rolling.

The method used in the transient rolling analysis can also be applied to the pitching analysis. A car in a rigid barrier test with the impulsive force located at a distance, y, below the CG, and at the horizontal distance, x, from the CG to the force application point is shown in Fig. 6.78. The pitching of the vehicle about the contact point becomes more severe when the CG is closer to the front in the test. This is because the distance x is shorter and the angular acceleration is larger. To minimize the roof buckling at the A-pillar area and rotation of the dummy, pitching of the vehicle should be

reduced. This can be accomplished by shifting the vehicle weight so the CG is moved backward and/or downward such that the numerator in Eq. (6.121) is minimized.

6.7.4 Rollover and Yaw Detections

The roll rate of a vehicle can be measured by a roll rate sensor [6]. Likewise, the yaw rate of a vehicle can be measured by a yaw rate sensor. To understand the basic dynamic principles involved in roll and yaw rate sensing, a gimbaled gyroscope can be used for demonstration. Shown in Fig. 6.79, the base of the gyroscope is in the yz plane (perpendicular to x) along the center line of the vehicle. The shaft of the rotor is supported by two gimbal bearings on the inner gimbal. The rotor spins at a high speed, and as the vehicle rolls about the x axis, the inner gimbal will rotate about the z axis to proportionate angular deflection. The amount of angular movement of the inner gimbal is proportional to the moment M_z which is equal to the product of moment of inertia of the rotor, I_y, and the angular velocities, ω_y and ω_x.

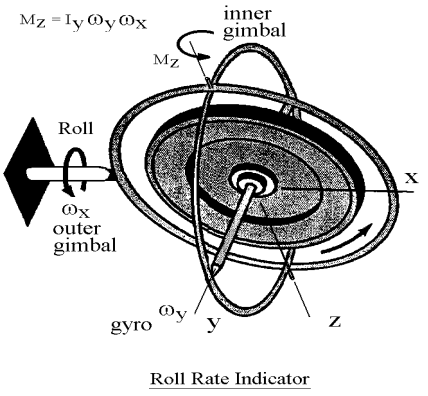

Fig. 6.79 Gimbaled Gyroscope for Roll Rate Detection

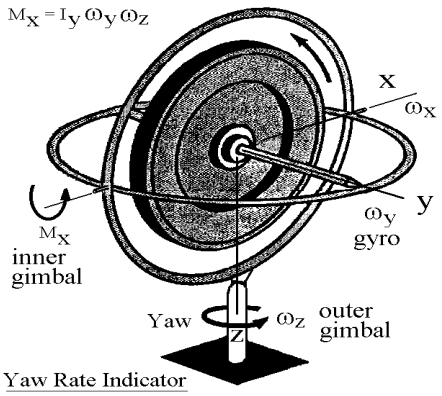

Fig. 6.80 Gimbaled Gyroscope for Yaw Rate Detection

The yaw rate of a vehicle can be measured using the setup of the gimbaled gyroscope shown in Fig. 6.80. Shown in Fig. 6.80, the base of the gyroscope is in the xy plane, perpendicular to the z-axis, the vertical line of the vehicle. The shaft of the rotor is supported by two gimbal bearings of the inner gimbal. As the rotor spins at a high speed, and the vehicle is making a turn about the z-axis, the inner gimbal then rotates about the x-axis with a finite angular deflection. This amount of angular movement of the inner gimbal is proportional to the moment M_x which is equal to the product of moment of inertia of the rotor, I_y, and the angular velocities, ω_y and ω_z.

6.8 ECCENTRIC LOADING ON VEHICLE ROLLOVER

In Section 6.4.6, an analytical method was used to analyze the deceleration of a rigid body subjected to an impulsive loading. To alleviate the complexity of this analytical approach, the analysis was simplified by assigning a local x-y coordinate system (a moving reference frame) such that the impulsive loading is perpendicular to the x-axis, and the direction of the loading is along the y-axis. In this section, a vector method is utilized to analyze the impact loading of a vehicle in rollover using a fixed reference frame. This approach helps determine, for example, the acceleration of a point on the vehicle at a different roll angle without reassigning the local coordinate system.

6.8.1 Vector Method for Eccentric Loading Analysis

A central collision of two vehicles is an impact where the principle direction of force (PDOF) passes through the center of gravity of each vehicle. Since there is no eccentricity, the moment arm

of the force about the CG is zero. Therefore, the rigid body undergoes translation only. In a non-central impact, the PDOF does not pass through the CG of the body; therefore, every point except the CG experiences a direct force and a moment. This is based on the statics principle that a force acting at a point on the rigid body can be transformed into a parallel force acting at another point plus a couple. The vector sum of the direct acceleration and moment-induced acceleration constitutes the resultant acceleration at that point.

Using a vector method helps in solving a general eccentric loading problem. This is because the eccentric loading is a directional problem which requires a proper sign for a quantity, such as force, distance, and moment. Fig. 6.81 shows a force acting on a rigid body at point E. By transforming this force into a force and a couple about an arbitrary point, G, one gets the applied force and moment acting at G. Force EF is perpendicular to GN which is the moment arm P.

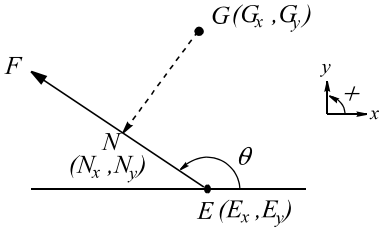

Fig. 6.81 Moment of Force about a Point G

Using a functional minimization technique applied to the distance GN, the coordinates (N_x and N_y) of point N can be obtained in closed-form. They are in terms of the given coordinates (E_x and E_y) of point E, and the horizontal angle, θ of the applied force. Eq.(6.122) shows the procedures used to solve for the coordinates of point N. For the following special cases, when the horizontal angles of the force vector are 0 and 90°, the coordinates of point N can be found from Eq. (6.122) and verified by rotating the force vector shown in Fig. 6.81.

(1) When θ = 0, from (4) and (5) of Eq. (6.122), one gets $N_x = G_x$ and $N_y = E_y$

(2) When θ =90°, from (4) and (5), one gets $N_x = E_x$ and $N_y = G_y$

Define $\vec{F}$: *applied force,* E: *appliccation point of the force*
θ: *horizontal angle of* $\vec{F}$, $\bar{p}$: *position vector, N to G*
G:a point of interest, G_x, G_y: *x, y coordinates of point G*
Given: *points G and E and a force vector at E*
Find: 1) *the coordinates of point N, where GN is perpendicular to* $\vec{F}$
2) *the moment of* $\vec{F}$ *about G, the sign of rotation* (*CCW is* +)

Since $p^2 = |GN|^2 = (G_x - N_x)^2 + (G_y - N_y)^2$ . . . . . (1)

Since vector EN has the same slope as that of EF,

$$\tan\theta = \frac{N_y - E_y}{N_x - E_x} \quad \text{. . . . . (2)} \tag{6.122}$$

Substituting N_y *from* (2) *into* (1), *it becomes*

$$p^2 = (G_x - N_x)^2 + \left[(G_y - E_y) - (N_x - E_x)\tan\theta\right]^2 \quad \text{. . . . . (3)}$$

Minimizing the distance p by setting: $\frac{dp}{dN_x} = 0$, *and solve for* N_x.

$$N_x = \left[(G_y - E_y)\sin\theta\cos\theta + G_x\cos^2\theta + E_x\sin^2\theta\right] \quad \text{. . . . . (4)}$$

From (2): $N_y = E_y + \tan\theta\,(N_x - E_x)$ . . . . . (5)

Since the position vector GN and the force vector EF are now defined, the direction of angular rotation can be obtained by computing the moment which is the product of the position vector and the force vector. The computation of the moment is shown in (1) of Eq. (6.123). The angular rotation is positive (ccw, counterclockwise) if the moment is positive; and it is negative (cw, clockwise) if the moment is negative.

$$
\begin{aligned}
&\textit{Define}\quad \bar{p}\text{: } \textit{position vector,}\\
&\qquad\quad \bar{F}\text{: } \textit{force vector, and}\\
&\qquad\quad \bar{M}\text{: } \textit{moment, (+ if counterclockwise; - if clockwise)}\\
&\textit{then}\quad \bar{M} = \bar{p}\times\bar{F} \quad \ldots\ldots\ldots\ldots\ldots\ldots \quad (1)\\
&\\
&\textit{Define}\quad I_G\text{: } \textit{moment of inertia about G (center of gravity),}\\
&\qquad\quad \bar{\alpha}\text{: } \textit{angular acceleration}\\
&\textit{then}\quad \bar{\alpha} = \frac{\bar{M}}{I_G} \quad \ldots\ldots\ldots\ldots\ldots\ldots \quad (2)\\
&\\
&\textit{Define}\quad \bar{r}_{GQ}\text{: } \textit{position vector from point G to point Q,}\\
&\qquad\quad a_Q\text{: } \textit{acceleration at point Q,}\\
&\qquad\quad a_G\text{: } \textit{acceleration at point G, then}\\
&\qquad\quad a_Q = a_{\bar{G}} + \bar{r}_{GQ}\times\bar{\alpha} \quad \ldots\ldots\ldots\ldots \quad (3)
\end{aligned}
\tag{6.123}
$$

Consequently, the direction of the angular acceleration, α, in the force or moment problem or the torsional stress, τ, in the torsional problem can be defined. The angular acceleration of the rigid body, α, is then equal to M/I_G shown in (2) of Eq. (6.123) and I_G is the moment of inertia of the rigid body about point G.

From Section 6.4, it is known that the acceleration at G is the same as the acceleration at the point of impulsive force. The acceleration at any other point Q can be computed by using (3) of Eq. (6.123). The construction of a circle of constant acceleration can be added by following the procedures adopted in Section 6.4.7.

6.8.2 Rollover Kinematics Using the Vector Method

As part of the requirements for occupant protection in FMVSS 208, a vehicle is placed on a tilt table at 23° and the table is mounted on a cart, which hits a curb at 30 mph. The purpose of the test is to check for occupant containment during rollover. Since the impulsive loading is due to the impact between the cart (carrying the tilt table) and the stopper, the direction of the impulse is horizontal. The accelerations at both sides of the roof rails immediately after impact can then be computed by using the vector method described in the previous section.

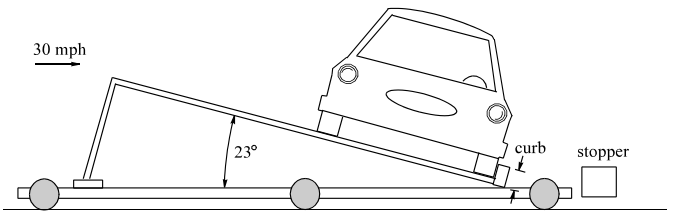

Fig. 6.82 FMVSS 208 Tilt Table Rollover Test.

The x-y axes in the plot shown in Fig. 6.83 are set in a global coordinate system. The CG (center of gravity) location of the vehicle is located at the point with a symbol of a triangle, and the radius of gyration in a roll is 2 ft. An SUV shown in Fig. 6.83 is subjected to an impulsive loading at the left side wheel. The angle between the impulsive loading and the tilt table is 23° as shown in Figs. 6.83 and 6.84. Every point on the COCA (circle of constant acceleration; see Section 6.4.3 for its construction) is shown as a solid curve passing through the CG (point G), and has the same acceleration as that at the curb contact. However, the acceleration at the right roof rail location Q is greater than that at the contact point or at the CG. The ratio of the acceleration at the right roof rail to that at the CG equals the ratio of the radius of the outer circle to that of the inner circle. The acceleration at the roof rail therefore is about 1.6 times higher than that at the CG. Fig. 6.84 shows the same problem as that in Fig. 6.83, except that the roof rail Q is at the left side of the vehicle instead. The acceleration at the left roof rail is about 2.1 times that at the CG.

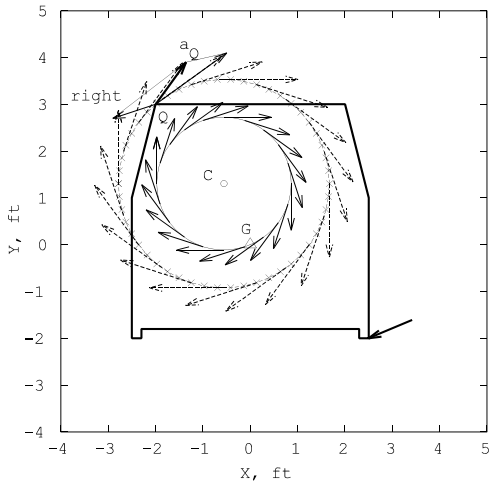

Fig. 6.83 Right Roof Rail Acceleration in a 23° Tilt Table Test.

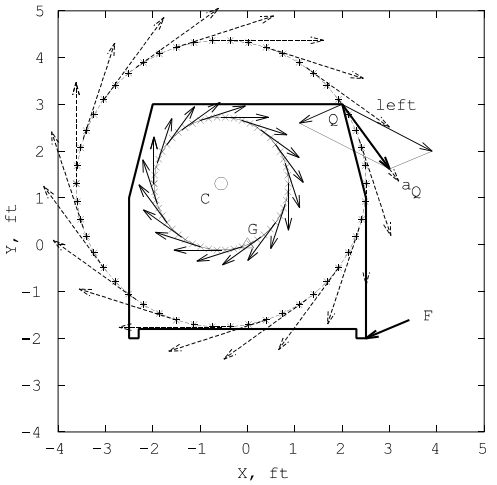

Fig. 6.84 Left Roof Rail Acceleration in a 23° Tilt Table Test.

Although the two cases shown in Figs. 6.83 and 6.84 use the same input data, locations of the CG, and center of the COCA circle, C, the acceleration at the left roof rail in Fig. 6.84 is higher than that at the right roof rail in Fig. 6.83. This is because the acceleration at point Q consists of a linear acceleration component which is parallel to the loading at the contact point and an acceleration component perpendicular to GQ which is due to the moment. Although the magnitudes of each of the two components in two cases are the same, the two components at the right roof rail are about 160° apart and at the left roof rail, 120° apart. This explains why the resultant acceleration, a_Q, at the left roof rail is larger than that at the right roof rail.

In the tilt table rollover test, one of the accelerations at the roof rails is higher than at other locations in the vehicle. In theory, the roof rails are the ideal locations for installing rollover crash sensors, especially, considering the roof rails are where the side air bag curtains for rollover protection are installed. However, in practice, due to the cost and manufacturing issues, the rollover sensor is located at the centerline tunnel where the frontal and side impact crash sensors are located.

Figs. 6.85 and 6.86 show the new cases where the impulsive loading is at a horizontal angle of -23°, i.e., opposite to that shown in Figs. 6.83 and 6.84. Because the moment arm of the impulsive loading about the CG is smaller than before, the angular acceleration is also smaller. At both roof rail locations, the two acceleration components don't add up; instead, they tend to cancel out each other. Therefore, the accelerations at both roof rail locations are smaller than those at the CG.

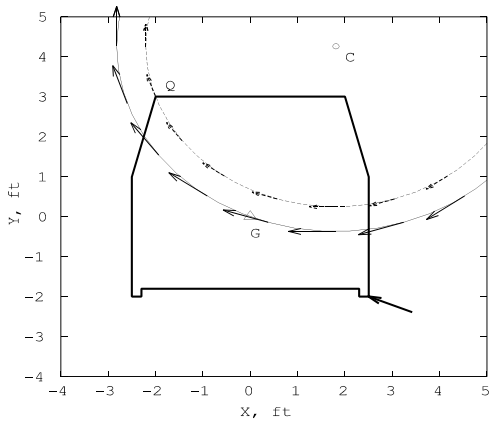

Fig. 6.85 Acceleration at Right Roof Rail in a -23° Tilt Table Test.

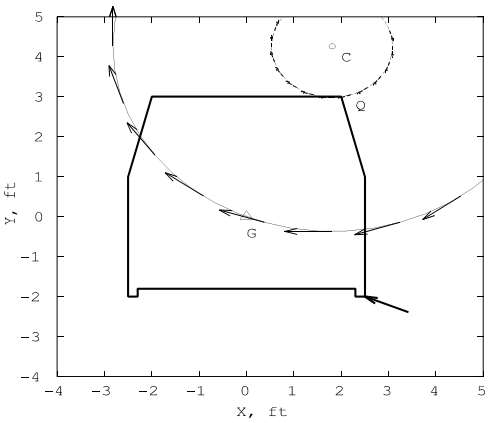

Fig. 6.86 Acceleration at Left Roof Rail in a -23° Tilt Table Test.

With a zero tilt table angle, the vehicle is in an upright position and the direction of the impulsive loading is horizontal, as shown in Fig. 6.87. The resultant accelerations at both right and left roof rails are the same and about 10% more than that at the CG.

Fig. 6.88 shows a situation where the SUV has rolled over a quarter turn and the left roof rail has hit the ground. Due to the fact that the two acceleration components at the left roof rail are in the upward direction, they add up to a resultant acceleration of about 3.5 times that at the CG. This is also the case for the right roof rail location.

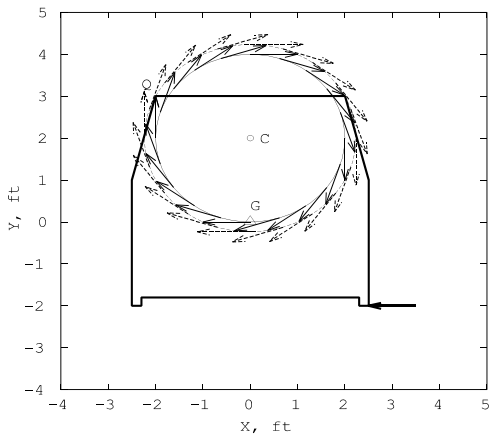

Fig. 6.87 Accelerations at L. and R. Roof Rail in a Level Impact

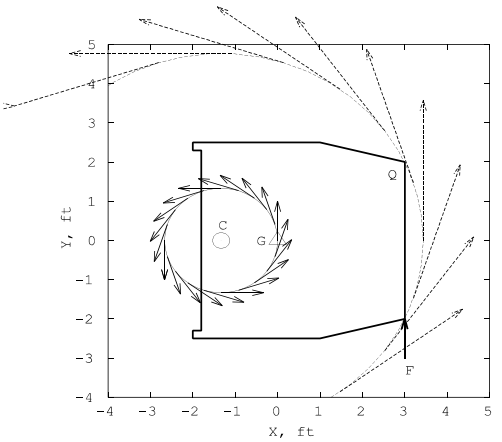

Fig. 6.88 Accelerations at L. and R. Roof Rail in a Quarter Turn Impact

6.8.3 Conditions for a Vehicle to Stop Rolling Following Rollover

In a vehicle rollover, if the initial sliding velocity is large compared to the critical sliding velocity, the vehicle may become airborne and tumble in the air before it contacts the ground. In this section, kinematic principles are presented to determine whether the vehicle will stop rolling upon impacting after being airborne.

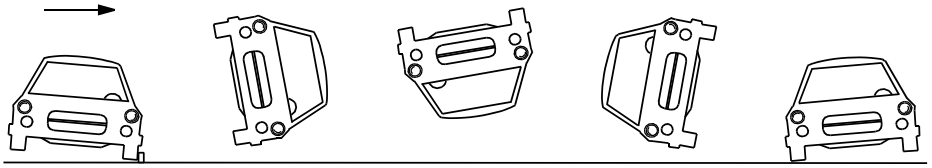

Fig. 6.89 Vehicle Tripped Rollover and Air-borne

During rollover, the transient angular motion of a vehicle upon landing on the ground can be modeled using the equation of angular acceleration shown in Eq.(6.120) of Section 6.7.3. At any given moment, the angular velocity of the vehicle, ω_1, at a roll angle θ can be determined. This is Event #1, as shown in Fig. 6.90. As the vehicle pivots about A, the reaction at point A does no work, since the contact point does not move. At Event #2, just before the vehicle impacts the ground, no impact occurs between Events #1 and #2; therefore, no energy is gained or lost. The only force which does work is the weight of the vehicle. Conservation of energy can then be applied to determine the angular velocity ω_2 at Event #2, as shown in Eq. (6.124).

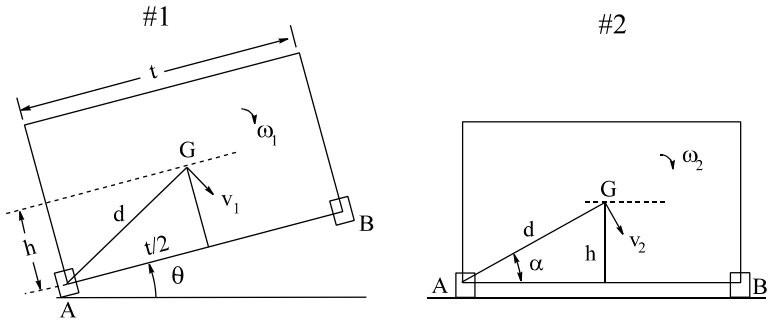

Fig. 6.90 Vehicle Rollover Before Hitting the Ground

$$T_1 + U_{12} = T_2, \quad \textit{where}$$

$$T_1 = \frac{1}{2}mv_1^2 + \frac{1}{2}I_G\omega_1^2 = \frac{1}{2}m(d\omega_1)^2 + \frac{1}{2}(mK^2)\omega_1^2 \qquad (I_G = mK^2)$$

$$= \frac{1}{2}m(K^2 + d^2)\omega_1^2 \qquad K\text{: radius of gyration}$$

$$U_{12} = mg\left[\frac{t}{2}\sin\theta + h\cos\theta - h\right] \qquad (\textit{Reference potential at ground})$$

$$T_2 = \frac{1}{2}m(K^2 + d^2)\omega_2^2, \quad \textit{therefore} \qquad (6.124)$$

$$\omega_2^2 = \omega_1^2 + \frac{2g}{K^2 + d^2}\left[\frac{t}{2}\sin\theta + h(\cos\theta - 1)\right] \quad \ldots\ldots\ldots \quad (1)$$

Special case:

1. $\theta = 0°$ $\qquad \omega_2 = \omega_1$
2. $\theta = 90°$ $\qquad \omega_2^2 = \omega_1^2 + \dfrac{2g}{K^2 + d^2}\left[\dfrac{t}{2} - h\right]$

After Event #2, point B impacts the ground. It is assumed that this impact is inelastic (plastic), and the ground is sufficiently rough to prevent any slipping. We propose to determine whether the vehicle stops after hitting the ground or keeps rotating. If the vehicle stops, the vertical components

of the impulsive loading exerted on both points A and B can be determined. If the vehicle keeps rotating, one can determine how high the CG will rise above the ground.

Since we do not know whether the vehicle will stop after hitting the ground or keep rotating, we must make an assumption and choose either one of the two scenarios and then check whether the result obtained is consistent with the assumption. If it is, the assumption is correct.

Let us assume that from the moment that the vehicle impacts the ground (immediately after Event #2) the vehicle impacts the ground at two points shown in Event #3 of Fig. 6.91. Since there is an impact between Events #2 and #3 which involves energy loss, one should use the principle of impulse and momentum to solve for the unknown vertical impulses acting at points A and B.

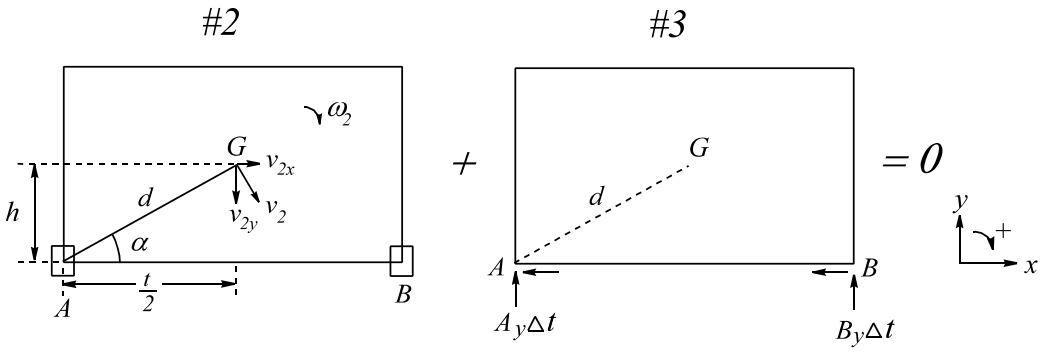

Fig. 6.91 Assuming Vehicle Stops Rolling after Impacting the Ground

Assuming the vehicle stops after impact, the initial momentum at Event #2 plus the angular impulse acting on the vehicle during Event #3 equals the final momentum. Here, the final momentum is zero since we will assume that the vehicle stops rolling after impacting the ground.

Solving the two unknown impulses involves the equilibrium relationships where the total angular impulse and the total linear impulse are set to zero as shown by (1) and (3) of Eq. (6.125), respectively. (2) and (4) of Eq. (6.125) show the expressions for the linear impulses acting at points A and B, respectively. In the following, let us define

A_y = Vertical impact force at point A, B_y = Vertical impact force at point B, and

Δt = Duration of impact forces

$$v_2 = d\omega_2, \quad v_{2x} = v_2 \cdot \sin\alpha = d\omega_2 \cdot \frac{h}{d} = \omega_2 h$$

$$v_{2y} = v_2 \cdot \cos\alpha = d\omega_2 \cdot \frac{t}{2d} = \omega_2 \frac{t}{2}$$

$$\sum M_B = 0 \quad (CW+) \quad \ldots\ldots\ldots\ldots\ldots\ldots \quad (1)$$

$$m v_{2x} \cdot h - m v_{2y} \frac{t}{2} + I\omega_2 + (A_y \Delta t)t = 0 \qquad \Delta t = Duration$$

$$\therefore A_y \Delta t = \frac{m\omega_2}{t}\left[\left(\frac{t}{2}\right)^2 - (h^2 + K^2)\right] \quad \ldots\ldots\ldots \quad (2) \qquad (6.125)$$

$$\sum p_y = 0 \quad (\uparrow +) \quad \ldots\ldots\ldots\ldots\ldots\ldots \quad (3)$$

$$A_y \Delta t + B_y \Delta t - m v_{2y} = 0, \quad therefore$$

$$B_y \Delta t = \frac{m\omega_2}{t}\left[\left(\frac{t}{2}\right)^2 + (h^2 + K^2)\right] = \frac{m\omega_2}{t}[d^2 + K^2] \quad \ldots \quad (4)$$

Due to the inelastic impact, the vertical loading B_y at point B is always positive. However, the vertical loading at point A, A_y, is positive (reaction force pointing upward) if the vehicle stops rolling

after impact. Therefore, from (2) of Eq. (6.125), the necessary condition for the vehicle to stop rolling after impact is shown in Eq. (6.126).

$$\text{For } A_y \Delta t > 0, \qquad \left(\frac{t}{2}\right)^2 > (h^2 + K^2)$$
$$\frac{t}{2} > \sqrt{h^2 + K^2} \quad \ldots \quad \textit{Vehicle stops after impact.} \tag{6.126}$$

In order for the vehicle to stop rolling after one side of vehicle hitting on the ground, the half track width of the vehicle should be greater than the hypotenuse of a right triangle with CG height on one side and the roll radius of gyration on the other. A diagram depicting the stop-rolling condition is shown in Fig. 6.92. A quarter circular arc is drawn about center O using the half track width as the radius. The CG height along the vertical axis and the radius of gyration along the horizontal axis form a right triangle OGA. A block (or a vehicle) with smaller radius of gyration and/or smaller CG height would yield a hypotenuse such as OB. Since OB is less than the radius the circular arc, the vehicle stops rolling (or moving) after hitting the ground. Any combination of h and K having the hypotenuse such as OC greater than the radius of the circular arc would result in lifting up the non-impacting side of the block.

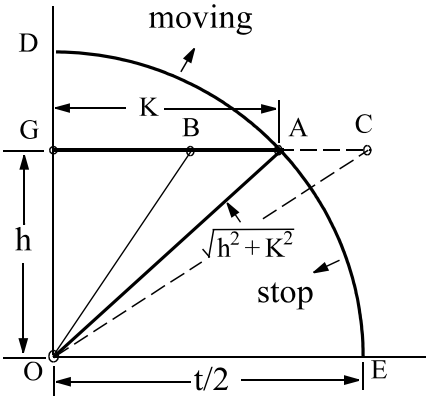

Fig. 6.92 Condition to Stop after One side of Vehicle hits the Ground

Case Study 1: A typical mid-size truck has the following geometric and inertial properties:
h (CG height) = 27.5 in, t (track width) = 60 in, K (radius of gyration in roll) = 25 in.

Following the drawing shown in Fig. 6.92, the hypotenuse = 37.2 in, since OE = t/2 = 30 in, which is less than the hypotenuse that is OC shown in Fig. 6.92. Therefore, under the assumption stated in the beginning of this section, the truck in this Case Study would not stop and the point A will lift up following the impact.

Case Study 2: Given a rectangular block with a width of t and a height of 2h, similar to the one shown in Fig. 6.90, with the data shown in Eq. (6.127), the block is positioned at an angle of $\theta = 40^o$ and released from rest. Assume the ground is sufficiently rough to prevent the block from slipping. Determine whether the block will stop or keep moving after impacting the ground.

$$\textit{A rectangular block } (t \times 2h) \textit{ with } t = .6m,\ h = .2m,\ M = 50kg,$$
$$I = \frac{M}{12}[t^2 + (2h)^2] = MK^2, \quad \textit{where} \quad K^2 = \frac{t^2 + (2h)^2}{12} = .043\ m^2 \tag{6.127}$$
$$d^2 = \left(\frac{t}{2}\right)^2 + h^2 = .13m^2$$

Using the condition that the vehicle stops after impact, we get

$$\frac{t}{2} = \frac{0.6m}{2} = 0.3\,m, \quad \sqrt{h^2+K^2} = \sqrt{(0.2)^2+0.043} = 0.29\,m$$
$$\text{Since } \frac{t}{2} > \sqrt{h^2+K^2}, \quad \text{block stops after impact.} \tag{6.128}$$

Substituting $\theta = 40°$ and $\omega_1 = 0$ into (1) of Eq. (6.124), the angular velocity of the block just before hitting the ground is computed and shown in Eq. (6.129).

$$\begin{aligned}\omega_2^2 &= \omega_1^2 + \frac{2g}{K^2+d^2}\left[\frac{t}{2}\sin\beta + h(\cos\beta - 1)\right] \\ &= 0 + \frac{2\times 9.81}{.043+.13}\left[\frac{.6}{2}\sin 40° + .2(\cos 40° - 1)\right] \\ \omega_2 &= 4.07\ rad/s\end{aligned} \tag{6.129}$$

The vertical loadings at the two corners of the block are computed using Eq. (6.125) and the results as shown in Eq. (6.130).

$$\begin{aligned}&\frac{M\omega_2}{t} = \frac{50\times 4.07}{.6} = 339 \\ &\left(\frac{t}{2}\right)^2 = .09\,m^2, \quad h^2+K^2 = .04+.043 = .083\,m^2 \\ &\left(\frac{t}{2}\right)^2 + (h^2+K^2) = .173\,m^2, \quad \left(\frac{t}{2}\right)^2 - (h^2+K^2) = .007\,m^2 \\ &\therefore A_y\Delta t = 339\times .007 = 2.37\,N\text{-}s, \quad B_y\Delta t = 339\times .173 = 58.6\,N\text{-}s\end{aligned} \tag{6.130}$$

Since both A_y and B_y are positive, the solution is physically possible; the block stops after impact. Note that vertical impulse at point A is fairly small compared to that at point B, this is an indication that point A is on the verge of lifting up from the ground. If, for example, the CG height were a little higher or the track width a little shorter, the vertical impulse at point A might become negative, and the block could start a new phase of rotation.

6.9 REFERENCES

1. Juvinall, R.C., "Stress, Strain, and Strength," McGraw Hill, 1967. pp. 170,171, 175.
2. Spotts, M.F., "Impact Stress in Elastic Bodies Calculated by the Energy Method," from "Spring Design and Application," Edited by N.P. Chironis, Product Engineering, McGraw-Hill Co., 1961.
3. Prasad, A. K., "Coefficient of Restitution of Vehicle Structures and its Use in Estimating the Total V in Automobile Collisions," pp.217–246, Crashworthiness and Occupant Protection in Transportation Systems, 1991 ASME Winter Annual Meeting.
4. "Characterization and Dynamic Testing of Utility Vehicles, Volume 1 — Executive Summary, Volume 2 — Vehicle Characterization Tests, Volume 3 — Vehicle Dynamic Tests," Report No: FaAA-AZ-R-89-4-2, Failure Analysis Associates, April, 1993.
5. Gillespie, T.D., "Fundamentals of Vehicle Dynamics," Published by Society of Automotive Engineers, Inc., 1992.
6. Chou, C. C., and Amin, M., "A Review of the State of the Art of Angular Rate Sensors," SAE Paper No. 2000-01-2668, Society of Automotive Engineers, 2000.

CHAPTER 7

CRASH SEVERITY AND RECONSTRUCTION

7.1 INTRODUCTION

In the development of a new vehicle platform, its crashworthiness is an important concern, and it is imperative to compare the impact severity of the vehicle and occupants under various test and design conditions. Since an impact is a physical event that involves analyses of impulses and energy components, such as kinetic energy, energy absorption, and energy dissipation, the analyses require both the principle of work and energy and that of impulse and momentum. Although both principles are derived from Newton's Second Law, they are not mutually exclusive when it comes to solving problems involving impact and excitation.

It will be shown that any crash event, modeled by either a single-mass or a multi-mass system, involves impact and/or excitation. Recognizing the existence of the impact and/or excitation, the closed-form formulas derived in Section 4.11 of Chapter 4 can be utilized to solve problems. Case studies, such as the dynamic principles of pyrotechnic pretensioner on the occupant responses, are investigated. The preloading effect of a restraint system on the occupant response and ridedown efficiency are discussed. Many crashworthiness topics related to single and multi-vehicle collisions are analyzed by the engineering principles presented so far for determining the degree of crash severity. Applications of these principles to vehicle-to-vehicle compatibility, shear loading of truck body mounts due to eccentric loading, and the methodology of accident reconstruction methodology are also presented.

7.2 OCCUPANT MOTION UNDER IMPACT AND EXCITATION

Occupant motion in the vehicle compartment is controlled by both the vehicle and restraint impact factors. Both factors complement each other in producing the occupant responses in a particular test condition. Since any vehicle produced needs to be certified to meet the federal vehicle safety standard, it is not unusual to see a truck equipped with a pyrotechnic device or a pretensioner. This is because the truck in general is stiffer than a passenger car, and the pretensioner affects the motion of an occupant. The chest deceleration rises up earlier and the ensuing ridedown efficiency increases. In the following sections, a simple 2-dimensional occupant model is presented to show the translation and rotational kinematics of the occupant in a crash. The theory and effect of the pretensioner in improving the occupant crashworthiness are presented in the following sections.

7.2.1 Two-Degree-of-Freedom Occupant Model

A generalized two-degree-of-freedom (TWODOF) dynamic model based on a simple restrained occupant model [1] is developed to simulate occupant motion and response in the event of a vehicle frontal collision. The TWODOF model and the variables used are shown in Fig. 7.1 and Table 7.1, respectively. Unrestrained and restraint systems, including lap, shoulder belts, air bag, and their combinations are incorporated in the model. The occupant-vehicle contact surfaces are defined by the upper and lower panels. The occupant body consists of a chest (upper mass) and a hip (lower mass). The chest is able to rotate about the link pivot, and the hip is able to translate horizontally. The vehicle compartment is defined by the inclinations and the locations of the upper and lower panels and their force deflection (F-D) data. In the case of an air bag restraint system, the air bag F-D data is combined together with the upper panel F-D characteristics.

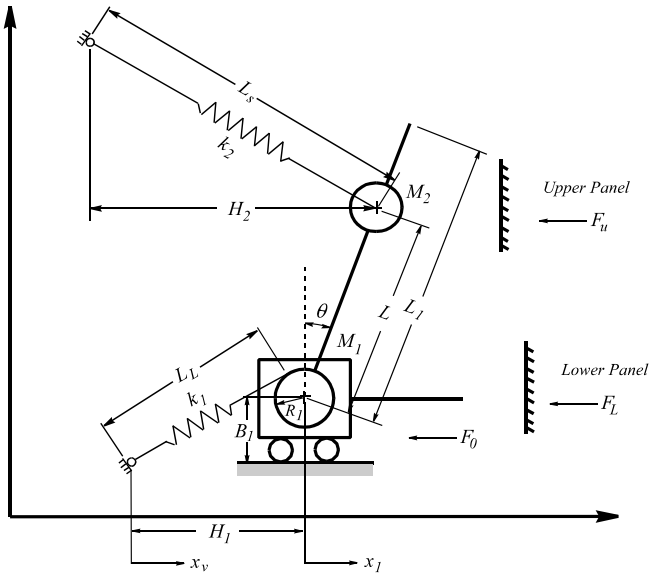

Fig. 7.1 A Two-Degree-of-Freedom Occupant Model

Table 7.1 Definitions of Model Variables

M_1: Lower mass (Hip),
M_2: Upper mass (Chest)
X_1: Lower mass displacement
X_v: Vehicle displacement (Crush)
L: Distance from link pivot to upper mass
L_1: Distance from link pivot to head center
L_s: Distance from D-ring to upper mass
L_L: Distance from lap belt anchor to tangent point on hip circle
R_1: Radius of hip circle
B_1: Vertical distance from lap belt anchor to center of hip circle
δ_1: Lap belt stretch
F_0: Friction between hip and seat
F_L: Knee and lower panel contact force
F_u: Effective torso and upper panel contact force which produces a moment about link pivot
K_1: Lap belt stiffness
K_2: Shoulder belt stiffness
H_1: Horizontal distance from lap belt anchor to hip center
H_2: Horizontal distance from D-ring to torso center
θ: Angular displacement of body segment from vertical

The model also simulates an unrestrained occupant impact. The derivation of the equations of motion of the "TWODOF" model is based on a lap and shoulder restraint system. The occupant undergoes the two-dimensional motion and is subjected to restraint interactions and external forces. The shoulder belt load is applied to the chest, and the lap belt load is applied tangentially to the hip circle. The lap belt is "wound up" on the hip as the chest rotates. The lap belt load is thus a function of the relative displacement of hip-to-vehicle and chest rotation.

The dynamic solution of the occupant model is obtained using the LaGrange's Equations as shown in Eq. (7.1). The independent variables in the equation are q_i: (1) $i = 1$, $q_i = x_1$, the linear displacement of the hip joint, and (2) $i = 2$, $q_2 = \theta$, the angular displacement of the upper torso. The kinetic and potential energies of the system are expressed in terms of the two independent variables as shown in Eq. (7.2).

$$\textit{LaGrange's Equation:}\quad \frac{d}{dt}\left(\frac{\partial T}{\partial q_i}\right)-\frac{\partial T}{\partial q_i}+\frac{\partial V}{\partial q_i}=Q_{qi} \tag{7.1}$$

Where q_i and Q_{qi} are defined as follows:

i	1	2
q_i	x_1	θ
Q_{qi}	$-(F_0 + F_L)$	$-F_u$

$$\textit{System Kinetic energy and System Potential energy:}$$
$$T = \frac{1}{2}M_1\dot{x}_1^2+\frac{1}{2}M_2[\dot{x}_1^2+(L\dot{\theta})^2+2\dot{x}_1L\dot{\theta}\cos\theta] \tag{7.2}$$
$$V = \frac{1}{2}(K_1\delta_1^2+K_2\delta_2^2)-M_2gL(1-\cos\theta)$$

By completing the partial differentiations with respect to the independent variables x_1 and θ shown in Eq. (7.1), the equations of motion of the model in terms of the linear acceleration of the hip and the angular acceleration of the chest are thus derived as shown in Eq. (7.3).

$$\begin{bmatrix} M_1+M_2 & M_2L\cos\theta \\ M_2\cos\theta & M_2L \end{bmatrix}\begin{bmatrix}\ddot{x}_1 \\ \ddot{\theta}\end{bmatrix}=\begin{bmatrix}F_{AB} \\ F_{BC}\end{bmatrix} \tag{7.3}$$

Solving for the linear and angular accelerations in Eq. (7.3), one gets the closed-form solutions for the two accelerations as shown in Eq. (7.4).

The model has been generalized to include the following main variables and features:

$$\textit{Closed-Form Formulas for } \ddot{x}_1 \textit{ and } \ddot{\theta}\textit{:}$$
$$\ddot{x}_1 = \frac{F_{AB}-F_{BC}\cos\theta}{M_1+M_2\sin^2\theta},\qquad \ddot{\theta} = \frac{-F_{AB}\cos\theta+F_{BC}\dfrac{M_1+M_2}{M_2}}{L(M_1+M_2\sin^2\theta)},\qquad \textit{where} \tag{7.4}$$
$$F_{AB} = -(F_0+F_l)-\left(K_1\delta_1\frac{H_1L_l+R_1B_1}{H_1^2+B_1^2}+K_2\delta_2\frac{H_2}{L_s}\right)+M_2L\dot{\theta}^2\sin\theta$$
$$F_{BC} = -F_u-K_1\delta_1\frac{R_1}{L}-K_2\delta_2+M_2g\sin\theta$$

1. Chest force-deflection characteristics (see Fig. 7.2).
2. Seat friction and friction coefficient between shoulder belt and chest.
3. Restraint systems: unrestrained, lap, shoulder belts, air bag, and their combinations.
4. Lap and shoulder belt slacks.
5. Air bag deployment time.

6. Chest and knee targets.
7. Upper and lower panel general F-D characteristics (see Fig. 7.3).
8. Linear belt stiffness (with minor program modification, non-linear belt stiffness or general belt F-D curve can be simulated).

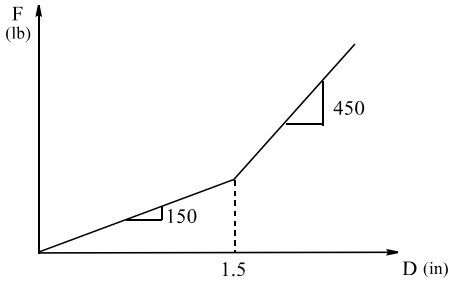

Fig. 7.2 Chest Force-Deflection Data

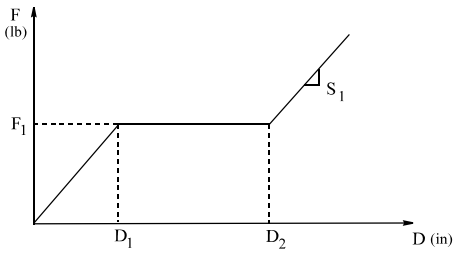

Fig. 7.3 Vehicle Contact Surface Force-Deflection Curve

7.2.2 Effect of Seat Belt and Pretensioner on Occupant Kinematics

In a vehicle frontal crash, an unbelted occupant undergoes a free-flight motion until impacting on the vehicle interior surfaces, such as windshield, steering wheel, and instrument panel as shown in the left column of Fig. 7.4.

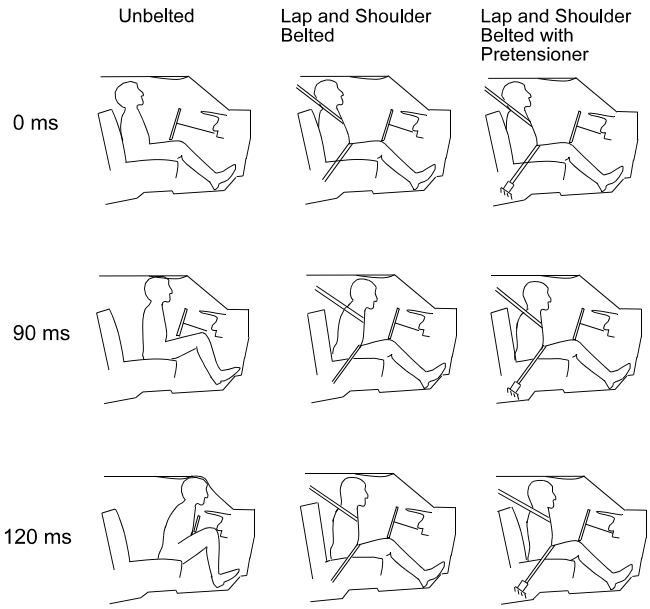

Fig. 7.4 Unrestrained and Restrained Occupant Kinematics in a Crash

The motion of an occupant without and with a pretensioner installed on the retractor anchor side or buckle side of the 3-point (lap and shoulder belt) restraint system is shown in columns 2 and 3 of Fig. 7.4, respectively. The dynamic effects of the pretensioner on the occupant dynamics are the subjects to be presented in the following sections.

7.3 PRELOADING ON AN OCCUPANT

Any crash event involves impact and/or excitation. A vehicle passenger compartment in a frontal rigid barrier test undergoes an impact process, while a restrained occupant undergoes an excitation by the vehicle crash pulse and an impact at high speed test by the intruding toe board on the lower extremities of the occupant. The outcome of the impact can be quite different from that of the excitation. As an example, the occupant in a vehicle crash has the benefit of riding down with the deforming vehicle structure, thus diverting some of the occupant energy away from interacting with the restraint system. The occupant response, such as chest deceleration, depends on the distribution of the remaining restraint energy. In a laboratory, a Hyge sled test is intended to replicate the occupant dynamics in a vehicle-to-rigid barrier condition. Except for the effect of vehicle intrusion and vehicle pitch, the sled test captures most of the effects of the vehicle crash pulse on the occupant response.

In Section 6.6.4 of Chapter 6, the kinetics of a preloaded safety belt is briefly discussed. Depending on the test condition, it may have different effects on the dynamics of the subject being tested. In this section, the effects of a pretensioner on impact responses are presented. The kinetic relationships for both component and sled test conditions (due to excitation and impact) are described, respectively.

7.3.1 Modeling Pretensioning Effects in a System Test

The main function of the pretensioner is to take out any restraint slack as early as possible in an impact. By zeroing in the slack, the pretensioner in a system test reduces the torso deceleration while the vehicle is undergoing the "deformation phase" and the occupant is undergoing "ridedown."

A summary of a series of tests conducted in the laboratory using a Hyge sled is shown in Fig. 7.5.

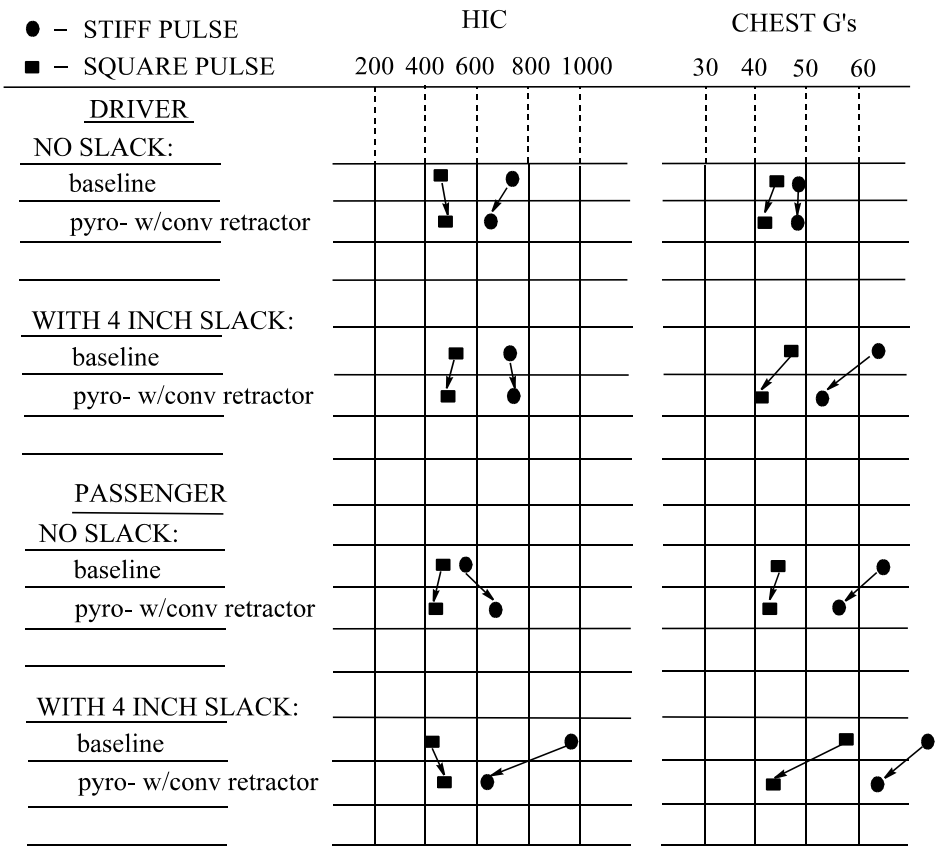

Fig. 7.5 Effects of Pretensioner on Occupant Responses

There are four factors in the tests, and two occupant responses (HIC and Chest G).

The factors are (1) pulse: stiff and approximated square pulses, (2) driver and passenger, (3) with and without restraint slack (four inches), and (4) with and without pretensioner. A total combination of 8 tests were conducted and the chest g and HIC for each of the 8 tests are shown in the chart.

Looking at the effect of pulse shape on occupant responses in Fig. 7.6, the square pulse is seen to be an idealized optimal pulse, the resulting chest g and HIC being lower than those of stiff pulse. Regardless of the type of pulse used in the test, the effect of the pretensioner on reducing the occupant responses, especially the chest g, is quite obvious. The pretensioning effect is even more pronounced for the cases where a stiff pulse was used and the occupant had a 4-inch restraint slack.

Assuming that restraint slack is taken out as soon as the impact is initiated, the occupant will be restrained by the pretensioning force, F_O, at time zero as shown in Fig. 7.6. The magnitude of the pretensioning force is assumed to be on the high side of 600 lbs.

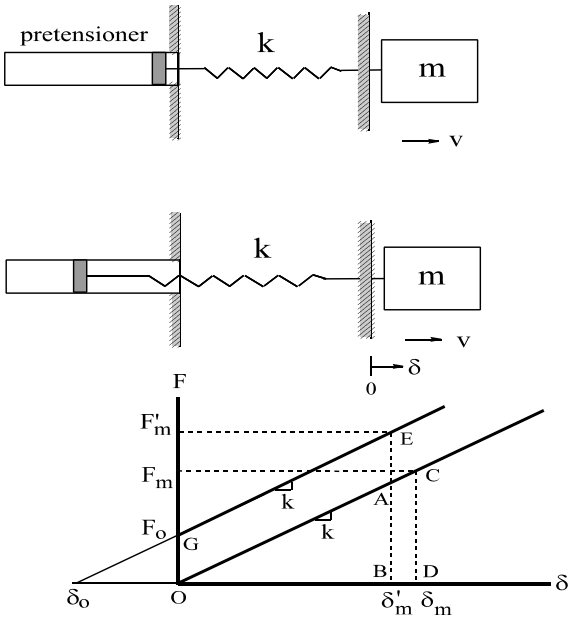

Fig. 7.6 Restraint System w/ Pretensioner and F vs. D

Using the CRUSH II model for a 30 mph rigid barrier test, the input data needed for the model are listed in Table 7.2. Note that the occupant weight of 100 lbs is an approximated effective weight of torso interacting with the restraint system. The model parameters for the vehicle, occupant, frame, and restraint (spring) are shown in Fig.7.7.

Table 7.2 Input Data for Vehicle-Occupant Models w/ and w/o Restraint Preload

Model, 30 mph Barrier	Weight, klb		Stiffness, klb/in		Restraint Preload, F_o klb
	Vehicle	Occupant	Frame	Restraint	
w/o preload	M1: 3 klb	M2: 0.1 klb	3	0.5	0
w/ preload	M3: 3 klb	M4: 0.1 klb	3	0.5	0.6

Note: w/o : without; w/ : with

The motion and chest g responses of an occupant (M_2 or M_4) riding in a vehicle for the two cases, without and with a pretensioner, are shown in Fig. 7.7. The restrained occupant decelerations vs. time for the two cases are also marked on the model. The simulation results of the modeling are summarized in Table 7.3. The responses of an occupant, such as the maximum displacement, restraint deflection, restraint force, and restraint energy, are smaller in the model with a pretensioner (for M_4) than in the model without a pretensioner (for M_2). Therefore, overall, the crash severity of the occupant in this system test with a pretensioner is less than that without a pretensioner.

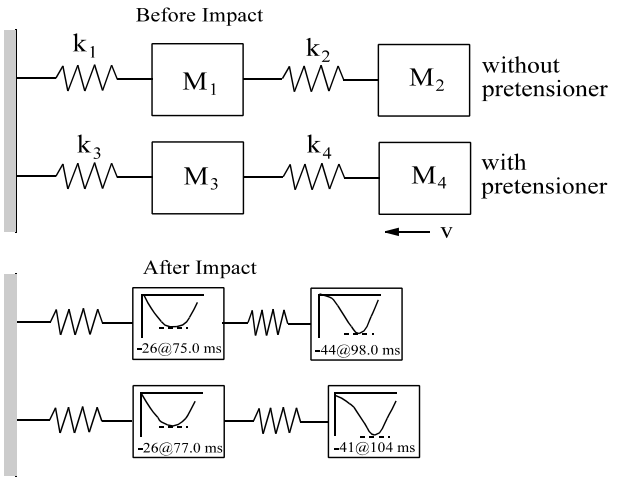

Fig. 7.7 A Vehicle-Occupant Model w/ and w/o Restraint Preload

Table 7.3 Restrained Occupant Responses w/ and w/o Restraint Preload

Model, 30 mph Barrier	Occupant		Restraint Peak Values		
	Max.Displ., in @ ms	Chest Decel, g @ ms	Deflection, in	Force, klb	Restraint Energy, klb-ft
w/o preload	35.3 @ 88	-44 @ 98	8.8	4.4	1.6
w/ preload	33.2 @ 90	-41 @ 104	7.1	4.1	1.4

The occupant deceleration profile with a preload of 0.6 klb and an occupant effective weight of 0.1 klb yields an initial deceleration of 6 g at time zero, as shown in Fig. 7.8.

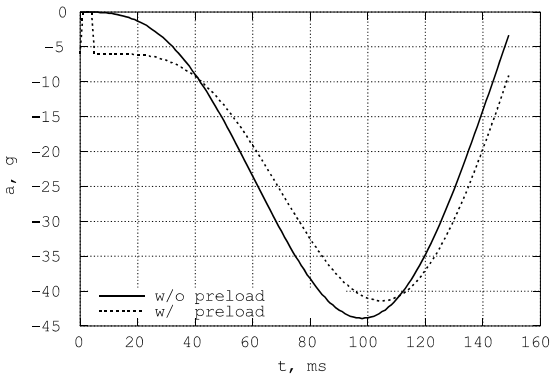

Fig. 7.8 Pretensioner Effect on Chest Response

However, the final peak occupant deceleration of the preloaded model is about 3 g smaller than that without preloading. The lower chest g in the preloaded case is also confirmed by the restraint force-deflection curves for the two cases as shown in Fig. 7.9. Both the peak force and energy of the restraint system for the preloaded case are smaller than those of the non-preloaded case (see Table 7.3 for numerical values).

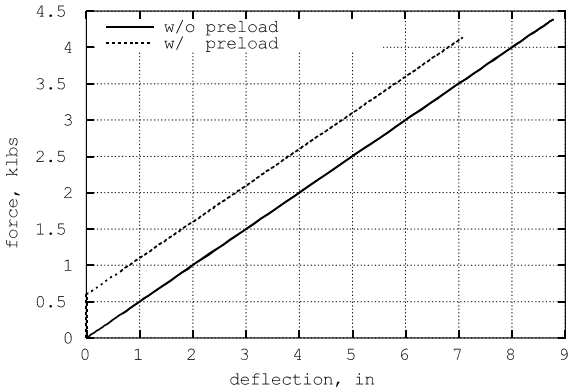

Fig. 7.9 Force vs. Deflection of Models w/ and w/o Preload

To compare the occupant ridedown efficiencies for both cases, the occupant kinetic energy, E_o, in the 30 mph test is computed in Eq. (7.5) and is equal to 3 klb-ft.

$$
\begin{aligned}
&E_o = We_o = 0.4WV^2 \\
&\text{where } E_o\text{: Occupant kinetic energy, klb-in,} \\
&\qquad e_o\text{: Occupant energy density, g-in} \\
&\qquad W\text{: Occupant weight, klb} \\
&\qquad V\text{: Impact speed, mph} \\
&\text{For } W = 0.1 \text{ klb}, \quad V = 30 \text{ mph}, \\
&\text{then } E_o = 36 \text{ klb-in} (=3 \text{ klb-ft})
\end{aligned}
\tag{7.5}
$$

The ridedown efficiencies, μ, for both models have been computed and shown in Table 7.4. For the model with a pretensioner, μ equals 54%. This compares with 46% for the model without a pretensioner. The underlying reason for the higher ridedown efficiency is due to a larger force in the early portion of the occupant deceleration curve that results in a higher ridedown energy density. The higher occupant deceleration in the beginning of the crash pulse is attributed to the use of the pretensioner.

Table 7.4 Output Responses of Models w/ and w/o Preload

Model	E_o , Occupant Kinetic Energy, klb-ft	E_{rs} ,Restraint Energy, klb-ft	E_{rd} ,Ridedown Energy, klb-ft	μ , Ridedown Efficiency, %
w/o Preload	3	1.62	1.38	46
w/ Preload	3	1.38	1.62	54

7.3.2 Modeling Pretensioning Effects in a Component Test

In a component test on a seat belt restraint system, the test setup is shown in Fig. 7.10. The restraint system with and without pretentioner is impacted by a black tuffy (a body block) at a preset speed. For the test with pretensioner, it is assumed that the pretensioning takes effect at time zero when impact occurs. The corresponding initial stretch, δ therefore depends on the initial preload.

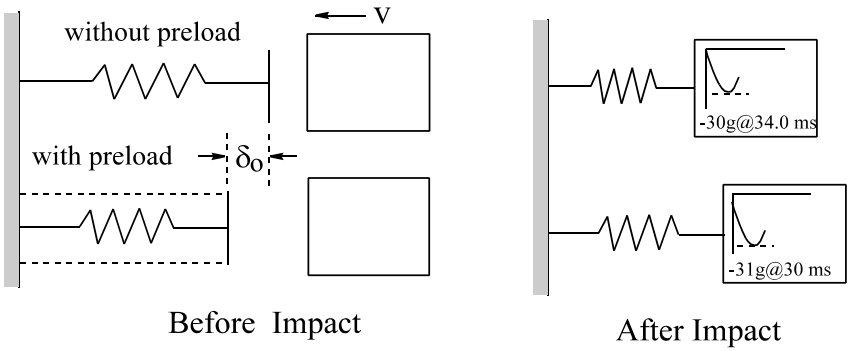

Fig. 7.10 Component Impact Model without and with Preload

Let us define the parameters for the force-deflection curves for the component tests with and without preload as shown in Fig. 7.10:

F_m, F'_m : Maximum force developed without or with pretensioner, respectively,
δ_m, δ'_m : Maximum deflection developed without or with pretensioner, respectively,
F_o : Preload at time zero,
δ_o : Initial belt stretch (or compression) due to preload.
E, E′ : Energy absorption without or with preloading, respectively
v : Impactor speed

We propose to derive the following relationships among the three forces, F_m, F'_m, and F_o, and the three deflections δ_m, δ'_m, and δ_o, respectively.

Based on the geometry in the force-deflection plots for the two cases, with and without a pretensioner, shown in Fig. 7.11, the area in the triangle OCD, and the area in the trapezoid OGEB are the energy absorptions. These two areas are the same and equal to the initial kinetic energy of the impactor. By equating the energies of the two areas, and rearranging the geometric terms, the relationships between the forces and deflections are then derived as shown by the formulas (3) and (4) of Eq. (7.6), respectively.

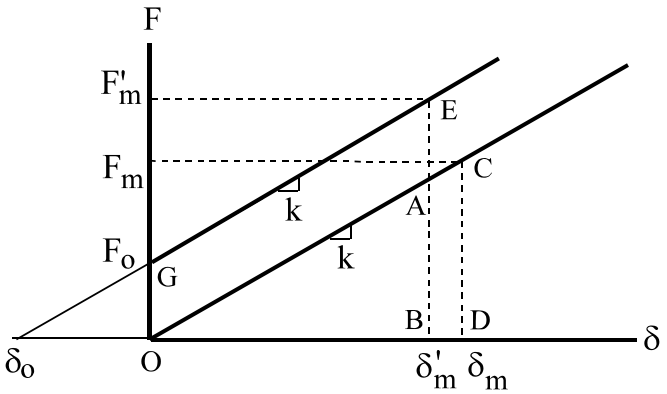

Fig. 7.11 Force vs. Deflection of Impact Model w/ and w/o Preload

$$E = \frac{1}{2}mv^2 = \Delta OCD = \Delta OAB + \diamond BACD, \quad E' = \frac{1}{2}mv^2 = \Delta OGEB = \Delta OAB + \diamond OGEA$$

$$\text{Since } E = E', \quad \text{then} \quad \diamond BACD = \diamond OGEA, \text{ or } \frac{AB + CD}{2} BD = OG \times OB$$

$$\left[\frac{(F_m' - F_o) + F_m}{2}\right](\delta_m - \delta_m') = F_o \delta_m' \quad \ldots\ldots\ldots\ldots\ldots\ldots \quad (1)$$

$$\text{Since } GE // OC, \text{ and slope} = k, \quad \frac{EB - OG}{OB} = \frac{CD}{OD} \qquad (7.6)$$

$$\frac{F_m' - F_o}{\delta_m'} = \frac{F_m}{\delta_m} \quad \ldots\ldots\ldots\ldots\ldots\ldots\ldots\ldots\ldots\ldots \quad (2)$$

Given: k, δ_m, F_m, and F_o, the two unknowns: δ_m' and F_m' can then be solved from equations (1) *and* (2):

$$F_m' = \sqrt{F_o^2 + F_m^2} \qquad \text{where } F_m' \geq F_m \quad \text{for } F_o \geq 0 \quad \ldots \quad (3)$$

$$\delta_m' = \sqrt{\delta_o^2 + \delta_m^2} - \delta_o \qquad \text{where } \delta_m' \leq \delta_m \quad \text{for } \delta_o \geq 0 \quad \ldots \quad (4)$$

The geometric relationships among the forces and deflections in the cases with and without preloading are shown in Figs. 7.12(a) and (b), respectively. These relationships are defined by the Pythagorian Rule. It can be concluded that in a component test at a given impact velocity, the test object in a preloaded condition is subjected to a higher impact force but with less deflection than the test without preload.

Depending on the test setup, the effects of the pretensioner on the dynamic responses of an object can be different. In a component test setup, the impactor is propelled to a certain speed and impacts the test component. In a system test, such as in a vehicle-to-barrier or a Hyge sled test, an occupant undergoes both impact and excitation processes. The excitation is due to the crash pulse of the vehicle and the impact between the occupant and restraint system is the second collision.

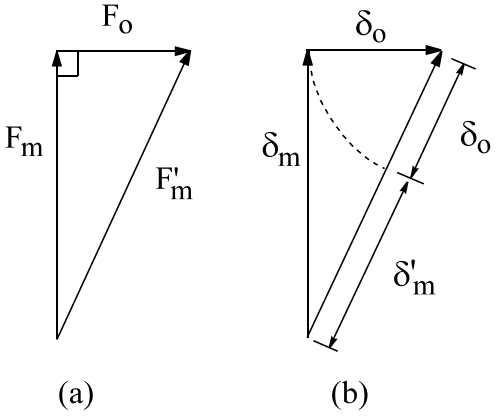

Fig. 7.12 Force and Deflection Relationships
(a) w/o, and (b) with Pretensioner

The solutions of F_m' and δ_m' can be further normalized by F_m and δ_m, respectively, as shown in Eq. (7.7).

$$\begin{aligned}
&\textit{Define the ratios:}\quad r_f = \frac{F_m'}{F_m},\quad r_d = \frac{\delta_m'}{\delta_m},\quad r_o = \frac{\delta_o}{\delta_m} = \frac{F_o}{F_m} \\
&\textit{then } F_m' = \sqrt{F_o^2 + F_m^2} \quad \textit{becomes} \quad r_f = \sqrt{1 + r_o^2} \\
&\delta_m' = \sqrt{\delta_o^2 + \delta_m^2} - \delta_o \quad \textit{becomes} \quad r_d = \sqrt{1 + r_o^2} - r_o
\end{aligned} \tag{7.7}$$

The normalized force and deflection ratios, r_f and r_d, are plotted against the normalized preload ratio, r_o, in Fig. 7.13. If r_o equals 1, an extreme case where the preload F_o is the same as F_m, then F_m' is the largest force acting on the object ($r_f = 1.414$), and δ_m' is the smallest ($r_d = .414$) within the range considered.

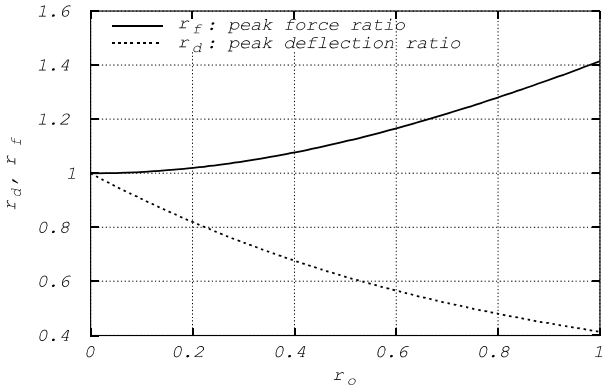

Fig. 7.13 Peak Load and Deflection Ratios w/ and w/o Preload of A One-Mass Model

7.3.3 Transient Analysis of a Preloaded Model — Impact and Excitation

The dynamics of the preloading spring-mass model shown in Fig. 7.10 can be formulated by a second order differential equation. The effect of preloading on the output responses can then be studied using the closed-form solutions presented in the Section 4.11 of Chapter 4.

The forcing function (excitation) in (1) of Eq. (7.8) is a constant in the second-order differential equation. The preloaded g-force, F_o, produces the preloaded deflection, δ_o. If the preloaded force equals the weight of an object in a horizontal impact, the corresponding deflection is then the same as the static deflection due to the weight of an object in a vertical drop test.

$$\begin{aligned}
&\textstyle\sum F = ma, \qquad -k(\alpha + \delta_o) = ma, \quad \textit{since } a = \ddot{\alpha} \\
&\textit{where } \alpha\textit{: relative displacement of mass } m, \\
&m\ddot{\alpha} + k\alpha = -k\delta_o = -F_o, \textit{ then } \ddot{\alpha} + \omega_e^2\alpha = E_o \\
&\textit{where } \quad E_o = -\frac{F_o}{m} = -\frac{k\delta_o}{m} = -\omega_e^2\delta_o
\end{aligned} \tag{7.8}$$

Since the initial test speed of the impactor is v_o, and the preloaded g-force acting on the mass is E_o, the preloaded model is a special component test subjected to a constant excitation due to the preload in addition to the impact.

In Section 4.11, the impact and excitation of a Kelvin model are presented and a set of closed form solutions is presented. The solutions for the model subjected to various pulses such as a TESW (tipped equivalent square wave), halfsine, or haversine pulse are expressed in terms of homogeneous and particular solutions. In general, the initial conditions are a*, the initial acceleration due to excitation, v*, the velocity due to impact, and d*, the relative displacement.

Using the solution formula for the TESW shown in Eq. (4.88) and Table 4.11, one gets the output transient acceleration of the mass as shown in Eq. (7.9). Note that a* = E is a constant deceleration which will be shown due to the equivalent preloading, and v* = v_o is the initial impact velocity.

$$\textit{Initial conditions: } a^* = E \textit{ (due to excitation)}, \quad v^* = v_o \textit{(due to impact)},$$
$$\textit{and } d^* = 0 \textit{ (relative displacement)}$$
$$\textit{From Eq. (4.88) and Table 4.11 of Chapter 4:}$$
$$\textit{the integration constants are: } c_2 = -\frac{E^*}{\omega_e}, \quad c_1 = -\frac{v^*}{\omega_e}$$
$$\textit{Define } \ddot{\alpha}_c\textit{: homogeneous solution}, \quad \ddot{\alpha}_p\textit{: particular solution}$$
$$\ddot{\alpha}_c = e_1 \sin(\omega_e t) + e_2 \cos(\omega_e t), \quad \textit{where } e_1 = -v^* \omega_e, \quad e_2 = E \tag{7.9}$$
$$\ddot{\alpha}_c = -v^* \omega_e \sin(\omega_e t) + E \cos(\omega_e t)$$
$$\textit{From Table 4.11 of Chapter 4: } \ddot{\alpha}_p = 0, \textit{ therefore}$$
$$\ddot{\alpha} = \ddot{\alpha}_c + \ddot{\alpha}_p = -v^* \omega_e \sin(\omega_e t) + E \cos(\omega_e t) = R \sin(\omega_e t + \phi) \quad \ldots\ldots\ (1)$$
$$\textit{where } R = \sqrt{(v^* \omega_e)^2 + E^2}, \quad \ldots \quad (2), \qquad \phi = \tan^{-1} \frac{-E}{v^* \omega_e} \quad \ldots\ (3)$$

The maximum g-force in the component test consists of two acceleration components, shown in (1) of Eq. (7.9). One acceleration component is v*ω_e, attributed to the impact, and the other component, E, is attributed to the excitation caused by preloading.

Case Study: In a component test, a test object with an effective weight of 100 lbs is propelled to a speed of 15 mph. The restraint stiffness is assumed to be 500 lbs/in. The object is tested under two restraint conditions: One model in Fig. 7.10 has no preload, and the other has a preload of 300 lbs obtained by precompressing the spring 0.6 inches. We propose to perform the transient analysis for both models and to identify the parameters that affects the output responses.

$$\textit{Initial conditions:}$$
$$a^*(E^*) = \frac{F_o}{m} = \frac{K\delta \times g}{W} = \frac{(500 \times 0.6) \times 386.4}{100} = 1159 \textit{ in/s}^2 \textit{ (excitation)}$$
$$v^* = v_o = 15 \textit{ mph} = 264 \textit{ in/s (due to impact), and } d^* = 0 \textit{ (relative displacement)}$$
$$\textit{From Eq.(4.88) of Chapter 4: the integration constants then become}$$
$$\omega_e = \sqrt{\frac{k}{m}} = \sqrt{\frac{kg}{W}} = \sqrt{\frac{500 \times 386.4}{100}} = 44 \textit{ rad/s}$$
$$c_2 = -\frac{E^*}{\omega_e} = 26.34 \textit{ in/s}, \quad c_1 = -\frac{v^*}{\omega_e} = 6 \textit{ in}$$
$$\textit{Define } \ddot{\alpha}_c\textit{: homogeneous solution}, \quad \ddot{\alpha}_p\textit{: particular solution} \tag{7.10}$$
$$\ddot{\alpha}_c = e_1 \sin(\omega_e t) + e_2 \cos(\omega_e t),$$
$$\textit{where } e_1 = -v^* \omega_e = -11{,}616 \textit{ in/s}^2, \quad e_2 = E = 1159 \textit{ in/s}^2$$
$$\ddot{\alpha}_c = \left[-11{,}616 \sin(\omega_e t) + 1159 \cos(\omega_e t)\right] \textit{in/s}^2 = \left[30 \sin(\omega_e t) + 3 \cos(\omega_e t)\right] g$$
$$\textit{From Table 4.11 of Chapter 4: } \ddot{\alpha}_p = 0, \textit{ therefore}$$
$$\ddot{\alpha} = \ddot{\alpha}_c + \ddot{\alpha}_p = -v^* \omega_e \sin(\omega_e t) + E \cos(\omega_e t) = R \sin(\omega_e t + \phi) \quad \ldots\ldots\ (1)$$
$$\textit{where } R = \sqrt{(v^* \omega_e)^2 + E^2} = 11674 \textit{ in/s}^2 = 30.2 \textit{ g.} \quad \ldots\ldots\ (2)$$
$$\phi = \tan^{-1} \frac{-E}{v^* \omega_e} = 5.7^\circ \quad \ldots\ldots\ (3)$$

Using the formula shown in Eq. (7.9), the output acceleration components due to the impact and excitation are computed and shown in Eq. (7.10).

The output transient response due to impact is 30 $\sin(\omega_e t)$, g, and that due to constant excitation (equivalent g-force due to preload) is 3 $\cos(\omega_e t)$, g. The total output transient response is the sum of those due to impact and excitation as shown in Fig. 7.8.

The timing, t_g, that the maximum acceleration incurs can be found from (1) of Eq. (7.10) and is shown in Eq. (7.11).

$$\textit{Output acceleration}: \quad \ddot{\alpha} = R\sin(\omega_e t + \phi)$$

$$\textit{Define} \quad t_g: \textit{time when } \ddot{\alpha} \textit{ is maximum}, \quad \textit{therefore} \quad (\omega_e t_g + \phi) = \frac{\pi}{2},$$

$$\textit{or} \quad t_g = \frac{\frac{\pi}{2} - \phi}{\omega_e} \quad \ldots\ldots\ldots\ldots \quad (1) \tag{7.11}$$

$$\textit{for } \phi = 5.7° = 0.1 \textit{ rad. and } \omega_e = 44 \textit{ rad., then}$$

$$t_g = 0.033 \textit{ s} = 33 \textit{ ms}$$

Shown in Fig. 7.14 are two output acceleration components and one resultant acceleration computed by the closed-form formulas shown in Eq. (7.10). Additional two curves superimposed on the first three curves are from the numerical method using the CRUSH II model. Note that the maximum resultant acceleration of 30.2 g occurs at 33 ms. In this component test at 15 mph, the single-mass model without preloading (impact only without excitation) yields a maximum acceleration of 30 g which is slightly lower than that with preloading.

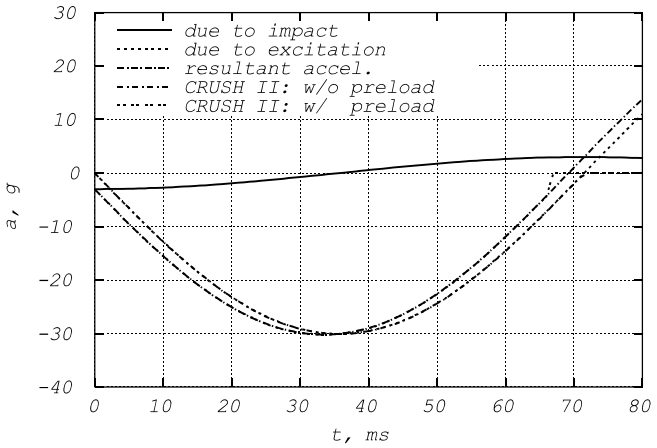

Fig. 7.14 Acceleration vs. Time for Models w/ and w/o Preload

7.4 CENTRAL COLLISIONS

Two approaches are used in the analysis of central collisions. One uses the relative motion concept to analyze the total crush energy absorbed and dissipated in the two-vehicle collision, and the other uses a fixed-frame reference to relate the total and individual crush energy to the crash severity in terms of barrier equivalent velocity (BEV).

It will be shown that the concept of an effective mass system is very useful in simplifying the expression for the energy absorption in a vehicle-to-vehicle impact (VTV). In a rigid barrier test, the energy absorbed by the vehicle structure is ½ mv^2. It can be shown that in a two-vehicle impact, the energy absorbed by the combined structure is also ½ $m_e p^2$, where m_e is the effective mass and p is the relative approach velocity.

Any crash event involves not only impact and excitation, but also energy absorption and loss. In collisions among multiple vehicles, the crush energy absorbed by each vehicle determines the crash severity for that vehicle. Although, the principle of work and energy and the principle of impulse and momentum are derived from Newton's Second Law of Motion, they are not mutually exclusive when it comes to solving dynamic collision problems. In the following two-bob impact problem, although it involves energy transfer between two events, the momentum principle must be used (not discretionary) to account for the energy loss during the collision.

7.4.1 A Collision Experiment

In an experiment, a ping-pong ball exits from a toy gun and strikes a stationary fishing bob, as shown in Fig. 7.15. The masses of the ball and bob are m and M, respectively, and the coefficient of restitution between them is e. After impact, the bob swings up to a maximum height, where the angle is $\alpha°$. Derive the closed-form formula for the muzzle velocity of the ping-pong ball, v_m, and the percentage of energy loss (with respect to the initial kinetic energy of the ball) during impact.

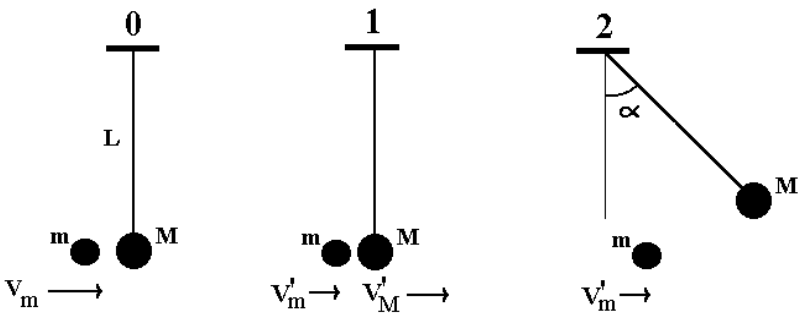

Fig. 7.15 Two-Particle Impact to Determine Impact Velocity

Case Study (Exercise): Before proceeding to solve the general problem, we propose to solve a special case in order to review basic principles. Given the following information: L = 12 inches, $\alpha = 30°$, mass ratio of M/m = 3.0, and e = 0 (using a Velcro pad attached to the ball and bob), determine the initial impact velocity of the ball and the percentage of the energy loss due to impact (Answer: 8 mph and 75%).

Hint: Note that if only the conservation of energy is applied to the two events (before and after impact), this will lead to a substantially lower initial impact velocity because the energy loss occurred between the two events is not accounted for.

Impacts involve generally energy loss, which occurs in two phases: a deformation phase and a restitution phase. In the deformation phase, the crush energy is absorbed by the engaging structures, and in the restitution phase, a portion of the energy absorbed is returned as rebound energy. The final energy loss, termed as the energy dissipation, is equal to energy absorption minus rebound energy. It will be shown in this chapter that the total crush energy depends on the effective mass of the two masses and the closing speed, i.e., the relative approach velocity of the two masses. The general problem shown in Fig. 7.15 is solved for the initial impact velocity of the ball and the energy loss. The solution procedures are shown in Eq. (7.12).

Let v_m: *Initial velocity of mass m*

v_m', v_M': *separation velocities of m and M, respectively*; *then*

Applying the conservation of energy to events 1 *and* 2,

$$1-2:\ v_M' = \sqrt{2gh} \quad \ldots\ldots\ldots\ldots\ldots\ldots\ (1)$$

where $h = L(1-\cos\alpha)$ . . . . . *maximum height reached by M*

Applying the conservation of momentum to the events 0 *and* 1 *and the definition of e, the ratio of relative separation velocity to the relative approach velocity, one gets*

$$0-1:\quad mv_m = mv_m' + Mv_M', \ldots (2), \qquad e = \frac{v_m' - v_M'}{0 - v_m} \ldots (3)$$

Solving for v_m' *and* v_M' *using* (2) *and* (3), *one gets*

$$\frac{v_m'}{v_m} = \frac{1-R_m e}{1+R_m}, \quad \frac{v_M'}{v_m} = \frac{1+e}{1+R_m} \quad \ldots\ldots\ldots\ldots\ (4) \tag{7.12}$$

where $R_m = \dfrac{M}{m}$ . . . *mass ratio of M to m*

The initial velocity of mass m is then equal to

$$v_m = \frac{1+R_m}{1+e} v_M' = \frac{1+R_m}{1+e}\sqrt{2gh} \quad \ldots\ldots\ldots\ (5)$$

Let $\%E_{loss}$: *percent of energy loss during impact*

$$\%E_{loss} = \frac{E_{loss}}{K.E._i} = \frac{K.E._i - K.E._f}{K.E._i} = \left(1 - \frac{K.E._f}{K.E._i}\right) \times 100\% \quad . \ (6)$$

$$K.E._i = .5mv_m^2 \quad \text{and} \quad K.E._f = .5mv_m'^2 + .5Mv_M'^2 \quad \ldots\ (7)$$

Substituting (4) *and* (7) *into* (6), *it becomes*

$$\%E_{loss} = \frac{R_m}{1+R_m}(1-e^2) \times 100\% = \frac{M}{m+M}(1-e^2) \times 100\% \quad . \ (8)$$

The initial velocity of mass m, v_m, normalized by the square root of 2gh, is plotted against mass ratio for five levels of coefficients of restitution, e, and shown in Fig. 7.16. The percent energy loss, $\%E_{loss}$, during impact with respect to the initial kinetic energy can then be computed using (8) of Eq. (7.12).

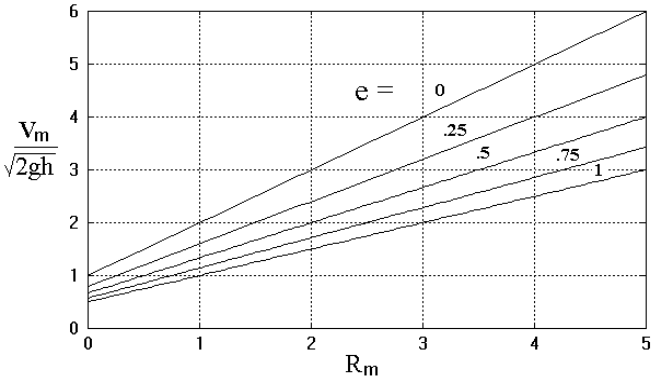

Fig. 7.16 Normalized Impact Velocity of Mass m

Special Cases:

(1) For $m \ll M$, then $R_m = M/m \approx \infty$. The general problem degenerates into a vehicle-to-rigid barrier impact. From (8) of Eq. (7.12), $\%E_{loss} = (1 - e^2) \times 100\%$.

(2) For $m \gg M$, then $R_m \approx 0$. The general problem degenerates into a simple pendulum problem where there is no impact, there is no energy loss. From (8) of Eq. (7.12), $\%E_{loss} \approx 0$.

7.4.2 Relative Motion During Impact

Assuming point masses (m_1 and m_2) to represent two vehicles and limiting the discussion to collinear, central impacts, we can treat the motions of the vehicles as a one-dimensional process. Vectors can be omitted and velocities can be treated as scalars, where a positive value represents motion to the right and a negative value to the left. Velocities after impact will be identified by primes (′).

A staged crash test where an SUV (sport utility vehicle, #1) impacts on a mid-size car (#2) at a closing speed of 58 mph in a central collision is shown in Fig. 7.17. Since the struck car has its parking brake released before impact, the frictional impulse is negligible, and the conservation of momentum applies.

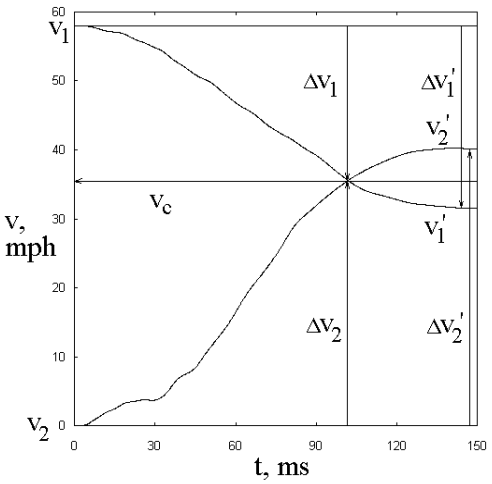

Fig. 7.17 Velocities of a SUV (#1) and Mid-Size Car in a 58 mph Central Collision

The term P is defined as the relative approach velocity of the two masses and is equal to $(v_1 - v_2)$. Assuming v_1 is moving to the right before collision, this term is always positive. The term P' is defined as the relative separation velocity and is $(v_1' - v_2')$. P' is always negative or zero, since after a collision v_2' is necessarily never less than v_1'.

Three cases can be defined, depending on the directions and magnitudes of the velocities, as shown in Table 7.5. In each case, the initial velocity of mass m_1 will be assumed to be to the right (in the positive direction). The second mass can be directed to the right (Case 1), can be at rest (Case 2), or can move to the left, having a negative speed (Case 3).

Fig. 7.18 shows a plot of relative velocity P versus time t for a typical encounter. The value P is always positive before collision and negative afterward. In every case the value is zero at some point during the collision. At t_{cv} , the time at common velocity, the two masses momentarily have the same speed. Since at t_{cv} , vehicle crush is at its maximum, t_{cv} is also referred to as t_m , time of dynamic crush. At this time the deformation phase (plastic and elastic) ends and the restitution phase (elastic) begins and continues up to the time of total separation of the two vehicles.

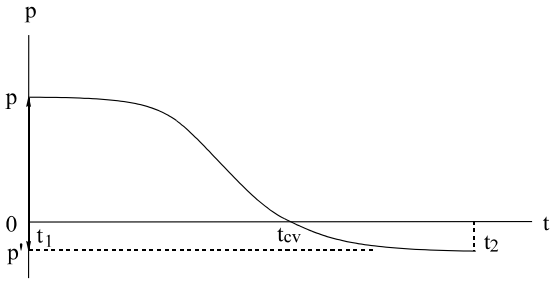

Fig. 7.18 Velocity Plot of Relative Motion

Table 7.5 Relative Motion of Two Particles During Impact

Case 1: Mass m_1 catching up with m_2 $\rightarrow p = v_1 - v_2$ $v_1 \rightarrow$ m_1 $v_2 \rightarrow$ m_2 $\vdash^{+}$ $v_c \rightarrow$ m_1 m_2 $v_1' \rightarrow$ $v_2' \rightarrow$ m_1 m_2 OR $\leftarrow v_1'$ $v_2' \rightarrow$ m_1 m_2 $\leftarrow p' = v_1' - v_2'$ $\longleftarrow p' = v_1' - v_2'$	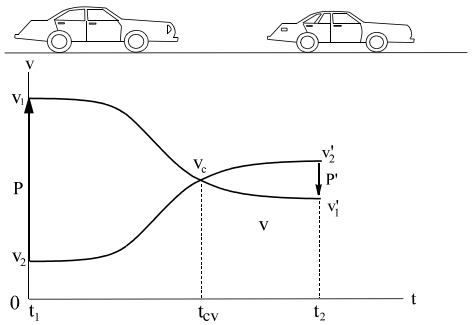
Case 2: Mass m_1 moving toward stationary m_2 $\rightarrow p = v_1$ $v_1 \rightarrow$ m_1 $v_2 = 0$ m_2 $\vdash^{+}$ $v_c \rightarrow$ m_1 m_2 $v_1' \rightarrow$ $v_2' \rightarrow$ m_1 m_2 OR $\leftarrow v_1'$ $v_2' \rightarrow$ m_1 m_2 $\leftarrow p' = v_1' - v_2'$ $\longleftarrow p' = v_1' - v_2'$	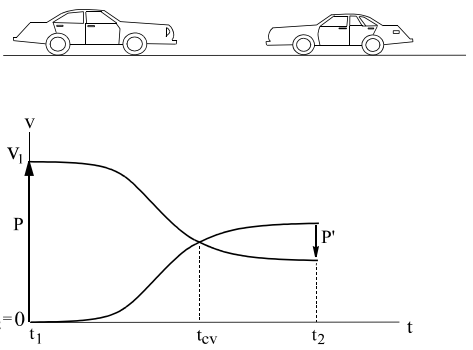
Case 3: Masses m_1 and m_2 in head-on $\rightarrow p = v_1 + v_2$ $v_1 \rightarrow$ m_1 $\leftarrow v_2$ m_2 $\vdash^{+}$ $v_c \rightarrow$ m_1 m_2 $v_1' \rightarrow$ $v_2' \rightarrow$ m_1 m_2 OR $\leftarrow v_1'$ $v_2' \rightarrow$ m_1 m_2 $\leftarrow p' = v_1' - v_2'$ $\longleftarrow p' = v_1' - v_2'$	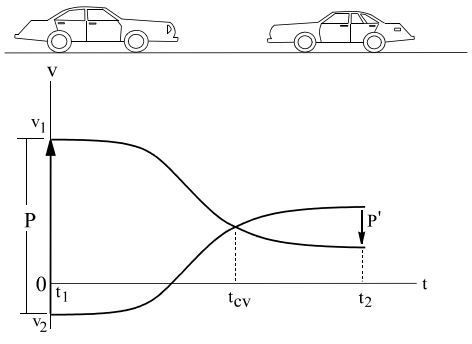

During the duration of the collision, when the two masses are in intimate contact with each other, impact forces come into play. These forces are both dissipative, losing energy, primarily in the deformation of the bodies and non-dissipative, storing and releasing energy. The integral of these forces over time is termed linear impulse. By Newton's Third Law, the force acting on mass m_1 will be equal and opposite to the force acting on mass m_2. If F is the force acting on m_1, the impulse acting on that body will be given by:

$$I = \int_{t}^{t'} F\,dt \qquad F = \textit{Collision force} \qquad I = \textit{Linear impulse} \tag{7.13}$$

Applying the principles of impulse and momentum to each of the two masses at the initial approach and final separation times, one gets

$$\begin{aligned} &m_1 v_1 - I = m_1 v_1' \qquad (1)\\ &m_2 v_2 + I = m_2 v_2' \qquad (2)\\ &v_1, v_2 \;:\; \textit{Initial velocities of masses } 1 \textit{ and } 2\\ &v_1', v_2' \;:\; \textit{final velocities of masses } 1 \textit{ and } 2 \end{aligned} \tag{7.14}$$

Considering only one-dimensional motion and central impacts one can write for any time, t, during the collision: Initially, the total energy starts as kinetic energy and after the collision, ends up as final kinetic energy plus the energy dissipated in the collision process, $\Delta E'$:

$$\frac{m_1}{2} v_1^2 + \frac{m_2}{2} v_2^2 = \frac{m_1}{2} v_1'^2 + \frac{m_2}{2} v_2'^2 + \Delta E' \tag{7.15}$$

This equation can be rewritten as follows:

$$\frac{m_1}{2}(v_1 - v_1')(v_1 + v_1') = \left(\frac{m_2}{2}\right)(v_2' - v_2)(v_2' + v_2) + \Delta E' \tag{7.16}$$

From (1) and (2) of Eq. (7.14), one can determine I and substitute it in Eq. (7.16):

$$\frac{I}{2}(v_1 + v_1') = \frac{I}{2}(v_2' + v_2) + \Delta E' \tag{7.17}$$

Solving for $\Delta E'$ and reordering the velocity terms in the bracket yields:

$$\Delta E' = \frac{I}{2}[(v_1 - v_2) + (v_1' - v_2')] \tag{7.18}$$

The velocity terms now can be seen to be the relative velocities before and after the collision:

$$\Delta E' = \frac{I}{2}[P + P'] \tag{7.19}$$

7.4.3 Kelvin's Theorem, Total Crush, and Dissipated Energies

The expression for dissipated energy shown in Eq. (7.19) is called Kelvin's Theorem [2] which states: *The dissipated energy in a collision is equal to the product of the total impulse generated and one-half of the sum of the approach and separation relative velocities.*

Note that P and P′ are always taken to be positive. An alternate expression is available which uses the coefficient of restitution, e, in place of the impulse. This relies on the definition of e which can be stated as follows.

$$e = \frac{\textit{relative separation velocity}}{\textit{relative approach velocity}} = \frac{P'}{P}$$
$$\textit{and} \quad P' = eP \tag{7.20}$$

Values of e range from 1.0 for a perfectly elastic collision, with no loss of energy, down to 0.0 for a totally dissipative collision. Note that in this case the separation velocity is also zero, so the two vehicles move as one body after collision.

Now (1) and (2) of Eq. (7.14) can be rewritten as follows:

$$v_1 = \frac{I}{m_1} + v_1' \qquad v_2 = \frac{-I}{m_2} + v_2' \tag{7.21}$$

Subtracting the second equation from the first leaves:

$$(v_1 - v_2) = P = I\left(\frac{1}{m_1} + \frac{1}{m_2}\right) + P' \tag{7.22}$$

Solving for I yields:

$$I = m_e(P - P'), \quad \textit{where}$$
$$m_e \textit{ is defined as the effective mass of the system,}$$
$$m_e = \frac{m_1 m_2}{m_1 + m_2} \tag{7.23}$$

Substituting p′ = e p and I in Kelvin's expression, i.e., Eq. (7.19), gives:

$$\Delta E' = (1 - e^2)\left[\frac{1}{2} m_e P^2\right] \quad \ldots\ldots \quad (1)$$
$$\because \quad \Delta E = \frac{1}{2} m_e P^2 \quad \ldots\ldots\ldots \quad (2) \tag{7.24}$$
$$\therefore \quad \Delta E' = (1 - e^2)\,\Delta E \quad \ldots\ldots\ldots \quad (3)$$

Note that ΔE is the total crush energy absorbed by the engaging structure of the two vehicles involved in the collision. ΔE′ is the total crush energy dissipated by the engaging structure of the two vehicles. As described in Chapter 4, Section 4.4.4, the dynamic equivalency between two-mass and effective mass system simplifies the analysis of vehicle-to-vehicle impact by vehicle-to-rigid barrier impact. In the rigid barrier impact, the total energy absorbed by the structure is the same as the total crush energy shown in (2) of Eq. (7.24).

For two specific vehicles and a given value of e, the amount of dissipated energy, ΔE′, is the same, no matter what speeds the vehicles have, as long as their approach speed is the same! When a parked car is rear-ended by a car at 30 mph, the collision should produce about the same dissipation energy as when it is going 30 mph and is hit by the same car going 60 mph .

Note also that in the energy term, the approach speed is squared. A car hitting a parked car at 60 mph should produce about *four* times the dissipation energy as the same car at 30 mph. The term e, of course, depends on various factors. Generally, it is not very dependent on speed except at very low speeds. In most vehicle-vehicle collisions e is a small number, about .12, much less than one. Then, its variability is not significant, since the term ($1 - e^2$) is quite insensitive to e when e is much less than one.

7.4.4 Total Crush Energy

Assume two colliding vehicles, vehicle 1 and vehicle 2, with the line of action of the collision forces being collinear and passing through the center of masses of the two bodies. Also, assume the initial velocities are along the same line and the coefficient of restitution is zero, such that the two vehicles have the same speed, v_c , after their collision.

The conservation of momentum of a system of two masses is applied to a two-time event: one is at the time of contact and the other at the time of maximum deformation when both masses reach the same velocity. The common velocity shown in (1) of Eq. (7.25) is derived using the vector operation, and the common speed shown in (2) is based on scalar operation where direction of initial velocity v_1 (to the right) is assumed to be positive.

$$\bar{v}_c = \frac{m_1\bar{v}_1 + m_2\bar{v}_2}{m_1 + m_2} \qquad (1)$$
$$v_c = \frac{m_1 v_1 - m_2 v_2}{m_1 + m_2} \qquad (2) \qquad (7.25)$$

Using the Case 3 configuration from the previous section for a head-on collision of two vehicles, the magnitudes of the velocity change of vehicles #1 and #2 are defined and shown in Fig. 7.19.

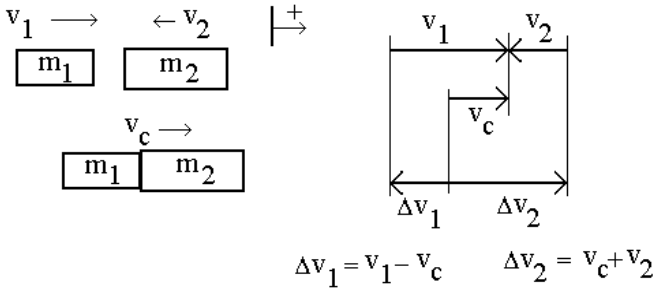

Fig. 7.19 Definition of Velocity Changes

$$\Delta E = \frac{1}{2} m_e P^2 = \frac{1}{2} m_e v_{close}^2 \qquad (1)$$
$$\text{where } m_e\text{: the effective mass of the system,} \qquad (7.26)$$
$$m_e = \frac{m_1 m_2}{m_1 + m_2} = \frac{m_1}{1 + R_m} = \frac{m_2}{1 + R_m'} \qquad (2)$$

Substituting v_c from Eq. (7.25) into the definition of Δv_1 shown in Fig. 7.19, one gets the relationships between the velocity changes of the two masses and closing speed, $v_{close} = v_1 + v_2$. Note that the sum of the speed changes equals the closing speed: $\Delta v_1 + \Delta v_2 = v_1 + v_2$.

$$\Delta v_1 = \frac{m_2}{m_1 + m_2} v_{close} = \frac{1}{1 + R_m} v_{close} \qquad (1)$$
$$\Delta v_2 = \frac{m_1}{m_1 + m_2} v_{close} = \frac{1}{1 + R_m'} v_{close} \qquad (2) \qquad (7.27)$$
$$\text{where } v_{close} = v_1 + v_2, \quad R_m = \frac{m_1}{m_2}, \quad R_m' = \frac{m_2}{m_1}$$

Eliminating v_{close} between (1) in Eq. (7.26) and Eq. (7.27) and repeating between (2) in Eq. (7.26) and Eq. (7.27), one gets expressions for Δv_1 and Δv_2 in terms of total crush energy, ΔE:

$$\Delta v_1 = \sqrt{\frac{2\,\Delta E}{m_1(1 + R_m)}} \quad \ldots \quad (1), \qquad \Delta v_2 = \sqrt{\frac{2\,\Delta E}{m_2(1 + R_m')}} \quad \ldots \quad (2) \qquad (7.28)$$
$$\text{where } R_m = \frac{m_1}{m_2}, \qquad R_m' = \frac{m_2}{m_1}$$

These equations can be used to compute Δv_1 and Δv_2 when the total crush energy, ΔE, is known or can be computed from accident reconstruction software such CRASH3 [3], where the damage profile and stiffness coefficients are available.

Note that dividing Δv_1 by Δv_2 in Eq. (7.28) shows that the speed change of a vehicle is inversely proportional to its mass, i.e., the heavier the vehicle, the smaller its change in speed.

$$\frac{\Delta v_1}{\Delta v_2} = \frac{m_2}{m_1} \tag{7.29}$$

7.4.5 Individual Crush Energy

A vehicle-to-vehicle impact model is shown in Fig. 7.20, For each vehicle, assume a linear force-crush distance relationship defined by F = k x , where x is the amount of deformation in the crush, k is a proportionality factor (stiffness), and F is the force generated during the crush process.

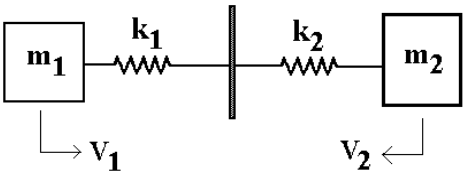

Fig. 7.20 Vehicle-to-Vehicle Impact

The form of this relationship is the same as that for the well-known spring force equation. However, two major differences are to be noted:

1) The force in the spring equation stays constant at any given value of x, while in the collision process, the force is transient in nature, dropping to zero if x doesn't continue to increase (unloading process).

2) The stored energy in the spring is available as potential energy (stored in the spring) while in the collision process most of the energy obtained from the force acting through a distance (crush energy) is dissipated as heat in the deformation of the body structures and is not stored as potential energy.

$$\begin{aligned} &\textit{Define: } x_1, x_2\textit{: Deformation of } m_1 \textit{ and } m_2\textit{, respectively} \\ &\Delta E_1\,(\textit{Crush energy of } m_1) = \int F\,dx_1 = \int k_1 x_1\,dx_1 = \frac{1}{2} k_1 x_1^2 \\ &\Delta E_2\,(\textit{Crush energy of } m_2) = \frac{1}{2} k_2 x_2^2 \end{aligned} \tag{7.30}$$

Taking the ratio of the crush energies for both vehicles:

$$\frac{\Delta E_1}{\Delta E_2} = \frac{k_1 x_1^2}{k_2 x_2^2} = \frac{F x_1}{F x_2} = \frac{x_1}{x_2} = \frac{k_2}{k_1} \tag{7.31}$$

Note that the amount of crush energy is inverse to the "spring" constant of the structure involved in the crash. Thus, the stiffer a vehicle, the less of the total crush energy absorbed.

Using Eq. (7.31), the partition of energy into vehicle 1 and 2 can be obtained as follows:

$$\frac{\Delta E_1}{\Delta E} = \frac{\Delta E_1}{\Delta E_1 + \Delta E_2} = \frac{k_2}{k_1 + k_2} = \frac{1}{1 + R_k} \quad \ldots\ldots\ldots\ldots \quad (1)$$

$$\textit{similarly,} \quad \frac{\Delta E_2}{\Delta E} = \frac{\Delta E_2}{\Delta E_1 + \Delta E_2} = \frac{k_1}{k_1 + k_2} = \frac{1}{1 + R_k'} \quad \ldots\ldots \quad (2) \qquad (7.32)$$

$$\textit{where} \quad R_k = \frac{k_1}{k_2}, \qquad R_k' = \frac{k_2}{k_1}$$

As an example, for a rigid crash barrier, k_2 can be assumed to be infinitely large. Then, in Eq. (7.32), the term R_k becomes zero and ΔE_1 becomes equal to ΔE ; i.e., all of the crush energy is absorbed by the vehicle and none by the barrier.

The relationship between ΔE_1 and Δv_1 shown in Eq. (7.33) can be obtained by eliminating ΔE between (1) of Eq. (7.28) and (1) of Eq. (7.32).

$$\Delta v_1 = \sqrt{\frac{2}{m_1} \frac{(1 + R_k)}{(1 + R_m)} \Delta E_1} \qquad (7.33)$$

For vehicle 1, the relationship between ΔE_1 and v_{close} shown in Eq. (7.34) can be obtained by eliminating ΔE between (1) of Eq. (7.27) and (1) of Eq. (7.32). From this, one gets:

$$\Delta E_1 = \frac{m_1}{2} \frac{1}{(1 + R_m)(1 + R_k)} v_{close}^2 \qquad (7.34)$$

For vehicle 2, eliminating ΔE between (1) of Eq. (7.27) and (2) of Eq. (7.32) yields:

$$\Delta E_2 = \frac{m_2}{2} \frac{1}{(1 + R_m')(1 + R_k')} v_{close}^2 \qquad (7.35)$$

7.5 NON-CENTRAL COLLISIONS

As shown in Fig. 7.21, assume two colliding vehicles, vehicles 1 and 2, with the line of action of the collision forces being collinear but offset from the center of mass of each vehicle. Also, assume that the directions of the initial velocities are parallel to each other. Vehicle 1 is at the left and moving to the right. Its speed is v_1, taken to be positive in the positive x-direction.

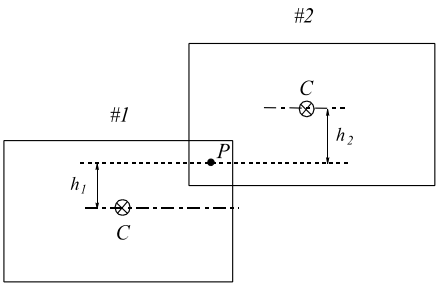

Fig. 7.21 Non-Central Collision

For simplicity, v_1 is assumed to be always positive. The speed of vehicle 2, at the right, v_2, is taken to be positive in the negative x-direction. Thus, for a head-on collision, vehicle 2 will be traveling in the negative x-direction and will have a positive speed. It is assumed that the coefficient of restitution is zero, such that the two vehicles have the same speed, v_c , after their collision. Considering vehicle 1, Fig. 7.22 shows the relationship that the angular acceleration has to the vehicle coordinate system.

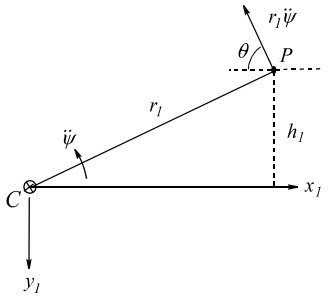

Fig. 7.22 Angular Acceleration in Vehicle 1

The collision region for vehicle 1 is defined by the point P, which is laterally offset a distance h_1 from the vehicle centerline passing through the center of mass, C. The acceleration of P will equal the acceleration of point C plus the product of the radial distance from C to P (r_1) and the angular acceleration of the body ($d\psi^2/d^2t$) (which is taken to be positive in a counterclockwise direction). The direction of the angular acceleration will be perpendicular to the radial vector, r_1. Resolving the x components of these terms gives:

$$\ddot{x}_P = \ddot{x}_C + r_1\ddot{\psi}_1\cos\theta \tag{7.36}$$

Here, θ is the projection angle that the velocity vector of point P relative to C ($v_{P/C}$) makes with the x-axis. Then, the cosine is:

$$\cos\theta = \frac{h_1}{r_1} \tag{7.37}$$

Substituting in for the cosine and rearranging terms gives:

$$\begin{aligned} \ddot{x}_p &= \ddot{x}_C + h_1\ddot{\psi}_1 \quad \ldots\ldots\ldots \quad (1) \\ \ddot{x}_C &= \ddot{x}_P - h_1\ddot{\psi}_1 \quad \ldots\ldots\ldots \quad (2) \end{aligned} \tag{7.38}$$

The x component of the force acting on vehicle 1 at P is F_x. One can write a force equation in the x-direction for the center of mass plus an equation for the moment created by F_x about the center of mass. Once the collision begins and the bodies start to rotate, some smaller amount of force in the y-direction may ensue; this is neglected in this analysis.

Force equation, collision force acting on the center of mass:

$$F_x = m_1\ddot{x}_C = m_1(\ddot{x}_P - h_1\ddot{\Psi}_1) \quad \ldots\ldots\ldots\ldots\ldots \quad (1)$$

Moment equation about the center of mass, C

$$F_x h_1 = I_1\ddot{\Psi}_1 = m_1 k_1^2\ddot{\Psi}_1 \quad \ldots\ldots\ldots\ldots\ldots\ldots \quad (2) \tag{7.39}$$

Rearranging (2) yields: $\quad \ddot{\Psi}_1 = \dfrac{F_x h_1}{m_1 k_1^2} = \ddot{x}_C \dfrac{h_1}{k_1^2} \quad \ldots \quad (3)$

Here, the term k_1 is the radius of gyration of vehicle 1 (in yaw motion). The square of k_1 is equal to the moment of inertia about the center of mass divided by the mass. Substituting (3) of Eq. (7.39) into (1) of Eq. (7.38), one gets a functional relationship between the accelerations at the damage centroid P, and the center of gravity C of vehicle 1 as shown in Eq. (7.40)

$$\ddot{x}_P = \ddot{x}_C + h_1\left(\ddot{x}_C\frac{h_1}{k_1^2}\right) = \ddot{x}_C\left(1 + \frac{h_1^2}{k_1^2}\right) \quad \textit{and, solving for } \ddot{x}_C\textit{:}$$

$$\ddot{x}_C = \left(\frac{k_1^2}{k_1^2 + h_1^2}\right)\ddot{x}_P \tag{7.40}$$

Setting the term $[k_1^2/(k_1^2 + h_1^2)]$ to γ_1 and identifying this as the "mass reduction factor" for vehicle 1, we can state:

$$\ddot{x}_C = \gamma_1\ddot{x}_P \quad \ldots\ldots\ldots \quad (1)$$

$$\ddot{x}_P = \frac{\ddot{x}_C}{\gamma_1} = \frac{F_X}{(\gamma_1 m_1)} \tag{7.41}$$

Here, the mass term ($\gamma_1 m_1$) can be considered to be an"effective mass" of vehicle 1 acting at the point P. Defining γ_2 to be $(k_2^2 / (k_2^2 + h_2^2)$ leads to an effective mass for vehicle 2 of $\gamma_2 m_2$ at the point P. Note that in any offset case, where $h_1 > 0.0$ and $h_2 > 0.0$, the acceleration along the x-axis of the center of mass, C, will always be less than that of point P, since both γ_1 and γ_2 are less than 1.0. The reason for this difference in acceleration is the contribution to the motion at P in the x_1 direction, of the yaw acceleration ($h_1 \cdot d\psi^2/dt^2$), this being attributable to the torque imparted to the body by the collision force, F_X.

Integrating over the duration of the impact using (1) of Eq. (7.41), we get for vehicle 1:

$$\int\ddot{x}_C dt = \Delta\dot{x}_C = \gamma_1\Delta\dot{x}_P \quad \textit{or} \quad \Delta v_C = \gamma_1\Delta v_P \tag{7.42}$$

In the same manner we can obtain for vehicle 2:

$$\Delta v_C = \gamma_2\Delta v_P \tag{7.43}$$

Note that for each vehicle, the change in velocity along the x-axis is greater at P than at the center of mass, C, since the effective mass term, γ_1 or γ_2, is less than 1.0 for an offset collision.

The Calspan program CRASH3 allows the energy partition developed earlier in Eqs. (7.32) and (7.33) to be used for offset collisions, also. For the point P, the centroid of the collision process, the effective masses should be used in place of the actual vehicle masses. Then, using Eqs. (7.32) and (7.33) and substituting the effective masses obtained above, one gets for the change in speed in the x-direction:

At damage centroid:

$$\textit{For vehicle 1 at damage centroid, P:}\quad \Delta v_P = \sqrt{\frac{2\gamma_2 m_2}{\gamma_1 m_1(\gamma_1 m_1 + \gamma_2 m_2)}\Delta E}$$
$$\textit{For vehicle 2 at damage centroid, P:}\quad \Delta v_P = \sqrt{\frac{2\gamma_1 m_1}{\gamma_2 m_2(\gamma_1 m_1 + \gamma_2 m_2)}\Delta E} \tag{7.44}$$

At center of mass:

$$\textit{For vehicle 1 at the center of mass, C:}\quad \Delta v_C = \sqrt{\frac{2\gamma_1\gamma_2 m_2}{m_1(\gamma_1 m_1 + \gamma_2 m_2)}\Delta E}$$
$$\textit{For vehicle 2 at the center of mass, C:}\quad \Delta v_C = \sqrt{\frac{2\gamma_1\gamma_2 m_1}{m_2(\gamma_1 m_1 + \gamma_2 m_2)}\Delta E} \tag{7.45}$$

In the above, the term γ_1 is the mass reduction factor for vehicle 1 and is equal to $[k_1^2/(k_1^2 + h_1^2)]$, there being a similar term for γ_2 using k_2 and h_2 .

Two examples are presented below, one for a head-on central collision of two cars and one for the same collision but with the cars being offset. In each case the collision is considered to be totally inelastic; thus, the value of e is assumed to be 0.0.

7.5.1 Case Study 1: Central Collision

Car 1 and car 2 suffer a head-on central collision. Car 2 has a weight of 3 kips (kilo-pounds) and a speed of 10 mph to the left. Car 1 has a weight of 2 kips and a speed to the right of 20 mph.

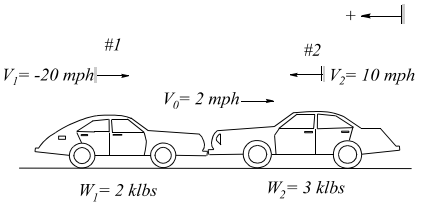

Fig. 7.23 Vehicle-to-Vehicle Central Collision

Using the conservation of momentum and assuming the positive x-direction is to the left:

$$m_1 v_1 + m_2 v_2 = (m_1 + m_2) v_C$$
$$\textit{Solving for } v_C \textit{ gives:}\quad v_C = -2.0\ \textit{mph} \qquad (\textit{to the right}) \tag{7.46}$$

next applying the conservation of energy:

Total energy before collision = Total energy after collision:

$$m_1\frac{v_1^2}{2} + m_2\frac{v_2^2}{2} = (m_1 + m_2)\frac{v_C^2}{2} + \Delta E$$
$$\textit{where } \Delta E \textit{ is the energy dissipated in the collision}$$
$$\textit{Solving this equation for } \Delta E \textit{ yields:}\quad \Delta E = 540.0\ \textit{klbs (mph)}^2 \tag{7.47}$$

By applying Eq. (7.45), the change in velocity for each vehicle can be obtained:

$$\Delta v_1 = \sqrt{\frac{2m_2}{m_1(m_1+m_2)}\Delta E} = \sqrt{\frac{2\times 3}{2\times 5}\times 540} = 18.0\ mph$$
$$(Velocity\ change\ of\ v_1\ at\ common\ velocity)$$
$$\Delta v_2 = \sqrt{\frac{2m_1}{m_2(m_1+m_2)}\Delta E} = 12.0 \tag{7.48}$$
$$(Velocity\ change\ of\ v_2\ at\ common\ velocity)$$

Thus, car 2 (large car) changes in speed from 10 to -2 mph with a Δv_2 of -12 mph, and car 1 (small car) changes in speed from -20 mph (to the right) to -2 mph with a Δv_1 of 18 mph. As expected, the vector sum of the two velocity changes is the same as the closing speed which is 30 mph.

7.5.2 Case Study 2: Non-central or Offset Collision

Assume that the offset of car 1 (h_1 = lateral distance from the centerline of the car to the line through the collision point) is 20". Assume the value of k_1^2 is 4040 in^2, a typical value for a full-size car. Then, $\gamma_1 = k_1^2/(k_1^2 + h_1^2) = 0.91$. For car 2, assume the offset is 95% of h_1 or 19" and that k_2^2 is 91% of that of k_1^2 or 3676 in^2. With these values, $\gamma_2 = 0.91$ also.

$$For\ car\ 1\ at\ the\ center\ of\ mass,\ C:\quad \Delta v_C = \sqrt{\frac{2\gamma_1\gamma_2 m_2}{m_1(\gamma_1 m_1+\gamma_2 m_2)}\Delta E} = 17.1\ mph$$
$$For\ car\ 2\ at\ the\ center\ of\ mass,\ C:\quad \Delta v_C = \sqrt{\frac{2\gamma_1\gamma_2 m_1}{m_2(\gamma_1 m_1+\gamma_2 m_2)}\Delta E} = 11.4\ mph \tag{7.49}$$

$$For\ car\ 1\ at\ damage\ centroid,\ P:\quad \Delta v_P = \sqrt{\frac{2\gamma_2 m_2}{\gamma_1 m_1(\gamma_1 m_1+\gamma_2 m_2)}\Delta E} = 19.0\ mph$$
$$For\ car\ 2\ at\ damage\ centroid,\ P:\quad \Delta v_P = \sqrt{\frac{2\gamma_1 m_1}{\gamma_2 m_2(\gamma_1 m_1+\gamma_2 m_2)}\Delta E} = 12.7\ mph \tag{7.50}$$

Comparing the two cases, it can be seen that the change in speed of the center of mass for the offset collision is slightly less than for the central collision while the change in speed in the collision region is a little greater than for the central collision.

7.6 USE OF ΔV AND BEV IN CRASH SEVERITY ASSESSMENT

This section presents an analytical comparison of the degree of impact severity in a vehicle-to-fixed perpendicular barrier and vehicle-to-object (non-perpendicular barrier) tests. A nonlinear model with power curve force-deflection is presented to compare the crash severity of the two vehicles involved in a crash.

The barrier equivalent velocity (BEV) is a reference speed that yields the same amount of crush energy in a subject vehicle between a fixed barrier and a non-perpendicular barrier test [4,5]. The energy is used as a reference value such that the speed conversion between non-perpendicular and fixed barrier tests in terms of mass and stiffness ratios of the two objects can be formulated. Equal energy, however, does not necessarily produce the same force or deformation in the subject vehicle

in rigid barrier tests. This will depend on the mass and stiffness ratios of the two vehicles involved in the collision.

Let BEV_1 be the barrier equivalent velocity of vehicle 1. It is assumed that the final speed of vehicle 1 is zero. It is assumed that all of the crush energy is developed in the vehicle, none in the barrier. In this case the crush energy equals the initial kinetic energy of the vehicle, i.e., all of the kinetic energy is absorbed and dissipated in the crush energy of the vehicle. Then, for vehicle 1:

$$Kinetic\ energy = \frac{m_1}{2}(BEV_1)^2 = Crush\ energy = \Delta E_1 \tag{7.51}$$

Equating Eq. (7.34) to Eq. (7.51), one gets

$$\frac{BEV_1}{v_{close}} = \frac{1}{\sqrt{(1+R_m)(1+R_k)}} \tag{7.52}$$

Eliminating v_{close} between (1) of Eq. (7.26) and Eq. (7.52), it becomes

$$BEV_1 = \sqrt{\frac{1+R_m}{1+R_k}}\,\Delta v_1 \tag{7.53}$$

Eliminating BEV_1 between Eq. (7.52) and Eq. (7.53) yields:

$$\frac{\Delta v_1}{v_{close}} = \frac{1}{1+R_m} \tag{7.54}$$

Similarly, for vehicle 2, one gets:

$$\begin{aligned} &Kinetic\ energy = \frac{m_2}{2}(BEV_2)^2 = Crush\ energy = \Delta E_2 \\ &\frac{BEV_2}{v_{close}} = \frac{1}{\sqrt{(1+R_m')(1+R_k')}} \quad \ldots\ldots\ldots \quad (1) \\ &BEV_2 = \sqrt{\frac{1+R_m'}{1+R_k'}}\,\Delta v_2 \quad \ldots\ldots\ldots\ldots \quad (2) \\ &\frac{\Delta v_2}{\Delta v_{close}} = \frac{1}{1+R_m'} \quad where\ R_m' = \frac{1}{R_m} \quad \ldots\ldots \quad (3) \end{aligned} \tag{7.55}$$

For a central collision of two vehicles with a closing speed of $(v_1 + v_2)$ (regardless of the individual speeds of the two vehicles), the crush energy developed in a subject vehicle will be the same when the subject vehicle impacts a fixed perpendicular barrier at the BEV speed (given by Eq. (7.52) for vehicle 1 or Eq. (7.55) for vehicle 2). Two vehicle parametric constants are needed in this equation, the mass ratio and stiffness ratio of the two vehicles involved in the collision.

For a special case (1), two identical vehicles are involved in a head-on collision. The ratio of BEV of a subject vehicle to closing speed is 0.5.

For a special case (2), the other vehicle having the same weight but being two times as stiff as the subject vehicle, then $R_m = 1$, $R_k = ½ = .5$, and from Eq. (7.52), the BEV of the subject vehicle is 0.58 of the closing speed. The reason that BEV is higher for vehicle 1 is that the stiffer vehicle 2 imparts more damage and more crush energy on vehicle 1. Therefore, given the same closing speed, the BEV of vehicle 1 in case (2) is higher than in case (1).

7.6.1 Crash Severity Index

The term BEV_1/V_{close} shown in Eq. (7.52) is defined as the crash severity index of vehicle 1 (subject vehicle) in a vehicle-to-vehicle collision. It is a measure of BEV experienced by the subject vehicle per unit of closing speed in a two-vehicle collision. Fig. 7.24 shows the value of the crash severity index as a function of R_m and R_k, the mass and stiffness ratios of vehicle 1 to 2, respectively. It ranges from zero (subject vehicle hitting something very light and soft, $R_m = \infty$, $R_k = \infty$) to one

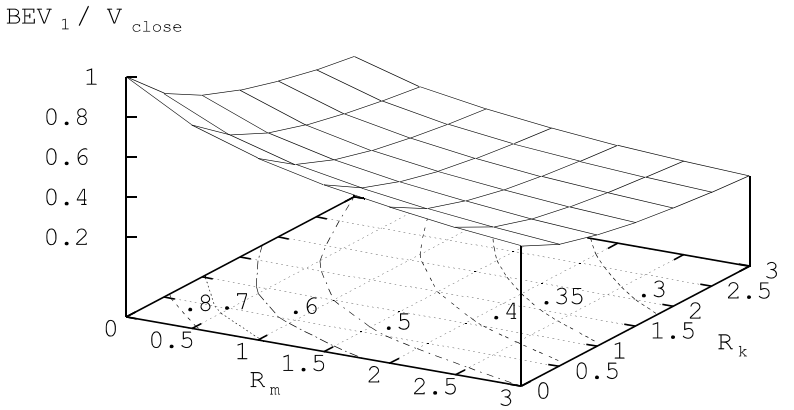

Fig. 7.24 3-D Relationship Between BEV_1 and Closing Speed

(subject vehicle hitting something very heavy and stiff, such as a rigid barrier, $R_m = 0$, $R_k = 0$).

Depending on the R_m and R_k, the higher the crash severity index (BEV_1/V_{close}), the worse off the subject vehicle is in the collision. As an example, in a vehicle compatibility study, assuming the mass ratio of the subject vehicle to the other heavier vehicle is 0.5, the value of BEV_1/V_{close} shown in the base contour plot of Fig. 7.24 is 0.67 when R_k (stiffness ratio of the subject to other vehicle) is 0.5. This crash severity index drops to 0.47 when R_k is 2. Therefore, in order to minimize the lighter vehicle crash severity index, R_k needs to be increased, which can be accomplished by increasing the stiffness of the lighter vehicle and/or decreasing the stiffness of the heavier vehicle.

As shown in Eq. (7.52), the stiffness ratio carries the same weight as the mass ratio when it comes to determine the crash severity of the subject vehicle.

Similarly, the crash severity index of vehicle 2 (i=2) can be plotted in terms of R_m and R_k. The surface of this plot is superimposed with that of vehicle 1 (i=1) and shown in Fig. 7.25.

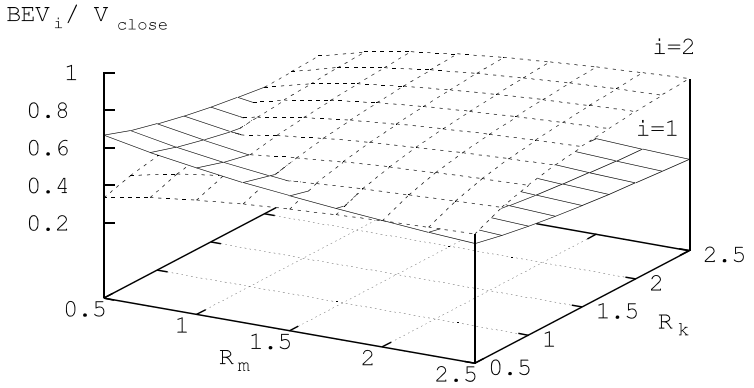

Fig. 7.25 3-D Plot of Crash Severity Indices for Vehicles 1 and 2

Note that the crash severity indices for the two vehicles have opposite trends. As far as the subject vehicle 1 is concerned, as the mass ratio R_m goes up, crash severity index goes down. A similar trend exists for the stiffness ratio, R_k. For the other vehicle 2, the trends are just opposite to those of subject vehicle 1.

The two surfaces shown in Fig. 7.25 for the two vehicles intersect within the ranges of mass ratio and stiffness ratio. At the intersection of the two surfaces, the crash severity indices of the two vehicles are equal. Therefore, in a vehicle-to-vehicle impact, the condition for both vehicles to have the same crash severity index or the same BEV is that the product of mass ratio and stiffness ratio is equal to 1. This condition is derived in Eq. (7.56).

$$
\begin{aligned}
&\text{Let } \frac{BEV_1}{V_{close}} = \frac{BEV_2}{V_{close}}, \text{ then} \\
&\frac{1}{\sqrt{(1+R_m)(1+R_k)}} = \frac{1}{\sqrt{(1+\frac{1}{R_m})(1+\frac{1}{R_k})}} \\
&(1+R_m)(1+R_k) = (1+\frac{1}{R_m})(1+\frac{1}{R_k}) = \frac{(1+R_m)(1+R_k)}{R_m R_k} \\
&\text{therefore, } R_m R_k = 1
\end{aligned}
\tag{7.56}
$$

7.6.1.1 Compatibility by Equal Crash Severity Index

Using the simple criterion, $R_m R_k = 1$, both vehicles in the vehicle-to-vehicle collision would have the same crash severity index (BEV/Vclose). Since FMVSS 208 mandates that every new vehicle has to be certified to meet the crash safety requirements in a 30 mph rigid barrier test, the corresponding closing speed for a vehicle-to-vehicle test can then be derived as shown in Eq. (7.57),

$$
\begin{aligned}
&\frac{BEV_1}{v_{close}} = \frac{1}{\sqrt{(1+R_m)(1+R_k)}}. \quad \text{For } BEV_1 = BEV_2, \\
&\text{substituting } R_k = \frac{1}{R_m} \text{ into the equation above yields:} \\
&\frac{BEV_1}{v_{close}} = \frac{\sqrt{R_m}}{1+R_m} \quad \ldots\ldots\ldots\ldots\ldots\ldots (1) \\
&v_{close} = BEV_1 \frac{1+R_m}{\sqrt{R_m}} \quad \ldots\ldots\ldots\ldots\ldots\ldots (2)
\end{aligned}
\tag{7.57}
$$

In a vehicle-to-vehicle compatibility test, the condition for both vehicles to have the same crash severity index, the vehicles should have the following attributes: the stiffness ratio of the subject vehicle to the other vehicle is inversely proportional to the mass ratio of the subject to the other vehicle. Condition shown by (1) of Eq. (7.57) is plotted in Fig. 7.26. Note that for any mass ratio, the maximum crash severity index is 0.5.

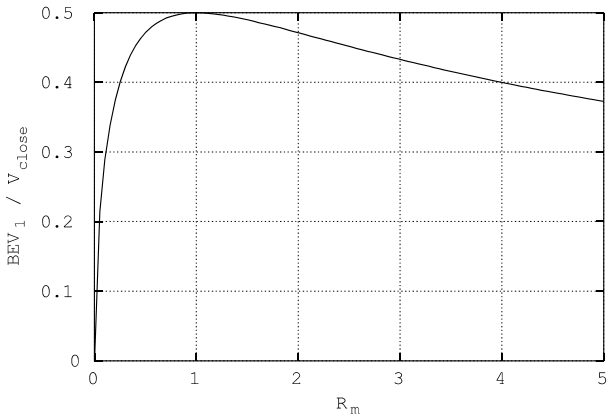

Fig. 7.26 Crash Severity Index as a Function of Mass Ratio with Condition $R_m R_k = 1$

If the vehicles involved in the VTV test are identical, then the condition of having the equal crash severity index for both vehicles is met. Letting the BEV be 30 mph, the closing speed in a VTV test should be two times BEV, which is 60 mph, or it can be computed by (2) of Eq. (7.57).

7.6.2 Crash Momentum Index

Another parametric relationship used in the analysis of vehicle-to-vehicle collisions deals with the change of momentum of a subject vehicle. This relationship, $\Delta v_1/v_{close} = 1/(1+R_m)$, derived and shown in Eq. (7.27) of Section 7.4.4 and also in Eq. (7.54) of Section 7.6, is plotted in Fig. 7.27.

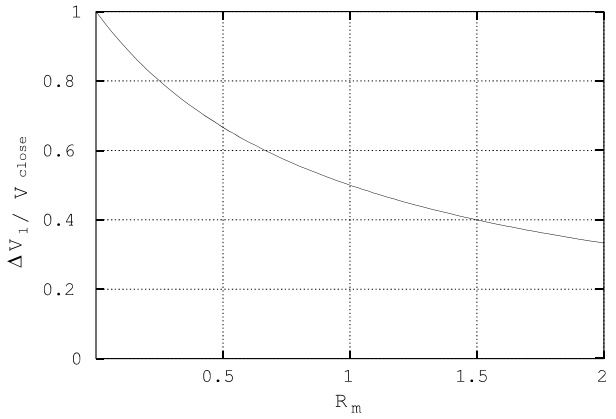

Fig. 7.27 Crash Momentum Index of Vehicle 1 in Two-Vehicle Collision

Unlike the crash severity index, which is based on the crash energy absorbed by the subject vehicle, the crash momentum index is based solely on the velocity change of the subject vehicle in the two-vehicle collision. Since it deals only with the velocity change, the effect of time, the crash duration, is out of the context. The momentum method alone deals only with the gross motion, not the transient motion. The steps used to derive the crash momentum index are only necessary in defining the total energy absorbed by the combined structure of the two vehicles. However, the momentum method alone is not sufficient to define the individual energy absorption by each of the two vehicles, since the energy distribution depends on the stiffness ratio of the two vehicles.

In general, it is the BEV (not the ΔV) that describes the VTV crash severities in a complete manner. Only in the fixed barrier test condition or when the stiffness ratio equals the mass ratio, will BEV (or crash severity index) be the same as ΔV (or crash momentum index). This relationship can be proved by simply making $R_m = R_k$ and substituting into Eq. (7.52). Then $BEV_1/V_{close} = \Delta V/V_{close} = 1/(1+R_m)$.

7.6.3 Crash Severity Assessment by a Power Curve Model

This section presents a model with power curve force deflection, as shown in Fig. 7.28. The model is used to assess the crash severity of a mid-size passenger vehicle in a vehicle-to-vehicle test. The velocity change and fixed barrier equivalent velocity (BEV) of a 1985 Merkur which is struck from the front by a NHTSA Moving Deformable Barrier (MDB) at 70 mph will be estimated. This test, a central collinear impact, was conducted at Calspan Corp. under a contract to NHTSA. The crash severity of the Merkur will then be analyzed and compared with that of NCAP (New Car Assessment Program) at a 35 mph rigid barrier test condition.

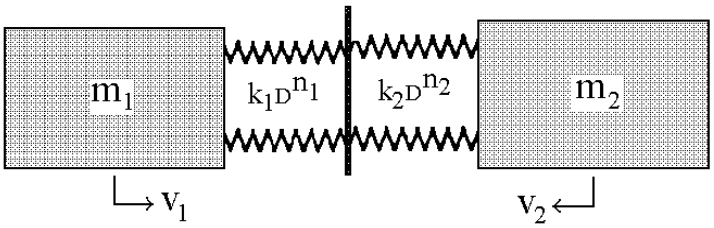

Fig. 7.28 A Non-linear Two-Mass Impact Model

7.6.3.1 *Power Curve Model and Methodology*

Power curve force-deflection model can be utilized to perform the following tasks: (1) impact modeling, with loading and unloading simulations, (2) computations of the barrier equivalent velocity (BEV), and (3) velocity change (V.C.) of a vehicle during impact.

Modeling of the two-vehicle impact was effected using a two-mass and two-EA (non-linear-spring Energy Absorber) model. This was used for both validation and prediction. The model simulates vehicle-fixed barrier and vehicle-vehicle impacts. In the vehicle-fixed barrier impact, only one set of data for the subject vehicle is specified. The other set of data for the second vehicle in the model is simply the mirror-image of the first set. Note that in the vehicle-fixed barrier impact, the velocities of the two vehicles are equal and opposite. The mass and velocity of the two vehicles are defined as follows:

m_1, m_2: masses of struck and striking vehicles, respectively.
V_1: initial velocity of struck vehicle.
V_2: initial velocity of striking vehicle.

7.6.3.2 *Power Curve Force-Deflections*

A power curve describing the force-deflection characteristics of the energy absorber of vehicle i is defined as:

$F = k_i D^{n_i}$ Where

F: force level of the energy absorber.
D: deflection of the energy absorber.
k_i, n_i: stiffness and power factors of vehicle i, respectively.

The test data for (1) the NHTSA MDB used in the vehicle side impact tests, and (2) the Merkur's frontal fixed barrier certification tests at 35 mph and the NCAP test are shown in Table 7.6.

Table 7.6 Merkur Test Data at 35 mph Rigid Barrier Tests

Crash Test No.	Test Weight, lb	Dynamic Crush, in @ ms	Static Crush, in
1	3426	27.0 @ 82	22.2
2	3443	27.0 @ 82	23.3
NCAP (TRC-85-NOT)	3452	(N/A)	23.9

The power curve formulas for both MDB and Merkur are obtained that approximate the force-deflection characteristics of both structures (see Figs. 7.29 and 7.30). They are:

NHTSA MDB: $F = 29.86D^{.47}$, and Merkur: $F = 21.50D^{.44}$

where F is the force level in klbs and Dis the deformation in inches.

Since both k (stiffness coefficient) and n (power) for the MDB are larger than those for the Merkur, MDB is definitely stiffer than the Merkur structure.

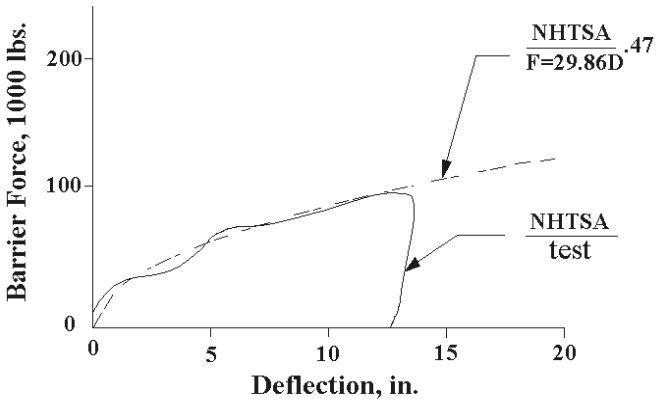

Fig. 7.29 NHTSA Moving Deformable Barrier (MDB) Force/Deflection Characteristics

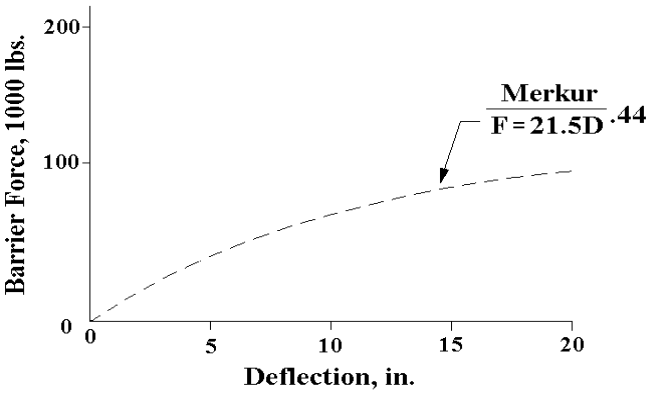

Fig. 7.30 Simulated '85 Merkur XR4 Frontal Structure Characteristics

The first stage of simulation computes the maximum dynamic crush and the fixed barrier equivalent velocity of each vehicle. The structural unloading properties are taken into account, which yields the static crush in the second stage of simulation.

Following the schematic shown in Fig. 7.31, the BEV can be computed. In the loading phase of a vehicle-vehicle impact, the structure of each vehicle undergoes a process of absorbing kinetic energy. The amount of absorbed energy (crush energy) in each vehicle depends on its structural characteristics. The energy absorption reaches its maximum when both vehicles reach the common velocity, where the maximum deformation (or dynamic crush) of each vehicle occurs. Since the vehicle structure is not perfectly plastic, part of the energy absorbed is transformed into kinetic energy due to spring back effect when unloading occurs. For the numerical methods on the power curve loading and unloading simulations, the reader is referred to Sections 5.6.1 and 5.6.2 of Chapter 5.

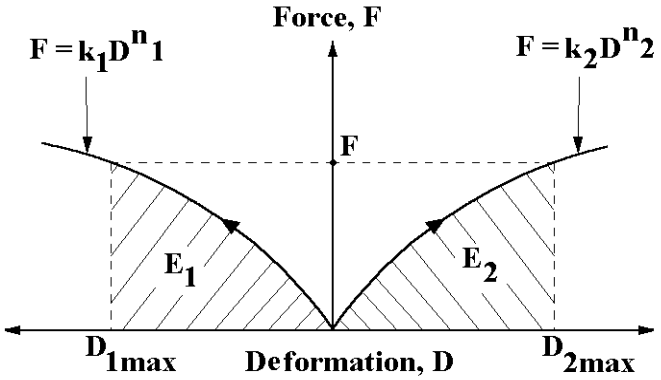

Fig. 7.31 Individual Crush Energy and BEV

Define:
Event 1: *at time zero,*
Event c: *at time of common velocity,*
Event 2: *t time of separation, and*
i: *vehicle index*

$\Delta\bar{V}_i$: *velocity change of vehicle # i at time of common velocity* (7.58)

$\Delta\bar{V}_i'$: *velocity change of vehicle # i at time of separation*

In the deformation phase: $\Delta\bar{V}_i = \bar{V}_i|_c - \bar{V}_i|_1$

In the restitution phase: $\Delta\bar{V}_i' = \bar{V}_i|_2 - \bar{V}_i|_c$

The crush energy absorbed by the vehicle structure up to the dynamic crush can then be computed. By equating the crush energy to that absorbed by the subject vehicle in a fixed barrier impact, one obtains the fixed Barrier Equivalent Velocity of the subject vehicle (BEV).

7.6.3.3 *Computation of Barrier Equivalent Velocity (BEV)*

Consider one of the two vehicles (Vehicle i): E_i is the maximum dynamic crush energy absorbed by the vehicle in a vehicle-vehicle impact, where:

$$E_i = \int F_i\, dx_i = \int_0^{D_{imax}} k_i x^{n_i}\, dx = \frac{k_i}{n_i+1} D_{imax}^{n_i+1} \tag{7.59}$$

By equating E_i to the energy absorbed by the subject vehicle in a fixed barrier impact, one obtains:

$$E_i = \frac{1}{2} m_i (BEV_i)^2, \quad and \quad BEV_i = \sqrt{2 E_i / m_i} \tag{7.60}$$

where BEV_i is the barrier equivalent velocity of vehicle i and m_i is the mass of the subject vehicle i.
Case Study: For the struck vehicle (i=1), BEV_1 is computed as follows:

$$\begin{aligned}
&Power\ curve:\ F = k_1 D^{n_1}\ \ (Units:\ lb,\ in)\\
&D\ (Dynamic\ crush) = 32.7\ in.\\
&k_1 = 21500.0,\ \ n_1 = 0.44\\
&m_1 = 3420\ lb/(32.2*12) = 8.85\ lb{\cdot}sec^2/in\\
&Then:\ \ E_1 = \left(\frac{21500.0}{0.44+1.00}\right) 32.7^{(0.44+1.00)} = 2.26{\cdot}10^6\ in{\cdot}lb\\
&BEV_1 = \sqrt{2E_1/m_1} = 715.4\ in/sec = 40.6\ mph
\end{aligned} \tag{7.61}$$

The velocity change (ΔV) of each vehicle involved in the two-vehicle impact can be computed either by using a numerical searching technique during the simulation or by the application of the conservation of linear momentum. Note that the sum of the absolute values of the velocity changes of the two vehicles is equal to the "closing speed" of the two vehicles — or the relative approach velocity of the two vehicles.

It should also be noted that ΔV of a vehicle in a two-vehicle impact is not necessarily the same as the BEV (fixed barrier equivalent velocity). As mentioned in Section 7.6.2, the ΔV and BEV of a vehicle are the same only when mass ratio equals stiffness ratio of the two vehicles. The analytical computation of the BEV of a vehicle in a two-vehicle impact involves the application of the principle of work and energy in addition to the principle of impulse and momentum.

The dynamic responses of the striking and struck vehicles are shown in Table 7.7. The dynamic crush and BEV of the Merkur are 32.7 inches and 40.6 mph, respectively. The estimated characteristic length of Merkur equals 32.7/40.6 = 0.81 inches/mph. Compared to the Merkur test data at 35 mph in rigid barrier tests shown in Table 7.7 where the characteristic length is about 0.80 inches/mph, the model's prediction is fairly reasonable.

Table 7.7 Dynamic Responses of Merkur and MDB

	Merkur (struck)	MDB (strike)
BEV, mph	40.6	27.1
Dynamic Crush, in	32.7	13
ΔV, mph	32.7	37.3
T_m, ms	65.5	65..5

Under the test condition where a NHTSA MDB (moving deformable barrier) strikes a mid-size passenger car (Merkur) at 70 mph, the velocity change of Merkur (32.7 mph) is less than NCAP test speed of 35 mph. However, based on the actual crush from the test, Merkur suffered a greater damage than that in the NCAP tests at 35 mph. Based on the power curve model simulation, the BEV of Merkur is 40.6 mph as shown in Table 7.7.

Therefore, in order to achieve the same crash severity for the Merkur as that in NCAP rigid barrier test, the striking speed of MDB should be scaled back from 70 mph to about 60 mph.

7.7 VEHICLE ACCELERATION AND CRASH SEVERITY

The acceleration of a vehicle involved in a two-vehicle collision is an indicator of crash severity. Using the relative acceleration response of an effective mass system shown in Eq. (4.70) in Section 4.9.1.1, the acceleration of the subject vehicle can be derived. Eq. (7.62) shows the acceleration of the subject vehicle as a function of relative approach velocity, mass ratio ($r_m = m_1/m_2$) , structure natural frequency, and damping factor. It should be noted that the acceleration of the subject vehicle is not governed by its own initial velocity; rather, it is governed by the relative approach velocity of the two vehicles.

$$\textit{Since } \ddot{x}_1 = \ddot{\alpha}(t)\frac{m_2}{m_1 + m_2} = \ddot{\alpha}(t)\frac{1}{1 + r_m} \quad \ldots\ldots\ldots\ldots\ldots\ldots (1)$$

from Eq.(4.70), *one gets*

$$\ddot{\alpha}(t) = (v_o\omega_e)e^{-\zeta\tau}\left[-2\zeta\cos\left(\sqrt{1-\zeta^2}\,\tau\right) + \frac{2\zeta^2-1}{\sqrt{1-\zeta^2}}\sin\left(\sqrt{1-\zeta^2}\,\tau\right)\right] \qquad (7.62)$$

therefore:

$$\ddot{x}_1 = \left(\frac{v_o\omega_e}{1 + r_m}\right)e^{-\zeta\tau}\left[-2\zeta\cos\left(\sqrt{1-\zeta^2}\,\tau\right) + \frac{2\zeta^2-1}{\sqrt{1-\zeta^2}}\sin\left(\sqrt{1-\zeta^2}\,\tau\right)\right] \quad \ldots\ldots (2)$$

where v_o: *relative approach velocity of two vehicles*

7.7.1 Damage Boundary Curve

To assess crash severity, a method adopted in the packaging industry called Damage Boundary Curve (DBC) [6] is used in the following crashworthiness analysis. Based on the effective mass and effective stiffness in assessing the impact severity, DBC defines the threshold of crash severity that the packaged components (such as a computer and peripheral products) can sustain without incurring damage. The specification is expressed in terms of peak acceleration (due to stiffness effect) and velocity change (due to mass effect) as shown in Fig. 7.32. Any impact condition sustained by the product which is above and/or to the right of the curve is in a damage zone. If the impact condition is below and /or to the left of the curve, it is a safe condition.

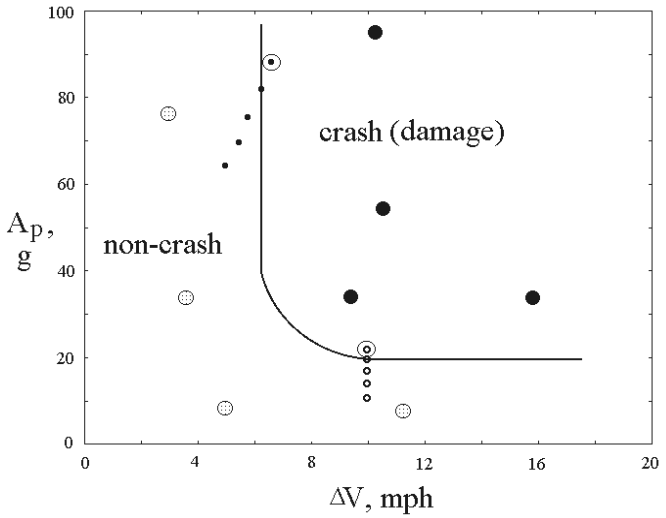

Fig. 7.32 A Damage Boundary Curve

Case Study 1: A product (component) is protected by a cushion material with stiffness given by a natural frequency of either 3 or 4 Hz. It is further assumed that the impact speed of the component striking a fixed barrier is kept at a constant 15 mph. Plot the transient velocity and acceleration responses and locate the two points on a DBC plot.

Using the transient and major response formulas shown in Section 4.5.1 in Chapter 4, the transient responses of the two tests are shown in Fig. 7.33. Both velocity curves between time zero and the time of dynamic crush have the same velocity change of 15 mph. However, the timings at the dynamic crush is 84 ms with the softer cushion (3 Hz) and 62 ms with the stiffer cushion (4 Hz). The peak sinusoidal deceleration is 13 g with the softer cushion and 17 g with the stiffer one.

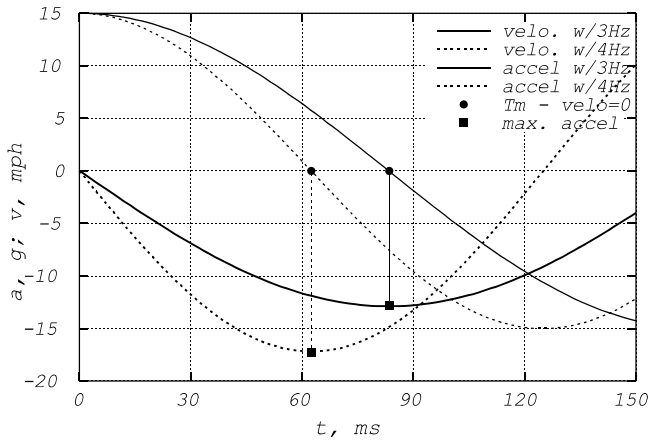

Fig. 7.33 Transient Velocity and Deceleration of a Product at Two Impact Speeds

Since the two points of the tests (15 mph, 13 g), and (15 mph, 17 g) have the same ΔV, they are located along a vertical in a DBC plot.

7.7.1.1 *Construction Steps for DBC*

Step 1: Determine the critical velocity change for a product. Using a drop test setup, the product is dropped from a given height onto a pad of known stiffness. The test is repeated with increasing drop test height until the product is damaged. Record the data points in terms of peak acceleration and velocity change. Circle the damage data point as shown in Fig. 7.32. The critical velocity change, Δv_c is the velocity change of a point immediately preceding the damage point. A vertical line is drawn through Δv_c.

Step 2: Replace the pad with a softer pad and choose a drop height such that the velocity change exceeds $(\pi/2)\Delta v_c$. By using this new velocity, the new test point will be located on the flat part of the lower right portion of DBC. Conduct a series of drop tests at the chosen drop height with an increasing pad stiffness for each succeeding test. The data points in terms of peak acceleration and velocity change are recorded. Circle the damage data point. The critical acceleration, A_c, is the acceleration of a point immediately preceding the damage point. A horizontal line is drawn through A_c .

Step 3: Round off the corner between the vertical through Δv_c and the horizontal through A_c. By fitting part of an ellipse between the two points $(\Delta v_c, 2A_c)$ and $((\pi/2)\Delta v_c, A_c)$, finish the final DBC construction.

7.7.1.2 *Mechanic Principles of DBC*

The mechanic principles of DBC involve the transient response of a two-mass system subjected to an impact. The two-mass system has been analyzed by an effective mass system in Section 4.4.4, Chapter 4. The impact response of a subject mass is controlled by its momentum (x-axis of DBC, due to the mass ratio) and energy absorption (y-axis of DBC, due to the stiffness ratio) relationship. Since the momentum principle describes the gross motion of the system, the impact duration is controlled by the natural frequency of the system. From Eq. (4.81), the contact (or impact) duration is inversely proportional to the undamped natural frequency.

Velocity change is the product of acceleration and impact duration. Given a velocity change on the DBC, the point that has a higher acceleration will have a shorter impact duration and the point that has a lower acceleration will have a longer one. Similarly, given an acceleration on the DBC, a smaller velocity change will have a shorter impact duration and a larger velocity change will have a longer one.

Case Study 2:

For a vehicle where the fuel is delivered to the engine by an electric fuel pump, a fuel shutoff switch is installed either in the trunk or in the passenger compartment. The switch is designed to shutoff the fuel supply when the impact severity in a certain impact mode is severe enough. A typical fuel shutoff switch is a mechanical device similar to the ball-in-tube (BIT) safing (or confirmation) sensor with a magnet to provide the bias g-force. Similar in function to the BIT safing sensor, the amount of damping in the fuel shutoff device is negligible.

A typical DBC of the fuel shutoff switch used in a full-size vehicle is shown in Fig. 7.34. The DBC is plotted in terms of deceleration and contact duration. The product of the two quantities yields the velocity change. There are two outer DBC curves shown in the top and bottom of the plot. When the deceleration is in the "must actuate region," the crash severity is the highest; while the deceleration is in the "must not actuate region," the severity is very low.

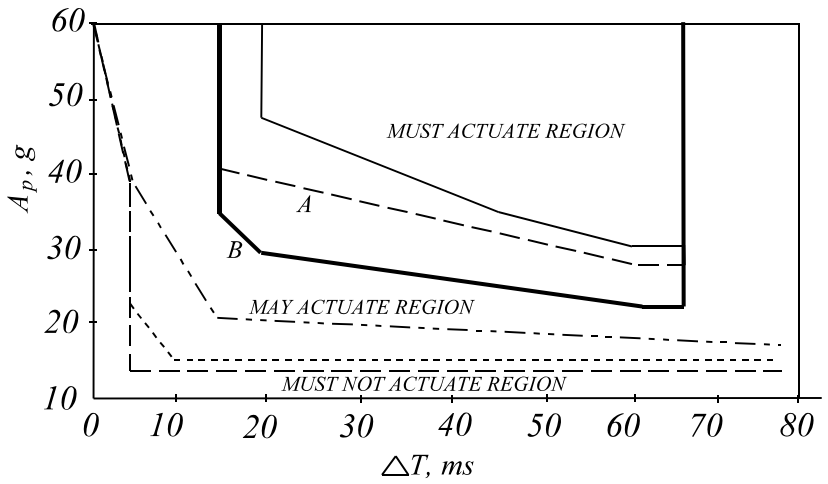

Fig. 7.34 DBC Curves for a Fuel Shutoff Switch of a Full-Size Vehicle

The two curves with indices A and B were obtained from tests. Curve A is based on a test where a full-size vehicle struck a rigid barrier at 35 mph. Curve B is based on both a test where a full-size vehicle was hit in the rear by a mid-size car at 50 mph, and a test where the full-size vehicle was hit in a frontal 50% offset by a mid-size car.

7.7.2 Crash Severity Assessment in Vehicle-to-Vehicle Compatibility Test

7.7.2.1 *Vehicle Crush Characteristics*

Fig. 7.35 shows the crush characteristics of three vehicles in a fixed barrier test condition. The characteristic length (c/v, in/mph) of the full-size car is the largest, followed by the mid-size car and then the truck/SUV. The relationship between the specific stiffness (K/W, lb/in/lb) and characteristic length (C/V, in/mph) has been shown in Eq. (4.26). This relationship is repeated in Eq. (7.63), and plotted in Fig. 7.35.

$$\frac{K}{W} = \frac{.8}{\left(\frac{C}{V}\right)^2} \tag{7.63}$$

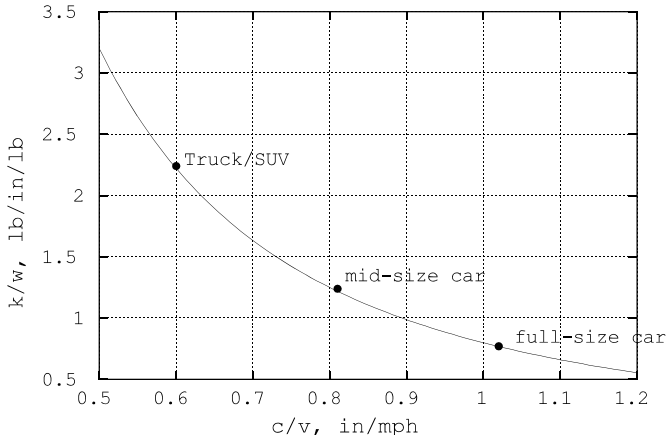

Fig. 7.35 Specific Stiffness vs. Characteristic Length

It has been shown in Section 4.5.2.5, Chapter 4, that in a vehicle-to-vehicle impact, the relative magnitudes of the mass ratio and stiffness ratio of two vehicles are determined by the specific stiffness of each of the two vehicles.

Since the specific stiffness of the truck is larger than those for either of the two cars, as shown in Fig. 7.35, the relative magnitudes of the mass ratio and stiffness ratio between the truck and car can be determined as shown in Eq. (7.64) (a repeat of Eq. (4.31) in Chapter 4).

$$\begin{aligned} &\textit{Since} \quad \frac{K_t}{M_t} > \frac{K_c}{M_c}, \quad \textit{and} \quad K>0, \quad M>0, \\ &\textit{after interchanging } K_c \textit{ and } M_t, \textit{ one gets} \\ &\qquad \frac{K_t}{K_c} > \frac{M_t}{M_c}, \qquad \textit{or} \quad r_k > r_m \\ &r_k\textit{: stiffness ratio of truck to car}, \quad r_m\textit{: mass ratio of truck to car} \end{aligned} \tag{7.64}$$

In order to show the differences of the crash severity index and crash momentum index clearly on a 3-D plot, the mass and stiffness ratios in the two expressions have been inverted. Substituting $r_m = 1/ r'_m$ and $r_k = 1/ r'_k$ in the respective expression, they become the ones shown in Fig. 7.36. The two crash indices of the subject vehicle #1 are now expressed in terms of the mass ratio, r'_m and stiffness ratio r'_k of vehicle #2 to #1.

The crash severity index is not equal to the crash momentum index in general, as shown in Fig. 7.36. The two indices are equal to each other when the mass ratio equals the stiffness ratio. This condition exists when the two surfaces shown in Fig. 7.36 intersect along the diagonal of the base.

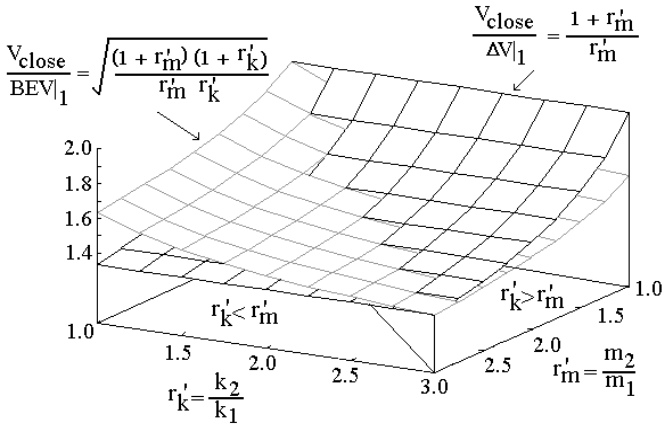

Fig. 7.36 Closing Speed Comparison Based on ΔV and BEV

The closing speed will be determined such that the full-size car would have the same ΔV and BEV of 35 mph as in a rigid barrier test.

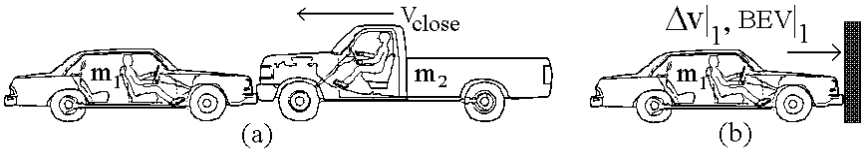

Fig. 7.37 Truck to Full-Size Car Compatibility Test — Case 1

Table 7.8 Closing Speeds Based on 35 mph Rigid Barrier Test ($BEV|_1$ and $\Delta V|_1$=35 mph)

Case #	vehicle-to-vehicle						r_m' m_2/m_1	r_k' k_2/k_1	$V_{close,\ mph}$	
	#1			#2					based on ΔV	based on BEV
	w_1, klb	k_1/w_1, klb/in/klb	k_1, klb/in	w_2, klb	k_2/w_2, klb/in/klb	k_2, klb/in				
1	4.5	0.77	3.5	5.5	2.2	12.1	1.2	3.5	64	54
2	3.5	1.24	4.3	4.5	0.77	3.47	1.3	0.8	62	70

In a rigid barrier test, the striking speed of a vehicle is the same as ΔV in the deformation phase and is also the same as the BEV. If the barrier impact speed is set at 35 mph, then the closing speed based on the momentum formula is 64 mph, while that based on the energy absorption formula is only 54 mph. Consequently, using the ΔV momentum method overestimates the closing speed by almost 20%. In Case 2, a full-size car strikes a mid-size car as shown in Fig. 7.38. The closing speed is determined in such a way that the subject mid-size vehicle m_1 would yield a BEV or ΔV of 35 mph, as in the rigid barrier test.

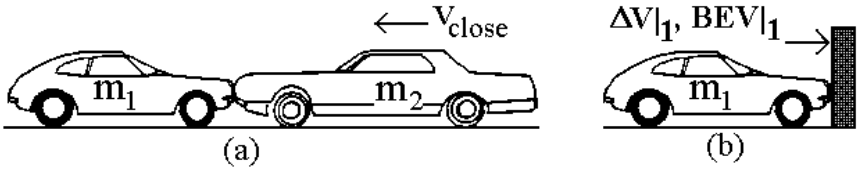

Fig. 7.38 Full-Size to Mid-Size Car Compatibility Test — Case 2

From Table 7.8 for case 2, $r_m' > r_k'$, the closing speed based on the momentum formula is 62 mph, while that based on the energy absorption formula is 70 mph. Consequently, using the ΔV momentum method underestimates the closing speed by about 11% in this test condition.

7.7.2.2 *Vehicle Peak Responses*

In the vehicle-to-vehicle test shown in (a) of Fig. 7.38, the subject vehicle m_1 absorbs a certain amount of the total crush energy during an impact. This energy absorption is equal to that absorbed by m_1 when it impacts on a rigid barrier at a speed of BEV_1, as shown in (b) of Fig. 7.38.

It will be proved that the peak sinusoidal deceleration of vehicle m_1 in the two-vehicle impact shown in part (a) is the same as that vehicle-rigid barrier test in part (b) of Fig. 7.38.

The peak sinusoidal deceleration of an effective mass is:

$$A_p = V_{close}\,\omega_e = V_{close}\sqrt{\frac{k_e}{m_e}} \qquad \ldots\ldots\ldots\ldots \quad (1)$$

where $k_e = \dfrac{k_1 k_2}{k_1 + k_2}$, *and* $m_e = \dfrac{m_1 m_2}{m_1 + m_2}$

The peak sinusoidal deceleration of mass #1 *is*: (7.65)

$$A_{p1} = A_p \frac{m_2}{m_1 + m_2} \qquad \ldots\ldots\ldots\ldots\ldots\ldots \quad (2)$$

Substituting (1) *into* (2), *and rearranging, one gets*

$$A_{p1} = \left(V_{close}\sqrt{\frac{1}{(1 + r_m)(1 + r_k)}} \right)\sqrt{\frac{k_1}{m_1}} = BEV_1\,\omega_1 \quad \ldots \quad (3)$$

The right hand side of (3) of Eq. (7.65) is the peak sinusoidal acceleration of vehicle #1 in a rigid barrier test where the impact speed is BEV_1 and the circular natural frequency of vehicle #1 is ω_1. The left hand side of (3) is the peak sinusoidal acceleration of vehicle #1 in the vehicle-to-vehicle test. Consequently, as long as the crash severity index is used in establishing the crush energy relationship between the vehicle-to-vehicle (VTV) and vehicle-to-barrier (VTB) tests, the peak sinusoidal acceleration of the subject vehicle will be the same in both VTV and VTB tests.

Note that the magnitude of the effective stiffness (or mass) expressed in terms of individual stiffness (or mass) is shown in Fig. 7.39. The magnitude of k_e becomes larger when both k_1 and k_2 are larger (e.g., $k_1 = k_2 = 10$, $k_e = 5$) and the magnitude of k_e becomes smaller when both k_1 and k_2 are smaller (e.g., $k_1 = k_2 = 2$, $k_e = 1$). Similar relationship applies to the effective mass. By knowing the magnitudes of the effective mass and stiffness, the change in vehicle response in a two-vehicle impact can be quickly assessed.

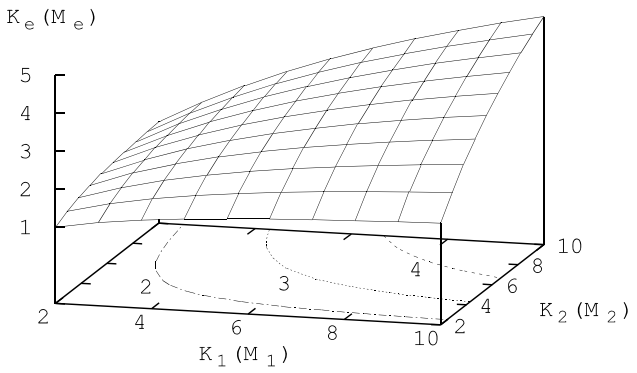

Fig. 7.39 Effective Spring (or Mass) in 2-Vehicle Impact

In a crashworthiness study, the velocity change (ΔV) and barrier equivalent velocity (BEV) are frequently used to describe the crash severity of an impact event. Although the two parameters are related by the impact conditions such as the velocities, masses, and stiffnesses of the vehicles involved, they are fundamentally different in describing the crash dynamics of the vehicles involved. This is due to the fact that ΔV is momentum based, and that BEVis momentum and energy based parameters. Because of the difference in the definition, ΔV describes the gross motion of the impact event, such as changes in the kinematic responses such as acceleration, velocity, and displacement of the vehicles involved, while BEV describes the changes in the kinetic responses such as the crush, force, and energy which are measures of the impact severity of the engaging vehicles.

7.8 VELOCITY AND ENERGY DISTRIBUTIONS IN TWO-VEHICLE IMPACT

Two methods are used to evaluate the velocity and energy components in a vehicle-to-vehicle impact. One method is based on the principles of impulse and momentum on which the Kelvin's Theorem is based, and the other is based on the Newton's Second Law from which the lumped mass model, CRUSH II, was established.

7.8.1 Kelvin's Theorem

Using the methodologies presented in Section 7.4 for the two-vehicle central impact, two cases of vehicle-to-vehicle central impacts are presented. The two vehicles are a full-size truck and a compact car. The mass and stiffness ratios of the truck to car are 2.5 and 3, respectively. The relative approach velocities for both cases are 40 m/s. However, the initial velocities of the two vehicles in the two cases are different as shown in Table 7.9.

Table 7.9 Initial Velocities of Car and Truck in Two Cases of Central Impact

Case #	Initial Velocity, m/s		Closing Speed, m/s
	Car, m	Truck, M	
1	25	15	40
2	0	40	

The input data, the procedures of computing the velocity and energy components, are listed in Table 7.10. The energy dissipation by Kelvin's theorem and the barrier equivalent velocities (BEV) of each vehicle in terms of energies absorbed and dissipated for Case 1 central impact are also computed.

Table 7.10 Velocity and Energy Components for Case 1 Vehicle in Central Impact

```
 ** ENERGY DISTRIBUTION OF TWO VEHICLES IN CENTRAL IMPACT **
ENTER m (MASS m, Kg) <1000> 1000
ENTER M (MASS M, Kg) <2500> 2500
ENTER v1 (INITIAL VELOCITY OF m, m/sec) => 25
 V1 (INITIAL VELOCITY OF M, m/sec) => 15
ENTER e (COeFFICIENT OF RESTITUTION) => .15
 k (RELATIVE STIFFNESS OF m) => 1
 K (RELATIVE STIFFNESS OF M) => 3
 IMPACT PARAMETERS:
 RM (MASS RATIO, m/M) = .4
 RV (VELOCITY RATIO, v1/V1) = 1.666667
 RE (ENERGY RATIO, Δ Em/Δ EM, OR K/k) = 3
vo = Vo (COMMON VELOCITY OF m AND M) = 3.571429 m/sec
v2 (FINAL OR SEPARATION VELOCITY OF m) = -7.857143 m/sec
 V2 (FINAL OR SEPARATION VELOCITY OF M) = 1.857143 m/sec
 Δvo (VELOCITY CHANGE OF m @ COMMON VELOCITY) = 28.57143 m/sec
 ΔVo (VELOCITY CHANGE OF M @ COMMON VELOCITY) = 11.42857 m/sec
 Δv (VELOCITY CHANGE OF m @ SEPARATION) = 32.85714 m/sec
 ΔV (VELOCITY CHANGE OF M @ SEPARATION) = 13.14286 m/sec
 P1 (=v1+V1, RELATIVE APPROACH VELOCITY) = 40 m/sec
 P2 (=v2+V2, RELATIVE SEPARATION VELOCITY) = -6 m/sec
 P (=P1+P2, RELATIVE APPROACH + SEPARATION VELOCITIES) = 34 m/sec
 I12 [m(v1-v2)=M(V1-V2), LINEAR IMPULSE] = 32857.14 kg*m/sec
 ΔE [CRUSHING ENERGY DISSIPATED] (= I12*P/2 .. Kelvin's Theorem) = 558.5714 kJ
```

The comparisons of the velocity and energy components for the two cases are shown in Table 7.11. Note that the magnitudes of those variables that are defined with respect to the fixed reference frames are different between the two cases. Those variables, related to the boundary conditions of the problem, are the common velocity, separation velocity, initial kinetic energy, kinetic energy at the time of common velocity, and final (separation) kinetic energy. However, those quantities in terms of relative responses are identical between the two cases. They are related to the impact severity such as velocity changes, relative velocities, the energy absorbed, the rebound energy, and the energy dissipated by the vehicle structures.

Table 7.11 Velocity and Energy Components of Two Central Impacts

Parameters	Case 1	Case 2
m (mass m), Kg	1000	
M (mass M), Kg	2500	
v_1 (initial velocity of m), m/sec	25	0
V_1 (initial velocity of M), m/sec	15	40
e (coefficient of restitution)	0.15	
k (relative stiffness of m)	1	

K (relative stiffness of M)	3	
r_m (mass ratio, m/M)	0.4	
r_v (velocity ratio, v_1/V_1)	1.667	0
r_e (energy ratio, $\Delta E_m/\Delta E_M$, or K/k)	3	
Velocity Distribution		
$v_o = V_o$ (common velocity of m and M), m/sec	3.57	27.57
v_2 (final or separation velocity of m), m/sec	-7.86	-32.86
V_2 (final or separation velocity of M), m/sec	1.86	26.86
Δv_o (velocity change of m @ common velocity)	27.57	
ΔV_o (velocity change of M @ common velocity)	11.43	
Δv (velocity change of m @ separation), m/sec	32.86	
ΔV (velocity change of M @ separation), m/sec	13.14	
P_1 ($=v_1+V_1$, relative approach velocity), m/sec	40	
P_2 ($=v_2+V_2$, relative separation velocity), m/sec	-6	
P ($=P_1+P_2$, relative approach + separation velocities), m/sec	34	
I_{12} [$m(v_1-v_2)=M(V_1-V_2)$, linear impulse], kg*m/s	32857.14	
Energy Distribution		
Crushing energy dissipated (= I_{12}*P/2 .. Kelvin's Theorem), kJ	557.57	
E_{m1} (initial K.E. of m), kJ	312.5	0
E_{M1} (initial K.E. of M), kJ	281.25	2000
E_1 (total initial K.E.), kJ	593.75	2000
E_o (total K.E. @ common velocity), kJ	22.32	1427.57
ΔE_a (total energy absorbed)	571.43	
E_{m2} (final K.E. of m), kJ	30.87	539.8
E_{M2} (final K.E. of M), kJ	4.31	901.63
E_2 (total final K.E.), kJ	35.18	1441.43
ΔE_r (total rebound energy), kJ	12.86	
ΔE (crushing energy dissipated), kJ	557.57	

ΔE_m (energy dissipated by m), kJ	417.93	
ΔE_M (energy dissipated by M), kJ	139.64	
E_t (energy transferred, M => m), kJ	137.3	957.72
ΔE_{am} (energy absorbed by m), kJ	427.57	
ΔE_{aM} (energy absorbed by M), kJ	142.86	
ΔE_{am} (energy rebounded by m), kJ	9.64	
ΔE_{aM} (energy rebounded by M), kJ	3.21	
BEV_a (Barrier Equivalent Velocity based on energy Absorbed):		
BEV_a OF m, m/sec	29.28	
BEV_a OF M, m/sec	10.69	
BEV_d (Barrier Equivalent Velocity based on energy Dissipated):		
BEV_d OF m, m/sec	27.95	
BEV_d OF M, m/sec	10.57	

To understand the energy relationships between the two vehicles, the velocity and energy component distributions are graphed and shown in Fig. 7.40. The bars at the left side are those energy and velocity components for the compact car, and at the right side for the truck. The initial velocities of the car and truck are 25 and 15 m/s, respectively, and the closing speed is 40 m/s. Although the car has only 313 kJ of initial kinetic energy, it ended up with 429 kJ of absorbed energy. This is due to the soft structure of the small car absorbing most of the total energy in the impact between the car and truck. After subtracting the rebound energy of the car from the absorbed energy of the car, the energy dissipated by the car is 419 kJ, as shown in Fig. 7.40.

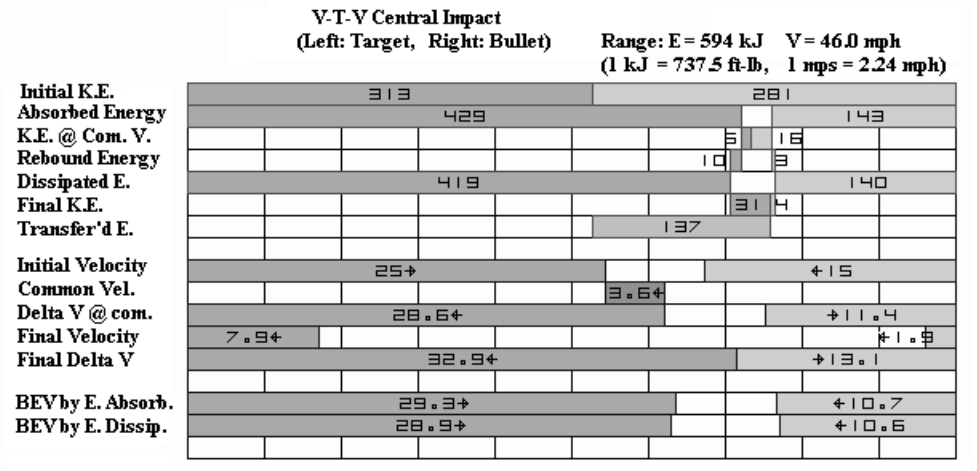

Fig. 7.40 Energy and Velocity Distribution Map for Central Impact (v=25, V=15 m/s)

At the end of the energy dissipation phase by the small car, it still has 31 kJ of final kinetic energy. Therefore, the total energy available to the small car in the collision process is 419 + 31 = 450

kJ. Since the small car has only 313 kJ of initial kinetic energy, the net increase of 450 – 313=137 kJ is referred to as the transferred energy. It is a kinetic energy transferred from the vehicle with larger initial momentum to the other vehicle. If the initial velocities of the two vehicles are chosen such that the closing speed remains the same and the initial momenta of the two vehicles equal, then there is no kinetic energy transferred. Graphically, the transferred energy is the energy from the boundary (interface) between the final kinetic energy segments of the two vehicles to the boundary between the initial kinetic energy segments of the two vehicles as shown in the bar graph of Fig. 7.40.

As long as the closing speed of the two vehicles is kept the same, different initial velocities of the two vehicles will not change the crash severities of the two vehicles. Fig. 7.41 shows the energy and velocity distribution map for Case 2. The collision speeds of car and truck are 0 and 40 m/s, respectively. Compared to Fig. 7.40, although the kinetic energies are different, including the transferred energy, the crash severities such as the energy absorption, the energy dissipation, and the corresponding BEV remain the same. This is because it is the closing speed in a two-vehicle impact that determines the crash severity.

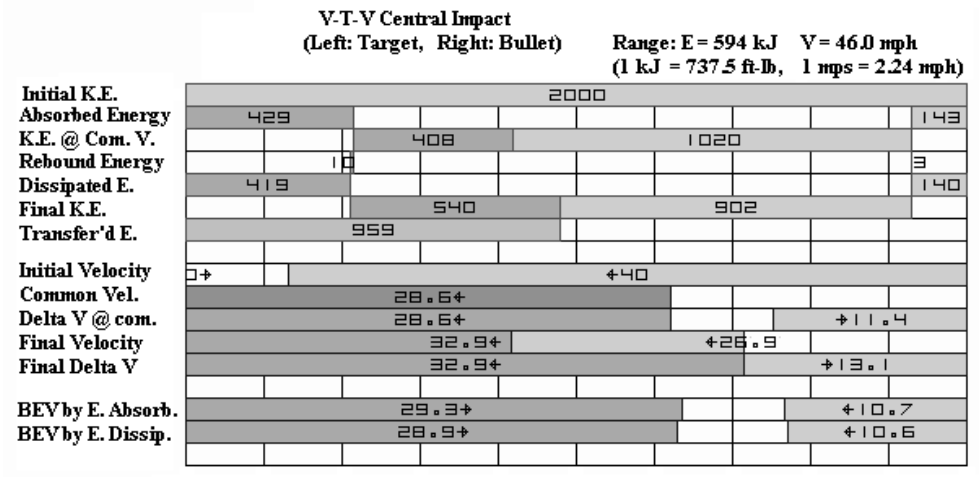

Fig. 7.41 Energy and Velocity Distribution Map for Central Impact (v=0, V=40 m/s)

To compare the energy and velocity distribution of the vehicle-to-vehicle in an offset (non-central) impact with those in the central impact, the basic formulas developed in Section 7.5 on non-central impact are utilized for the following analysis shown in Table 7.11. For a more comprehensive analysis on the oblique and offset impact modes, the reader should refer to the work done by MacMillan [2]. Similar to the coefficient of restitution used along the line of impact between two objects, the tangential moment coefficient is used along the contact surface to take into account the friction and inter-locking phenomenon between the contacting component surfaces. The input data listed in Table 7.11 represents the conditions of a 50% offset impact between two vehicles with a closing speed of 40 m/s. The longitudinal and lateral distances between the C.G. of each vehicle and the damage centroid are x and y, respectively. The computations of velocity and energy components are shown in Table 7.11 and Fig. 7.42. Since it is an offset impact, the final velocity of each vehicle consists of horizontal and vertical components where the magnitudes and directions are shown in the plot. Since in the offset impact, a portion of kinetic energy is expended in the rotation, the resulting BEV of each vehicle based on energy dissipated is about 15% less than that for the central impact.

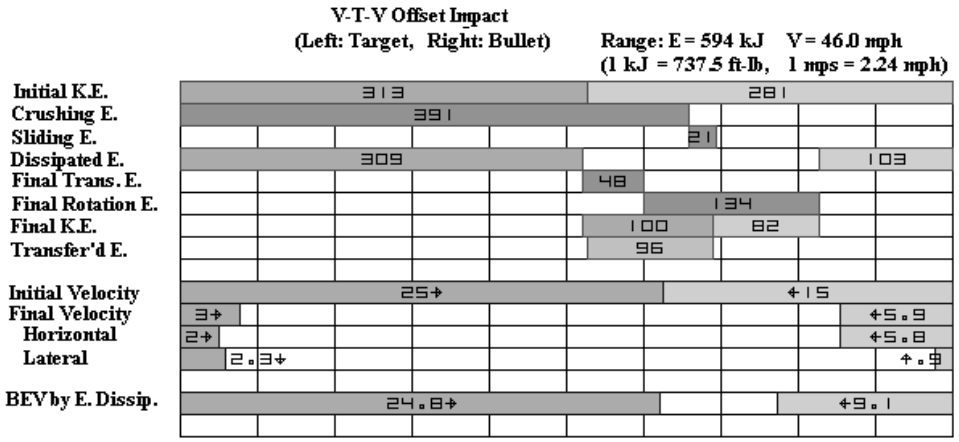

Fig. 7.42 Energy and Velocity Distribution Map for Offset Impact (v=25, V=15 m/s)

Table 7.11 Velocity and Energy Components for Case 1 Vehicle in Offset Impact

5. ENERGY DISTRIBUTION IN VEHICLE-TO-VEHICLE OFFSET IMPACT
ENTER m (MASS m, Kg) <1000> 1000
M (MASS M, Kg) <2500> 2500
k^2 (RADIUS OF GYRATION SQUARED OF m, m^2) <2> 2
K^2 (RADIUS OF GYRATION SQUARED OF M, m^2) <3> 3
ENTER x (X LOCATION OF C.G. OF m, m) <1.5> 1.5
X (X LOCATION OF C.G. OF M, m) <2> 2
y (Y LOCATION OF C.G. OF m, m) <1> 1
Y (Y LOCATION OF C.G. OF M, m) <1.25> 1.25
ENTER v1 (INITIAL VELOCITY OF m, m/sec) <25> 25
V1 (INITIAL VELOCITY OF M, m/sec) <15> 15
ENTER L (LAMBDA, TANGENTIAL IMPACT COEFFICIENT) <.1> .1
e (COeFFICIENT OF RESTITUTION) <.15> .15
k (RELATIVE STIFFNESS OF m) <1> 1
K (RELATIVE STIFFNESS OF M) <3> 3
IMPACT PARAMETERS:
RM (MASS RATIO, m/M) = .4
RE (ENERGY RATIO, DELTA Em/DELTA EM, OR K/k) = 3
v2 (FINAL OR SEPARATION VELOCITY OF m) = 3.04795 m/sec
@ ANGLE ALPHA2 = -48.99091 degrees
: HORIZONTAL VELOCITY = 2 m/sec
: LATERAL VELOCITY = -2.3 m/sec
w2 (FINAL ANGULAR VELOCITY OF m) = 9.775 rad/sec
V2 (FINAL OR SEPARATION VELOCITY OF M) = 5.872512 m/sec
@ ANGLE BETA2 = -9.013205 degrees
: HORIZONTAL VELOCITY = 5.8 m/sec
: LATERAL VELOCITY = -.92 m/sec
W2 (FINAL ANGULAR VELOCITY OF M) = 3.22 rad/sec
P1 (RELATIVE APPROACH VELOCITY) = 40 m/sec
P2 (RELATIVE SEPARATION VELOCITY) = -6 m/sec
NOTE: e = -P2 / P1
P (RELATIVE APPROACH + SEPARATION VELOCITIES) = 34 m/sec
I12 (COMPRESSIVE IMPULSE) = 23000 kg*m/sec
CRUSHING ENERGY DISSIPATED (= I12*P/2 .. Kelvin's Theorem) = 391 kJ
Q1 (RELATIVE INITIAL SLIDING VELOCITY) = 0 m/sec
Q2 (RELATIVE FINAL SLIDING VELOCITY) = 17.8825 m/sec
Q (=Q1+Q2) = 17.8825 m/sec
J12 (TANGENTIAL IMPULSE = LAMBDA * I12) = 2300 kg*m/sec
SLIDING ENERGY DISSIPATED (= J12*Q/2 .. Kelvin's Theorem) = 20.56487 kJ
K.E. (KINETIC ENERGY WITH RESPECT TO A FIXED FRAME OF REFERENCE):
1. E1t (INITIAL TOTAL tRANSLATIONAL K.E.) = 593.75 kJ
2. E1r (INITIAL TOTAL rOTATIONAL K.E.) = 0 kJ
3. E1 (INITIAL TOTAL K.E.) = 593.75 kJ
4. Em1 (INITIAL TOTAL K.E. OF m) = 312.5 kJ

5. EM1 (INITIAL TOTAL K.E. OF M) = 281.25 kJ
6. E2t (FINAL TOTAL tRANSLATIONAL K.E.) = 47.753 kJ
7. E2r (FINAL TOTAL rOTATIONAL K.E.) = 134.4321 kJ
8. E2 (FINAL TOTAL K.E.) = 182.1851 kJ
9. Em2 (FINAL TOTAL K.E. OF m) = 100.1956 kJ
10. EM2 (FINAL TOTAL K.E. OF M) = 81.9895 kJ
11. Δ Ep (CRUSHING ENERGY DISSIPATED) = 391 kJ
12. ΔEq (SLIDING ENERGY DISSIPATED) = 20.56487 kJ
13. Δ Em (ENERGY DISSIPATED BY m) = 308.6736 kJ
14. Δ EM (ENERGY DISSIPATED BY M) = 102.8912 kJ
15. Δ E (TOTAL ENERGY DISSIPATED) = 411.5649 kJ
16. Et (ENERGY TRANSFERRED, M => m) = 96.36927 kJ

BEVd (Barrier Equivalent Velocity based on energy Dissipated):

BEVd OF m = 24.84648 m/sec

BEVd OF M = 9.07265 m/sec

7.8.2 Lumped Mass Modeling on Crash Severity

The lumped mass modeling technique utilizing the CRUSH II model is used here to assess the crash severity of each of the two vehicles involved in a central impact. There are three cases to be analyzed for their relative crash severities. The closing speed is 31 mph for all three cases, as shown in Table 7.12; however, the individual velocities in the three cases are different.

One of the frequently asked questions is "Assuming the other vehicle is a full-size truck and the subject vehicle is a mid-size sedan, in which of the three cases will the subject sedan undergo the most severe impact?"

Table 7.12 Crash Severity in Vehicle-to-Vehicle Impact

Case #	Initial Speed , mph **Other** **Subject**	Closing Speed, mph	Crash Pulse of Subject Vehicle **Body**	**Engine**
1	0 <= 31	31	Fig. 7.44	Fig. 7.44
2	15 => <= 16			
3	31 => 0			

A 12-mass and 23-EA lumped mass CRUSH II model is shown in Fig. 7.43. The model is set up for simulating a vehicle-to-vehicle central impact with the front bumpers represented by the interface mass. The simulation results of the transient deceleration at the body (passenger compartment) and engine for the other vehicle in the three cases are shown in Fig. 7.44. The transient decelerations at the body location in the three cases are on top of each other. Similarly, those deceleration curves at the engine location for the three cases are also identical. For the subject vehicle, the observation of the transient deceleration responses shown in Fig. 7.45 is the same as that for the other vehicle.

However, the velocity and displacement responses (w.r.t. the absolute reference frame) at the body location are different for the three cases as shown in Figs. 7.46 and 7.47, respectively. However, looking at the relative velocity of the subject vehicle w.r.t. the other vehicle, the velocity changes for the three cases are identical.

Consequently, it can be fairly stated that the crash severity such as deceleration, BEV, energy absorbed, and energy dissipated in a vehicle-to-vehicle impact is determined by the closing speed (relative speed), relative mass (mass ratio), and relative stiffness (stiffness ratio) of the two vehicles.

Such an observation of the relationship has also been proved out by the finite element method (FEM) where each vehicle is modeled by 50,000 elements. Such an FEM model, executed on a supercomputer, yields the same results as those by the two previous methods.

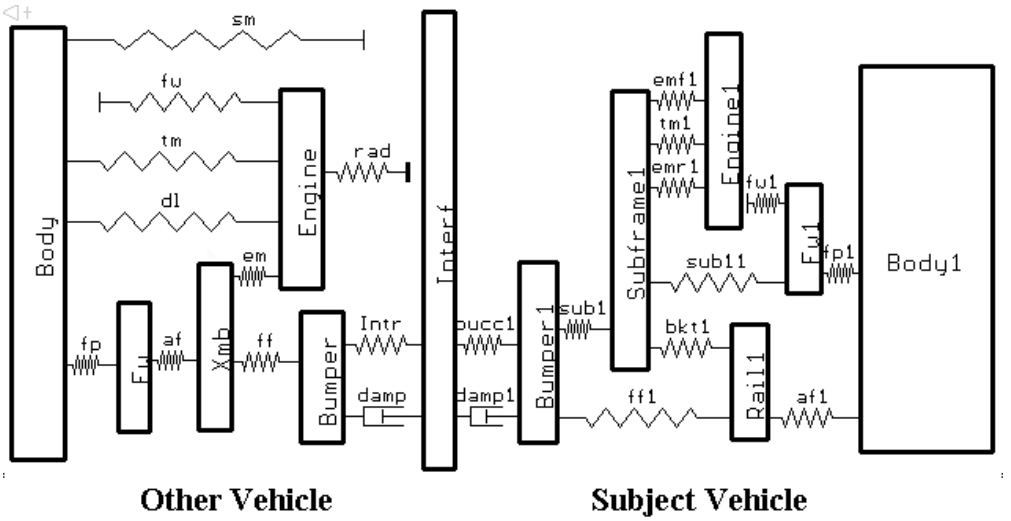

Fig. 7.43 A Vehicle-to-Vehicle Impact Model

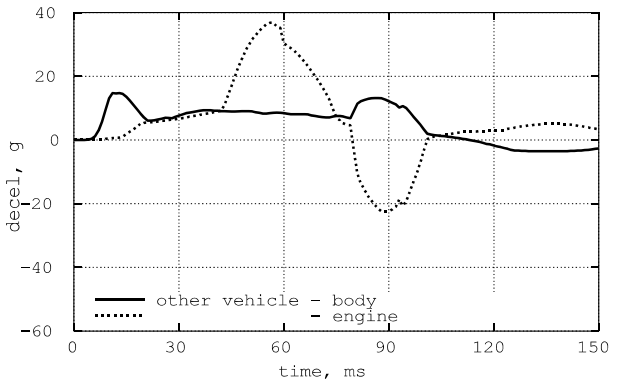

Fig. 7.44 Other Vehicle Decelerations at Body and Engine for 3 Cases

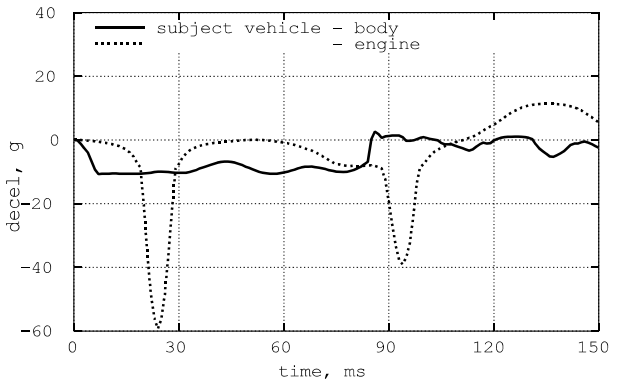

Fig. 7.45 Subject Vehicle Decelerations at Body and Engine for 3 Cases

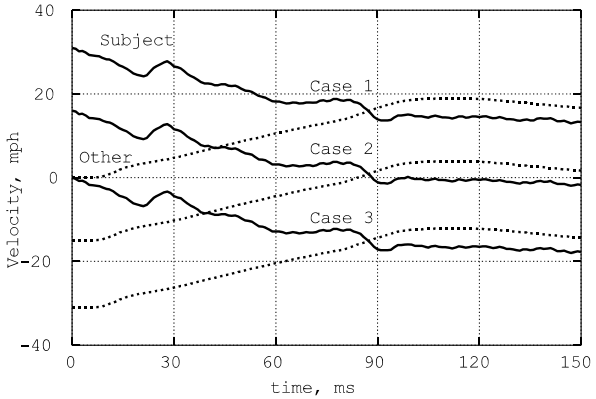

Fig. 7.46 Vehicle Body Velocities for 3 Cases

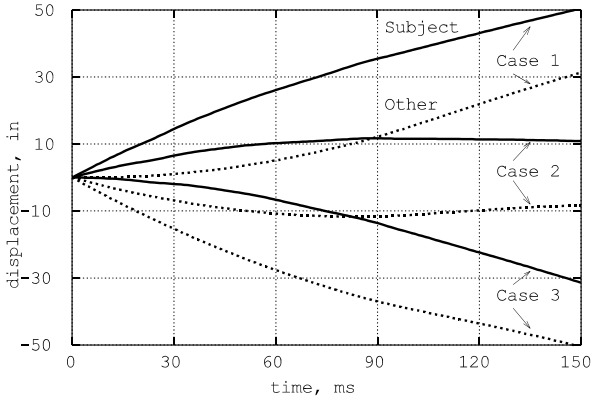

Fig. 7.47 Vehicle Body Displacements for 3 Cases

7.9 INTERMEDIATE MASS EFFECT

In a vehicle frontal test, the subsystem of mass(es) located between the rigid barrier and vehicle compartment is referred to as the intermediate mass. Therefore, the load-cell plate and engine-power train are the major intermediate masses of a vehicle in the frontal impact. Assume that the load-cell plate is securely fastened to the rigid barrier, the test load-cell transient loading is shown in Fig. 7.48.

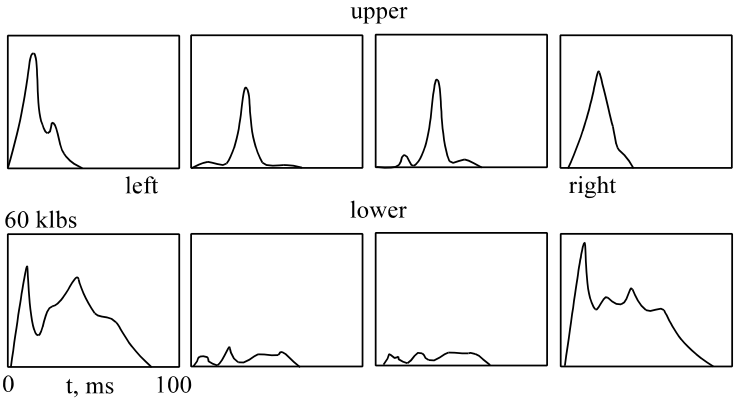

Fig. 7.48 Load Cell Plate Loadings, Frame Vehicle at 35 mph Test

Among all the load-cells, the outer load-cells carry the most loadings. This is because in the 35 mph frame vehicle to rigid barrier impact, the stiff frame rails on both sides of the vehicle carry most of the impact loading.

Using the barrier load-cell data and vehicle crash data, the energy distribution on the front end can be computed. Fig. 7.49 shows a frame vehicle energy distribution in a high speed rigid barrier test. 35% of the crush energy is absorbed by the upper part of the front end structure, and 65% by the lower part where the frame rails are located.

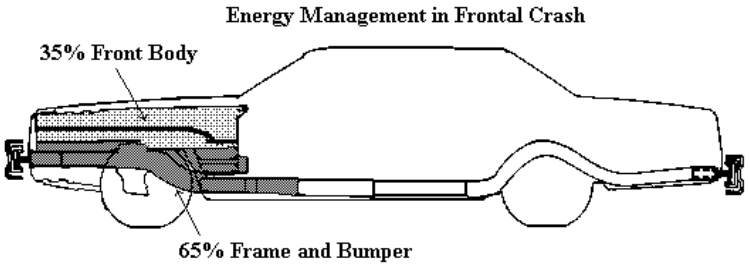

Fig. 7.49 Energy Distribution on a Vehicle Front

The lumped-mass vehicle model with the engine (and power train) as the intermediate mass is shown in Fig. 7.50. At any instant during impact, the load-cell loading is the sum of forces due to those springs in contact with the load-cell plate. Since the load cells and steel plate are fastened securely to the barrier, the load-cell loading is also referred to as the barrier loading.

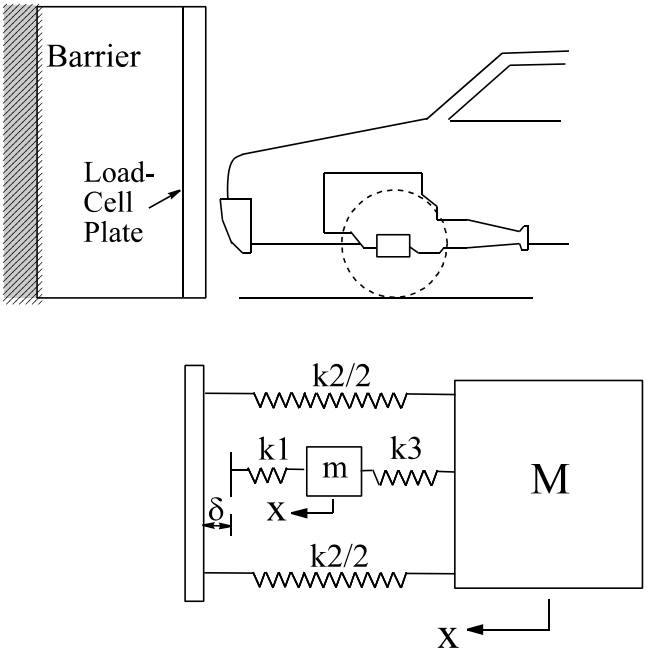

Fig. 7.50 Vehicle Model with Intermediate Mass, m.

Shown in the model in Fig. 7.50, the mass of the engine is m, and that of the passenger compartment is M. Assuming a typical engine in the truck weighs about 760 lbs and the compartment, 4580 lbs, the compartment to engine weight ratio is about 6. Since the mass of the engine is appreciable, it yields certain dynamic effects on the compartment loading [7]. The compartment loading is defined as the product of compartment mass and compartment deceleration.

The compartment loading alone without the engine effect in a crash can be estimated using the principle of impulse and momentum. Assuming no frictional impulse between contact surfaces during the crash, the momentum change of the vehicle between time zero and time of dynamic crush is then equal to the external impulse during this period. The external impulse is mainly due to barrier reaction loading acting on the vehicle in the horizontal direction. Shown in Eq. (7.66), the compartment loading is the same as the barrier loading and equals 80,000 lbs for the 35 mph rigid barrier test.

$$
\begin{aligned}
&M\Delta V = F\Delta T \\
&For\ M = 4580\,lbs\,(=142\,slugs) \\
&\quad \Delta V = 35\,mph = 51.3\,ft/\text{sec} \\
&\quad \Delta T = .091\,\text{sec} \\
&\quad g = 32.2\,ft/\text{sec/sec} \\
&F(average\ loading) = M\Delta V/\Delta T/g = 80{,}000\,lbs \\
&A'(average\ deceleration\ loading) = 80{,}000/4580 = 17.5\,g
\end{aligned}
\tag{7.66}
$$

We will see the role that the engine plays in the barrier loading and the compartment loading by formulating the equations of motion of the two masses as shown in Eq. (7.67).

$$
\begin{aligned}
&M\ddot{X} = -K3(X-x) - K2X \quad \ldots\ldots\ldots\ldots\ldots\ldots \quad (1) \\
&M\ddot{x} = \ \ K3(X-x) - K1\,|x-\delta| \quad \ldots\ldots\ldots\ldots\ldots\ldots \quad (2) \\
&where \quad |x-\delta| > 0, \\
&summing\ up\ both\ sides\ of\ (1)\ and\ (2)\ yields \\
&m\ddot{x} = -M\ddot{X} - (K2X + K1\,|x-\delta|) \quad \ldots\ldots\ldots\ldots\ldots\ldots \quad (3) \\
&m\ddot{x} = Compartment\ loading - Barrier\ loading \quad \ldots \quad (4)
\end{aligned}
\tag{7.67}
$$

Therefore, the inertia of the engine has a direct effect on the compartment loading. Based on crash test data of a frame vehicle in a 35 mph rigid barrier test, the compartment, engine, and barrier load cell crash data are shown in Fig. 7.51.

Based on the loading and acceleration relationship (4) of Eq. (7.67), the following observations on the test data are made:

(I) When the compartment loading is greater than the barrier loading, the intermediate mass (e.g., engine) is accelerating. Fig. 7.51(c) shows that the compartment loading is greater than the barrier loading 15 ms after the crash. The vehicle structural components are all decelerating right after the impact and the engine starts decelerating 15 ms later, as shown in Fig. 7.51(b). Consequently, the intermediate mass, dominated by the barrier load plate, is the only mass that is accelerating within that short period of time.

(II) When the compartment loading is less than the barrier loading, the intermediate mass (e.g., engine) is decelerating. Fig. 7.51(b) shows that the engine starts decelerating at 15 ms and continues to about 45 ms. It bottoms out at 40 ms and reaches its maximum deceleration. Within this period, the compartment loading is less than the barrier loading, as shown in Fig. 7.51(c).

Since the inertia and location of the engine have a direct bearing on the magnitude and crash pulse shape at the vehicle compartment, the design of the front end structure should consider the design guidelines for the low speed, compatibility, and high speed test conditions as shown in Fig. 7.52.

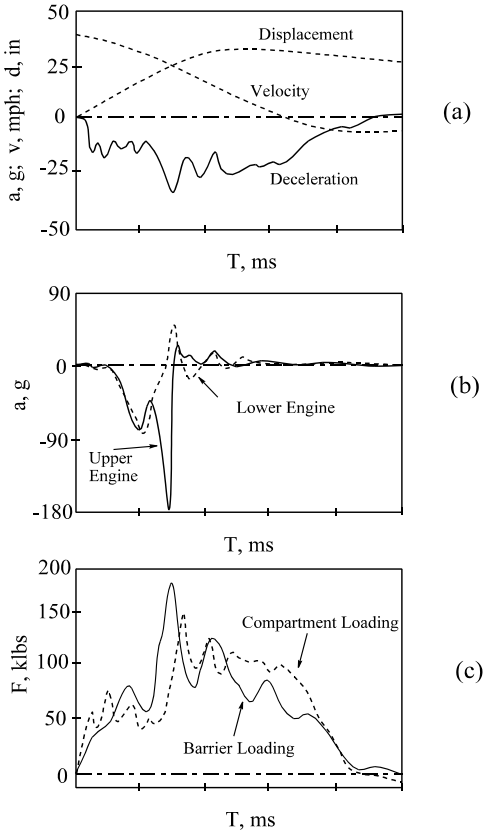

Fig. 7.51 Kinematics of Frame Vehicle, Engine and Loadings in a 35mph Test

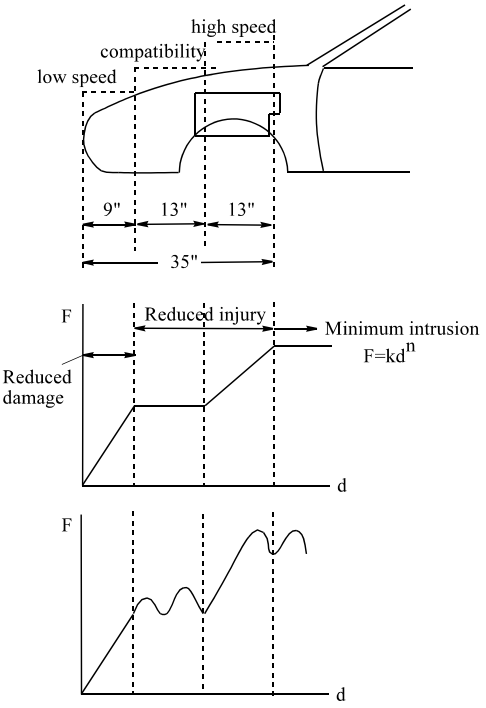

Fig. 7.52 Front End Design Considerations

7.10 MODELING THE VEHICLE-TO-VEHICLE COMPATIBILITY TEST

In a vehicle-to-vehicle compatibility test, the mass and stiffness are the vehicle parameters that need to be considered in addition to the vehicle geometry such as bumper height. In a typical compatibility test, a full-size truck is used to impact on a mid-size car which is the baseline setup. It has been known that the stiffnesses of a truck and car can be manipulated to give better protection to the occupant in the car which is lighter in weight than the truck.

However, the compatibility study should be looked at from the point of view of the vehicle and occupant dynamic responses as a whole. In the following two sections, compatibility modeling based on the change in structural stiffness of truck and/or car will be exercised.

7.10.1 Models with Same Effective Stiffness

There are three fundamental parameters to be addressed. They are "MSG": mass, stiffness, and geometry of both vehicles involved in the collision. Since small vehicles do not have as much available crash space as large vehicles, it is imperative to make small vehicles stiffer.

Shown in Fig. 7.53 are two vehicle-occupant models, top and bottom. Each model represents a vehicle-to-vehicle collision. Let v3 be a truck and v4 a car compartment with 4 and 2 klb (kilo-pounds), respectively. o3 and o4 represent the torso weights (.1 klb), and r3 and r4 represent the stiffness (.25 klb/in) of the restraint with zero slack for the truck and car, respectively. Interface mass i represents the bumper mass of .005 klb; this is rigidly attached to the truck only. The initial speed of the truck impacting on the stationary car is 70 mph.

The bottom model has the same effective structural stiffness as the top one. Given s3 and s4 in the top model, and assume s2 in the bottom model is twice as much as s4, then s1 can be computed which would yield the same effective structure stiffness of 1.86 klb/in. The computation of s1 is shown in Eq. (7.68).

The simulation and animation is executed with the CRUSH II package. In setting up the model, EAs s3 and s1 are the ones capable of having tension and compression. The rest of the EAs are good only for compression (for modeling purposes, only compression is used, not tension). The stiffness values shown in Fig. 7.53 are for loading only. The unloading stiffness of the structure is set equal to 44.4 times the loading stiffness. Similarly, the unloading stiffness of the restraint is set equal to 4 times the loading stiffness. The parametric relationship between the loading and unloading stiffness related by the coefficient of restitution or percentage of permanent deformation is described in Section 5.6 of Chapter 5 on Loading and Unloading Simulation.

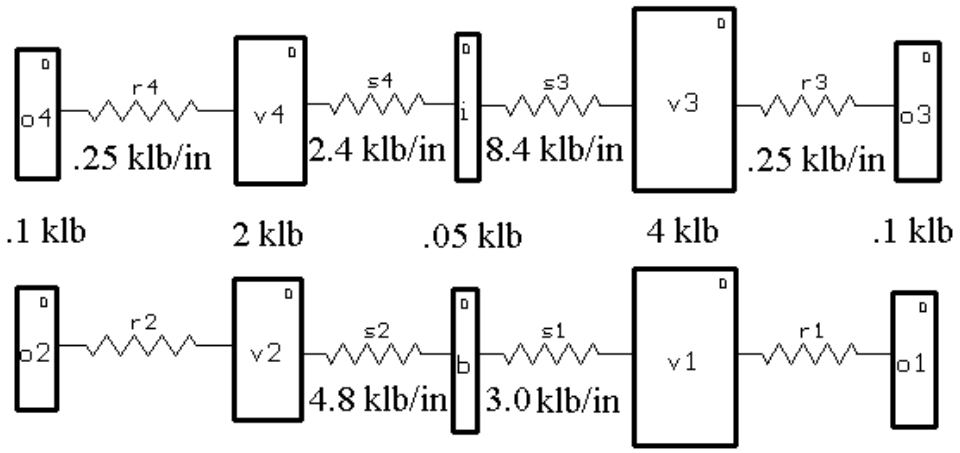

Fig. 7.53 Models I (top) and II (bottom) with Same Effective Structure Stiffness

$$
\begin{aligned}
&\textit{Given:}\quad s_3 = 8.4\ \textit{klb/in}, \quad \textit{and}\ s_4 = 2.4\ \textit{klb/in} \\
&\therefore\ \textit{effective stiffness:}\quad s_e = \frac{s_3 s_4}{s_3 + s_4} = 1.86\ \textit{klb/in} \\
&\textit{Since Model II has the same effective stiffness, then} \\
&s_e = \frac{s_1 s_2}{s_1 + s_2} = 1.86\ \textit{klb/in}, \quad \textit{let}\ \ s_2 = 2\ \ \textit{and}\ \ s4 = 4.8\ \textit{klb/in} \\
&\textit{then}\quad s_1 = \left(\frac{s_2}{s_2 - s_e}\right) s_e = 3.0\ \textit{klb/in}
\end{aligned}
\tag{7.68}
$$

The model responses due to changes in the structural stiffness of the two vehicles but having the same effective stiffness are analyzed using the models shown in Fig. 7.53. The numbers below the spring element (EA) represent the maximum crush energy absorbed, kips-ft, by that EA.

Define: d4: deformation of spring s4, e4: max. crush energy absorbed by spring s4,
d3: deformation of spring s3 e3: max. crush energy absorbed by spring s3,
d2: deformation of spring s2 e2: max. crush energy absorbed by spring s2,
d1: deformation of spring s1 e1: max. crush energy absorbed by spring s1.

Then:

$$
\begin{aligned}
&\because\ F\,(force) = (s4)(d4) = (s3)(d3),\\
&\therefore\ \frac{e4}{e3} = \frac{s4\,(d4)^2/2}{s3\,(d3)^2/2} = \frac{d4}{d3} = \frac{s3}{s4}\\
&To\ check:\ \frac{e4}{e3} = \frac{172}{49.3} = \frac{s3}{s4} = \frac{8.4}{2.4} = 3.5\\
&\quad and\ \ e4 + e3 = 221.3\ \ (total\ crush\ energy)\\
&Similarly:\ \frac{e2}{e1} = \frac{85.6}{136} = \frac{s1}{s2} = \frac{3.0}{4.8} = .63\\
&\quad and\ \ e2 + e1 = 221.6\ \ (total\ crush\ energy)
\end{aligned}
\tag{7.69}
$$

The energy capable of being absorbed by the effective spring in each of the two models (due to s4 and s3 in top model, and s2 and s1 in bottom model of Fig. 7.53) is the same. The amount of crush energy absorbed can be computed using the energy equation for the effective mass system (See Section 4.4.4 on the dynamic equivalency) as shown in Eq. (7.70).

$$
\begin{aligned}
&In\ natural\ units:\ \ \Delta E = \frac{1}{2} m_e v_{close}^2\\
&Define\ \ \Delta E:\ \ total\ crush\ energy,\ klb\text{-}ft\\
&\qquad w_e:\ \ effective\ weight,\ klb\ (kilo\text{-}pound)\\
&\qquad v_{close}:\ \ closing\ speed,\ mph,\ \ then\\
&\qquad \Delta E = .0334\, w_e v_{close}^2\\
&where\ \ w_e = \frac{w_1 w_2}{w_1 + w_2} = \frac{2\times 4}{2+4} = 1.333\,klb\\
&v_{close} = 70\ mph,\ \ and\ \ \ \Delta E = 218\,klb\text{-}ft\\
&In\ metric\ units:\\
&1\,J(Joule) = 8.85\ lb\text{-}in,\ \ 1\ KJ = 8.85\ klb\text{-}in = .738\ klb\text{-}ft\\
&therefore,\ \ total\ crush\ energy:\ \ \Delta E = 296\ KJ
\end{aligned}
\tag{7.70}
$$

Note that the minor difference in the numerical values of the energy between the computed and the simulation is due to the dynamic coupling effect of the occupants in the simulation model. The energy absorption in the model with same effective stiffness is simply redistributed between the two springs in the two models. It can be shown that the decelerations of the truck (24 g) and car (48 g) remain the same in both models under the same effective stiffness condition.

$$
\begin{aligned}
&In\ a\ two\text{-}mass\ system:\\
&A_1,\ A_2:\ \ acceleration\ magnitudes\ of\ car\ and\ truck.\\
&\qquad \frac{A_1}{A_2} = \frac{w_2}{w_1} \quad \ldots\ldots \quad (1)\\
&In\ one\ effective\ mass\ system:\ \ \ Define\\
&A_p:\ peak\ acceleration\ of\ the\ effective\ mass\ system.\\
&A_p = A_1 + A_2 = \omega_e v_{close} \quad \ldots\ldots \quad (2)
\end{aligned}
\tag{7.71}
$$

For each of the two models, the two vehicle masses and the effective stiffness remain the same. Therefore, (1) and (2) of Eq. (7.71) are the same for both models, and the solutions of A_1 and A_2 remain the same.

Using the crash severity index formula, it can also be shown that the magnitude of peak acceleration of the car in each of the two models remains the same. As far as the car is concerned, the energy absorption in Model I is twice as much as that in Model II; therefore, the corresponding ratio of BEV of the car in Model I to that in Model II is equal to squared root of two. However, the ratio of the structural natural frequency of the car in Model I to that in Model II is just the reverse of that

BEV ratio. Therefore, the vehicle peak acceleration, product of BEV and the natural frequency, is the same in both models where the effective stiffnesses are the same. Eqs. (7.72) and (7.73) show the numerical computations of the car accelerations in the two models.

For Car 1 in model I:

$$r_m = \frac{\text{car weight}}{\text{truck weight}} = \frac{2\ klb}{4\ klb} = .5 \quad \text{and} \quad r_k = \frac{2.4\ klb/in}{8.4\ klb/in} = .3$$

$$\frac{BEV_1}{V_{close}} = \frac{1}{\sqrt{(1+r_m)(1+r_k)}} = 0.72, \quad \therefore \quad BEV_1 = 0.72 \times 70 = 50.4\ mph \tag{7.72}$$

Let A_1: Car 1 peak acceleration in the fixed barrier test:

$$A_1 = BEV_1\,\omega_1 = BEV_1\sqrt{\frac{k_1 g}{w_1}} = (50.4\times 17.6)\sqrt{\frac{2.4\times 386.4}{2}}/386.4 = 49\ g$$

For Car 1 in model II:

$$r_m = \frac{\text{car weight}}{\text{truck weight}} = \frac{2\ klb}{4\ klb} = .5 \quad \text{and} \quad r_k = \frac{4.8\ klb/in}{3.0\ klb/in} = 1.6$$

$$\frac{BEV_1}{V_{close}} = \frac{1}{\sqrt{(1+r_m)(1+r_k)}} = 0.51 \quad \therefore \quad BEV_1 = 0.51 \times 70 = 35.7\ mph \tag{7.73}$$

Let A_1: Car 1 peak acceleration in the fixed barrier test:

$$A_1 = BEV_1\,\omega_1 = BEV_1\sqrt{\frac{k_1 g}{w_1}} = (35.7\times 17.6)\sqrt{\frac{4.8\times 386.4}{2}}/386.4 = 49\ g$$

Since vehicle decelerations in both models remain unchanged, the torso decelerations in the car (64 g) and truck (33 g) also remain the same in both models as shown in Fig. 7.54. Note that the discrepancy in the torso deceleration in the truck in both models (32 g compared to 33 g) is due to numerical roundoff. The curve inside the rectangular box is the deceleration versus time of that particular mass. The numbers at the bottom of the box are the peak deceleration value in g and the corresponding timing in ms. The numbers below the spring element (EA) represent the maximum crush energy absorbed, kips-ft, by that EA and the corresponding timing in ms.

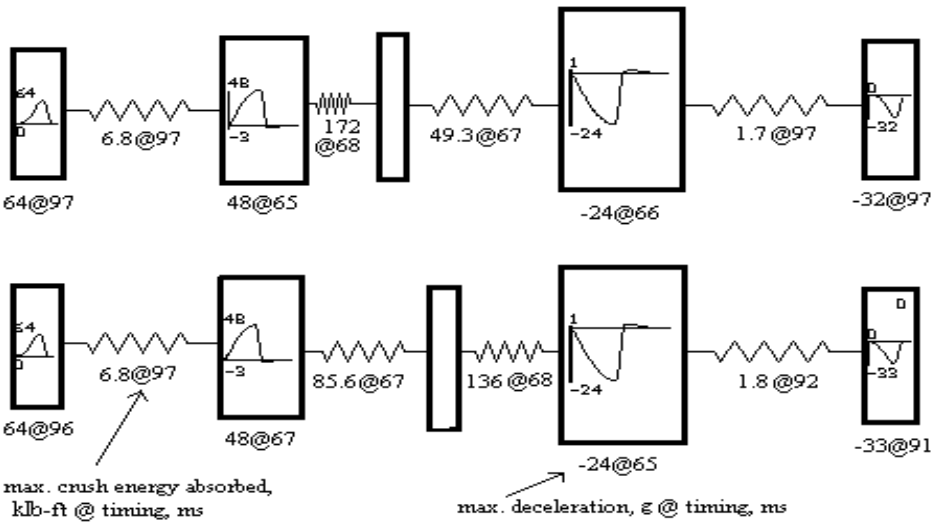

Fig. 7.54 Responses of Models I and II with Same Effective Structure Stiffness

7.10.2 Models with Different Effective Stiffness

In general, any change in the car and/or truck stiffness would change the car deceleration. Rearranging the A_1 formula in Eq. (7.73), it becomes as shown in Eq. (7.74).

$$\begin{aligned}
&\textit{For Car 1 in the car-truck model:}\\
&r_m = \frac{\textit{car weight}}{\textit{truck weight}} = \frac{w_1}{w_2}, \quad r_k = \frac{\textit{car stiffness}}{\textit{truck stiffness}} = \frac{k_1}{k_2}\\
&\textit{Let } A_1\textit{: Car 1 peak acceleration in the fixed barrier test:}\\
&A_1 = \left[BEV_1\right]\omega_1 = \left[\frac{V_{close}}{\sqrt{(1+r_m)(1+r_k)}}\right]\sqrt{\frac{k_1 g}{w_1}}
\end{aligned} \tag{7.74}$$

If only the truck stiffness, k_2, is decreased, then the car-to-truck stiffness ratio, r_k, is increased. The impact severity of the car in terms of $BEV|_1$ is lowered, so is the peak deceleration of Car 1, A_1. Therefore, softening the truck structure would decrease both the car and truck decelerations. However, due to the limited available crush space in the front end and the resulting larger deformation of the truck, decreasing the truck stiffness may result in excessive intrusion of the dash panel into the passenger compartment (cab).

An optimization problem can then be formulated such that the constraints on the intrusions on both car and truck, the available crush space, and an acceptable vehicle acceleration are taken into consideration.

Case Study:

A vehicle having mass M and stiffness K is tested in two cases. Case 1 (Fig. 7.55): The vehicle impacts on a fixed rigid barrier at a speed of V; and Case 2 (Fig. 7.56): The vehicle impacts on a movable rigid block of same weight with a negligible sliding resistance at a speed of 2V.

(I) Determine the energy absorption by the vehicle structure, deceleration level, dynamic crush, and the impact duration for both cases (a) and (b), and

(II) In which case is the vehicle subjected to a higher crash severity?

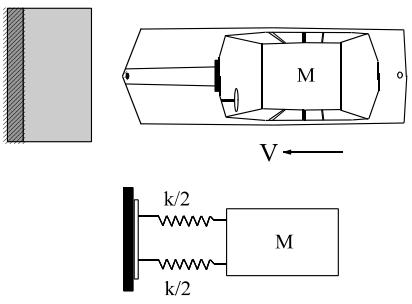

Fig. 7.55 Vehicle-Rigid Barrier Test

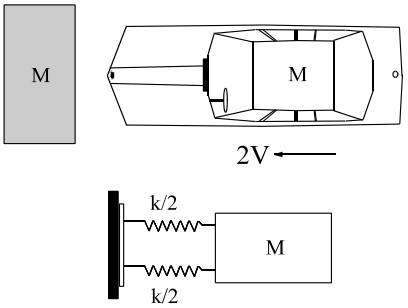

Fig. 7.56 Vehicle-Rigid Block Impact

Using the closed form formula for the spring-mass model for the vehicle-rigid barrier test, the major responses in terms of acceleration and crush can be computed as shown in Eq. (7.75). The subscript 1 used in the variables denotes case number 1, and subscript 2 for case number 2.

Case 1 (Fig. 7.55):

$$\textit{Energy absorbed by the structure}: \quad \Delta E_1 = \frac{1}{2}MV^2$$

$$\textit{Peak sinusoidal acceleration}: \quad A_1 = V\omega = V\sqrt{\frac{K}{M}}$$

$$\textit{Dynamic Crush}: \quad C_1 = \frac{V}{\omega} = V\sqrt{\frac{M}{K}} \tag{7.75}$$

$$\textit{Time of dynamic crush}: \quad T_{M_1} = \frac{T}{4} = \frac{1}{4f} = \frac{\pi}{\omega}$$

Similarly, the vehicle-rigid movable block impact shown in Fig. 7.56 can be analyzed by using the effective mass approach; the crush energy, deceleration, and crush of the vehicle can also be computed.

Case 2 (Fig. 7.56):

From the analysis on Case 2, (1) of Eq. (7.76) shows that the energy absorption by the Case 2 vehicle is twice as much as that by Case 1 vehicle. The peak sinusoidal acceleration and dynamic crush of Case 2 vehicle is 1.414 (square root of 2) times as much as those for Case1 vehicle. Lastly, the timings when those maximum responses occur are shorter for Case 2 vehicle which is 0.707 (inverse of square root of 2) times those for Case 1 as shown in (4) of Eq. (7.76).

Therefore, Case 2 vehicle in Fig. 7.56 is subjected to a higher crash severity than Case1 vehicle in Fig. 7.55.

$$\textit{effective mass}: \quad M_e = \frac{MM}{M+M} = \frac{M}{2}$$

Energy absorbed by the structure in Case2:

$$\Delta E_2 = \frac{1}{2}M_e(2V)^2 = MV^2 = 2\Delta E_1 \quad \ldots\ldots\ldots\ldots \quad (1)$$

Peak sinusoidal acceleration of the effective mass M_e:

$$A_e = (2V)\omega_e = (2V)\sqrt{\frac{K}{M_e}} = 2\sqrt{2}V\omega \tag{7.76}$$

Using mass reduction factor to compute the acceleration of mass M,

$$A_2 = \frac{M}{M+M}A_e = \sqrt{2}V\omega = \sqrt{2}A_1 \quad \ldots\ldots\ldots\ldots \quad (2)$$

$$\textit{Dynamic Crush}: \quad C_2 = \frac{2V}{\omega_e} = \frac{2V}{\sqrt{2}\omega} = \sqrt{2}C_1 \quad \ldots\ldots\ldots \quad (3)$$

$$\textit{Time of dynamic crush}: \quad T_{M_2} = \frac{\pi}{2\omega_e} = \frac{1}{\sqrt{2}}T_{M_1} \quad \ldots \quad (4)$$

7.11 ACCIDENT RECONSTRUCTION METHODOLOGY

CRASH3 [3A, 3B], a later version of CRASH2, is a computer program developed by CALSPAN Corporation under a contract with National Highway Traffic Safety Administration. Released in 1976, it is intended to interpret the physical evidence from a traffic accident. The program provides estimates of impact speeds and speed changes on the basis of analytical techniques covered in Section 7.5 on non-central collisions and is used to analyze vehicle crashes and determine speeds, energies, vehicle directions, etc. occurring in a crash. The term CRASH is an acronym for CALSPAN Reconstruction of Accident Speeds on Highways.

7.11.1 Background

Campbell [8] has developed a method for utilizing energy methods to evaluate crash phenomena. One major proposal by him for a vehicle-fixed barrier collision is a linear relationship between the speed of the vehicle just before impact and the residual crush distance shown in Eq. (7.77). The residual crush is the crush distance measured after the impact. It is also named static crush, the amount of crush after the elastic rebound from the dynamic crush.

$$v = b_0 + b_1 x \quad \ldots\ldots\ldots\ldots\ldots\ldots \quad (1) \tag{7.77}$$

where:

v : *Vehicle speed at impact. v must equal or exceed the Bumper Standard speed*

b_0, b_1 : *Constants (vehicle structure dependent)*

x (*or C*) : *Residual crush distance*

Shown in Fig. 7.57 are sample data points from barrier crashes at different speeds and the linear regression line. A typical regression line intercepts y-axis at b_o, a positive number.

The positive b_o is due to the fact that modern vehicles are designed to meet the bumper standard according to Part 581, Bumper Standard (49 CFR, Code of Federal Regulations). This standard establishes requirements for the impact resistance of vehicles in low speed front and rear collisions. In the U.S., the standard calls for a fixed barrier speed of 2.5 mph (5 mph according to Canadian standard) at which the exterior surfaces of a vehicle should have no "permanent deviations from their original contours 30 minutes after completion of barrier impact."

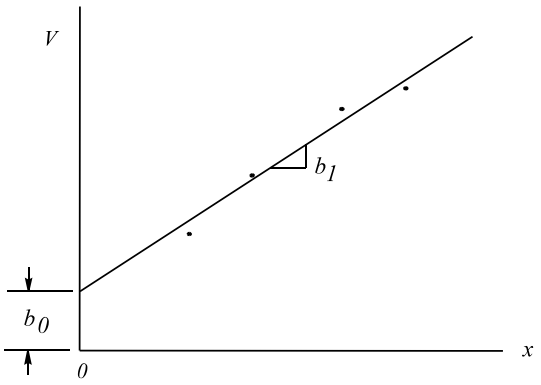

Fig. 7.57 Barrier Impact Speed vs. Residual Crush

Along with this equation, Campbell proposed a linear force versus deflection (residual crush) equation shown in Eq. (7.78) to relate to the velocity equation in terms of energy relationship.

$$\frac{F}{W} = A + Bx, \quad \text{where}$$

$$\begin{aligned} x &: \text{Residual crush} \\ F &: \text{Crush force at a given } x \\ A, B &: \text{stiffness coefficients, structure dependent} \\ W &: \text{Width of section of body being crushed} \end{aligned} \tag{7.78}$$

The force per unit width of damage section versus residual crush relationship is plotted in Fig. 7.58. Similar to the barrier impact velocity versus residual crush, every point on the straight line is a data point approximated by the regression to the sets of data.

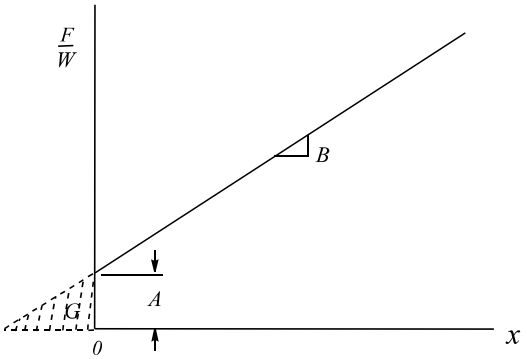

Fig. 7.58 Unit Crush Force versus Residual Crush

Assuming zero restitution, e = 0 (i.e., the final velocity of the impacting vehicle is equal to that of the barrier, essentially a speed of zero in this case), one can apply the conservation of momentum and conservation of energy theorems as follows:

$$\begin{aligned} &\text{Work done on vehicle} = \text{Integral of force function over} \\ &\text{distance traversed, Thus:} \quad \int F\,dx = \frac{M}{2}v^2 \end{aligned} \tag{7.79}$$

To this work must be added a constant term, GW, to account for work done on an energy-absorbing bumper, for which the crush distance is held at zero. Then, the work done (or crush energy) and the initial kinetic energy are:

$$\begin{aligned} &\text{Use } C \text{ as Residual Crush, then} \\ &\text{Crush energy} = W\left(G + AC + \frac{B}{2}C^2\right) \quad \ldots\ldots \quad (1) \\ &T = \frac{M}{2}v^2, \quad T = \frac{M}{2}(b_0 + b_1 C)^2 = \frac{M}{2}(b_0^2 + 2b_0 b_1 C + b_1^2 C^2) \\ &\text{Equating like terms gives:} \\ &A = \frac{Mb_0 b_1}{W} \qquad B = \frac{Mb_1^2}{W} \qquad G = \frac{Mb_0^2}{W} \quad \ldots \quad (2) \end{aligned} \tag{7.80}$$

By combining terms the coefficient G can be expressed in terms of A and B:

$$G = \frac{A^2}{2B} \tag{7.81}$$

The crush energy per unit width of vehicle shown in (1) of Eq. (7.80) is plotted and shown in Fig. 7.59. Note that the value of G when residual crush is zero depends solely on the square of b_0. Since b_0 is the intercept of the line on the v vs. x plot shown in Fig. 7.57, it affects the accuracy of the speed estimate. If b_0 is higher than what it should be, the actual speed of a subject vehicle involved in a low speed accident would be overestimated.

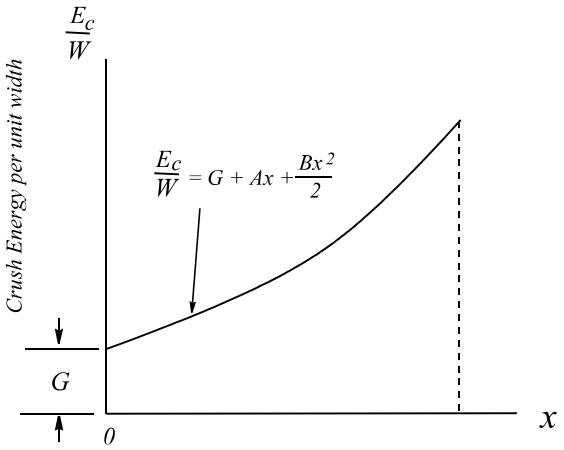

Fig. 7.59 Crush Energy vs. Residual Crush

Expressing the coefficients in terms of mph (miles per hour), in (inches), and lbs (pounds) and letting the mass, M, be represented by its weight in pounds (Mg = w) gives:

$[b_0] = mph \qquad [b_1] = mph/in$

$[Mg] = [w] = lb \qquad [W] = in$

$[A] = lb/in \qquad [B] = lb/in^2$

$[G] = lb$

In terms of these units for the coefficients, the equations for A, B, and G become:

$$A = 0.8\frac{wb_0b_1}{W},$$

$$B = 0.8\frac{wb_1^2}{W} \quad \ldots\ldots\ldots \quad (1) \qquad (7.82)$$

$$G = 0.4\frac{wb_0^2}{W}$$

Rearranging the expressions above to solve for b_0, and b_1:

$$b_0 = 1.12A\sqrt{\frac{W}{Bw}} \quad \ldots\ldots \quad (2)$$

$$b_1 = 1.12\sqrt{\frac{BW}{w}} \quad \ldots\ldots \quad (3)$$

7.11.2 Vehicle Size and Stiffness Coefficient Categories

The data for the vehicle size and stiffness coefficients used in the original CRASH3 accident reconstruction program were based on the vehicle model years from the 1970's. Laboratory collision test data for later model vehicles is being obtained by NHTSA and will be added. Tables 7.13 and 7.14 show the vehicle size and stiffness categories from the original data base.

Table 7.13 Vehicle Size Categories

Size Category	1	2	3	4	5	6	7
	Mini-Car	Sub-compact	Compact	Inter-mediate	Full-Size	Luxury	Vans
W_b (in)	80.9-94.8	94.8-101.6	101.6-110.4	110.4-117.5	117.5-123.2	123.2-150	109-130
T (in)	51.1	54.6	58.9	61.8	63.7	63.7	67.6
L (in)	159.8	174.9	196.2	212.8	223.7	229.4	183.6
W (in)	60.8	67.2	72.6	77	79.8	79.8	79
a (in)	45.1	46.3	51.3	54.7	58.1	60.1	48.5
b (in)	48.1	50.1	55.5	59.2	63	65.1	68.5
x_f (in)	76	83.3	89.8	98.8	101.8	104.2	75.6
x_r (in)	-83.8	-91.6	-106.4	-114	-121.9	-125.2	-107
y_s (in)	30.4	33.6	36.3	38.5	39.9	39.9	39.5
RSQ (in)	2006	2951	3324	3741	4040	4229	3713

Definitions:
W_b = wheel base, in, T = track, in,
L = length, in, W = width, in,
a = distance from c.g. to front axle,
b = distance from c.g. to rear axle,
x_f = distance from c.g. to front of vehicle,
x_r = distance from c.g. to rear of vehicle,
y_s = distance from c.g. to side of vehicle,
RSQ = radius of gyration in yaw squared.

Table 7.14 Vehicle Stiffness Categories

Stiffness Category		1	2	3	4	5	6	7	8
		Mini-Car	Sub-compact	Com pact	Inter-mediate	Full-Size	Luxury	Vans	Pick-up
(F) Front	A	302	259	317	356	325	325	383	480
	B	47	43	56	34	37	37	126	50
	G	967	778	901	1874	1429	1429	580	2315
(B) Rear	A	366	391	410	357	297	297	300	346
	B	38	41	44	13	70	70	55	25
	G	1755	1874	1931	4986	628	628	818	2373
(R,L) Side	A	77	140	173	143	177	177	See Note 1	See Note 1
	B	37	67	57	50	47	47		
	G	81	148	263	203	331	331		

Note 1: For side damage, pick a size category (1 to 6) by wheelbase.

7.11.2.1 *Computing Stiffness Coefficients, Intercept and Slope*

Case Study 1: A set of crash test data using eight F-150 trucks conducted at frontal barrier impact speeds of 8, 14, 31, and 35 mph (see data points in Fig. 7.60) is used as a data base. The regression line has been computed and is $V = b_0 + b_1 x = 5.07 + x$ as shown in Fig. 7.60. Compute the stiffness coefficients of F-150 in the frontal impact. [Answer is shown in Table 7.15]

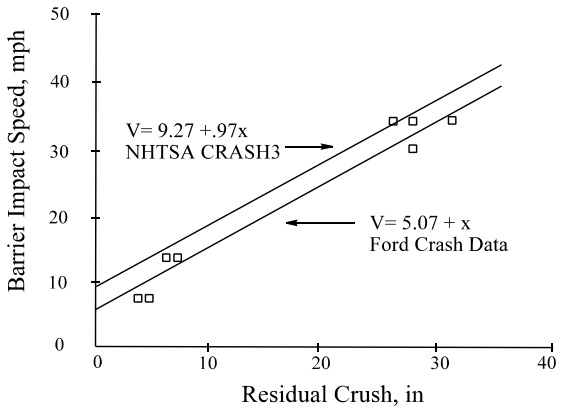

Fig. 7.60 Truck-Barrier Speed vs. Residual Crush (Test Data)

Case Study 2: Given the stiffness coefficients of A (lb/in) = 480 and B (lb/in^2) = 50 of a generic truck from a CRASH3 data base (see Table 7.14, Vehicle Stiffness Categories), the given parameters are w (test weight) = 5276 lb, and W (Width) = 79 inches.

Using the formula (2) of Eq. (7.82) for the intercept b_o and (3) for slope b_1, one gets

$$b_0 = 1.12A\sqrt{\frac{W}{Bw}} = 1.12\times 480\times\sqrt{\frac{79}{50\times 5276}} = 9.3\,mph$$
$$b_1 = 1.12\sqrt{\frac{BW}{w}} = 1.12\times\sqrt{\frac{50\times 79}{5276}} = .97\,mph/in \qquad (7.83)$$
$$therefore \quad V = 9.3 + .97X$$

Using the formulas shown in Eq. (7.82), A, B, and G are computed and shown in Fig. 7.61.

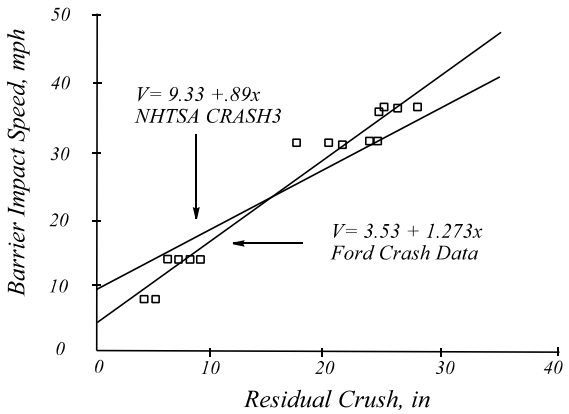

Fig. 7.61 Car-Barrier Speed vs. Residual Crush (Test Data).

7.11.3 Stiffness Coefficient Comparison Between Data Base and Crash Tests

According to the vehicle size and stiffness categories shown in Tables 7.14 and 7.15, the light truck (F-150) and car (Taurus) used in this analysis are categorized as Pick-Up (#8) and Intermediate (#4) vehicles, respectively. Table 7.15 compares the barrier speed vs. residual crush equations and stiffness coefficients between NHTSA and Ford vehicle data.

Table 7.15 Stiffness Coefficient Comparison Between Data Base and Test

Vehicle	Barrier Speed, mph as a Function of Residual Crush, in	Front	
		A (lb/in)	B (lb/in/in)
Light Truck (F-150)	NHTSA V = 9.27 + .97X FORD V = 5.07 + X	480 271	50 53
Car (Taurus)	NHTSA V = 9.33 + .89X FORD V = 3.53 + 1.27 X	356 193	34 70

There are eight barrier crash tests used in the Ford light truck analysis and nineteen tests in the Ford passenger car analysis with barrier impact speeds ranging from 8 to 35 mph. The data points showing the residual crush at a given barrier impact speed are shown in Figs. 7.60 and 7.61 for the light truck and car, respectively. These data points are fitted by a straight line using the least square technique.

The actual barrier impact speed corresponding to zero residual crush is determined by the energy absorption capability in the bumper design. However, by setting the residual crush to zero in the barrier impact speed equations, NHTSA formulae yield about 9 mph for both light truck and car, while Ford data yield about 5 and 4 mph for the light truck and car, respectively. Considering the 5 mph bumper design criterion used by Ford, the equations seem to be logical and reasonably accurate as far as speed at zero residual crush.

From Fig. 7.60 for light truck, it shows that NHTSA CRASH3 tends to over-estimate the barrier impact speed given a residual crush within the speed range of 8 to 35 mph. However, for the car used in this analysis as shown in Fig. 7.61, NHTSA CRASH3 tends to over-estimate the speed when the residual crush is less than 15 inches which is corresponding to 22 mph barrier impact speed. Beyond 15 inches, NHTSA CRASH3 tends to under-estimate the impact severity of the car.

In a study by Smith and Noga [3C] on the accuracy and sensitivity of CRASH3 program, the results of 53 independent staged collisions were used to compare with those from CRASH3. The sensitivity to error in the stiffness coefficients of the force-deflection relationship is examined. It was estimated that errors of 10 percent in the force-deflection (stiffness) coefficients resulted in errors of 2-5 percent in ΔV calculation.

7.11.4 Four-Way Plot of Stiffness Coefficients and Responses

A four-way plot is created to help easing the computation of response variables given the values of test parameters and stiffness coefficients. Fig. 7.62 shows four plots based on four equations. Equations (1) and (4) show the relationships between crush energy (CE), BEV, and ΔV of the target vehicle when it is subjected to an impact by a moving rigid barrier. Equations (2) and (3) relate the stiffness coefficients to the crush energy, residual crush (C), and BEV. The intercept and slope of the straight line on the BEV vs. C plot can be computed from Equation (3) when the stiffness coefficients are given. Similar to the characteristic length (dynamic crush/BEV), the intercept and slope on the BEV vs. C plot characterize the post-crush behavior of the vehicle structure.

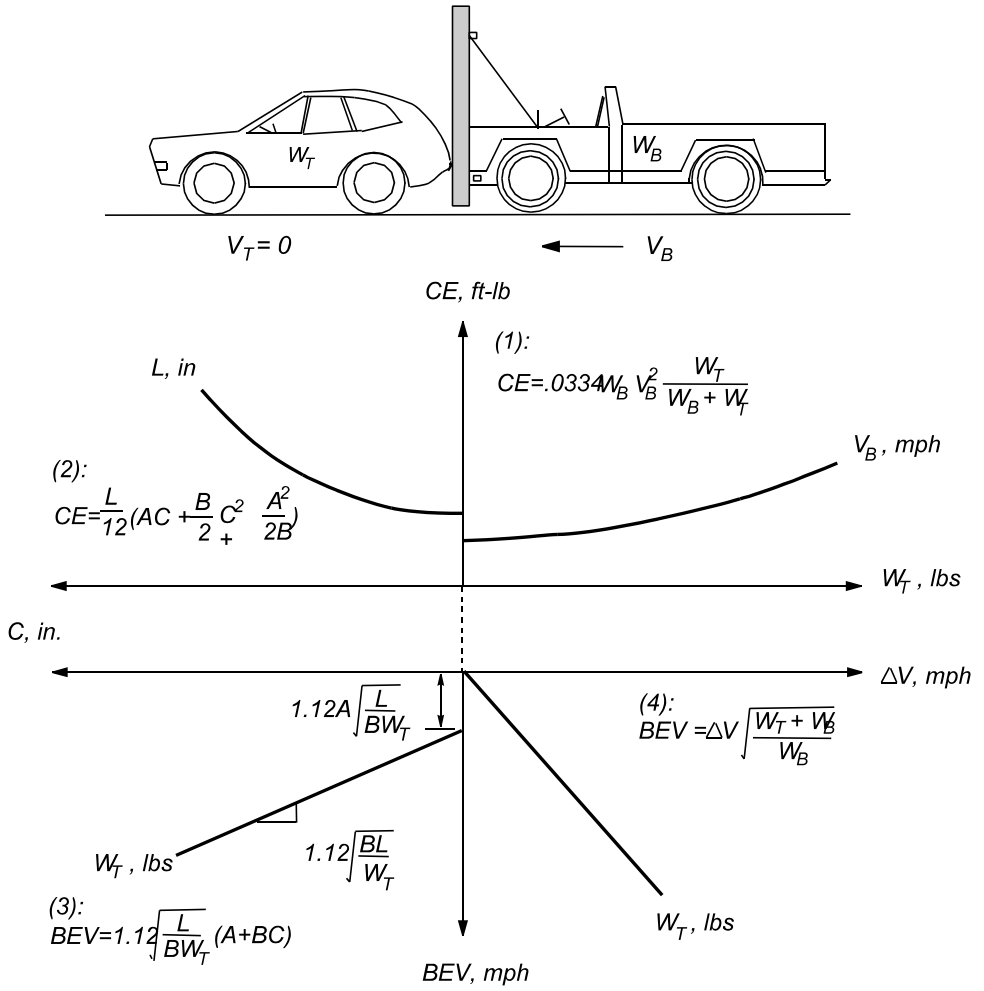

Fig. 7.62 A Four-Way Crash Severity Plot

The variables used in the four-way plot are defined as follows:

W_B = weight of bullet vehicle (moving rigid barrier), lbs
W_T = weight of target vehicle, lbs
V_B = impact speed of bullet vehicle, mph
CE = crush energy absorbed by target vehicle, ft-lb
L = frontal width of the target vehicle, in
A, B = stiffness coefficients of the target vehicle (lb/in, lb/in/in)
C = residual (static) crush, in
BEV = barrier equivalent velocity of the target vehicle, mph
ΔV = velocity change of the target vehicle, mph

7.11.5 Non-Linear Crush Profile and Force Deflection Data

In a real world accident, the damage profile is usually not uniform across the width of the vehicle and the force-deflection data of the structure are not elastic. To enhance the accident reconstruction methodology, crush energy for damage profile with various shapes has been formulated by Smith et al. [9], and the elasto-plastic force deflection characteristics can be utilized to model the vehicle structure.

7.11.5.1 *Non-Linear Crush Profile*

The formula for the crush energy shown in (1) of Eq. (7.80) can be generalized to account for the non-linear damage profiles. The coefficients α and β shown in Eq. (7.84) depend on the geometry of the damage profile. For the special case where the damage is uniform across the front end of the vehicle, α = β = 1.

$$E_C\ (Crush\ Energy) = \left[\alpha AC + \frac{\beta BC^2}{2} + \frac{A^2}{2B}\right] W \tag{7.84}$$

For the damage profiles induced by the rigid pole and the offset barrier, the corresponding coefficients α and β are shown in Fig. 7.63. For the offset damage profile, k has the value between 0 and 1; for the angular barrier impact, k = 1 (α = 1/2 and β = 1/3); for the perpendicular barrier impact (fixed rigid barrier impact, k = 0 (α = 1 and β = 1).

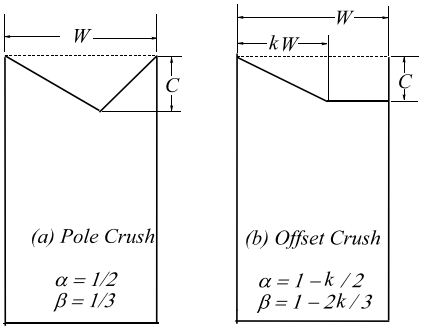

Fig. 7.63 Non-Linear Damage Profiles

7.11.5.2 *Elasto-Plastic Force Deflection*

Shown in Fig. 7.64 is a elasto-plastic force deflection which can model the vehicle structure more realistically than just the elastic force deflection. The crush energy for the elasto-plastic force deflection model can be obtained by the integration over the elastic range as shown in Eq. (7.85).

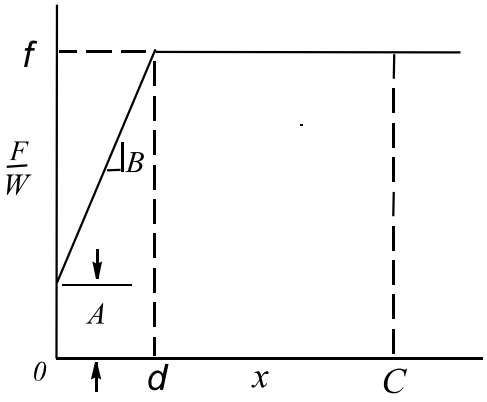

Fig. 7.64 Elasto-Plastic Force Deflection

$$\frac{CE}{W} = \int_0^C \frac{F}{W}dx = \int_0^d (A+Bx)dx + \int_d^C \frac{f}{W}dx \quad \ldots \ldots (1)$$

where f *(constant force)* $= A + Bd$

d : *deflection at the end of elastic range*

C : *residual crush* $(C > d)$ (7.85)

Integrating (1) *yields*

$$\frac{CE}{W} = (A+Bd)C + \left(\frac{A^2}{2B} - \frac{B}{2}d^2\right) \quad \ldots \ldots \ldots (2)$$

7.11.5 Estimate of the Impact Severity and Sensor Performance in a Van Impact

On an icy road, an Aerostar was involved in an offset collision with a full-size pickup of unknown make. The Aerostar rear-ended the pickup at a speed of approximately 25 mph. The Aerostar exhibited front end crush on the left-hand side only, as shown in Fig. 7.65.

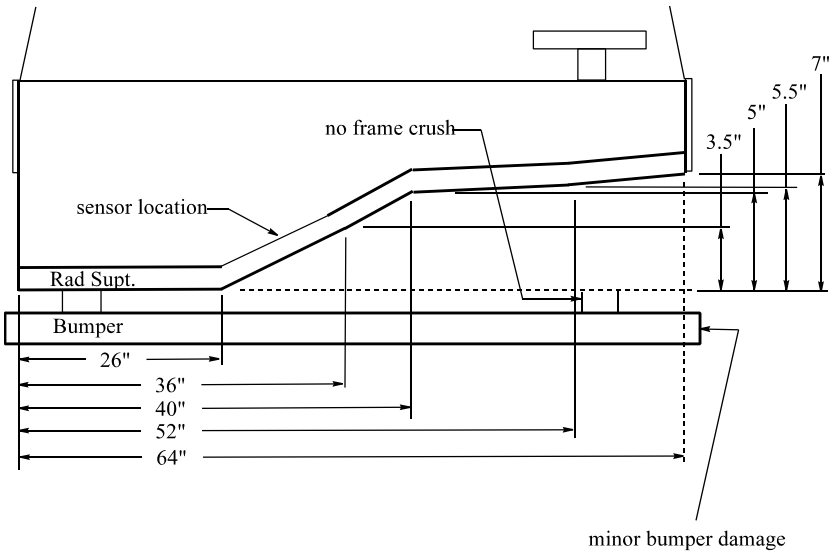

Fig. 7.65 Aerostar Front End Damage

The air bag in the Aerostar did not deploy. The upper-center radiator support (rad supt.) where the air bag sensor metal can is attached was moderately bent. The sensor metal can did not appear to be directly involved in the impact, since there were no surface imperfections on the can. The bending of one of the attachment arms appeared to be attributed to the twisting of the upper radiator support.

Case Studies: (1) estimate the impact severity of the vehicle in the crush zone and in the passenger compartment and (2) estimate the performance of the crash sensor and safing sensors.

7.11.5.1 *Estimate of the Vehicle Impact Severity*

Case Study 1 (Exercise): Use CRASH3 methodology for accident reconstruction and estimate the crush energy, velocity changes in the crush zone and in the compartment, and BEV (barrier equivalent velocity) of the Aerostar in the collision. Assume the depth of the damage on the pickup was two inches across the damage width.

7.11.5.2 *Estimate of the Sensor Performance*

Based on the calibrations of the crash sensors and safing (confirmation) sensor, the threshold levels of the sensors can be constructed using the DBC (damage boundary curve) approach presented in Section 7.7.1.

The calibration of a ball-in-tube (BIT) sensor is expressed in terms of velocity change at the time of activation, ΔV. A typical range of calibration for a crash sensor is between 7 and 10 mph and that for the safing (confirmation) sensors in the occupant compartment zone (Safing 1) and crush zone (Safing 2) sensors is between 1.2 and 4.0 mph.

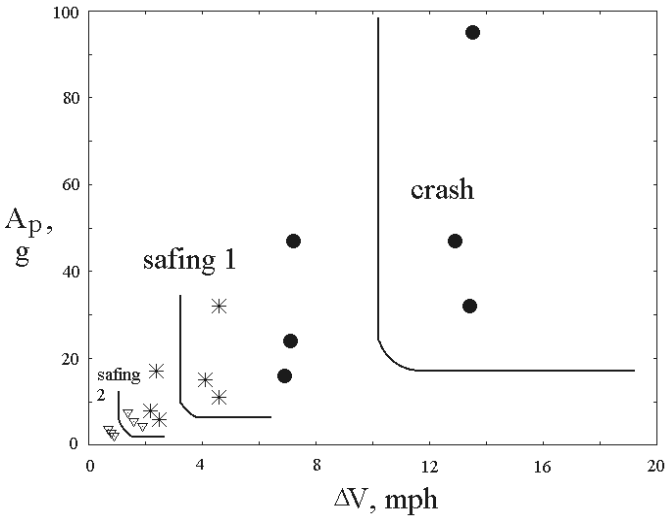

Fig. 7.66 Damage Boundary Curves of Ball-in-Tube Crash and Safing Sensors

The testing and calibration of the sensors are performed by a power thruster in the production plant. A simple power thruster can produce a harmonic pulse such as a haversine or a halfsine excitation. For the BIT sensor, six haversine pulses with various magnitudes and durations are required to test each type of sensor. For the crash sensor, the first three pulses marked with a circle symbol (○) shown in the upper right location of Fig. 7.66 are required to activate the sensor; while the last three pulses should not activate the sensor. Similarly, the six pulses for the safing 1 sensor are shown marked with a star symbol (∗) and those for the safing 2 sensor are shown marked with a triangle symbol (▽).

The test pulse specification is expressed by ΔV (total area or velocity change of the haversine pulse) and A_p (the magnitude of peak acceleration) and is shown as a data point in the figure. The first three of the six haversine pulses, having higher velocity changes than the other three, ensure that the sensor must activate; while the other three must not.

Using the damage boundary curve (DBC) approach described in Section 7.7.1, the two groups of data points of each sensor are separated by DBC, as shown in Fig. 7.66. Thus, the DBC is transformed into a threshold level for that specific sensor. The first three tests, which are located to the right and above the threshold level are in the must-activate zone, and the last three tests, located to the left and lower of the threshold level are in the must-not-activate zone.

Case Study 2 (Exercise):

Using the computed velocity changes from Case Study 1 and the threshold levels of the sensors shown by the DBC's in Fig. 7.66, evaluate the sensor performance and estimate the likelihood of the sensor activation that would result in an air bag deployment.

7.12 REFERENCES:

1. Weaver, J.R., "A Simple Occupant Dynamics Model," J. Biomechanics, Vol. 1, Pergamon Press, 1968, pp. 185–191.
2. MacMillan, R.H., "Dynamics of Vehicle Collisions," Inderscience Enterprises Ltd., U.K., 1983.
3. A. McHenry, R.R. and Lynch, J.P., "CRASH2 User's Manual", Interim Report for NHTSA under Contract No. DOT-HS-5-01124, September, 1976,
   B. "CRASH3 User's Guide and Technical Manual," NHTSA Report, DOT-HS-805-732, February, 1981,
   C. Smith, R.A. and Noga, T., "Accuracy and Sensitivity of CRASH, " National Center for Statistics and Analysis Research and Development, DOT-HS-806-152, March, 1982.
4. Henson, S.E., "A Relationship Between Barrier Collisions and Car-To-Car Collisions," Technical Report, Automotive Safety Affairs Office, Ford Motor Company, November 20, 1970.
5. Carpenter, N.J. and Welcher, J.B., "Stiffness and Crush Energy Analysis for Vehicle Collision and its Relationship to Barrier Equivalent Velocity (BEV)," SAE Paper No. 2001-01-0500, SAE 2001 World Congress, Detroit, Michigan, March 5–8, 2001.
6. Brandenburg, R.K. and Lee, J.L., "Fundamentals of Packaging Dynamics," 4th Edition, 1991, L.A.B.
7. Huang, M. and Chen, R., "Use of an Advanced CRUSH Model in Estimating Vehicle Impact Loading and Energy Absorption," AMD-Vol. 210/BED-Vol. 30, Crashworthiness and Occupant Protection in Transportation Systems, ASME International Mechanical Engineering Congress and Exposition, San Francisco, California, November 12–17, 1995, pp.273–285.
8. Campbell, K., "Energy Basis for Collision Severity,"SAE paper 740565 Presented at the 3rd International SAE Conference on Occupant Protection, July, 1974.
9. Smith, G.C., James, M.B., Perl, T.R., and Struble, D.E., "Frontal Crush Energy and Impulse Analysis of Narrow Object Impacts," 87-WA/SAF-5, ASME Winter Annual Meeting, Boston, Massachusetts, December 13–18, 1987.